

Structural and Mechanistic Studies on PHD2 and the Discovery of Potential Inhibitors

William Douglas Figg, Jr.

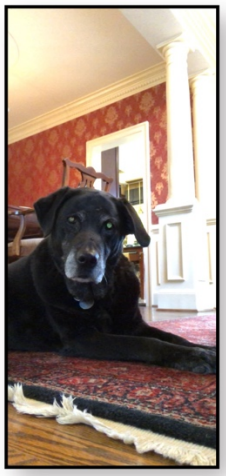
St. Hugh's College, University of Oxford

Michaelmas Term 2021

A thesis submitted to the Board of the faculty of Chemistry at the University of Oxford in partial fulfilment of the requirements for the degree of *Doctor of Philosophy*.



Mr. Clarence Levi Rice, Jr.
8/5/1943 - 13/12/2020



Aspen Figg
28/9/2006 - 15/3/2021

In loving memory to,

Levi – my devoted Grandfather

and

Aspen – my faithful companion

"From this high place all things flow:
Land of divided streams, of water spilled
Eastward, westward without memento;
Land where the morning mist is curled
Like smoke about the ridgepole of the world.
This mist is furled.

The sunset hawk now rides
The tall light up the climbing deep of air.
Beneath him swings the rooftree that divides
The east and west. His gold eyes scan
The crumpled shade on gorge and crest,
And streams that creep and disappear, appear,
Past fingered ridges and their shrivelling span.
Under the broken eaves men take their rest.

Forever, should they stir, their thought would keep
This place. Not love, happiness past, constrains,
But certitude. Enough, and it remains;
Though they who thread the flood and neap
Of earth itself have felt the earth creep,
In pastures hung against and the sweat of stone,
Knowing thereby no constant moon
Sustains the hill's lost granite surge."

1932

– Robert Penn Warren, 'Watershed'

Abstract

Human prolyl hydroxylases isoforms 1-3 (*Hs*PHD1-3) are hypoxia sensing 2-oxoglutarate (2OG)-dependent oxygenases that catalyse post-translational modifications of hypoxia-inducible factor (HIFα). The PHDs catalyse the *trans*-4-prolyl hydroxylation of the oxygen degradation domains (ODDs) in HIFα isoforms, which promotes their subsequent degradation *via* the von-Hippel Lindau-E3-Ligase-26s proteasomal pathway, *i.e.*, PHD catalysis suppresses expression of HIFα target genes. Molecular analyses, including a crystal structure of PHD2 in complex with a HIF1α fragment peptide, have revealed the PHDs form a discrete 2OG oxygenase subfamily with unusual kinetic properties, though the precise structural basis of the latter have been unclear. PHD inhibition is a therapeutic option for treatment of anaemia/ischaemia-related diseases. In-depth biophysical characterisation of the PHDs could provide insights into their 'O_2-sensing' ability which may aid the development of therapeutics that differ than the current late-stage/approved 2OG-mimicking PHD inhibitors in use. The work described in this thesis aimed to reveal insights into the mechanism of the PHDs and aid in the development of improved inhibitors through the structural analyses on PHD2.

Significant efforts were made to obtain conditions suitable for producing PHD2-substrate complexes in anaerobic conditions that may enable future O_2-initiated time-resolved mechanistic studies. Such studies may reflect key catalytic intermediates and active site interactions that are involved in the reaction of the PHDs and may provide useful data for novel inhibitor discovery. After initiating the reaction with O_2 with timepoints exceeding 17 minutes to 5-days, the crystals were cryo-cooled in liquid-N_2 to quench catalysis and allow for structural characterisation with X-ray crystallographic methods. Four previously unreported PHD2 crystal forms were obtained with a truncated form of $PHD2_{181-407}$ and a total of 41 structures were refined with resolutions ranging from 1.17 Å to 3.10 Å. Of the new crystal forms, those for the anaerobic $PHD2_{181-407}$.Fe(II).2OG.$HIF2\alpha_{523-542}$-CODD complex (obtained with an acetate-based precipitant) and the $PHD2_{181-407}$.Mn(II).succinate complex (Mn(II) is substituted for Fe(II) and is catalytically inert) are notable as they are suitable for mechanistic and co-crystallisation/soaking-based studies, respectively. The acetate-based crystallisation condition provides a robust-high-resolution (achieved 1.07 Å resolution) anaerobic system suitable for time-resolved work, as evidenced by the demonstration of *in crystallo* catalysis (without apparent crystal degradation) to give the first structure of a $PHD2_{181-407}$.Fe.product complex (timepoint was 5-days O_2-exposure in a 200 μm x 30 μm x 15 μm crystal). The acetate-derived crystallisation condition, from this work, has enabled further mechanistic-based crystallographic studies that are in progress, *e.g.*, including high pressure O_2 experiments. The $PHD2_{181-407}$.Mn(II).succinate conditions yielded the first structure of $PHD2_{181-407}$ with Molidustat, a clinically applied inhibitor. The $PHD2_{181-407}$.Mn(II).succinate crystal form was optimised for high-throughput soaking of small-molecule fragments and monodentate Fe-binding compounds to explore potential allosteric and orthosteric sites within PHD2 in a structure-guided approach to drug discovery. The combined studies provide insights into PHD catalysis and a foundation for the development of novel PHD inhibitors.

Table of Contents

Abstract **IV**

Table of Contents **V**

Acknowledgments **X**

List of Contributors **XIII**

Abbreviations **XIV**

List of Figures **XIX**

List of Tables **XXIII**

Chapter 1 – Introduction **1**

1.1 An Introduction to the 2-Oxoglutarate-Dependent Oxygenases **2**

1.2 Structural Overview of 2OG Oxygenases **4**
1.2.1 Comparison of DSBH Fold of PHD2 with Homologues and Other 2OG Oxygenases 6

1.3 The Hypoxic Response Pathway **8**
1.3.1 Hypoxia-Inducible Factor 11
1.3.2 VCB-E3 Ligase-Proteasome Degradation Pathway 13
1.3.3 CREBs Binding-p300 Proteins 14
1.3.4 Factor-Inhibiting Hypoxia-Inducible Factor 16
1.3.5 Prolyl Hydroxylases 19

1.4 Medicinal Chemistry Approaches for PHD Inhibition **23**
1.4.1 Carboxylic Acid-Based PHD Inhibitors 25
1.4.2 Non-Carboxylic Acid-Based PHD Inhibitors 27
1.4.3 Non-Conventional PHD Inhibitors 29
1.4.4 Clinically Used PHD Inhibitors 30

1.5 Research Objectives of the Work Described in this Thesis **36**

1.6 References **37**

Chapter 2 – Mechanistics Studies of PHD2 **50**

2.1 Background on PHD2 Mechanistic Studies **51**
2.1.1 Proposed Catalytic Mechanism for the PHDs 55
2.1.2 3C Cyclic Peptide and Time-Resolved Crystallography 58

2.2 The Formate-Derived Crystallisation Condition with the 3C Cyclic Peptide **60**

2.2.1 Optimisation of the Formate-Derived PHD2$_{181-407}$.HIF2α$_{523-543}$-CODD Crystals 66
2.2.2 Comparisons Between tPHD2.NOG/2OG and HIF1α$_{556-575}$/HIF2α$_{523-542}$ Substrate Complexes 70
2.2.3 Structure of a Formate-Derived Anaerobic-PHD2$_{181-407}$.Fe(II).2OG.HIF2α$_{523-542}$-CODD Complex 73
2.2.4 Use of the 3C Cyclic Peptide and Reproducibility 80

2.3 A Novel Zn(II)-Based Crystallisation Condition for the PHD2$_{181-407}$.Mn(II).2OG.HIF2α$_{523-542}$-CODD Complex 81

2.4 A Novel PHD2$_{181-407}$.Mn(II).2OG.HIF2α$_{523-542}$-CODD Crystallisation Condition Without the Cyclic Peptide 87
2.4.1 The Anaerobic Optimisation of the Acetate-Derived Condition 91

2.5 Summary and Future Directions 106

2.6 References 111

Chapter 3 – Structural Analyses on PHD2 Inhibition *via* Co-Crystallisation 117

3.1 Background 118

3.2 A Novel PHD2$_{181-407/426}$ *P* 2$_1$ Crystal Form 124
3.2.1 Development of a Crystallisation System to Soak Inhibitors 124
3.2.2 PHD2$_{181-407}$.Mn(II).Succinate *P* 2$_1$ Crystal Form 129
3.2.3 Structural analysis of PHD2$_{181-407}$ in Complex with Fumarate 140
3.2.4 Co-Crystallisation of PHD2$_{181-407}$ with Molidustat, IOX4, and Takeda-17 using the Succinate *P* 2$_1$ Crystal System 146

3.3 A Novel PHD2$_{181-407}$ *P* 6$_1$ 2 2 Crystal Form in Complex with Pre-Clinical Candidate ZXJ-1 154

3.4 The Substrate Binding Induced-Fit-Mechanism by tPHD2 160

3.5 Summary and Future Directions 166

3.6 References 172

Chapter 4 – Structural Analyses on PHD2 Inhibition *via* Co-Crystallisation 177

4.1 Background 178
4.1.1 Technical Overview of XChem Fragment-Based Screening 178
4.1.2 Biological Background 182

4.2 XChem Fragment-Based Screen of PHD2 185

4.2.1 XChem Binding Site 1 193
4.2.2 XChem Binding Site 2 195
4.2.3 XChem Binding Site 3 197
4.2.4 XChem Binding Site 4 199
4.2.5 XChem Binding Site 5 200
4.2.6 XChem Summary 201

4.3 $PHD2_{181-407}$ in Complex with Derivatives of Takeda-17 202
4.3.1 Active Site Chemistry with Monodentate Derivatives 205

4.4 Summary and Future Directions 210

4.5 References 212

Chapter 5 – Summary 218

5.1 Chapter 2 – Summary 219

5.2 Chapter 3 – Summary 223

5.3 Chapter 3 – Summary 228
5.3.1 Soaked-Based Studies with XChem Fragment Screening 228
5.3.2 Soaking-Based Studies with Monodentate Binding Derivatives 230

5.4 Summary and Future Outlook 231

5.5 References 233

Chapter 6 – Methods 238

6.1 General Methods and Reagents 239

6.2 Molecular Biology 241
6.2.1 SDS-PAGE 241
6.2.2 Plasmid Deoxyribonucleic Acid (DNA) Mini-Prep 242
6.2.3 Sequencing 242
6.2.4 DNA Concentration – NanoDrop™ 243

6.3 Microbiology Techniques 243
6.3.1 Luria-Bertani (LB) and 2xYeast and Tryptone (2YT) Media 243
6.3.2 LB Agar Media 243
6.3.3 Antibiotic Preparation 244
6.3.4 Transformations 244
6.3.5 Small-Scale Bacterial Culture 245
6.3.6 Optical Density (OD) Calculation-UV/Vis Spectrophotometry 245
6.3.7 Large-Scale Bacterial Culture and Induction 245

6.3.8 Cell Harvesting and Storage 246
6.3.9 Glycerol Stocks 246

6.4 Protein Purification 246
6.4.1 Pre-Purification Cell Treatment 246
6.4.2 Ni(II)-Affinity Chromatography 247
6.4.3 Gel-Filtration (Size-Exclusion Chromatography) 248
6.4.4 Ion-Exchange (IX) Chromatography 248
6.4.5 Protein Concentration 249
6.4.6 Buffer Exchange 249
6.4.7 Protein Purification Buffers 249
6.4.8 NanoDrop™ Protein Concentration Analysis 250
6.4.9 His_6-Tag Cleavage 251
6.4.10 EDTA-Treatment for Apo-Enzyme 251

6.5 tPHD2 Turnover Assays 251
6.5.1 Cofactor Preparation 251
6.5.2 Hydroxylation Reaction 252
6.5.3 Mass Spectrometry (MS) 253
6.5.4 RapidFire® - Solid Phase Extraction (SPE)-Coupled MS 253

6.6 X-ray Crystallography 254
6.6.1 Protein Sample and Reagents Preparation 254
6.6.2 Broad Screen 254
6.6.3 Optimisation Blocks 255
6.6.4 Crystallisation Robot 255
6.6.5 Additive and Detergent Screens 256
6.6.6 Crystal Manipulation 256
6.6.7 Data Collection 258
6.6.8 Data Processing 259
6.6.9 PHENIX Software Suite (version 1.19.1) 261
6.6.10 Protein Data Bank (PDB) Extract Tool 263
6.6.11 PDB Validation Service 263
6.6.12 PDB Onedep Server 264

6.7 Chapter 2 Methods 264
6.7.1 Formate Condition Protein-Substrate Preparation 264
6.7.2 $PHD2_{181-407}$.HIF2α-CODD Complex Structure 265
6.7.3 Anaerobic Formate Condition Crystal 265
6.7.4 O_2-Exposure Formate condition Crystals 266
6.7.5 Zn Condition Crystals 266
6.7.6 Acetate Condition Anaerobic Crystals 267
6.7.7 O_2-Exposure Acetate condition Crystals 268

6.8 Chapter 3 Methods 269
6.8.1 $PHD2_{181-426}$.Mn(II) Complex Structure 269
6.8.2 $PHD2_{181-407}$.Mn(II).Succinate Complex Structure 270
6.8.3 $PHD2_{181-407}$.Mn(II).Fumarate Complex Structure 270
6.8.4 $PHD2_{181-407}$.Mn(II).Molidustat Complex Structure 271
6.8.5 $PHD2_{181-407}$.Mn(II).IOX4 Complex Structure 271

6.8.6 PHD2$_{181-407}$.Mn(II).Takeda-17 Complex in the *P* 2$_1$ Crystal Form 272
6.8.7 PHD2$_{181-407}$.Mn(II).ZXJ1 Complex Structure
Ammonium Sulfate Condition 272

6.9 Chapter 4 Methods 273
6.9.1 Seeding Protocol 273
6.9.2 Solvent Characterisation 273
6.9.3 TexRank and Echo® Dispensing 275
6.9.4 SoakDB 274
6.9.5 Crystal Shifter 275
6.9.6 Data Collection and Parameters 275
6.9.7 XCE and Downstream Processing (DIMPLE and PanDDA) 277
6.9.8 Crystal Soaking with Monodentate Binding Derivatives 277

6.10 References 278

Appendix I 284

Appendix II 287

Appendix III 294

Declaration of Authorship 304

Acknowledgements

First and foremost, I would like to express my sincere appreciation and gratitude to Prof. Christopher Schofield for his close mentorship and supervision over the past four years. Thank you for allowing me the opportunity to work on such an exciting project as the prolyl hydroxylases. As I came from a Genetics background, I particularly wish to thank him for his encouragement and trust as I learned skills outside my repertoire. A true highlight has been our one-on-one discussions while pouring over the data together. These learning moments have left a lasting impact on me and they will be forever cherished.

Secondly, to Dr. Michael McDonough for his supervision and guidance in the ways of the 'Jedi', or structural biology. Thank you for all the times that you checked my crystal plates, fished crystals, collected numerous datasets, requested access to synchrotron facilities (*e.g.*, XChem-Diamond and HPMX-ESRF), and refined my crystallographic data. Furthermore, thank you for teaching me to do these tasks on my own. All the out-of-hour beamtime sessions have genuinely felt like the Master and the Padawan shooting crystals.

Thank you to Dr. Yu Nakashima and Giorgia Fiorini, both of whom I worked closely with on this project. Dr. Nakashima was instrumental in teaching me the core modelling skills needed to refine crystal structures. Thank you to Giorgia for her efforts in optimising the acetate-derived crystals that can be grown in the anaerobic glovebox. I look forward to our exciting results to come on the time-resolved prolyl-hydroxylase project.

I wish to thank members of the CJS group who helped me significantly in the lab. In particular, thank you to Dr. Zhihong Zhang for his 'Yoda'-level skills in protein purification and who helped me improve my own skills in the technique substantially. Thank you to Dr. Anthony Tumber for his extensive efforts on the high-throughput mass spectrometry assay. I am grateful to Dr. Rasheduzzaman Chowdhury for his significant contribution to the initial optimisation and structural characterisation of prolyl-hydroxylases. Dr. Chowdhury's work was the foundation for this study. Thank you to Dr. Kerstin Lippl and Dr. Tongri Liu for their supervision and training in my initial months in the CJS group. Thank you to Dr. James Holt-Martyn for the numerous discussion and insight into the medicinal chemistry of the prolyl hydroxylases. Thank you to Dr. Patrick Rabe for his help in organising and scheduling weekly beamtime, collecting remote datasets, and experimental advice. Thank you to Dr. Martine Abboud for her guidance on the writing of this thesis and our insightful discussions on the project. Thank you to Dr. Christopher Lohans, who helped significantly with the molecular biology methods at the start of my project. Thank you to Dr. Shuang Liu for her help with several NMR

assays. Thank you to Dr. Adam Hardy, our laboratory manager, for his daily operation of the laboratory and technical advice throughout this project. Thank you to Manso Jubier, who prepared media for cell growth and helped with autoclaving flasks for large-scale cultures. I want to thank Dr. Ji Luo (NIH) for his advice and comments during this study. Thank you to Dr. Chiara Maniaci, Prof. Emily Flashman, Dr. Gareth Langley, Dr. Illaria Pettinati, Dr. Joanna Storr, Dr. Jürgen Brem, Dr. Leah Taylor-Kearney, Dr. Lennart Brewitz, Dr. Louise Walport, and to Dr. Mark White for their advice, training, and assistance during this project. In addition, I would like to express my appreciation to all the CJS-AK-EF group members and the CRL mass spectrometry, stores, workshop, and catering staff for all their support the past four years.

Thank you to Diamond Light Source Ltd. (MX18069, MX23459, MX19458, and LB24500), Synchrotron SOLEIL, and European Synchrotron Research Facility (MX-2289) for the allocated beamtime and laboratory access. I would also like to thank the beamline staff, particularly Dr. Alice Douangamath, Dr. Romain Talon, Dr. Alexandre Dias, and Dr. Philippe Carpentier for their extensive help on the experiments conducted at these facilities. Thank you to Dr. Edward Lowe for all his help in organising the shipment of samples to the synchrotron facilities and collecting several crystal datasets at Synchrotron SOLEIL. I thank the International Centre for Diffraction Data-Ludo Frevel for partial funding of this project.

While there are too many teachers, instructors, and professors to name, I need to acknowledge the outstanding scientific education I received until this point: Congressional Schools of Virginia, Woodberry Forest School, and Trinity College Dublin.

I wish to express my gratitude and special appreciation to my friends who have supported and encouraged me over the years, even when the times were the hardest: Aisling Hourihane, Aislinn Crawford, Alex Crean, Ashley Dey, Caoimhe Slevin, Dan Ball, Daniel Chaplin, Darren O'Dowling, Eoin Colleary, Freddie Foster, Georgia Gebler, Ines Niarchos, Jacob Liefland Berntsson, James Linyard, Joe Fitzpatrick, John Bethell, Katie Toal, Klem Šimelis, Louis Murray Brown, Dr. Oluwatobi Arisa, Pac O'Shea, PD Duncan, Raphael Reinbold, Dr. Roman Belle, Shannon McGann, Tim Suits, Tobi John, and many more. To the future fond memories that lay ahead.

To Dr. Alen Krajnc, it has not been the same without you in Oxford. Thank you for all the life-long memories, encouragement, and support during some of the most challenging periods during this study. I could always find solace knowing we were experiencing the same hurtles together as we tackled one failed experiment at a time.

Thank you to Martin Dirr, Kerstin Dirr, Tobi Dirr, Oli Dirr, and Carina Gruber for your support, warm hospitality, and company during the critical stages of writing this thesis. There is no better treat than waking up and having a weisswurst with bretzen, weissbier (alcohol-free of course), and süßer senf to begin the day of writing. The

afternoon dips in the sea truly saved my mind and kept me fresh for the following tasks at hand.

Thank you to my family, particularly Levi-Edith-Rice, Dudley-Margaret Manley, Judith-Joe Davenport, David-Meredith Figg, Bobby-Cathie Holderfield, Mike-Hollie James, Fred-Janie Luzzio, Clay-Mary Meininger, and Mark-Beth Risinger for their support, care, and encouragement during each sector of my life. I will always cherish the family days in Kentucky and Florida, especially all the fond memories with my cousins: Drake-Emily Duncan, Andrew Figg, Ava Figg, Alex Gaither, Olivia Luzzio, Julia Luzzio, Hayley Meininger, Clayton Meininger, Tyler-Caitlin Phelps, and Connor Wilson. They have always been special to bring everyone together.

Last, but not least, thank you to the three closest people to me, Anna Dirr, Jennifer Figg, and Dr. William Figg, Sr. To Mom and Dad, thank you for your unreserved love, care, sacrifice, and support over the years. Thank you for all the life experiences and lessons from an early age. They have made me the man I am today. To my Dad, thank you for your belief in me even when I had lost faith in myself. Finally, to Anna, my life partner, thank you for your love and companionship, especially during the isolation challenges caused by the COVID-19 pandemic. To have your company each day was a true blessing. Also, thank you to Anna for keeping me sane (90% of the time at least) while writing this thesis. Mom, Dad, and Anna, I look forward to our next chapters together.

List of Contributors

Supervisor

Prof. Christopher Schofield

Chapter 2

Dr. Rasheduzzaman Chowdhury – Conducted the preliminary work for this study

Dr. Michael McDonough – Crystallographic manipulation, data collection, data analysis, and training

Dr. Anthony Tumber – Conducted the RapidFire® hydroxylation assay

Ms. Giorgia Fiorini – Further optimization of acetate-derived crystallisation condition

Dr. Patrick Rabe – Advice on time-resolved crystallographic studies

Dr. Philippe Carpentier (ESRF) – Performing high-pressure experiments and data collection

Chapter 3

Dr. Michael McDonough – Crystallographic manipulation, data collection, data analysis, and training

Dr. Yu Nakashima – Crystal manipulation, crystallographic refinements, and training

Dr. Zhihong Zhang – Optimisation of the purification strategy

Dr. Edward Lowe – Collected data at SOLEIL and organized regular beamtime

Dr. James Holt-Martyn – Synthesised Molidustat

Prof. Xiaojin Zhang – Synthesised ZXJ-1

Chapter 4

Dr. Michael McDonough – Applied for XChem, crystallographic manipulation, data collection, data analysis, and training

Dr. Yu Nakashima – XChem, Soaking of inhibitors, Crystal manipulation, and crystallographic refinements

Dr. Alice Douangamath (DLS) – Assisted with wet laboratory XChem efforts

Dr. Romain Talon (DLS) – Assisted with wet/dry laboratory XChem efforts

Dr. Alexandre Dias (DLS) – Clustered XChem data and ran PanDDA2 on the clusters

Dr. Anthony Tumber – RapidFire MS IC_{50} data on the Takeda-17 derivatives

Ms. Caitlin Gold – Synthesised the CG Takeda-17 derivatives

Mr. Marcin Bielinski – Synthesised Takeda-17 and derivatives

Editors – *Prof. Christopher Schofield, Dr. Michael McDonough, Dr. Zhihong Zhang, Dr. Yu Nakashima, Ms. Anna Dirr, Dr. Oluwatobi Arisa, Dr. Alen Krajnc, Dr. James Holt-Martyn, and Dr. William Figg, Sr.*

List of Abbreviations

2D	2-Dimensional
2OG	2-Oxoglutarate/alpha-ketoglutarate
2OG-diacid	Diacidic form of 2OG
2OG-disalt	Disodium salt of 2OG
2YT	2X yeast and tryptone
3C	Cyclic peptide
3D	3-Dimensional
5GP	Guanosine-5'-monophosphate
Å	Angstrom
Å²	B-factor
ACT	Acetate
ACV	L-(alpha-aminoadipoyl)-L-cysteinyl-D-valine
ADP	Atomic displacement parameters
AI	Artificial intelligence
AlkB	alpha-Ketoglutarate-dependent hydroxylase
ALKBH5	AlkB homolog 5
AMP	Adenosine monophosphate
AMPL	ATOM Modelling PipeLine
APS	Ammonium persulfate
ARD	Ankyrin repeat domain
AspH	Aspartyl/asparaginyl beta-hydroxylase
ASU	Asymmetric unit
ATOM	Accelerating Therapeutics Opportunity in Medicine
BBB	Blood brain barrier
BBOX	Gamma-butyrobetaine hydroxylase
bHLH	Basic helix-loop-helix domain
CAD	*C*-terminal transactivation domain
CBP	CREB protein
CCD	Charge coupled device
CCP4	Collaborative Computational Project Number 4
cGMP	Cyclic GMP
CIF	Crystallographic information files
CKD	Chronic kidney disease
CNS	Central nervous system
CoA	Coenzyme A
CODD	*C*-terminal oxygen degradation domain
CP4H	Collagen prolyl-4-hydroxylase
CPH	Collagen prolyl hydroxylase
CREB	Cyclic AMP response element binding
CSV	Comma-separated values

CUL	Cullin 2 protein
CV	Column volume
Da	Dalton
DAOCS	Deacetoxycephalosporin-C synthase
Diamond	Diamond Light Source Ltd.
DMOG	Dimethyloxalylglycine
DMSO	Dimethylsulfoxide
DNA	Deoxyribonucleic acid
DSBH	Double-stranded beta-helix
E. coli	*Escherichia coli*
EDTA	Ethylenediaminetetraacetic acid
EF-Tu	Elongation factor-Tu
EPO	Erythropoietin
ESRF	European Synchrotron Research Facility
FAS	$(NH_4)_2Fe(II)(SO_4)$
FASTA	Fast-All
Ferric	$Fe(II)^{I}$
Ferryl	$Fe^{IV}=O$
FIH	Factor-inhibiting HIF
FKBP38/FKBP8	Peptidyl-prolyl *cis-trans* isomerase FKBP38
FPLC	Fast-protein LC
FTO	alpha-Ketoglutarate-dependent dioxygenase
FUM	Fumarate
GDA	Generic Data Acquisition
GMP	Guanosine monophosphate
GSK	GlaxoSmithKline Plc.
GUI	Graphical user interface
HCl	hydrochloride
HIF	Hypoxia-inducible factor
HIF1-3alpha	HIF isoform 1-3alpha
HIFbeta	HIF beta-subunit
His_6	Hexa-histidine
HP	High performance
HPMX	High-Pressure-MX
hr	Hour
HRE	Hypoxic response element
Hs	*Homo sapiens*
HSP90	Heat-shock protein 90
HT/-S	High-throughput screen
Hyp	Hydroxyproline
IC_{50}	Half-maximal inhibitory concentration
ID	Identification/Identifier

IOX4-A	Acidic derivative of IOX4 inhibitor
IPNS	Isopenicillin *N* synthase
IPTG	Isopropyl beta-D-1-thiogalactopyranoside
ISPyB	Information system for protein crystallography beamlines
IX	Ion-exchange
JmjC	Jumonji C demethylase
KDM	Histone lysine demethylase
KSCN	Potassium SCN
LAA	Sodium-L-ascorbate
LB	Luria-Bertani
LC	Liquid chromatography
LCD	Liquid crystal display
m/z	Mass-to-charge ratio
MES	2-(*N*-morpholino)ethanesulfonic acid
Milli-Q	Water purified using a Millipore Elix® 10 system (Merck Life Sciences, Ltd.)
mmCIF	Macromolecular CIF
MOPS	3-morpholinopropane-1-sulfonic acid
MR	Molecular replacement
mRNA	Messenger RNA
Ms	*Mus musculus*
MS	Mass spectrometry
MTZ	McLaughlin, Terry and Zelinka file
MW	Molecular weight
MX	Macromolecular-crystallography
MYND	Myeloid, Nervy, and DEAF-1
NEDD	Neural precursor cell expressed developmentally down-regulated protein
NMR	Nuclear magnetic resonance
NO	Nitric oxide
NODD	*N*-terminal ODD
NOG	*N*-Oxalylglycine
OD	Optical density
ODD	Oxygen degradation domain
OLT	Oxford Lab Technologies, Ltd.
p23	Co-chaperone protein p23
p300	E1A binding protein
PanDDA	Pan-Dataset Density Analysis
PAS	Per-Arnt-Sim domain
PDB	Protein data bank
PDE5	Phosphodiesterase 5A1
PEG	Polyethylene glycol
PEG 550 MME	Polyethylene glycol monomethyl ether 550
PHD	Prolyl hydroxylase

PHD1-3	PHD isoform 1-3
PHF8	PHD finger protein 8
PK	Pharmacokinetic
PPHD	*Pseudomonas putida* PHD
PSDVB	Polystyrene-divinylbenzene
QTOF	Quadrople-time-of-flight
RaPID	Random nonstandard Peptide Integrated Discovery
RBX	Ring box 1 protein
RCSB	Research Collaboratory for Structural Bioinformatics
RMSD	Root-mean-square-deviation
RNA	Ribonucleic acid
ROS	Reactive oxygen species
RT	Room temperature
SAR	Structure activity relationship
SCA	Scalepack file
SCN	thiocyanate
SDH	Succinate Dehydrogenase
SDS	Sodium-dodecyl-sulfate
SDS-PAGE	SDS polyacrylamide gel electrophoresis
SIN	Succinate
SM	Small-molecule
SoakDB	Soak Database
SOC	Super optimal broth medium
Sparged	O_2-saturated
SPE	Solid phase extraction
SpO_2	Haemoglobin O_2 saturation
T. adharens	*Trichoplax adharens*
***Ta*PHD**	*Trichoplax adharens* PHD
TAZ1	Transcription Adaptor putative Zn Finger 1 domain
TCA cycle	Tricarboxylic acid cycle
TEMED	N,N,N',N'-tetramethylethylenediamine
TET	Ten-eleven translocation methylcytosine dioxygenase
TFT	Thin-film-transistor
TFZ	Translation function Z
TLS	Torsion-Liberation-Screw
Tm	Melting temperature
tPHD	Truncated PHD
Tris	Tris(hydroxymethyl)aminomethane
Ub	Ubiquitin
UDC	Unattended data collection
UPLC	Ultra-performance LC
UV	Ultraviolet

SMILES	Simplified Molecular Input Line Entry System
V	Volt
v/v	Volume per volume
VCB	VHL-elongin-B-elongin-C-complex
VEGF	Vascular endothelial growth factor
VHL	von Hippel-Lindau protein
VioC	Alpha-ketoglutarate-dependent L-arginine hydroxylase / Viomycin biosynthesis protein C
Vis	Visible
w/v	Weight per volume
W1	Active site water 1
W2	Active site water 2
XCE	XChemExplorer
XFEL	X-ray Free-Electron Laser source

List of Figures

Chapter 1 – Introduction

Figure 1-1| Collagen Hydroxylation by Prolyl Hydroxylases. 2
Figure 1-2| A 2D Topography Diagram of the Conserved 2OG Oxygenase DSBH (or Jelly-Roll) Fold. 5
Figure 1-3| Core Domain Comparison of PHD2 with its Evolutionary Homologues PPHD and TaPHD**.** 6
Figure 1-4| DSBH and Domain Comparison of FIH, AlkBH5, IPNS. 8
Figure 1-5| Overview of the Hypoxic Response Pathway. 10
Figure 1-6| View from a Crystal Structure the MsHIF2α,β-PAS-bHLH Domains Bound to a Hypoxic Response Element. 11
Figure 1-7| Views from Structures of HIF1α-peptides Complexed Structure with pVHL and Histone Acetyltransferases CBP/p300 Proteins. 12
Figure 1-8| View from a pVHL-Elongin B-Elongin C in Complex with HIF1$\alpha_{549\text{-}582}$ Peptide. 14
Figure 1-9| View from a Solution Structure of MsCBP/p300 in Complex with HsHIF1$\alpha_{776\text{-}826}$-CAD Peptide. 15
Figure 1-10| The Reaction Mechanism of Asparaginyl Hydroxylation by FIH. 16
Figure 1-11| HIF1-3α NODD and CODD Sequence Alignment and Conservation 17
Figure 1-12| View from a Structure of FIH in Complex with HIF1$\alpha_{788\text{-}806}$-CAD Peptide and a Synthetic Consensus Ankyrin Repeat Peptide. 19
Figure 1-13| PHD1-3 Sequence Alignment and Conservation with Observed Secondary Structure Features 20
Figure 1-14| View from tPHD2$_{181\text{-}416/426}$ in Complex with 2OG and HIF1$\alpha_{588\text{-}574}$-CODD. 22
Figure 1-15| Comparison of the 2OG Binding Pockets of tPHD2 and FIH. 24
Figure 1-16| Core Scaffolds of 2OG Derived Carboxylic Acid-Based PHD Inhibitors. 26
Figure 1-17| Core Scaffolds of Non-Carboxylic Acid-Containing PHD Inhibitors. 28
Figure 1-18| Non-Conventional PHD Inhibitors. 30
Figure 1-19| Clinically Applied Small-Molecule PHD Inhibitors**.** 31

Chapter 2 – Mechanistic Studies of PHD2

Figure 2-1| View from a Crystal Structure of PHD2$_{181\text{-}426}$-NOG in Complex with HIF1$\alpha_{556\text{-}575}$-19-mer Fragment Peptide. 51
Figure 2-2| Superimposition and Active Site View of PHD2$_{181\text{-}426}$ Structures in Complex with HIF1$\alpha_{556\text{-}575}$-CODD and HIF1$\alpha_{395\text{-}413}$-NODD. 53
Figure 2-3| Non-hydroxylated and Hydroxylated HIFα-ODD Pyrrolidine Conformation Ring Pucker. 54
Figure 2-4| The Proposed Consensus Catalytic Cycle of 2OG Oxygenases. 56
Figure 2-5| PHD2$_{181\text{-}407}$ in Complex with RaPID-derived 3C Cyclic and HIF1α-CODD Peptides. 59
Figure 2-6| A Succinyl-Peroxide Intermediate Observed During Mechanistic Crystallographic Studies of L-Arginine Hydroxylase, VioC. 60
Figure 2-7| The Two-Column Purification Strategy to Purify PHD2$_{181\text{-}407}$. 61
Figure 2-8| Mass Spectra of PHD2$_{181\text{-}407}$ Construct Thrombin Cleavage and Hydroxylation Assay with HIF2$\alpha_{523\text{-}542}$-CODD Peptide. 62
Figure 2-9| Optimisation of the Formate Crystallisation Condition and View of the HIF2$\alpha_{523\text{-}542}$-CODD Peptide's Role in Crystal Packing. 68
Figure 2-10| The 3C Peptide is Not Complexed in the PHD2$_{181\text{-}407}$.Mn(II).NOG.HIF2α523-542-CODD Complex Structure. . 69
Figure 2-11| PHD2$_{181\text{-}407}$.Mn(II).NOG.HIF2$\alpha_{523\text{-}542}$-CODD Complex Structure. 70

Figure 2-12 | PHD2$_{181-407}$.Mn(II).2OG.HIF2α$_{523-542}$-CODD Complex Structure. 71
Figure 2-13 | Comparison of *Xtal-A* with Previously reported Monoclinic Structure (PDB:5L9B) and with *Xtal-B*. 72
Figure 2-14 | Formate Condition Anaerobic and O_2-Exposed Crystal Structures of PHD2$_{181-407}$.Fe(II).2OG.Timepoints T17, T19, T25-Minutes.. 76
Figure 2-15 | Crystallographic Validation of Anaerobic and O_2-Exposed Formate-Derived Structures. 77
Figure 2-16 | Normalised Cα B-Factor Analysis Between Formate Condition Crystal Structures. 78
Figure 2-17 | All Atoms B-Factor Heat-Map of the Formate Anaerobic and O_2-Exposed Data. 79
Figure 2-18 | Zn Condition Optimisation of the PHD2$_{181-407}$.Mn(II).2OG.HIF2α$_{523-542}$-CODD Complex 84
Figure 2-19 | The Zn Condition Derived PHD2$_{181-407}$.2OG.HIF2α$_{523-542}$-CODD Complex Structure. 85
Figure 2-20 | Hydroxylation Assay to Compare Activity of EDTA-treated PHD2$_{181-407}$ versus PHD2$_{181-407}$. 88
Figure 2-21 | Crystallisation Optimisation of the Acetate Condition for Anaerobic Growth. 85
Figure 2-22 | Initial PHD2$_{181-407}$.Mn(II).2OG.HIF2α$_{523-542}$-CODD Complex Structure Obtained Using the Acetate Condition. 91
Figure 2-23 | PHD2$_{181-407}$.ACT.HIF2α$_{523-542}$-CODD (*Xtal-I*) Structure and Alignment with the Anaerobic Acetate Crystal Structure (*Xtal-J*). 93
Figure 2-24 | A Representation of the Space Group Change After O_2-Exposure. 97
Figure 2-25 | Inter-Chain Interactions of the *P* 2_1 O_2-Exposed PHD2$_{181-407}$.Fe(II).2OG.HIF2α$_{523-542}$-CODD Crystal Lattice. 98
Figure 2-26 | The Active site of Anaerobic and O_2-Exposed Acetate-Derived Complex Structures. 95
Figure 2-27 | The Close-up Views of the Active Site Changes Acetate-Derived Crystals O_2-Exposure. 101
Figure 2-28 | Crystallographic Validation of Anaerobic and O_2-Exposed Acetate-Derived PHD2$_{181-407}$-HIF2α$_{523-542}$-CODD Complex Structures. 102
Figure 2-29 | Normalised Cα B-Factor Analysis Between Acetate Condition Crystal Structures. 103
Figure 2-30 | All Atoms B-Factor Heat-Map of the Acetate Anaerobic and O_2-Exposed Data. 104
Figure 2-31 | Optimisation of the PHD2$_{181-407}$.Fe(II)/Mn(II).HIF2α$_{523-542}$-CODD Crystallisation System. 108

Chapter 3 – Structural Analyses on PHD2 Inhibition *via* Co-crystallisation

Figure 3-1 | Crystal Systems for Various Reported tPHD2-Inhibitor Complex Structures. 121
Figure 3-2 | Overview of Clinically Applied PHD and Other 2OG Oxygenase Inhibitors. 122
Figure 3-3 | Overview of Reported tPHD2-Ligand Complex Structure Active Sites. 123
Figure 3-4 | Crystallisation and Crystal form of the PHD2$_{181-426}$ Construct in Complex with Mn. 126
Figure 3-5 | A View from the PHD2$_{181-426}$.Mn(II) Complex Structure. 128
Figure 3-6 | SDS-PAGE Gel Characterisation of PHD2$_{181-407}$ After Each Purification Step and Crystallisation of both 2 and 3-Column Products. 130
Figure 3-7 | Hit and Optimised PHD2$_{181-407}$.Mn(II).Succinate Crystals**.** 132
Figure 3-8 | An Overview of PHD2$_{181-407}$.Succinate *P* 2_1 Crystal Form. 133
Figure 3-9 | A Surface Overview of the Asymmetric Unit of the PHD2$_{181-407}$ *P* 2_1 Crystal Form 135
Figure 3-10 | A View from the Active Sites of PHD2$_{181-407}$.Mn(II).Succinate and AsqJ.Fe(II).Succinate Complex Structures. 137
Figure 3-11 | Views from the Active sites of PHD2$_{181-407}$.Mn(II).2OG, PHD2$_{181-407}$.Mn(II).Succinate, and FIH-1.Fe(II).Succinate Complexes. 135
Figure 3-12 | A View from the Active Sites of the Six-Chains of the PHD2$_{181-407}$ in complex with Fumarate. 144
Figure 3-13 | A View from the Active Sites FIH in complex with Fumarate. 146

Figure 3-14 | A View from 3D and 2D Active Site Representations of $PHD2_{181-407}$ in Complex with Molidustat (20) and IOX4 (28). 149
Figure 3-15 | A View from the Active Site of Aligned Complex Structures of PHD1, $PHD2_{181-416}$, and $PHD2_{181-407}$ Complexed with Takeda-17 (17). 153
Figure 3-16 | Overview of $PHD2_{181-407}$ *P* 6_1 2 2 Crystal Form with the Pre-Clinical Candidate ZXJ-1 (33). 156
Figure 3-17 | A View from Structures of $PHD2_{181-407/426}$ in Complex with ZXJ-1 (33) and Vadadustat (23). 159
Figure 3-18 | An Overview of Variation of the β2-β3 Finger Loop of tPHD2 Between Crystal Forms and Ligands Bound. 162
Figure 3-19 | A Continued Overview of Variation of the β2-β3 Finger Loop of tPHD2 Between Crystal Forms and Ligands Bound. 163
Figure 3-20 | A View of tPHD2's Active Site Residues Induced-Fit Mechanism Between Various Complex Structures. 165
Figure 3-21 | 2D Depiction of the $PHD2_{181-407}$ Active site in Complex with 2OG (Anaerobic), SIN (O_2-Exposed), SIN (Condition), and FUM (Condition). 168
Figure 3-22 | Structural Alignment of AlphaFold Predicted Collagen P4H and $PHD2_{181-426}$ with a View of the Active Site Residues. 170

Chapter 4 – Structural Analyses on PHD2 Inhibition *via* Soaking-Based Studies

Figure 4-1 | Introduction and Overview of the XChem Fragment Screen Pipeline at Diamond. 179
Figure 4-2 | Overview of the Wet Laboratory XChem Pipeline. 181
Figure 4-3 | Alignment of Complex Structures of PDE5 and View of the Active Site. and Dynamic Loop Regions. 183
Figure 4-4 | Optimisation Flowchart of the $PHD2_{181-407}$.Mn(II).Succinate-*P* 2_1 Crystal form for Use in the XChem Fragment Screen at Diamond. 188
Figure 4-5 | An Overview Flowchart of the Dry Laboratory Component and Data Processing. Steps of the XChem Pipeline. 189
Figure 4-6 | An Overview of the Five Binding Sites of $PHD2_{181-407}$.Mn(II).Succinate Identified for the Soaked XChem Fragments. 192
Figure 4-7 | Surface Representation View of the Five Binding Sites of Soaked XChem Fragments and $PHD2_{181-407}$. 193
Figure 4-8 | View of Binding Site 1 of $PHD2_{181-407}$ with Soaked XChem Fragments. 194
Figure 4-9 | Views from Binding Site 2 of $PHD2_{181-407}$ with Soaked XChem Fragments. 196
Figure 4-10 | Views from Binding Site 3 of $PHD2_{181-407}$ with Soaked XChem Fragments. 198
Figure 4-11 | A View from Binding Site 4 of $PHD2_{181-407}$ in Complex with Fragment-x0042. 199
Figure 4-12 | A View from Binding Site 5 of $PHD2_{181-407}$ in Complex with Fragment-x0033 and Superimposed with the $PHD2_{181-426}$-$HIF1\alpha_{556-574}$-Substrate Structure. 200
Figure 4-13 | A View from Superimposed Monodentate Binding Derivatives in Complex with $PHD2_{181-407}$ and the Interaction with the Active Site 'Back'-Pocket. 203
Figure 4-14 | 2D Overview of the $PHD2_{181-407}$ Active Site in Complex with Takeda-17 Derivatives. 206
Figure 4-15 | Structures of $PHD2_{181-407}$ in Complex with Derivatives of Takeda-17 (17) and Views of the Active Site Interactions. 207
Figure 4-16 | Comparison of the Back Pocket Loop between PHD1-3 Isoforms and View from the Active Site. 209

Figure 4-17| Chemical Moieties that can Modulate the Biophysics of the Paired $PHD2_{181-407}$ Active Site Sidechains. 211

Chapter 5 – Summary

Figure 5-1| View from the Active Sites of $PHD2_{181-407}$ Crystals in Different States; Anaerobic, O_2-Exposed, and Aerobic Conditions (with or without Ligands). 221
Figure 5-2| A Close-up View of Anaerobic and Intermediate $PHD2_{181-407}$.$HIF2\alpha_{523-542}$-CODD Complex Structures. 222
Figure 5-3| An Alignment and View from $PHD2_{181-407}$ Complex Structures with Co-Substrates, Co-Products, and Inhibitors. 224
Figure 5-4| Structural Alignment of Complex Structures and Asymmetric Unit Chains of the 12 XChem Fragment Hits and Depiction of the Five Binding Sites. 229
Figure 5-5| An Alignment of PHD1-3 Active Sites with the Acrive Site Conformational Change Induced by the Monodentate Binding Derivative, CG22. 231

Appendices

Figure AII-1| Validation Tables for the Crystallographic Data from the XChem Fragment Screen. 288
Figure AII-2| Validation Tables for the Crystallographic Data from the Soaking-Based Studies. 291
Figure AIII-1| 3D and 2D Active Site Comparisons of FIH and $PHD2_{181-407}$ Complex Structures with Molidustat (20). 296
Figure AIII-2| Sequence and Amino Acid Composition of the $PHD2_{181-407}$ Construct with an *N*-Terminal His_6 Affinity-Tag. 297
Figure AIII-3| Sequence and Amino Acid Composition of the $PHD2_{181-407}$ Construct Post Thrombin Cleavage of *N*-Terminal His_6-Tag. 298
Figure AIII-4| Sequence and Amino Acid composition of the $PHD2_{181-426}$ Construct with an *N*-Terminal His_6 Affinity-Tag. 299
Figure AIII-5| Sequence and Amino Acid Composition of the $PHD2_{181-426}$ Construct Post Thrombin Cleavage of *N*-Terminal His_6-Tag 300
Figure AIII-6| RADDOSE-3D Calculation of the X-ray dosage of $PHD2_{181-407}$.Mn(II).Molidustat crystal (20, *Xtal-R*) Collected at the Diamond-I04 Beamline. 301
Figure AIII-7| RADDOSE-3D Calculation of the X-ray dosage of $PHD2_{181-407}$.Mn(II).Molidustat crystal (20, *Xtal-R*) Collected on an In-House FR-E+ SuperBright Rotating Anode Source. 302

List of Tables

Chapter 1 – Introduction

Table 1-1| FIH and tPHD2 Km Values for 2OG and O_2. Values reported are from *Tarshonkaya, H. et al., J. Bio. Chem. 2015*. 17

Chapter 2 – Mechanistic Studies of PHD2

Table 2-1| Formate-Derived Crystallographic Data Processing and Refinement Statistics. 64

Table 2-2| Formate-Derived Anaerobic and O_2-Exposed Crystallographic and Refinement Statistics. 65

Table 2-3| Zn Condition Crystallographic Data and Refinement Statistics. 83

Table 2-4| Crystallographic Data and Refinement Statistics. 90

Table 2-5| Acetate-Derived Crystallographic Data Processing and Refinement Statistics. 95

Table 2-6| An Overview of the Conditions of Harvested $PHD2_{181-407}$.$HIF2\alpha_{523-542}$-CODD Crystals. 107

Chapter 3 – Structural Analyses on PHD2 Inhibition *via* Co-crystallisation

Table 3-1| Crystallisation Conditions of Reported tPHD2-Ligand Complex Structures. 120

Table 3-2| Crystallographic Data Processing and Refinement Statistics (*Xtal-O*). 127

Table 3-3| Crystallographic Data Processing and Refinement Statistics (*Xtal-P*). 134

Table 3-4| Crystallographic Data Processing and Refinement Statistics (*Xtal-Q*). 142

Table 3-5| Crystallographic Data Processing and Refinement Statistics (*Xtal-R and Xtal-S*). 147

Table 3-6| Crystallographic Data Processing and Refinement Statistics (*Xtal-T*). 152

Table 3-7| Crystallographic Data Processing and Refinement Statistics (*Xtal-U*). 157

Table 3-8| Harvested Crystals from Co-Crystallised Complex Structures of $PHD2_{181-407}$. 167

Chapter 4 – Structural Analyses on PHD2 Inhibition *via* Soaking-Based Studies

Table 4-1| Overview of Soak Conditions from SoakDB and Datasets Collected During the $PHD2_{181-407}$ XChem Fragment Screen. 191

Table 4-2| Overview of Soaked Based Studies of $PHD2_{181-407}$ in Complex with the Takeda-17 Derivatives. 204

Chapter 6 – Materials and Methods

Table 6-1| Reagents and Buffers Used to Prepare a 12.5% SDS-PAGE Gel. 242

Table 6-2| Reagents used to Prepare LB Broth Media. 243

Table 6-3| Reagents used to Prepare LB Agar media. 243

Table 6-4| List of tPHD2 Protein Purification Buffers. 250

Appendices

Table AI-1| The *Xtal-ID* Information Reported in this Thesis and Coupled with the Data Quality and Refinement Statistics. 277

Table AI-2| Conventional Rotation-Based Macromolecular Crystallography Diffraction Parameters. 286

Table AII-1| The XChem Fragment Screen Crystallographic Data and Refinement Statistics. 289

Table AII-2| The XChem Fragment Screen Crystallographic Data and Refinement Statistics. 290

Table AII-3| The Crystallographic Data and Refinement Statistics for $PHD2_{181-407}$ in Complex with Takeda-17 (17) Derivatives. 292

Table AII-4| The Crystallographic Data and Refinement Statistics for $PHD2_{181-407}$ in Complex with Takeda-17 (17) Derivatives. 293
Table AIII-I| tPHD2 Constructs Used in the Research Described in this Thesis. 295

Chapter 1

Introduction

Chapter 1

1.1 An Introduction to the 2-Oxoglutarate-Dependent Oxygenases

In 1962, collagen prolyl hydroxylases (CPH) were reported to require O_2 for catalysis, of which one oxygen atom is incorporated into their hydroxylated product.[1–3] *Trans*-3- or *trans*-4-prolyl hydroxylation of the repeating Gly-Pro-Pro tripeptide was observed in the presence of ferrous Fe(II), 2-oxoglutarate/alpha-ketoglutarate (2OG), and ascorbic acid (**Figure 1-1**).[4]

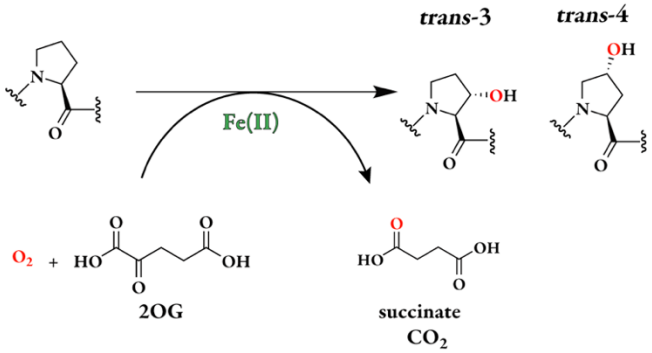


Figure 1-1| Collagen Hydroxylation by Prolyl Hydroxylases. Fe(II), 2OG, and O_2 are the required cofactors for the conversion of the target proline to either *trans*-3- or *trans*-4-hydroxyproline in the biosynthesis of collagen. 2OG reacts with O_2 to form succinate and CO_2. Abbreviations: 2-Oxoglutarate (2OG).

The CPHs were a pioneering example of oxygenases, *i.e.*, enzymes that catalyse formation of products in which one or two oxygens from O_2 are introduced. The oxidation of Gly-Pro-Pro units gives Gly-Pro-Hydroxyproline (Hyp) during collagen biosynthesis (**Figure 1-1**).[5] During the reaction, 2OG is decarboxylated to form the succinate and CO_2 coproducts.[6,7] There are two broadly classified families of haem and non-haem Fe(II)-dependent oxygenases. Within the non-haem family there are both monooxygenases and

dioxygenases.[8–11] The monooxygenases incorporate one oxygen atom of O_2 into their prime substrates, while the other oxygen is reduced to water.[8,10,12] The related family of dioxygenases, however, incorporate both atoms of O_2 into their substrates/co-substrates, as evidenced by reported $^{18}O_2$ experiments conducted with the CPHs and other oxygenases.[1,3,9–15]

The 2OG-dependent oxygenase superfamily emerged following the pioneering studies on the CPHs and subsequent work on the structurally-related isopenicillin *N* synthase (IPNS).[16] The structure of IPNS revealed that the superfamily of enzymes is widely distributed across multiple species.[17–19] The family of non-haem Fe(II)-dependent dioxygenases catalyse a wide range of biological processes and functions. Previous studies have evidenced roles for the 2OG oxygenases and structurally related enzymes in (i) human O_2-sensing (prolyl hydroxylases, PHDs), (ii) transcriptional regulation (*e.g.*, the Jumonji C demethylases, JmjCs), (iii) deoxyribonucleic acid (DNA) oxidation (*e.g.*, the Ten-eleven translocation methylcytosine dioxygenases, TETs), (iv) DNA repair (alpha-ketoglutarate-dependent hydroxylases, (v) AlkB homologues), (vi) fatty acid metabolism (phytanoyl-Coenzyme A (CoA) hydroxylase), (vii) chromatin epigenetic modifications (*e.g.*, histone lysine demethylases, KDMs), (viii) the biosynthesis of antibiotics *via* halogenating enzymes (SyrB2), (ix) and related enzymes that do not utilise 2OG such as (*e.g.*, IPNS, deacetoxycephalosporin-C synthase (DAOCS), and plant specific-ethylene-forming enzyme (EFE)).[17–24]

The 2OG oxygenases can catalyse oxidative reactions ranging from simple hydroxylation reactions of biomacromolecules (as seen with the CPHs), to demethylations *via* hydroxylation of substrate methyl groups, to complex cyclisations and epimerisations.[17–19] Whole-genome sequencing initiatives have revealed 2OG oxygenases are present in most aerobic organisms. The conservation has helped the functional

assignment and characterisation of individual 2OG oxygenases.[17,19,23,25] In humans, it is reported that there are between 60-70 genes encoding for 2OG oxygenases.[17,19,23,25] Structural analyses implemented through X-ray crystallographic studies of 2OG oxygenases has revealed a conserved structural fold, known as the double-stranded beta-helix (DSBH, or jelly-roll) core fold which exhibits conserved motifs, but not identical, for cofactor and cosubstrates binding.[16,17,19,25]

1.2 Structural Overview of 2OG Oxygenases

Crystallographic evidence has revealed the 2OG oxygenases have a conserved DSBH based core fold (or jelly roll), which consists of an *N*-terminal extension of the DSBH, the eight β-strands of the DSBH fold (βI-βVIII), a βIV-βV loop-domain, and a *C*-terminal extension of the DSBH (labelled in **Figure 1-2**).[16,17,19,26–28] The *N*-terminal extension varies between the 2OG oxygenases and typically contains several α-helices, although some oxygenases contain a discrete *N*-terminal domain, *e.g.,* the human PHD (plant homeodomain) finger protein 8 (PHF8).[26–28] 2OG oxygenases have additional β-strands near the *N*-terminus that are not part of the DSBH fold.[26–28] The conserved DSBH motif contains eight β-strands forming minor (βII, βIV, βV, βVII) and major (βI, βIII, βVI, βVIII) sheets in an anti-parallel conformation that provide a rigid scaffold for Fe(II) and 2OG binding.[16,26–29]

The βIV-βV insert varies significantly in 2OG oxygenases. It can comprise only two residues (*e.g.*, IPNS, PDB: 1IPS) or can be a large substrate binding domain, *e.g.* as observed in Factor-inhibiting hypoxia-inducible factor (FIH, **Figure 1-4A** and **1-4C**, PDB: 4Z1V).[16,30]

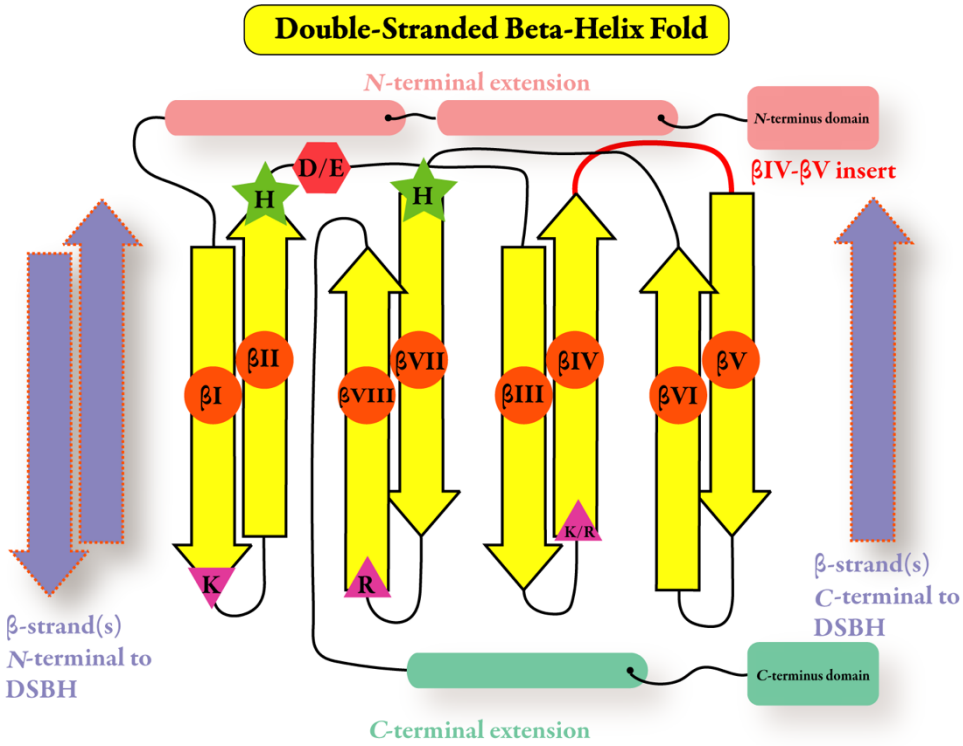


Figure 1-2| A 2D Topography Diagram of the Conserved 2OG Oxygenase DSBH (or Jelly-Roll) Fold. The *N*-terminal extension (salmon) typically consists of a *N*-terminal domain and several α-helices. The eight β strands of the DSBH (yellow) are labelled βI-βVIII. Additional secondary structure β-strands elements (blue) vary in number and type between the 2OG oxygenases. The conserved cofactor and cosubstrate binding residues are histidine (green, star), aspartate/glutamate (orange-red, hexagon), and lysine/arginine (magenta, triangle). The βIV/βV loop (red) can range from a small loop to a large extension domain, *e.g.* FIH. The *C*-terminal extension (green-cyan) consists of several α-helices and a *C*-terminal domain. Abbreviations: 2-Dimensional (2D), Double-stranded beta-helix (DSBH), 2-Oxoglutarate (2OG), Factor-inhibiting HIF (FIH).

The *C*-terminal extension typically includes α-helices, loops, strands, and in some cases a *C*-terminal domain, *e.g.*, as in human histone lysine demethylase 6A (*hs*KDM6A).[31] The *N*-/*C*-terminal extensions have been reported to play roles in substrate binding and in some cases dimerization, *e.g.*, γ-butyrobetaine hydroxylase (BBOX) and FIH.[32–37]

A 'facial-triad' of conserved metal binding residues, HXD/E...H motif (**Figure 1-2**), is observed in most, but not all 2OG oxygenases. Aspartyl/asparaginyl beta-hydroxylase (AspH) is an exception as it only contains two histidine residues to bind the Fe(II).[38]

The conserved 2OG binding pockets typically contain a basic residue, *i.e.*, a lysine or an arginine which interacts with the C5 carboxylate of 2OG (**Figure 1-2**).[17,19,26–28]

Although the overall folds of the 2OG oxygenases are structurally similar, comparisons between the 2OG oxygenases provide insights into mechanistic differences between each subfamily of enzymes.

1.2.1 Comparison of DSBH Fold of PHD2 with Homologues and Other 2OG Oxygenases

The following section provides a structural comparison of human PHD2 (*Hs*PHD2), the focus of this thesis, with related 2OG-dependent orthologues, *i.e.,* *Pseudomonas putida* prolyl hydroxylase (PPHD) and *Trichoplax adharens* (*Ta*PHD) (**Figure 1-3**).

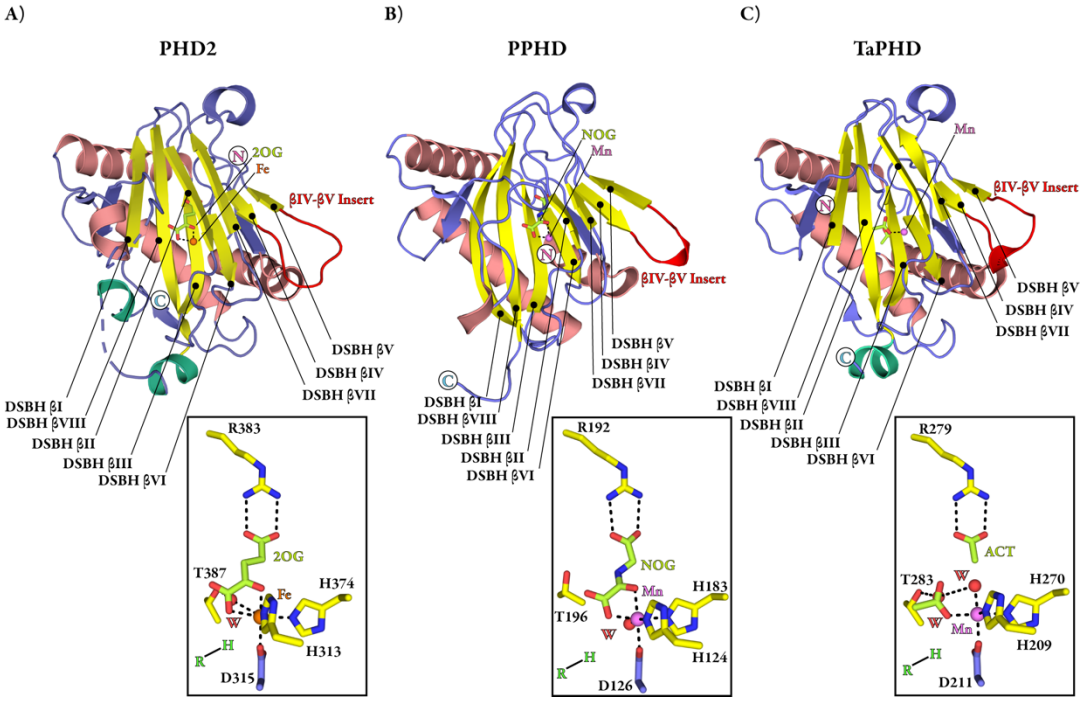


Figure 1-3|Core Domain Comparison of PHD2 with its Evolutionary Homologues PPHD and *Ta*PHD. The DSBH (yellow), βIV-βV insert (red), and *N* (salmon)/*C* (green-cyan)-terminal extensions are highlighted in the structures in reference to the DSBH 2D diagram (**Figure 1-2**). The PHD2.2OG (PDB: 3OUJ), PPHD.NOG (PDB: 4J25), and *Ta*PHD.Mn (PDB: 6EY1) complex structures are represented. Key active site residues and ligands are depicted as sticks. Electrostatic and hydrogen bonding interactions are displayed as dashes (black). Metal ions are represented by spheres (Fe-orange and Mn-violet). Prime substrate binding site is indicated by R–H (green). Catalytically inert Mn(II) is substituted for Fe(II) in the PPHD and *Ta*PHD structures. Abbreviations: Double stranded beta-helix (DSBH), Human prolyl hydroxylase 2 (PHD2), *Pseudomonas putida* prolyl hydroxylase (PPHD), *Trichoplax adhaerens* prolyl hydroxylase (*Ta*PHD), 2-Oxoglutarate (2OG), *N*-Oxalylglycine (NOG). PDB: 3OUJ, 4J25, 6EY1.

All three enzymes have a similar overall catalytic DSBH-containing fold

(**Figure 1-3**).[37,39,40] The minor fold strands βII and βVII of the metazoan *Hs*PHD2 DSBH (yellow) are longer in comparison to PPHD, a bacterial elongation factor-Tu (EF-Tu) modifying prolyl hydroxylase.[39] All three PHDs contain a relatively short βIV-βV insert loop compared to many other 2OG oxygenases (**Figure 1-3**).[37,39,40] *Hs*PHDs and *Ta*PHD both have a *C*-terminal α-helix/ces in the *C*-terminal extension region.[40–42] The α-helices in the PHDs are reported to play a role in substrate binding.[41,42] The *Hs*PHDs and orthologues contain a conserved mobile *N*-terminal finger loop between the β2-β3 strands that interacts with HIFα-substrates upon complexation (PDB: 3HQR).[39–42]

The *Hs*PHDs and orthologues form a discrete structural subgroup of the 2OG oxygenases. Comparisons with, *e.g.*, *Hs*AlkB, reveal subtle differences in the βIV and βV minor fold, including differences in the length of the core strands. FIH, an asparaginyl hydroxylase, and IPNS contain larger *N*-terminal extension regions than the *Hs*PHDs. Both FIH and IPNS lack a mobile β2-β3 finger loop that is observed in the PHD structures, though the conserved DSBH fold is maintained (**Figure 1-4**).[16,30,43]

FIH has an incorporated a substrate binding domain in the βIV-βV insert (red, **Figure 1-4A**).[44] FIH and IPNS both contain more α-helices in their *N*-terminal extensions compared to the *Hs*PHDs.[16,45,46] IPNS, compared to other members of the 2OG oxygenase structural family, has an α8-β6-β7 insert after βI of the DSBH fold (**Figure 1-4C**). [16,45,46] IPNS catalysis is a key step in the biosynthesis of penicillin and cephalosporins through the conversion of L-(α-aminoadipoyl)-L-cysteinyl-D-valine (ACV) with O_2 to isopenicillin *N*.[16,45,46] Although it does not employ 2OG as a cosubstrate, IPNS is closely related to the 2OG oxygenases; especially those involved in cephalosporin biosynthesis, *e.g.*, DAOCS.[16,21,46]

The structural comparison of 2OG oxygenases highlights variations in their primary substrate binding motifs and evolved dynamic mobile elements required for

enzymatic function,[26] in particular for the *Hs*PHDs, which are involved in the hypoxic response in animals.[47]

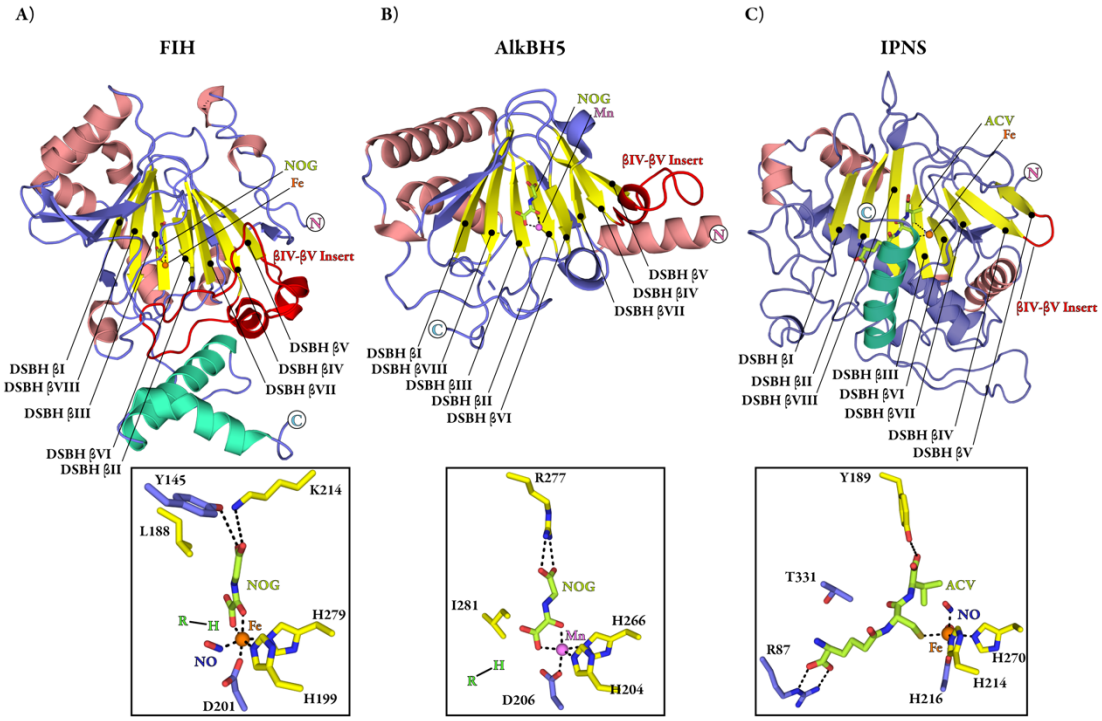


Figure 1-4| DSBH and Domain Comparison of FIH, AlkBH5, IPNS. The DSBH (yellow), βIV-βV insert (red), and *N* (salmon)/*C* (green-cyan)-terminal extensions are highlighted in the structures in reference to the DSBH 2D diagram (**Figure 1-2**). View from the FIH.NOG (PDB: 4Z1V), AlkBH5.NOG (PDB: 4NRP), and IPNS.ACV (PDB: 1BLZ) complexes structures are shown. Key active site residues and ligands are depicted as sticks. Electrostatic and hydrogen bonding interactions are displayed as dashes (black). Metal ions are represented by spheres (Fe-orange and Mn-violet). Prime substrate binding site is indicated by R–H (green). Catalytically inert Mn(II) is substituted for Fe(II) in the PPHD and *Ta*PHD structures Abbreviations: Factor-inhibiting HIF (FIH), Alpha-ketoglutarate-dependent dioxygenase homolog 5 (AlkBH5), Isopenicillin *N* synthase (IPNS), Double-stranded beta-helix (DSBH), *N*-Oxalylglycine (NOG), L-(α-aminoadipoyl)-L-cysteinyl-D-valine (ACV). PDB: 4Z1V, 4NRP, 1BLZ.

1.3 The Hypoxic Response Pathway

Molecular investigations have led to the discovery of a direct link in metazoans between the availability of O_2 and a transcriptional homeostatic response to hypoxia.[40,47,48] The maintenance of O_2 levels in aerobic life is a significant challenge in larger organisms that have high energy demands due to their large mass.[48] A transcriptional regulator, hypoxia-inducible factor (HIF)-α,β heterodimer, was shown to regulate promotion of

expression of the gene encoding for erythropoietin (*EPO*).[49,50] Subsequently HIF was reported to regulate transcription of many identified genes and observed to induce the genetic-upregulation of different hypoxia associated gene-clusters, including those encoding for *EPO* and vascular endothelial growth factor (*VEGF*) (**Figure 1-5C**).[47,51] The *Hs*PHDs were identified as hypoxia sensors which act by down regulation of HIFα levels, in aerobic conditions, *i.e.*, in a relatively O_2-rich environment.[47,52,53] The HIF-PHD pathway is likely conserved throughout metazoans, even in the simplest animal, *T. adharens,* having a rudimentary HIF system.[40,52]

In humans there are three PHD isoforms (PHD1-3), all of which catalyse the *trans*-4-prolyl hydroxylation of HIFα (**Figure 1-1**) in the presence of Fe(II), 2OG, and O_2 (**Figure 1-5A**).[39]

HIFα hydroxylation subsequently leads to its degradation *via* promoting its binding to the von Hippel-Lindau protein (pVHL)-elongin-B-elongin-C-complex (VCB); the complex is a component of the E3 ligase-26S proteasome pathway (**Figure 1-5A**).[54–57] In moderate hypoxia (O_2 saturation of haemoglobin (SpO_2) of 93-89%), PHDs are less active and HIFα levels increase, promoting transcription of genes implicated in the hypoxic response.[58] The structurally related 2OG-dependent hydroxylase, FIH, catalyses hydroxylation of the β-carbons of Asn803 and Asn851 of HIF1-2α, respectively, in a O_2-dependent manner.[47,59] The presence of hydroxyasparagine in HIFα prevents complexation with histones acetyltransferases, cyclic adenosine monophosphate (AMP) response element binding (CREB) protein (CBP)/E1A binding protein (p300), which promote transcription in response to hypoxia (**Figure 1-5B**).[60,61] The HIF system is reportedly involved in many biochemical and physiological pathways, including cell migration, cell growth, apoptosis, metabolism, and cellular transport.[47]

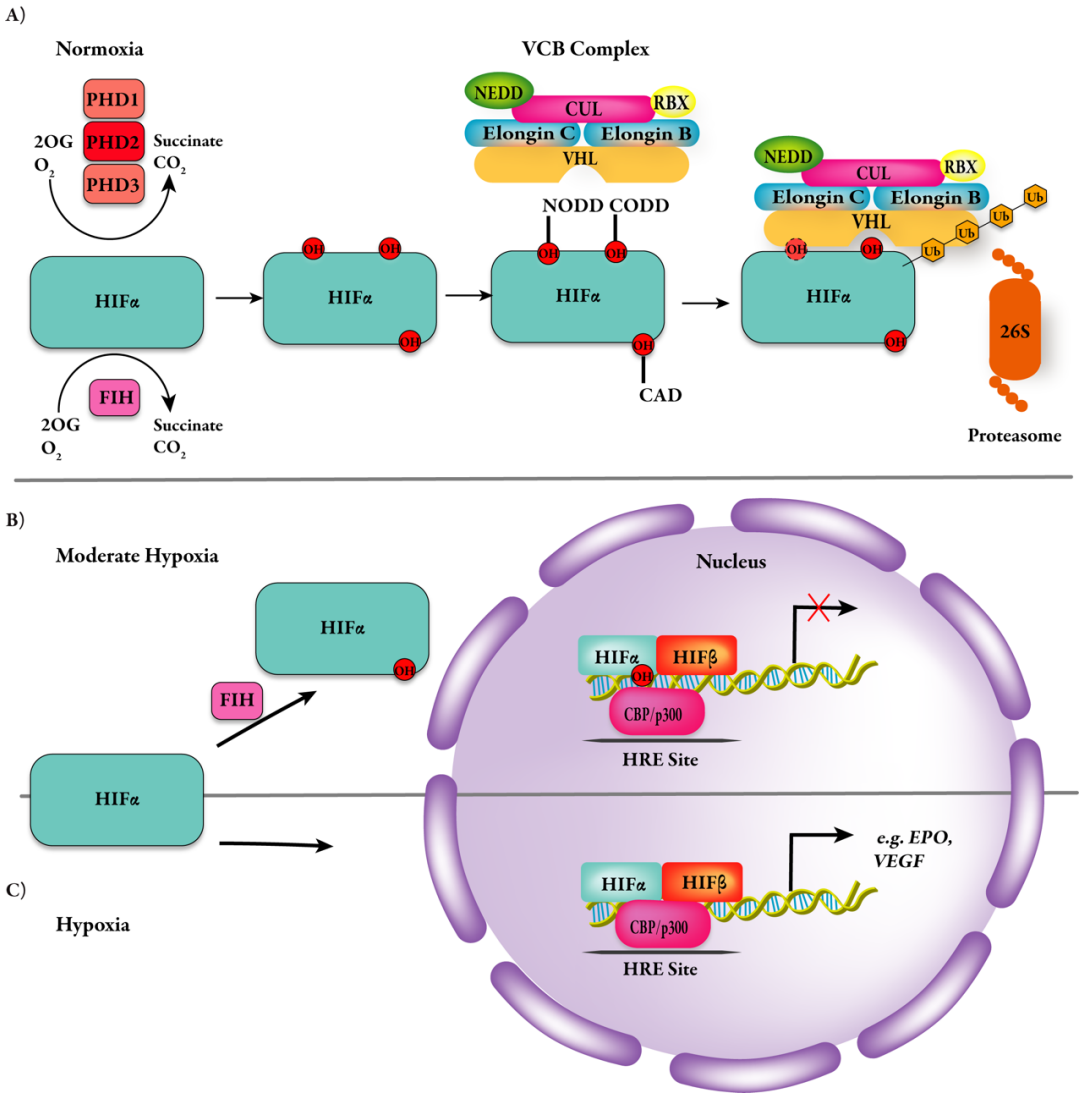


Figure 1-5| Overview of the Hypoxic Response Pathway. (A) In aerobic conditions, PHD1-3, hydroxylate proline residues in HIF1-3α-ODDs, in an O_2 available dependent manner. Formation of hydroxyprolines enhances HIFα binding to pVHL. The pVHL-HIFα complex recruits other subunits of the VCB complex to hydroxylated HIFα and subsequently leads to degradation of HIFα by the 26S proteasome *via* the E3-ligase-ubiquitination pathway. FIH, an asparaginyl hydroxylase, hydroxylates an asparagine residue in the *C*-terminal activation domain (CAD) of HIFα. (B) In moderate hypoxia (SpO_2 of 93-89%), the PHD1-3 are less active compared to FIH. HIFα and HIFβ form the transcriptionally active HIFα,β-heterodimer in the nucleus. The FIH catalysed hydroxyasparagine in the CAD domain of HIFα blocks the CBP/p300 subunit from binding to HIFα,β-heterodimer and prevents HIF induced gene regulation. (C) In hypoxia (SpO_2 of <89%), PHD1-3 and FIH are less active and the HIFα,β-heterodimer-CBP/p300 complex can regulate downstream genes under the transcriptional control of a HRE. Abbreviations: Human prolyl hydroxylase isoforms 1-3 (PHD1-3), Hypoxia-inducible factor isoform 1-3α (HIF1-3α), Oxygen degradation domain (*N*-or *C*-ODD), 2-Oxoglutarate (2OG), von Hippel-Lindau protein (pVHL), von Hippel-Lindau protein-elongin B-elongin C complex (VCB), Cullin 2 protein (CUL), Ring box 1 protein (RBX), neural precursor cell expressed developmentally down-regulated protein (NEDD), ubiquitin (Ub), Factor-inhibiting HIF (FIH), *C*-terminal transactivation domain (CAD), Hypoxia-inducible factor β-subunit (HIFβ), CREB protein (CBP/p300), Hypoxic response element (HRE), erythropoietin (*EPO*), vascular endothelial growth factor (*VEGF*).

1.3.1 Hypoxia-Inducible Factor

The isolated HIFα isoforms (HIF1-3α) subunits localise in the cytoplasm where they are hydroxylated by the PHDs; HIFα is reported to interact with the heat-shock protein 90, HSP90.[62] When HIFα escapes PHD hydroxylation, HIF1-3α are translocated to the nucleus where they bind with HIFβ (also referred to as the Aryl Hydrocarbon Receptor Nuclear Translocator) and work to promote the transcription of specific gene sets.[63,64] In hypoxia, formation of HIFα,β-heterodimer *via* two Per-Arnt-Sim domains (PAS-A or PAS-B) of the HIFα and HIFβ subunits (**Figures 1-5C** and **1-6**).[47,55,63–66] The basic helix-loop-helix (bHLH) domain of the HIFα,β-heterodimer binds to the hypoxic response elements (HRE) upstream of the promoter region of the HIF target gene (**Figure 1-6**).[66,67] All the HIF1-3α isoforms contain the PAS-A/B, bHLH, and oxygen degradation domains (ODD).[63–66] In comparison to HIF3α, HIF1-2α contain two ODDs and a *C*-terminal transactivation domain (CAD).[40]

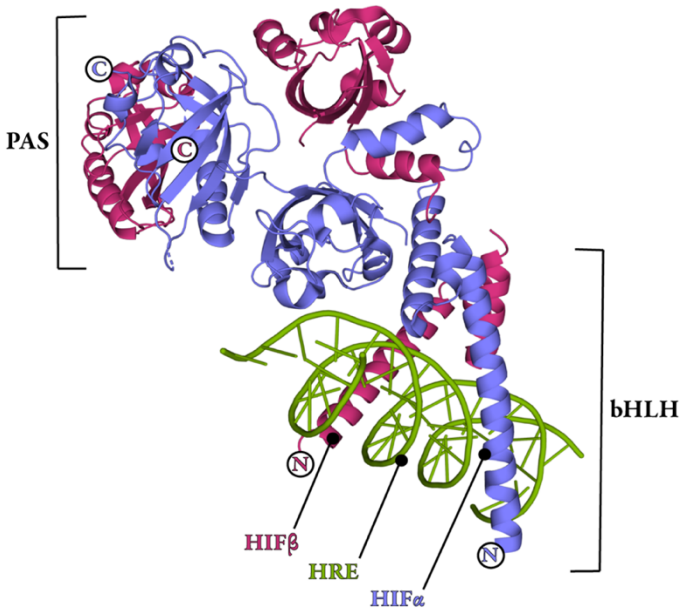


Figure 1-6| View from a Crystal Structure the *Ms*HIF2α,β-PAS-bHLH Domains Bound to an Hypoxic Response Element (HRE). The HIF2α (blue)-HIFβ (red)-heterodimer of the PAS domains in complex with the DNA of a HRE (green) bound by the bHLH domains of HIF2α and HIFβ (PDB: 4ZPK). Abbreviations: *Mus musculus* (*Ms*), Hypoxia-inducible factor 2α isoform and β subunit (HIF2α and HIFβ), Per-Arnt-Sim domain (PAS), basic helix-loop-helix domain (bHLH), deoxyribonucleic acid (DNA), Hypoxic response element (HRE). PDB: 4ZPK.

The two HIFα-ODDs are referred to as the *N*-terminal ODD (NODD) and *C*-terminal ODD (CODD) based on their respective position within HIF1-2α.[63–66] The ODDs have a conserved LXXLAP consensus motif where the PHDs bind and hydroxylate the proline residue in the HIFα-ODD.[47,55,63–66]

Hydroxylated HIFα subsequently recruits pVHL that complexes on the hydroxylated ODD (**Figure 1-7A**).[68] In aerobic conditions and moderate hypoxia (SpO_2 of 93-89%), FIH hydroxylates an asparagine residue within the CAD of HIFα (**Figure 1-7B**).[58]

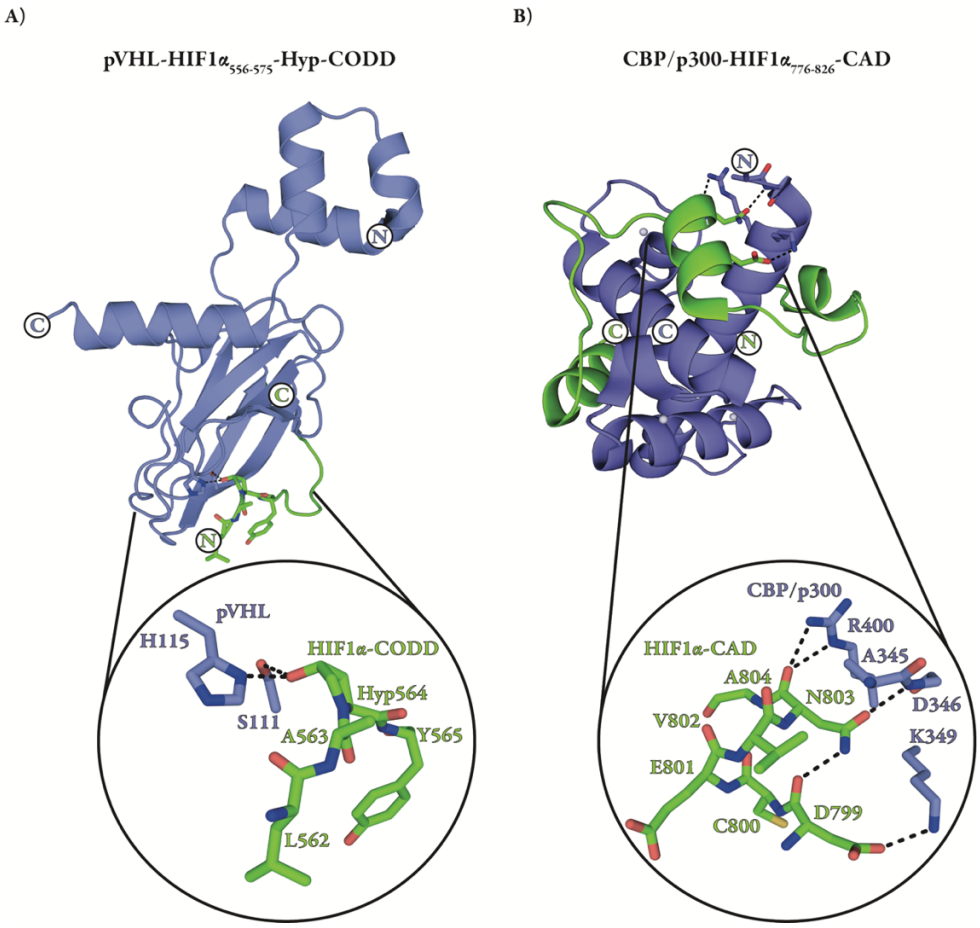


Figure 1-7| Views from Structures of HIF1α-peptides Complexed Structure with pVHL and Histone Acetyltransferases CBP/p300 Proteins. (A) A HIFα556-575-peptide (green) with Hyp564 in complex with pVHL (PDB: 1LM8). Residues His115 and Ser111 interact with HIF1α-Hyp564. (B) Solution structure of *Ms*CBP/p300 protein in complex with a *Hs*HIF1α776-826-CAD peptide (green) (PDB: 1L8C). The HIF1α776-826-CAD Asn803 interacts with residue Asp799 within the CAD domain and residues Arg400, Asp346, of CBP/p300 protein. (A-B) Key interactions are represented by dashes (black). Abbreviation: Hypoxia-inducible factor 1α isoform (HIF1α), Von Hippel-Lindau protein (pVHL), hydroxyproline 564 (Hyp564), *Mus musculus* (*Ms*), CREBs protein (CBP/p300), *Homo sapiens* (*Hs*), *C*-terminal transactivation

The presence hydroxyasparagine, unlike hydroxyproline-pVHL mediated degradation of HIFα, blocks the binding of the CBP/p300 complex and prevents HIFα,β-heterodimer induced transcriptional regulation of HIF target genes (**Figure 1-7B**).[69,70]

1.3.2 VCB-E3 Ligase-Proteasome Degradation Pathway

The pVHL was discovered through molecular investigation of individuals with vascular proliferation induced retinal haemangioblastomas, referred to as von Hippel-Lindau (VHL) disease.[54–56,68,71,72] In 1904, the German ophthalmologist Eugen von Hippel described the familial occurrence of retinal haemangioblastomas.[72] Arvid Lindau, a neuropathologist, identified inherited retinal vascular proliferation as a marker for increased risk of haemangioblastomas of the central nervous system (CNS), kidney cancer, and paragangliomas.[72]

Based on prior clinical observations, VHL disease is reported to be a high penetrance genotype that can be transmitted between generations in an autosomal dominant fashion, *i.e.*, individuals with one mutated allele will develop the VHL disease.[54,71,72] Tumorigenesis is promoted when biallelic inactivation of *VHL via* mutation, genetic silencing, or gene loss leading to an unregulated hypoxic response, *e.g.,* induced angiogenesis (overproduction of VEGF)[73] and increased erythrocytosis (increased EPO levels).[54,55,71,72] *VHL* inactivation is common in sporadic kidney cancer, haemangioblastomas, and is often the first mutation leading to the pathogenesis of clear cell renal carcinoma.[54,71,72] Through careful dissection of the hypoxic pathway, it was identified that the hydroxylated labile HIFα subunit is degraded *via* the E3 ligase-26S proteasome degradation pathway mediated through the essential interaction of pVHL and the protein-protein interactions of multiple other proteins, including elongin B-elongin C (also referred to as the VCB complex) and Ring Box 1 (RBX1), and Cullin 2 (Cul2)

(**Figure 1-5A,** and **Figure 1-8**).[47,55,68,72] pVHL, which shuttles between the cell cytoplasm and nucleus (*i.e.*, pVHL subcellular localisation is regulated in the cell),[74] consists of both an α-subunit-Elongin B/C, RBX1, Cul2 recruitment domain and β-subunit-substrate recognition domain.[54,71,72]

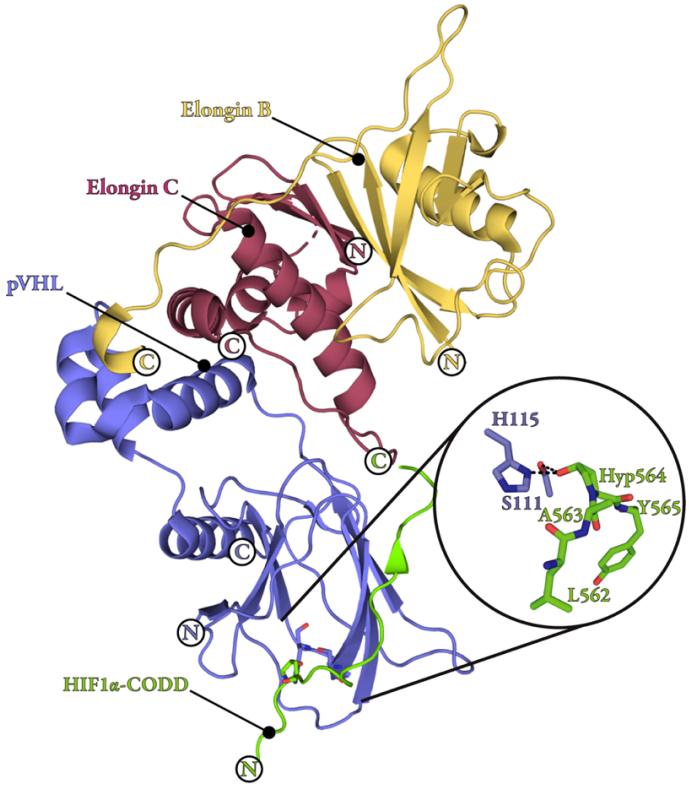


Figure 1-8| View from a pVHL-Elongin B-Elongin C in Complex with HIF1α$_{549-582}$ Peptide. Elongin B (light orange) and Elongin C (raspberry) complex structure with pVHL-HIFα$_{549-582}$ peptide (PDB: 1LQB). Abbreviations: von Hippel-Lindau protein (pVHL), Hypoxia-inducible factor 1α isoform (HIF1α). PDB: 1LQB.

HIFα hydroxylated-ODD permits the interaction with the pVHL residues Ser111 and His115 (**Figure 1-7A**, and **Figure 1-8**).[56,68] The HIFα-VCB complex recruits the E3 ligase and is subsequently poly-ubiquitinated and degraded through the 26S proteasome (**Figure 1-5A**).[47,55]

1.3.3 CREBs Binding-p300 Proteins

CBP/p300 histone acetyltransferases bind to the *C*-terminal CAD of the HIF1-2α subunit of the HIFα,β-heterodimer in the nucleus and are involved in the HIFα,β-

CBP/p300-complex recognition of HREs.[69,70] The isolated CAD is predominantly disordered, as observed through nuclear magnetic resonance (NMR) and crystallographic studies of FIH-CAD complex structures. Three Zn ions are observed to stabilise the Transcription Adaptor putative Zn Finger 1 domain (TAZ1) of CBP/p300.[69,70] Upon HIFα-substrate binding with CBP/p300, the CADs adopt a conformation forming three short α-helices with the FIH prime substrate residue $Asn803_{HIF1\alpha}$ and $Asn851_{HIF2\alpha}$ in the α2 helix (**Figure 1-9**).[69,70] The intermolecular interactions between $Asn803_{HIF1\alpha\text{-}CAD}$ and the main chain carbonyl of $Asp799_{CBP/p300}$ partially stabilise the α2-helix of CBP/p300. $Asn803_{HIF1\alpha\text{-}CAD}$ interacts with residues $Arg400_{CBP/p300}$ and $Asp346_{CBP/p300}$ guanidino group and mainchain peptidyl nitrogen.[66,67] Based on NMR evidence, the CAD α3-helix is buried in a hydrophobic groove of the CBP/p300 protein that locks it on the surface (**Figure 1-9B**).[69,70]

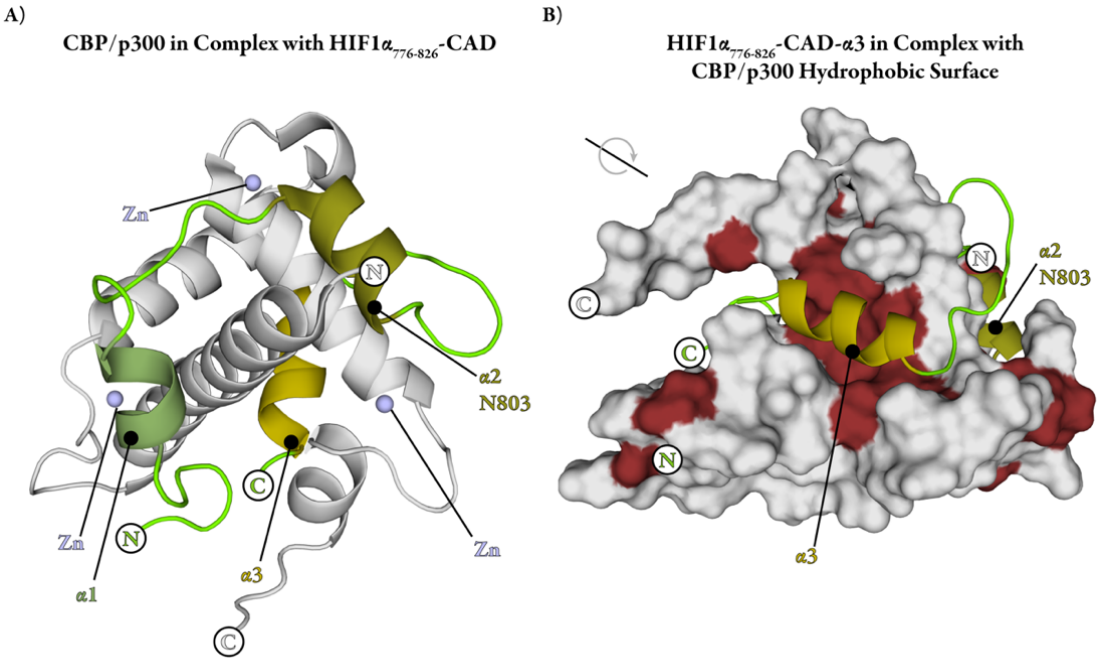


Figure 1-9| View from a Solution Structure of *Ms*CBP/p300 in Complex with *Hs*HIF1α$_{776\text{-}826}$-CAD Peptide. (A) The *Ms*CBP/p300 protein (grey-white is stabilised by three Zn(II) ions (blue) and is in complex with a *Hs*HIFα$_{776\text{-}826}$ peptide (green) (PDB: 1L8C). Three α-helices, α1-3 are coloured light green, dark olive and olive, respectivley. (B) Hydrophobic surface groove of the *Ms*CBP/p300 complex (red) bound to the α3 helix (olive) of the *Hs*HIF1α-CAD domain (green). Abbreviations: *Musculus mus* (*Ms*), CREBs binding protein (CBP/p300), Hypoxia-inducible factor 1α isoform (HIF1α), *C*-terminal transactivation domain (CAD). PDB: 1L8C.

In aerobic and moderately hypoxic conditions, FIH catalyses the hydroxylation of $Asn803_{HIF1\alpha}$ and disrupts the intra- and inter-molecular interactions between the $CAD_{HIF1\text{-}2\alpha}$-CBP/p300 complex which prevents transcriptional initiation of HIF1-2 target genes; that occur in hypoxia (SpO_2 of <89%).[69,70,75]

1.3.4 Factor-Inhibiting Hypoxia-Inducible Factor

The asparaginyl hydroxylase, FIH, was first identified as a protein that binds to HIF1-2α.[76] FIH catalyses the conversion of asparagine to 3-hydroxyasparagine (or β-hydroxyasparagine) in the presence of Fe(II) and O_2.[44] The hydroxylation is similar to the reaction catalysed by the PHDs, and is coupled to the conversion of 2OG to succinate and CO_2 (**Figure 1-10**).[77,78] FIH, consistent with most, but not all, 2OG-dependent oxygenases, contains a conserved 'facial-triad' of HXD/E...H Fe(II) chelating residues.[30]

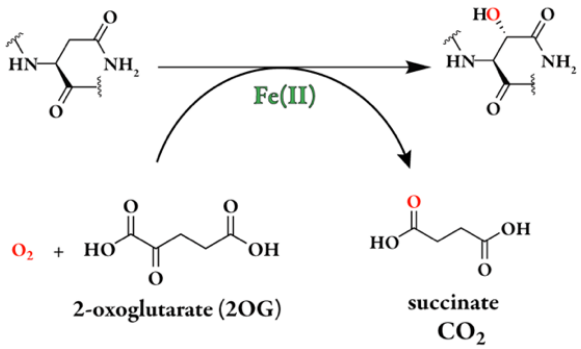


Figure 1-10| The Reaction Mechanism of Asparaginyl Hydroxylation by FIH. The catalysis of 3-hydroxyasparagine (or β-hydroxyasparagine), while in the presence of Fe(II), is coupled to the conversion of cofactor, 2OG, and O_2 to succinate and the release of carbon dioxide. O_2 is split and incorporated into both the prime substrate, asparagine, and the co-product, succinate. Abbreviations: Factor-inhibiting hypoxia-inducible factor (FIH), 2-Oxoglutarate (2OG).

FIH is proposed to act as a second regulator of the hypoxic response through hydroxylation of HIF1-2α subunits that evade prolyl hydroxylation mediated degradation, *e.g.*, in moderate hypoxia (SpO_2 of 93-89%).[47,55,58] Unlike PHD1-3, FIH has only one reported isoform and lacks a redundant effect on HIF-dependent transcriptional regulation as observed through genetic manipulation of FIH in various conditions.[47,76]

The O_2 sensitivity of FIH and the PHDs differ. The role of FIH is, however, likely more complex as there is evidence that it is involved in the regulation of a set of HIF target genes.[79] It has been reported that FIH has a low K_m for O_2, approximately 90-110 μM (**Table 1-1**), whereas for the PHDs the K_m for oxygen has been observed between 230-250 μM for each of the isoforms (in one study >450 μM for $PHD2_{181-426}$ in the presence of HIF1-2α-substrates, **Table 1-1** and **Figure 1-11**).[77,80–82]

Table 1-1| FIH and tPHD2 K_m Values for 2OG and O_2. Values reported are from *Tarshonskaya, H. et al., J. Bio. Chem. 2015.*

Enzyme	Substrate (peptides)	K_m 2OG (μM)	K_m O_2 (μM)
FIH	$HIF1\alpha_{789-822}$-CAD	110 ± 20	110 ± 30
FIH	$HIF2\alpha_{832-850}$-CAD	19 ± 6	110 ± 10
$PHD2_{181-426}$	$HIF1\alpha_{395-413}$-NODD	30 ± 9	>450
$PHD2_{181-426}$	$HIF1\alpha_{556-574}$-CODD	13 ± 2	460 ± 30
$PHD2_{181-426}$	$HIF2\alpha_{398-416}$ NODD	17 ± 5	410 ± 80
$PHD2_{181-426}$	$HIF2\alpha_{523-541}$-CODD	9 ± 2	>450

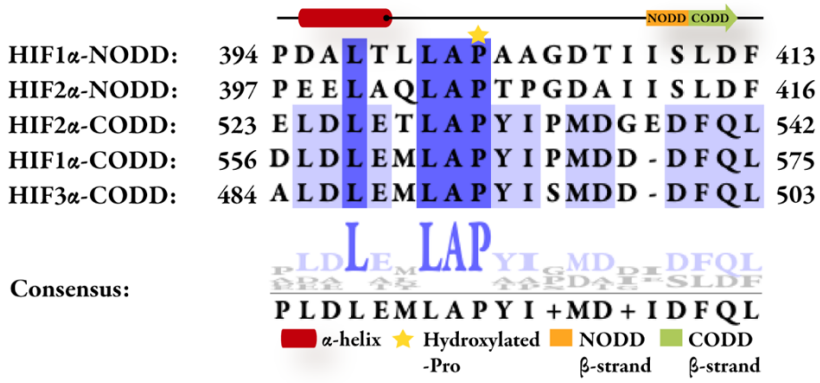


Figure 1-11| HIF1-3α NODD and CODD Sequence Alignment and Conservation. HIF1-3α hydroxylation ODDs sequence similarity and conservation. The secondary structure of the HIFα sequences is shown above, α-helix (red cylinder) and β-strand (orange-green arrow). The β-strand for NODD sequences forms in the orange region (Ile-Ser, PDB: 5L9V) and the β-strand for CODD sequences forms in the green region (Phe-Gln, PDB: 3HQR). The *trans*-4-hydroxylated Pro residues of the HIFα-sequences are indicated by a star (yellow). Abbreviations: Hypoxia-inducible factor (HIF1-3α), *N*/*C*-terminal oxygen degradation domains (NODD, CODD, or ODD).

The precise roles of ascorbate in 2OG oxygenase catalysis are still unclear, especially in cells. Ascorbate is thought to be involved in the reduction of ferric (Fe(III)) or ferryl (Fe(IV)=O) species inadvertently produced during the catalysis of 2OG oxygenases.[83,84] Ascorbate is thus proposed to potentially reset over-oxidised enzymes for

catalysis, *i.e.*, may also reduce reactive oxygen species (ROS) present which might oxidise or damage the enzyme.[83,84] However, it has recently been reported that ascorbate can also react with O_2 to produce H_2O_2.[83,84]

Both solution and crystallographic studies have provided evidence for the promiscuous nature of FIH. Unlike the PHDs, there is strong evidence that FIH can accept multiple other substrates, principally, but not exclusively from the consensus ankyrin repeat domain (ARD) structural family (**Figure 1-12**).[85,86]

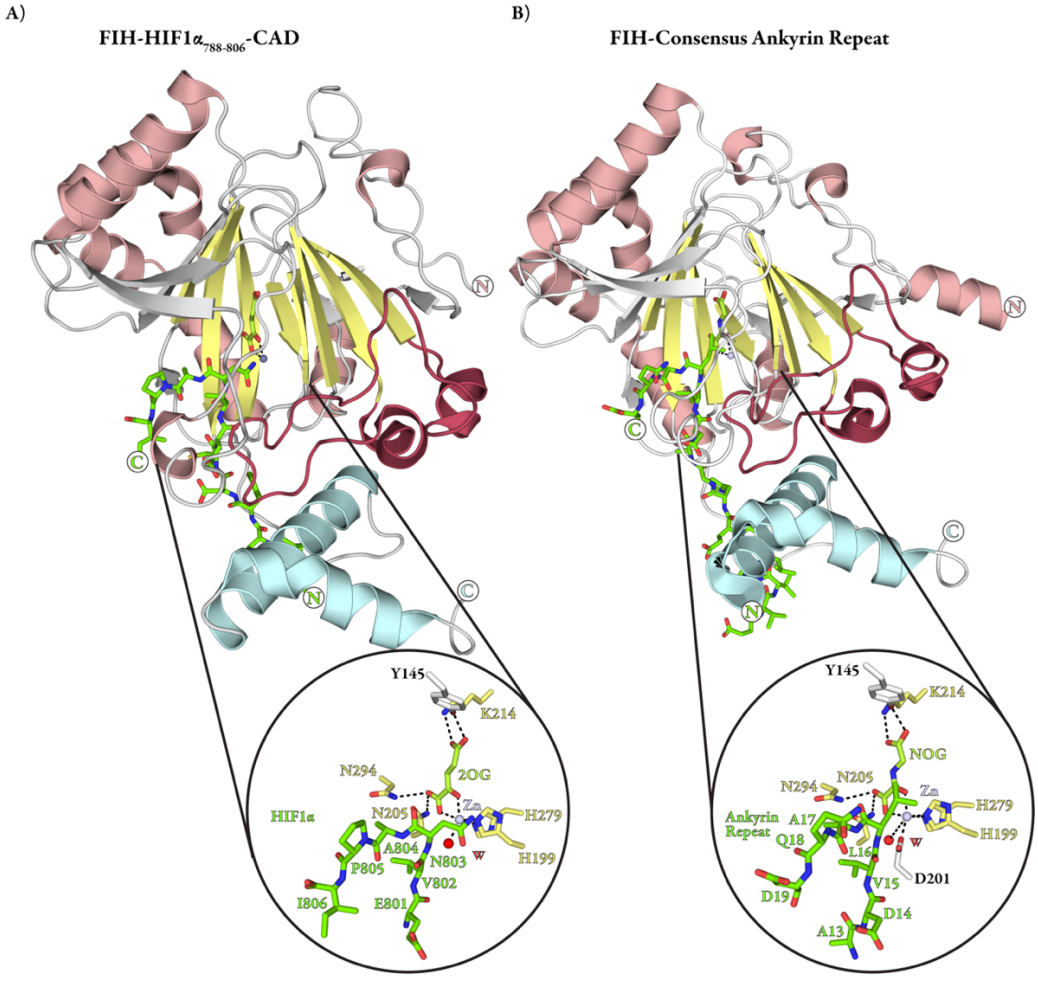


Figure 1-12| View from a Structure of FIH in Complex with HIF1α$_{788-806}$-CAD Peptide and a Synthetic Consensus Ankyrin Repeat Peptide. (A) FIH is complexed with 2OG (lemon) and a HIFα-CAD peptide (PDB: 3D8C). (B) FIH is complexed with NOG (lemon) and a synthetic consensus ankyrin repeat peptide (20-mer, PDB: 4B7E). (A-B) The DSBH (yellow), *N*-terminal extension (salmon), *C*-terminal extension (cyan), HIFα/Ankyrin repeat substrate (green), and βIV-βV insert (red) are highlighted. Active site residues (white/yellow), water (red), and metal (Zn, blue) are shown. Catalytically inert Zn(II) ions are substituted for Fe(II). Yellow residues are included in the DSBH of FIH. Key interactions are represented as dashes (black). Abbreviations: Factor-inhibiting HIF (FIH), Hypoxia-inducible factor-*C*-terminal activation domain (HIF1α-CAD), Double-stranded beta-helix (DSBH), 2-Oxoglutarate (2OG), *N*-Oxalylglycine (NOG). PDB: 3D8C, 4B7E.

FIH can form a complex with the CAD as well as the ankyrin repeat with its large βIV-βV insert substrate recognition domain, with similar binding properties to the Jmjc demethylase family (**Figure 1-12**).[35,44] Upon binding the CAD domain to FIH, a network of hydrogen bonds is formed with the HIFα domain, including an unusual hydrogen bond between the Fe-coordinating $Asp201_{FIH}$ and $Asn803_{HIF1\alpha}$ sidechains, an interaction that might modulate the O_2-sensitivity of the FIH catalysed hydroxylation reaction.[44] The reported structures of FIH in complex with *N*-oxalylglycine (NOG), an isosteric analogue and inhibitor of 2OG, and HIFα/ARD-peptides allows for structural comparisons with the related hypoxic 'sensors', PHD1-3.[85,86]

1.3.5 Prolyl Hydroxylases

As described above (**1.3.4**), the human PHD1-3 isoforms are the 'O_2-sensors' and negative regulators of the hypoxic response pathway.[47,52,53,55,57,87,88] The PHD2 isoform is the most conserved across animals and is widely expressed across human cell types (**Figure 1-13**).[88] The reported messenger ribonucleic acid (mRNA) levels of PHD1 and PHD3 suggests their transcription levels are tissue-specific, *i.e.,* higher levels of PHD1 present in the testis and PHD3 present in cardiac muscle.[88,89] However, the PHD isoforms have different substrate specificities of the five HIFα-substrate domains (**Figure 1-7** and **Table 1-1**).[41,42,88,90] For example, PHD3 does not fully turnover NODD sequences (*i.e.*, <~10% hydroxylation is observed), a property that might be a feature of tissue-specific regulation, it is possible that PHD3 binding to HIFα-NODD sequences results in inhibition.[88,91] PHD2 has a preference for the HIF1α-CODD sequence, whereas PHD1 has a preference for the HIF2α-CODD sequence.[41,42,88] The observed substrate and tissue-specificity of the human PHD1-3 isoforms indicates a deeper level of regulation and feedback loops of the hypoxic response in higher animals. There is evidence for simple

HIF systems exist in early animals, *e.g., T. adhaerens* only contains one PHD and HIFα isoforms.[40,48,88–90]

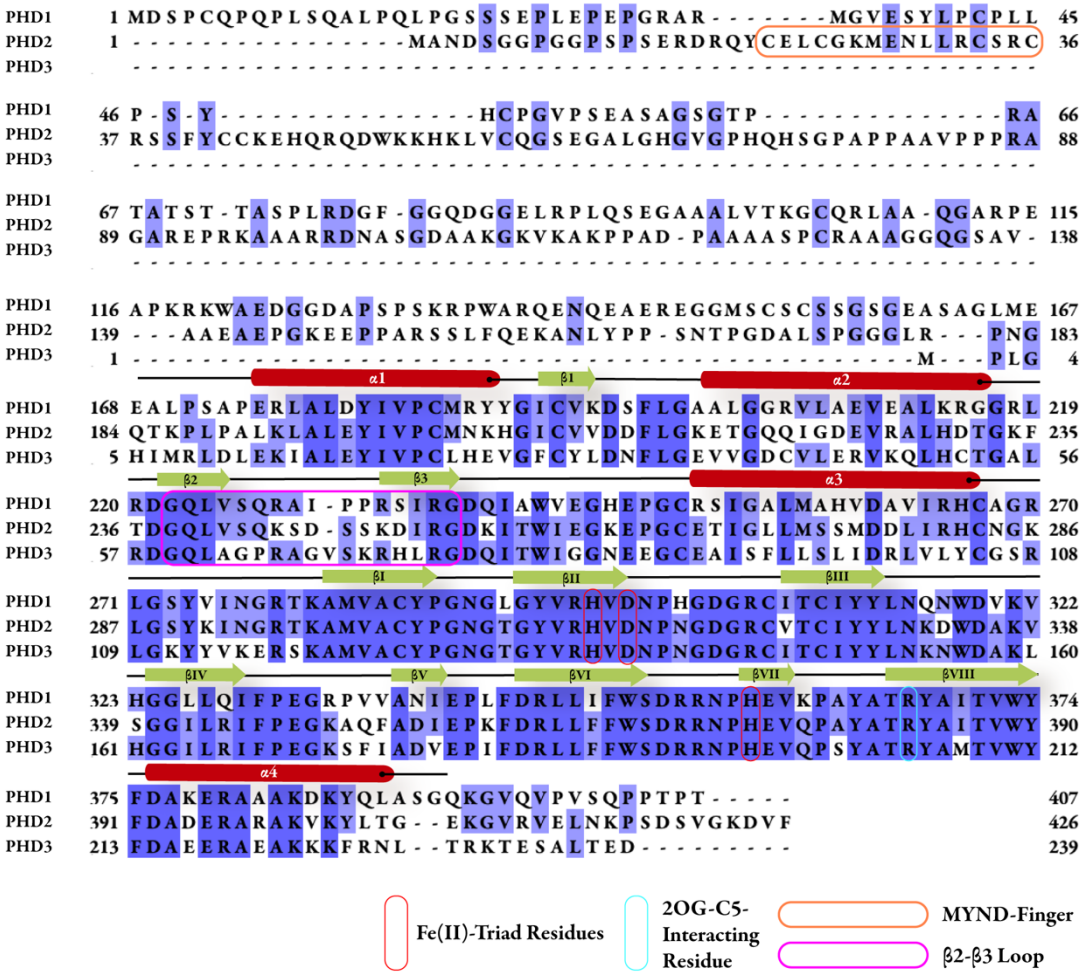


Figure 1-13| PHD1-3 Sequence Alignment and Conservation with Observed Secondary Structure Features. The PHD paralogues 1-3 aligned sequences are illustrated with conservation shown (blue). Secondary structures of features of PHD2 from structural data are depicted above the sequences (PDB: 3HQR). Orange regions indicates areas of interest; for PHD2 the *N*-terminal orange region highlights the MYND-finger and the *C*-terminal orange region represents the β2-β3 finger loop variation the PHDs. The metal chelating (red) and 2OG-C5 (cyan) interacting residues are marked. Abbreviations: Prolyl hydroxylase (PHD1-3), Myeloid, Nervy, and DEAF-1 (MYND). UniProt IDs: PHD1-Q96KS0, PHD2-Q9GZT9, PHD3-Q9H6Z9.

As previously discussed (**1.3.4**), PHD1-3 have a reported K_m for O_2 in the range of 230-250 μM (another study observed >450 μM K_m for truncated PHD2 (tPHD2) in the presence of HIF1-2α-substrates); *i.e.*, the high K_m values highlight the weak affinity the PHDs have for O_2.[77,82,92,93] Recent computational evidence has proposed an O_2 diffusion channel in tPHD2 that is lined with hydrophobic residues from both the

enzyme and bound substrate.[94] There is evidence that different HIFα-substrates may interact with the PHDs in a manner that affects the rate of O_2 diffusion.[94] The authors proposed a 2OG rearrangement from bidentate to monodentate coordination of the metal to allow for O_2 binding at the 2OG C1 carboxylate position.[94] The 2OG rearrangement was proposed as potential evidence for the PHDs slow reaction with O_2 (discussed further in **2.1**).[94] Other studies have investigated the tight binding of the metal bound water and hydrogen bond network formed with Thr387, *i.e.*, in some proposed mechanisms, O_2 would have to displace the Fe-coordinated water in the PHDs (**2.1**).[41,95] The insights have led to metazoan PHDs being termed 'O_2-sensors'.[40,55,77,82] As dissolved O_2 decreases in tissue under hypoxic conditions (SpO_2 <89%), the PHDs become less active, and leads to subsequent HIFα,β stabilization.[47,58]

Inhabitants living in high altitudes, such as Tibetans and Andeans natives, have adapted to their environment where O_2 is not as readily available as at closer to sea levels due to the partial pressure of these climates.[96,97] The mutations D4E and C127S in PHD2 are observed in the high-altitude populations, *i.e.*, specific mutations in the *N*-terminus of PHD2 have been identified.[93,94] The mutations lead to suppression of PHD2 activity and may be linked to an increased fitness for the hypoxic climates mediated through HIF stabilisation.[96,97] From a structural perspective, sequence variation between the PHD isoforms in the *N*-terminal extension to the DSBH fold, the β2-β3 finger loop, and the *C*-terminal helix may explain the adaptation of humans to different environments with various O_2-levels (**Figure 1-13**).

PHD2 contains a conserved *N*-terminal Zn(II)-binding Myeloid, Nervy, and DEAF-1 (MYND) domain and its function has not been clearly defined, but is likely to interact with the HIFα substrate and related cytoplasm packaging proteins, co-chaperone

protein p23 (p23) and peptidyl-prolyl *cis-trans* isomerase FKBP38 (FKBP38, also known as FKBP8).[98]

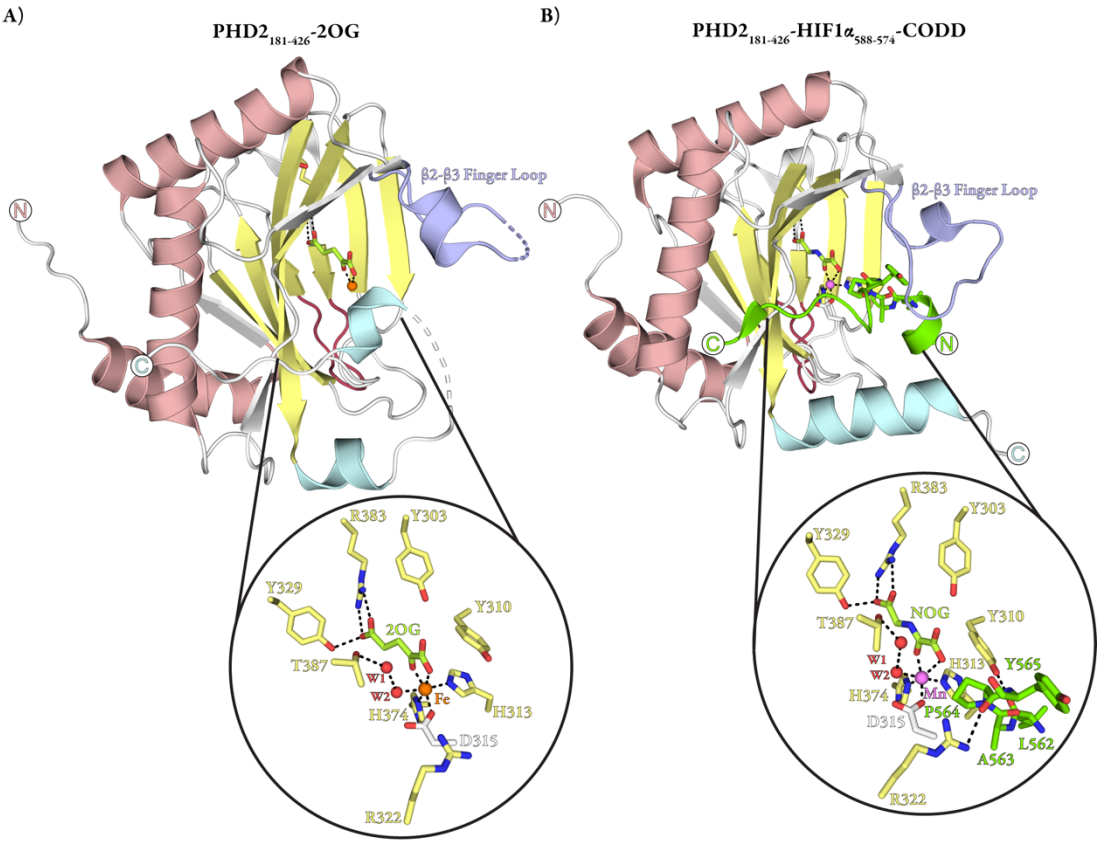


Figure 1-14| View from tPHD2$_{181-416/426}$ in Complex with 2OG and HIF1α$_{588-574}$-CODD. (A) PHD2$_{181-416}$ is complexed with 2OG (PDB: 3OUJ). (B) PHD2$_{181-426}$ is complexed with NOG and HIF1α-CODD peptide (PDB: 3HQR). (A-B) The DSBH (yellow), *N*-terminal extension (salmon), *C*-terminal extension (cyan), HIFα substrate (green), βIV-βV insert (red), and β2-β3 finger loop (blue) are highlighted. Active site residues (white/yellow), waters (red), and metal (Fe-orange and Mn-violet) are shown. Yellow residues are included in the DSBH. Key interactions are represented by dashes (black). Abbreviations: Prolyl hydroxylase isoform 2 (PHD2), Hypoxia-inducible factor *C*-terminal oxygen degradation domain (HIF1α-CODD), Double-stranded beta-helix (DSBH), 2-Oxoglutarate (2OG), *N*-Oxalylglycine (NOG). PDB: 3OUJ, 3HQR.

Both p23 and FKBP38 are reported to be involved in the HSP90 pathway.[62,96,99,100] The β2-β3 finger loop has been shown through solution NMR and crystallographic studies to be involved in substrate binding.[42,90] The labile β2-β3 finger loop has been observed to close over and interacts with the HIFα substrate once bound (**Figure 1-14B**, PDB: 3HQR).[41] The variation in the loop region between the PHDs may provide an explanation for difference in reported substrate specificity between the isoforms (**Figure 1-14**).[42]

Although there are no reported structures of PHD3, to date, the key active site residues are conserved, evidence by sequence alignment. Future structural data may elucidate subtle features of PHD catalysis and variation between the PHD1-3 that may aid the discovery of novel PHD isoform-selective inhibitors.

1.4 Medicinal Chemistry Approaches for PHD Inhibition

Co(II) was used as a medicine to promote erythropoiesis long before the discovery of the PHDs.[101] Fe(II) antagonists, such as Co(II), Cu(II), and Ni(II), are PHD inhibitors because the PHDs require a single Fe(II)-cofactor for catalysis (**Figure 1-15A-B**).[102,103] Furthermore, Fe-chelators (*e.g.,* deferoxamine [104] and 1,10-phenanthroline[105]) inhibit the PHDs *via* sequestration of available Fe ions. However, due to the importance of Fe bioavailability, use of the chelators as a therapeutic agents would likely dysregulate other Fe-dependent pathways and potentially lead to toxicities.[102]

The 2OG binding pocket of the PHDs is 'tight' relative to many other human 2OG oxygenases, especially with HIFα-substrates bound, as evidenced by computational and crystallographic studies.[41,92,94] The active site of the PHDs contain many hydrophobic and polar residues that are potentially involved in the O_2-diffusion into the PHDs (displayed as magenta lines in **Figure 1-15**).[37,41,82]

As the PHDs are 2OG-dependent enzymes, analogues, and derivatives of 2OG were explored as inhibitors (**Figure 1-16**). Most clinical therapeutics currently in the late-stage/approved are 2OG derivatives. Initially, *N*-oxalylglycine (NOG)[106] and the related cell-penetrating pro-drug dimethyloxalylglycine (DMOG, **3**)[107] were both designed as 2OG mimetics to bind in an analogous mode to the PHDs (**Figure 1-16A**).[102]

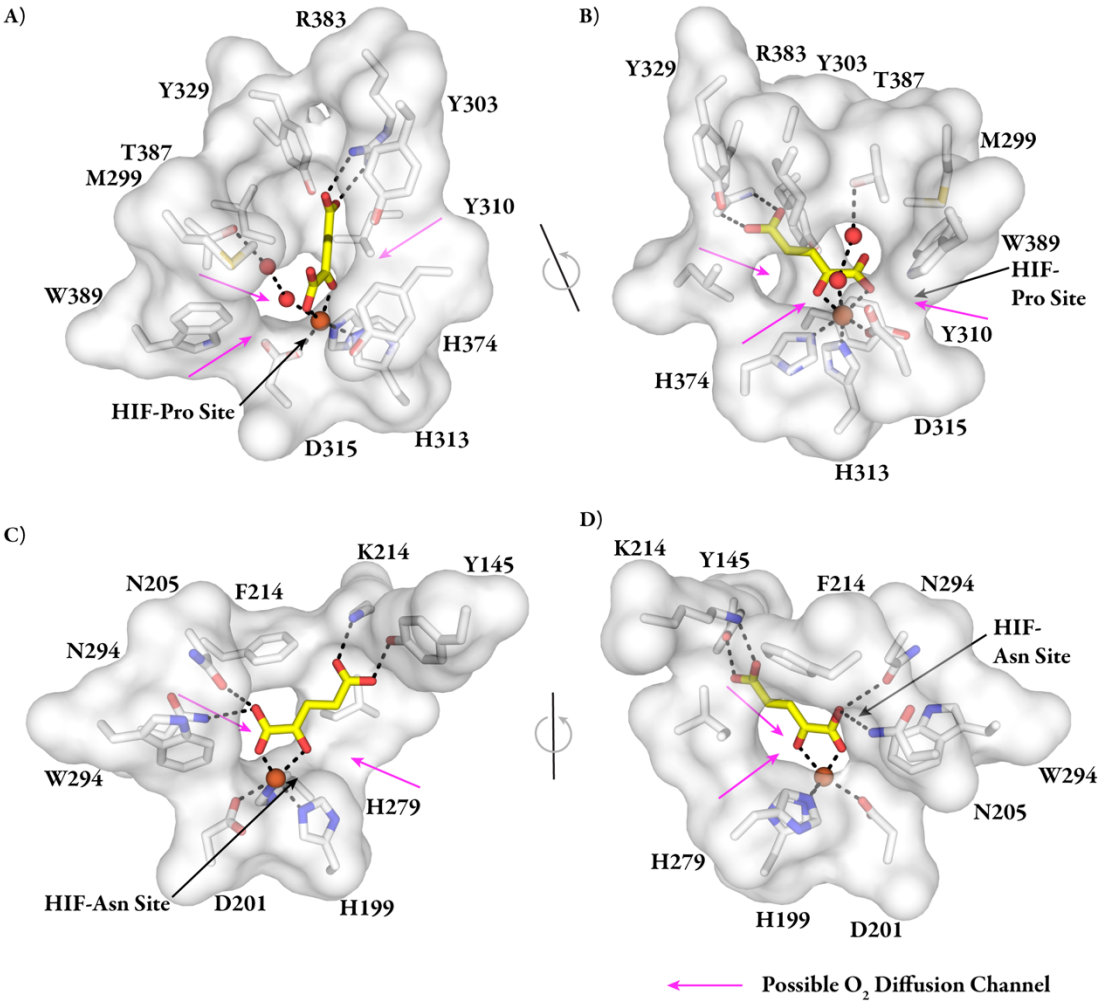


Figure 1-15| Comparison of the 2OG Binding Pockets of tPHD2 and FIH. (A-B) The 2OG binding pocket of PHD2 with the active site residues displayed with surface representation, waters (red), and metal (Fe, orange) (PDB: 3OUJ). (A) 1st orientation represents the HIF1α-ODD proline binding pocket. (B) 2nd orientation highlights the proposed O_2 diffusion pathway (PDB: 3OUJ). (C-D) The 2OG binding pocket of FIH with the active site residues shown in the electron cloud and metal (Fe, orange) (PDB: 1MZF). (C) 1st orientation represents the HIF1α-CAD asparagine binding pocket (PDB: 1MZF). (D) 2nd orientation highlights a potential FIH O_2 diffusion route (PDB: 1MZF). Abbreviations: 2-Oxoglutarate (2OG), Truncated prolyl hydroxylase isoform 2 (tPHD2), Factor-inhibiting HIF (FIH), Hypoxia-inducible factor isoform 1α (HIF1α), *C*-terminal oxygen degradation domain (CODD), *C*-terminal activation domain (CAD). PDB: 3OUJ, 1MZF.

Both the C1 carboxylate and C2 ketone of 2OG bind to Fe with a bidentate chelation mode (**Figure 1-15**, PDB: 3OUJ).[108] The C5 carboxylate is buried further into the active site and forms a salt-bridge with the guanidino group of $Arg383_{PHD2}$ and hydrogen bonds with $Tyr329_{PHD2}$ phenolic OH (**Figure 1-15A-B**, PDB: 3OUJ).[108] In FIH the C5 carboxylate of 2OG interacts with $Lys214_{FIH}$ and $Tyr145_{FIH}$ (**Figure 1-15C-D**, PDB: 1MZF).[34]

In some cases, dual inhibition of both PHDs and FIH may be advantageous to activate a subset of HIF regulated gene clusters (*e.g.*, complete induction of *CA9*, *ADM*, *EGLN3*, and *HK2* genes requires the inhibition of both PHDs and FIH that leads to a varied response to hypoxia).[109] Though, as the active site differs substantially between the two sub-families of enzymes, a very good inhibitor would achieve PHD isoform-selective inhibition and limit the off-target effects as a result of inhibition of other 2OG-dependent oxygenases.[17,19,110] Currently, there are three major classes of inhibitors of the PHDs that were first classified in Joharapurkar *et al.*, 2018: (i) carboxylic acid-based inhibitors working by Fe(II) chelation and 2OG competition, (ii) non-carboxylic acid-based inhibitors working by Fe(II) chelation and 2OG competition, and (iii) non-conventional inhibitors (*i.e.*, those with a different mode of inhibition) .[102,111]

1.4.1 Carboxylic Acid-Based PHD Inhibitors

The bicyclic isoquinolines (**4**) were established CPHs inhibitors, and subsequently further developed as PHD inhibitors.[112,113] The inhibitors contain a glycinamide sidechain linked to the isoquinoline bicyclic core scaffold (**Figure 1-16B**).[102] In the quinolone (**5**)[114] and monocyclic pyridine (**6**)[115] scaffolds, the ring carbonyl oxygen and the glycinamide carbonyl group, respectively, can coordinate the Fe-centre.[102,111] The carboxylic acid-based inhibitors were diversified to include 5,6-membered bicyclic (**7** and **9**) and tricyclic (**7**-**8**) ring scaffolds.[102,116] Most carboxylic acid containing PHD inhibitors use a glycinamide sidechain moiety linked to the heterocyclic ring that interacts with the 2OG binding $Arg383_{PHD2}$ and $Tyr329_{PHD2}$ (**Figure 1-15A**).[102,111] Researchers from GlaxoSmithKline Plc. (GSK) have reported a series of benzimidazole derivatives (**7**-**8**), which manifest replacement of the isoquinoline phenolic OH revealing an alternative binding mode to the PHDs.[102,111]

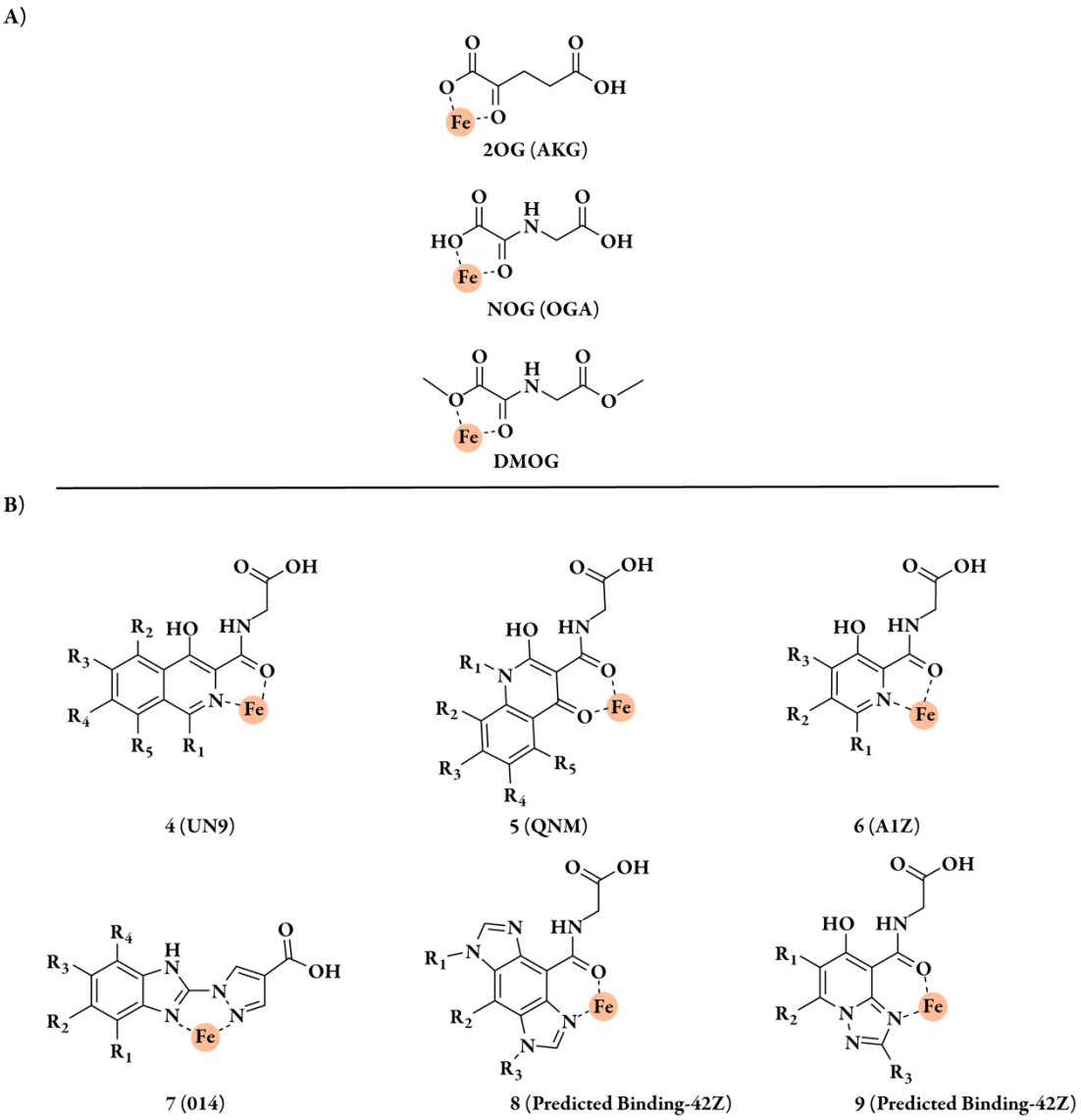


Figure 1-16| Core Scaffolds of 2OG Derived Carboxylic Acid-Based PHD Inhibitors. (A) 2OG is depicted with NOG and DMOG mimetics. (B) Core Scaffolds of bicyclic, tricyclic, and monocyclic carboxylic acid-based 2OG derivatives. Abbreviations: 2-Oxoglutarate (2OG), *N*-Oxalylglycine (NOG), Dimethyloxalylglycine (DMOG). PDB: UN9, QNM, A1Z, 014, and 42Z.

Researchers from Johnson and Johnson Ltd. have reported a co-crystal structure of a benzimidazole derivatives of **7** that revealed an electrostatic interaction between the phenolic OH sidechain of $Tyr303_{PHD2}$ with the NH of the imidazole ring (PDB: 3OUI).[108,117] The presence of the pyrazole ring is reported to help provide strong Fe chelation (**7**).[118] A series of quinazolines, with an incorporated carbonyl following ring expansion of the benzimidazole core (**7**), to enable a hydrogen bond interaction with $Tyr303_{PHD2}$.

The multiple 2OG-mimicking PHD inhibitors have employed a carboxylate-based/glycinamide containing sidechain as a pharmacophore for binding and inhibition highlighting its utility.[102,111,117] Subtle changes to the ligand scaffolds through crystallographic observations illustrate the unique tightness of the PHDs active site compared to other 2OG oxygenases.[37,108,110,119,120]

An example of a high-throughput screen (HTS) on the PHDs comes from work by Bayer AG, which conducted an HTS to discover a small-molecule hits for the PHDs (see **1.4.2**). The identified hit was later developed into BAY 85-3934, also known as Molidustat (**20**).[112,113] The triazole-containing compounds are distinct from many PHD inhibitors as they lack a carboxylic acid sidechain, *i.e.*, they are part of the class of non-carboxylic acid-based PHD inhibitors.[121,122]

1.4.2 Non-Carboxylic Acid-Based PHD Inhibitors

The HTS of the PHDs yielded three different series of non-carboxylic based PHD inhibitors (work conducted by Merck KGaA, GSK, and Bayer AG **Figure 1-17**).[102,111] HTS hits identified pyrazole-hydroxypyrimidine (**10**,)[123] and spiroindolone (**11**)[124] scaffolds as potent PHD inhibitors.[102,111] The pyrazole-hydroxypyrimidine (**10**) series chelates Fe *via* the two nitrogen atoms of the heterocyclic rings in a bidentate manner.[102,111] The spiroindolone (**11**) and spiroazaindoles derivative were found to require the 2-pyridylmethyl moiety for potency.[125] Merck further optimised the pyrazole-pyrimidine series through the incorporation of a pyridazine ring in replacement of the pyrazole (**12**).[126]

The GSK quinazoline series (**13**) contains a pyrimidinedione core fused to a *N*3-azaheterocycle.[102,127,128] The Fe binding atoms are likely the pyrimidinedione N1 and

keto-O atoms (**13**).[102,127,128] However, the fused pyrimidinedione-thiophene ring likely coordinates Fe *via* the keto-O and thiol-S atoms (**14**).

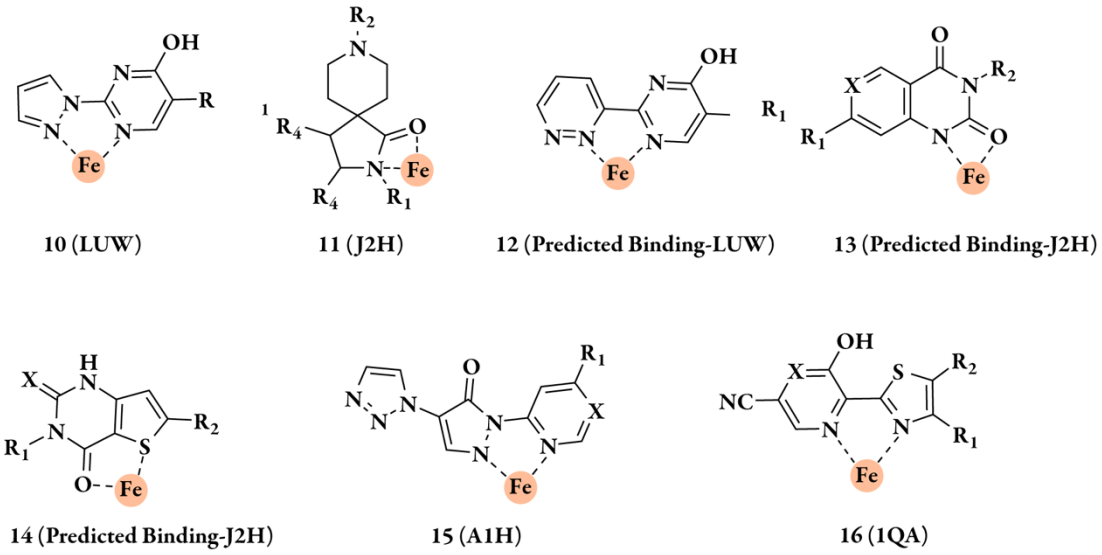


Figure 1-17 | Core Scaffolds of Non-Carboxylic Acid-Containing PHD Inhibitors. Core scaffolds of PHD inhibitor classes lacking the carboxylic acid/glycinamide sidechain moiety. Abbreviations: Prolyl hydroxylase domain (PHD). PDB: LUW, J2H, A1H, and 1QA.

Bayer AG have reported a class of potent triazole based PHD inhibitors with a pyrazolone-pyrimidine core with analogues that contain a pyridine ring in substitution for the pyrimidine (**15**).[121,122] The triazole based scaffold was of significant interest as the triazole sidechain is a reported bioisostere of carboxylic acids.[129] Thus, the triazole was considered and validated as an very good substitute of the 2OG-derived carboxylic acid-based inhibitors.[119,122] Another non-carboxylic acid core scaffold, the thiazole-hydroxypyrimidines (**16**), was reported by Crystal Genomics, Inc. as a series of PHD inhibitors.[130] The cyano group was determined to be a key pharmacophore for PHD2 inhibition *via* predicted interaction with active site residues $Tyr329_{PHD2}$ and $Arg383_{PHD2}$; the differs with the nitrile of Takeda-17 (**17**, **1.4.3**, Figure 1-18) which interacts with the sidechain of Asn331 (PDB: 5V18, discussed in **3.2.4.2**).[102,130,131] The thiazole-hydroxypyrimidines bind to Fe with both nitrogen heterocyclic atoms as evidence by a reported co-crystal structure of $tPHD2_{184-419}$ with a related analogue (PDB: 4KBZ).[102,130,131]

Non-carboxylic acid-based small-molecule inhibitors add another dimension in the design and optimisation of novel PHD inhibitors. Compounds lacking the charge polarity induced by the carboxylate have been shown to cross the blood-brain-barrier (BBB) and inhibit the PHDs in a brain tissue-model as a potential utility to treat CNS related disorders.[119,132]

1.4.3 Non-Conventional PHD Inhibitors

There are several other classes of PHD inhibitors that do not fall into the two described classes (**Figure 1-18**). One example is the novel monodentate Fe binding 5,6-bicyclic heteroaryl triazolopyridine inhibitor of the PHDs, also known as Takeda-17 (**17**) (designed by Takeda Pharmaceuticals Co. Ltd.).[132] The reported half-maximal inhibitory concentration (IC_{50}) values of the triazolopyridine inhibitor **17** imply a isoform-selective-manner of inhibition, with a lower reported IC_{50} for PHD1 compared to PHD2-3.[132] The triazolopyridine coordinates the active site metal *via* the N1 atom in a monodentate mode of inhibition, as evidenced by two crystal structures of $PHD1_{167\text{-}403}$ (PDB: 5V1B) and $PHD2_{181\text{-}416}$ (PDB: 5V18) in complex with **17**.[132] The N3 atom exhibits a water mediated interaction with the phenolic OH of $Tyr313_{PHD1}$ and $Tyr329_{PHD2}$ (**Figure 1-18**).[132] Structure activity relationship (SAR) showed a preference for a 4-CN group that forms an electrostatic interaction with $Asn315_{PHD1}$ and $Asn331_{PHD2}$.[102,132] The phenyl ring of **17** forms a π-π stacking interaction with $Tyr287_{PHD1}$ and $Tyr303_{PHD2}$.[102,132]

Previous work in the Schofield group has led to the diacylhydrazines (**18**) series of 'dual-action' inhibitors of the prolyl hydroxylases. The diacylhydrazines (**18**) function by Fe-centre chelation/2OG competition and by inducing binding of a second Fe ion at the active site, *i.e.*, the 'dual-action'.[133]

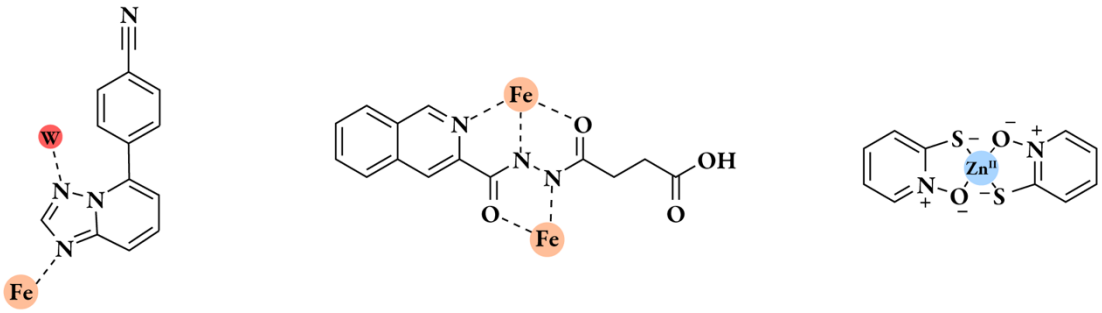


Figure 1-18| Non-Conventional PHD Inhibitors. Core scaffolds and inhibitors of the PHDs with novel binding modes; monodentate coordination (**17**) and reported allosteric inhibition (**19**). Abbreviations: Prolyl hydroxylase (PHD). PDB: 8UY, and 2JP.

18 exemplified a strong non-specific chelation affinity for tPHD2 bound Fe, with binding of a second Fe observed *via* mass spectrometry analysis.[133] An inhibitor bound with two Fe ions in tPHD2 may be vulnerable to oxidation. **18** inhibited tPHD2 with an IC_{50} of 18.4 μM.[133]

The Korean Institute of Technology conducted a screen of 1040 FDA-approved drugs and bioactive compounds with the PHDs, which led to the discovery of a Zn(II) bound small-molecule, known as pyrithione zinc (**19**).[102,134] It has been previously approved as a microbicidal agent, **19** has been reported to inhibit PHD3 at 0.98 μM IC_{50} and >1 mM IC_{50} for tPHD2; although its mode of inhibition is not known.[102,134]

Similar to the non-carboxylic acid-based inhibitors, the Takeda compounds (**17**) and small-molecules such as/or related to **19** may provide a starting point for solutions to obtain future isoform-selective PHD inhibitors that display a good profile and utility as therapies to target various tissue-specific diseases and disorders.

1.4.4 Clinically Used PHD Inhibitors

1.4.4.1 Overview and Perspective of PHD Clinical Therapeutics

Several PHD inhibitors have recently been approved for clinical use and some other candidates are in the late-stage of clinical trials for treatment of chronic kidney disease (CKD) associated anaemia (**Figure 1-19**).[135]

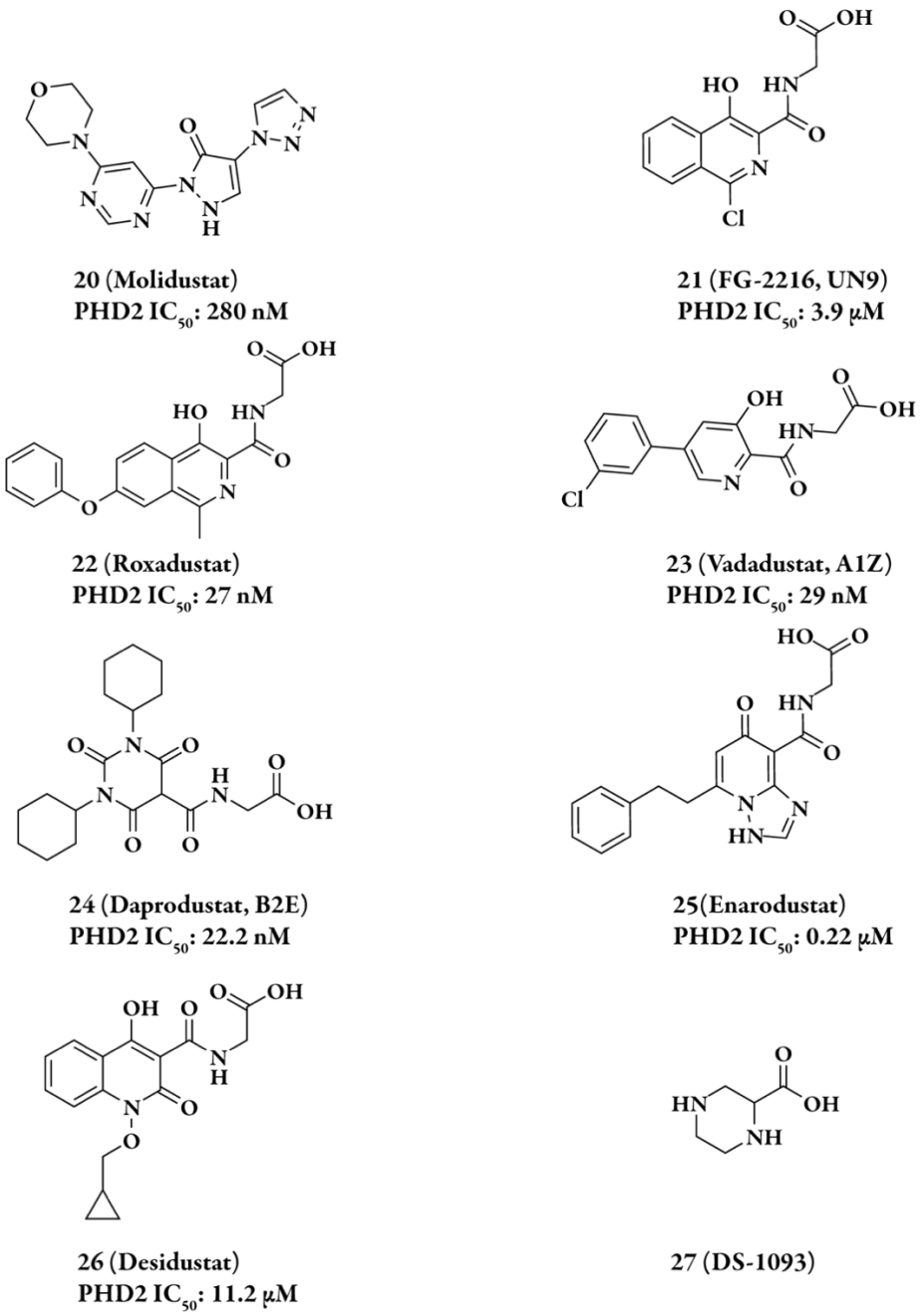


Figure 1-19| Clinically Applied Small-Molecule PHD Inhibitors. Structures of PHD inhibitors approved for clinical use, in late-stage development, or which have been discontinued**.** Abbreviations: Prolyl hydroxylase (PHD).

Molidustat (**20**, Bayer AG) is member of the major non-carboxylic acid-based class of PHD-selective inhibitors.[121,122] **20** has been approved in Japan (January 2021) for clinical use (trade name: Musredo®).[136] **20** has displayed a good bioavailability and potency of PHD1-3 with reported IC_{50} values of 480 nM, 280 nM, and 450 nM, respectively. Previous members of the Schofield group have shown that **20** manifests an IC_{50} value of 3 nM for the catalytic domain $PHD2_{181-426}$ in an *in vitro* assay.[110]

Roxadustat (**22**, formerly FG-4592; Fibrogen Inc.) is a member of the major carboxylic acid-based PHD selective inhibitors. **22** was first in class of PHD inhibitor to be approved for clinical use in China (trade name: Ai Rui Zhuo®)[137], Japan (trade name: Evrenzo®),[138] and Chile. Recently the Federal Drug Administration (FDA, USA) did not approve **22** for use, requiring additional clinical studies to be conducted.[139] **22** was derived from the initial clinical candidate, FG-2216 (**21**), that was discontinued due to safety concerns. **22** contains an isoquinoline core with a glycinamide sidechain and additional 7-phenoxy sidechain incorporated (**21**).[102,111,140,141] Previous studies determined an IC_{50} value of **22** for tPHD2 at 27 nM.[110] **22** has shown to increase and maintain haemoglobin levels in individuals with CKD.[142] Increases in EPO levels and decreases in hepcidin are observed without reported tumorigenic initiation, progression, or metastasis in a VEGF-sensitive breast cancer model.[142,143]

Vadadustat (**23**, formerly AKB-6548; invented by Proctor and Gamble Co. and licensed to Akebia Therapeutics Inc.) is also member of the carboxylic acid-based PHD inhibitors and is approved in Japan for clinical use (trade name Vafseo®).[135] Solution studies of tPHD2 reported an IC_{50} of 29 nM for **23**.[110] Observations from the clinical trials have exhibited the ability of **23** to upregulate haemoglobin and EPO levels without effecting blood pressure or VEGF levels.[144,145]

Daprodustat (**24**, formerly GSK1278863; GSK) is approved in Japan (trade name Duvroq®).[135] **24** contains the common glycinamide sidechain and is a member of the major carboxylic acid-based PHD inhibitors.[102,111] The core scaffold is a pyrimidine-trione.[102,111] Inhibition data of PHD1-3 with **24** reported IC_{50} values of 3.5 nM, 22.2 nM, and 5.5 nM, respectively.[146] Data from the pre-clinical studies has shown good bioavailability and low blood clearance for **24** administered *in vivo*.[146] Furthermore, **24** has displayed dose-dependent regulation of haemoglobin and EPO levels. Although, cardiac repolarisation and gastrointestinal events have been recorded.[147]

Enarodustat (**25**, formerly JTZ-951; discovered by Japan Tobacco Inc. and licensed to Shenzhen Salubris Pharmaceuticals Co., Ltd.) is a member of the carboxylic acid-based PHD inhibitors, and has been approved for clinical use in Japan (ENAROY®).[148,149] Due to cellular permeability issues with a precursor analogue, a lipophilic 2-phenylethyl substituent was added to the benzimidazole core, which reported an IC_{50} value of 0.22 μM for tPHD2.[102,149] **25** displayed good preclinical characteristics with nominal bioavailability and solubility in the *in vivo* models.[149] Data from a clinical trial shows that **25** is effective in maintaining haemoglobin levels in a dose-dependent manner with associated decreases in hepcidin and ferritin.[150]

Desidustat (**26**, formerly ZYAN-1; Cadila Healthcare Ltd.) is one of the carboxylic acid-based class of PHD inhibitors and is in Phase III clinical trials in India.[151,152] **26** contains a *N*-alkoxyquinolone core ring.[102] Preclinical studies indicated **26** as a candidate to treat both chemotherapy-induced anaemia and CKD-associated anaemia with a reported IC_{50} value of 11.2 μM for tPHD2.[102,152] Phase II studies reported an increase haemoglobin levels compared to placebo in a dose-dependent manner upon administration of **26**.[152–154]

DS-1093 (**27**; Daiichi Sankyo Ltd.) is the final reported carboxylic acid-based PHD inhibitor to reach clinical trials.[111,135] At the end of Phase I trials the company discontinued the development of **27** as a treatment for CKD related anaemia.[111,135]

1.4.4.2 Structural Characterisation of Clinically Applied Inhibitors in Complex with tPHD2

The first tPHD2-isoquinoline complex structures were reported by a group at Procter and Gamble Co. and from current group members (PDB: 2HBT and 2G1M, respectively.[37,155] Based on the crystallographic evidence, the bicyclic inhibitors bound to the active site Fe *via* a bidentate mode analogous to 2OG and **2**-**3**.[37,155] The heterocyclic nitrogen and the glycinamide sidechain carbonyl oxygen atoms coordinate the Fe-centre (**4**).[37,108,155] The glycinamide carboxylate is positioned to form a salt-bridge with the guanidinium moiety of $Arg383_{PHD2}$ and a hydrogen bond with the phenolic OH of $Tyr329_{PHD2}$ in the 2OG pocket, similar to the C5 carboxylate of 2OG (PDB: 3OUJ).[37,108,155] Other characteristics of the glycinamide-containing inhibitors are the π-π-stacking interaction between the phenolic sidechain of $Tyr310_{PHD2}$ and the hydrogen bond between $Tyr303_{PHD2}$-4-phenolic sidechain of the core isoquinoline ring.[37,155]

Vadadustat (**23**) contains a monopyridine core and has a glycinamide sidechain.[102,111] A structure has been reported for the complex of **23** and $tPHD2_{181-426}$ (PDB: 5OX6), which reveals that the inhibitor binds Fe *via* its pyridine N1 nitrogen and glycinamide carbonyl oxygen.[110] The glycinamide carboxylate of **23** forms a salt-bridge interaction with the guanidinium sidechain of Arg383, as seen with other compounds in the class.[110] A crystal structure of $PHD2_{181-426}$ with a **24** related analogue (CCT6, PDB: 5OX5) was reported by previous Schofield group members.[110] CCT6 was observed to chelate the metal *via* the heterocyclic carbonyl oxygen and the carbonyl oxygen of the glycinamide sidechain.[110] Currently, there are no reported crystal structures of the PHDs

in complex with **22**. Based on previous work, it is likely the phenoxy sidechain of **22** interferes with ordered crystal packing of the PHDs due to ligand induced heterogeneous conformations. The piperazine-carboxylate based compound, **27**, likely chelates the metal *via* the N1 of the piperazine and carbonyl oxygen. Currently, there are no reported crystal structures of **27** with the PHDs. Due to the polarity of the glycinamide sidechain, the inhibitors cannot pass the BBB and are often targeted for degradation once administered.[156]

Molidustat (**20**), a member of the non-carboxylic acid class, has four contiguous rings with a triazole based sidechain moiety.[121,122] The metal chelating residues, evidenced by a crystal structure of $PHD2_{181-426}$ with a related acid-based analogue (PDB: 5A3U), are the NH nitrogen of the pyrazolone and N1 atom of the pyrimidine rings.[119] Further studies should be aimed at structurally characterising more of the PHD clinically relevant inhibitors.

1.5 Research Objectives of the Work Described in this Thesis

The first objective of the work presented in this thesis was to further understand the catalytic mechanism of the PHDs, in particular the catalysis by tPHD2, principally through crystallographic studies. The second objective was to develop a novel structure guided approach to inhibitor design using a robust crystallisation system for use in co-crystallisation, crystal soaking, and XChem fragment-based screening.[157,158]

Specific Research Aims

1. *Develop a robust tPHD2-HIFα-substrate crystallisation system for mechanistic studies.*
2. *Develop a co-crystallisation system to obtain further tPHD2-inhibitor complexes.*
3. *Develop a soaking-based condition for tPHD2 crystals to be used for XChem fragment-based and other small-molecule screening.*

It was envisaged that results from the work presented here may one day, in part, aid the field in specific understanding of the PHDs from a mechanistic and structural perspective. It was also envisaged that the tPHD2 complex structures may be useful in structure-guided development of isoform-selective inhibitors that could potentially regulate the PHDs in a tissue-specific manner.

1.6 References

(1) Prockop, D.; Kaplan, A.; Udenfriend, S. Oxygen-18 Studies on the Conversion of Proline to Hydroxyproline. *Biochemical and Biophysical Research Communications* **1962**, *9* (1–2), 162–166. https://doi.org/10.1016/0006-291X(62)90107-9.

(2) Udenfriend, S. Formation of Hydroxyproline in Collagen. *Science* **1966**, *152* (3727), 1335–1340. https://doi.org/10.1126/science.152.3727.1335.

(3) Cardinale, G. J.; Rhoads, R. E.; Udenfriend, S. Simultaneous Incorporation of 18O into Succinate and Hydroxyproline Catalyzed by Collagen Proline Hydroxylase. *Biochemical and Biophysical Research Communications* **1971**, *43* (3), 537–543. https://doi.org/10.1016/0006-291X(71)90647-4.

(4) Hutton, J. J.; Tappel, A. L.; Udenfriend, S. Requirements for α-Ketoglutarate, Ferrous Ion and Ascorbate by Collagen Proline Hydroxylase. *Biochemical and Biophysical Research Communications* **1966**, *24* (2), 179–184. https://doi.org/10.1016/0006-291X(66)90716-9.

(5) Hutton, J. J.; Kaplan, A.; Udenfriend, S. Conversion of the Amino Acid Sequence Gly-Pro-Pro in Protein to Gly-Pro-Hyp by Collagen Proline Hydroxylase. *Archives of Biochemistry and Biophysics* **1967**, *121* (2), 384–391. https://doi.org/10.1016/0003-9861(67)90091-4.

(6) Cardinale, G. J.; Udenfriend, S. Prolyl Hydroxylase. In *Advances in Enzymology and Related Areas of Molecular Biology*; John Wiley & Sons, Ltd, 2006; Vol. 41, pp 245–300. https://doi.org/10.1002/9780470122860.ch6.

(7) Counts, D. F.; Cardinale, G. J.; Udenfriend, S. Prolyl Hydroxylase Half Reaction: Peptidyl Prolyl-Independent Decarboxylation of α-Ketoglutarate. *Proceedings of the National Academy of Sciences of the United States of America* **1978**, *75* (5), 2145–2149. https://doi.org/10.1073/pnas.75.5.2145.

(8) Hayaishi, O.; Katagiri, M.; Rothberg, S. Studies on Oxygenases; Pyrocatechase. *Journal of Biological Chemistry* **1957**, *229* (2), 905–920. https://doi.org/10.1016/S0021-9258(19)63695-1.

(9) Wang, Y.; Li, J.; Liu, A. Oxygen Activation by Mononuclear Nonheme Iron Dioxygenases Involved in the Degradation of Aromatics. *Journal of Biological Inorganic Chemistry* **2017**, *22* (2–3), 395–405. https://doi.org/10.1007/s00775-017-1436-5.

(10) Mason, H. S. Mechanisms of Oxygen Metabolism. *Science* **1957**, *125* (3259), 1185–1188. https://doi.org/10.1126/science.125.3259.1185.

(11) Raven, E. L. A Short History of Heme Dioxygenases: Rise, Fall and Rise Again. *Journal of Biological Inorganic Chemistry* **2017**, *22* (2–3), 175–183. https://doi.org/10.1007/s00775-016-1412-5.

(12) Hayaishi, O.; Katagiri, M.; Rothberg, S. Communications to the Editor: Mechanism of the Pyrocatechase Reaction. *Journal of the American Chemical Society* **1955**, *77* (20), 5450–5451. https://doi.org/10.1021/ja01625a095.

(13) Mason, H. S.; Fowlks, W. L.; Peterson, E. Oxygen Transfer and Electron Transport by the Phenolase Complex. *Journal of the American Chemical Society* **1955**, *77* (10), 2914–2915. https://doi.org/10.1021/ja01615a088.

(14) Fujimoto, D.; Tamiya, N. Incorporation of 18O from Air into Hydroxyproline by Chick Embryo. *Biochemical Journal* **1962**, *84* (2), 333–335. https://doi.org/10.1042/bj0840333.

(15) Posner, H. S.; Mitoma, C.; Rothberg, S.; Udenfriend, S. Enzymic Hydroxylation of Aromatic Compounds. III. Studies on the Mechanism of Microsomal

Hydroxylation. *Archives of Biochemistry and Biophysics* **1961**, *94* (2), 280–290. https://doi.org/10.1016/0003-9861(61)90042-X.

(16) Roach, P. L.; Clifton, I. J.; Fülöp, V.; Harlos, K.; Barton, G. J.; Hajdu, J.; Andersson, I.; Schofield, C. J.; Baldwin, J. E. Crystal Structure of Isopenicillin N Synthase Is the First from a New Structural Family of Enzymes. *Nature* **1995**, *375* (6533), 700–704. https://doi.org/10.1038/375700a0.

(17) Rose, N. R.; McDonough, M. A.; King, O. N. F.; Kawamura, A.; Schofield, C. J. Inhibition of 2-Oxoglutarate Dependent Oxygenases. *Chem. Soc. Rev.* **2011**, *40* (8), 4364–4397. https://doi.org/10.1039/C0CS00203H.

(18) Flashman, E.; Schofield, C. J. The Most Versatile of All Reactive Intermediates? *Nature Chemical Biology* **2007**, *3* (2), 86–87. https://doi.org/10.1038/nchembio0207-86.

(19) Islam, Md. S.; Leissing, T. M.; Chowdhury, R.; Hopkinson, R. J.; Schofield, C. J. 2-Oxoglutarate-Dependent Oxygenases. *Annual Review of Biochemistry* **2018**, *87* (1), 585–620. https://doi.org/10.1146/annurev-biochem-061516-044724.

(20) Rabe, P.; Kamps, J. J. A. G.; Schofield, C. J.; Lohans, C. T. Roles of 2-Oxoglutarate Oxygenases and Isopenicillin N Synthase in β-Lactam Biosynthesis. *Nat. Prod. Rep.* **2018**, *35* (8), 735–756. https://doi.org/10.1039/C8NP00002F.

(21) Tarhonskaya, H.; Szöllössi, A.; Leung, I. K. H.; Bush, J. T.; Henry, L.; Chowdhury, R.; Iqbal, A.; Claridge, T. D. W.; Schofield, C. J.; Flashman, E. Studies on Deacetoxycephalosporin C Synthase Support a Consensus Mechanism for 2-Oxoglutarate Dependent Oxygenases. *Biochemistry* **2014**, *53* (15), 2483–2493. https://doi.org/10.1021/bi500086p.

(22) Hausinger, R. P.; Herr, C. Q.; Hu, J. Nonheme Fe(II)- and 2-Oxoglutarate-Dependent Ethylene-Forming Enzyme. In *Encyclopedia of Inorganic and Bioinorganic Chemistry*; John Wiley & Sons, Ltd, 2019; pp 1–9. https://doi.org/https://doi.org/10.1002/9781119951438.eibc2703.

(23) Hausinger, R. P. Fe(II)/α-Ketoglutarate-Dependent Hydroxylases and Related Enzymes. *Critical Reviews in Biochemistry and Molecular Biology* **2004**, *39* (1), 21–68. https://doi.org/10.1080/10409230490440541.

(24) Matthews, M. L.; Neumann, C. S.; Miles, L. A.; Grove, T. L.; Booker, S. J.; Krebs, C.; Walsh, C. T.; Bollinger, J. M. Substrate Positioning Controls the Partition between Halogenation and Hydroxylation in the Aliphatic Halogenase, SyrB2. *Proceedings of the National Academy of Sciences* **2009**, *106* (42), 17723–17728. https://doi.org/10.1073/pnas.0909649106.

(25) Loenarz, C.; Schofield, C. J. Expanding Chemical Biology of 2-Oxoglutarate Oxygenases. *Nature Chemical Biology* **2008**, *4* (3), 152–156. https://doi.org/10.1038/nchembio0308-152.

(26) McDonough, M. A.; Loenarz, C.; Chowdhury, R.; Clifton, I. J.; Schofield, C. J. Structural Studies on Human 2-Oxoglutarate Dependent Oxygenases. *Current Opinion in Structural Biology* **2010**, *20* (6), 659–672. https://doi.org/10.1016/j.sbi.2010.08.006.

(27) Aik, W. S.; McDonough, M. A.; Thalhammer, A.; Chowdhury, R.; Schofield, C. J. Role of the Jelly-Roll Fold in Substrate Binding by 2-Oxoglutarate Oxygenases. *Current Opinion in Structural Biology* **2012**, *22* (6), 691–700. https://doi.org/10.1016/j.sbi.2012.10.001.

(28) Clifton, I. J.; McDonough, M. A.; Ehrismann, D.; Kershaw, N. J.; Granatino, N.; Schofield, C. J. Structural Studies on 2-Oxoglutarate Oxygenases and Related Double-Stranded β-Helix Fold Proteins. *Journal of Inorganic Biochemistry* **2006**, *100* (4), 644–669. https://doi.org/10.1016/j.jinorgbio.2006.01.024.

(29) Hewitson, K. S.; Granatino, N.; Welford, R. W. D.; McDonough, M. A.; Schofield, C. J. Oxidation by 2-Oxoglutarate Oxygenases: Non-Haem Iron Systems in Catalysis and Signalling. *Philosophical Transactions of the Royal Society A: Mathematical, Physical and Engineering Sciences* **2005**, *363* (1829), 807–828. https://doi.org/10.1098/rsta.2004.1540.

(30) Taabazuing, C. Y.; Fermann, J.; Garman, S.; Knapp, M. J. Substrate Promotes Productive Gas Binding in the α-Ketoglutarate-Dependent Oxygenase FIH. *Biochemistry* **2016**, *55* (2), 277–286. https://doi.org/10.1021/acs.biochem.5b01003.

(31) Sengoku, T.; Yokoyama, S. Structural Basis for Histone H3 Lys 27 Demethylation by UTX/KDM6A. *Genes and Development* **2011**, *25* (21), 2266–2277. https://doi.org/10.1101/gad.172296.111.

(32) Leung, I. K. H.; Krojer, T. J.; Kochan, G. T.; Henry, L.; von Delft, F.; Claridge, T. D. W.; Oppermann, U.; McDonough, M. A.; Schofield, C. J. Structural and Mechanistic Studies on γ-Butyrobetaine Hydroxylase. *Chemistry and Biology* **2010**, *17* (12), 1316–1324. https://doi.org/10.1016/j.chembiol.2010.09.016.

(33) Tars, K.; Rumnieks, J.; Zeltins, A.; Kazaks, A.; Kotelovica, S.; Leonciks, A.; Sharipo, J.; Viksna, A.; Kuka, J.; Liepinsh, E.; Dambrova, M. Crystal Structure of Human Gamma-Butyrobetaine Hydroxylase. *Biochemical and Biophysical Research Communications* **2010**, *398* (4), 634–639. https://doi.org/10.1016/j.bbrc.2010.06.121.

(34) Dann, C. E.; Bruick, R. K.; Deisenhofer, J. Structure of Factor-Inhibiting Hypoxia-Inducible Factor 1: An Asparaginyl Hydroxylase Involved in the Hypoxic Response Pathway. *Proceedings of the National Academy of Sciences of the United States of America* **2002**, *99* (24), 15351–15356. https://doi.org/10.1073/pnas.202614999.

(35) Elkins, J. M.; Hewitson, K. S.; McNeill, L. A.; Seibel, J. F.; Schlemminger, I.; Pugh, C. W.; Ratcliffe, P. J.; Schofield, C. J. Structure of Factor-Inhibiting Hypoxia-Inducible Factor (HIF) Reveals Mechanism of Oxidative Modification of HIF-1α. *Journal of Biological Chemistry* **2003**, *278* (3), 1802–1806. https://doi.org/10.1074/jbc.C200644200.

(36) Öster, L. M.; van Scheltinga, A. C. T.; Valegård, K.; Hose, A. M. K.; Dubus, A.; Hajdu, J.; Andersson, I. Conformational Flexibility of the C Terminus with Implications for Substrate Binding and Catalysis Revealed in a New Crystal Form of Deacetoxycephalosporin C Synthase. *Journal of Molecular Biology* **2004**, *343* (1), 157–171. https://doi.org/10.1016/j.jmb.2004.07.049.

(37) McDonough, M. A.; Li, V.; Flashman, E.; Chowdhury, R.; Mohr, C.; Liénard, B. M. R.; Zondlo, J.; Oldham, N. J.; Clifton, I. J.; Lewis, J.; McNeill, L. A.; Kurzeja, R. J. M.; Hewitson, K. S.; Yang, E.; Jordan, S.; Syed, R. S.; Schofield, C. J. Cellular Oxygen Sensing: Crystal Structure of Hypoxia-Inducible Factor Prolyl Hydroxylase (PHD2). *Proceedings of the National Academy of Sciences of the United States of America* **2006**, *103* (26), 9814–9819. https://doi.org/10.1073/pnas.0601283103.

(38) Brasnett, A.; Pfeffer, I.; Brewitz, L.; Chowdhury, R.; Nakashima, Y.; Tumber, A.; McDonough, M. A.; Schofield, C. J. Human Oxygenase Variants Employing a Single Protein Fe(II) Ligand Are Catalytically Active. *Angewandte Chemie - International Edition* **2021**, *60* (26), 14657–14663. https://doi.org/10.1002/anie.202103711.

(39) Scotti, J. S.; Leung, I. K. H.; Ge, W.; Bentley, M. A.; Paps, J.; Kramer, H. B.; Lee, J.; Aik, W.; Choi, H.; Paulsen, S. M.; Bowman, L. A. H.; Loik, N. D.; Horita, S.;

Ho, C. H.; Kershaw, N. J.; Tang, C. M.; Claridge, T. D. W.; Preston, G. M.; McDonough, M. A.; Schofield, C. J. Human Oxygen Sensing May Have Origins in Prokaryotic Elongation Factor Tu Prolyl-Hydroxylation. *Proceedings of the National Academy of Sciences of the United States of America* **2014**, *111* (37), 13331–13336. https://doi.org/10.1073/pnas.1409916111.

(40) Lippl, K.; Boleininger, A.; McDonough, M.; Abboud, M. I.; Tarhonskaya, H.; Chowdhury, R.; Loenarz, C.; Schofield, C. J. Born to Sense: Biophysical Analyses of the Oxygen Sensing Prolyl Hydroxylase from the Simplest Animal Trichoplax Adhaerens. *Hypoxia* **2018**, *6*, 57–71. https://doi.org/10.2147/hp.s174655.

(41) Chowdhury, R.; McDonough, M. A.; Mecinović, J.; Loenarz, C.; Flashman, E.; Hewitson, K. S.; Domene, C.; Schofield, C. J. Structural Basis for Binding of Hypoxia-Inducible Factor to the Oxygen-Sensing Prolyl Hydroxylases. *Structure* **2009**, *17* (7), 981–989. https://doi.org/10.1016/j.str.2009.06.002.

(42) Chowdhury, R.; Leung, I. K. H.; Tian, Y. M.; Abboud, M. I.; Ge, W.; Domene, C.; Cantrelle, F. X.; Landrieu, I.; Hardy, A. P.; Pugh, C. W.; Ratcliffe, P. J.; Claridge, T. D. W.; Schofield, C. J. Structural Basis for Oxygen Degradation Domain Selectivity of the HIF Prolyl Hydroxylases. *Nature Communications* **2016**, *7* (1), 12673. https://doi.org/10.1038/ncomms12673.

(43) Feng, C.; Liu, Y.; Wang, G.; Deng, Z.; Zhang, Q.; Wu, W.; Tong, Y.; Cheng, C.; Chen, Z. Crystal Structures of the Human RNA Demethylase Alkbh5 Reveal Basis for Substrate Recognition. *Journal of Biological Chemistry* **2014**, *289* (17), 11571–11583. https://doi.org/10.1074/jbc.M113.546168.

(44) Hewitson, K. S.; Holmes, S. L.; Ehrismann, D.; Hardy, A. P.; Chowdhury, R.; Schofield, C. J.; McDonough, M. A. Evidence That Two Enzyme-Derived Histidine Ligands Are Sufficient for Iron Binding and Catalysis by Factor Inhibiting HIF (FIH). *Journal of Biological Chemistry* **2008**, *283* (38), 25971–25978. https://doi.org/10.1074/jbc.M804999200.

(45) Burziaff, N. I.; Rutledge, P. J.; Clifton, I. J.; Hensgens, C. M. H.; Pickford, M.; Adlington, R. M.; Roach, P. L.; Baldwin, J. E. The Reaction Cycle of Isopenicillin N Synthase Observed by X-Ray Diffraction. *Nature* **1999**, *401* (6754), 721–724. https://doi.org/10.1038/44400.

(46) Roach, P. L.; Clifton, I. J.; Hensgens, C. M. H.; Shibata, N.; Schofield, C. J.; Hajdu, J.; Baldwin, J. E. Structure of Isopenicillin N Synthase Complexed with Substrate and the Mechanism of Penicillin Formation. *Nature* **1997**, *387* (6635), 827–830. https://doi.org/10.1038/42990.

(47) Schofield, C. J.; Ratcliffe, P. J. Oxygen Sensing by HIF Hydroxylases. *Nat. Rev. Mol. Cell Biol.* **2004**, *5* (5), 343–354. https://doi.org/10.1038/nrm1366.

(48) Loenarz, C.; Coleman, M. L.; Boleininger, A.; Schierwater, B.; Holland, P. W. H.; Ratcliffe, P. J.; Schofield, C. J. The Hypoxia-Inducible Transcription Factor Pathway Regulates Oxygen Sensing in the Simplest Animal, Trichoplax Adhaerens. *EMBO Reports* **2011**, *12* (1), 63–70. https://doi.org/10.1038/embor.2010.170.

(49) Semenza, G. L.; Wang, G. L. A Nuclear Factor Induced by Hypoxia via de Novo Protein Synthesis Binds to the Human Erythropoietin Gene Enhancer at a Site Required for Transcriptional Activation. *Molecular and Cellular Biology* **1992**, *12* (12), 5447–5454. https://doi.org/10.1128/mcb.12.12.5447-5454.1992.

(50) Wood, S. M.; Gleadle, J. M.; Pugh, C. W.; Hankinson, O.; Ratcliffe, P. J. The Role of the Aryl Hydrocarbon Receptor Nuclear Translocator (ARNT) in Hypoxie Induction of Gene Expression: Studies in Arnt-Deficient Cells. *Journal of*

Biological Chemistry **1996**, *271* (25), 15117–15123. https://doi.org/10.1074/jbc.271.25.15117.
(51) Serganova, I.; Cohen, I. J.; Vemuri, K.; Shindo, M.; Maeda, M.; Mane, M.; Moroz, E.; Khanin, R.; Satagopan, J.; Koutcher, J. A.; Blasberg, R. LDH-A Regulates the Tumor Microenvironment via HIF-Signaling and Modulates the Immune Response. *PLoS ONE* **2018**, *13* (9), 1–22. https://doi.org/10.1371/journal.pone.0203965.
(52) Jaakkola, P.; Mole, D. R.; Tian, Y. M.; Wilson, M. I.; Gielbert, J.; Gaskell, S. J.; von Kriegsheim, A.; Hebestreit, H. F.; Mukherji, M.; Schofield, C. J.; Maxwell, P. H.; Pugh, C. W.; Ratcliffe, P. J. Targeting of HIF-α to the von Hippel-Lindau Ubiquitylation Complex by O2-Regulated Prolyl Hydroxylation. *Science* **2001**, *292* (5516), 468–472. https://doi.org/10.1126/science.1059796.
(53) Bruick, R. K.; McKnight, S. L. A Conserved Family of Prolyl-4-Hydroxylases That Modify HIF. *Science* **2001**, *294* (5545), 1337–1340. https://doi.org/10.1126/science.1066373.
(54) Kaelin, W. G. The von Hippel-Lindau Tumour Suppressor Protein: O2 Sensing and Cancer. *Nature Reviews Cancer* **2008**, *8* (11), 865–873. https://doi.org/10.1038/nrc2502.
(55) Kaelin Jr., W. G.; Ratcliffe, P. J. Oxygen Sensing by Metazoans: The Central Role of the HIF Hydroxylase Pathway. *Mol Cell* **2008**, *30* (4), 393–402. https://doi.org/10.1016/j.molcel.2008.04.009.
(56) Stebbins, C. E.; Kaelin, W. G.; Pavletich, N. P. Structure of the VHL-ElonginC-ElonginB Complex: Implications for VHL Tumor Suppressor Function. *Science* **1999**, *284* (5413), 455–461. https://doi.org/10.1126/science.284.5413.455.
(57) Maxwell, P. H.; Wlesener, M. S.; Chang, G. W.; Clifford, S. C.; Vaux, E. C.; Cockman, M. E.; Wykoff, C. C.; Pugh, C. W.; Maher, E. R.; Ratcliffe, P. J. The Tumour Suppressor Protein VHL Targets Hypoxia-Inducible Factors for Oxygen-Dependent Proteolysis. *Nature* **1999**, *399* (6733), 271–275. https://doi.org/10.1038/20459.
(58) Ekström, M.; Ringbaek, T. Which Patients with Moderate Hypoxemia Benefit from Long-Term Oxygen Therapy? Ways Forward. *International Journal of Chronic Obstructive Pulmonary Disease* **2018**, *13*, 231–235. https://doi.org/10.2147/COPD.S148673.
(59) Lando, D.; Peet, D. J.; Whelan, D. A.; Gorman, J. J.; Whitelaw, M. L. Asparagine Hydroxylation of the HIF Transactivation Domain: A Hypoxic Switch. *Science* **2002**, *295* (5556), 858–861. https://doi.org/10.1126/science.1068592.
(60) Dames, S. A.; Martinez-Yamout, M.; de Guzman, R. N.; Dyson, H. J.; Wright, P. E. Structural Basis for Hif-1 /CBP Recognition in the Cellular Hypoxic Response. *Proceedings of the National Academy of Sciences* **2002**, *99* (8), 5271–5276. https://doi.org/10.1073/pnas.082121399.
(61) Freedman, S. J.; Sun, Z. Y. J.; Poy, F.; Kung, A. L.; Livingston, D. M.; Wagner, G.; Eck, M. J. Structural Basis for Recruitment of CBP/P300 by Hypoxia-Inducible Factor-1α. *Proceedings of the National Academy of Sciences of the United States of America* **2002**, *99* (8), 5367–5372. https://doi.org/10.1073/pnas.082117899.
(62) Song, D.; Li, L. S.; Heaton-Johnson, K. J.; Arsenault, P. R.; Master, S. R.; Lee, F. S. Prolyl Hydroxylase Domain Protein 2 (PHD2) Binds a Pro-Xaa-Leu-Glu Motif, Linking It to the Heat Shock Protein 90 Pathway. *Journal of Biological Chemistry* **2013**, *288* (14), 9662–9674. https://doi.org/10.1074/jbc.M112.440552.
(63) Semenza, G. L. Hypoxia-Inducible Factors in Physiology and Medicine. *Cell* **2012**, *148* (3), 399–408. https://doi.org/10.1016/j.cell.2012.01.021.

(64) Semenza, G. L. HIF-1, O2, and the 3 PHDs: How Animal Cells Signal Hypoxia to the Nucleus. *Cell* **2001**, *107* (1), 1–3. https://doi.org/10.1016/S0092-8674(01)00518-9.
(65) Semenza, G. L. Hydroxylation of HIF-1: Oxygen Sensing at the Molecular Level. *Physiology* **2004**, *19* (4), 176–182. https://doi.org/10.1152/physiol.00001.2004.
(66) Semenza, G. L.; Nejfelt, M. K.; Chi, S. M.; Antonarakis, S. E. Hypoxia-Inducible Nuclear Factors Bind to an Enhancer Element Located 3' to the Human Erythropoietin Gene. *Proceedings of the National Academy of Sciences of the United States of America* **1991**, *88* (13), 5680–5684. https://doi.org/10.1073/pnas.88.13.5680.
(67) Wang, G. L.; Jiang, B. H.; Rue, E. A.; Semenza, G. L. Hypoxia-Inducible Factor 1 Is a Basic-Helix-Loop-Helix-PAS Heterodimer Regulated by Cellular O2 Tension. *Proceedings of the National Academy of Sciences of the United States of America* **1995**, *92* (12), 5510–5514. https://doi.org/10.1073/pnas.92.12.5510.
(68) Min, J. H.; Yang, H.; Ivan, M.; Gertler, F.; Kaelin, W. G.; Pavietich, N. P. Structure of an HIF-1α-PVHL Complex: Hydroxyproline Recognition in Signaling. *Science* **2002**, *296* (5574), 1886–1889. https://doi.org/10.1126/science.1073440.
(69) Dames, S. A.; Martinez-Yamout, M.; de Guzman, R. N.; Dyson, H. J.; Wright, P. E. Structural Basis for Hif-1 /CBP Recognition in the Cellular Hypoxic Response. *Proceedings of the National Academy of Sciences* **2002**, *99* (8), 5271–5276. https://doi.org/10.1073/pnas.082121399.
(70) Freedman, S. J.; Sun, Z. Y. J.; Poy, F.; Kung, A. L.; Livingston, D. M.; Wagner, G.; Eck, M. J. Structural Basis for Recruitment of CBP/P300 by Hypoxia-Inducible Factor-1α. *Proceedings of the National Academy of Sciences of the United States of America* **2002**, *99* (8), 5367–5372. https://doi.org/10.1073/pnas.082117899.
(71) Kaelin, W. G. Von Hippel-Lindau Disease. *Annual Review of Pathology* **2007**, *2* (1), 145–173. https://doi.org/10.1146/annurev.pathol.2.010506.092049.
(72) Kaelin, W. G. The VHL Tumor Suppressor Gene: Insights into Oxygen Sensing and Cancer. *Transactions of the American Clinical and Climatological Association* **2017**, *128*, 298–307.
(73) Figg, W. D.; Folkman, J. *Angiogenesis: An Integrative Approach from Science to Medicine*; Springer, 2008. https://doi.org/10.1007/978-0-387-71518-6.
(74) Ye, Y.; Vasavada, S.; Kuzmin, I.; Stackhouse, T.; Zbar, B.; Williams, B. R. G. Subcellular Localization of the von Hippel-Lindau Disease Gene Product Is Cell Cycle-Dependent. *International Journal of Cancer* **1998**, *78* (1), 62–69. https://doi.org/10.1002/(SICI)1097-0215(19980925)78:1<62::AID-IJC11>3.0.CO;2-7.
(75) Vincent, K. A.; Feron, O.; Kelly, R. A. Harnessing the Response to Tissue Hypoxia: HIF-1α and Therapeutic Angiogenesis. *Trends in Cardiovascular Medicine* **2002**, *12* (8), 362–367. https://doi.org/10.1016/S1050-1738(02)00186-X.
(76) Mahon, P. C.; Hirota, K.; Semenza, G. L. FIH-1: A Novel Protein That Interacts with HIF-1α and VHL to Mediate Repression of HIF-1 Transcriptional Activity. *Genes and Development* **2001**, *15* (20), 2675–2686. https://doi.org/10.1101/gad.924501.
(77) Tarhonskaya, H.; Hardy, A. P.; Howe, E. A.; Loik, N. D.; Kramer, H. B.; McCullagh, J. S. O.; Schofield, C. J.; Flashman, E. Kinetic Investigations of the Role of Factor Inhibiting Hypoxia-Inducible Factor (FIH) as an Oxygen Sensor. *Journal of Biological Chemistry* **2015**, *290* (32), 19726–19742. https://doi.org/10.1074/jbc.M115.653014.

(78) McNeill, L. A.; Hewitson, K. S.; Claridge, T. D.; Seibel, J. F.; Horsfall, L. E.; Schofield, C. J. Hypoxia-Inducible Factor Asparaginyl Hydroxylase (FIH-1) Catalyses Hydroxylation at the β-Carbon of Asparagine-803. *Biochemical Journal* **2002**, *367* (3), 571–575. https://doi.org/10.1042/BJ20021162.

(79) Chan, M. C.; Ilott, N. E.; Schödel, J.; Sims, D.; Tumber, A.; Lippl, K.; Mole, D. R.; Pugh, C. W.; Ratcliffe, P. J.; Ponting, C. P.; Schofield, C. J. Tuning the Transcriptional Response to Hypoxia by Inhibiting Hypoxia-Inducible Factor (HIF) Prolyl and Asparaginyl Hydroxylases. *Journal of Biological Chemistry* **2016**, *291* (39), 20661–20673. https://doi.org/10.1074/jbc.M116.749291.

(80) Koivunen, P.; Hirsilä, M.; Günzler, V.; Kivirikko, K. I.; Myllyharju, J. Catalytic Properties of the Asparaginyl Hydroxylase (FIH) in the Oxygen Sensing Pathway Are Distinct from Those of Its Prolyl 4-Hydroxylases. *Journal of Biological Chemistry* **2004**, *279* (11), 9899–9904. https://doi.org/10.1074/jbc.M312254200.

(81) Hirsilä, M.; Koivunen, P.; Günzler, V.; Kivirikko, K. I.; Myllyharju, J. Characterization of the Human Prolyl 4-Hydroxylases That Modify the Hypoxia-Inducible Factor. *Journal of Biological Chemistry* **2003**, *278* (33), 30772–30780. https://doi.org/10.1074/jbc.M304982200.

(82) Tarhonskaya, H.; Chowdhury, R.; Leung, I. K. H.; Loik, N. D.; McCullagh, J. S. O.; Claridge, T. D. W.; Schofield, C. J.; Flashman, E. Investigating the Contribution of the Active Site Environment to the Slow Reaction of Hypoxia-Inducible Factor Prolyl Hydroxylase Domain 2 with Oxygen. *Biochemical Journal* **2014**, *463* (3), 363–372. https://doi.org/10.1042/BJ20140779.

(83) Deutsch, J. C. Ascorbic Acid Oxidation by Hydrogen Peroxide. *Analytical Biochemistry* **1998**, *255* (1), 1–7. https://doi.org/10.1006/abio.1997.2293.

(84) Khan, A.; Schofield, C. J.; Claridge, T. D. W. Reducing Agent-Mediated Nonenzymatic Conversion of 2-Oxoglutarate to Succinate: Implications for Oxygenase Assays. *ChemBioChem* **2020**, *21* (20), 2898–2902. https://doi.org/10.1002/cbic.202000185.

(85) Wilkins, S. E.; Karttunen, S.; Hampton-Smith, R. J.; Murchland, I.; Chapman-Smith, A.; Peet, D. J. Factor Inhibiting HIF (FIH) Recognizes Distinct Molecular Features within Hypoxia-Inducible Factor-α (HIF-α) versus Ankyrin Repeat Substrates. *Journal of Biological Chemistry* **2012**, *287* (12), 8769–8781. https://doi.org/10.1074/jbc.M111.294678.

(86) Yang, M.; Chowdhury, R.; Ge, W.; Hamed, R. B.; McDonough, M. A.; Claridge, T. D. W.; Kessler, B. M.; Cockman, M. E.; Ratcliffe, P. J.; Schofield, C. J. Factor-Inhibiting Hypoxia-Inducible Factor (FIH) Catalyses the Post-Translational Hydroxylation of Histidinyl Residues within Ankyrin Repeat Domains. *FEBS Journal* **2011**, *278* (7), 1086–1097. https://doi.org/10.1111/j.1742-4658.2011.08022.x.

(87) Mole, D. R.; Maxwell, P. H.; Pugh, C. W.; Ratcliffe, P. J. Regulation of HIF by the von Hippel-Lindau Tumour Suppressor: Implications for Cellular Oxygen Sensing. *IUBMB Life* **2001**, *52* (1–2), 43–47. https://doi.org/10.1080/15216540252774757.

(88) Appelhoffl, R. J.; Tian, Y. M.; Raval, R. R.; Turley, H.; Harris, A. L.; Pugh, C. W.; Ratcliffe, P. J.; Gleadle, J. M. Differential Function of the Prolyl Hydroxylases PHD1, PHD2, and PHD3 in the Regulation of Hypoxia-Inducible Factor. *Journal of Biological Chemistry* **2004**, *279* (37), 38458–38465. https://doi.org/10.1074/jbc.M406026200.

(89) Lieb, M. E.; Menzies, K.; Moschella, M. C.; Ni, R.; Taubman, M. B. Mammalian EGLN Genes Have Distinct Patterns of MRNA Expression and Regulation.

Biochemistry and Cell Biology **2002**, *80* (4), 421–426. https://doi.org/10.1139/o02-115.

(90) Abboud, M. I.; Chowdhury, R.; Leung, I. K. H.; Lippl, K.; Loenarz, C.; Claridge, T. D. W.; Schofield, C. J. Studies on the Substrate Selectivity of the Hypoxia-Inducible Factor Prolyl Hydroxylase 2 Catalytic Domain. *ChemBioChem* **2018**, *19* (21), 2262–2267. https://doi.org/10.1002/cbic.201800246.

(91) Cockman, M. E.; Lippl, K.; Tian, Y. M.; Pegg, H. B.; Figg, W. D.; Abboud, M. I.; Heilig, R.; Fischer, R.; Myllyharju, J.; Schofield, C. J.; Ratcliffe, P. J. Lack of Activity of Recombinant HIF Prolyl Hydroxylases (PHDs) on Reported Non-HIF Substrates. *eLife* **2019**, *8*, e46490. https://doi.org/10.7554/eLife.46490.

(92) Flashman, E.; Hoffart, L. M.; Hamed, R. B.; Bollinger, J. M.; Krebs, C.; Schofield, C. J. Evidence for the Slow Reaction of Hypoxia-Inducible Factor Prolyl Hydroxylase 2 with Oxygen. *FEBS Journal* **2010**, *277* (19), 4089–4099. https://doi.org/10.1111/j.1742-4658.2010.07804.x.

(93) Hirsilä, M.; Koivunen, P.; Günzler, V.; Kivirikko, K. I.; Myllyharju, J. Characterization of the Human Prolyl 4-Hydroxylases That Modify the Hypoxia-Inducible Factor. *Journal of Biological Chemistry* **2003**, *278* (33), 30772–30780. https://doi.org/10.1074/jbc.M304982200.

(94) Domene, C.; Jorgensen, C.; Schofield, C. J. Mechanism of Molecular Oxygen Diffusion in a Hypoxia-Sensing Prolyl Hydroxylase Using Multiscale Simulation. *Journal of the American Chemical Society* **2020**, *142* (5), 2253–2263. https://doi.org/10.1021/jacs.9b09236.

(95) Pektas, S.; Taabazuing, C. Y.; Knapp, M. J. Increased Turnover at Limiting O2 Concentrations by the Thr387 → Ala Variant of HIF-Prolyl Hydroxylase PHD2. *Biochemistry* **2015**, *54* (18), 2851–2857. https://doi.org/10.1021/bi501540c.

(96) Song, D.; Li, L. S.; Arsenault, P. R.; Tan, Q.; Bigham, A. W.; Heaton-Johnson, K. J.; Master, S. R.; Lee, F. S. Defective Tibetan PHD2 Binding to P23 Links High Altitude Adaption to Altered Oxygen Sensing. *Journal of Biological Chemistry* **2014**, *289* (21), 14656–14665. https://doi.org/10.1074/jbc.M113.541227.

(97) Lorenzo, F. R.; Huff, C.; Myllymäki, M.; Olenchock, B.; Swierczek, S.; Tashi, T.; Gordeuk, V.; Wuren, T.; Ge, R. L.; McClain, D. A.; Khan, T. M.; Koul, P. A.; Guchhait, P.; Salama, M. E.; Xing, J.; Semenza, G. L.; Liberzon, E.; Wilson, A.; Simonson, T. S.; Jorde, L. B.; Kaelin, W. G.; Koivunen, P.; Prchal, J. T. A Genetic Mechanism for Tibetan High-Altitude Adaptation. *Nature Genetics* **2014**, *46* (9), 951–956. https://doi.org/10.1038/ng.3067.

(98) Arsenault, P. R.; Song, D.; Bergkamp, M.; Ravaschiere, A. M.; Navalsky, B. E.; Lieberman, P. M.; Lee, F. S. Identification of Small-Molecule PHD2 Zinc Finger Inhibitors That Activate Hypoxia Inducible Factor. *ChemBioChem* **2016**, *17* (24), 2316–2323. https://doi.org/10.1002/cbic.201600493.

(99) Song, D.; Navalsky, B. E.; Guan, W.; Ingersoll, C.; Wang, T.; Loro, E.; Eeles, L.; Matchett, K. B.; Percy, M. J.; Walsby-Tickle, J.; McCullagh, J. S. O.; Medina, R. J.; Khuran, T. S.; Bigham, A. W.; Lappin, T. R.; Lee, F. S. Tibetan PHD2, an Allele with Loss-of-Function Properties. *Proceedings of the National Academy of Sciences of the United States of America* **2020**, *117* (22), 12230–12238. https://doi.org/10.1073/pnas.1920546117.

(100) Sinnema, M.; Song, D.; Guan, W.; Janssen, J. W. H.; van Wijk, R.; Navalsky, B. E.; Peng, K.; Donker, A. E.; Stegmann, A. P. A.; Lee, F. S. Loss-of-Function Zinc Finger Mutation in the EGLN1 Gene Associated with Erythrocytosis. *Blood*. American Society of Hematology September 27, 2018, pp 1455–1458. https://doi.org/10.1182/blood-2018-06-854711.

(101) Wang, G. L.; Semenza, G. L. Desferrioxamine Induces Erythropoietin Gene Expression and Hypoxia- Inducible Factor 1 DNA-Binding Activity: Implications for Models of Hypoxia Signal Transduction. *Blood* **1993**, *82* (12), 3610–3615. https://doi.org/10.1182/blood.v82.12.3610.3610.
(102) Joharapurkar, A. A.; Pandya, V. B.; Patel, V. J.; Desai, R. C.; Jain, M. R. Prolyl Hydroxylase Inhibitors: A Breakthrough in the Therapy of Anemia Associated with Chronic Diseases. *Journal of Medicinal Chemistry* **2018**, *61* (16), 6964–6982. https://doi.org/10.1021/acs.jmedchem.7b01686.
(103) Salnikow, K.; Donald, S. P.; Bruick, R. K.; Zhitkovich, A.; Phang, J. M.; Kasprzak, K. S. Depletion of Intracellular Ascorbate by the Carcinogenic Metals Nickel and Cobalt Results in the Induction of Hypoxic Stress. *Journal of Biological Chemistry* **2004**, *279* (39), 40337–40344. https://doi.org/10.1074/jbc.M403057200.
(104) Nagle, Dale G. and Zhou, Y.-D. Natural Product-Derived Small Molecule Activators of Hypoxia-Inducible Factor-1 (HIF-1). *Current Pharmaceutical Design* **2006**, *12* (21), 2673–2688.
(105) Shui, Y. B.; Arbeit, J. M.; Johnson, R. S.; Beebe, D. C. HIF-1: An Age-Dependent Regulator of Lens Cell Proliferation. *Investigative Ophthalmology and Visual Science* **2008**, *49* (11), 4961–4970. https://doi.org/10.1167/iovs.08-2118.
(106) Baader, E.; Tschank, G.; Baringhaus, K. H.; Burghard, H.; Gunzler, V. Inhibition of Prolyl 4-Hydroxylase by Oxalyl Amino Acid Derivatives in Vitro, in Isolated Microsomes and in Embryonic Chicken Tissues. *Biochemical Journal* **1994**, *300* (2), 525–530. https://doi.org/10.1042/bj3000525.
(107) Cunliffe, C. J.; Franklin, T. J.; Hales, N. J.; Hill, G. B. Novel Inhibitors of Prolyl 4-Hydroxylase. 3. Inhibition by the Substrate Analogue N-Oxaloglycine and Its Derivatives. *Journal of Medicinal Chemistry* **1992**, *35* (14), 2652–2658. https://doi.org/10.1021/jm00092a016.
(108) Rosen, M. D.; Venkatesan, H.; Peltier, H. M.; Bembenek, S. D.; Kanelakis, K. C.; Zhao, L. X.; Leonard, B. E.; Hocutt, F. M.; Wu, X.; Palomino, H. L.; Brondstetter, T. I.; Haugh, P. v.; Cagnon, L.; Yan, W.; Liotta, L. A.; Young, A.; Mirzadegan, T.; Shankley, N. P.; Barrett, T. D.; Rabinowitz, M. H. Benzimidazole-2-Pyrazole HIF Prolyl 4-Hydroxylase Inhibitors as Oral Erythropoietin Secretagogues. *ACS Medicinal Chemistry Letters* **2010**, *1* (9), 526–529. https://doi.org/10.1021/ml100198y.
(109) Chan, M. C.; Ilott, N. E.; Schödel, J.; Sims, D.; Tumber, A.; Lippl, K.; Mole, D. R.; Pugh, C. W.; Ratcliffe, P. J.; Ponting, C. P.; Schofield, C. J. Tuning the Transcriptional Response to Hypoxia by Inhibiting Hypoxia-Inducible Factor (HIF) Prolyl and Asparaginyl Hydroxylases. *The Journal of Biochemistry* **2016**, *291* (39), 20661–20673. https://doi.org/10.1074/jbc.M116.749291.
(110) Yeh, T.-L.; Leissing, T. M.; Abboud, M. I.; Thinnes, C. C.; Atasoylu, O.; Holt-Martyn, J. P.; Zhang, D.; Tumber, A.; Lippl, K.; Lohans, C. T.; Leung, I. K. H.; Morcrette, H.; Clifton, I. J.; Claridge, T. D. W.; Kawamura, A.; Flashman, E.; Lu, X.; Ratcliffe, P. J.; Chowdhury, R.; Pugh, C. W.; Schofield, C. J. Molecular and Cellular Mechanisms of HIF Prolyl Hydroxylase Inhibitors in Clinical Trials. *Chemical Science* **2017**, *8* (11), 7651–7668. https://doi.org/10.1039/C7SC02103H.
(111) Wu, Y.; Wang, N.; Lei, Y.; Hu, T.; You, Q.; Zhang, X. Small-Molecule Inhibitors of HIF-PHD2: A Valid Strategy to Renal Anemia Treatment in Clinical Therapy. *MedChemComm* **2016**, *7* (7), 1271–1284. https://doi.org/10.1039/c6md00240d.

(112) Cunliffe, C. J.; Franklin, T. J. Inhibition of Prolyl 4-Hydroxylase by Hydroxyanthraquinones. *Biochemical Journal* **1986**, *239* (2), 311–315. https://doi.org/10.1042/bj2390311.
(113) Arend, M. P.; Flippin, L. A.; Volkmar, G. P.; Ho, W. B.; Turtle, E. D.; Du, X. Nitrogen-Containing Heteroaryl Compounds and Their Use in Increasing Endogenous Erythropoietin, 2004.
(114) Gotchev, D. B. Prolyl Hydroxylase Inhibitors, September 13, 2009.
(115) Kawamoto, R. M.; Wu, S.; Evdokimov, A. G.; Greis, K. D.; Boyer, A. S.; Warshakoon, N. C. Prolyl Hydroxylase Inhibitors and Method of Use, May 13, 2014.
(116) Gotchev, D. B. Prolyl Hydroxylase Inhibitors, 2009.
(117) Rabinowitz, M. H. Inhibition of Hypoxia-Inducible Factor Prolyl Hydroxylase Domain Oxygen Sensors: Tricking the Body into Mounting Orchestrated Survival and Repair Responses. *Journal of Medicinal Chemistry* **2013**, *56* (23), 9369–9402. https://doi.org/10.1021/jm400386j.
(118) Barrett, T. D.; Palomino, H. L.; Brondstetter, T. I.; Kanelakis, K. C.; Wu, X.; Yan, W.; Merton, K. P.; Schoetens, F.; Ma, J. Y.; Skaptason, J.; Gao, J.; Tran, D. T.; Venkatesan, H.; Rosen, M. D.; Shankley, N. P.; Rabinowitz, M. H. Prolyl Hydroxylase Inhibition Corrects Functional Iron Deficiency and Inflammation-Induced Anaemia in Rats. *British Journal of Pharmacology* **2015**, *172* (16), 4078–4088. https://doi.org/10.1111/bph.13188.
(119) Chan, M. C.; Atasoylu, O.; Hodson, E.; Tumber, A.; Leung, I. K. H.; Chowdhury, R.; Gómez-Pérez, V.; Demetriades, M.; Rydzik, A. M.; Holt-Martyn, J.; Tian, Y. M.; Bishop, T.; Claridge, T. D. W.; Kawamura, A.; Pugh, C. W.; Ratcliffe, P. J.; Schofield, C. J. Potent and Selective Triazole-Based Inhibitors of the Hypoxia-Inducible Factor Prolyl-Hydroxylases with Activity in the Murine Brain. *PLoS ONE* **2015**, *10* (7), e0132004. https://doi.org/10.1371/journal.pone.0132004.
(120) Chowdhury, R.; Candela-Lena, J. I.; Chan, M. C.; Greenald, D. J.; Yeoh, K. K.; Tian, Y. M.; McDonough, M. A.; Tumber, A.; Rose, N. R.; Conejo-Garcia, A.; Demetriades, M.; Mathavan, S.; Kawamura, A.; Lee, M. K.; van Eeden, F.; Pugh, C. W.; Ratcliffe, P. J.; Schofield, C. J. Selective Small Molecule Probes for the Hypoxia Inducible Factor (HIF) Prolyl Hydroxylases. *ACS Chemical Biology* **2013**, *8* (7), 1488–1496. https://doi.org/10.1021/cb400088q.
(121) Flamme, I.; Oehme, F.; Ellinghaus, P.; Jeske, M.; Keldenich, J.; Thuss, U. Mimicking Hypoxia to Treat Anemia: HIF-Stabilizer BAY 85-3934 (Molidustat) Stimulates Erythropoietin Production without Hypertensive Effects. *PLoS ONE* **2014**, *9* (11), 1–14. https://doi.org/10.1371/journal.pone.0111838.
(122) Beck, H.; Jeske, M.; Thede, K.; Stoll, F.; Flamme, I.; Akbaba, M.; Ergüden, J. K.; Karig, G.; Keldenich, J.; Oehme, F.; Militzer, H. C.; Hartung, I. v.; Thuss, U. Discovery of Molidustat (BAY 85-3934): A Small-Molecule Oral HIF-Prolyl Hydroxylase (HIF-PH) Inhibitor for the Treatment of Renal Anemia. *ChemMedChem* **2018**, *13* (10), 988–1003. https://doi.org/10.1002/cmdc.201700783.
(123) Clements, M. J.; Debenham, J. S.; Hale, J. J.; Madsen-Duggan, C. B.; Walsh, T. F. Substituted 4-Hydroxypyrimidine-5-Carboxamides, October 2, 2012.
(124) Fletcher, J. M.; Hale, J. J.; Miao, S.; Vachal, P. Spiroindolones, November 13, 2008.
(125) Vachal, P.; Miao, S.; Pierce, J. M.; Guiadeen, D.; Colandrea, V. J.; Wyvratt, M. J.; Salowe, S. P.; Sonatore, L. M.; Milligan, J. A.; Hajdu, R.; Gollapudi, A.; Keohane,

C. A.; Lingham, R. B.; Mandala, S. M.; Demartino, J. A.; Tong, X.; Wolff, M.; Steinhuebel, D.; Kieczykowski, G. R.; Fleitz, F. J.; Chapman, K.; Athanasopoulos, J.; Adam, G.; Akyuz, C. D.; Jena, D. K.; Lusen, J. W.; Meng, J.; Stein, B. D.; Xia, L.; Sherer, E. C.; Hale, J. J. 1,3,8-Triazaspiro[4.5]Decane-2,4-Diones as Efficacious Pan-Inhibitors of Hypoxia-Inducible Factor Prolyl Hydroxylase 1-3 (HIF PHD1-3) for the Treatment of Anemia. *Journal of Medicinal Chemistry* **2012**, *55* (7), 2945–2959. https://doi.org/10.1021/jm201542d.

(126) Debenham, J. S.; Madsen-Duggan, C.; Clements, M. J.; Walsh, T. F.; Kuethe, J. T.; Reibarkh, M.; Salowe, S. P.; Sonatore, L. M.; Hajdu, R.; Milligan, J. A.; Visco, D. M.; Zhou, D.; Lingham, R. B.; Stickens, D.; Demartino, J. A.; Tong, X.; Wolff, M.; Pang, J.; Miller, R. R.; Sherer, E. C.; Hale, J. J. Discovery of N-[Bis(4-Methoxyphenyl)Methyl]-4-Hydroxy-2-(Pyridazin-3-Yl)Pyrimidine-5-Carboxamide (MK-8617), an Orally Active Pan-Inhibitor of Hypoxia-Inducible Factor Prolyl Hydroxylase 1-3 (HIF PHD1-3) for the Treatment of Anemia. *Journal of Medicinal Chemistry* **2016**, *59* (24), 11039–11049. https://doi.org/10.1021/acs.jmedchem.6b01242.

(127) Gotchev, D. B. Prolyl Hydroxylase Inhibitors, November 25, 2009.

(128) Gotchev, D. B. Prolyl Hydroxylase Inhibitors, 2009.

(129) Bonandi, E.; Christodoulou, M. S.; Fumagalli, G.; Perdicchia, D.; Rastelli, G.; Passarella, D. The 1,2,3-Triazole Ring as a Bioisostere in Medicinal Chemistry. *Drug Discovery Today*. Elsevier Ltd October 1, 2017, pp 1572–1581. https://doi.org/10.1016/j.drudis.2017.05.014.

(130) Hong, Y. R.; Kim, H. T.; Ro, S.; Cho, J. M.; Lee, S. H.; Kim, I. S.; Jung, Y. H. Discovery of Novel 2-[2-(3-Hydroxy-Pyridin-2-Yl)-Thiazol-4-Yl]-Acetamide Derivatives as HIF Prolyl 4-Hydroxylase Inhibitors; SAR, Synthesis and Modeling Evaluation. *Bioorganic and Medicinal Chemistry Letters* **2014**, *24* (14), 3142–3145. https://doi.org/10.1016/j.bmcl.2014.05.003.

(131) Hong, Y. R.; Shin, D.; Ro, S.; Cho, J. M.; Kim, H. T.; Lee, J. H.; Kim, J. M.; Lee, W. S.; Choi, J. R. Phenol Derivatives and Methods of Use Thereof, 2010.

(132) Ahmed, S.; Ayscough, A.; Barker, G. R.; Canning, H. E.; Davenport, R.; Downham, R.; Harrison, D.; Jenkins, K.; Kinsella, N.; Livermore, D. G.; Wright, S.; Ivetac, A. D.; Skene, R.; Wilkens, S. J.; Webster, N. A.; Hendrick, A. G. 1,2,4-Triazolo-[1,5-a]Pyridine HIF Prolylhydroxylase Domain-1 (PHD-1) Inhibitors with a Novel Monodentate Binding Interaction. *Journal of Medicinal Chemistry* **2017**, *60* (13), 5663–5672. https://doi.org/10.1021/acs.jmedchem.7b00352.

(133) Yeoh, K. K.; Chan, M. C.; Thalhammer, A.; Demetriades, M.; Chowdhury, R.; Tian, Y. M.; Stolze, I.; McNeill, L. A.; Lee, M. K.; Woon, E. C. Y.; MacKeen, M. M.; Kawamura, A.; Ratcliffe, P. J.; Mecinović, J.; Schofield, C. J. Dual-Action Inhibitors of HIF Prolyl Hydroxylases That Induce Binding of a Second Iron Ion. *Organic and Biomolecular Chemistry* **2013**, *11* (5), 732–745. https://doi.org/10.1039/c2ob26648b.

(134) Na, Y. R.; Woo, D. J.; Kim, S. Y.; Yang, E. G. Pyrithione Zn Selectively Inhibits Hypoxia-Inducible Factor Prolyl Hydroxylase PHD3. *Biochemical and Biophysical Research Communications* **2016**, *472* (2), 313–318. https://doi.org/10.1016/j.bbrc.2016.02.115.

(135) Haase, V. H. Hypoxia-Inducible Factor–Prolyl Hydroxylase Inhibitors in the Treatment of Anemia of Chronic Kidney Disease. *Kidney International Supplements* **2021**, *11* (1), 8–25. https://doi.org/10.1016/j.kisu.2020.12.002.

(136) Pharmaceuticals and Medical Devices Agency. Molidustat (MUSREDO) Approval in Japan https://www.info.pmda.go.jp/go/pack/39990D7F1028_1_01/.
(137) Dhillon, S. Roxadustat: First Global Approval. *Drugs* **2019**, *79* (5), 563–572. https://doi.org/10.1007/s40265-019-01077-1.
(138) Akizawa, T.; Yamaguchi, Y.; Otsuka, T.; Reusch, M. A Phase 3, Multicenter, Randomized, Two-Arm, Open-Label Study of Intermittent Oral Dosing of Roxadustat for the Treatment of Anemia in Japanese Erythropoiesis-Stimulating Agent-Naïve Chronic Kidney Disease Patients Not on Dialysis. *Nephron* **2020**, *144* (8), 372–382. https://doi.org/10.1159/000508100.
(139) AstraZeneca. Update on US regulatory review of roxadustat in anaemia of chronic kidney disease https://www.astrazeneca.com/media-centre/press-releases/2020/update-on-us-regulatory-review-of-roxadustat-in-anaemia-of-chronic-kidney-disease.html (accessed 2021 -09 -21).
(140) Guenzler-Pukall, V.; Wang, Q.; Parobok, I. L.; Guo, G. Methods for Reducing Blood Pressure, June 12, 2009.
(141) MacDougall, I. C. New Anemia Therapies: Translating Novel Strategies from Bench to Bedside. *American Journal of Kidney Diseases* **2012**, *59* (3), 444–451. https://doi.org/10.1053/j.ajkd.2011.11.013.
(142) Seeley, T. W.; Sternlicht, M. D.; Klaus, S. J.; Neff, T. B.; Liu, D. Y. Induction of Erythropoiesis by Hypoxia-Inducible Factor Prolyl Hydroxylase Inhibitors without Promotion of Tumor Initiation, Progression, or Metastasis in a VEGF-Sensitive Model of Spontaneous Breast Cancer. *Hypoxia* **2017**, *Volume 5*, 1–9. https://doi.org/10.2147/hp.s130526.
(143) Becker, K.; Saad, M. A New Approach to the Management of Anemia in CKD Patients: A Review on Roxadustat. *Advances in Therapy* **2017**, *34* (4), 848–853. https://doi.org/10.1007/s12325-017-0508-9.
(144) Pergola, P. E.; Spinowitz, B. S.; Hartman, C. S.; Maroni, B. J.; Haase, V. H. Vadadustat, a Novel Oral HIF Stabilizer, Provides Effective Anemia Treatment in Nondialysis-Dependent Chronic Kidney Disease. *Kidney International* **2016**, *90* (5), 1115–1122. https://doi.org/10.1016/j.kint.2016.07.019.
(145) Martin, E. R.; Smith, M. T.; Maroni, B. J.; Zuraw, Q. C.; DeGoma, E. M. Clinical Trial of Vadadustat in Patients with Anemia Secondary to Stage 3 or 4 Chronic Kidney Disease. *American Journal of Nephrology* **2017**, *45* (5), 380–388. https://doi.org/10.1159/000464476.
(146) Ariazi, J. L.; Duffy, K. J.; Adams, D. F.; Fitch, D. M.; Luo, L.; Pappalardi, M.; Biju, M.; DiFilippo, E. H.; Shaw, T.; Wiggall, K.; Erickson-Miller, C. Discovery and Preclinical Characterization of Gsk1278863 (Daprodustat), a Small Molecule Hypoxia Inducible Factor-Prolyl Hydroxylase Inhibitor for Anemias. *Journal of Pharmacology and Experimental Therapeutics* **2017**, *363* (3), 336–347. https://doi.org/10.1124/jpet.117.242503.
(147) Caltabiano, S.; Collins, J.; Serbest, G.; Morgan, L.; Smith, D. A.; Ravindranath, R.; Cobitz, A. R. A Randomized, Placebo- and Positive-Controlled, Single-Dose, Crossover Thorough QT/QTc Study Assessing the Effect of Daprodustat on Cardiac Repolarization in Healthy Subjects. *Clinical Pharmacology in Drug Development* **2017**, *6* (6), 627–640. https://doi.org/10.1002/cpdd.342.
(148) Markham, A. Enarodustat: First Approval. *Drugs* **2021**, *81* (1), 169–174. https://doi.org/10.1007/s40265-020-01444-3.
(149) Ogoshi, Y.; Matsui, T.; Mitani, I.; Yokota, M.; Terashita, M.; Motoda, D.; Ueyama, K.; Hotta, T.; Ito, T.; Hase, Y.; Fukui, K.; Deai, K.; Yoshiuchi, H.; Ito,

S.; Abe, H. Discovery of JTZ-951: A HIF Prolyl Hydroxylase Inhibitor for the Treatment of Renal Anemia. *ACS Medicinal Chemistry Letters* **2017**, *8* (12), 1320–1325. https://doi.org/10.1021/acsmedchemlett.7b00404.

(150) Akizawa, T.; Nangaku, M.; Yamaguchi, T.; Arai, M.; Koretomo, R.; Matsui, A.; Hirakata, H. A Placebo-Controlled, Randomized Trial of Enarodustat in Patients with Chronic Kidney Disease Followed by Long-Term Trial. *American Journal of Nephrology* **2019**, *49* (2), 165–174. https://doi.org/10.1159/000496929.

(151) Desai, R. C.; Pandya, V.; Patel, P. R. Quinolone Derivatives, July 19, 2016.

(152) Kansagra, K. A.; Parmar, D.; Jani, R. H.; Srinivas, N. R.; Lickliter, J.; Patel, H. v.; Parikh, D. P.; Heading, H.; Patel, H. B.; Gupta, R. J.; Shah, C. Y.; Patel, M. R.; Dholakia, V. N.; Sukhadiya, R.; Jain, M. R.; Parmar, K. v.; Barot, K. Phase I Clinical Study of ZYAN1, A Novel Prolyl-Hydroxylase (PHD) Inhibitor to Evaluate the Safety, Tolerability, and Pharmacokinetics Following Oral Administration in Healthy Volunteers. *Clinical Pharmacokinetics* **2018**, *57* (1), 87–102. https://doi.org/10.1007/s40262-017-0551-3.

(153) Patel, H.; Joharapurkar, A. A.; Pandya, V. B.; Patel, V. J.; Kshirsagar, S. G.; Patel, P.; Gevriya, B.; Jain, M. R.; Srinivas, N. R.; Patel, P. R.; Desai, R. C. Influence of Acute and Chronic Kidney Failure in Rats on the Disposition and Pharmacokinetics of ZYAN1, a Novel Prolyl Hydroxylase Inhibitor, for the Treatment of Chronic Kidney Disease-Induced Anemia. *Xenobiotica* **2018**, *48* (1), 37–44. https://doi.org/10.1080/00498254.2016.1278287.

(154) Jain, M. R.; Joharapurkar, A. A.; Pandya, V.; Patel, V.; Joshi, J.; Kshirsagar, S.; Patel, K.; Patel, P. R.; Desai, R. C. Pharmacological Characterization of ZYAN1, a Novel Prolyl Hydroxylase Inhibitor for the Treatment of Anemia. *Drug Research* **2015**, *66* (2), 107–112. https://doi.org/10.1055/s-0035-1554630.

(155) Warshakoon, N. C.; Wu, S.; Boyer, A.; Kawamoto, R.; Renock, S.; Xu, K.; Pokross, M.; Evdokimov, A. G.; Zhou, S.; Winter, C.; Walter, R.; Mekel, M. Design and Synthesis of a Series of Novel Pyrazolopyridines as HIF 1-α Prolyl Hydroxylase Inhibitors. *Bioorganic and Medicinal Chemistry Letters* **2006**, *16* (21), 5687–5690. https://doi.org/10.1016/j.bmcl.2006.08.017.

(156) Casey Laizure, S.; Herring, V.; Hu, Z.; Witbrodt, K.; Parker, R. B. The Role of Human Carboxylesterases in Drug Metabolism: Have We Overlooked Their Importance? *Pharmacotherapy* **2013**, *33* (2), 210–222. https://doi.org/10.1002/phar.1194.

(157) Williams, S. P.; Kuyper, L. F.; Pearce, K. H. Recent Applications of Protein Crystallography and Structure-Guided Drug Design. *Current Opinion in Chemical Biology* **2005**, *9* (4), 371–380. https://doi.org/10.1016/j.cbpa.2005.06.007.

(158) Douangamath, A.; Fearon, D.; Gehrtz, P.; Krojer, T.; Lukacik, P.; Owen, C. D.; Resnick, E.; Strain-Damerell, C.; Aimon, A.; Ábrányi-Balogh, P.; Brandão-Neto, J.; Carbery, A.; Davison, G.; Dias, A.; Downes, T. D.; Dunnett, L.; Fairhead, M.; Firth, J. D.; Jones, S. P.; Keeley, A.; Keserü, G. M.; Klein, H. F.; Martin, M. P.; Noble, M. E. M.; O'Brien, P.; Powell, A.; Reddi, R. N.; Skyner, R.; Snee, M.; Waring, M. J.; Wild, C.; London, N.; von Delft, F.; Walsh, M. A. Crystallographic and Electrophilic Fragment Screening of the SARS-CoV-2 Main Protease. *Nature Communications* **2020**, *11* (1), 5047. https://doi.org/10.1038/s41467-020-18709-w.

Chapter 2

Mechanistic Studies on PHD2

Chapter 2

2.1 Background on PHD2 Mechanistic Studies

In 2009, research from the Oxford Chemistry Department resulted in the report of the first PHD-substrate structure, *i.e.*, of a $PHD2_{181-426}$.Mn(II).NOG.$HIF1\alpha_{556-575}$-substrate complex structure (**Figure 2-1**, PDB: 3HQR).[1]

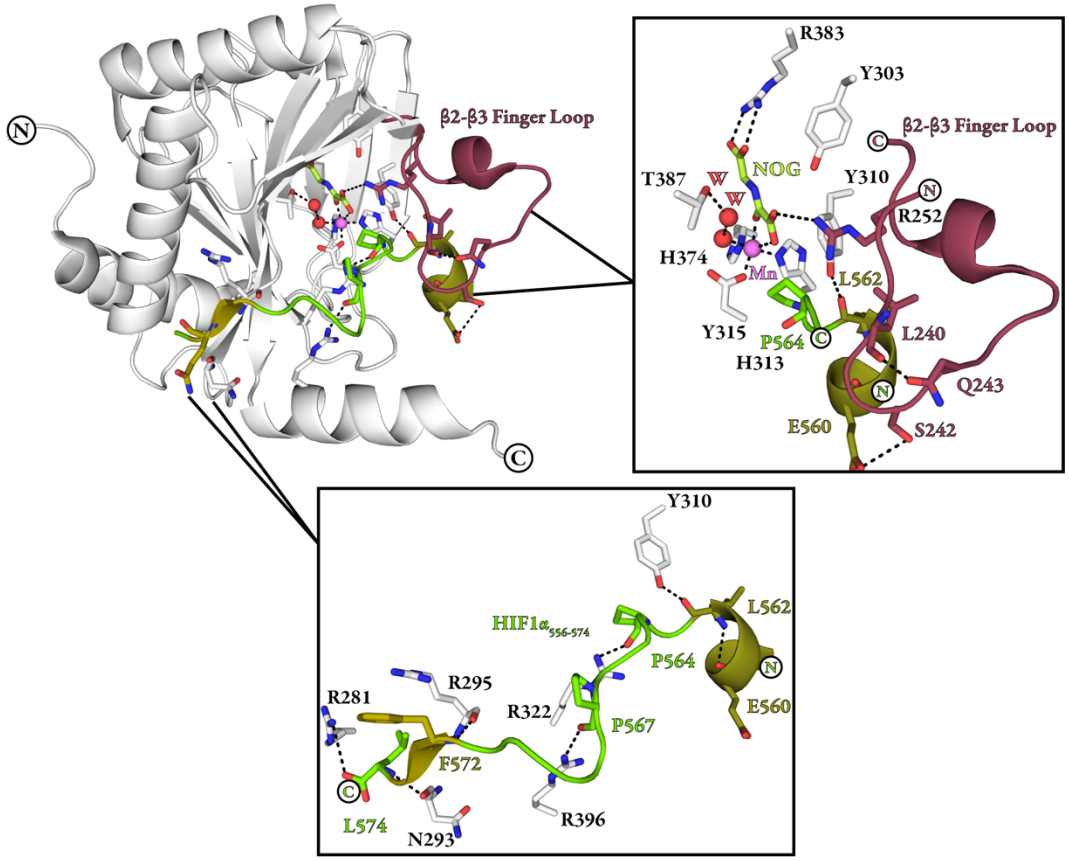


Figure 2-1 | View from a Crystal Structure of $PHD2_{181-426}$.NOG in Complex with $HIF1\alpha_{556-575}$-19-mer Fragment Peptide. The active site residues of $PHD2_{181-426}$ are shown as sticks (white). $PHD2_{181-426}$ (white) and its β2-β3 finger loop (raspberry) are depicted in cartoons. The $HIF1\alpha_{556-575}$-CODD peptide (green) is displayed as cartoon with observed secondary structure elements (olive). Residue interactions are displayed with dashes (black). The Mn ion (violet) and water molecules (red) are represented as spheres. Abbreviations: Prolyl hydroxylase isoform 2 (PHD2), Hypoxia-inducible factor (HIF), and *N*-Oxalylglycine (NOG). PDB: 3HQR.

The initial hit crystal of $PHD2_{181-426}$.Mn(II).NOG.$HIF1\alpha_{556-575}$-CODD complex took approximately 6 months to grow and was apparently formed *via* nucleation within heavy amorphous precipitation.[1] In complex were Mn(II) (replacing Fe(II)), inhibitor NOG (replacing 2OG), and a 19-mer peptide of $HIF1\alpha_{556-575}$ with $PHD2_{181-426}$ to obtain the structure (PDB: 3HQR, **Figure 2-1**).[1] tPHD2 is inactive with Mn(II). Both Mn(II) and NOG were typically used to prepare aerobic tPHD2.HIFα substrate crystals. The initial crystallisation condition (obtained by screening) was around 20% (w/v) polyethylene glycol (PEG) 3350, 200 mM $MgCl_2$, at pH 7.5 (temperature 298 K).[1] Optimisation of the initial conditions was carried out to obtain higher resolution crystals. A $PHD2_{181-426}$-$HIF1\alpha_{556-575}$ complex crystal diffracted to a 2.00 Å resolution (**Figure 2-1**).[1] The resultant structure revealed the key substrate binding residues and secondary structure features of $PHD2_{181-426}$ upon binding of $HIF1\alpha_{556-575}$-peptide. HIF1α, which is typically disordered at its ODD region, forms a *N*-terminal α-helix and a *C*-terminal β-strand once bound with the PHDs.[1] Active site residues $Tyr310_{PHD2}$ and $Arg322_{PHD2}$ form a hydrogen bond and electrostatic interaction with residues $Leu562_{HIF1\alpha}$ and $Pro564_{HIF1\alpha}$, respectively (**Figure 2-1**).[1,2] The $PHD2_{181-426}$.HIF1α structure provided new insights into the residues of tPHD2 that interact with HIFα and the induced-fit mechanism of substrate binding, in particular the conformation of the mobile β2-β3 finger loop (**Figure 2-1**).[1–5]

The β2-β3 finger loop is characteristic of the PHD paralogues and evolutionary orthologues compared to other 2OG-dependent oxygenases.[6–8] As previously discussed (**Figure 1-13,** in section **1.3.5**), there are significant sequence variations in the β2-β3 finger loop region of PHD1-3 and related PHDs. The lack of sequence conservation may, in part, reflect the observed differences in substrate specificity between the PHD isoforms and HIF1-3α substrates.[2,9]

In 2016, previous Schofield group members managed to obtain a complex structure of PHD2$_{181\text{-}426\text{-}(R281C/P317C)}$.Mn(II).NOG.HIF1α$_{395\text{-}413}$-NODD$_{(L397C/A412C)}$ through disulfide cross-linking of the substrate into the active site (**Figure 2-2**).[2]

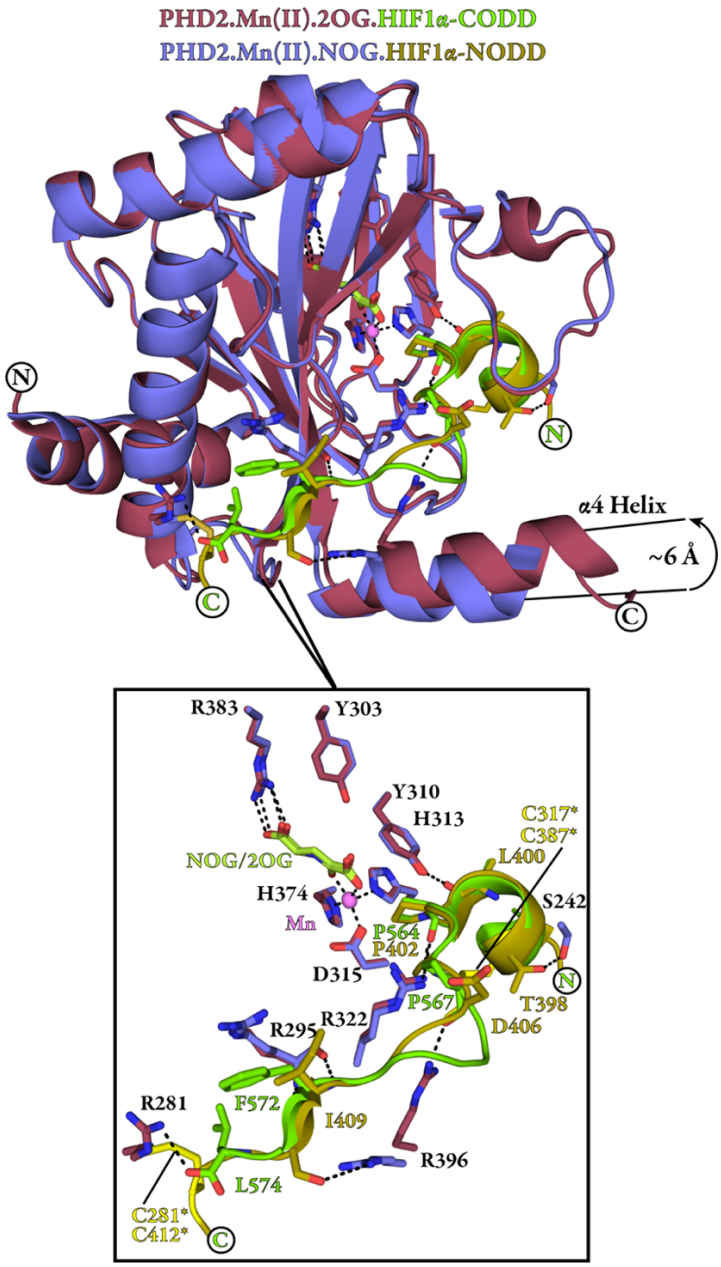


Figure 2-2|Superimposition and Active Site View of PHD2$_{181\text{-}426}$ Structures in Complex with HIF1α$_{556\text{-}575}$-CODD and HIF1α$_{395\text{-}413}$-NODD. PHD2$_{181\text{-}426}$ is in complex with fragment peptides of the *N*-/*C*-terminal oxygen degradation domains. The aligned structures of PHD2$_{181\text{-}426}$.HIF1α$_{556\text{-}575}$-CODD (red) and PHD2$_{181\text{-}426}$.HIF1α$_{395\text{-}413}$-NODD (blue) highlight variations in the *C*-terminal α4 helix induced by the different substrate binding. The active site residues are displayed as sticks. The CODD (green) and NODD (olive) fragment peptides are depicted as a cartoon and sticks. Active site interactions are shown as dashes (black). 2OG and NOG are represented as sticks (lemon). Disulfide cross-link depicted as sticks (yellow). Abbreviations: Prolyl hydroxylase isoform 2 (PHD2), Hypoxia-inducible factor (HIF), *C*-/*N*-terminal oxygen degradation domain (*C*-/*N*-ODD), 2-Oxoglutarate (2OG), and *N*-Oxalylglycine (NOG). PDB: 5L9B, 5L9V.

Comparisons of the PHD2$_{181-426}$.Mn(II).2OG.HIF1α$_{556-575}$-CODD and PHD2$_{181-426}$.Mn(II).NOG.HIF1α$_{395-413}$-NODD complexes reveals the apparent importance of the PHD2$_{181-426}$-*C*-terminal α4-helix in binding HIFα substrates (**Figure 2-2**). An ~6 Å shift of the α4-helix is observed between their structures and may be linked to the conformational variation of Arg396$_{PHD2}$. The guanidinium moiety of Arg396 is observed to interact with two different residues in the NODD and CODD fragment structures, *i.e.*, Pro567$_{HIF1α-CODD}$ and Ser410$_{HIF1α-NODD}$ (**Figure 2-2**).[2]

After ODD substrate binding and loop closure, PHD catalyses the *trans*-4-prolyl hydroxylation of its target prolines (**Figure 2-3**). Pro564$_{HIF1α}$ is proposed to change the preferred ring pucker from a C^4 *endo*- to a C^4 *exo*-conformation due, in part, to the operation of a stereo-electronic 'Gauche' effect induced by hydroxylation.[1]

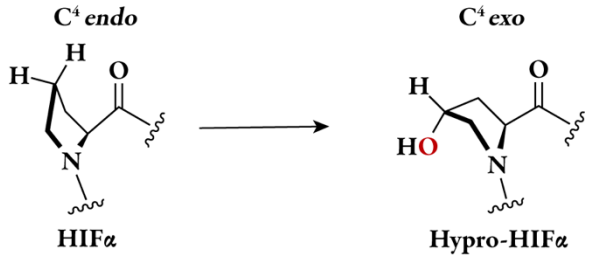


Figure 2-3| Non-hydroxylated and Hydroxylated HIFα-ODD Pyrrolidine Conformation Ring Pucker. Upon *trans*-4-hydroxylation, it is proposed that the HIFα-ODD target proline changes its preferred ring pucker from the C^4 *endo*- to the C^4 *exo*-conformation. Abbreviations: Hypoxia-inducible factor α (HIFα), Oxygen degradation domain (ODD), Hydroxylated proline (Hypro).

The pyrrolidine ring of Pro564 is observed to be in the C^4 *endo* conformation in the PHD2$_{181-426}$.HIF1α$_{556-574}$ complex and C^4 *exo* conformation in the VCB.HIF1α$_{Hyp564}$-CODD complex (**Figure 2-3**).[10] It has been proposed that the switch in pyrrolidine ring conformation helps promote the release of the HIFα product release.[1] Previous NMR studies have shown that the hydroxylated HIFα can inhibit tPHD2 by blocking the non-hydroxylated HIFα-substrate from binding when hydroxylated HIFα is present, but note the same inhibition can occur for 2OG and hydroxylated Pro.[11]

The conserved hydroxylation ODD motif, LXXLAP, can be visualised in the $PHD2_{181-426}$.$HIF1\alpha_{556-575}$ complex structure (**Figure 2-1**, PDB: 3HQR).[1] The alanine-proline unit is conserved in most of metazoan HIFα-ODD sequences.[9] The alanine is proposed to enable flexibility that allows the target proline to adopt a catalytically productive conformation in the orthosteric site.[1] The relatively "tight" nature of the active site of the PHDs, along with the binding mechanism of HIFα substrates, likely help make the PHDs very specific, non-promiscuous enzymes.[9,12,13] There have been previously reported alternative substrates of the PHDs, but previous Schofield group members and collaborators have not been able to validate the targets as PHD substrates through proteomic and other investigations.[9]

2.1.1 Proposed Catalytic Mechanism for the PHDs

In PHD catalysis, as observed in other 2OG oxygenases, 2OG binding precedes the HIFα-substrate complexing (**Figure 2-4**).[12,14] The octahedral geometry of Fe(II) (or Mn(II)) accommodates complexation of 2OG in a bidentate coordination mode and one bound water molecule (**Figure 2-4**).[12,14] Upon binding of HIFα-substrate, the reaction is proposed to be initiated by O_2 (**Figure 2-4**).[12,14] It is proposed that the water molecule is displaced on O_2 binding and/or that 2OG reorganises to allow O_2 to bind at the 2OG C1 carboxylate-Fe(II) binding position next to $Pro564_{HIF1\alpha}$; 2OG-Fe rearrangement has been observed in other 2OG oxygenases (**Figure 2-4B**).[14,15] Recent computational analyses have led to the proposal of a 2OG rearrangement occurring in the PHDs (**Figure 2-4C**).[13] In the $PHD2_{181-426}$.HIF1α structure (PDB: 3HQR), the Fe bound water forms a hydrogen bond network involving Asp315 (coordinating the metal ion), an unbound water molecule, and the alcohol side chain of Thr387 (**Figure 2-1**).[1,16] The uncoordinated carboxylate of Asp315 Oδ1 atom likely interacts with the Fe-coordinated water molecule

and increases the displacement energy required for O_2 to substitute for this water.[1,14] Previous literature has reported that the T387A mutation can increase the rate hydroxylation approximately 15-fold in an *in vitro* assay compared to wild-type PHD2.[16] The T387A mutation may enable more efficient O_2-diffusion to the Fe, *i.e.*, diffusion of O_2 in the proposed pathway to the catalytic site.[16] The Thr387 active site residue is conserved in the related-metazoan orthologue, *Ta*PHD, and bacterial orthologue, PPHD.[6,7]

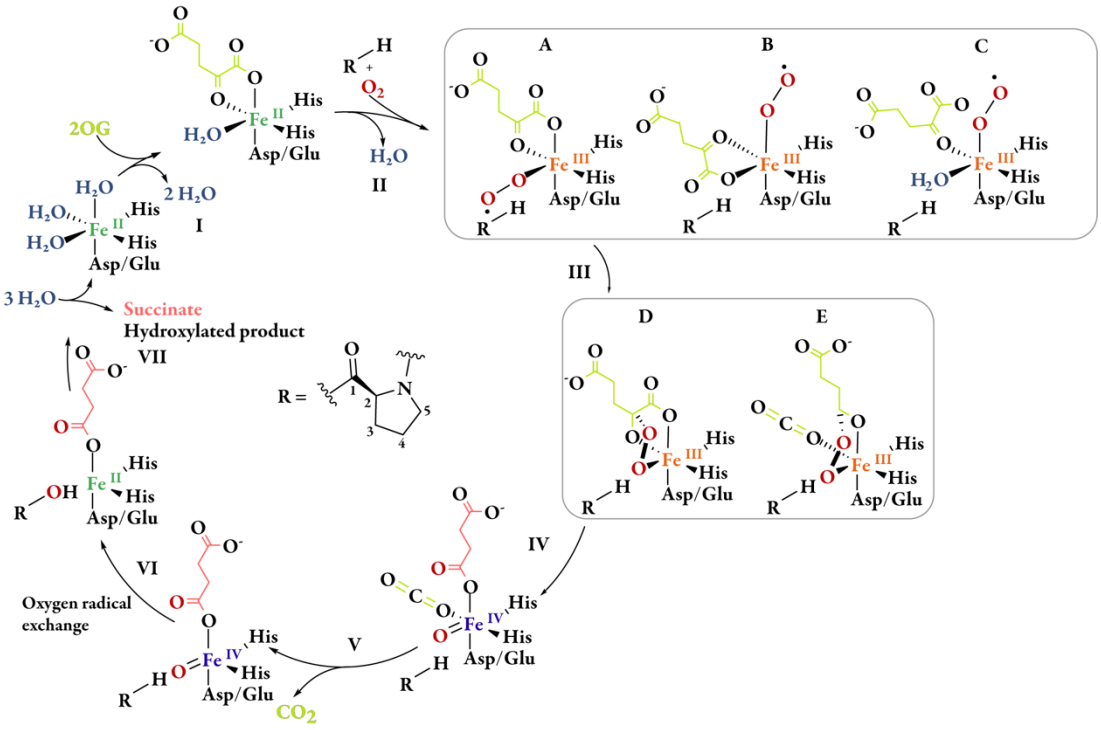


Figure 2-4| The Proposed Consensus Catalytic Cycle of Prolyl Hydroxylases. (I) Two water molecules are displaced upon 2OG coordinating Fe(II) in a bidentate manner. (II) HIFα-substrate binding is followed by O_2 displacement of the remaining water molecule and oxidation of Fe(II) to Fe(III). It has been proposed that 2OG can potentially rearrange or form a monodentate coordination of Fe(II) during catalysis (A-C). (III) Oxidation of 2OG leads to the subsequent decarboxylation of the 2OG C1 carboxylate (C-D). (IV) Formation of succinate and oxidation of Fe(III) to a reactive ferryl Fe(IV) intermediate. (V) CO_2 is released. (VI) The ferryl Fe(IV)=O abstracts a hydrogen that leads to hydroxylation of the HIFα-substrate. (VII) Succinate and hydroxylated products are released, and three water molecules re-coordinate the Fe-centre. Abbreviations: 2-Oxoglutarate (2OG).

In 1974, Cardinale and Udenfriend proposed a mechanism for the CPHs post-translational modification of collagen.[17] Their mechanism proposed the formation of a peroxide-bridge between succinate (post-decarboxylation of 2OG) and the target

proline.[17,18] Following the peroxobridge, Cardinale and Udenfriend proposed the formation of a peroxyproline intermediate prior to 2OG decarboxylation.[18] The consensus catalytic cycle of 2OG-dependent enzymes, based on detailed crystallographic and spectroscopic data, has shown evidence for formation of different, but related, intermediate complexes. In particular, there is good evidence for the formation of a reactive ferryl Fe(IV)=O complex (in some cases, but not all).[19] Detailed stopped flow/ultraviolet (UV)-visible (Vis) and Mössbauer spectroscopy of tPHD2 have provided evidence for a slow reaction of tPHD2 with O_2 and formation of a relative stable species at 320 nm.[12] The stable species is likely not the Fe(IV)=O complex that has been observed with some other 2OG oxygenases, evidenced by the species appearing and slowly decaying over time in tPHD2.[12] The Fe(IV)=O species has been observed to rapidly form and decompose during the hydrogen abstraction from the substrate and the subsequent radical recombination to form the product in other 2OG-dependent enzymes (visualised through Mössbauer spectroscopy).[12,20–22] The tPHD2.Fe(II).2OG complex has been observed to be relatively stable in the presence of O_2 and substrate uncoupled 2OG turnover was slower in tPHD2 then with other 2OG-dependent enzymes, *e.g.*, AlkB is reported to have increased levels of 2OG uncoupled turnover in the presence of O_2.[23] A consistent shift from a λ_{max} 527 nm to a 521 nm species was seen, potentially representing a change from a six- to a five- coordinated Fe-centre.[12] The evolution of the PHDs as metazoans' 'O_2-sensors', may in part, be enabled by the stability of the tPHD2.Fe(II).2OG complex and tight binding of the HIFα substrates when available. It is thus proposed that the PHDs are essentially 'primed' for catalysis in a manner sensitive to the O_2-tension in the cytoplasm.[12]

2.1.2 3C Cyclic Peptide and Time-Resolved Crystallography

Due to the difficulties in growing the PHD2$_{181-426}$.Mn(II).NOG.HIF1α$_{556-575}$-CODD substrate crystals and the packing clashes observed in the *P* 6_3 space group of PHD2$_{181-426}$.Fe(II).NOG.HIF1α$_{556-575}$-CODD$_{Hyp564}$, studies were conducted to identify a cyclic peptide that could be used to promote crystallisation.[5] Previous work described the identification of a high-affinity cyclic peptide (3C) that binds tightly to PHD2$_{181-426}$ at the *N*-terminal extension of the DSBH fold (discussed in section **1.2**) and the *C*-terminus.[5,24] A 14-mer cyclic peptide (molecular weight: 1751.20) and was obtained through the application of the established Random nonstandard Peptide Integrated Discovery (RaPID) mRNA-display system (**Figure 2-5**).[5,24] The reported 3C cyclic peptide can be used as a molecular tool to stabilise the enzyme and promote crystallisation of PHD2$_{181-407}$ with HIFα-substrate (**Figure 2-5**).[5,24] Furthermore, the 3C peptide could potentially be used also to stabilise tPHD2 constructs and help promote co-crystallisation with structurally uncharacterised inhibitors.[5,24]

In theory, the 3C cyclic peptide could be utilised to assist in the scale-up of crystallisation of PHD2$_{181-407}$.HIFα complexes for time-resolved mechanistic studies that require large amounts of crystals for data collection.[5,24] For studies conducted by *Dr. Rasheduzzaman Chowdhury*, the 3C helped to promote the PHD2$_{181-407}$.Mn(II).HIF1α$_{556-575}$-CODD.3C complex structure (PDB: 6YW3).[5,24] The reproduction and optimisation of the PHD2$_{181-407}$.Mn(II).HIF1α$_{556-575}$-CODD.3C crystallisation conditions was carried out in anaerobic conditions substituting Fe(II) and 2OG for Mn(II) and NOG. The anaerobically grown PHD2.HIFα crystals could then be exposed to O_2 and initiate a reaction *in crystallo*. Subsequent conventional quench-cryo-cooling or serial crystallography methods might trap an intermediate reaction state with O_2-exposed crystals.[28–36]

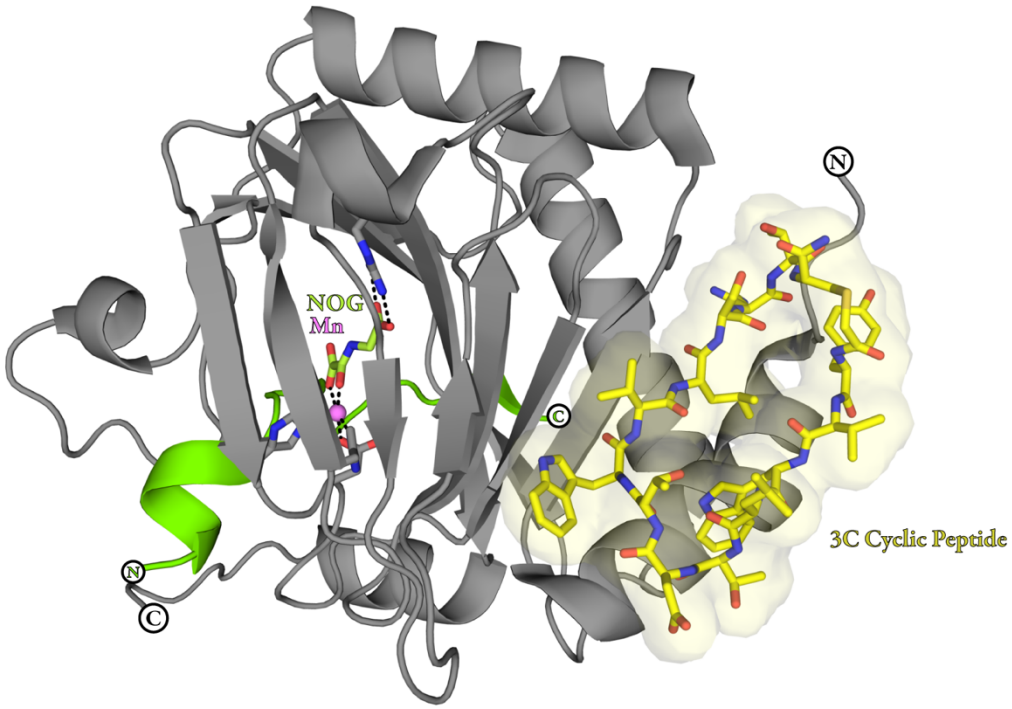


Figure 2-5 | PHD2$_{181-407}$ in Complex with RaPID-derived 3C Cyclic and HIF1α-CODD Peptides. A surface representation of the 3C cyclic peptide (yellow) is displayed. The 3C is bound to the *N*-terminal extension to the DSBH (or jelly roll) fold. The HIF1α-CODD peptide (green) is bound in the normal substrate binding groove and is unaffected by the 3C peptide. PHD2$_{181-407}$ is depicted as a cartoon (grey). Abbreviations: Prolyl hydroxylase isoform 2 (PHD2), Random nonstandard Peptide Integrated Discovery (RaPID), 3C cyclic peptide (3C) and *C*-terminal oxygen degradation domain (CODD). PDB: 6YW3.

The development of tuneable, brilliant energy X-ray beamlines and improved pixel-array detectors at synchrotron light sources has led to the ability to obtain higher resolution crystallographic data.[25–27] Advancements in X-ray Free-Electron Laser sources (XFELs), have enabled new capabilities in time-resolved based serial crystallographic studies.[28–36] These technological developments provide an ability to capture snapshots of the enzyme catalysis with femtosecond pulses that can be coupled with spectroscopic data.[28,34–36] The application of time-resolved synchrotron crystallography has led to the potential characterisation of intermediates in the mechanisms of the 2OG oxygenases and other enzymes.[28,30,33–35] In 2017, researchers from Pennsylvania State University reported synchrotron based time-resolved mechanistic studies on 2OG-dependent L-arginine hydroxylase violacein synthase (VioC), a bacterial 2OG-dependent enzyme.[37] The group

reported observation of a potential succinyl-peroxide intermediate following the decarboxylation of 2OG (**Figure 2-6**).[37] A part of my work was the time-resolved studies of tPHD2 to determine a suitable anaerobic crystallisation condition to investigate the unique nature of the PHDs and relative slow reaction with O_2 using X-ray crystallography.

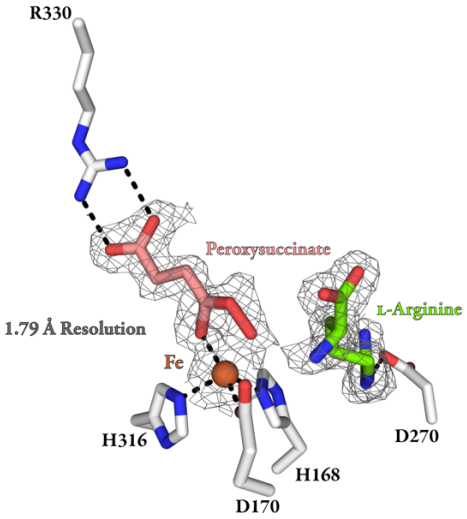


Figure 2-6| A Succinyl-Peroxide Intermediate Observed During Mechanistic Crystallographic Studies of L-Arginine Hydroxylase, VioC. The active site of VioC is depicted as sticks (active site residues-white, succinyl-peroxide (pink), and L-Arginine (green)). The key active site interactions are depicted as dashes (black). The $2mF_o$-DF_c map (contoured at 1.0 σ) displayed as mesh (grey). Abbreviations: L-arginine hydroxylase violacein synthase (VioC). PDB: 6ALO.

2.2 The Formate-Derived Crystallisation Condition with the 3C Cyclic Peptide

Recombinant $PHD2_{181\text{-}407}$ was purified using a two-column purification strategy, that involved Ni(II)-affinity chromatography (**6.4.2**), a procedure encompassing the removal of the hexa-histidine (His_6)-tag with thrombin protease (**6.4.9**), and size-exclusion chromatography (SEC, **6.4.3**, **Figure 2-7**). His_6-tag removal using thrombin was confirmed *via* mass spectrometry (MS). A +178 Dalton (Da) shift on the mass spectra of $PHD2_{181\text{-}407}$ was observed prior to His_6-tag removal; with evidence to suggest that this shift likely corresponds to a gluconylation of the His_6-tag using thrombin (**Figure 2-8A**).[38]

The +178 Da shift was not present after thrombin cleavage of the His_6-tag (**Figure 2-8A**). The activity of $PHD2_{181-407}$ was analysed using a reported hydroxylation assay.[9] MS analyses were conducted to determine the level of hydroxylation after 30 minutes incubations of $PHD2_{181-407}$ with the $HIF2\alpha_{523-542}$-CODD peptide (**Figure 2-8B**, **6.5.2**).[9] Turnover was observed for the purified construct of $PHD2_{181-407}$ and highlights the *N-/C*-terminally truncated construct is catalytically active. (*Thank you to Dr. Rasheduzzaman Chowdhury for his significant preliminary work to optimise the crystallisation of the tPHD-HIFα complex.*)

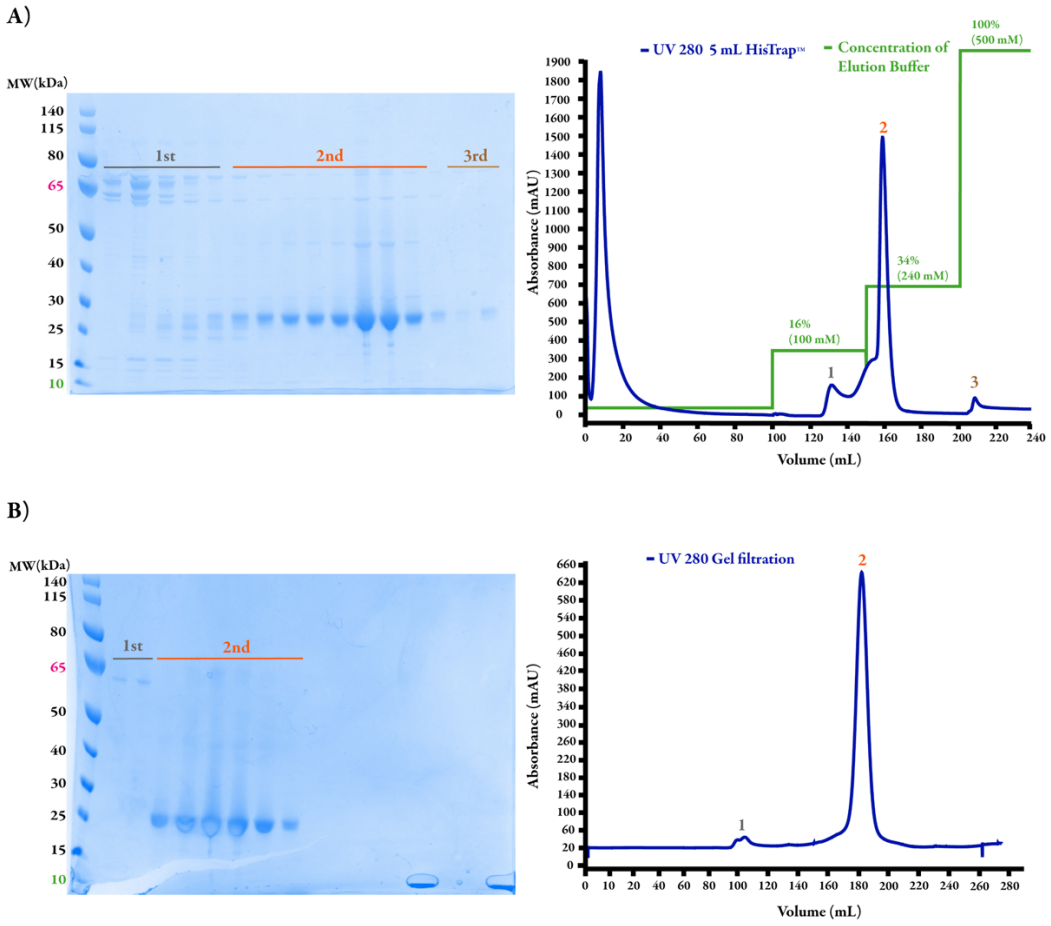


Figure 2-7| The Two-Column Purification Strategy to Purify $PHD2_{181-407}$. (A) The SDS-PAGE gel and chromatogram of the affinity chromatography step provides characterisation of purity of the construct at this step and the step elution gradient (green) used to elute protein from the column. (B) SDS-PAGE and chromatogram of the gel filtration column provide final characterization of purity the two-column strategy before crystallisation. Bands in the 2nd peak (orange) were collected for crystallisation studies. Abbreviations; Molecular weight (MW), Dalton (Da), Prolyl hydroxylase isoform 2 (PHD2), Sodium-dodecyl-sulfate polyacrylamide gel electrophoresis (SDS-PAGE).

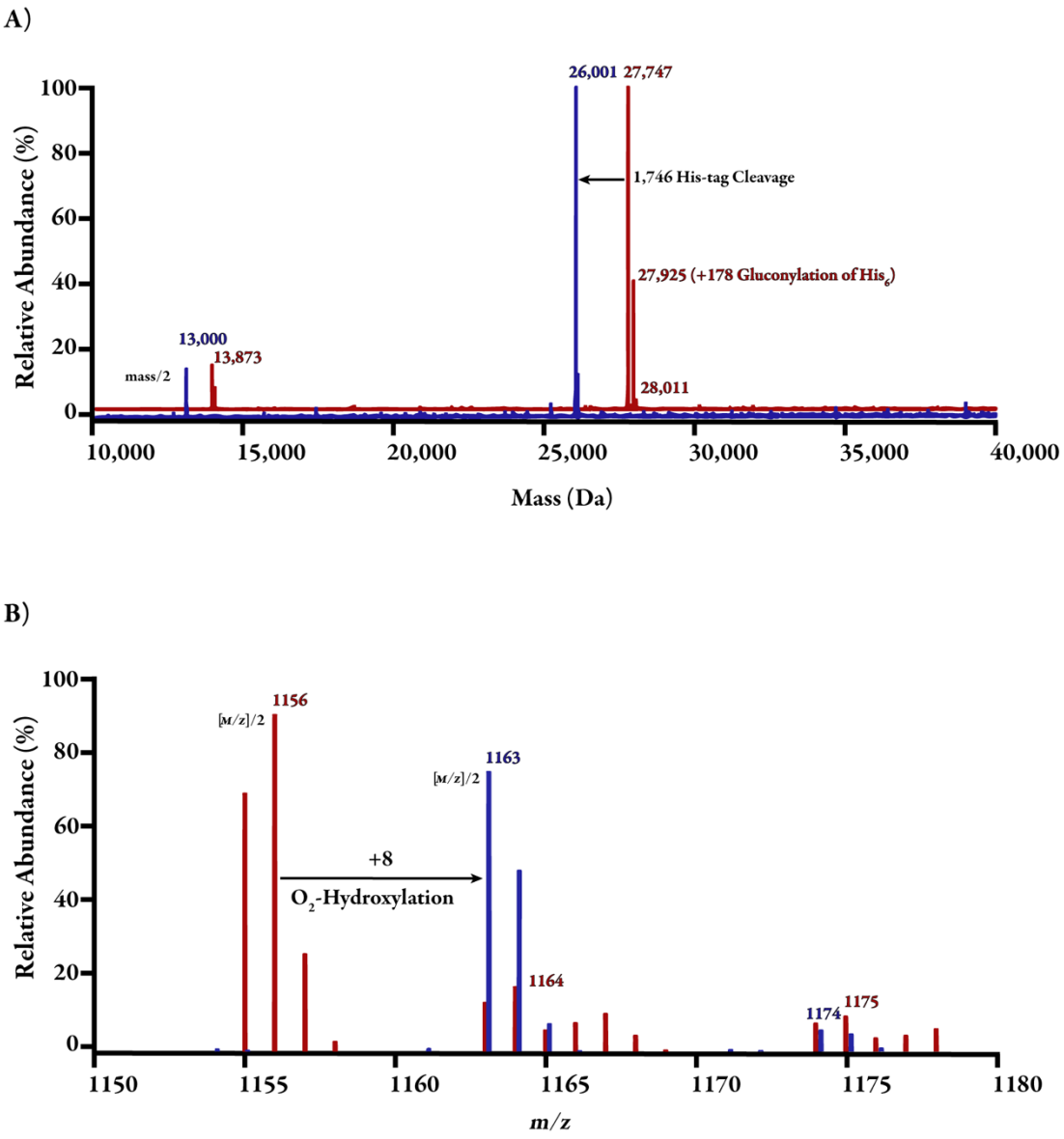


Figure 2-8| Mass Spectra of PHD2$_{181-407}$ Construct Thrombin Cleavage and Hydroxylation Assay with HIF2α$_{523-542}$-CODD Peptide. (A) The deconvoluted thrombin cleavage spectra are overlayed and of His$_6$-PHD2$_{181-407}$ (red) and cleaved-PHD2$_{181-407}$ (blue) indicate that the His$_6$-tag purification has been removed from the construct. A +178 gluconylation modification of the His$_6$-tag is observed. The reaction was left overnight at 4 °C. (B) Spectra of the HIF2α$_{523-542}$-CODD (red) and hydroxylated-HIF2α$_{523-542}$-CODD (blue) from the hydroxylation assay are overlaid and indicates the construct is active through the +16 O_2 adduct (+8 [*m*/*z*]/2) of the HIF2α peptide. The reaction was prepared with 1 μM PHD2$_{181-407}$, 100 μM, 300 μM 2OG, 300 μM L-ascorbate, and 50 μM $(NH_4)Fe(II)(SO_4)$. Abbreviations: Prolyl hydroxylase isoform 2 (PHD2), Hypoxia-inducible factor (HIF), *C*-terminal oxygen degradation domain (CODD), and Hexa-histidine (His$_6$).

Initial attempts were aimed to optimise the crystallisation of the PHD2$_{181-407}$.HIFα-substrate complex, both in aerobic and anaerobic conditions in a manner suitable for further mechanistic studies on tPHD2. The 3C cyclic peptide (**Figure 2-5**), was used to promote crystallisation of PHD2$_{181-407}$ with HIFα-substrate.[5,24] A former Schofield group

member obtained a crystallisation condition with magnesium formate and 18-22% (w/v) PEG 3350 (the formate-derived condition developed by *Dr. Rasheduzzaman Chowdhury*).[5] Reproduction of the PHD2$_{181-407}$.Mn(II).NOG.HIF1α$_{556-575}$-CODD complex was screened for in 24-well sitting-drop (**6.6.4**) and hanging-drop vapour diffusion crystallisation plates (**6.7.1** and **6.7.3**).[5]

Six complex structures incubated with the 3C cyclic peptide were derived from the formate condition following a protocol from *Dr. Rasheduzzaman Chowdhury* (6.7.1). The structures correspond to:

(i) PHD2$_{181-407}$.Mn(II).NOG.HIF2α$_{523-542}$-CODD.3C (*Xtal-A*),

(ii) PHD2$_{181-407}$.Mn(II).2OG.HIF2α$_{523-542}$-CODD.3C (*Xtal-B*),

(iii) PHD2$_{181-407}$.Fe(II).2OG.HIF2α$_{523-542}$-CODD.3C-O_2 fragment (anaerobic *Xtal-C*),

(iv) PHD2$_{181-407}$.Fe(II).2OG.HIF2α$_{523-542}$-CODD.3C.Rest-O_2-1-min.17/19/25-min.+O_2

(**6.7.4**, T17-*Xtal-D,* T19-*Xtal-E,* and T25-*Xtal-F*; *Xtal IDs* are listed in **Appendix I**).

Table 2-1| Formate-Derived Crystallographic Data Processing and Refinement Statistics.

	Formate Mn(II).NOG (*Xtal-A*)	Formate Mn(II).2OG (*Xtal-B*)
Beamline	Diamond Light Source-I24	Diamond Light Source-I24
Detector	Dectris Pilatus3 6M	Dectris Pilatus3 6M
Data Processing	Xia2 DIALS	Xia2 DIALS
Wavelength (Å)	0.96861	0.97962
Resolution range (Å)	40.75 - 1.17 (1.21 - 1.17)	36.64 - 1.21 (1.25 - 1.21)
Space group	*P* 21 21 2	*P* 21 21 2
Unit cell (Å, °)	130.91 38.32 42.88	130.45 38.17 42.75
Total reflections	1764477 (121954)	808554 (71010)
Unique reflections	73707 (7148)	66188 (6526)
Multiplicity	23.9 (17.1)	12.2 (10.9)
Completeness (%)	99.75 (98.07)	99.94 (99.85)
Mean I/sigma(I)	11.13 (1.20)	10.05 (1.15)
Wilson B-factor (Å²)	13.75	14.13
R-merge†	0.1467 (3.871)	0.1317 (4.204)
R-meas	0.1499 (3.99)	0.1376 (4.413)
R-pim	0.03046 (0.9422)	0.03926 (1.322)
CC1/2	0.999 (0.39)	0.999 (0.432)
CC*	1 (0.749)	1 (0.777)
Reflections used in refinement	73635 (7115)	66154 (6516)
Reflections used for R-free	3746 (345)	3326 (334)
R-work✧	0.1613 (0.3095)	0.1598 (0.3118)
R-free✧	0.1852 (0.3188)	0.1792 (0.3075)
CC(work)	0.975 (0.722)	0.973 (0.775)
CC(free)	0.961 (0.705)	0.961 (0.805)
Number of non-hydrogen atoms	2416	2269
macromolecules	2105	2036
ligands	65	111
solvent	276	163
Protein residues	243	240
RMS(bonds, Å)	0.008	0.011
RMS(angles, °)	1.02	1.22
Ramachandran favored (%)	97.91	97.88
Ramachandran allowed (%)	2.09	2.12
Ramachandran outliers (%)	0	0.00
Rotamer outliers (%)	1.37	1.43
Clashscore	5.94	4.63
Average B-factor (Å²)	20.46	22.72
macromolecules	18.5	20.92
ligands	46.57	49.15
solvent	32.16	33.86
Number of TLS groups	9	10

Single crystal diffraction data was collected from samples held at 100 K with conventional, rotation-based methods. Ligands: Mn, 2OG, FMT, GOL, Cl, Mg, and PEG. Statistics for the highest-resolution shell are shown in parentheses.

† R-merge (or Rsym) is equal to $\sum|I-\langle I\rangle|/\sum I$. R-merge represents the data quality of merged reflection data. *I* is equal to the intensity of individual measurements and <I> is equal to the average of multiple measurements.

✧R_{free} is the R_{factor} for 5% of the reflections which are excluded during refinement.
R_{factor} is equal to $\sum_{hkl}||Fobs_{(hkl)}| - |Fcalc_{(hkl)}||/\sum_{hkl}|Fobs_{(hkl)}|$ and was calculated for the working set of reflections (R_{work}).
Appendix I contains information on the crystal contents and *Xtal-IDs*.

Table 2-2|Formate-Derived Anaerobic and O_2-Exposed Crystallographic and Refinement Statistics.

	Anaerobic.Fe(II).2OG (*Xtal-C*)	T17.Fe(II).2OG (*Xtal-D*)	T19. Fe(II).2OG (*Xtal-E*)	T25.Fe(II).2OG (*Xtal-F*)
Beamline	Diamond Light Source-I24	Diamond Light Source-I24	Diamond Light Source-I24	Diamond Light Source-I24
Detector	Dectris Pilatus3 6M	Dectris Pilatus3 6M	Dectris Pilatus3 6M	Dectris Pilatus3 6M
Data Processing	Xia2 DIALS	Xia2 DIALS	Xia2 DIALS	Xia2 DIALS
Wavelength (Å)	0.96876	0.96877	0.96876	0.96876
Resolution range (Å)	32.67 - 1.48 (1.53 - 1.48)	41.13 - 1.65 (1.70 - 1.65)	65.53 - 1.65 (1.70 - 1.65)	43.17 - 1.48 (1.53 - 1.48)
Space group	*P* 21 21 2	*P* 21 21 2	*P* 2_1 2_1 2	*P* 21 21 2
Unit cell (Å, °)	129.50 37.84 42.23	130.94 38.20 43.32	131.05 38.26 43.32	130.71 38.14 43.17
Total reflections	411005 (37506)	334919 (32236)	332357 (32147)	388150 (31703)
Unique reflections	35559 (3514)	26993 (2609)	27086 (2650)	36914 (3618)
Multiplicity	11.6 (10.7)	12.4 (12.4)	12.3 (12.1)	10.5 (8.8)
Completeness (%)	99.94 (100.00)	99.82 (99.24)	99.91 (99.96)	99.94 (100.00)
Mean I/sigma(I)	11.57 (1.13)	7.34 (1.00)	9.80 (1.63)	13.14 (1.23)
Wilson B-factor (Å²)	19.69	19.25	17.18	18.47
R-merge†	0.1215 (1.971)	0.1986 (2.417)	0.161 (1.651)	0.1004 (1.671)
R-meas	0.1273 (2.071)	0.2072 (2.522)	0.168 (1.724)	0.1054 (1.775)
R-pim	0.03748 (0.6265)	0.05857 (0.7135)	0.04765 (0.4908)	0.0317 (0.588)
CC1/2	0.999 (0.504)	0.997 (0.504)	0.999 (0.685)	0.999 (0.523)
CC*	1 (0.819)	0.999 (0.819)	1 (0.902)	1 (0.829)
Reflections used in refinement	35552 (3514)	26961 (2604)	27085 (2649)	36910 (3618)
Reflections used for R-free	1794 (190)	1333 (142)	1347 (139)	1879 (179)
R-work✧	0.2494 (0.3612)	0.1816 (0.3064)	0.1808 (0.2607)	0.1748 (0.2864)
R-free✧	0.2774 (0.4135)	0.2013 (0.3377)	0.2113 (0.2701)	0.2061 (0.3030)
CC(work)	0.954 (0.659)	0.972 (0.777)	0.967 (0.868)	0.972 (0.783)
CC(free)	0.956 (0.458)	0.970 (0.713)	0.954 (0.797)	0.968 (0.689)
Number of non-hydrogen atoms	2075	2247	2184	2300
macromolecules	1975	2018	2044	2059
ligands	15	15	19	38
solvent	89	218	126	215
Protein residues	239	242	242	242
RMS(bonds, Å)	0.013	0.004	0.007	0.01
RMS(angles, °)	1.08	0.78	0.99	0.96
Ramachandran favored (%)	97.42	97.48	97.48	97.06
Ramachandran allowed (%)	2.58	2.52	2.52	2.94
Ramachandran outliers (%)	0	0	0.00	0
Rotamer outliers (%)	0.99	1.9	1.42	1.39
Clashscore	3.34	3.26	2.48	3.42
Average B-factor (Å²)	31.81	23.31	20.66	25.76
macromolecules	31.83	22.32	20.36	24.73
ligands	26.5	22.88	17.07	39.53
solvent	31.84	32.51	26.05	33.98
Number of TLS groups	6	9	9	9

Single crystal diffraction data was collected from samples held at 100 K with conventional, rotation-based methods. Ligands: Fe, 2OG, and FMT. Statistics for the highest-resolution shell are shown in parentheses.

† R-merge (or Rsym) is equal to $\sum|I-\langle I\rangle|/\sum I$. R-merge represents the data quality of merged reflection data. *I* is equal to the intensity of individual measurements and <I> is equal to the average of multiple measurements. ✧R_{free} is the R_{factor} for 5% of the reflections which are excluded during refinement.
R_{factor} is equal to $\sum_{hkl}||Fobs_{(hkl)}| - |Fcalc_{(hkl)}||/\sum_{hkl}|Fobs_{(hkl)}|$ and was calculated for the working set of reflections (R_{work}).
Appendix I contains information on the crystal contents and *Xtal-IDs*.

2.2.1 Optimisation of the Formate-Derived $PHD2_{181-407}$.$HIF2\alpha_{523-543}$-CODD Crystals

Some of the challenges with the formate-derived crystallisation system relate to the use of the 3C and HIF1α-peptides, both of which are largely insoluble in aqueous solutions. Thus, different methods were used to overcome the solubility issue that led to crystallisation of $PHD2_{181-407}$ in complex with the $HIF2\alpha_{523-542}$-CODD peptide. Multiple attempts to reproduce the $PHD2_{181-407}$.Mn(II).NOG.$HIF1\alpha_{556-575}$-CODD.3C crystallisation condition were initially tried using 24-well hanging-drop plates (**6.7.1-6.7.3**). Later, 288 sitting-drop vapour diffusion plates (**6.6.3**) were prepared with a crystallisation robot (Crystal Phoenix, Art Robbins Instruments, LLC., **6.6.4**) to increase the probability of obtaining an optimised condition.

Technical issues arose with Ni(II)-leeching into the $PHD2_{181-407}$ active site during the affinity chromatography purification step (**6.4.2**). Ni(II)-leeching has been previously reported to lead to instability of tPHD2, evidenced by results from a melting temperature (T_m)-shift assay.[39] To prevent this issue, it was suggested (*by Dr. Rasheduzzaman Chowdhury*) to use 5 column volumes (CV) of buffer containing high imidazole (0.5 M, **6.4.7**) to wash unbound Ni(II) ions from the affinity chromatography column prior to the loading of $PHD2_{181-407}$.[39] Furthermore, a laboratory wide phage infection required optimisation of the cell growth and expression conditions. During the infection, the induction point and expression temperatures were modified from the previously reported protocols.[2] An optimised protocol with growth of *Escherichia coli* (*E. coli*) cells to an $OD_{600\ nm}$ of 1.2 prior to induction with 0.5 mM isopropyl β-D-1-thiogalactopyranoside (IPTG); the cells were incubated overnight at 18 °C before harvesting (**6.3.7-6.3.8**; note that the induction conditions were only used for the formate-derived crystals).

As solubility was an issue with the $HIF1\alpha_{556-575}$-CODD and 3C peptides, dimethylsulfoxide (DMSO) and base (approximately 50-100 mM NaOH) were used to

assist solubilisation. All attempts to solubilise the peptides led to heavy amorphous precipitation in the crystallisation drops. Of the HIFα-CODD peptides tested (*i.e.*, HIF1$\alpha_{556-575}$, HIF2$\alpha_{523-542}$, and HIF3$\alpha_{484-503}$), the HIF2$\alpha_{523-542}$-CODD was found to be the most soluble when the protein solution was added to lyophilised substrate.

Initial haystack clusters of the PHD2$_{181-407}$.Mn(II).NOG.HIF2$\alpha_{523-542}$-CODD.3C microcrystals were first identified in 0.33 M magnesium formate and 19.6% (w/v) PEG 3350 after one day of equilibration (**Figure 2-9**, **6.7.2**). A subsequent optimised screen around the initial microcrystal condition yielded both a 1 mm x 100 μm x 80 μm and a 250 μm x 50 μm x 30 μm plate-like morphology crystals *(Xtal-A* and *Xtal-B,* respectively; *Xtal-IDs* are listed in **Appendix I**) after one week of equilibration (**Figure 2-9**, **6.7.2**). The crystal formed in 0.31 M magnesium formate and 16.6% (w/v) PEG 3350. The crystal was cryo-cooled in liquid-N_2 and diffraction data collected at 100 K to 1.17 Å resolution at a synchrotron source (**6.6.7.2**). The *Xtal-A* (**Table 2-1**) structure was solved by molecular replacement (MR)-phasing (**6.6.9.2**) using PDB: 3HQR as a starting model.[1] The solved structure of *Xtal-A* revealed no apparent evidence for binding of the 3C cyclic peptide (**Figures 2-10** and **2-11**). Further structural characterisation of *Xtal-A* revealed that the HIF2$\alpha_{523-542}$-CODD peptide helps promote crystallisation through an interaction between the Gly537$_{HIF2\alpha}$-Glu538$_{HIF2\alpha}$ insert and Glu538$_{HIF2\alpha\text{-symmetry}}$ from the neighbouring symmetry-related chain (**Figure 2-9**).

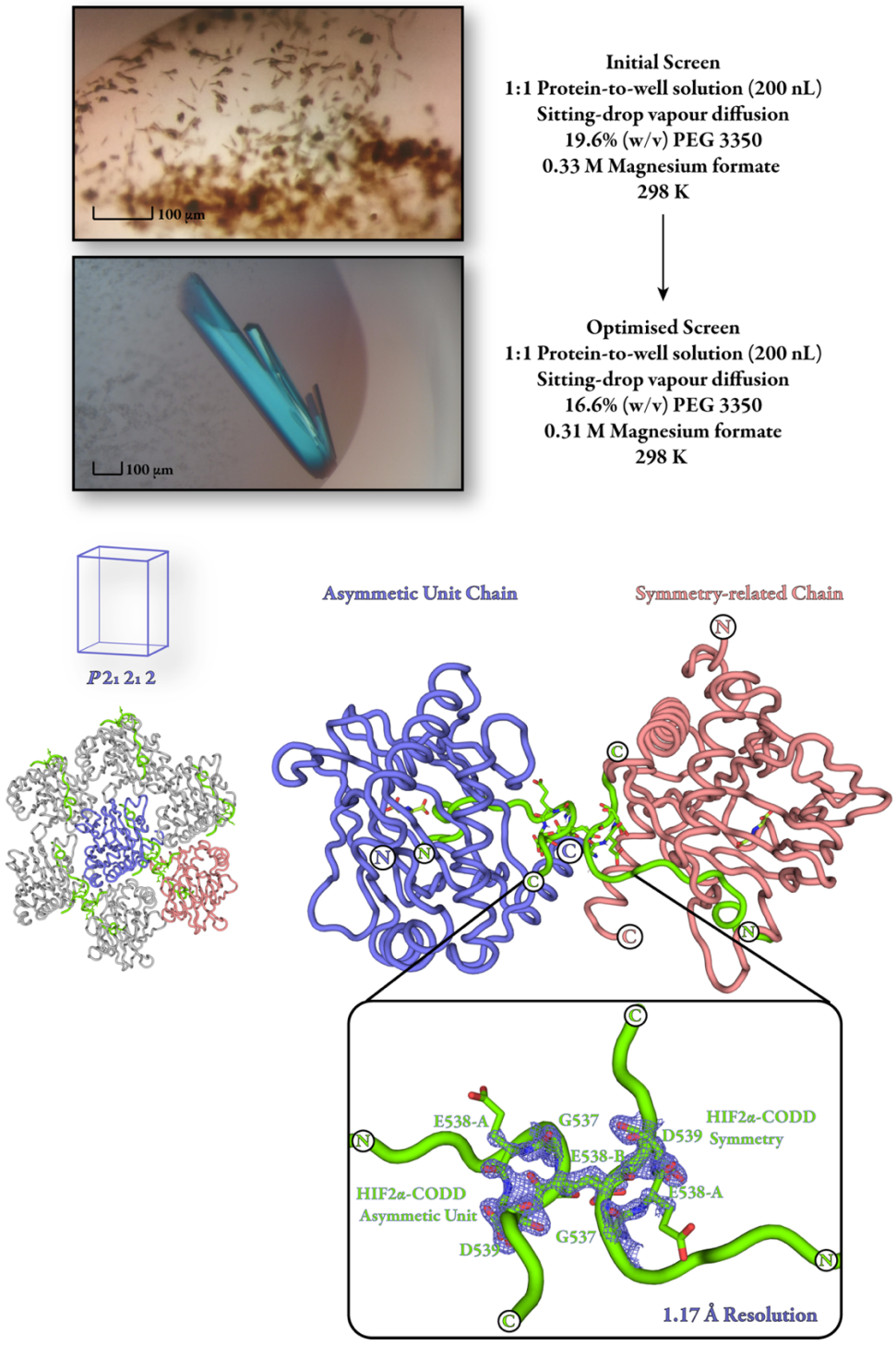


Figure 2-9| Optimisation of the Formate Crystallisation Condition and View of the HIF2α$_{523-542}$-CODD Peptide's Role in Crystal Packing. Initial PHD2$_{181-407}$.Mn(II).NOG.HIF2α$_{523-542}$-CODD.3C microcrystals were obtained and optimised to form a 1 mm x 100 µm x 80 µm plate-like shaped crystal (*Xtal-A*). Note that the Gly537-Glu538 insert the HIF2α$_{523-542}$-CODD peptide flips away from the core protein to interact with the Glu538 residue from the neighbouring symmetry-related chain (interacts with-pink and surrounding-grey). The $2mF_o$-DF_c maps (contoured to 1.0 σ) are displayed as mesh (blue). Abbreviations: Prolyl hydroxylase isoform 2 (PHD2), Hypoxia-inducible factor (HIF), and *C*-terminal oxygen degradation domain (CODD).

The inherent flexibility of glycine likely helps to enable a 'flip-out' of the Gly537-Glu538 residues, relative to the core fold of $PHD2_{181-407}$ (**Figure 2-9**). The symmetry-related molecule interaction between $Glu538_{HIF2\alpha}$-$Glu538_{HIF2\alpha\text{-symmetry}}$, that forms a 3.30 Å hydrogen bond between $Glu538_{HIF2\alpha}$ and $Asp539_{HIF2\alpha\text{-symmetry}}$ (*vice versa* interactions when the residues are in the alternate conformation) may help promote the oligomerisation during crystallization by further stabilising the lattice of $PHD2_{181-407}$.HIF2α that extends the data to 1.17 Å, whereas the $PHD2_{181-426}$.Mn(II).NOG.HIF1α complex only diffracts to 2.00 Å (PDB: 3HQR, **Figure 2-9**). It is possible that the nature of the oligomerisation induced by the $HIF2\alpha_{523-542}$-peptide may disrupt the reported 3C binding sites (**Figure 2-10**).[5,24]

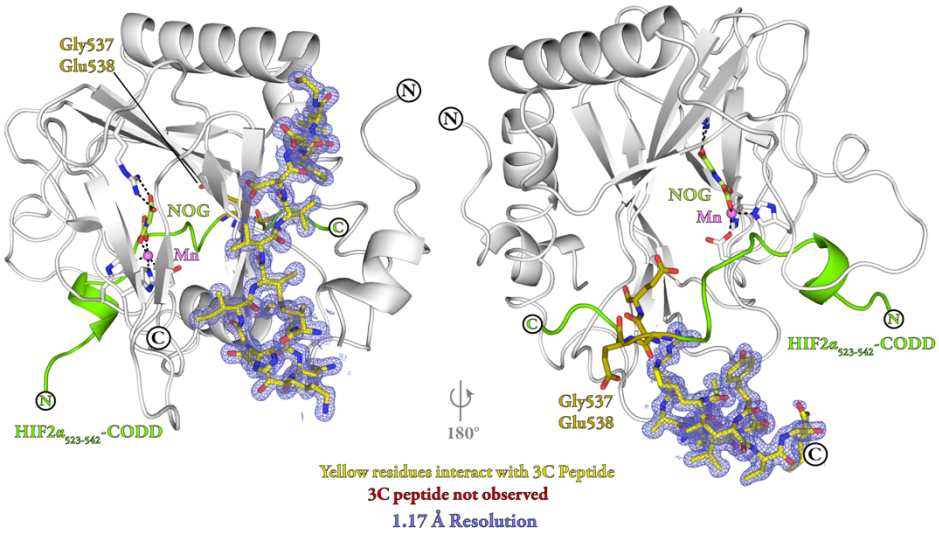


Figure 2-10|| The 3C Peptide is Not Complexed in the $PHD2_{181-407}$.Mn(II).NOG.$HIF2\alpha_{523-542}$-CODD Complex Structure. The $2mF_o$-DF_c electron density map (contoured to 1.0 σ) is displayed in blue mesh around the *N*-terminal and *C*-terminal residues, depicted as sticks (yellow), that interact with the 3C peptide. Active site residues (white), key HIF2α (olive) residues, and NOG (lemon) are displayed as sticks. HIF2α is represented as a cartoon (green). Mn ion is shown as a sphere, and electrostatic and hydrogen bonds are illustrated as dashes (black). Abbreviations: Prolyl hydroxylase isoform 2 (PHD2), Hypoxia-inducible factor (HIF), *N*-Oxalylglycine (NOG), and *C*-terminal oxygen degradation domain (CODD). *Xtal-ID*: *A*.

2.2.2 Comparisons Between tPHD2.NOG/2OG and HIF1α$_{556-575}$/HIF2α$_{523-542}$ Substrate Complexes

The high resolution structures of Mn(II) substituted PHD2$_{181-407}$.HIF2α$_{523-542}$-CODD co-crystallised with NOG or 2OG are very similar to each other. The *Xtal-A*-NOG complex structure aligned with PHD2$_{181-407}$.Mn(II).2OG.HIF2α$_{523-542}$-CODD complex (*Xtal-B*, **Table 2-1**) revealed a root-mean-square deviation (RMSD) value of 0.078 (measured in PyMOL™, **6.1**). Thus, indicating there are no significant conformational changes between the structures (**Figure 2-11**). The hydrogen bond network of water molecules from Thr387 to metal bound water is conserved in both the NOG and 2OG bound states (*Xtal-A* and *Xtal-B,* respectively).

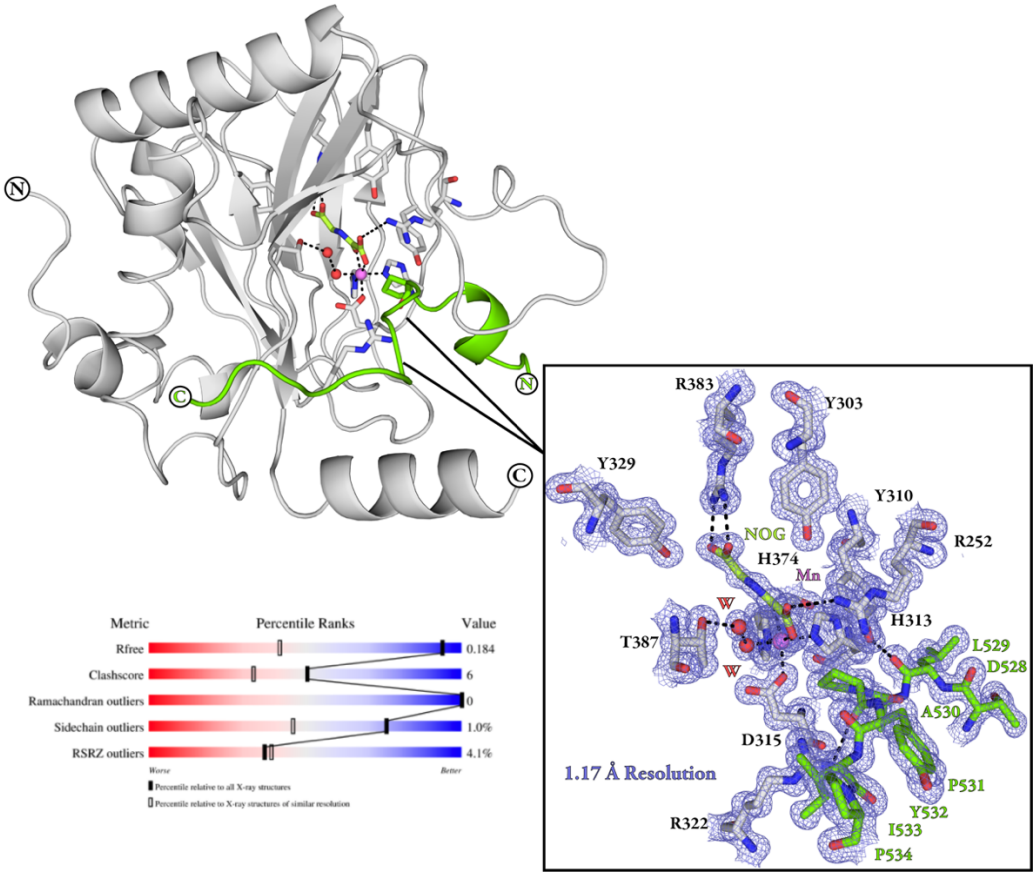


Figure 2-11| PHD2$_{181-407}$.Mn(II).NOG.HIF2α$_{523-542}$-CODD Complex Structure. The crystal diffracted to a 1.17 Å resolution. Active site residues (white), NOG (yellow), and HIF2α$_{523-542}$-CODD peptide residues (green) are shown in sticks. The 2mF_o-DF_c electron density map (contoured to 1.0 σ) is displayed as mesh (blue). Active site interactions are shown in black dashes. Mn (pink) and water molecules (red) are shown in spheres. Validation heat chart is shown and was generated using the PDB validation service. Abbreviations: Prolyl hydroxylase isoform 2 (PHD2), Hypoxia-inducible factor (HIF), *N*-Oxalylglycine (NOG), *C*-terminal oxygen degradation domain (CODD), and Protein Data Bank (PDB). *Xtal-ID*: *A*.

Similar to that of *Xtal-A*, the *Xtal-B* structure manifests the HIF2α$_{523-542}$-peptide Gly537-Glu538 conformational 'flip-out'. Thus, it seems this may be a conserved feature between the PHD2$_{181-407}$.Mn(II).NOG/2OG.HIF2α$_{523-542}$-CODD.3C complexes (**Figure 2-9**). In the *Xtal-B* complex, the density around the 2OG methylenes is not as clear as the density around the N1 atom of NOG in the *Xtal-A* (**Figure 2-12**). The weak density may, in part, reflect a small portion of 2OG uncoupled turnover from co-purifying Fe(II) with the crystallised PHD2$_{181-407}$ (*i.e.*, the added Mn(II) did not fully exchange with the bound Fe(II), **6.4**).[40]

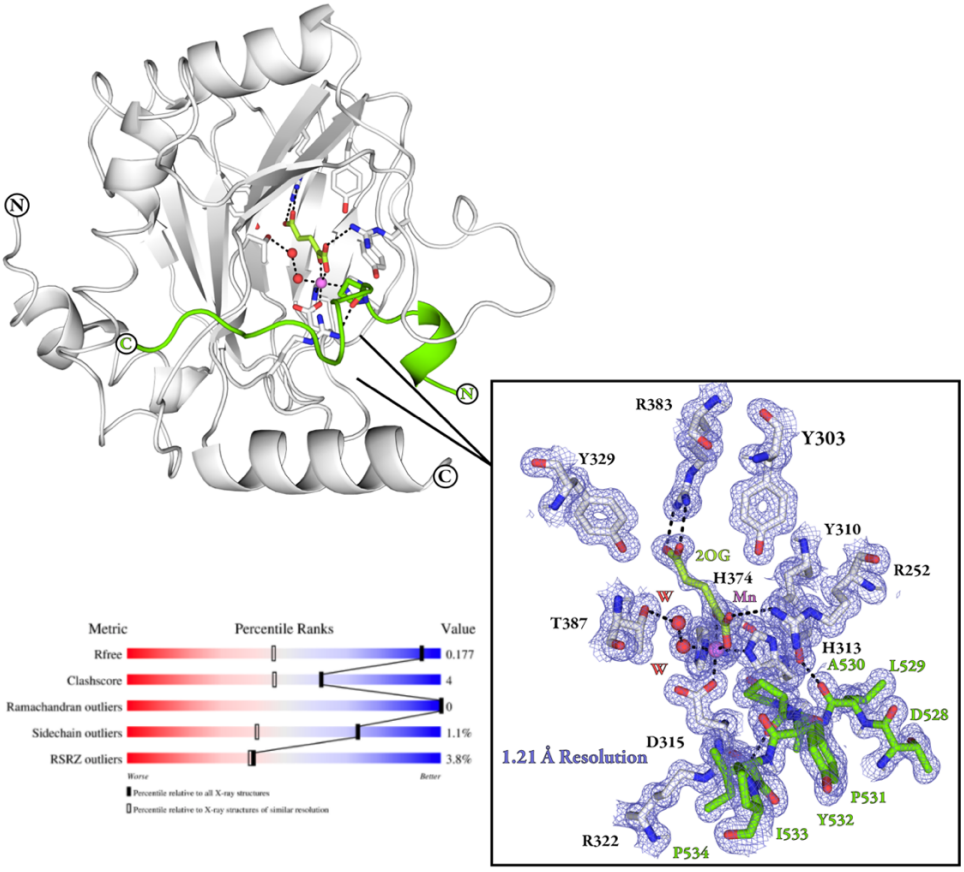


Figure 2-12| PHD2$_{181-407}$.Mn(II).2OG.HIF2α$_{523-542}$-CODD Complex Structure. The crystal diffracted to 1.21 Å resolution and active site residues (white), 2OG (yellow), and HIF2α$_{523-542}$-CODD peptide residues (green) are shown in sticks. The 2mF$_o$-DF$_c$ electron density map (contoured to 1.0 σ) of the residues is indicated in blue mesh. Active site interactions are shown in dashes (black). Mn (violet) and water molecules (red) are shown in spheres. Validation heat chart is shown and was generated using the PDB validation service. Abbreviations: Prolyl hydroxylase isoform 2 (PHD2), Hypoxia-inducible factor (HIF), 2-Oxoglutarate (2OG), *C*-terminal oxygen degradation domain (CODD), and Protein Data Bank (PDB). *Xtal-ID*: *B*.

The structure of *Xtal-A*-Mn(II).NOG (*P* 2_1 2_1 2, a = 130.91 Å, b = 38.32 Å, c = 42.99 Å) when aligned with the previously reported PHD2$_{181-426}$.Mn(II).2OG.HIF1α$_{556-575}$-CODD (PDB: 5L9B) complex structure, reveals similar conformations, that results in a RMSD of 0.238 (calculated with PyMOL™, **6.1**), but with subtle changes that might be induced during substrate binding (**Figure 2-13A**).[2]

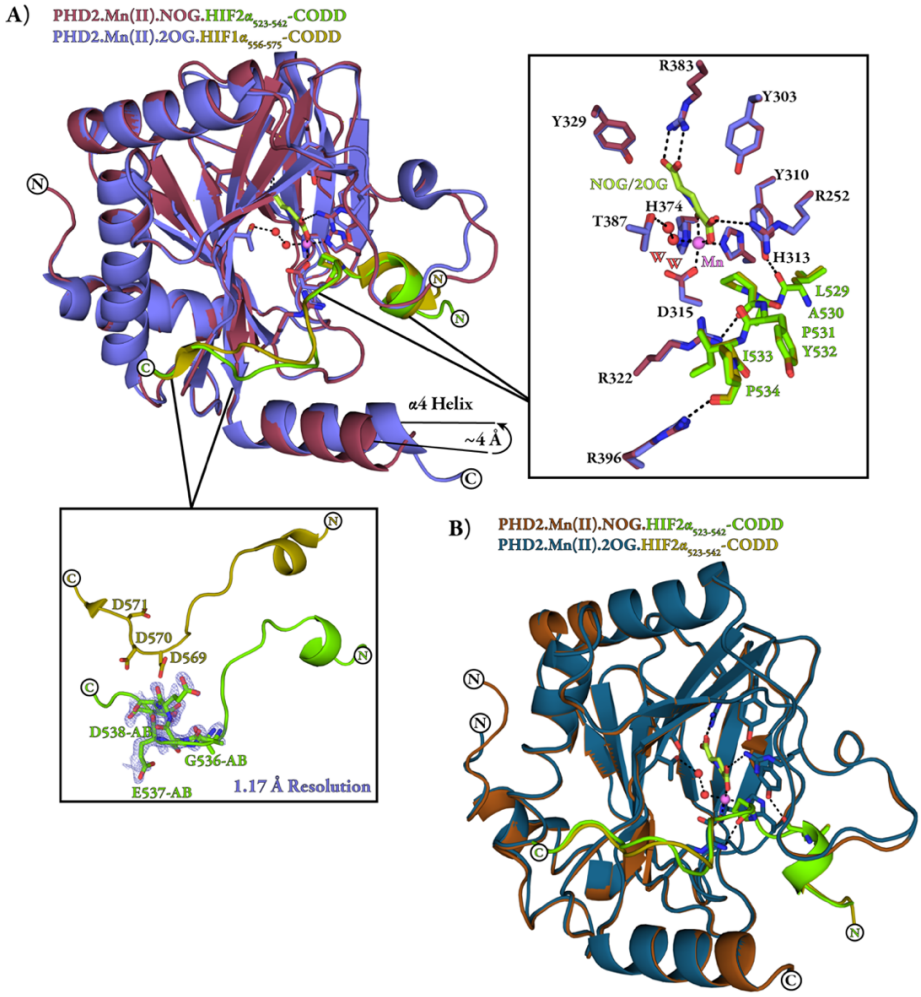


Figure 2-13| Comparison of *Xtal-A* with the Previously Reported Monoclinic Structure (PDB: 5L9B) and with *Xtal-B*. (A) PHD2$_{181-407}$.NOG (red) and PHD2$_{181-426}$.2OG (blue; PDB: 5L9B) are displayed as cartoons. Active site residues, NOG or 2OG, and peptides are depicted as sticks and coloured based on their associated complex structure. A comparison of HIF2α$_{523-542}$-CODD (green) versus the HIF1α$_{556-575}$-CODD (olive) peptides with 2mF_o-DF_c electron density (contoured to 1.0 σ) illustrates the observed 'flip-out' of the Gly537-Glu538 residues in the PHD2$_{181-407}$.Mn(II).2OG.HIF2α$_{523-542}$-CODD.3C complex. (B) The formate condition PHD2$_{181-407}$.NOG (orange) and PHD2$_{181-407}$.2OG (teal) structures are aligned. (A-B) Mn (violet) and water molecules (red) are shown as spheres. Key interactions are represented by dashes (black). Abbreviations: Prolyl hydroxylase isoform 2 (PHD2), Hypoxia-inducible factor (HIF), 2-Oxoglutarate (2OG), and *C*-terminal oxygen degradation domain (CODD). PDB: 5L9B. *Xtal-IDs*: *A*, *B*.

Other possibilities for the structural differences might be explained by the construct variation and its effect on the crystal lattice packing because the space groups differ between the structures (PDB: 5L9B: *P* 2_1, a = 40.19 Å, b = 76.40 Å, c = 70.96 Å, β = 90.03°). Structural comparison of the HIF2α$_{523-542}$-CODD and HIF1α$_{556-575}$-CODD peptides bound to tPHD2 reveals the sequence variation between the substrate ODDs. HIF2α contains the Gly537$_{HIF2α}$-Glu538$_{HIF2α}$ insert, whereas HIF1α contains three Asp residues, *i.e.*, Asp569-Asp571(**Figure 2-13A**). An ~4 Å shift is observed between the α4 helices between the *Xtal-A* structure and PHD2$_{181-426}$.Mn(II).2OG.HIF1α$_{556-575}$-CODD complexes (measured in COOT, **6.6.9.3**; PDB: 5L9B, **Figure 2-13A**).[2]

Although, the *C*-terminal helix shift is not as prominent as the shift seen in the superimposed structures of PHD2$_{181-426}$.Mn(II).NOG.HIF1α$_{556-575}$-CODD and 2OG.HIF1α$_{395-413}$-NODD structures (PDB: 5L9B and 5L9V, **Figure 2-2**).[2]

2.2.3 Structure of a Formate-Derived Anaerobic-PHD2$_{181-407}$. Fe(II).2OG.HIF2α$_{523-542}$-CODD.3C Complex

After obtaining the high-resolution datasets from the formate crystallisation condition (*Xtal-A* and *Xtal-B*), with the crystallisation of the complex, in part, due to the HIF2α$_{523-542}$-CODD. An attempt to form the Fe(II) substituted PHD2$_{181-407}$. 2OG.HIF2α$_{523-542}$-CODD complex in the anaerobic glovebox was conducted (**6.7.3**). However, optimisation of the PHD2$_{181-407}$.Fe(II).2OG.HIF2α$_{523-542}$-CODD.3C.-O_2 crystallisation in anaerobic conditions was achieved only once (**6.7.3**). The HIF2α$_{523-542}$-CODD peptide was added to PHD2$_{181-407}$.Fe(II).2OG under anaerobic conditions and incubated for 1 hr. The protein was heavily precipitated due to the temperature (25-30 °C) within the anaerobic glovebox. In the prepared hanging-drop vapour diffusion plates, one clustered crystal formed with approximately 500 μm x 250 μm dimensions and

appeared as a large fan morphology of crystals. An approximately 55 μm x 25 μm x 10 μm fragment of the anaerobic crystal in the formate-derived condition was cryo-cooled in liquid-N_2 and diffraction data was collected at 100 K at a synchrotron source (**6.6.7.2**) to a 1.48 Å resolution (*Xtal-C*, **Tables 2-2** and **2-7**).

2.2.3.1 Initial O_2-Exposure on the Anaerobic Formate Crystals

An initial O_2-exposure experiment was attempted by exposing fragments of an anaerobic crystal to atmospheric-O_2 and an O_2-saturated (sparged) solution (~1.22 mM)[41] to determine if the formate-derived PHD2$_{181\text{-}407}$.Fe(II).2OG.HIF2α$_{523\text{-}542}$-CODD.3C crystals were active *in crystallo*. If successful, it was envisaged that the crystallisation condition may be optimised to obtain a PHD2$_{181\text{-}407}$.hydroxylated-HIF2α product structure. The PHD2$_{181\text{-}407}$.Fe(II).2OG.HIF2α$_{523\text{-}542}$-CODD.3C.Rest-1-min.+O_2 crystal fragments were quenched with a rapid quench-cryo-cooling method (timepoints collected were from 2.45-25 minutes, **6.7.4**). During the exposure to O_2, the crystals changed from clear to a yellow-orange colour, potentially of the ferric PHD2$_{181\text{-}407}$.Fe(III).2OG.HIF2α$_{523\text{-}542}$-CODD.3C.Rest-1-min.+O_2 (due to ligand-to-metal charge transfer) and started to dissolve from this reaction point.[42] The crystals began to dissolve likely due to product release as HIF2α$_{523\text{-}542}$-CODD forms a crystal lattice contact point. To release the product, the β2-β3 loop undergoes enzymatic ordered-sequential mechanism and may disrupt the crystal contact points. The crystal drop contained 1 mM PHD2$_{181\text{-}407}$, 1 mM Fe(II), 2 mM 2OG, and 2 mM HIF2α$_{523\text{-}542}$-CODD. The reaction could complete one further turnover, but PHD2 has been observed to be inhibited by hydroxylated product.[43] Thus, the structures obtained from the crystal fragments reflect either anaerobic or early timepoints of catalysis prior to product release. Three timepoints diffracted:

(i) PHD2$_{181-407}$.Fe(II).2OG.HIF2α$_{523-542}$-CODD.3C.Rest-O_2-1-min.T17-min.+O_2. (*Xtal-D*), (ii) PHD2$_{181-407}$.Fe(II).2OG.HIF2α$_{523-542}$-CODD.3C.Rest-O_2-1-min.+O_2.T19-min (*Xtal-E*), and (iii) PHD2$_{181-407}$.Fe(II).2OG.HIF2α$_{523-542}$-CODD.3C.Rest-O_2-1-min.+O_2.T25-min (*Xtal-F*). It is important to note that the recorded timepoints are a gauge and may not reflect the true level of O_2-exposure within the crystals. O_2-diffusion into macromolecular crystals can be inconsistent and portions of the crystal can turnover at different rates compared to others.[31,36] The inconsistency of the O_2-diffusion can lead to a mixture of species being observed within the electron density of the time-resolved crystal structures.[36] However as the crystals were saturated for long timepoints, O_2 should have equilibrated in ~5 min into the crystals.[31]

There was no evidence of hydroxylated-HIF2α$_{523-542}$-CODD in the O_2-exposed PHD2$_{181-407}$.Fe(II).2OG.HIF2α$_{523-542}$-CODD.3C.Rest-O_2-1-min.+O_2 crystals (**Figure 2-14**). The $2mF_o$-DF_c electron density around the 2OG is similar between T17 and T25 as *Xtal-B* (previously described in **2.2.2**, **Figure 2-14**). In the T19 structure (*Xtal-E*), there was no apparent density observed for the 2OG methylene units. The lack of density may, in part, reflect the competition of formate with the 2OG (PDB: 6ST3, **Figure 2-14**).[44] It had been previously reported that formate can interact with the guanidinium of Arg383 in a manner similar to the C5 carboxylate of 2OG, *i.e.*, formate may inhibit the reaction, PDB: 6ST3).[44] Other than the apparent weak density for 2OG in the *Xtal-E*, there are no significant conformational changes observed between *Xtal-C-F*, evidenced by RMSD values between 0.112-0.131 (calculated in PyMOL™, **6.1**; **Figure 2-14**).

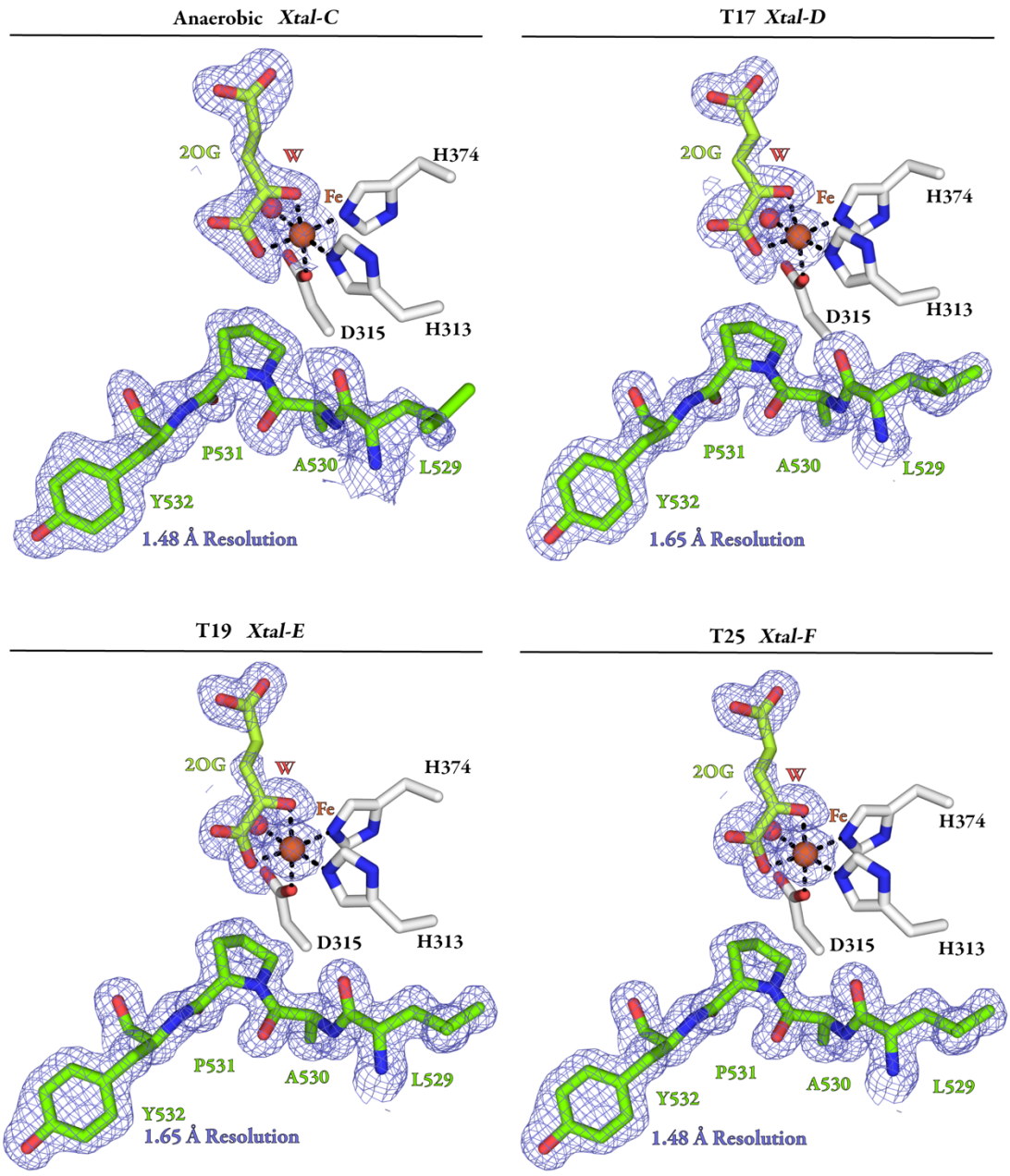


Figure 2-14| Formate Condition Anaerobic and O_2-Exposed Crystal Structures of $PHD2_{181-407}$.Fe(II).2OG.Timepoints T17, T19, and T25-Minutes. The active site residues (white), 2OG (yellow), and $HIF2\alpha_{523-542}$-CODD peptide residues (green) are shown in sticks. The $2mF_o$-DF_c electron density map (contoured to 1.0 σ) of the residues is indicated in mesh (blue). Active site interactions are shown in dashes (black). Fe (orange) and water molecules (red) are displayed as spheres. Abbreviations: Prolyl hydroxylase isoform 2 (PHD2), Hypoxia-inducible factor (HIF), 2-Oxoglutarate (2OG), and *C*-terminal oxygen degradation domain (CODD). *Xtal-IDs*: *C*, *D*, *E*, *F*.

The overall resolution (1.48-1.65 Å) and validation statistics were generally considered to be acceptable for the O_2-exposed formate-derived $PHD2_{181-407}$.Fe(II).2OG.$HIF2\alpha_{523-542}$-CODD.3C.±O_2 crystals (**Figure 2-15**). However, the clustered nature of the anaerobic-*Xtal-C* or cracks introduced during manipulation of the crystal in the anaerobic glovebox

may have caused overlapping reflections produced from diffraction from more than one crystal lattice. This is reflected in the high R_{free} value of the dataset that does not decrease with further modelling and refinements.

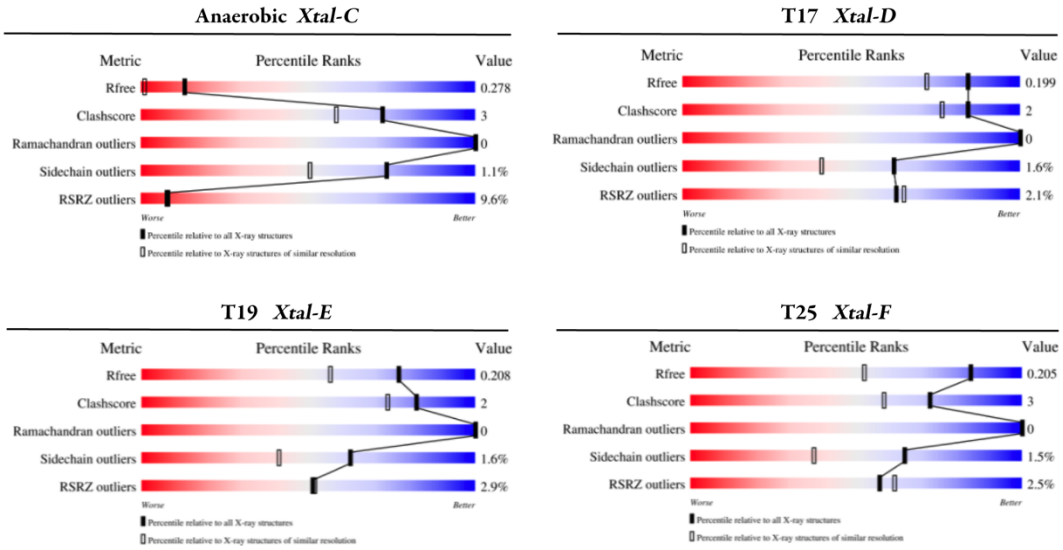


Figure 2-15| Crystallographic Validation of Anaerobic and O_2-Exposed Formate-Derived Structures. The validation tables were generated with the PDB validation service Abbreviations: Protein Data Bank (PDB).

The aerobic (*Xtal-A-B*), anaerobic (*Xtal-C*), and O_2-exposed (*Xtal-D-F*) normalised Cα atom B-factors for the structure (*i.e.*, 'an expression of the B-factor in units of standard deviation about the mean value', $Å^2$)[45] were analysed with reference to the secondary structure of $PHD2_{181-407}$ (analysis described in **6.6.9.5**, **Figure 2-16**).[46,47] The regions with the most variation in their B-factors were residues Gln243-Lys244 (β2-β3 finger loop) and Cys283-Gly285 (*N*-terminal extension of the DSBH fold, **Figure 2-16**). The reduction in B-factors at the two sites when exposed to O_2 may, in part, reflect the substrate dynamics of $PHD2_{181-407}$ in complex with the $HIF2α_{523-542}$-CODD peptide. It may be that the anaerobic structure is an outlier relative to the other structures due to the overlapping reflections caused from the clustered/cracked nature of the crystal (**Figure 2-16**). The observations may reflect small amounts of turnover in the aerobically prepared

complexes (*Xtal-A* and *Xtal-B*) and/or 2OG-uncoupled turnover prior to the preparation of the anaerobic formate-derived crystal.

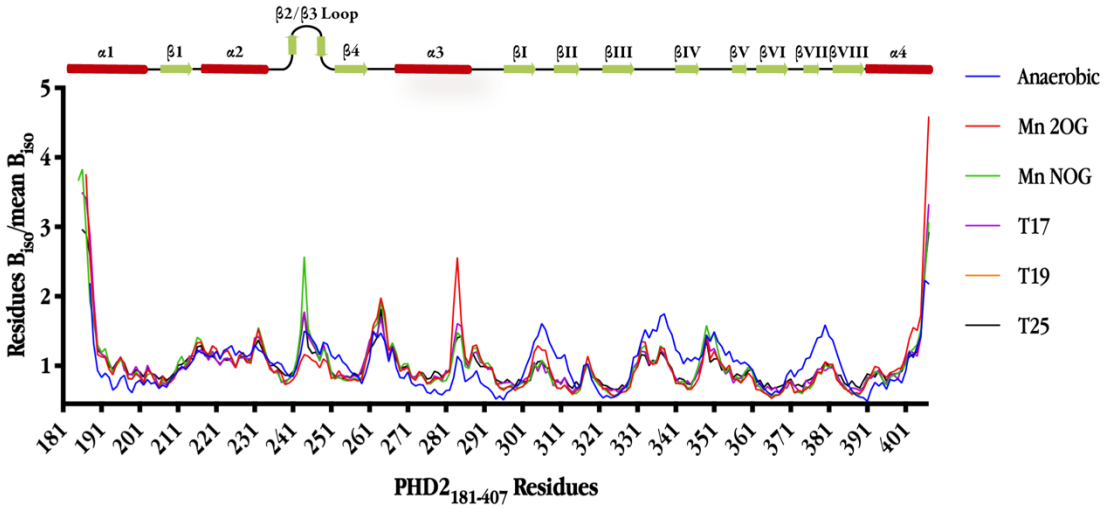


Figure 2-16| Normalised Cα B-Factor Analyses Between Formate Condition Crystal Structures. All $PHD2_{181-407}$ residues Cα atom B-factors (Å^2) were normalised based on the mean B-factor of the crystal structure. The formate condition crystal structures were analysed with normalised B-factors (Å^2): anaerobic (*Xtal-C*, blue), *Xtal-A* (green, NOG), *Xtal-B* (red, 2OG), T17 (*Xtal-D*-purple), T19 (*Xtal-E*-orange), and T25 (*Xtal-F*-black). α-helix (red cylinder) and β-strand (green arrow) secondary structure features are aligned above in correspondence with residues. Data was analysed with the Structure Comparison tool in PHENIX. Abbreviations: Prolyl hydroxylase isoform 2 (PHD2), 2-Oxoglutarate (2OG), and *N*-Oxalylglycine (NOG). *Xtal IDs*: *C*, *D*, *E*, *F*.

An overall B-factor heat-map (*i.e.*, all atoms) of the $PHD2_{181-407}$.Fe(II).2OG.$HIF2\alpha_{523-542}$-CODD.3C.±O_2 crystals are displayed for the anaerobic (*Xtal-C*) and O_2-exposed timepoints (*Xtal-D-F,* **Figure 2-17**). The structural depiction of the B-factor temperatures provides a visual reference to compare with the normalised Cα B-factor graph (**Figure 2-16**). Of note, the β2-β3 finger loop is not disordered in any of the formate-derived structures (**Figure 2-17**). (*Thank you to Dr. Michael McDonough for his help in harvesting the crystals, performing the O_2-exposure, and collecting the datasets on the formate-derived crystals.)*

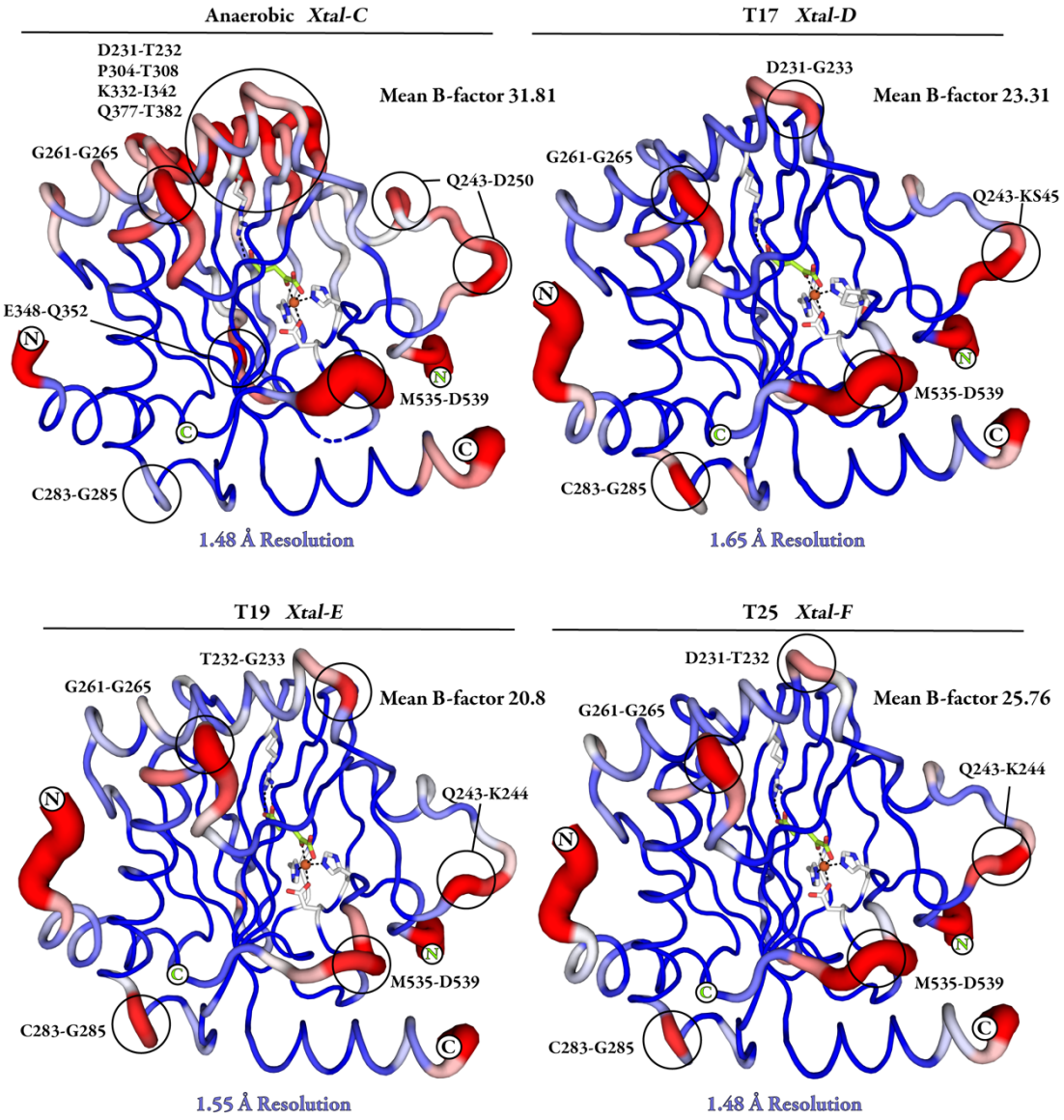


Figure 2-17| All Atoms B-Factor Heat-Map of the Formate Anaerobic and O_2-Exposed Data. $PHD2_{181-407}$.$HIF2\alpha_{523-542}$-CODD complex structures are depicted as a putty cartoon (the relative size of the cartoon correlates to high B-factor (Å^2) values). The blue-white-red heat map (blue-low B-factor temperature and red-high B-factor temperatures, Å^2) has been normalised to the mean B-factor (Å^2) of the structures and areas of interest are highlighted with circles (black). Abbreviations: Prolyl hydroxylase isoform 2 (PHD2), Hypoxia-inducible factor isoform 2α, C-terminal oxygen degradation domain (CODD). *Xtal-IDs*: *C*, *D*, *E*, *F*.

2.2.4 Use of the 3C Cyclic Peptide and Reproducibility

Reasons the anaerobic crystallisation condition of the $PHD2_{181-407}$.Fe(II).2OG.$HIF2\alpha_{523-542}$-CODD.3C.-O_2 complex may not have been reproducible are because 2OG-cosubstrate was added under aerobic conditions to the protein mixture (**6.7.3**). In the absence of substrate, uncoupled decarboxylation of 2OG (2 mM) may have occurred when the $PHD2_{181-407}$.2OG mixture was incubated with 3C peptide overnight under aerobic conditions, *i.e.*, due to residual Fe(II) that copurified with $PHD2_{181-407}$.[39,48] Although, how the reaction occurs without the presence of ascorbate is unclear.[48] Other reasons for non-reproducibility of the anaerobic crystal (*Xtal-C*) are that the $PHD2_{181-407}$ sample had heavily precipitated during the incubation with substrate. The precipitation would change the final concentrations of enzyme prior to preparation of the crystallisation plates.

Numerous attempts to reproduce the anaerobic *Xtal-C* formate-derived crystallisation condition failed. Solubilising $HIF2\alpha_{523-542}$-CODD and 3C by adding the protein solution directly to the lyophilised peptides (**6.7.1**) led to inconsistencies in the concentration between crystallisation set-ups. Overall, the results suggested that a new robust, reliable, and active crystallisation condition would be required for future $PHD2_{181-407}$.Fe(II).2OG.$HIF2\alpha_{523-542}$-CODD mechanistic based crystallographic analyses.

2.3 A Novel Zn(II)-Based Crystallisation Condition for the $PHD2_{181-407}$.Mn(II).2OG.$HIF2\alpha_{523-542}$-CODD.3C Complex

With the aim of detailed mechanistic studies of the $PHD2_{181-407}$.Fe(II).2OG.$HIF2\alpha_{523-542}$-CODD.3C complex, a broad screen (**6.6.2**) of conditions was carried out in the search for a new crystallisation condition. To aid in reproducibility of the system, preparation of the $PHD2_{181-407}$.Mn(II).2OG.$HIF2\alpha_{523-542}$-CODD.3C mixture was simplified, *i.e.*, the incubation times and protocol steps were reduced to allow for consistent reproduction. Previous overnight incubations of $PHD2_{181-407}$ to dissolve the $HIF2\alpha_{523-542}$-CODD (2-4 mM) and 3C peptides (~600-700 μM) were reduced to 1 hour (hr, **6.7.5**).

During one of the purifications of $PHD2_{181-407}$, a fine precipitation was noticed after a buffer exchange (**6.4.6**) into acidic 2-(*N*-morpholino)ethanesulfonic acid (MES, pH 5.8, **6.4.7**). The precipitation of $PHD2_{181-407}$ was most likely due to the acidic pH of the buffer; this observation led to a comparison between the use of diacidic form of 2OG (2OG-diacid) against the disodium salt of 2OG (2OG-disalt) for crystallisation. Use of the 2OG-diacid yielded more nucleation of $PHD2_{181-407}$ in the broad screens (**6.6.2**) compared to the 2OG-disalt, *i.e.*, $PHD2_{181-407}$ has an apparent preference for acidic pHs for crystallisation (some reported crystallisation conditions are shown in **Table 3-1**, in section **3.1**).

The $PHD2_{181-407}$.Mn(II).2OG.$HIF2\alpha_{523-542}$-CODD.3C mixture was subjected to broad screening; microcrystals were observed to form after one day of equilibration using the Classics Lite Suite™ screen (Qiagen N.V.). Microcrystals were formed in the well condition with 10 mM Zn(II)SO_4, 26 mM MES pH 6.5, and 11% (w/v) PEG 550 monomethyl ether (MME, **Figure 2-18**, **6.7.5**). Conditions were optimised around the initial hits; a 20 μm x 10 μm x 5 μm crystal formed in 0.01 M Zn(II)SO_4, 11% (w/v) PEG

550 MME, and 26 mM MES pH 6.5. The crystal was cryo-cooled in liquid-N_2 and diffraction data was collected at 100 K to a 2.07 Å resolution at a synchrotron source (*Xtal-G*, **6.6.7.2**; **Tables 2-4** and **2-7**). The dataset is in the *P* 2_1 space group (*Xtal-G***, Figure 2-18,** and **Table 2-4**). The monoclinic space group had been previously reported for $PHD2_{181-426}$.HIF1α-NODD/CODD complex structures (PDB: 5L9B: a = 40.19 Å, b= 76.40 Å, c = 70.96 Å, β = 90°, and 5L9V: a = 43.81 Å, b= 73.09 Å, c = 70.41 Å, β = 91.17°) that were obtained, but the cell dimensions differ with the Zn(II)-based condition (*Xtal-G*, a = 43.97 Å, b= 70.24 Å, c = 90.72 Å, β = 101.3°).[1,2]

The condition was initially thought to be a very good candidate for further mechanistic studies as microcrystals formed of $PHD2_{181-407}$.Mn(II).2OG.$HIF2\alpha_{523-542}$-CODD.3C if (i) Zn(II)SO_4 could be replaced with Fe(II)SO_4, (ii) Fe(II) could be substituted for Mn(II), and (iii) prevent the heavy precipitation of $PHD2_{181-407}$. Needle morphology microcrystals are preferred for efficient O_2-diffusion into the crystals.[31,36] Microcrystal slurries are used for chip-based fix-target and XFEL data collections using serial data collection and processing strategies.[31,36] The needle morphology and micro-scale can provide a more efficient O_2-diffusion into the crystal and limit the O_2-gradient that may be observed in some time-resolved structures, *i.e.*, with the aim to have a more uniform substrate turnover within the complex.[31,36] As $PHD2_{181-407}$.$HIF2\alpha_{523-542}$-CODD crystallised as plate-like microcrystals in this condition.[31,36] Thus, further optimisation of crystal morphology would not be required.[31]

Table 2-3| Zn Condition Crystallographic Data and Refinement Statistics.

	Zn Condition: Mn(II).2OG.HIF2α-CODD.3C (*Xtal-G*)
Beamline	Diamond Light Source-I24
Detector	Dectris Pilatus3 6M
Data Processing	Xia2 DIALS
Wavelength (Å)	0.96862
Resolution range (Å)	88.98 - 2.07 (2.14 - 2.07)
Space group	$P\ 1\ 2_1\ 1$
Unit cell (Å, °)	43.97 70.24 90.72, 101.26
Total reflections	216107 (21374)
Unique reflections	33147 (3252)
Multiplicity	6.5 (6.6)
Completeness (%)	99.78 (98.52)
Mean I/sigma(I)	6.34 (0.64)
Wilson B-factor (Å²)	37.72
R-merge†	0.2153 (0.9256)
R-meas	0.235 (1.006)
R-pim	0.09244 (0.3909)
CC1/2	0.69 (0.86)
CC*	0.904 (0.962)
Reflections used in refinement	33147 (3204)
Reflections used for R-free	1644 (154)
R-work✧	0.2041 (0.3443)
R-free✧	0.2243 (0.3524)
CC(work)	0.958 (0.844)
CC(free)	0.958 (0.824)
Number of non-hydrogen atoms	3878
macromolecules	3713
ligands	79
solvent	114
Protein residues	489
RMS(bonds, Å)	0.004
RMS(angles, °)	0.65
Ramachandran favored (%)	96.44
Ramachandran allowed (%)	3.56
Ramachandran outliers (%)	0.00
Rotamer outliers (%)	1.93
Clashscore	3.18
Average B-factor (Å²)	52.36
macromolecules	52.58
ligands	48.65
solvent	46.73
Number of TLS groups	15

Single crystal diffraction data was collected from samples held at 100 K with conventional, rotation-based methods. Ligands: Mn, Zn, 2OG, Cl, and Mg. Statistics for the highest-resolution shell are shown in parentheses.

† R-merge (or Rsym) is equal to $\sum|I-\langle I\rangle|/\sum I$. R-merge represents the data quality of merged reflection data. *I* is equal to the intensity of individual measurements and <I> is equal to the average of multiple measurements. ✧R_{free} is the R_{factor} for 5% of the reflections which are excluded during refinement. R_{factor} is equal to $\sum_{hkl}||Fobs_{(hkl)}| - |Fcalc_{(hkl)}||/\sum_{hkl}|Fobs_{(hkl)}|$ and was calculated for the working set of reflections (R_{work}).
Appendix I contains information on the crystal contents and the *Xtal-ID*.

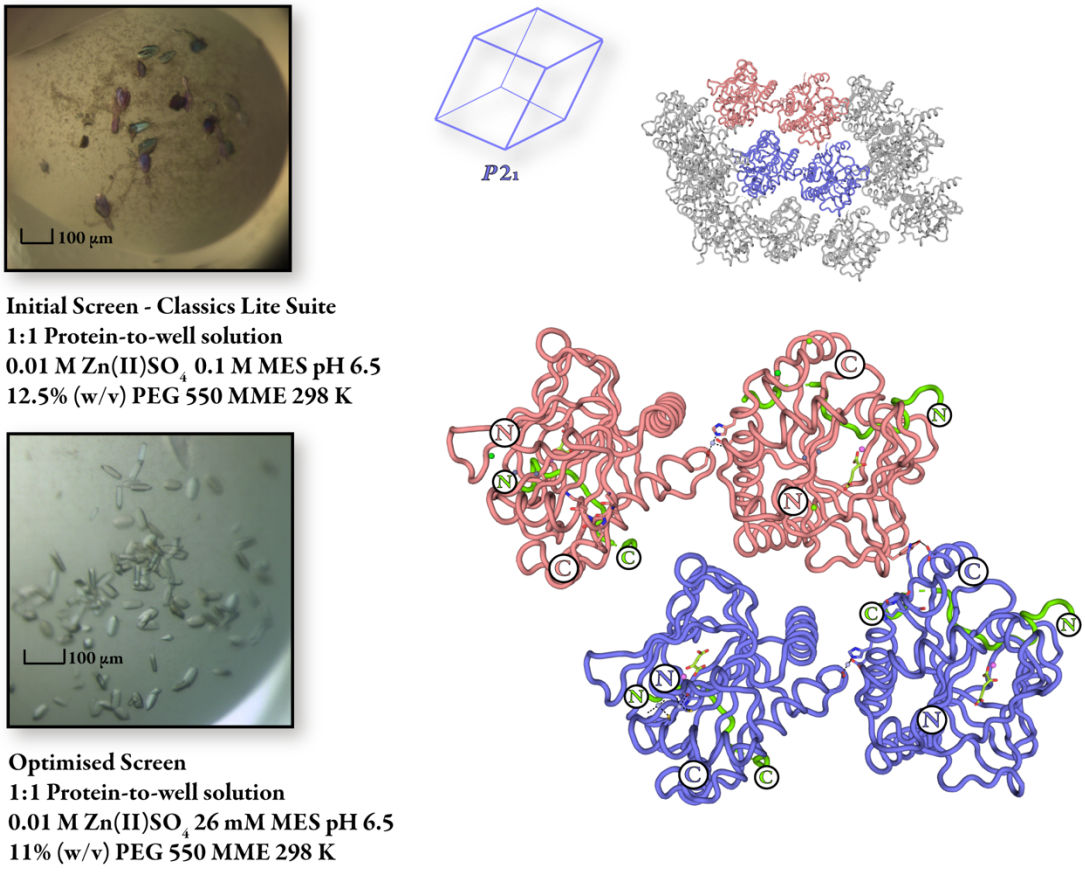


Figure 2-18| Zn Condition Optimisation of the PHD2$_{181-407}$.Mn(II).2OG.HIF2α$_{523-542}$-CODD.3C Complex. Microcrystals in a needle morphology were obtained after a broad screen with the Classics Lite Suite™ screen. As the morphology was potentially useful for O_2-diffusion into the crystals, the condition was optimised and a structure was obtained at 1.97 Å resolution in the *P* 2_1 space group. The crystal oligomerisation is depicted with cartoon chains of the asymmetric unit (blue) and the symmetry-related chains (interacts with ASU-pink and surrounding-grey). HIF2α$_{523-542}$-CODD peptide, displayed as a cartoon (green), is displayed for all four chains. The metals (Mn-violet and Zn-blue) are depicted as spheres. Abbreviations: Asymmetric unit (ASU), Hypoxia-inducible factor isoform 2α (HIF2α), and *C*-terminal oxygen degradation domain (CODD). *Xtal-ID*: *G*.

The Zn-based PHD2$_{181-407}$.Mn(II).2OG.HIF2α$_{523-542}$-CODD.3C crystal form (*Xtal-G*) was structurally characterised (MR-phased using *Xtal-A* as a starting model, **6.6.9.3**) and, similar to the formate-derived structures, revealed no apparent evidence for 3C cyclic peptide binding. The asymmetric unit (ASU) content contains two chains of PHD2$_{181-407}$.Mn(II).2OG.HIF2α$_{523-542}$-CODD.

In the Zn-derived PHD2$_{181-407}$.Mn(II).2OG.HIF2α$_{523-542}$-CODD.3C complex structure (*Xtal-G*), apparently a Zn ion is coordinated by both ASU chains (**Figure 2-19**). Residues Glu263$_{Chain-C}$, Asp278$_{Chain-A}$, and His282$_{Chain-A}$ form a Zn-binding 'facial-triad'

(**Figure 2-19**). A similar interaction is seen in the *Xtal-G* structure near the *N*-terminus of the construct, the carboxylates of residues Asp246$_{symmetry}$ and Asp250$_{symmetry}$ of the β2-β3 finger loop and the thiol sidechains of Cys201 and Cys208 coordinate two Zn ions (**Figure 2-19**).

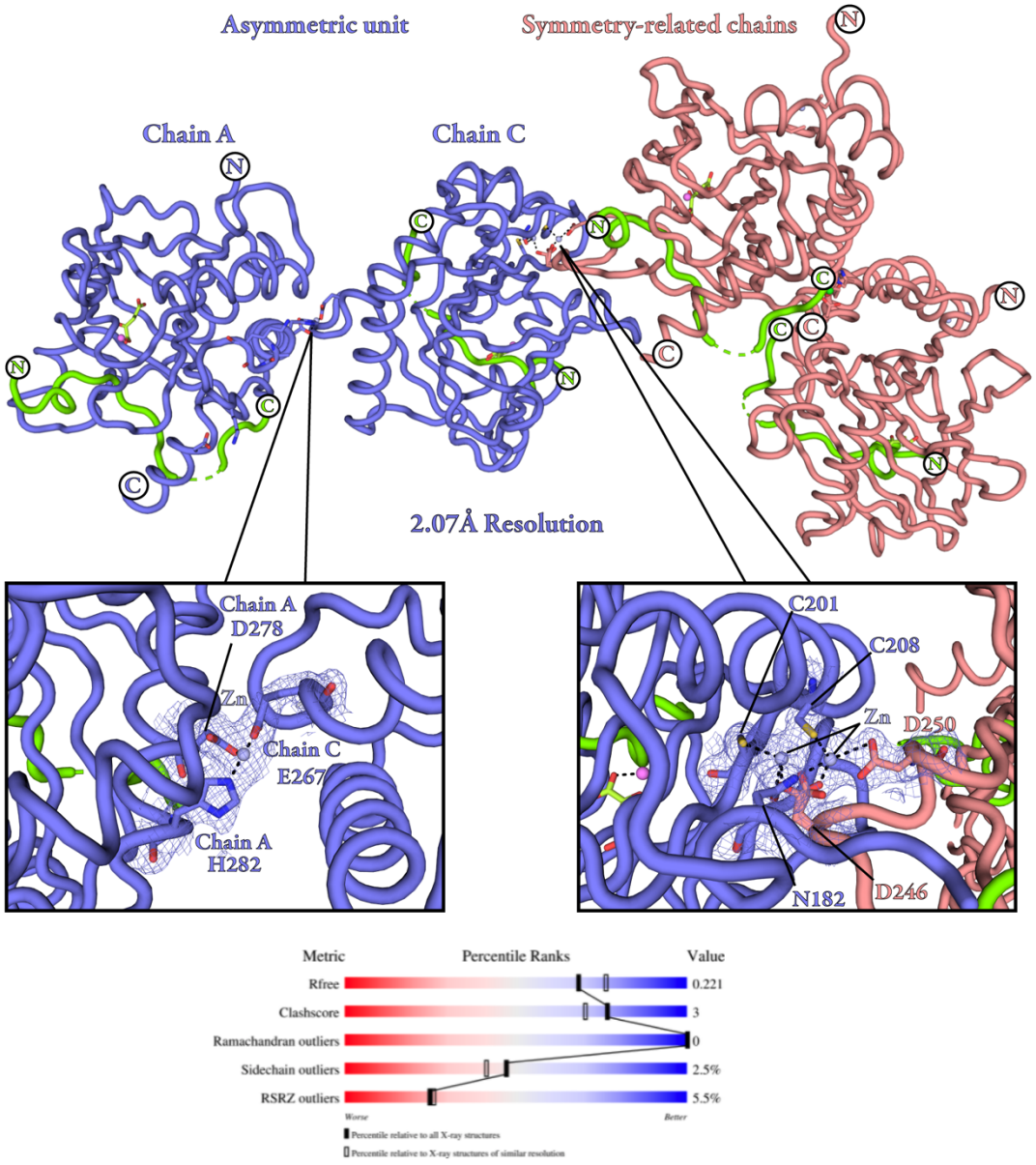


Figure 2-19| The Zn Condition Derived PHD2$_{181-407}$.Mn(II).2OG.HIF2α$_{523-542}$-CODD.3C Complex Structure. Key inter-chain interactions are shown between chains in the asymmetric unit (blue) and symmetry-related chains (pink). The specific residues that interact are depicted in sticks and metal ions in complex are displayed as spheres (Mn-violet and Zn-blue). 2mF_o-DF_c electron density map (blue, contoured to 1.0 σ) is shown as mesh for the specific residues and metal ions. HIF2α$_{523-542}$-CODD peptide is shown as a cartoon (green). The crystallographic validation heat table is shown below for the structure and was generated with the PDB validation service. Abbreviations: Prolyl hydroxylase isoform 2 (PHD2), Hypoxia-inducible factor (HIF), 2-Oxoglutarate (2OG), *C*-terminal oxygen degradation domain (CODD), and Protein Data Bank (PDB). *Xtal-ID*: *G*.

Cys201-Cys208 typically forms a disulfide bridge in approximately half of the reported tPHD2 structures.[49] The *N*-terminal residues of the $PHD2_{181-407}$ construct are typically not observed in the electron density. The Zn ion stabilises the $PHD_{181-407}$ construct to the *N*-terminal Met (-3 residue) of the pET-28a(+) NheI restriction site (**Appendix III**). Another distinct feature of the *Xtal-G* complex was the disordering of the HIF2$\alpha_{523-542}$-CODD substrate between the Gly537-Glu538 insert of the peptide (*i.e.*, the HIF2α symmetry interaction, discussed in section **2.2.1**, is not observed in the *P* 2_1 crystal form). However, since Gly537-Glu538 was not visible in the electron density of in the *Xtal-G* complex, this provides evidence for conformational flexibility of these residues.

Even though the inter-chain coordinated Zn ions are likely a crystallographic artefact, it is of interest that the Zn ions bind at the observed sites. As previously mentioned (section **1.3.5**), the full-length version of PHD2 contains a conserved Zn-finger binding MYND-domain that binds Zn ions.[50] The specific role of the Zn-finger has not be fully characterised, but has been reported to interacts with the HSP90 pathway.[50]

The Zn ions potentially are involved in the oligomerisation of the complex structure, the Zn-based crystallisation conditions could not be optimised without the use of Zn(II)SO_4. Efforts were made to use Fe(II)SO_4, to substitute for the Zn(II)SO_4 in the condition, but the attempts were unsuccessful. Furthermore, the Zn(II)SO_4 was required for crystallisation of $PHD2_{181-407}$.HIF2$\alpha_{523-542}$-CODD (*Xtal-G*), and/or would likely inhibit the substrate turnover if used for time-resolved studies. The Zn condition also formed heavy precipitation, which was considered to potentially disrupt downstream data collection. Thus, the search for a more suitable $PHD2_{181-407}$.HIF2$\alpha_{523-542}$-CODD condition for mechanistic studies was continued.

2.4 A Novel Acetate-Based PHD2$_{181-407}$.Mn(II).2OG.HIF2α$_{523-542}$-CODD Crystallisation Condition

After the solubility issues of the 3C peptide and HIF2α$_{523-542}$-peptide.[5,24] A screen for a new condition with DMSO-solubilised HIF2α$_{523-542}$-CODD peptide was conducted (**6.6.2**). Using the PHD2$_{181-407}$ crystallisation tools, such as the 2OG-diacid and HIF2α$_{523-542}$-CODD peptide, suitable crystallisation conditions were screened using in both the Crystal Screen™ I/II and PEG/Ion Screen™ I/II (Hampton Research Corp.). Both screens have yielded multiple crystallisation conditions for the tPHD2 constructs (**Table 3-1**, in section **3.1**). Based on a procedure used in time-resolved work by *Dr. Patrick Rabe*, an ethylenediaminetetraacetic acid (EDTA) treated batch of PHD2$_{181-407}$ was prepared (**6.4.10**). EDTA is a strong chelator that should bind any bound metal ions and trace metals that had copurified with the protein during the purification. The PHD2$_{181-407}$ batch was analysed *via* a hydroxylation assay (**Figure 2-20**, **6.5** and **6.5.2.2**) to determine if the protein was in the apo form and check activity. Approximately 33.33 turnover events were observed in 19 mins (~0.029 turnover/seconds (s)) with 150 nM PHD2$_{181-407}$ and 5 μM of HIF2α$_{523-542}$-CODD; slower than previously reported K_{cat} values (0.069 ± 0.006 s^{-1}) and provides kinetic evidence for the slow reaction of the PHDs with O_2.[14] The in-solution activity of the EDTA-treated PHD2$_{181-407}$ was compared against non-treated PHD2$_{181-407}$. The results revealed that the apo-protein was inactive with low levels of HIF2α$_{523-542}$-CODD methionine oxidation observed in the no-enzyme control (**Figure 2-20**). The results imply that all the copurified Fe(II), and by implication other metals, had been removed (**Figure 2-20**). Further, it was observed that addition of Fe(II) could restore the activity of PHD2$_{181-407}$ (**Figure 2-20**). The ability to add ferrous Fe(II) into the active site would help to ensure there was no heterogenous mixture of oxidised or

contaminant (*i.e.*, Ni(II) from the affinity chromatography) metal in the protein batch that could inhibit catalysis.

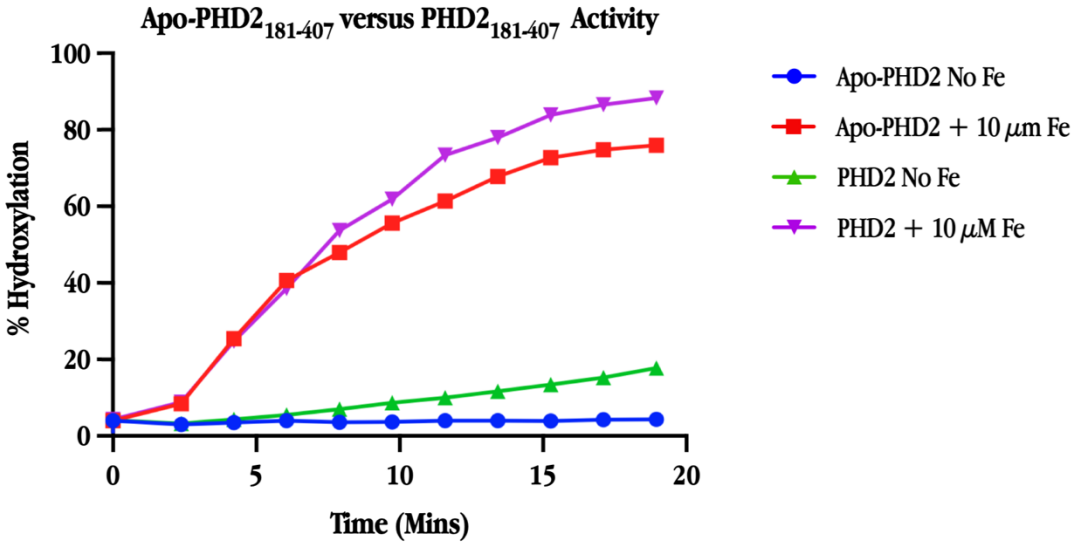


Figure 2-20| Hydroxylation Assay to Compare Activity of EDTA-treated PHD2$_{181-407}$ versus PHD2$_{181-407}$ as isolated. Both EDTA-treated (apo)-PHD2$_{181-407}$ and non-treated PHD2$_{181-407}$ (PHD2 No Fe) were assayed for activity ± 10 μM Fe(II)SO_4. The percent hydroxylation of the HIF1α peptide was measured over 19 minutes. The reaction conditions contained 150 nM PHD2$_{181-407}$, 5 μM HIF2α$_{523-542}$-CODD, 10 μM Fe(II)SO_4, 10 μM 2OG, and 100 μM L-ascorbic acid. Abbreviations: Ethylenediaminetetraacetic acid (EDTA), Prolyl hydroxylase isoform 2 (PHD2), and Hypoxia-inducible factor isoform 1α (HIF1α). *(Thank you to Dr. Anthony Tumber for conducting the RapidFire® based hydroxylation experiment).*

After one week of equilibration, a 420 μm x 45 μm x 15 μm plate-like morphology crystal of apo-PHD2$_{181-407}$.Mn(II) (1.2 mM).2OG (5 mM).HIF2α$_{523-542}$-CODD (*Xtal-H*) was observed in 0.2 M ammonium acetate, 0.1 M sodium acetate pH 4.6, and 30% (w/v) PEG 4000 (**Figure 2-21**, **6.7.6**). An initial crystal was cryo-cooled in liquid-N_2 (**6.6.6.2**) and diffraction data collected at 100 K to a 1.70 Å resolution and reported in the *P* 2_1 2 2_1 space group at a synchrotron source (*Xtal-H*, **6.6.7.2**; **Tables 2-4** and **2-7**). The structure was solved through MR-phasing using *Xtal-A* as a starting model (**6.6.9.2**). Weak electron density was observed for the 2OG and a coordinated Mn(II) ion (**Figure 2-22**).

The weak density observed for the active site ligand may be caused by a mixture of acetate (ACT) and 2OG in the active site of PHD2$_{181-407}$. As PHD2$_{181-407}$ was EDTA-

treated, it is possible that the added Mn(II) was not completely bound, *i.e.*, likely there is residual EDTA in the protein solution that chelates Mn(II) (**6.4.10**). The observed metal ion and ligands occupancies were refined to (i) Mn ion at 25%, (ii) 2OG at 55%, and (iii) ACT at 45% (**Figure 2-22**).

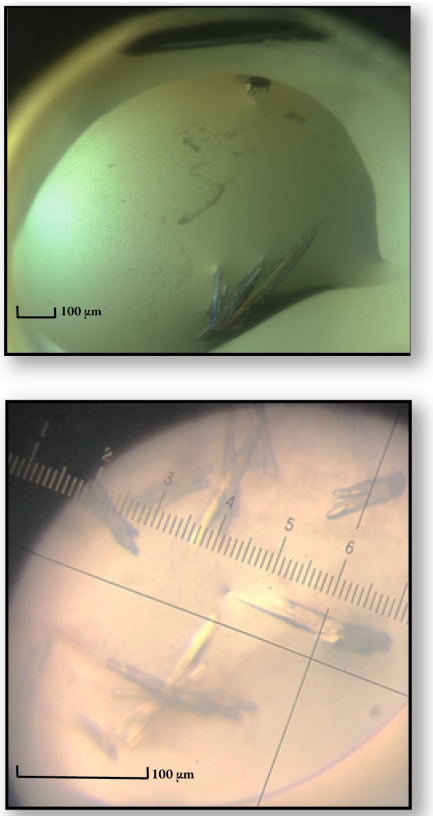


Figure 2-21| Crystallisation Optimisation of the Acetate Condition for Anaerobic Growth. The initial crystal hits were observed in the Crystal Screen™ I/II. The crystallisation condition was further optimised for 24-well sitting-drop plates in the anaerobic glovebox.

After obtaining the *Xtal-H* structure, the acetate condition was considered a candidate for mechanistic-based crystallographic studies (**Figure 2-22**). Apart from viscosity concerns, the observed metal occupancy was low and that acetate may inhibit hydroxylation by binding/competing with 2OG at the Arg383 position, *i.e.*, which has been seen in a *Ta*PHD structure (PDB: 6EY1) and may act in a similar manner to the formate interaction (PDB: 6ST3).[7,44] Efforts began, taking the above mentioned concerns into consideration, on optimising the acetate-derived condition for growth in an anaerobic glovebox.

Table 2-4| Crystallographic Data and Refinement Statistics.

	Acetate Screen (*Xtal-H*)	Acetate Complex (*Xtal-I*)
Beamline	Diamond Light Source-I04	Diamond Light Source-I03
Detector	Dectris Eiger2 XE 16M	Dectris Eiger2 XE 16M
Data Processing	Fast DP	Xia2 DIALS
Wavelength (Å)	0.97949	0.97625
Resolution range (Å)	28.50 - 1.70 (1.76 - 1.70)	40.70 - 1.55 (1.60 - 1.55)
Space group	P 21 2 21	*P* 21 2 21
Unit cell (Å, °)	38.22 42.77 131.15	37.89 42.82 130.80
Total reflections	240218 (19832)	363355 (36424)
Unique reflections	24028 (2172)	31810 (3104)
Multiplicity	10.0 (9.1)	11.4 (11.7)
Completeness (%)	98.00 (89.86)	99.92 (99.55)
Mean I/sigma(I)	14.57 (2.70)	8.84 (0.39)
Wilson B-factor (Å²)	16.91	22.59
R-merge†	0.2186 (0.9807)	0.1303 (2.296)
R-meas	0.2305 (1.035)	0.1363 (2.401)
R-pim	0.07153 (0.3222)	0.03982 (0.6929)
CC1/2	0.996 (0.863)	0.999 (0.471)
CC*	0.999 (0.963)	1 (0.8)
Reflections used in refinement	24022 (2172)	31789 (3091)
Reflections used for R-free	1999 (181)	1591 (146)
R-work✧	0.1687 (0.2623)	0.1859 (0.3387)
R-free✧	0.1976 (0.3095)	0.2173 (0.3485)
CC(work)	0.966 (0.911)	0.971 (0.674)
CC(free)	0.968 (0.796)	0.962 (0.711)
Number of non-hydrogen atoms	2376	2235
macromolecules	2121	2004
ligands	22	21
solvent	240	219
Protein residues	242	240
RMS(bonds, Å)	0.004	0.005
RMS(angles, °)	0.84	0.81
Ramachandran favored (%)	97.48	96.61
Ramachandran allowed (%)	2.52	3.39
Ramachandran outliers (%)	0.00	0.00
Rotamer outliers (%)	2.16	1.48
Clashscore	3.31	3.79
Average B-factor (Å²)	21.71	28.77
macromolecules	20.78	28.02
ligands	19.59	34.55
solvent	30.00	35.38
Number of TLS groups	9	9

Single crystal diffraction data was collected from samples held at 100 K with conventional, rotation-based methods. Ligands: Mn, 2OG, and ACT. Statistics for the highest-resolution shell are shown in parentheses.

† R-merge (or Rsym) is equal to $\sum|I-\langle I\rangle|/\sum I$. R-merge represents the data quality of merged reflection data. *I* is equal to the intensity of individual measurements and <I> is equal to the average of multiple measurements. ✧R_{free} is the R_{factor} for 5% of the reflections which are excluded during refinement. R_{factor} is equal to $\sum_{hkl}||Fobs_{(hkl)}| - |Fcalc_{(hkl)}||/\sum_{hkl}|Fobs_{(hkl)}|$ and was calculated for the working set of reflections (R_{work}).

Appendix I contains information of the crystal contents and the *Xtal-IDs*.

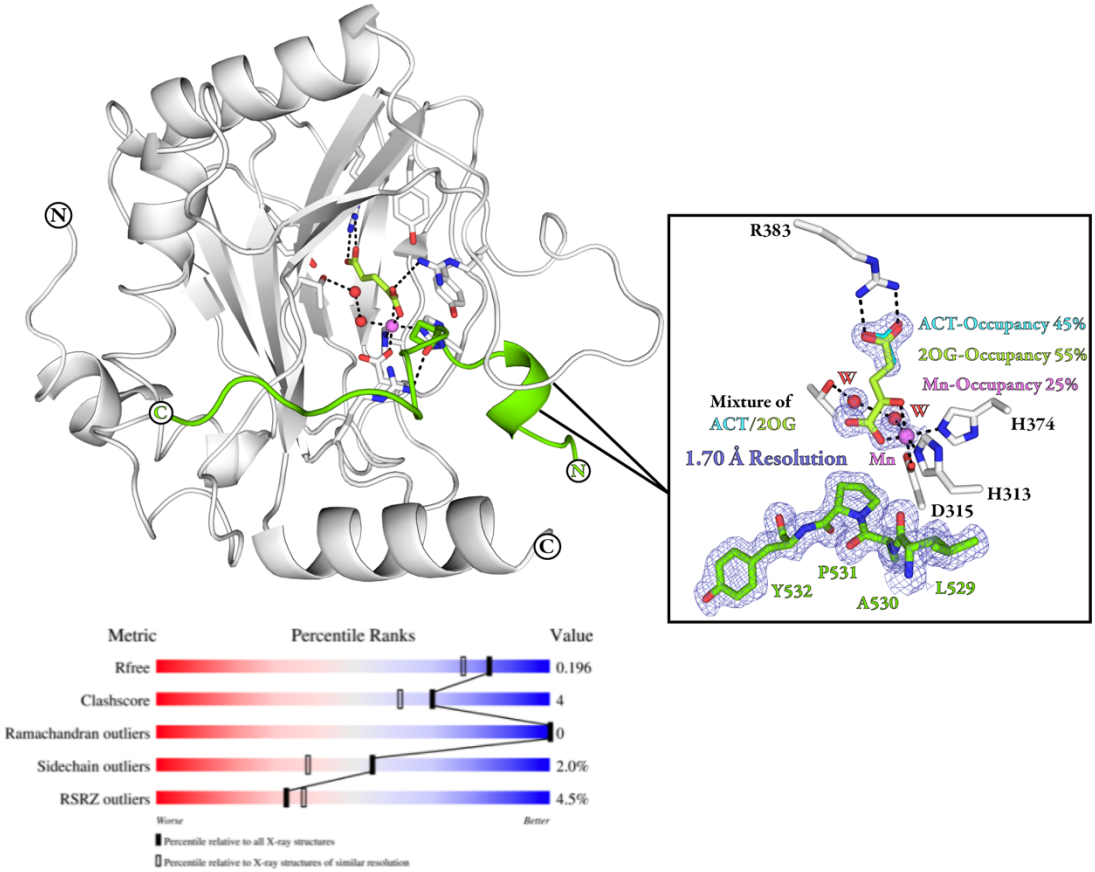


Figure 2-22| Initial PHD2$_{181-407}$.Mn(II).2OG.HIF2α$_{523-542}$-CODD Complex Structure Obtained Using the Acetate Condition. Whole protein (white) and substrate peptide (green) are shown in cartoons. The active site residues (white), 2OG (yellow) ACT (cyan), and HIF2α$_{523-542}$-CODD peptide residues (green) are shown in sticks. The 2mF_o-DF_c electron density map (contoured to 1.0 σ) of the residues is indicated in mesh (blue). Active site interactions are displayed as dashes (black). Mn (violet) and water molecules (red) are shown as spheres. Abbreviations: Prolyl hydroxylase isoform 2 (PHD2), Hypoxia-inducible factor (HIF), 2-Oxoglutarate (2OG), Acetate (ACT), *C*-terminal oxygen degradation domain (CODD), and Protein Data Bank (PDB). *Xtal-ID*: *H*.

2.4.1 The Anaerobic Optimisation of the Acetate-Derived Condition

In contrast with the previously discussed formate condition (**2.2**), the anaerobic preparation of the acetate-derived condition, Fe(II) and 2OG solutions were prepared in the anaerobic glovebox. Prior to the protein-substrate preparation, a mini-fridge (Great Gadgets, Ltd.) had been ported into the glovebox to control the crystallisation temperature and hopefully prevent PHD2$_{181-407}$ precipitation induced from the relatively high temperatures (~25-30 °C) within the anaerobic environment (**6.7.6**). 1.2-1.5 mM (NH_4)Fe(II)(SO_4), 5 mM 2OG-diacid (*i.e.*, to have enough 2OG per molecule of protein

and account for any uncoupled turnover), and 1.2-1.5 mM DMSO-solubilised HIF2$\alpha_{523-542}$-CODD were added to PHD2$_{181-407}$ (**6.7.6**). The protein-substrate mixture was kept cool in the mini-fridge (~6-8 °C) during cofactor and substrate incubations (**6.7.6**). As PHD2$_{181-407}$ crystallisation solutions can often form a skin during equilibration, the volume of the crystallisation drops was reduced to 1.5 μL (*i.e.*, in a 1:1 protein-to-solution ratio) in sitting-drop vapour-diffusion plates (**6.7.6**). The conditions screened were 0.2 M ammonium acetate, 0.1 M sodium acetate pH 4.1-5.6, and 10-35% (w/v) PEG 4000. After 3 days of equilibration, 200 μm x 100 μm x 30 μm plate-like morphology crystals formed (*Xtal-I*, **Figure 2-21** and **2-23**). (*Crystallisation set-up was conducted by Ms. Giorgia Fiorini.*)

The harvested crystal diffracted to 1.55 Å resolution at a synchrotron source (**6.6.7.2**, **Figure 2-22**; **Tables 2-4** and **2-7**). The structure was solved (*Xtal-A* used as a MR-model, **6.6.9.2**) that led to the conclusion that there was no apparent metal ion present in the active site and raises the question of the biological relevance of the PHD2$_{181-407}$.HIF2α interaction in the absence of a bound metal ion (*Xtal-I*, **Figure 2-23**). Another feature observed was ACT interacting with guanidinium functionality of Arg383 in a similar manner as the *Ta*PHD complex (PDB: 6EY1).[7]

Another distinct feature of the *Xtal-I* structure is that an active site water, usually coordinated to the metal ion (in structures *Xtal-A-H*), is complexed between the Oδ1 of Asp315 and N1 atom of His374 structurally analogous to the active site metal that is not present (*Xtal-I*). The water interaction in the *Xtal-I* structure provides evidence for the Asp315 Oδ1 atom increasing the displacement energy required for O_2 to displace this active site water (discussed in section **2.1**, **Figure 2-23**).[1]

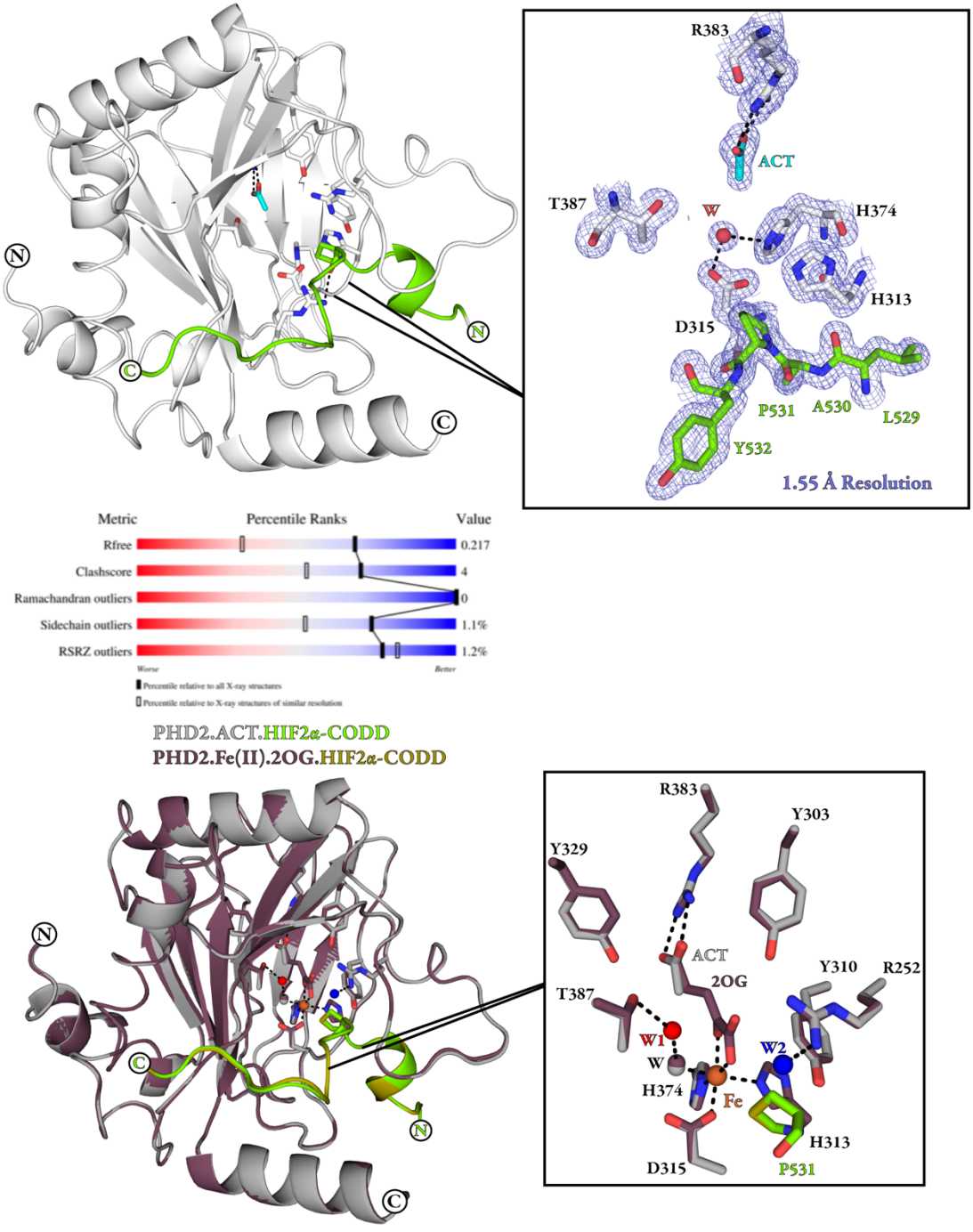


Figure 2-23| PHD2$_{181-407}$.ACT.HIF2α$_{523-542}$-CODD (*Xtal-I*) Structure and Alignment with the Anaerobic Acetate Crystal Structure (*Xtal-J*). Top panel: PHD2$_{181-407}$ is displayed as a cartoon (white). The active site residues, HIF2α-substrate residues, and ligand are depicted as sticks (active site-white, HIF2α-substrate-green, and ACT-ligand-cyan). The 2mF$_o$-DF$_c$ maps (contoured at 1.0 σ) are shown as mesh (blue). Bottom Panel: PHD2$_{181-407}$.ACT (grey) and PHD2$_{181-407}$.2OG (red) are illustrated as cartoons. The active site residues, HIF2α-substrate residues, and ligand are depicted as sticks (ACT-grey, 2OG-red, and HIF2α-substrate-green or olive). The red water molecule is observed in the PHD2$_{181-407}$.2OG complex, but not in the PHD2$_{181-407}$.ACT structure. The blue water molecule is observed in the PHD2$_{181-407}$.ACT complex, but not in the PHD2$_{181-407}$.2OG structure. Top and Bottom Panel: The waters molecules are depicted as spheres (red/raspberry-2OG, blue/grey-ACT) and key interactions are represented by dashes (black). Abbreviations: Prolyl hydroxylase isoform 2 (PHD2), Hypoxia-inducible factor (HIF), 2-Oxoglutarate (2OG), Acetate (ACT), *C*-terminal oxygen degradation domain (CODD). *Xtal-IDs*: *J, I.*

The structures of $PHD2_{181-407}$.Mn(II).2OG.$HIF2\alpha_{523-542}$-CODD (*Xtal-H*) and $PHD2_{181-407}$.ACT.$HIF2\alpha_{523-542}$-CODD (*Xtal-I*) were superimposed to compare active site water molecules present in the complexes (**Figure 2-23**). The W1 water molecule (red) in the *Xtal-H* structure, which interacts with Thr387, is not observed in *Xtal-I* (with no active site metal). The W2 water molecule (blue) in the *Xtal-I* structure, which interacts with Arg252, is not observed in the *Xtal-H* complex with 2OG (**Figure 2-23**). The precise function of the waters is not known, but they may be involved in 2OG binding.

As there was limited evidence for a metal ion in the active site of the $PHD2_{181-407}$.ACT.$HIF2\alpha_{523-542}$-CODD (*Xtal-I*) structure that was co-crystalliased with 1.2 mM Mn(II)Cl_2, the concentration and incubation time of $(NH_4)_2Fe(II)(SO_4)$ was increased to 1.5 mM and 30 minutes, respectively. A 600 μm x 200 μm x 75 μm plate-like morphology crystal formed after 3 days of equilibration and was harvested (**6.6.6.2** and **Table 2-7**). The anaerobic crystal diffracted to a 1.41 Å resolution at a synchrotron source (*Xtal-J*, **6.6.7.2**). The electron density corresponding to Fe and 2OG was observed in the active site of the *Xtal-J* complex structure (**Table 2-5**, **Figures 2-23** and **2-26**). The ability to obtain multiple crystals, prompted an initial O_2-exposure experiment in a similar fashion to that carried out with the formate-derived crystals (**2.2.3.1**). Five $PHD2_{181-407}$.Fe(II).2OG.$HIF2\alpha_{523-542}$-CODD.$\pm O_2$ structures were obtained: one anaerobic (*Xtal-J*) and four O_2-exposed datasets (*Xtal-K-N*, **Tables 2-5** and **2-6; Table 2-6 lists the O_2-timepoints**). (*Thank you to Ms. Giorgia Fiorini for her help on setting up the anaerobic crystal plates, further optimising the initial condition for anaerobic work, and assistance during sample preparation for data collection at Diamond Light Source Ltd.)*

Table 2-5| Acetate-Derived Crystallographic Data Processing and Refinement Statistics.

	Anaerobic.Fe(II).2OG *Xtal-J*	Fe(II).2OG.Rest-O_2-75-min *Xtal-K*	Fe(II).2OG.Rest-O_2-75-min *Xtal-L*	Fe(II).2OG.+O_2.60-min. *Xtal-M*	Fe(II).2OG.+O_2.7,200-min.+*Xtal-N*
Beamline	Diamond Light Source-I04	Diamond Light Source-I03	Diamond Light Source-I03	Diamond Light Source-I03	Diamond Light Source-I03
Detector	Dectris Eiger2 XE 16M	Dectris Eiger2 XE 16M	Dectris Eiger2 XE 16M	Dectris Eiger2 XE 16M	Dectris Eiger2 XE 16M
Data Processing	autoPROC Staraniso	autoPROC Staraniso	Xia2 DIALS	autoPROC Staraniso	Xia2 DIALS
Wavelength (Å)	0.97625	0.97627	0.97627	0.97627	0.97627
Resolution range (Å)	36.55 - 1.41 (1.46 - 1.41)	40.97 - 1.25 (1.29 - 1.25)	65.29 - 1.24 (1.28 - 1.24)	38.48 - 1.31 (1.36 - 1.31)	40.26 - 2.03 (2.10 - 2.03)
Space group	*P* 21 21 2	*P* 21 21 2	*P* 21 2 21	*P* 1 21 1	*P* 1 21 1
Unit cell (Å,°)	130.78 38.07 42.63	130.61 37.96 43.15	37.94 43.11 130.57	38.49 132.26 42.70, 91.68	38.38 131.93 42.29, 91.53
Total reflections	83579 (7808)	120353 (11502)	799023 (66134)	199766 (19487)	188964 (18342)
Unique reflections	41793 (3907)	60184 (5754)	61732 (6056)	99921 (9747)	27101 (2701)
Multiplicity	2.0 (2.0)	2.0 (2.0)	12.9 (10.9)	2.0 (2.0)	7.0 (6.8)
Completeness (%)	99.40 (94.15)	99.66 (97.02)	99.92 (99.77)	99.00 (96.63)	99.85 (99.30)
Mean I/sigma(I)	20.01 (3.28)	26.46 (3.87)	22.31 (2.19)	9.40 (0.71)	5.12 (0.51)
Wilson B-factor (Å²)	13.71	11.8	12.91	15.5	32.34
R-merge†	0.01713 (0.2582)	0.01536 (0.1917)	0.0543 (0.5191)	0.04109 (0.9461)	0.1689 (1.313)
R-meas	0.02423 (0.3652)	0.02172 (0.2711)	0.0566 (0.5453)	0.05811 (1.338)	0.1826 (1.423)
R-pim	0.01713 (0.2582)	0.01536 (0.1917)	0.01574 (0.1631)	0.04109 (0.9461)	0.06888 (0.542)
CC1/2	1 (0.746)	1 (0.873)	0.999 (0.951)	0.999 (0.383)	0.996 (0.642)
CC*	1 (0.924)	1 (0.966)	1 (0.987)	1 (0.744)	0.999 (0.884)
Reflections used in refinement	41780 (3894)	60184 (5754)	61702 (6051)	99867 (9742)	27064 (2682)
Reflections used for R-free	2077 (184)	2925 (282)	3118 (297)	5147 (556)	1371 (113)
R-work✧	0.1596 (0.2095)	0.1579 (0.2194)	0.1593 (0.2373)	0.1884 (0.3570)	0.1949 (0.3262)
R-free✧	0.1819 (0.2379)	0.1735 (0.2519)	0.1784 (0.2508)	0.2114 (0.3900)	0.2252 (0.2873)
CC(work)	0.969 (0.859)	0.965 (0.867)	0.968 (0.922)	0.964 (0.664)	0.961 (0.704)
CC(free)	0.963 (0.823)	0.965 (0.824)	0.952 (0.887)	0.963 (0.597)	0.945 (0.845)
Number of non-hydrogen atoms	2219	2236	2270	4488	4094
macromolecules	1982	2006	2041	3929	3869
ligands	15	64	57	26	26
solvent	226	188	193	541	207
Protein residues	239	240	241	476	477
RMS(bonds, Å)	0.008	0.010	0.012	0.009	0.003
RMS(angles, °)	1.02	1.20	1.46	1.03	0.61
Ramachandran favored (%)	97.02	98.28	97.86	97.6	97.82
Ramachandran allowed (%)	2.98	1.72	2.14	2.4	2.18
Ramachandran outliers (%)	0	0.00	0.00	0	0
Rotamer outliers (%)	1.48	1.46	2.82	1.51	2.3
Clashscore	2.3	2.49	3.95	2.07	1.71
Average B-factor (Å²)	18.95	16.97	19.28	22.93	38.92
macromolecules	18.02	15.80	18.28	21.81	38.93
ligands	10.68	27.12	21.52	17.43	34.77
solvent	27.5	27.21	29.52	31.26	39.09
Number of TLS groups	10	10	8	17	14

Single crystal diffraction data was collected from samples held at 100 K with conventional, rotation-based methods. Ligands: Fe, 2OG, Cl, GOL, and ACT.
Statistics for the highest-resolution shell are shown in parentheses.

† R-merge (or Rsym) is equal to $\sum|I-\langle I\rangle|/\sum I$. R-merge represents the data quality of merged reflection data. *I* is equal to the intensity of individual measurements and <I> is equal to the average of multiple measurements. ✧R_{free} is the R_{factor} for 5% of the reflections which are excluded during refinement.
R_{factor} is equal to $\sum_{hkl}||Fobs(_{hkl})| - |Fcalc(_{hkl})||/\sum_{hkl}|Fobs(_{hkl})|$ and was calculated for the working set of reflections (R_{work}).
Appendix I contains information of the crystal contents and the *Xtal-IDs*.

2.4.1.1 The O_2-Exposure of Acetate-Derived Crystals

To investigate whether the acetate-derived PHD2$_{181-407}$.HIF2α$_{523-542}$-CODD crystals could turnover *in crystallo*, a time-resolved O_2-experiment was conducted to test the system. Anaerobic crystals of PHD2$_{181-407}$.HIF2α$_{523-542}$-CODD were ported out of the glovebox and an O_2-sparged (5 minutes) well solution was prepared (**6.7.7**). The crystals were soaked with 5 μL of O_2-saturated solution. As the experiment ran over the course of 30 minutes, there was no apparent evidence of the reaction occurring, *i.e.*, there was no colour change or dissolving of the crystals to the extent observed with the formate-derived condition (**6.7.7**). The crystals were soaked for 45 minutes before harvesting (**6.6.6.2**). 12 crystals were removed for data collection from wells sparged with O_2. The resultant crystal structures diffracted to at 1.31 Å (*Xtal-M,* 60 minutes) and 2.03 Å (*Xtal-N,* ~7,200 minutes) resolutions in the *P* 2_1 space group. Note that after O_2-exposure the PHD2$_{181-407}$.HIF2α$_{523-542}$-CODD crystal form changed space groups, from *P* 2_1 2_1 2 to *P* 2_1 (**Figure 2-24**).

However, two PHD2$_{181-407}$.Fe(II).2OG.HIF2α$_{523-542}$-CODD.Rest-75-min crystals were not soaked with an O_2-sparged well solution (*Xtal-K* and *Xtal-L*, **Figures 2-26** and **2-27**, **6.7.7**). Instead *Xtal-K* and *Xtal-L* were exposed to atmospheric-O_2 for a resting time of 75 minutes and then soaked with a PHD clinically applied inhibitor, Roxadustat (**22**) to see if the HIF2α$_{523-542}$-peptide would be displaced by the inhibitor. Both *Xtal-K* and *Xtal-L* were soaked with 5 mM concentration of Roxadustat (**22**) for 15 minutes (only two soaked crystals were cryo-cooled with liquid-N_2, **6.7.7**). *Xtal-K* and *Xtal-L* were the last two crystals harvested from the O_2-exposure experiment to fill to the uni-puck (**6.6.6.2**, **Table 2-7**) and sent for diffraction data collection at 100 K at a synchrotron source (Diamond Light Source Ltd., **6.6.7.2**). There was no evidence of **22** of in the crystal structures of *Xtal-K* and *Xtal-L*.

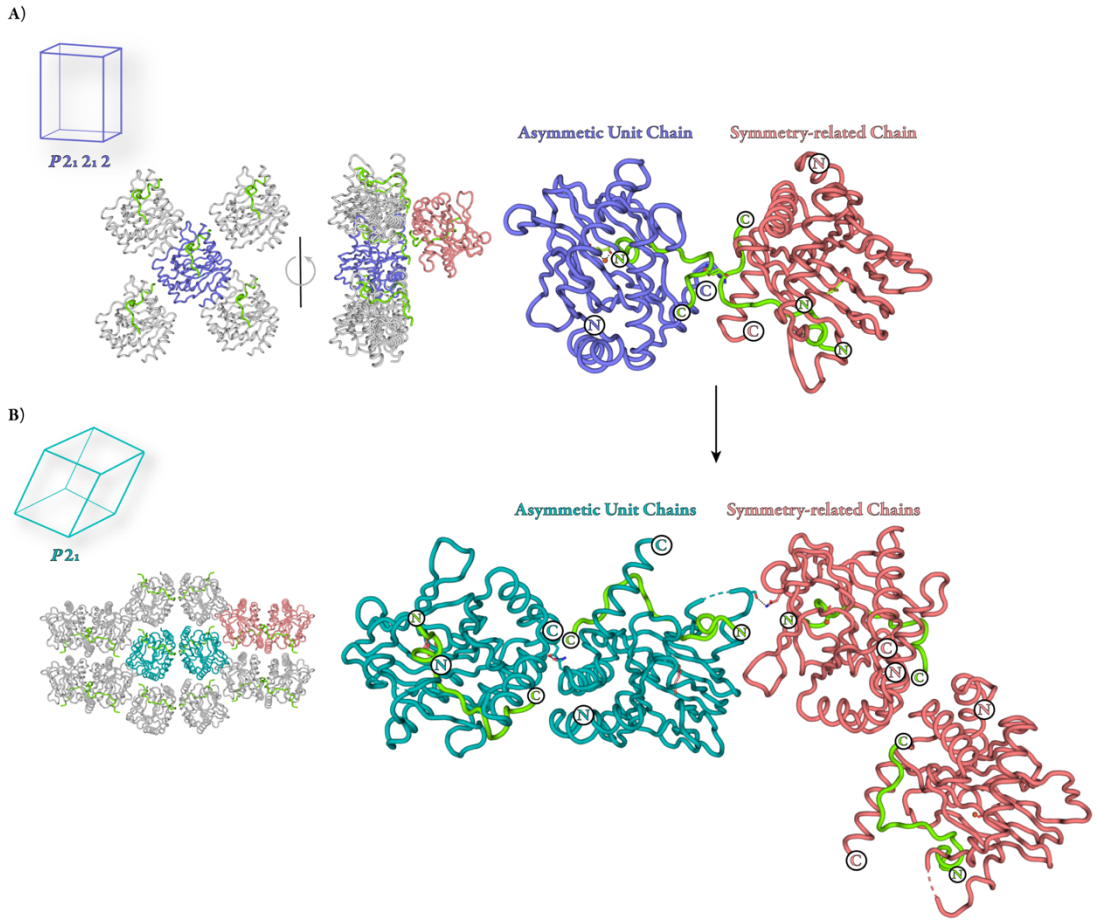


Figure 2-24| A Representation of the Space Group Change After O_2-Exposure. The $PHD2_{181-407}$.2OG-$HIF2\alpha_{523-542}$-CODD crystals change space groups from *P* 2_1 2_1 2 (A, *Xtal-J*) to *P* 2_1 (B, *Xtal-N*) during O_2-exposure. The asymmetric unit (blue and teal) and symmetry related chains (interacts with ASU-pink and surrounding-grey) are shown as cartoons. Abbreviations: Prolyl hydroxylase isoform 2 (PHD2), Hypoxia-inducible factor (HIF), 2-Oxoglutarate (2OG), and *C*-terminal oxygen degradation domain (CODD), Asymmetric unit (ASU). *Xtal-IDs*: *J*, *N*.

The ASU of the O_2-exposed *Xtal-M* and *Xtal-N* (also referred to as Product 1 and Product 2 in **Figures 2-26** and **2-27**) of the acetate-derived $PHD_{2181-407}$.$HIF2\alpha_{523-542}$-CODD contain two chains. The β2-β3 finger loop is observed to adopt a conformation that hinders substrate release and is induced by an interaction between chain C residues Ser245-Asp246 and chain A residues Arg322 and Gln377 (**Figure 2-25**). An electrostatic interaction between $Asn284_{chain-A}$ and $Asn284_{chain-C}$ stabilises the two $PHD2_{181-407}$ ASU chains (**Figure 2-25**).

The acetate-derived crystals are stable after O_2-exposure, evidenced by a dataset of two PHD2$_{181-407}$.Fe(II).2OG.HIF2α$_{523-542}$-CODD.Rest-1-min.+O_2.T~7,200-min (*Xtal-N*) that was collected 5-days after the initial exposure to O_2 (**Figure 2-26**).

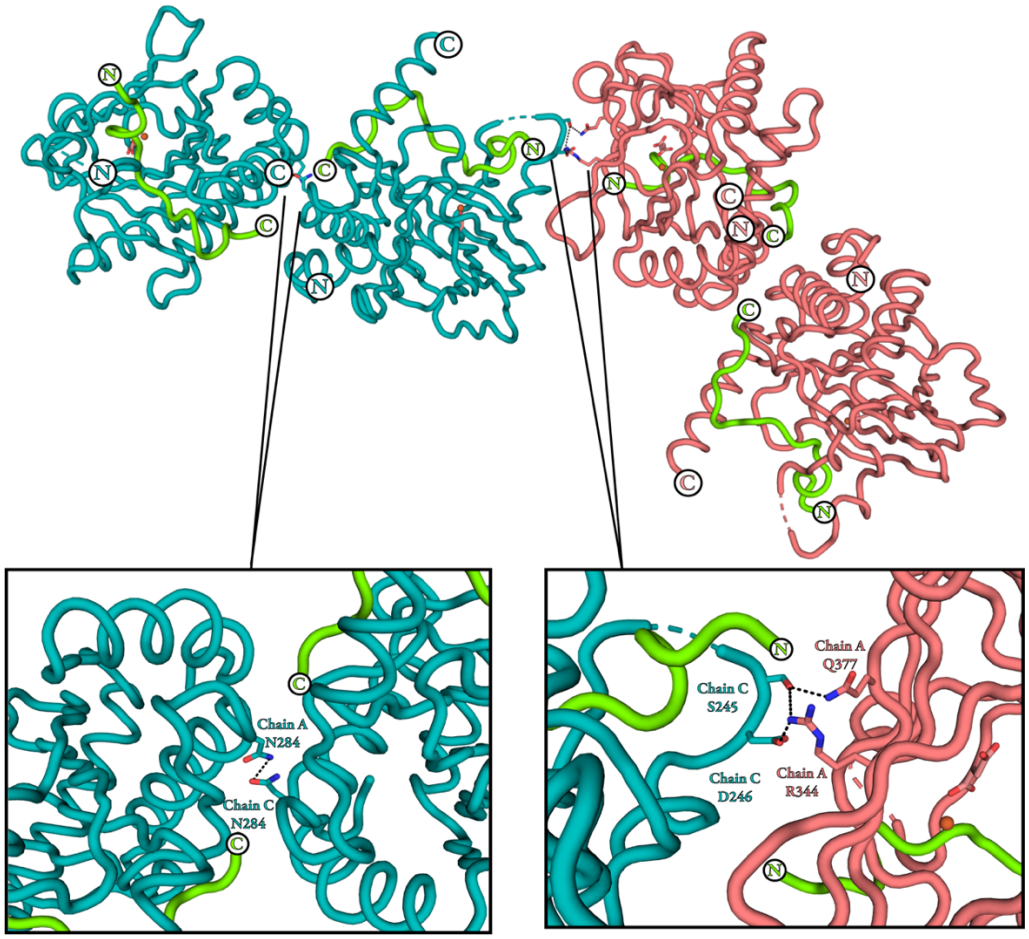


Figure 2-25| Inter-Chain Interactions of the *P* 2$_1$ O_2-Exposed PHD2$_{181-407}$.Fe(II).2OG.HIF2α$_{523-542}$-CODD Crystal Lattice. The asymmetric unit (teal) and symmetry related (pink) chains are shown as cartoons. The specific chain interactions are displayed as sticks. Abbreviations: Prolyl hydroxylase isoform 2 (PHD2), Hypoxia-inducible factor (HIF), 2-Oxoglutarate (2OG), and *C*-terminal oxygen degradation domain (CODD). *Xtal-ID*: *M*.

The active sites of the four O_2-exposed PHD2$_{181-407}$.Fe(II).2OG.HIF2α$_{523-542}$-CODD crystals were compared with that of the anaerobic PHD2$_{181-407}$.Fe(II).2OG.HIF2α$_{523-542}$-CODD (*Xtal-J*) complex (**Figure 2-26**). Evidence for the decarboxylation of 2OG in the O_2-exposed crystals is observed, as the presence of the 2mF_o-DF_c electron density corresponds to that of succinate in the 2OG binding pocket (*Xtal-K-N*, **Figure 2-26**).

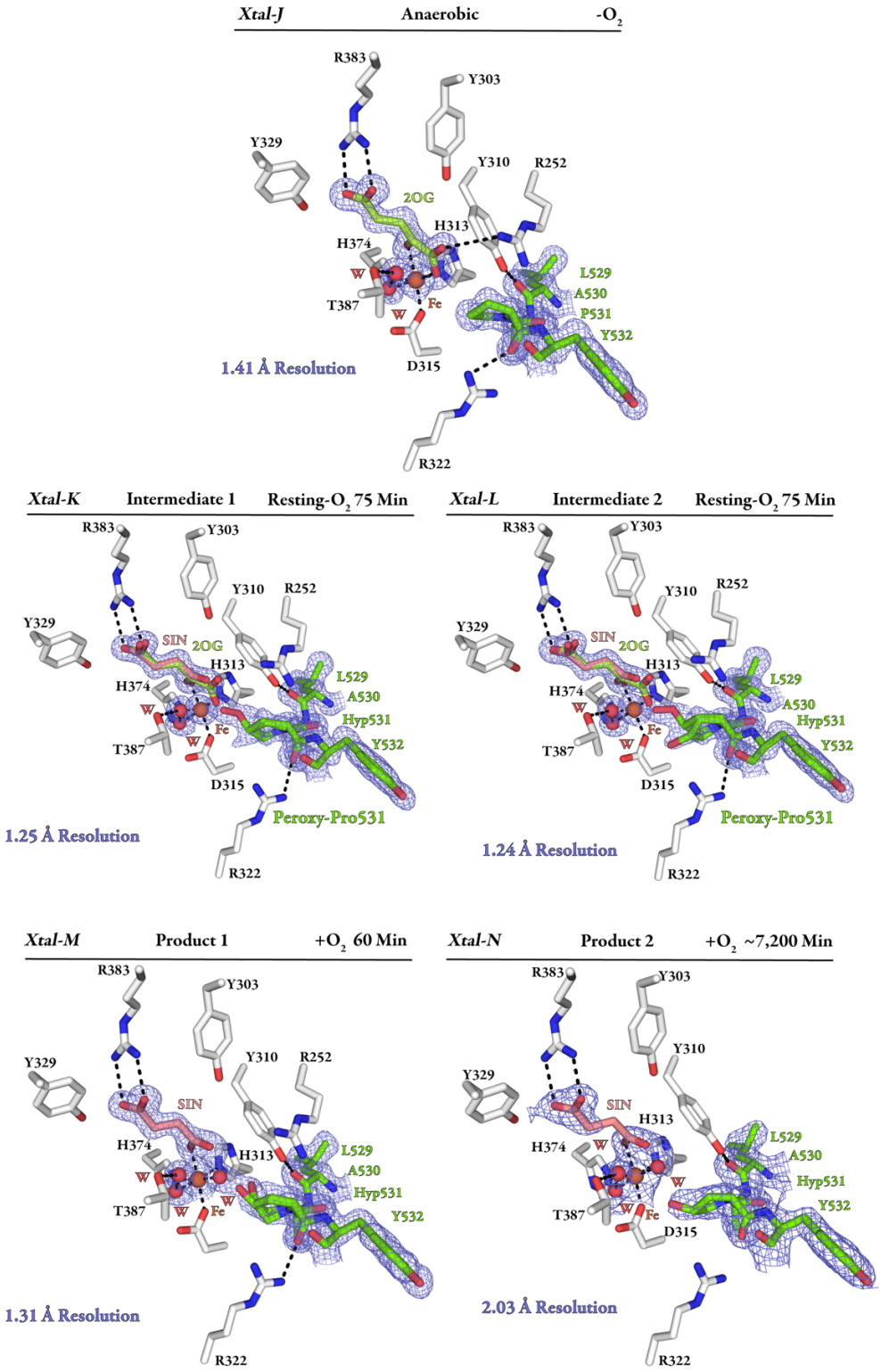


Figure 2-26| The Active site of Anaerobic and O_2-Exposed Acetate-Derived Complex Structures. The active site residues (white), 2OG (yellow), SIN (pink), and HIF2$\alpha_{523\text{-}542}$-CODD peptide residues (green) are shown as sticks. The $2mF_o$-DF_c electron density map (contoured to 1.0 σ) of the residues is displayed as mesh (blue). Electrostatic and hydrogen bonds interactions are represented as dashes (black). Fe (orange) and water molecules (red) are shown in spheres. The peroxy- and hydroxy-proline 531 is observed in multiple conformations. Abbreviations: Prolyl hydroxylase isoform 2 (PHD2), 2-Oxoglutarate (2OG), Succinate (SIN), Hypoxia-inducible factor (HIF), and *C*-terminal oxygen degradation domain (CODD). *Xtal-IDs*: *J*, *K*, *L*, *M*, *N*.

Pro531$_{HIF2\alpha}$ is hydroxylated in the O_2-exposed crystals (*Xtal-K-N*, **Figure 2-26** and **2-27**). The *Xtal-N* structure (exposed for 5-days) has fully turned over the HIF2$\alpha_{523-542}$-CODD peptide to give the hydroxylated product (Product 2, **Figure 2-26**).

The RMSD values of aligned structures of PHD2$_{181-407}$.Fe(II).2OG.HIF2α anaerobic (*Xtal-J*) and O_2-exposed structures revealed low deviations between the overall structures (*i.e.*, 0.079 for *Xtal-K* and *Xtal-L*; 0.136-0.143 for *Xtal-M* and *Xtal-N;* measured in PyMOL™, **6.1**). Note, however, time-resolved work with IPNS shows that low RMSD values does not mean that the complexes do not move during catalysis.[36] The hydrogen bond network of waters between the metal coordinated water and Thr387 is conserved in all structures (**Figure 2-26**). The Hyp531 hydroxyproline is also in the *trans*-position with the pyrrolidine ring pucker in the *exo*-conformation in the *Xtal-M* structure (**Figure 2-26** and **2-27**). As the resolution is lower for the *Xtal-N* structure the ring pucker is not as clear in the electron density (**Figure 2-26** and **2-27**). The hydroxyproline adopts different conformations between *Xtal-M* and *Xtal-N* structures, which could be the proposed product release or ejection mechanism.[1] The change in the pyrrolidine ring pucker may be involved in the initiation of hydroxylated HIFα release (**Figure 2-26** and **2-27**).[1] The succinate density beings to weaken around the 2OG methylenes, potentially as a result of partial loss of succinate from the active site and entry of acetate from the crystallisation condition (**Figure 2-26** and **2-27**).

The O_2-exposed PHD2$_{181-407}$.Fe(II).2OG.HIF2$\alpha_{523-542}$-CODD.Rest/+O_2 complex structures offer an initial mechanistic characterisation of the *in crystallo* reaction of PHD2$_{181-407}$ with HIF2$\alpha_{523-542}$-substrate. The structures of *Xtal-K* and *Xtal-L*, in part, reflect the formation of succinate and hydroxyproline (both refined as 60% and 40% occupancy, respectively).

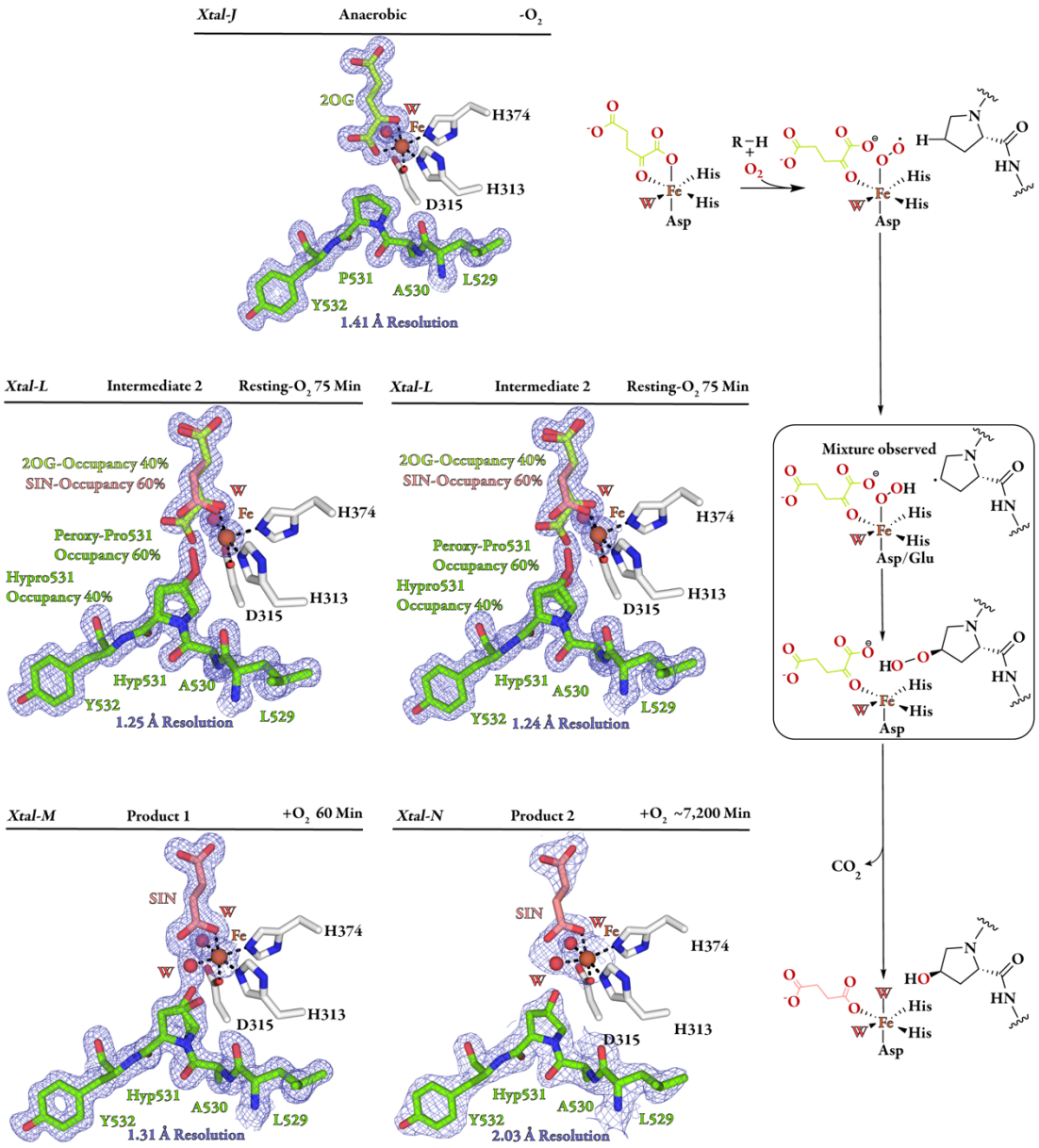


Figure 2-27| The Close-up Views of the Active Site Changes Acetate-Derived Crystals O_2-Exposure. The active site residues (white), 2OG (yellow), SIN (pink), and HIF2$\alpha_{523\text{-}542}$-CODD peptide residues (green) are shown in sticks. The $2mF_o$-DF_c electron density map (Contoured to 1.0 σ) of the residues displayed as mesh (blue). Active site interactions are represented as dashes (black). Fe (orange) and water molecules (red) are shown in spheres. The peroxy- and hydroxy-proline 531 is observed in multiple conformations. The accompanying proposed mechanism is displayed best on the observed crystal structures. Note, the intermediate reaction steps that are drawn in the black box are observed as a mixture in the crystal structures. Abbreviations: Prolyl hydroxylase isoform 2 (PHD2), 2-Oxoglutarate (2OG), Succinate (SIN), Hypoxia-inducible factor (HIF), and *C*-terminal oxygen degradation domain (CODD). *Xtal-IDs: J, K, L, M, N.*

The product is clearly observed in the *Xtal-M* and *Xtal-N* structures. 2OG is likely present and was refined at 40% occupancy (thought note the O1 atom of the 2OG C1 carboxylate has moved from the Fe. The formation of other 2OG derived species is possible and

cannot be ruled in this complex. It appears that two atoms maybe attached to the proline C4 position. Although its assignment as an intermediate must be regarded as speculative, this density was refined as C4 peroxyproline (i.e., R-O-OH). Such an intermediate was proposed for 2OG oxygenase catalysis by Cardinale and Udenfriend in 1971, though in their mechanism the peroxyproline attacks the 2OG 2-keto group; the structures of *Xtal-K* and *Xtal-L* do not appear to support this mechanism (**Figure 2-26**, **2-27**, and **2-28**).[18,20–22,37,51,52]

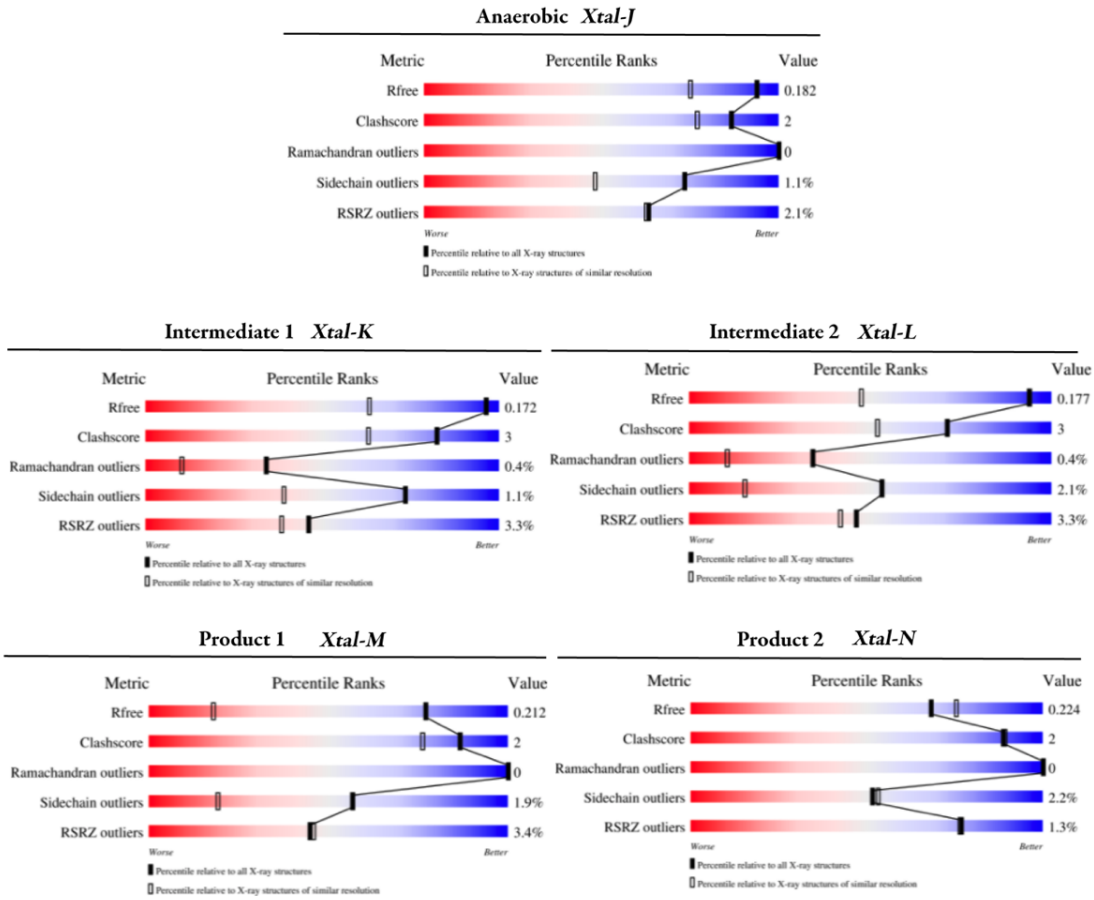


Figure 2-28| Crystallographic Validation of Anaerobic and O_2-Exposed Acetate-Derived PHD2$_{181-407}$.Fe(II).2OG.HIF2α$_{523-542}$-CODD Complex Structures. The validation tables were generated with the PDB validation tool. Abbreviations: Protein Data Bank (PDB).

If the presence of the speculative proline-peroxide intermediate could be validated, it would require revision of the current consensus 2OG oxygenase mechanism which employs a Fe(IV)=O intermediate to effect substrate oxidation. If valid, the

peroxyproline would have implications on the PHDs evolved slow reaction with O_2 and the role this enzyme plays in the hypoxic response. Note, however, at least in one case (VioC) a succinyl peroxide intermediate is proposed en route to the Fe(IV)=o intermediate.[37]

The anaerobic and O_2-exposed $PHD2_{181-407}$.Fe(II).2OG.$HIF2\alpha_{523-542}$-CODD crystals normalised B-factors (*i.e.*, 'an expression of the B-factor in units of standard deviation about the mean value', Å^2)[45] were compared in reference to the secondary structure elements shown in **Figure 2-29**, *i.e.*, in a similar manner as described in section **2.2.3.1**.

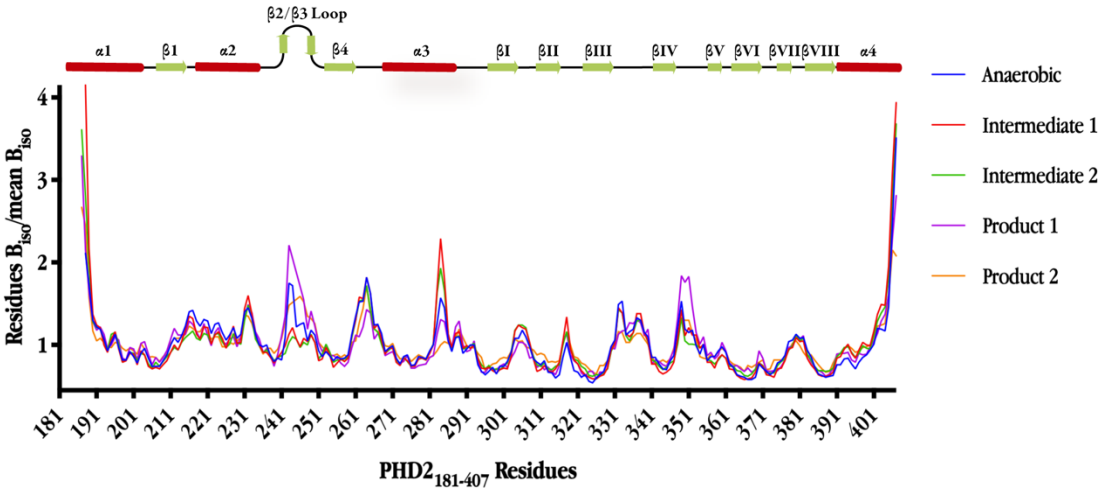


Figure 2-29| Normalised Cα B-Factor Analyses Between Acetate Condition Crystal Structures. All $PHD2_{181-407}$ residues Cα atom B-factors (Å^2) were normalised based on the mean B-factor of the crystal structure. The normalised B-factors were analysed for the anaerobic (blue, *Xtal-J*), Intermediate 1 (red, *Xtal-K*), Intermediate 2 (green, *Xtal-L*), Product 1 (chain A-purple, *Xtal-M*), and Product 2 (chain A-orange, *Xtal-N*) complex structures. α-helix (red cylinder) and β-strand (green arrow) secondary structure features are aligned above in correspondence with residues. Data was analysed with the Structure Comparison Tool in PHENIX. Abbreviations: Prolyl hydroxylase isoform 2 (PHD2). *Xtal-IDs*: *J*, *K*, *L*, *M*, *N*.

Analysis of variations in the Cα B-factors between $PHD2_{181-407}$.Fe(II).2OG.$HIF2\alpha_{523-542}$-CODD structures can potentially provide insight into the dynamics occurring during the O_2-catalysed reaction in the crystalline state (**Figure 2-29**).[45] An area of interest within $PHD2_{181-407}$ comprise residues Arg281-Gly285.

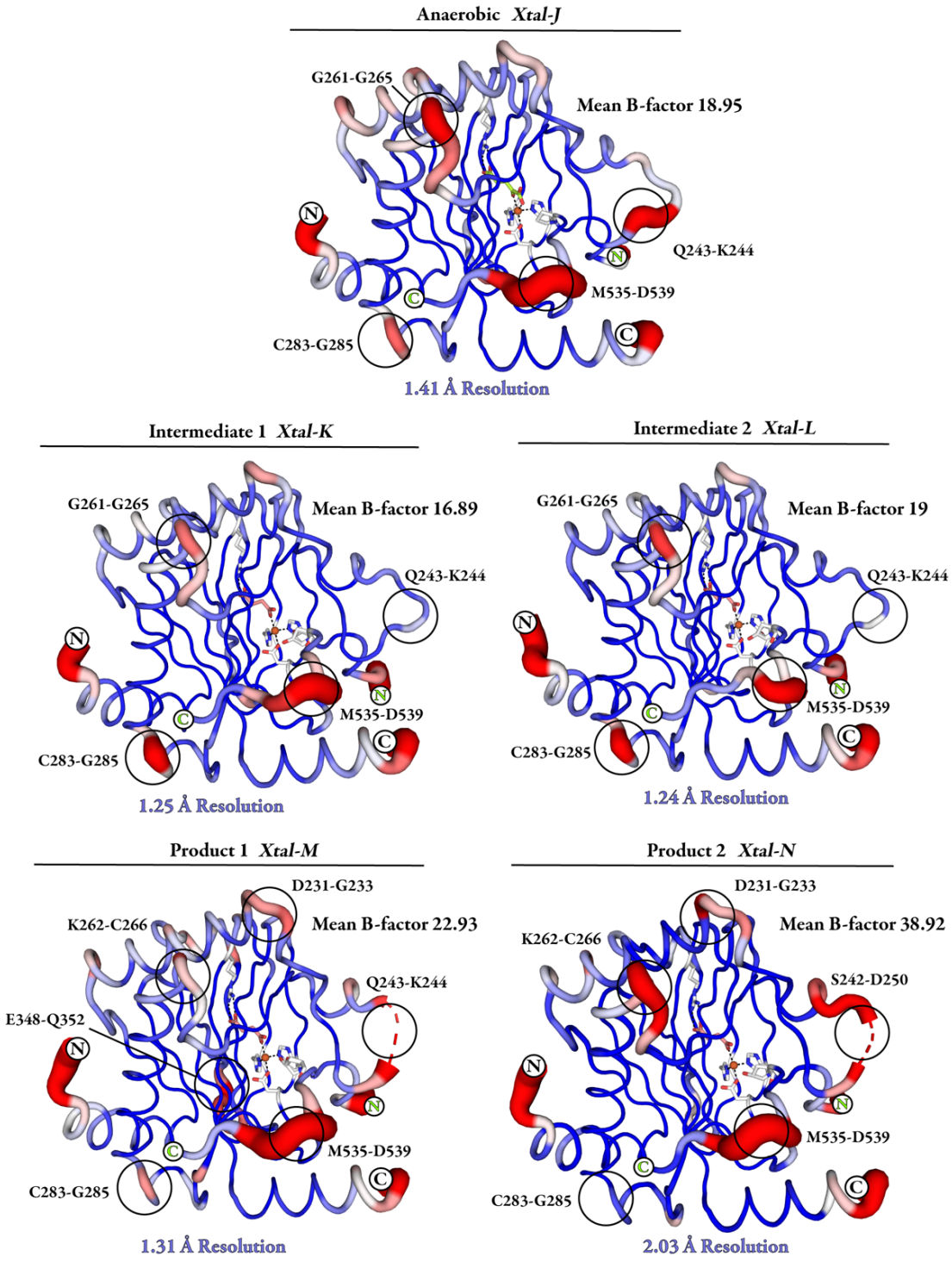


Figure 2-30| All Atoms B-Factor Heat-Map of the Acetate Anaerobic and O_2-Exposed Data. $PHD2_{181-407}$.$HIF2\alpha_{523-542}$-CODD Complex Structures are depicted with putty cartoons (relative size of the cartoon correlates to high B-factors, Å^2). The blue-white-red heat map (blue-low temperature and red high-temperature) is normalised to the average for all B-factors (Å^2) of the structures. Areas of interest are highlighted with circles (black). Abbreviations: Prolyl hydroxylase isoform 2 (PHD2), Hypoxia-inducible factor isoform 2α, C-terminal oxygen degradation domain (CODD). *Xtal-IDs*: *J*. *K*, *L*, *M*, *N*.

Both Arg281 and Asn284 electrostatically interact with Leu542 of the *C*-terminus of the HIF2α$_{523-542}$-CODD substrate (**Figure 2-29**). As seen in the oligomerisation of the ASU chains in the *P* 2$_1$ O$_2$-exposed crystal form, Asn284 forms a polar interaction with the same Asn284 from a neighbouring chain, and may, in part, reflect the observed decrease in B-factors observed for the residues between Arg281-Gly285 for *Xtal-M* and *Xtal-N* complexes (**Figures 2-29** and **2-30**).When PHD2$_{181-407}$.Fe(II).2OG.HIF2α$_{523-542}$-CODD.Rest-O$_2$-75-min *Xtal-K* and *Xtal-L* structures are compared to the anaerobic PHD2$_{181-407}$.Fe(II).2OG.HIF2α$_{523-542}$-CODD crystal (*Xtal-J*), an increase in B-factors for residues Arg281-Gly285 residues is apparent, probably reflecting conformational changes induced by the reaction with O$_2$ (**Figures 2-29** and **2-30**). It is possible that the dynamics of residues Arg281-Gly285 may act as a mechanism to assist in productively orienting the substrate at the active site (**Figure 2-30**). The dynamics of Arg281-Gly285 appear to be coupled with the β2-β3 finger loop stabilising the HIF2α$_{523-542}$-CODD substrate during intermediate reaction stages in *Xtal-K* and *Xtal-L* (**Figure 2-30**). The β2-β3 finger loop is observed to have high overall B-factors (Å^2) and is consistent between both formate-derived and acetate-derived PHD2$_{181-407}$.HIF2α$_{523-542}$-CODD complex structures.

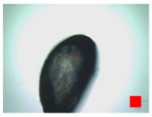
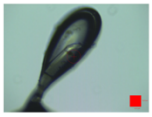
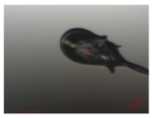
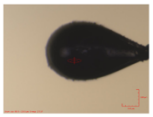
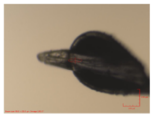
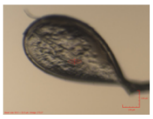
In *Xtal-M* and *Xtal-N* product structures, the β2-β3 finger loop is disordered (**Figure 2-30**).[53] The disordering of the β2-β3 finger loop is potentially the HIF2α$_{523-542}$-product ejection by PHD2$_{181-407}$. However, the product release is blocked by the symmetry-related chain during the point group change from *P* 2$_1$ 2$_1$ 2 to *P* 2$_1$ (discussed in **2.4.1.1**). The B-factor heat maps provide a visual tool to observe the dynamic regions of PHD2$_{181-407}$ during O$_2$-exposure. As the O$_2$-exposed structures are an initial characterisation, further time-resolved studies are required to characterise the nature of the observed intermediate species, with this work laying the foundation for future

mechanistic studies with the PHD2$_{181-407}$.Fe(II).2OG.HIF2α$_{523-542}$-CODD acetate-derived condition.

2.5 Summary and Future Directions

Two novel crystallisation conditions were developed to robustly obtain PHD2$_{181-407}$.HIF2α$_{523-542}$-CODD complex structures that are being used in ongoing mechanistic studies (**Figure 2-31**). In total, eleven structures: (i) *Xtal-A*.Mn(II).NOG.3C, (ii) *Xtal-B*.Mn(II).2OG.3C, (iii) *Xtal-C*.Fe(II).2OG.3C.-O_2, (iv) *Xtal-D*.Fe(II).2OG.3C.Rest-O_2-1-min.+O_2, (v) *Xtal-E*. Fe(II).2OG.3C.Rest-O_2-1-min.+O_2, (vi) *Xtal-F*. Fe(II).2OG.3C.Rest-O_2-1-min.+O2, (vi) *Xtal-G*.Mn(II).2OG.3C, (vii) *Xtal-I*.ACT, (viii) *Xtal-J*.Fe(II).2OG.-O_2, (ix) *Xtal-K*.Fe(II).2OG.Rest-O_2-75-min, (x) *Xtal-L*.Fe(II).2OG.Rest-O_2-75-min, (xi) *Xtal-M*.Fe(II).2OG.Rest-O_2-1-min.+O_2.60-min, (xii) *Xtal-N*.Fe(II).2OG.Rest-1-min.+O_2.7,200-min were obtained. Crystallisation protocols with use of the 2OG-diacid form and DMSO-solubilised-HIF2α$_{523-542}$-CODD substrate, helped to find a suitable condition for crystallisation of the PHD2$_{181-407}$.Fe(II).2OG.HIF2α$_{523-542}$-CODD complex (**Figure 2-31**). A reproducible protocol was developed to obtain PHD2$_{181-407}$.HIF2α$_{523-542}$-CODD crystals in the anaerobic glovebox during each preparation. As previously mentioned, (**2.2.1**), an important step was the removal of unbound Ni(II) during the affinity chromatography purification column (**6.4.2**). Ni(II)-leeching was observed during the optimisation of the purification of PHD2$_{181-407}$. A mixture of co-purified metal species with PHD2$_{181-407}$ would likely inhibit crystallisation. EDTA-treatment of PHD2$_{181-407}$ was conducted to remove any coordinated metal from the protein.

Table 2-6 | An Overview of the Conditions of Harvested $PHD2_{181-407}$.$HIF2\alpha_{523-542}$-CODD Crystals.

Crystal ID	Crystal Contents	Mount	Res (Å)	O_2-Exposure (min)	Cryo-protectant	Condition
Xtal-A	$PHD2_{181-407}$.Mn(II).NOG. $HIF2\alpha_{523-542}$-CODD.3C		1.17	Normoxic	Glycerol	Formate
Xtal-B	$PHD2_{181-407}$.Mn(II).2OG. $HIF2\alpha_{523-542}$-CODD.3C		1.21	Normoxic	Glycerol	Formate
Xtal-C	$PHD2_{181-407}$.Fe(II).2OG. $HIF2\alpha_{523-542}$-CODD.3C		1.48	Anaerobic	Glycerol	Formate
Xtal-D	$PHD2_{181-407}$.Fe(II).2OG. $HIF2\alpha_{523-542}$-CODD.3C		1.65	17	Glycerol	Formate
Xtal-E	$PHD2_{181-407}$.Fe(II).2OG. $HIF2\alpha_{523-542}$-CODD.3C		1.55	19	Glycerol	Formate
Xtal-F	$PHD2_{181-407}$.Fe(II).2OG. $HIF2\alpha_{523-542}$.CODD		1.48	25	Glycerol	Formate
Xtal-G	$PHD2_{181-407}$.Mn(II).2OG. $HIF2\alpha_{523-542}$.CODD		2.02	Normoxic	Glycerol	Zn
Xtal-H	$PHD2_{181-407}$.Mn(II).2OG. ACT.$HIF2\alpha_{523-542}$-CODD		1.70	Normoxic	Glycerol	Acetate
Xtal-I	$PHD2_{181-407}$.ACT. $HIF2\alpha_{523-542}$-CODD		1.55	Anaerobic	Glycerol	Acetate
Xtal-J	$PHD2_{181-407}$.Fe(II).2OG. $HIF2\alpha_{523-542}$-CODD		1.41	Anaerobic	DMSO	Acetate
Xtal-K	$PHD2_{181-407}$.Fe(II).2OG. Hyp$HIF2\alpha_{523-542}$-CODD		1.25	75*	DMSO	Acetate
Xtal-L	$PHD2_{181-407}$.Fe(II).2OG. Hyp$HIF2\alpha_{523-542}$-CODD		1.24	75*	DMSO	Acetate
Xtal-M	$PHD2_{181-407}$.Fe(II).2OG. Hyp$HIF2\alpha_{523-542}$-CODD		1.31	60	DMSO	Acetate
Xtal-N	$PHD2_{181-407}$.Fe (II).2OG. Hyp$HIF2\alpha_{523-542}$-CODD		2.03	7,200	DMSO	Acetate

* Resting time 75 min - Not soaked with O_2

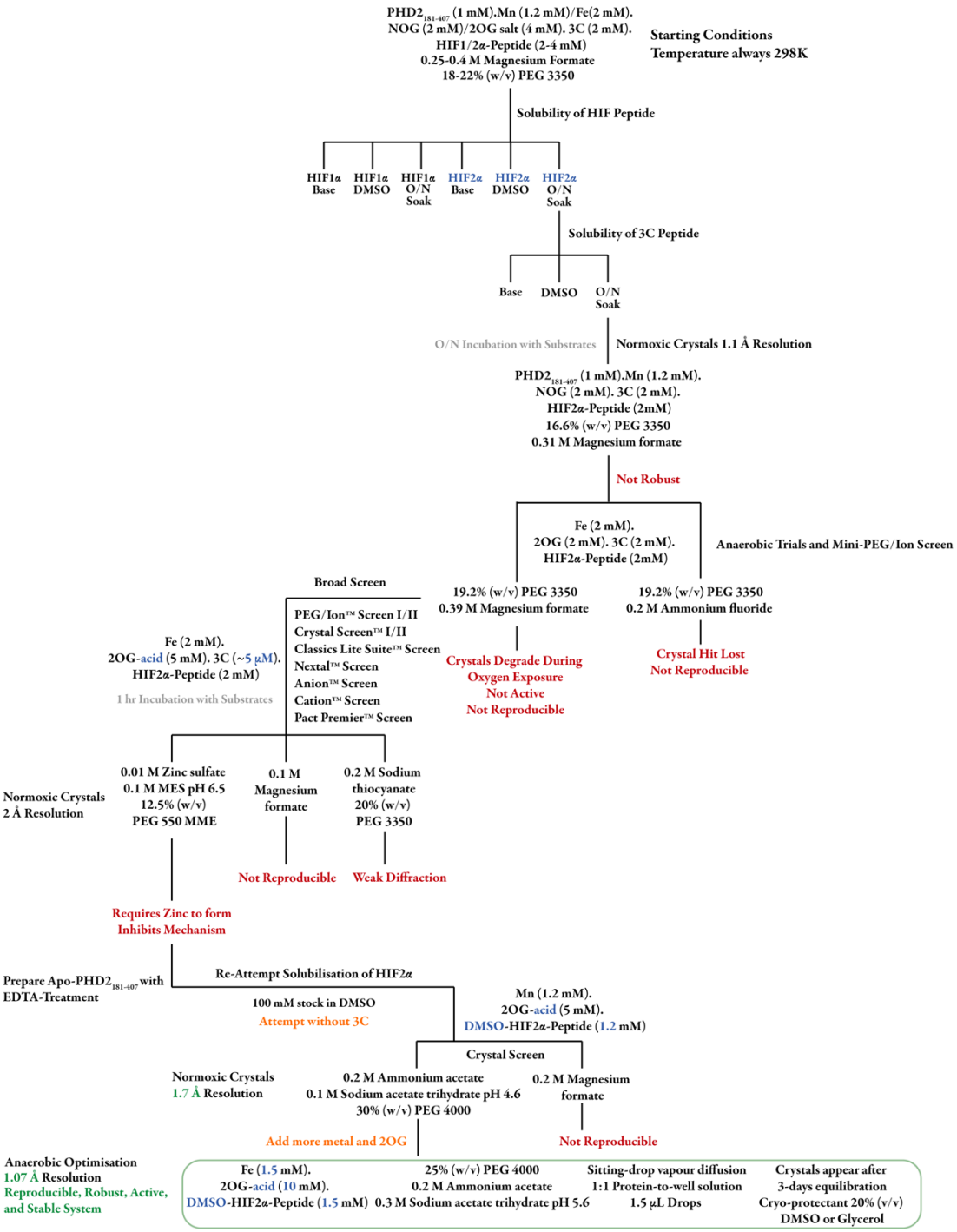


Figure 2-31| Optimisation of the PHD2$_{181-407}$.Fe(II)/Mn(II).NOG/2OG.HIF2α$_{523-542}$-CODD Crystallisation System. The flow-chart depicts the key improvements (blue and green)of the PHD2$_{181-407}$.HIF2α$_{523-542}$-CODD crystallisation system. Errors (orange) and failures (red) are also highlighted, along with advances that led towards the final crystallisation condition. Note the highest resolution (1.07 Å)was the achieved resolution, however, the dataset was not complete to that resolution. Abbreviations: Prolyl hydroxylase isoform 2, Hypoxia-inducible factor isoform 2α.

Of the crystallisation procedures presented here it is of particular interest how the presence of the HIF2α$_{523-542}$-CODD can help promote robust crystallisation of

PHD2$_{181-407}$.Mn(II)/Fe(II).HIF2α$_{523-542}$-CODD complexes. Potentially, the HIF2α$_{523-542}$-CODD peptide could be used to obtain substrate complexes with PHD1 or PHD3 isoforms. Furthermore, the strategy (*i.e.*, screening with different peptides) could be applied to other oxygenases to obtain their substrate complex structures.

Further solution-based studies are required to characterise the biological relevance of the observed Zn binding in the Zn-derived PHD2$_{181-407}$.HIF2α$_{523-542}$-CODD complex structure (*Xtal-G*). The function of the Zn ions in the *Xtal-G* complex (between residues Cys201-Cys208-Asn182 and Asp278-His282) may be involved with the *N*-terminal MYND-Zn-binding domain in the full-length PHD2.[50] Due to the difficult nature of crystallisation in anaerobic conditions, a reliable and robust system was needed to obtain PHD2$_{181-407}$.Fe(II).2OG.HIF2α$_{523-542}$-CODD crystals in the glovebox (**Figure 2-31**). In comparison to the formate-derived condition, the acetate condition provides a reliable, robust, stable, and catalytically active crystal. The acetate-derived crystallisation condition is a platform for future mechanistic-based studies.

Current and future work is ongoing to optimise a batch method protocol for microcrystal production of the PHD2$_{181-407}$.HIF2α$_{523-542}$-CODD complex. The efforts may help obtain further room temperature and nitric oxide (NO) structures *via* chip-based fixed-target data collection at Diamond Light Source Ltd. (I24 Beamline in collaboration with the XFEL-Hub).[31,34–36] The experiments may provide PHD2$_{181-407}$.HIF2α$_{523-542}$-CODD structures that can be compared against any cryogenic or O_2-bound complexes obtained during the mechanistic studies, *i.e.*, to validate the structural results and determine if there is a temperature bias to the conformation and reaction mechanism observed.[31,34,36,54] A room temperature structure could potentially corroborate the current preliminary findings and may provide further insight into the dynamics that are visualised upon exposure to O_2.[31,34,36] A NO-structure might reveal the O_2-binding position on the

Fe-centre.[31] Further O_2 experiments using high-pressure O_2-gas cells (55 Bar) have been conducted at the European Synchrotron Research Facility (ESRF)-High Pressure Macromolecular Crystallography (HPMX) laboratory.[55] The high pressure experiments offer an alternative way to overcome the slow O_2-diffusion into large macro-crystals through pressurisation of O_2-gas.[55] Another advantage to HPMX is that the crystal can be cryo-cooled in liquid-O_2 as the O_2 condenses in the pressure cell.[55–57] Cryo-cooling in liquid-O_2 may prevent O_2 gas molecules diffusing out of the crystals when cryo-cooled with liquid-N_2.[56] Also, other inert noble gases can be used for crystal derivatisation, such as Kr and Xe gas cells (up to 150 bar), the gases can potentially provide insight in the O_2-diffusion pathway as they have similar properties to O_2.[56,57] Both Kr and Xe gases have a higher electron density and can be visualised in the $PHD2_{181-407}$.$HIF2\alpha_{523-542}$-CODD crystallographic data. The derivatisation of by Kr or Xe may reveal the O_2-diffusion pathway of the $PHD2_{181-407}$.$HIF2\alpha_{523-542}$-CODD complex.[13,57]

The mechanistic studies of $PHD2_{181-407}$ may one day reveal the specific catalytic mechanisms of the PHDs and better insight into how this enzyme family has evolved as a hypoxic 'sensor' in animals.[58] Further investigations may provide novel approaches to PHD1-3 inhibition, *i.e.*, isoform-selectivity to control and regulate the hypoxic response in different tissues.[59] The structural analysis of $PHD2_{181-407/426}$ inhibition is explored in Chapters **3** and **4**.

2.6 References

(1) Chowdhury, R.; McDonough, M. A.; Mecinović, J.; Loenarz, C.; Flashman, E.; Hewitson, K. S.; Domene, C.; Schofield, C. J. Structural Basis for Binding of Hypoxia-Inducible Factor to the Oxygen-Sensing Prolyl Hydroxylases. *Structure* **2009**, *17* (7), 981–989. https://doi.org/10.1016/j.str.2009.06.002.

(2) Chowdhury, R.; Leung, I. K. H.; Tian, Y. M.; Abboud, M. I.; Ge, W.; Domene, C.; Cantrelle, F. X.; Landrieu, I.; Hardy, A. P.; Pugh, C. W.; Ratcliffe, P. J.; Claridge, T. D. W.; Schofield, C. J. Structural Basis for Oxygen Degradation Domain Selectivity of the HIF Prolyl Hydroxylases. *Nature Communications* **2016**, *7* (1), 12673. https://doi.org/10.1038/ncomms12673.

(3) Yeh, T.-L.; Leissing, T. M.; Abboud, M. I.; Thinnes, C. C.; Atasoylu, O.; Holt-Martyn, J. P.; Zhang, D.; Tumber, A.; Lippl, K.; Lohans, C. T.; Leung, I. K. H.; Morcrette, H.; Clifton, I. J.; Claridge, T. D. W.; Kawamura, A.; Flashman, E.; Lu, X.; Ratcliffe, P. J.; Chowdhury, R.; Pugh, C. W.; Schofield, C. J. Molecular and Cellular Mechanisms of HIF Prolyl Hydroxylase Inhibitors in Clinical Trials. *Chemical Science* **2017**, *8* (11), 7651–7668. https://doi.org/10.1039/C7SC02103H.

(4) McDonough, M. A.; Li, V.; Flashman, E.; Chowdhury, R.; Mohr, C.; Liénard, B. M. R.; Zondlo, J.; Oldham, N. J.; Clifton, I. J.; Lewis, J.; McNeill, L. A.; Kurzeja, R. J. M.; Hewitson, K. S.; Yang, E.; Jordan, S.; Syed, R. S.; Schofield, C. J. Cellular Oxygen Sensing: Crystal Structure of Hypoxia-Inducible Factor Prolyl Hydroxylase (PHD2). *Proceedings of the National Academy of Sciences of the United States of America* **2006**, *103* (26), 9814–9819. https://doi.org/10.1073/pnas.0601283103.

(5) Chowdhury, R.; Abboud, M. I.; McAllister, T. E.; Banerji, B.; Bhushan, B.; Sorensen, J. L.; Kawamura, A.; Schofield, C. J. Use of Cyclic Peptides to Induce Crystallization: Case Study with Prolyl Hydroxylase Domain 2. *Scientific Reports* **2020**, *10* (1). https://doi.org/10.1038/s41598-020-76307-8.

(6) Scotti, J. S.; Leung, I. K. H.; Ge, W.; Bentley, M. A.; Paps, J.; Kramer, H. B.; Lee, J.; Aik, W.; Choi, H.; Paulsen, S. M.; Bowman, L. A. H.; Loik, N. D.; Horita, S.; Ho, C. H.; Kershaw, N. J.; Tang, C. M.; Claridge, T. D. W.; Preston, G. M.; McDonough, M. A.; Schofield, C. J. Human Oxygen Sensing May Have Origins in Prokaryotic Elongation Factor Tu Prolyl-Hydroxylation. *Proceedings of the National Academy of Sciences of the United States of America* **2014**, *111* (37), 13331–13336. https://doi.org/10.1073/pnas.1409916111.

(7) Lippl, K.; Boleininger, A.; McDonough, M.; Abboud, M. I.; Tarhonskaya, H.; Chowdhury, R.; Loenarz, C.; Schofield, C. J. Born to Sense: Biophysical Analyses of the Oxygen Sensing Prolyl Hydroxylase from the Simplest Animal Trichoplax Adhaerens. *Hypoxia* **2018**, *6*, 57–71. https://doi.org/10.2147/hp.s174655.

(8) Loenarz, C.; Coleman, M. L.; Boleininger, A.; Schierwater, B.; Holland, P. W. H.; Ratcliffe, P. J.; Schofield, C. J. The Hypoxia-Inducible Transcription Factor Pathway Regulates Oxygen Sensing in the Simplest Animal, Trichoplax Adhaerens. *EMBO Reports* **2011**, *12* (1), 63–70. https://doi.org/10.1038/embor.2010.170.

(9) Cockman, M. E.; Lippl, K.; Tian, Y. M.; Pegg, H. B.; Figg, W. D.; Abboud, M. I.; Heilig, R.; Fischer, R.; Myllyharju, J.; Schofield, C. J.; Ratcliffe, P. J. Lack of Activity of Recombinant HIF Prolyl Hydroxylases (PHDs) on Reported Non-HIF Substrates. *eLife* **2019**, *8*, e46490. https://doi.org/10.7554/eLife.46490.

(10) Vitagliano, L.; Berisio, R.; Mastrangelo, A.; Mazzarella, L.; Zagari, A. Preferred Proline Puckerings in Cis and Trans Peptide Groups: Implications for Collagen

Stability. *Protein Science* **2001**, *10* (12), 2627–2632. https://doi.org/https://doi.org/10.1110/ps.ps.26601a.
(11) Abboud, M. I.; McAllister, T. E.; Leung, I. K. H.; Chowdhury, R.; Jorgensen, C.; Domene, C.; Mecinović, J.; Lippl, K.; Hancock, R. L.; Hopkinson, R. J.; Kawamura, A.; Claridge, T. D. W.; Schofield, C. J. 2-Oxoglutarate Regulates Binding of Hydroxylated Hypoxia-Inducible Factor to Prolyl Hydroxylase Domain 2. *Chemical Communications* **2018**, *54* (25), 3130–3133. https://doi.org/10.1039/c8cc00387d.
(12) Flashman, E.; Hoffart, L. M.; Hamed, R. B.; Bollinger, J. M.; Krebs, C.; Schofield, C. J. Evidence for the Slow Reaction of Hypoxia-Inducible Factor Prolyl Hydroxylase 2 with Oxygen. *FEBS Journal* **2010**, *277* (19), 4089–4099. https://doi.org/10.1111/j.1742-4658.2010.07804.x.
(13) Domene, C.; Jorgensen, C.; Schofield, C. J. Mechanism of Molecular Oxygen Diffusion in a Hypoxia-Sensing Prolyl Hydroxylase Using Multiscale Simulation. *Journal of the American Chemical Society* **2020**, *142* (5), 2253–2263. https://doi.org/10.1021/jacs.9b09236.
(14) Tarhonskaya, H.; Chowdhury, R.; Leung, I. K. H.; Loik, N. D.; McCullagh, J. S. O.; Claridge, T. D. W.; Schofield, C. J.; Flashman, E. Investigating the Contribution of the Active Site Environment to the Slow Reaction of Hypoxia-Inducible Factor Prolyl Hydroxylase Domain 2 with Oxygen. *Biochemical Journal* **2014**, *463* (3), 363–372. https://doi.org/10.1042/BJ20140779.
(15) Zhang, Z.; Smart, T. J.; Choi, H.; Hardy, F.; Lohans, C. T.; Abboud, M. I.; Richardson, M. S. W.; Paton, R. S.; McDonough, M. A.; Schofield, C. J. Structural and Stereoelectronic Insights into Oxygenase-Catalyzed Formation of Ethylene from 2-Oxoglutarate. *Proceedings of the National Academy of Sciences of the United States of America* **2017**, *114* (18), 4667–4672. https://doi.org/10.1073/pnas.1617760114.
(16) Pektas, S.; Taabazuing, C. Y.; Knapp, M. J. Increased Turnover at Limiting O2 Concentrations by the Thr387 → Ala Variant of HIF-Prolyl Hydroxylase PHD2. *Biochemistry* **2015**, *54* (18), 2851–2857. https://doi.org/10.1021/bi501540c.
(17) Cardinale, G. J.; Udenfriend, S. Prolyl Hydroxylase. In *Advances in Enzymology and Related Areas of Molecular Biology*; John Wiley & Sons, Ltd, 1974; Vol. 41, pp 245–300. https://doi.org/10.1002/9780470122860.ch6.
(18) Cardinale, G. J.; Rhoads, R. E.; Udenfriend, S. Simultaneous Incorporation of 18O into Succinate and Hydroxyproline Catalyzed by Collagen Proline Hydroxylase. *Biochemical and Biophysical Research Communications* **1971**, *43* (3), 537–543. https://doi.org/10.1016/0006-291X(71)90647-4.
(19) Valegård, K.; van Terwisscha Scheltinga, A. C.; Lloyd, M. D.; Hara, T.; Ramaswamy, S.; Perrakis, A.; Thompson, A.; Lee, H. J.; Baldwin, J. E.; Schofield, C. J.; Hajdu, J.; Andersson, I. Structure of a Cephalosporin Synthase. *Nature* **1998**, *394* (6695), 805–809. https://doi.org/10.1038/29575.
(20) Galonić, D. P.; Barr, E. W.; Walsh, C. T.; Bollinger, J. M.; Krebs, C. Two Interconverting Fe(IV) Intermediates in Aliphatic Chlorination by the Halogenase CytC3. *Nature Chemical Biology* **2007**, *3* (2), 113–116. https://doi.org/10.1038/nchembio856.
(21) Price, J. C.; Barr, E. W.; Tirupati, B.; Bollinger J. Martin; Krebs, C. The First Direct Characterization of a High-Valent Iron Intermediate in the Reaction of an α-Ketoglutarate-Dependent Dioxygenase: A High-Spin Fe(IV) Complex in Taurine/α-Ketoglutarate Dioxygenase (TauD) from Escherichia Coli. *Biochemistry* **2003**, *42* (24), 7497–7508. https://doi.org/10.1021/bi030011f.

(22) Hoffart, L. M.; Barr, E. W.; Guyer, R. B.; Bollinger, J. M.; Krebs, C. Direct Spectroscopic Detection of a C-H-Cleaving High-Spin Fe(IV) Complex in a Prolyl-4-Hydroxylase. *Proceedings of the National Academy of Sciences* **2006**, *103* (40), 14738–14743. https://doi.org/10.1073/pnas.0604005103.

(23) Ergel, B.; Gill, M. L.; Brown, L.; Yu, B.; Palmer, A. G.; Hunt, J. F. Protein Dynamics Control the Progression and Efficiency of the Catalytic Reaction Cycle of the Escherichia Coli DNA-Repair Enzyme AlkB*. *Journal of Biological Chemistry* **2014**, *289* (43), 29584–29601. https://doi.org/https://doi.org/10.1074/jbc.M114.575647.

(24) McAllister, T. E.; Yeh, T. L.; Abboud, M. I.; Leung, I. K. H.; Hookway, E. S.; King, O. N. F.; Bhushan, B.; Williams, S. T.; Hopkinson, R. J.; Münzel, M.; Loik, N. D.; Chowdhury, R.; Oppermann, U.; Claridge, T. D. W.; Goto, Y.; Suga, H.; Schofield, C. J.; Kawamura, A. Non-Competitive Cyclic Peptides for Targeting Enzyme-Substrate Complexes. *Chemical Science* **2018**, *9* (20), 4569–4578. https://doi.org/10.1039/c8sc00286j.

(25) Muench, S. P.; Antonyuk, S. v.; Samar, H. The Expanding Toolkit for Structural Biology: Synchrotrons, X-Ray Lasers and CryoEM. *IUCrJ* **2019**, *6* (2), 167–177. https://doi.org/10.1107/S2052252519002422.

(26) Grimes, J. M.; Hall, D. R.; Ashton, A. W.; Evans, G.; Owen, R. L.; Wagner, A.; McAuley, K. E.; von Delft, F.; Orville, A. M.; Sorensen, T.; Walsh, M. A.; Ginn, H. M.; Stuart, D. I. Where Is Crystallography Going? *Acta Crystallographica Section D: Structural Biology* **2018**, *74* (2), 152–166. https://doi.org/10.1107/S2059798317016709.

(27) Broennimann, C.; Eikenberry, E. F.; Henrich, B.; Horisberger, R.; Huelsen, G.; Pohl, E.; Schmitt, B.; Schulze-Briese, C.; Suzuki, M.; Tomizaki, T.; Toyokawa, H.; Wagner, A. The PILATUS 1M Detector. *Journal of Synchrotron Radiation* **2006**, *13* (2), 120–130. https://doi.org/10.1107/S0909049505038665.

(28) Orville, A. M. Recent Results in Time Resolved Serial Femtosecond Crystallography at XFELs. *Current Opinion in Structural Biology* **2020**, *65*, 193–208. https://doi.org/10.1016/j.sbi.2020.08.011.

(29) Johnson, L. N. Time-resolved Protein Crystallography. *Protein Science* **1992**, *1* (10), 1237–1243. https://doi.org/10.1002/pro.5560011002.

(30) Wiedorn, M. O.; Oberthür, D.; Bean, R.; Schubert, R.; Werner, N.; Abbey, B.; Aepfelbacher, M.; Adriano, L.; Allahgholi, A.; Al-Qudami, N.; Andreasson, J.; Aplin, S.; Awel, S.; Ayyer, K.; Bajt, S.; Barák, I.; Bari, S.; Bielecki, J.; Botha, S.; Boukhelef, D.; Brehm, W.; Brockhauser, S.; Cheviakov, I.; Coleman, M. A.; Cruz-Mazo, F.; Danilevski, C.; Darmanin, C.; Doak, R. B.; Domaracky, M.; Dörner, K.; Du, Y.; Fangohr, H.; Fleckenstein, H.; Frank, M.; Fromme, P.; Gañán-Calvo, A. M.; Gevorkov, Y.; Giewekemeyer, K.; Ginn, H. M.; Graafsma, H.; Graceffa, R.; Greiffenberg, D.; Gumprecht, L.; Göttlicher, P.; Hajdu, J.; Hauf, S.; Heymann, M.; Holmes, S.; Horke, D. A.; Hunter, M. S.; Imlau, S.; Kaukher, A.; Kim, Y.; Klyuev, A.; Knoška, J.; Kobe, B.; Kuhn, M.; Kupitz, C.; Küpper, J.; Lahey-Rudolph, J. M.; Laurus, T.; le Cong, K.; Letrun, R.; Xavier, P. L.; Maia, L.; Maia, F. R. N. C.; Mariani, V.; Messerschmidt, M.; Metz, M.; Mezza, D.; Michelat, T.; Mills, G.; Monteiro, D. C. F.; Morgan, A.; Mühlig, K.; Munke, A.; Münnich, A.; Nette, J.; Nugent, K. A.; Nuguid, T.; Orville, A. M.; Pandey, S.; Pena, G.; Villanueva-Perez, P.; Poehlsen, J.; Previtali, G.; Redecke, L.; Riekehr, W. M.; Rohde, H.; Round, A.; Safenreiter, T.; Sarrou, I.; Sato, T.; Schmidt, M.; Schmitt, B.; Schönherr, R.; Schulz, J.; Sellberg, J. A.; Seibert, M. M.; Seuring, C.; Shelby, M. L.; Shoeman, R. L.; Sikorski, M.; Silenzi, A.; Stan, C. A.; Shi, X.; Stern,

S.; Sztuk-Dambietz, J.; Szuba, J.; Tolstikova, A.; Trebbin, M.; Trunk, U.; Vagovic, P.; Ve, T.; Weinhausen, B.; White, T. A.; Wrona, K.; Xu, C.; Yefanov, O.; Zatsepin, N.; Zhang, J.; Perbandt, M.; Mancuso, A. P.; Betzel, C.; Chapman, H.; Barty, A. Megahertz Serial Crystallography. *Nature Communications* **2018**, *9* (1), 4025. https://doi.org/10.1038/s41467-018-06156-7.

(31) Rabe, P.; Beale, J. H.; Butryn, A.; Aller, P.; Dirr, A.; Lang, P. A.; Axford, D. N.; Carr, S. B.; Leissing, T. M.; McDonough, M. A.; Davy, B.; Ebrahim, A.; Orlans, J.; Storm, S. L. S.; Orville, A. M.; Schofielda, C. J.; Owen, R. L. Anaerobic Fixed-Target Serial Crystallography. *IUCrJ* **2020**, *7* (5), 901–912. https://doi.org/10.1107/S2052252520010374.

(32) Šrajer, V.; Schmidt, M. Watching Proteins Function with Time-Resolved x-Ray Crystallography. *Journal of Physics D: Applied Physics* **2017**, *50* (37), 373001. https://doi.org/10.1088/1361-6463/aa7d32.

(33) Kupitz, C.; Basu, S.; Grotjohann, I.; Fromme, R.; Zatsepin, N. A.; Rendek, K. N.; Hunter, M. S.; Shoeman, R. L.; White, T. A.; Wang, D.; James, D.; Yang, J. H.; Cobb, D. E.; Reeder, B.; Sierra, R. G.; Liu, H.; Barty, A.; Aquila, A. L.; Deponte, D.; Kirian, R. A.; Bari, S.; Bergkamp, J. J.; Beyerlein, K. R.; Bogan, M. J.; Caleman, C.; Chao, T. C.; Conrad, C. E.; Davis, K. M.; Fleckenstein, H.; Galli, L.; Hau-Riege, S. P.; Kassemeyer, S.; Laksmono, H.; Liang, M.; Lomb, L.; Marchesini, S.; Martin, A. v.; Messerschmidt, M.; Milathianaki, D.; Nass, K.; Ros, A.; Roy-Chowdhury, S.; Schmidt, K.; Seibert, M.; Steinbrener, J.; Stellato, F.; Yan, L.; Yoon, C.; Moore, T. A.; Moore, A. L.; Pushkar, Y.; Williams, G. J.; Boutet, S.; Doak, R. B.; Weierstall, U.; Frank, M.; Chapman, H. N.; Spence, J. C. H.; Fromme, P. Serial Time-Resolved Crystallography of Photosystem II Using a Femtosecond X-Ray Laser. *Nature* **2014**, *513* (7517), 261–265. https://doi.org/10.1038/nature13453.

(34) Orville, A. M. Entering an Era of Dynamic Structural Biology. *BMC Biology* **2018**, *16* (1), 55. https://doi.org/10.1186/s12915-018-0533-4.

(35) Aller, P.; Orville, A. M. Dynamic Structural Biology Experiments at XFEL or Synchrotron Sources. In *Methods in Molecular Biology*; Owens, R. J., Ed.; Springer US: New York, NY, 2021; Vol. 2305, pp 203–228. https://doi.org/10.1007/978-1-0716-1406-8_11.

(36) Rabe, P.; Kamps, J. J. A. G.; Sutherlin, K. D.; Linyard, J. D. S.; Aller, P.; Pham, C. C.; Makita, H.; Clifton, I.; McDonough, M. A.; Leissing, T. M.; Shutin, D.; Lang, P. A.; Butryn, A.; Brem, J.; Gul, S.; Fuller, F. D.; Kim, I.-S.; Cheah, M. H.; Fransson, T.; Bhowmick, A.; Young, I. D.; O'Riordan, L.; Brewster, A. S.; Pettinati, I.; Doyle, M.; Joti, Y.; Owada, S.; Tono, K.; Batyuk, A.; Hunter, M. S.; Alonso-Mori, R.; Bergmann, U.; Owen, R. L.; Sauter, N. K.; Claridge, T. D. W.; Robinson, C. v.; Yachandra, V. K.; Yano, J.; Kern, J. F.; Orville, A. M.; Schofield, C. J. X-Ray Free-Electron Laser Studies Reveal Correlated Motion during Isopenicillin N Synthase Catalysis . *Science Advances* **2021**, *7* (34), eabh0250. https://doi.org/10.1126/sciadv.abh0250.

(37) Mitchell, A. J.; Dunham, N. P.; Martinie, R. J.; Bergman, J. A.; Pollock, C. J.; Hu, K.; Allen, B. D.; Chang, W. C.; Silakov, A.; Bollinger, J. M.; Krebs, C.; Boal, A. K. Visualizing the Reaction Cycle in an Iron(II)- and 2-(Oxo)-Glutarate-Dependent Hydroxylase. *Journal of the American Chemical Society* **2017**, *139* (39), 13830–13836. https://doi.org/10.1021/jacs.7b07374.

(38) Kim, K. M.; Yi, E. C.; Baker, D.; Zhang, K. Y. J. Post-Translational Modification of the N-Terminal His Tag Interferes with the Crystallization of the Wild-Type and Mutant SH3 Domains from Chicken Src Tyrosine Kinase. *Acta*

Crystallographica Section D: Biological Crystallography **2001**, *57* (5), 759–762. https://doi.org/10.1107/S0907444901002918.
(39) Chowdhury, R. Structural and Mechanistic Studies on Prolyl Hydroxylases, Oxford University, UK, 2008.
(40) Mantri, M.; Zhang, Z.; McDonough, M. A.; Schofield, C. J. Autocatalysed Oxidative Modifications to 2-Oxoglutarate Dependent Oxygenases. *FEBS Journal* **2012**, *279* (9), 1563–1575. https://doi.org/10.1111/j.1742-4658.2012.08496.x.
(41) Xing, W.; Yin, M.; Lv, Q.; Hu, Y.; Liu, C.; Zhang, J. 1 - Oxygen Solubility, Diffusion Coefficient, and Solution Viscosity. In *Rotating Electrode Methods and Oxygen Reduction Electrocatalysts*; Xing, W., Yin, G., Zhang, J., Eds.; Elsevier: Amsterdam, 2014; pp 1–31. https://doi.org/https://doi.org/10.1016/B978-0-444-63278-4.00001-X.
(42) Huo, L.; Fielding, A. J.; Chen, Y.; Li, T.; Iwaki, H.; Hosler, J. P.; Chen, L.; Hasegawa, Y.; Que, L.; Liu, A. Evidence for a Dual Role of an Active Site Histidine in α-Amino-β-Carboxymuconate-ε-Semialdehyde Decarboxylase. *Biochemistry* **2012**, *51* (29), 5811–5821. https://doi.org/10.1021/bi300635b.
(43) Abboud, M. I.; Chowdhury, R.; Leung, I. K. H.; Lippl, K.; Loenarz, C.; Claridge, T. D. W.; Schofield, C. J. Studies on the Substrate Selectivity of the Hypoxia-Inducible Factor Prolyl Hydroxylase 2 Catalytic Domain. *ChemBioChem* **2018**, *19* (21), 2262–2267. https://doi.org/10.1002/cbic.201800246.
(44) Holt-Martyn, J. P.; Chowdhury, R.; Tumber, A.; Yeh, T. L.; Abboud, M. I.; Lippl, K.; Lohans, C. T.; Langley, G. W.; Figg, W.; McDonough, M. A.; Pugh, C. W.; Ratcliffe, P. J.; Schofield, C. J. Structure-Activity Relationship and Crystallographic Studies on 4-Hydroxypyrimidine HIF Prolyl Hydroxylase Domain Inhibitors. *ChemMedChem* **2020**, *15* (3), 270–273. https://doi.org/10.1002/cmdc.201900557.
(45) Johnson, T. W.; Gallego, R. A.; Brooun, A.; Gehlhaar, D.; McTigue, M. Reviving B-Factors: Retrospective Normalized B-Factor Analysis of c-Ros Oncogene 1 Receptor Tyrosine Kinase and Anaplastic Lymphoma Kinase L1196M with Crizotinib and Lorlatinib. *ACS Medicinal Chemistry Letters* **2018**, *9* (9), 878–883. https://doi.org/10.1021/acsmedchemlett.8b00147.
(46) Adams, P. D.; Afonine, P. v.; Bunkóczi, G.; Chen, V. B.; Davis, I. W.; Echols, N.; Headd, J. J.; Hung, L. W.; Kapral, G. J.; Grosse-Kunstleve, R. W.; McCoy, A. J.; Moriarty, N. W.; Oeffner, R.; Read, R. J.; Richardson, D. C.; Richardson, J. S.; Terwilliger, T. C.; Zwart, P. H. PHENIX: A Comprehensive Python-Based System for Macromolecular Structure Solution. *Acta Crystallographica Section D: Biological Crystallography* **2010**, *66* (2), 213–221. https://doi.org/10.1107/S0907444909052925.
(47) Moriarty, N. W.; Liebschner, D.; Klei, H. E.; Echols, N.; Afonine, P. v.; Headd, J. J.; Poon, B. K.; Adams, P. D. Interactive Comparison and Remediation of Collections of Macromolecular Structures. *Protein Science* **2018**, *27* (1), 182–194. https://doi.org/10.1002/pro.3296.
(48) Myllyla, R.; Majamaa, K.; Gunzler, V. Ascorbate Is Consumed Stoichiometrically in the Uncoupled Reactions Catalyzed by Prolyl 4-Hydroxylase and Lysyl Hydroxylase. *Journal of Biological Chemistry* **1984**, *259* (9), 5403–5405. https://doi.org/10.1016/s0021-9258(18)91023-9.
(49) Pijning, A. E.; Chiu, J.; Yeo, R. X.; Wong, J. W. H.; Hogg, P. J. Identification of Allosteric Disulfides from Labile Bonds in X-Ray Structures. *Royal Society Open Science* **2018**, *5* (2), 171058. https://doi.org/10.1098/rsos.171058.

(50) Arsenault, P. R.; Song, D.; Bergkamp, M.; Ravaschiere, A. M.; Navalsky, B. E.; Lieberman, P. M.; Lee, F. S. Identification of Small-Molecule PHD2 Zinc Finger Inhibitors That Activate Hypoxia Inducible Factor. *ChemBioChem* **2016**, *17* (24), 2316–2323. https://doi.org/10.1002/cbic.201600493.

(51) Park, K.; Li, N.; Kwak, Y.; Srnec, M.; Bell, C. B.; Liu, L. v.; Wong, S. D.; Yoda, Y.; Kitao, S.; Seto, M.; Hu, M.; Zhao, J.; Krebs, C.; Bollinger, J. M.; Solomon, E. I. Peroxide Activation for Electrophilic Reactivity by the Binuclear Non-Heme Iron Enzyme AurF. *Journal of the American Chemical Society* **2017**, *139* (20), 7062–7070. https://doi.org/10.1021/jacs.7b02997.

(52) Matthews, M. L.; Neumann, C. S.; Miles, L. A.; Grove, T. L.; Booker, S. J.; Krebs, C.; Walsh, C. T.; Bollinger, J. M. Substrate Positioning Controls the Partition between Halogenation and Hydroxylation in the Aliphatic Halogenase, SyrB2. *Proceedings of the National Academy of Sciences* **2009**, *106* (42), 17723–17728. https://doi.org/10.1073/pnas.0909649106.

(53) Chan, M. C.; Atasoylu, O.; Hodson, E.; Tumber, A.; Leung, I. K. H.; Chowdhury, R.; Gómez-Pérez, V.; Demetriades, M.; Rydzik, A. M.; Holt-Martyn, J.; Tian, Y. M.; Bishop, T.; Claridge, T. D. W.; Kawamura, A.; Pugh, C. W.; Ratcliffe, P. J.; Schofield, C. J. Potent and Selective Triazole-Based Inhibitors of the Hypoxia-Inducible Factor Prolyl-Hydroxylases with Activity in the Murine Brain. *PLoS ONE* **2015**, *10* (7), e0132004. https://doi.org/10.1371/journal.pone.0132004.

(54) Bradford, S. Y. C.; el Khoury, L.; Ge, Y.; Osato, M.; Mobley, D. L.; Fischer, M. Temperature Artifacts in Protein Structures Bias Ligand-Binding Predictions. *Chemical Science* **2021**, *12* (34), 11275–11293. https://doi.org/10.1039/d1sc02751d.

(55) Carpentier, P.; Leprêtre, C.; Basset, C.; Douki, T.; Torelli, S.; Duarte, V.; Hamdane, D.; Fontecave, M.; Atta, M. Structural, Biochemical and Functional Analyses of TRNA-Monooxygenase Enzyme MiaE from Pseudomonas Putida Provide Insights into TRNA/MiaE Interaction. *Nucleic Acids Research* **2020**, *48* (17), 9918–9930. https://doi.org/10.1093/nar/gkaa667.

(56) Kalms, J.; Schmidt, A.; Frielingsdorf, S.; Utesch, T.; Gotthard, G.; von Stetten, D.; van der Linden, P.; Royant, A.; Mroginski, M. A.; Carpentier, P.; Lenz, O.; Scheerer, P. Tracking the Route of Molecular Oxygen in O2-Tolerant Membrane-Bound [NiFe] Hydrogenase. *Proceedings of the National Academy of Sciences of the United States of America* **2018**, *115* (10), E2229–E2237. https://doi.org/10.1073/pnas.1712267115.

(57) Kalms, J.; Schmidt, A.; Frielingsdorf, S.; van der Linden, P.; von Stetten, D.; Lenz, O.; Carpentier, P.; Scheerer, P. Krypton Derivatization of an O2-Tolerant Membrane-Bound [NiFe] Hydrogenase Reveals a Hydrophobic Tunnel Network for Gas Transport. *Angewandte Chemie - International Edition* **2016**, *55* (18), 5586–5590. https://doi.org/10.1002/anie.201508976.

(58) Schofield, C. J.; Ratcliffe, P. J. Oxygen Sensing by HIF Hydroxylases. *Nat. Rev. Mol. Cell Biol.* **2004**, *5* (5), 343–354. https://doi.org/10.1038/nrm1366.

(59) Appelhoffl, R. J.; Tian, Y. M.; Raval, R. R.; Turley, H.; Harris, A. L.; Pugh, C. W.; Ratcliffe, P. J.; Gleadle, J. M. Differential Function of the Prolyl Hydroxylases PHD1, PHD2, and PHD3 in the Regulation of Hypoxia-Inducible Factor. *Journal of Biological Chemistry* **2004**, *279* (37), 38458–38465. https://doi.org/10.1074/jbc.M406026200.

Chapter 3

Structural Analyses on PHD2 Inhibition *via* Co-Crystallisation

Chapter 3

3.1 Background

In 2002, the first crystal structures of $PHD2_{181-417/426}$ in complex with an iodoisoquinolone analogue of FG-2216 (**21**, PDB: 2G19 and 2G1M, respectively) were reported by the Schofield group.[1] Soon after, a group at Proctor and Gamble Co. reported a complex of $PHD2_{188-426}$ and FG-2216 (**21**, PDB: 2HBT). The crystallographic studies of tPHD2 revealed the conserved DSBH fold (discussed in **1.2**) that is characteristic of the 2OG oxygenases. The molecular architecture of the PHD 2OG binding pocket was initially characterised as the isoquinolone inhibitors are 2OG-mimicking derivatives, in particular the glycinamide carboxylate of the inhibitors was shown to interact with the guanidino group of Arg383 in a manner analogous to that of 2OG.[1,2] The metal coordinating residues His313, Asp315, and His374 were observed to coordinate Fe.[1,2] The isoquinoline inhibitors were observed to bind in a bidentate coordination of the Fe-centre in a similar manner to 2OG complexation. His374 complexes the Fe *trans* to the N1 atom of the heterocycle and Asp325 *trans* to the O3 atom of the glycinamide sidechain of FG-2216 (**21**).[1,2] The structural analyses revealed key active site residues involved in binding of the ligands, including (i) Tyr303, (ii) Tyr310, (iii) Tyr329, and (iv) Arg383.[3] It also notable that the mobile β2-β3 finger loop was observed in different conformations in the inhibitor structures relative to that in the tPHD2.HIFα substrate structure (PDB: 3HQR, discussed in section **2.1**, **Figure 2-1**).[3]

To date, a search of the PDB shows that there are 22 reported tPHD2-small-molecule ligand crystal structures that are listed in **Table 3.1***. Analysis of the reported crystallisation conditions highlights an apparent preference of tPHD2 for lower pHs (4.8-7.5) and ammonium sulfate precipitants for crystal growth (**Table 3-1**).[1,2,4–12] The majority of the reported structures were crystallised in the high symmetry, hexagonal *P* 6_3 space group (**Figure 3-1D**). Of the 22 reported tPHD2-inhibitor structures, six space groups were observed to form for tPHD2 of varying construct length; typically, $PHD2_{181\text{-}426}$ was the construct used for crystallisation with either Fe(II) or Mn(II) ions (**Table 3-1**). [1,2,4–12] The *P* 6_3 space group for tPHD2 contains one chain in the ASU. Additionally, there have been three deposited tPHD2 structures each containing two, three, or six-chains in their ASUs (**Figures 3-1A** and **3-1B**).[5,11,12] Specific protomer and symmetry interactions of the common tPHD2 crystal forms may reflect necessary points-of-contact for lattice formation that potentially provide an explanation for why some clinically applied inhibitors have yet to be structurally characterised in complex with tPHD2.[7]

Structural investigations of the active sites from 21 reported tPHD2-inhibitor complexes (50% with Fe(II) and 50% with Mn(II)) reveal important active site interactions, possibly reflecting ligand induced-fit mechanism of these small-molecule inhibitors.[3] In 15 out of the 21 reported structures, the ligand contains a glycinamide (or carboxylic acid) sidechain moiety (**Figures 3-2** and **3-3A**).[1,2,4,6,7,9,12]

---

* Material in this chapter that is cited with 'CC BY 4.0 License' has been adapted with the permission of Figg Jr., W. D.; McDonough, M. A.; Chowdhury, R.; Nakashima, Y.; Zhang, Z.; Holt-Martyn, J. P.; Krajnc, A.; Schofield, C. J. Structural Basis of Prolyl Hydroxylase Domain Inhibition by Molidustat. *ChemMedChem* **2021**, *16* (13), 2082–2088, Wiley-VCH. https://doi.org/10.1002/cmdc.202100133. This is an open access article distributed under the terms of the Creative Commons CC BY license, which permits unrestricted use, distribution, and reproduction in any medium, provided the original work is properly cited. This work is licensed under the Creative Commons Attribution 4.0 International License. To view a copy of this license, visit http://creativecommons.org/licenses/by/4.0/ or send a letter to Creative Commons, PO Box 1866, Mountain View, CA 94042, USA.

Table 3-1| Crystallisation Conditions of Reported tPHD2-Ligand Complex Structures. Note that redundant structures for complexes with the same ligand and construct length were omitted.
This is a modified version of the Table in Figg Jr., W. D.; McDonough, M. A.; Chowdhury, R.; Nakashima, Y.; Zhang, Z.; Holt-Martyn, J. P.; Krajnc, A.; Schofield, C. J. Structural Basis of Prolyl Hydroxylase Domain Inhibition by Molidustat. ChemMedChem ***2021****, 16 (13), 2082–2088, Open Access, Wiley-VCH. https://doi.org/10.1002/cmdc.202100133. CC BY 4.0 License.*

PDB ID	2G1M	2G19	2HBT	3OUH	3OUI	3OUJ	4BQX	4BQY	4JZR	4KBZ	5A3U	5L9R	5OX5	5OX6	5V18	6NMQ	6QGV	6ST3	6YVT	6YVW	6YVX	6YVZ
Space Group	*P* 6_3	*P* 6_3	*P* 6_3	*P* 6_3	*P* 2_1 2_1 2_1	*P* 2_1 2_1 2_1	*P* 6_3	*P* 6_3	*P* 6_3	*P* 4_1	*P* 3_2 1 2	*P* 6_3	*P* 6_3	*P* 6_3	*P* 4_1	*H* 3 2	*H* 3 2	*P* 2_1 2 2_1	*P* 2_1 2_1 2_1	*P* 6_3	*P* 6_3	*P* 6_3
Resolution	2.20	1.70	1.60	2.51	1.70	2.30	1.79	1.55	2.10	2.15	3.30	1.81	2.25	1.99	2.15	1.58	1.40	2.43	2.85	1.97	1.80	1.91
Construct	181-426	181-417	188-426	181-416	181-392	181-416	181-426	181-426	181-426	181-426	181-426	181-426	181-426	181-426	181-417	180-392	181-407	181-407	181-426	181-426	181-426	181-426
MOL/ASU	1	1	1	1	1	1	1	1	1	1	3	1	1	1	1	1	1	2	6	1	1	1
Ligand	4HG	4HG	UN9 (**21**)	014	42Z	AKG	UN9 (**21**)	FNT	4JR	1QA	R8J (**35**)	OGA	B2E (**24**)	A1Z (**23**)	8UY (**17**)	KU1	J2H (**30**)	LUW (**29**)	PW2	PW5	2JP	PW8
Salt	$(NH_4)_2SO_4$	$(NH_4)_2SO_4$	$(NH_4)_2SO_4$ NaOAc	$(NH_4)_2SO_4$ $MgSO_4$	$(NH_4)_2SO_4$ NaOAc	$(NH_4)_2SO_4$ NaOAc	$(NH_4)_2SO_4$	$(NH_4)_2SO_4$	$(NH_4)_2SO_4$ NaOAc	$(NH_4)_2SO_4$	sodium citrate/ citric acid	$(NH_4)_2SO_4$	sodium citrate tribasic	sodium acetate tribasic $(NH_4)_2SO_4$		$(NH_4)_2SO_4$ $MgSO_4$	$(NH_4)_2SO_4$	sodium citrate tribasic NaOAc	$(NH_4)_2SO_4$ NaOAc	$(NH_4)_2SO_4$ succinic acid	$(NH_4)_2SO_4$ succinic acid	$(NH_4)_2SO_4$ succinic acid
Precipitant	dioxane	PEG 8000	PEG 4000		PEG 400	PEG 8000	dioxane	dioxane	PEG 3350	PEG 8000		PEG 400		PEG 8000	PEG 3350		2-propanol	PEG 4000	PEG 400	dioxane	dioxane	dioxane
Buffer/Additive	MES	MES		Imidazole			MES	MES		HEPES		HEPES			Bis-Tris/ASO4	Imidazole				MES/$FeSO_4$	MES/$FeSO_4$	MES/$FeSO_4$
pH	6.5	6.4	4.8-5.4	6.5	5.5	6.4	6.5	6.5	4.8	7.2	6.5	7.5	6.5	4.6	6.5	6.5	7.5	5.6	6.5	6.5	6.5	6.5

PDB ID	Reference	Ligands
2G1M	**1**	**4HG:** N-(4-hydroxy-8-iodoisoquinoline-3-carbonyl)glycine
2G19	**1**	**4HG:** N-(4-hydroxy-8-iodoisoquinoline-3-carbonyl)glycine
2HBT		**UN9:** N-(1-chloro-4-hydroxyisoquinoline-3-carbonyl)glycine
3OUH	**4**	**014:** 1-(5-chloro-6-fluoro-1H-benzimidazol-2-yl)-1H-pyrazole-4-carboxylic acid
3OUI	**4**	**42Z:** N-[(5,6-dichloro-1H-benzimidazol-2-yl)carbonyl]glycine
3OUJ	**4**	**AKG:** 2-oxoglutaric acid
4BQX	**2**	**UN9:** N-(1-chloro-4-hydroxyisoquinoline-3-carbonyl)glycine
4BQY	**2**	**FNT:** (2S)-2-{[(1-chloro-4-hydroxyisoquinolin-3-yl)carbonyl]amino}propanoic acid
4JZR	**2**	**4JR:** 2-(biphenyl-4-yl)-8-[(1-methyl-1H-imidazol-2-yl)methyl]-2,8-diazaspiro[4.5]decan-1-one
4KBZ	**2**	**1QA:** (2S)-({[2-(5-cyano-3-hydroxypyridin-2-yl)-1,3-thiazol-4-yl]acetyl}amino)(phenyl)ethanoic acid
5A3U	**5**	**R8J:** 6-(5-oxo-4-(1H-1,2,3-triazol-1-yl)-2,5-dihydro-1H-pyrazol-1-yl)nicotinic acid
5L9R	6	**OGA:** N-oxalylglycine
5OX5	**7**	**B2E:** (6-hydroxy-1,3-dimethyl-2,4-dioxo-1,2,3,4-tetrahydropyrimidine-5-carbonyl)glycine
5OX6	**7**	**AZ1:** 2-[[5-(3-chlorophenyl)-3-oxidanyl-pyridin-2-yl]carbonylamino]ethanoic acid
5V18	**8**	**8UY:** 4-([1,2,4]triazolo[1,5-a]pyridin-5-yl)benzonitrile
6NMQ	**9**	**KU1:** N-(4-oxo-1,4-dihydrocinnoline-3-carbonyl)glycine
6QGV	**10**	**J2H:** 8-[(3-methylpyridin-2-yl)methyl]-3-(4-phenylphenyl)-1-pyrimidin-2-yl-1,3,8-triazaspiro[4.5]decane-2,4-dione
6ST3	**11**	**LUW:** 4-oxidanyl-~{N}-[(4-phenoxyphenyl)methyl]-2-pyrazol-1-yl-pyrimidine-5-carboxamide
6YVT	**12**	**PW2:** 2-[[5-(6-methoxynaphthalen-2-yl)-3-oxidanyl-pyridin-2-yl]carbonylamino]ethanoic acid
6YVW	**12**	**PW5:** 4-[(5-bromanyl-4,6-dimethyl-pyridin-2-yl)amino]-4-oxidanylidene-butanoic acid
6YVX	**12**	**2JP:** 4-(isoquinolin-3-ylamino)-4-oxobutanoic acid
6YVZ	**12**	**PW8:** 4-[(5-bromanylisoquinolin-3-yl)amino]-4-oxidanylidene-butanoic acid

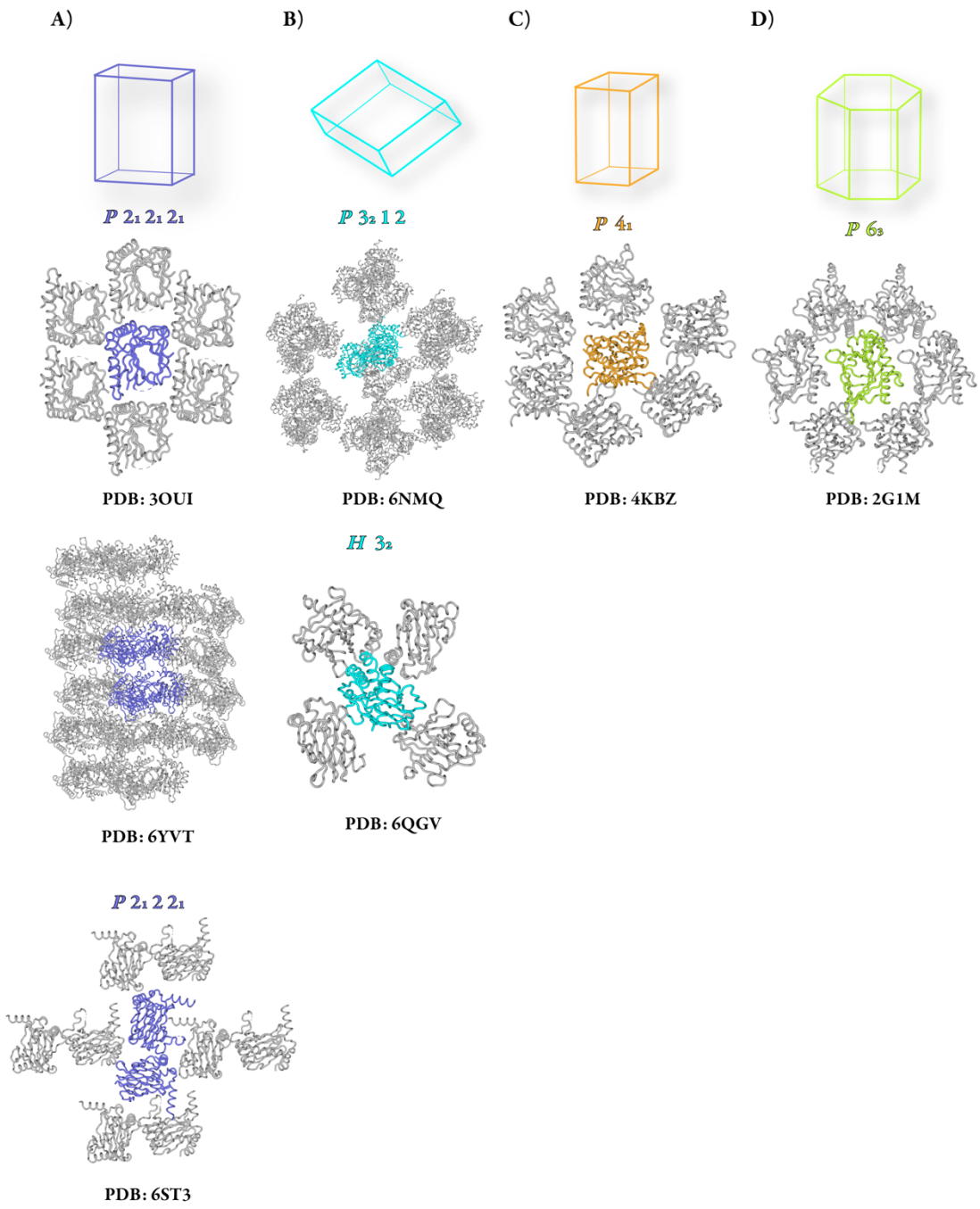


Figure 3-1|Crystal Systems for Various Reported tPHD2-Inhibitor Complex Structures. (A) The asymmetric unit (blue) and neighbouring symmetry chains (grey) for the orthorhombic tPHD2 crystal forms. (B) The asymmetric unit (cyan) and neighbouring symmetry chains (grey) for the trigonal tPHD2 crystal form. (C) The asymmetric unit (orange) and neighbouring symmetry chains (grey) for tetragonal tPHD2 crystal form. (D) The asymmetric unit (lemon) and neighbouring symmetry chains (grey) for the hexagonal tPHD2 crystal form. Abbreviations: Prolyl hydroxylase isoform 2 (PHD2). PDB: *listed within the figure.*

In five reported structures of the non-carboxylic acid-based class of inhibitors (*e.g.,* that lack the glycinamide sidechain, discussed in section **1.4.3**), there are tPHD2-complexes with a 4-hydroxypyrimidine (**29**), spiro[4.5]decanone (**30**), and IOX4-A (**35**, PDB: 5A3U

and 6ST3, **Figure 3-2**).[2,5,10,11] In 2017, structures were reported of a non-conventional PHD inhibitor, *i.e.*, Takeda-17 (**17**) co-crystallised with PHD1$_{167-403}$ and PHD2$_{181-416}$ were reported; these revealed a unique binding mode compared to other PHD-inhibitor complex structures (**Figures 3-2** and **3-3C**).[8]

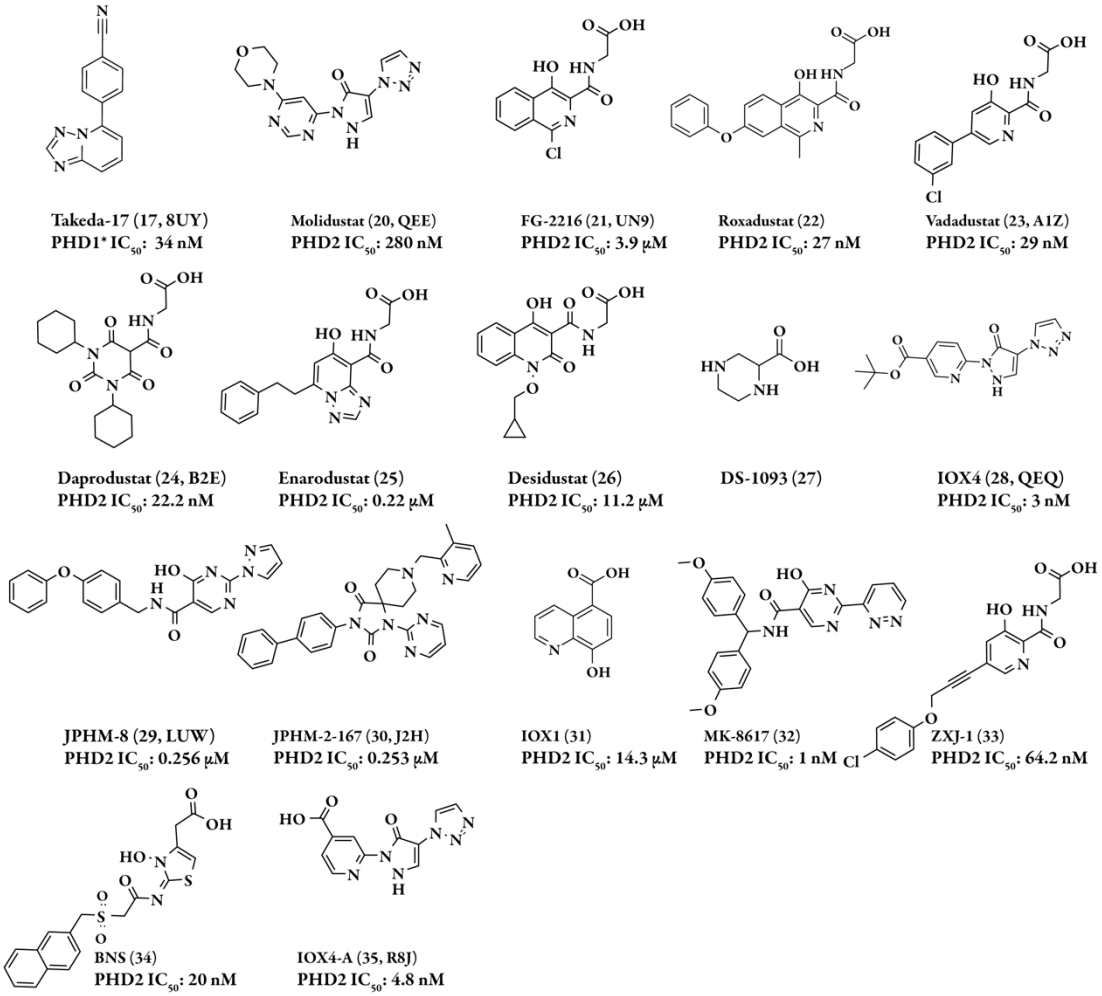


Figure 3-2| Overview of Clinically Applied PHD and Other 2OG Oxygenase Inhibitors. The PHD inhibitors displayed above are currently in late-stage/approved for clinical use, in pre-clinical stages, or discontinued (discussed in **1.4**). Abbreviations: Prolyl hydroxylase isoform 2 (PHD2), 2-Oxoglutarate (2OG). *References for IC_{50} values listed in text.*

Takeda-17 (**17**) complexes *via* monodentate coordination to the Fe-centre of tPHD2 and forms a π-π stacking interaction with the phenol ring of Tyr303 (**Figure 3-3C**, PDB: 5V18).[8] Further structural data is required to fully investigate the biophysical properties of PHD inhibition and gain better insight into the potency of the clinically used inhibitors. PHD inhibition may be improved by, not only elements of

Fe-chelation/2OG competition, but also as results of conformational changes (which are likely related to those involved in HIFα substrate binding) induced through ligand complexation.[3,7]

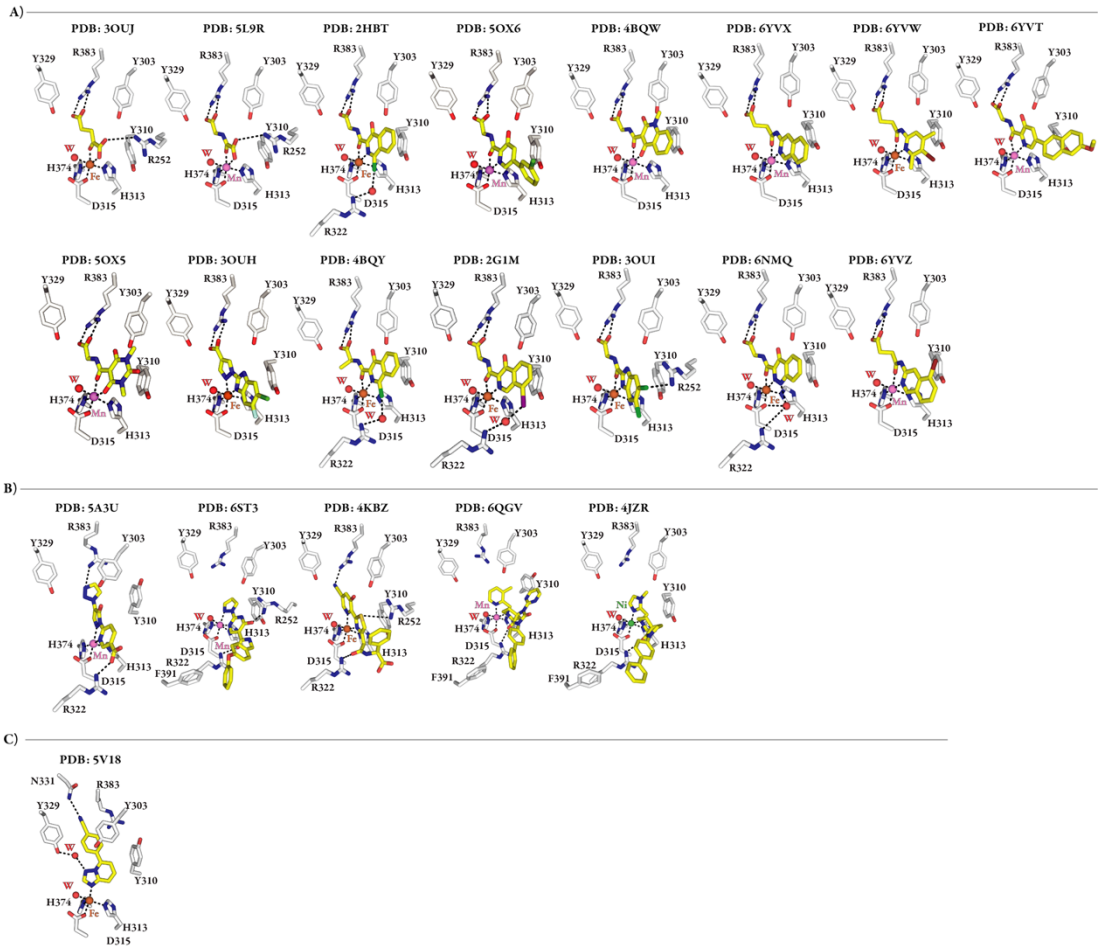


Figure 3-3|Overview of Reported tPHD2-Ligand Complex Structure Active Sites. (A) tPHD2 in complex with carboxylic acid and glycinamide based 2OG competing inhibitors. (B) tPHD2 in complex with non-carboxylic acid class of inhibitors; displayed as sticks (yellow). (C) tPHD2 in complex with non-conventional inhibitors. (A-B) Active site residues (white) and ligands (yellow) are depicted as sticks. Coordinated metal ions (Fe-orange, Mn-violet, and Ni-green) and waters (red) are shown as spheres. Dashed lines (black) correspond to key electrostatic/hydrogen bond interactions within the structures. Abbreviations: Prolyl hydroxylase isoform 2 (PHD2). PDB: *Listed within figure.*

At the onset of this study, only two of the reported PHD structures were complexed with clinically relevant inhibitors, *i.e.*, FG-2216 (**21**) and Vadadustat (**23**, PDB: 2HBT and 5OX6, respectively).[1,2,4–12] Further structural characterisation the tPHD2 in complex with clinically relevant inhibitors may reveal relative dynamics of protein-ligand interactions and the induced-fit mechanism of the PHDs.[3] Although, most of the

clinically applied PHD2 inhibitors have been challenging to crystallise,[7] and may be induced by the inhibitors direct or indirect interaction with the *C*-terminal residues that are involved in substrate binding.[7] Furthermore, these *C*-terminal interactions may, in part, reflect the potency of these small-molecules to the PHDs. Thus, further biophysical characterisation of these clinical inhibitors in complex with tPHD2 may provide an structural explanation for their potency that can aid development of novel inhibitors of the PHDs.[3,7]

One aim of my work was to overcome the above challenges by obtaining structural data on previously uncharacterised, clinically applied PHD inhibitors and other ligands (*e.g.*, succinic acid-coproduct and related fumaric acid). The work presented subsequently identifies three novel crystal forms, in the *P* 2_1 ($PHD2_{181-426}$), *P* 2_1 ($PHD2_{181-407}$), and *P* 6_1 2 2 ($PHD2_{181-407}$) space groups. The *P* 2_1 structure of $PHD2_{181-426}$.Mn(II) revealed an uncharacterised interaction of the β2-β3 finger loop. The *P* 2_1 and *P* 6_1 2 2 forms yielded six novel complex structures of $PHD2_{181-407}$ with co-crystallised ligands. These structural insights can potentially reveal important active site interactions as well as identify dynamic elements involved in inhibition of PHD2, such as: (i) the characterisation of active site water molecules that interact with residues Arg383-Tyr329, (ii) π-π-stacking interactions with Tyr303, and (iii) the conformation of the mobile-β2-β3 loop.[3]

3.2 A Novel $PHD2_{181-407/426}$ *P* 2_1 Crystal Form

3.2.1 Development of a Crystallisation System to Soak Inhibitors

To date there are no reported tPHD2 crystallisation conditions enabling routine soaking of ligands into the crystals. Initial work completed in Oxford *by Dr. Rasheduzzaman*

Chowdhury, attempted to use a cyclic peptide (3C, discussed earlier in **2.1**) to promote crystallisation of $PHD2_{181-407/426}$ with clinically used inhibitors, such as Molidustat (**20**), Roxadustat (**22**), and Daprodustat (**24**).[12,13] However as the 3C was not observed in the complex structures in Chapter **2**, the 3C was omitted from further crystallisation conditions.[12]

At the beginning of this project, the search for a novel crystal form to accommodate soaking-based studies (discussed further in Chapter **4**) was initiated with the $PHD2_{181-426}$ construct, a construct that contains the full *C*-terminus, as it had been reported that inhibitors may interact with the *C*-terminal residues of PHD2.[7] It was envisaged that a crystallisation condition with $PHD2_{181-426}$ in complex with Mn and no bound ligands could potentially permit soaking of small-molecules into the active site.

$PHD2_{181-426}$ was purified using the same protocol as for the $PHD2_{181-407}$ construct (**2.2** and **6.4**). A broad screen (**6.6.2**) of 0.8 mM $PHD2_{181-426}$ with 2.2 mM of $Mn(II)Cl_2$ was conducted (**6.8.1**). After a week of equilibration, micro-crystals formed in 0.02 M sodium/potassium phosphate and 20% (w/v) PEG 3350 from the PACT premier™ screen (298 K, Molecular Dimensions Ltd., **6.8.1**). The condition was optimised between 5-36 mM sodium/potassium phosphate and 15-26% (w/v) PEG 3350. After equilibration for 3 days, crystals of two different morphologies appeared in a single crystallisation drop (300 nL, 1:2 protein-to-well ratio) of 5 mM sodium/potassium phosphate and 15% (w/v) PEG 3350 (**6.8.1**, **Figure 3-4A**). Crystals of triangular plates and rod morphologies formed in the crystallisation drops (**Figure 3-4A**). They were harvested using 25% (v/v) glycerol as a cryo-protectant and were shown to diffract using both an in-house (**6.6.7.1,**) and synchrotron sources (**6.6.7.2**); the structures manifested *C* 2 (2.60 Å, plates, a=74.89 Å, b=129.93 Å, c=274.83 Å, β=90.16°; structure could not be solved) and *P* 2_1 (rods, **Table 3-1**) space groups. Unfortunately, these crystal forms exhibited weak diffraction.

The highest resolution dataset obtained was 2.97 Å in the *P* 2_1 space group (*Xtal-O*, **Table 3-2;** *Xtal-IDs* are listed in **Appendix I**). (*Thank you to Dr. Michael McDonough for harvesting and collecting the dataset on the PHD2$_{181-426}$.Mn crystal.)*

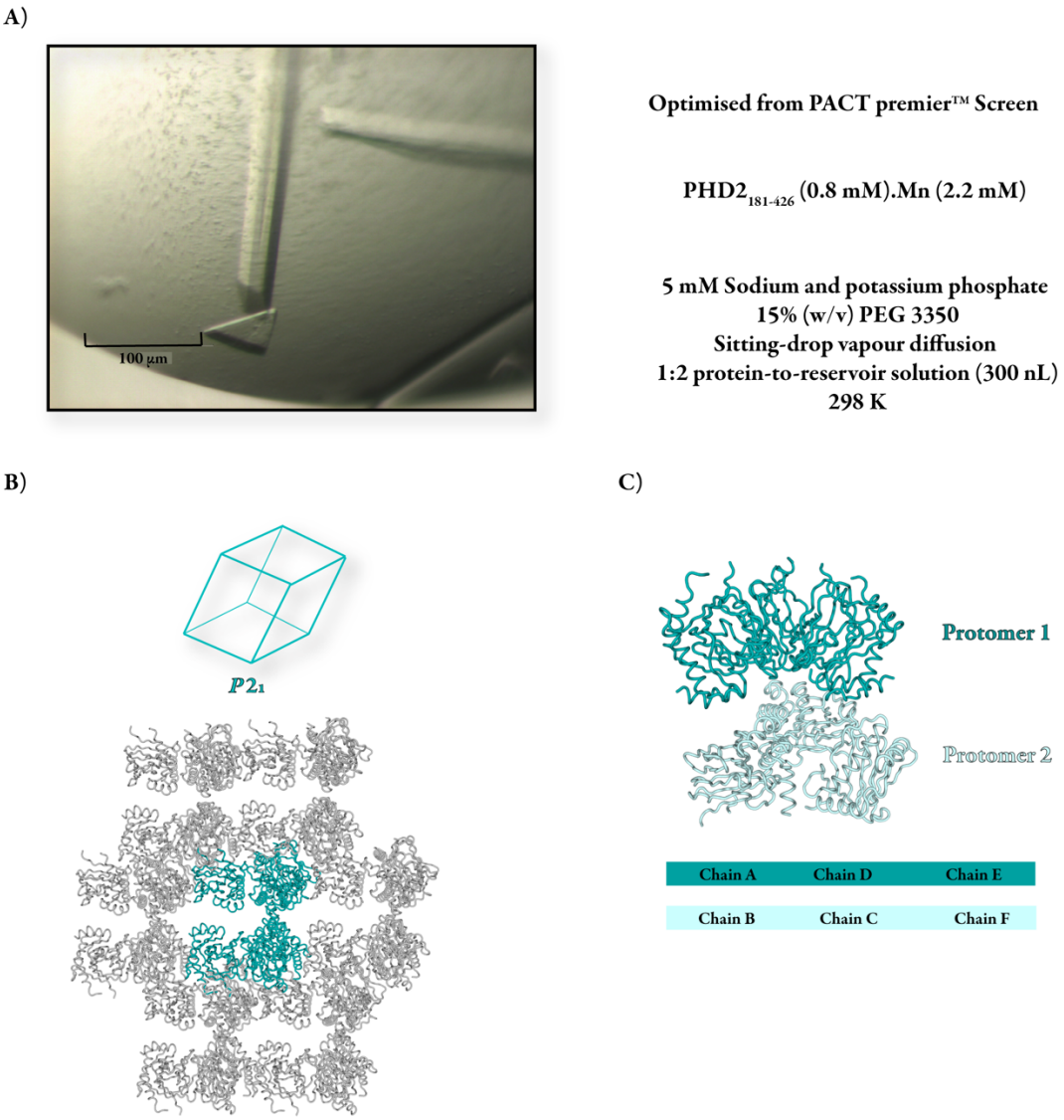


Figure 3-4| Crystallisation and Crystal form of the PHD2$_{181-426}$ Construct in Complex with Mn. (A) The optimised crystal condition yielded two crystal morphologies, *i.e.*, plate (*C* 2) and plate-like shaped (*P* 2_1) crystals. (B) The *P* 2_1 crystal form of PHD2$_{181-426}$ with the depicted six chain asymmetric unit in cartoon (teal) and symmetry related chains in cartoon (grey). (C) Two trimeric protomers (teal and light cyan) of the asymmetric unit are displayed in cartoon. Abbreviations: Prolyl hydroxylase isoform 2 (PHD2).

Based on the estimation of the solvent content with the Matthews coefficient, the novel crystal form exhibited six-chains in the ASU; tPHD2 is principally monomeric in solution.[6,14,15] A complex structure of tPHD2 with six-chains in the ASU was recently reported in the *P* 2_1 2_1 2_1 space group (PDB: 6YVT).[16]

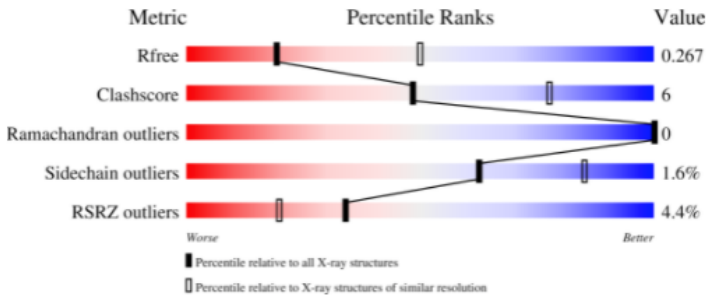
Table 3-2| Crystallographic Data Processing and Refinement Statistics (*Xtal-O*).

	$PHD2_{181-426}$.Mn(II) *Xtal-O*
Beamline	Diamond Light Source-I04-1
Detector	Dectris Pilatus 6M-F
Data Processing	autoPROC
Wavelength (Å)	0.9159
Resolution range (Å)	75.19 - 2.97 (3.07 - 2.97)
Space group	P 1 2_1 1
Unit cell (Å, °)	74.30 127.34 83.00, 115.05
Total reflections	283965 (27475)
Unique reflections	28908 (2874)
Multiplicity	9.8 (9.6)
Completeness (%)	99.39 (96.52)
Mean I/sigma (I)	10.62 (0.37)
Wilson B-factor (Å²)	91.24
R-merge†	0.07747 (0.8186)
R-meas	0.0817 (0.8654)
R-pim	0.02565 (0.2781)
CC1/2	0.999 (0.931)
CC*	1 (0.982)
Reflections used in refinement	28908 (2774)
Reflections used for R-free	1492 (115)
R-work✧	0.2451 (0.4182)
R-free✧	0.2672 (0.4520)
CC(work)	0.935 (0.747)
CC(free)	0.905 (0.810)
Number of non-hydrogen atoms	8836
macromolecules	8806
ligands	12
solvent	18
Protein residues	1180
RMS(bonds, Å)	0.005
RMS(angles, °)	0.77
Ramachandran favored (%)	97.23
Ramachandran allowed (%)	2.77
Ramachandran outliers (%)	0.00
Rotamer outliers (%)	2.40
Clashscore	6.69
Average B-factor (Å²)	105.29
macromolecules	105.39
ligands	80.08
solvent	73.64
Number of TLS groups	26

Single crystal diffraction data was collected from samples held at 100 K with conventional, rotation-based methods. Ligands: Mn and Cl. Statistics for the highest-resolution shell are shown in parentheses.

† R-merge (or Rsym) is equal to $\sum|I-\langle I\rangle|/\sum I$. R-merge represents the data quality of merged reflection data. *I* is equal to the intensity of individual measurements and <I> is equal to the average of multiple measurements. ✧R_{free} is the R_{factor} for 5% of the reflections which are excluded during refinement.

R_{factor} is equal to $\sum_{hkl}||Fobs_{(hkl)}| - |Fcalc_{(hkl)}||/\sum_{hkl}|Fobs_{(hkl)}|$ and was calculated for the working set of reflections (R_{work}). *Xtal-ID in* ***Appendix I***. Validation heat map generated by the PDB validation service.



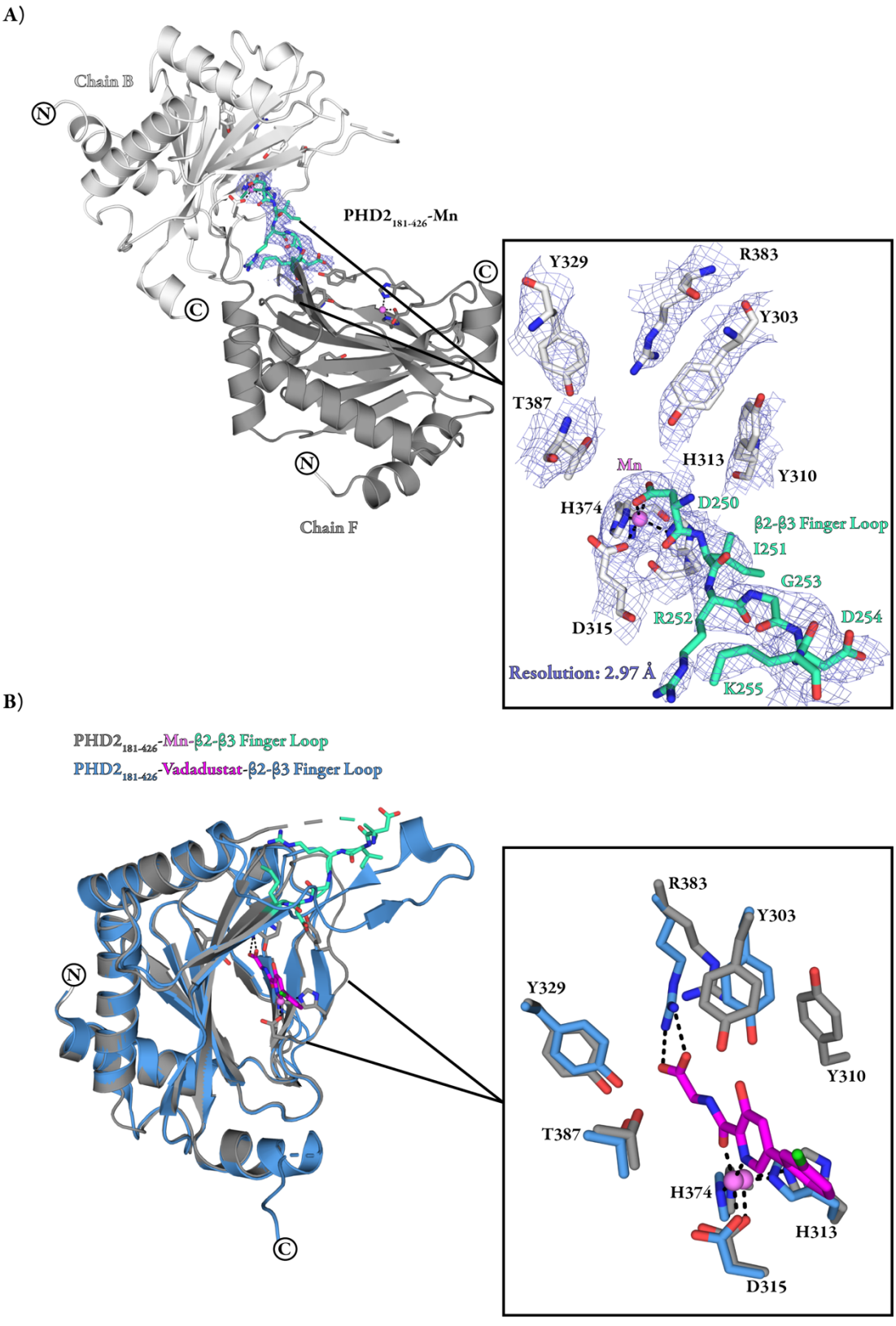


Figure 3-5|A View from the PHD2$_{181-426}$.Mn Complex Structure. PHD2$_{181-426}$ chains B and F are depicted as cartoons (white) and sticks (white). Chain C residues of the β2-β3 loop (raspberry) are displayed as sticks. The 2mF_o-DF_c electron density map (contoured to 1.0 σ) is illustrated as mesh over shown active site and loop residues. Mn ion (violet) is represented as a sphere. Dashes (black) represent highlighted active site interactions in the structure. Abbreviations: Prolyl hydroxylase isoform 2.

After solving the structure using a truncated model of PDB: 3HQR for molecular replacement (MR, **6.6.9.2**), two trimeric protomers were identified to form the ASU. Protomer 1 was comprised of chains A, D, and E (**Figure 3-4C**). Protomer 2 was formed from chains B, C, and F (**Figure 3-4C**). *Xtal-O* packs with an interaction between the mobile β2-β3 finger loop and the active site metal.[6] The active site-β2-β3 finger loop mediated interactions are observed between chains A-to-C, B-to-D, C-to-E, D-to-F, E-to-A, and F-to-B. The carboxylate of Asp250 was observed to coordinate the active site metal (Mn) *trans* to His374 *via* a bidentate interaction with the Oδ1 and Oδ2 atoms of Asp250 (**Figure 3-5**, note that $2mF_o$-DF_c electron density maps are displayed for the chain with the most complete density in the crystal form (either chain A, B, or C) and subsequently hereafter for complex structures with multiple chains in the ASU). The apparent β2-β3 loop interaction from Chain F appears to stabilise the active site of Chain B; and may, in part, accommodate formation of the crystal lattice in a complex without a ligand (**Figure 3-5**).

Although the loop-active site interaction is a notable feature observed in the *Xtal-O* structure, the interaction of the β2-β3 loop to the active site region would likely prevent the soaking of inhibitors into the crystals. Furthermore, the $PHD_{181-426}$.Mn crystal form (*Xtal-O*) was obtained once. As this crystallisation condition was not reproducible, efforts were refocused on the development of another method to obtain more structural data on tPHD2-inhibitor complexes, *i.e.*, utilising succinate co-product to stabilise the active site of $PHD2_{181-407}$ during co-crystallisation.

3.2.2 $PHD2_{181-407}$.Mn(II).Succinate *P* 2_1 Crystal Form

Until the $PHD2_{181-426}$.Mn complex (*Xtal-O*, **3.2.1**) that is described above, there had been no reported structures of tPHD2 that are uncomplexed with an active site-

ligand. The use of succinate co-product (which binds the PHD active site and displays weak inhibition with an IC_{50} for tPHD2 at >10 mM; for comparison the K_D of 2OG is reported to be <1 μM) as a crystallisation tool was initially proposed to stabilise the active site of tPHD2 in a manner that would enable the exchange of the co-product with DMSO-solubilised-PHD-inhibitors.[17,18]

A purified batch of the $PHD2_{181-407}$ construct, that had undergone an extra purification step (three-column batch, **Figure 3-6C, 6.4.4**) compared to the previous two-column batch (**2.2**, **Figure 3-6B**), was used to screen for crystals with $PHD2_{181-407}$ (1 mM), 1.2 mM ($Mn(II)Cl_2$), and succinic acid (2.2 mM) with conditions from the PEG/Ion screen™ I/II (Hampton Research Corp., **6.8.2**).

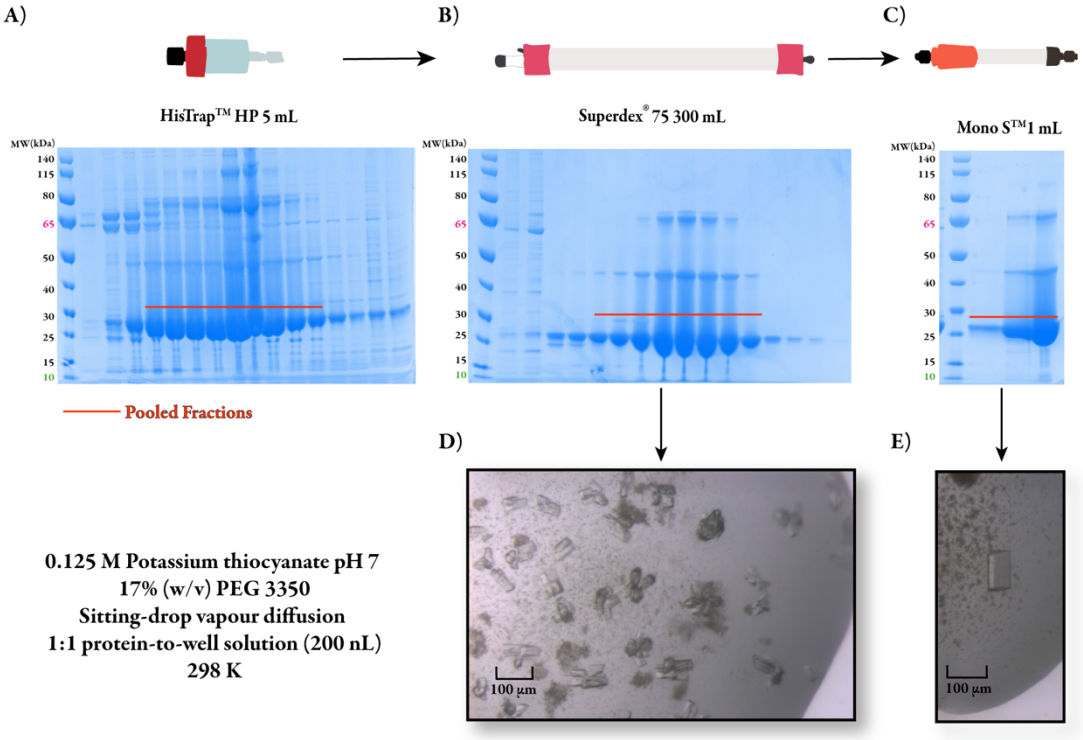


Figure 3-6| SDS-PAGE Gel Characterisation of $PHD2_{181-407}$ After Each Purification Step and Crystallisation of both 2 and 3-Column Products. (A) Gel characterisation of collected fractions from the affinity chromatography step. (B) SDS-PAGE characterization of collected fractions after size-exclusion chromatography. (C) SDS-PAGE gel characterisation after ion-exchange chromatography. (D-E) Crystal drops of the same condition highlight the differences in purity between the 2-column and 3-column batch of $PHD2_{181-407}$. Abbreviations: Sodium-dodecyl-sulfate polyacrylamide gel electrophoresis (SDS-PAGE), Prolyl hydroxylase isoform 2 (PHD2).

The three-column batch of protein was purified by ion-exchange chromatography (Mono S™, Cytiva Co.) as a final step before crystallisation trials (**Figure 3-6C**).[3] The negatively charged resin of the Mono S™ column assisted in the separation of contaminant proteins and oligomerisation that occurred during the purification (note that the fine packing of the MonoS™ resin can separate oligomerised proteins due to the increase positive charge on the surface of the oligomers relative to monomers).[19] The oligomerisation, at least in part, likely occurs due to the high concentrations of tPHD2 reached during the concentration of the protein and is potentially induced caused by the pH (7.5 at RT and 8.1 at 4 °C; note previous reported protocols used buffers at pH 7.0-7.5 at 4 °C).[3,6,14,20] The oligomerisation that is observed likely assists in the promotion of nucleation in the crystallisation drops (**Figure 3-6D**). The clustered nucleation that is observed reduces as the purity of the enzyme is increased (*i.e.*, with a further purification step there is less nucleation in the crystallisation drops, **Figure 3-6E**). (*Thank you to Dr. Zhihong Zhang for his help in the optimisation of the three-column purification strategy.)*

The three-column batch of $PHD2_{181-407}$ yielded crystals after one day of equilibration; 90 mm x 80 μm x 10 μm rhombohedral shaped crystals were obtained in 0.2 M potassium thiocyanate pH 7 and 20% (w/v) PEG 3350 at a 1:1 protein-to-well ratio (200 nL drops at 298 K, **Figure 3-7A**, **6.8.2**). The crystallisation condition was then further optimised and 100 μm x 50 μm x 20 μm (conditions listed in **Figure 3-7B**) and 200 μm x 120 μm x 35 μm (*Xtal-P*, conditions listed in **Figure 3-7C**, **6.8.2**) rhombohedral crystals were obtained after 3-5-days of equilibration. The hit crystals were initially tested for diffraction using an in-house source (3.10-3.30 Å resolution, **6.6.7.1**). Due to the weak diffraction, the $PHD2_{181-407}$.Mn(II).succinate crystals were sent to a synchrotron source (**6.6.7.2**) with the aim of obtaining higher resolution datasets. However, on the initial synchrotron visit, the highest resolution obtained was between 2.60-2.80 Å.

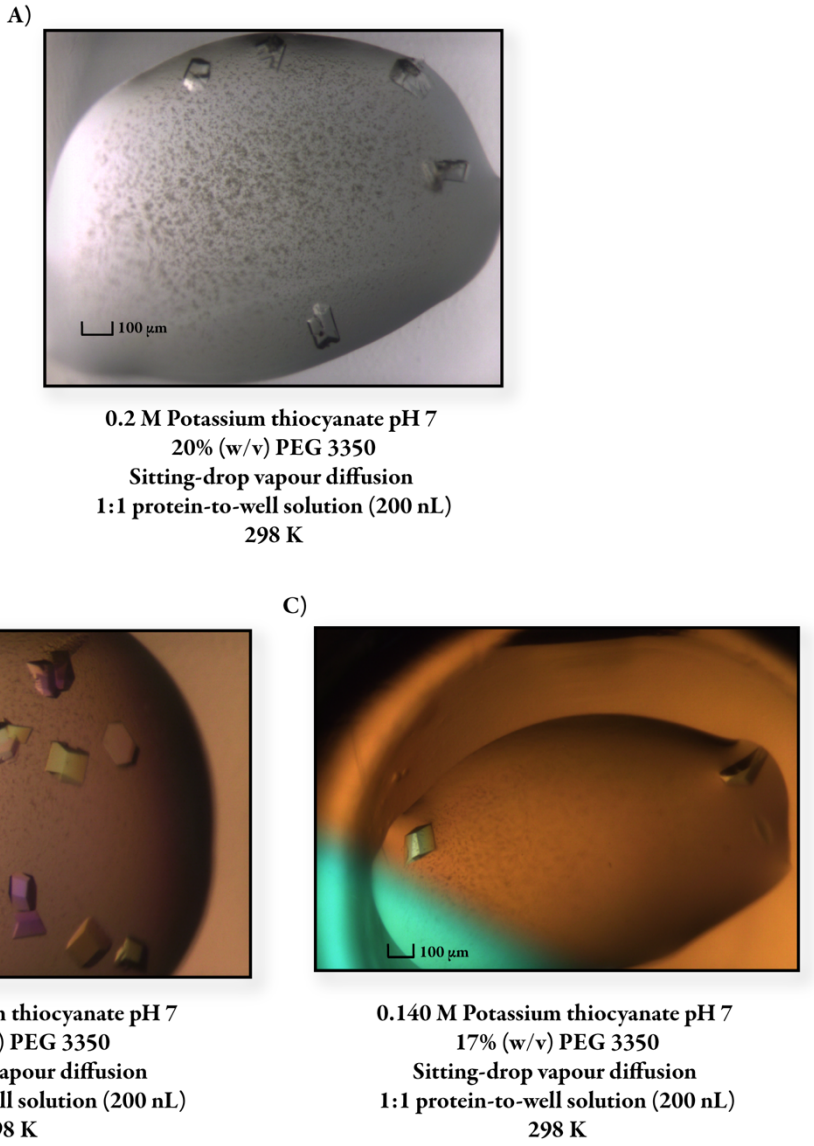


Figure 3-7| Hit and Optimised PHD2$_{181-407}$.Mn(II).Succinate Crystals. (A) PHD2$_{181-407}$.Mn(II).succinate crystals that formed from the PEG/Ion screen™ I/II. (B) Optimised crystals of PHD2$_{181-407}$.Mn(II).succinate. Abbreviations: Prolyl hydroxylase isoform 2 (PHD2).

Likely due to the low resolution and structural differences with the starting model (truncated PDB: 3HQR), the initial MR (**6.6.9.2**) solutions did not clearly display whether succinate was complexed in the PHD2$_{181-407}$ structure. As the model was refined through iterative steps (*i.e.*, phasing of multiple datasets and manual refinement), the quality of the electron density maps increased (these *P* 2$_1$ PHD2$_{181-407}$.Mn(II).succinate unit cells were from the datasets used for phasing a=77.05 Å, b=75.13 Å, b=126.98 Å, β=95.28° and a=75.96 Å, b=75.42 Å, c=130.38 Å, β=99.05°). An optimised batch of PHD2$_{181-407}$-

succinate crystals diffracted to 2.20 Å (**Figure 3-7B**) and 1.90 Å (*Xtal-P*, **Figures 3-7C** and **3-8A-B**, **Table 3-8**); with the higher resolution datasets, an improved starting model could be refined that allowed for structural investigation of the PHD2$_{181-407}$.Mn(II).succinate-derived active site. The PHD2$_{181-407}$.Mn(II).succinate-derived crystal form (*Xtal-P*) contained six-chains in its ASU, similarly to the PHD2$_{181-426}$ *P* 2$_1$ crystal form (*Xtal-O*, **3.2.1** and in PDB: 6YVT, **Figure 3-8C-E**).[16] PHD2$_{181-407}$ forms three protomers of two-chains in the ASU. For subsequent phasing of the datasets, one protomer was used (*i.e.*, a two-chain model of *Xtal-P*). (*Thank you to Dr. Yu Nakashima for his extensive help on developing a starting model for the MR phasing of structures in the P 2$_1$ crystal form.*)

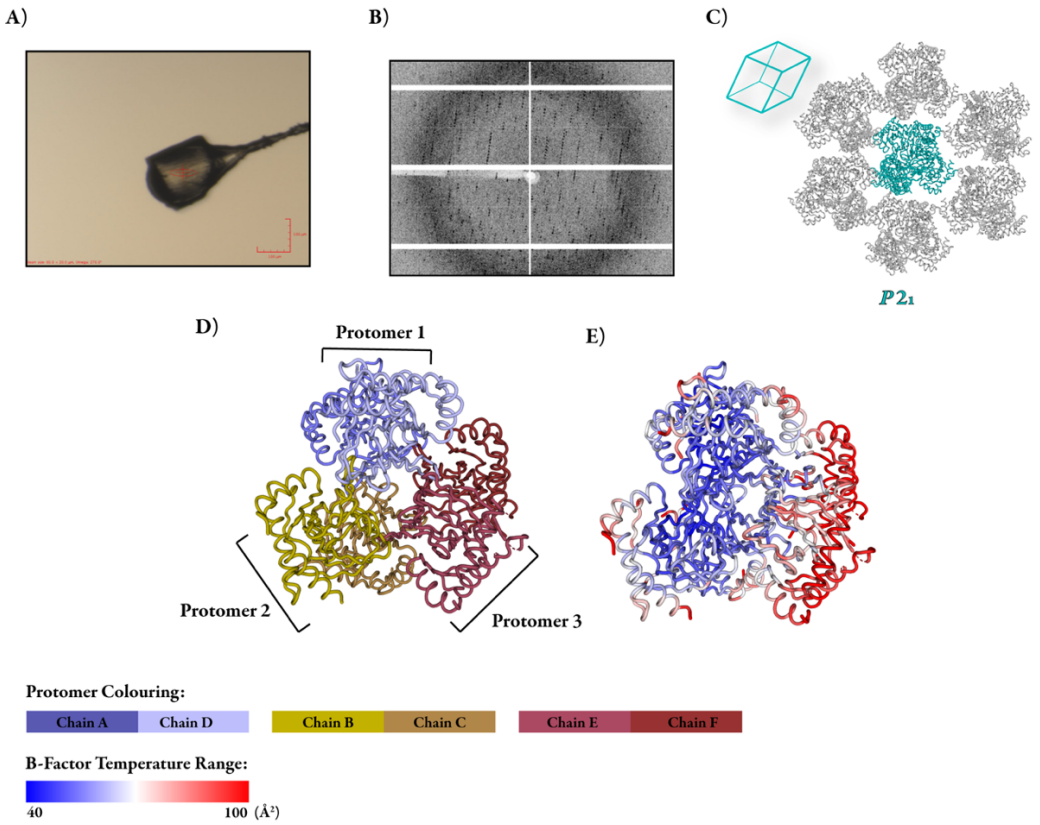


Figure 3-8| An Overview of PHD2$_{181-407}$.Mn(II).Succinate *P* 2$_1$ Crystal Form. (A) A PHD2$_{181-407}$ crystal load image on I03 Beamline (DLS) (B) Diffraction of reflections from a PHD2$_{181-407}$.succinate crystal using an Dectris Eiger2 XE 16M detector. (C) The asymmetric unit (teal) and neighbouring symmetry chains (grey) are depicted as cartoons. (E) Three two-chain protomers of the asymmetric unit are illustrated as cartoons (with a colour key shown highlighting the protomers). (E) The overall B-factor (Å^2) change throughout the PHD2$_{181-407}$ *P* 2$_1$ crystal form. Protomer 3 (chains E and F) exhibited high B-factors in comparison to the other protomers due to the moderate anisotropy of this crystal form. Abbreviations: Prolyl hydroxylase isoform 2 (PHD2), Diamond Light Source Ltd. (DLS).

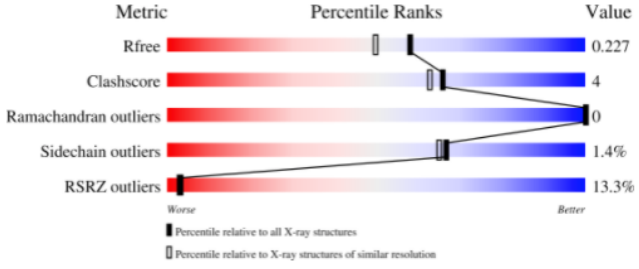
Table 3-3| Crystallographic Data Processing and Refinement Statistics (*Xtal-P*).

	$PHD2_{181-407}$.SIN (*Xtal-P*)
Beamline	Diamond Light Source-I03
Detector	Dectris Eiger2 XE 16M
Data Processing	Xia2 DIALS
Wavelength (Å)	0.9763
Resolution range (Å)	19.61 - 1.90 (1.96 - 1.90)
Space group	$P\,1\,2_1\,1$
Unit cell (Å, °)	75.93 74.89 126.88, 93.07
Total reflections	748372 (75703)
Unique reflections	111590 (11007)
Multiplicity	6.7 (6.9)
Completeness (%)	99.76 (99.07)
Mean I/sigma (I)	14.03 (1.33)
Wilson B-factor (Å²)	37.11
R-merge†	0.06314 (1.3)
R-meas	0.0685 (1.407)
R-pim	0.02627 (0.5326)
CC1/2	0.999 (0.695)
CC*	1 (0.906)
Reflections used in refinement	111590 (10997)
Reflections used for R-free	5375 (512)
R-work✧	0.2071 (0.3218)
R-free✧	0.2264 (0.3361)
CC(work)	0.949 (0.849)
CC(free)	0.944 (0.822)
Number of non-hydrogen atoms	9351
macromolecules	8969
ligands	170
solvent	274
Protein residues	1180
RMS(bonds, Å)	0.006
RMS(angles,°)	0.90
Ramachandran favored (%)	98.25
Ramachandran allowed (%)	1.75
Ramachandran outliers (%)	0.00
Rotamer outliers (%)	1.41
Clashscore	4.78
Average B-factor (Å²)	53.05
macromolecules	53.33
ligands	54.57
solvent	43.15
Number of TLS groups	35

Single crystal diffraction data was collected from samples held at 100 K with conventional, rotation-based methods. Ligands: Mn, SIN, K, SCN, DMS, and Cl. Statistics for the highest-resolution shell are shown in parentheses.

† R-merge (or Rsym) is equal to $\sum|I-\langle I\rangle|/\sum I$. R-merge represents the data quality of merged reflection data. *I* is equal to the intensity of individual measurements and <I> is equal to the average of multiple measurements. ✧R_{free} is the R_{factor} for 5% of the reflections which are excluded during refinement.

R_{factor} is equal to $\sum_{hkl}||Fobs_{(hkl)}| - |Fcalc_{(hkl)}||/\sum_{hkl}|Fobs_{(hkl)}|$ and was calculated for the working set of reflections (R_{work}). **Appendix I** contains the *Xtal-IDs*. Validation heat map generated by the PDB validation service.



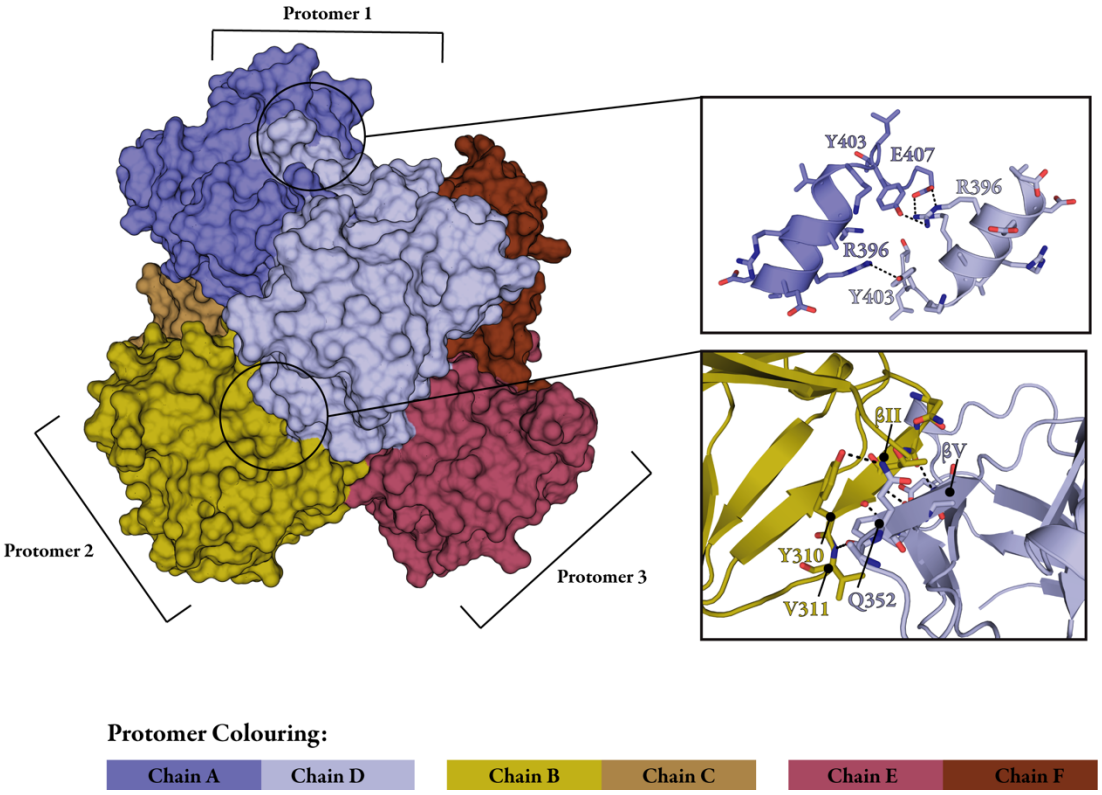


Figure 3-9| A Surface Overview of the Asymmetric Unit of the PHD2$_{181-407}$ *P* 2$_1$ Crystal Form and Specific Protomer Interactions. The surfaces of the each protomer are illustrated with each 2-chain protomer coloured coordinated based on dimer pair (protomer 1-slate-light blue; protomer 2-light olive-sand; protomer 3-raspberry-chocolate). Interactions of the C-terminus and DSBH strands are depicted as cartoons and highlighted residues are shown as sticks (slate, light olive, and light blue). Abbreviations: Prolyl hydroxylase isoform 2 (PHD2). *Figure adapted from Figg Jr., W. D.; McDonough, M. A.; Chowdhury, R.; Nakashima, Y.; Zhang, Z.; Holt-Martyn, J. P.; Krajnc, A.; Schofield, C. J. Structural Basis of Prolyl Hydroxylase Domain Inhibition by Molidustat. ChemMedChem* ***2021****, 16 (13), 2082–2088, Open Access, Wiley-VCH. https://doi.org/10.1002/cmdc.202100133. CC BY 4.0 License.*

The maximum resolution obtained for the PHD2$_{181-407}$.Mn(II).succinate *P* 2$_1$ crystal form was 1.79 Å (PDB: 6ZBO or *Xtal-R*, as discussed in section **3.2.1.1**). Moderate anisotropy was observed along the *a*/*c*-axis of the PHD2$_{181-407}$.Mn(II).succinate *P* 2$_1$ crystals (*i.e.*, there is variation on one axis of this crystal form).[21] The observed anisotropy is evidenced by the high B-factors of protomer 3 (>~90 Å^2) compared to protomers 1 and 2 (~45 Å^2, ~70 Å^2, respectively, **Figures 3-8D-E** and **3-9**). The protomers form *via* a *C*-terminal salt-bridge between the sidechains of residues Glu407 of chains A, C, and E and Arg396 in chains D, B, and F, reflecting interactions between adjacent protomers and the α4 helix (**Figure 3-9**).[3]

The DSBH core fold βII strand of chains A, B, C, D, E, and F interact with the neighbouring chains DSBH βV strand of chains B, F, D, E, C, and A, respectively, *via* anti-parallel interactions (**Figure 3-9**).[3] Active site residue, $Tyr310_{chain\text{-}B}$, of the βII strand interacts with residue $Gln352_{chain\text{-}D}$ of the βV strand (**Figure 3-9**). Notably, the $Tyr310_{chain\text{-}C}$-$Gln352_{chain\text{-}D}$ interaction impacts the positioning of Tyr310 in the $PHD2_{181\text{-}407}$.Mn(II).succinate-derived crystal form.

After the high-resolution datasets were collected, in the solved structures succinate was observed in complex with the Mn ion in the active site of $PHD2_{181\text{-}407}$ (**Figure 3-10**). Succinate coordinates the active site metal *via* its C1 carboxylate, while the C4 carboxylate interacts with the phenolic sidechain of Tyr329 and the guanidinium moiety of Arg383 (note that for succinate the C1 refers to the metal bound carboxylate, **Figure 3-10**). In the $PHD2_{181\text{-}407}$.Mn(II).succinate structure (*Xtal-P*), the C4 carboxylate of succinate forms an electrostatic interaction with the NH1 atom of Arg383 sidechain, which also binds 2OG. The C4 carboxylate of succinate also interacts *via* a hydrogen bond with an active site water (W1) and the ε-N of Arg383 (**Figures 3-10A** and **3-10C**). The water molecule prevents the formation of the salt-bridge that has been observed to form with the C4 carboxylate of succinate (*Xtal-K* and *Xtal-N*, **2.4.1.1**) and the guanidino sidechain of Arg383 (**Figure 3-10A**). Furthermore, the $2mF_o$-DF_c electron maps do not encapsulate the methylene units of succinate (**Figure 3-10A**). The non-observed density for the succinate methylenes may be caused by the weak binding of succinate co-product and/or conformation mobility of the succinate methylenes.[22] The apparent disordering of the methylenes has also been observed in a structure of AsqJ complexed with succinate (PDB: 6KD9, resolution 2.44 Å), another 2OG-dependent oxygenase (**Figure 3-10B**).[23] Note the lower resolution of the AsqJ.Fe(II).succinate (PDB: 6KD9) structure may have implications for the interpretation of the observed $2mF_o$-DF_c maps (**Figure 3-10B**).

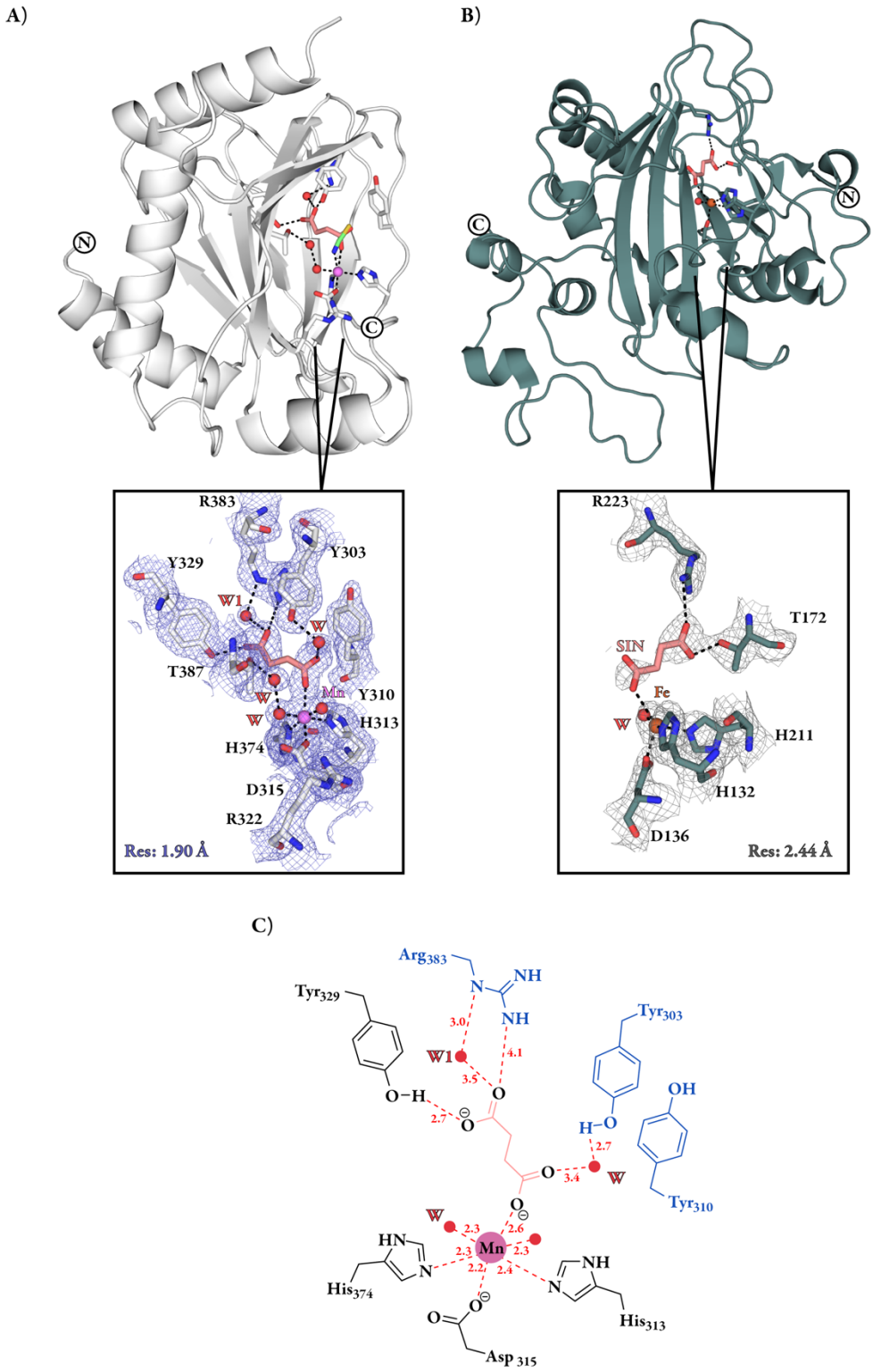


Figure 3-10| A View from the Active Sites of $PHD2_{181-407}$**.Mn(II).Succinate and AsqJ.Fe(II).Succinate Complex Structures.** (A) $PHD2_{181-407}$ in complex with succinate (salmon) is depicted as a cartoon (white) and active site residues are displayed as sticks (white). (B) AsqJ in complex with succinate (salmon; PDB: 6KD9) is depicted as a cartoon (green-blue) and active site residues are displayed as sticks (green-blue). (A-B) $2mF_o$-DF_c electron density (contoured to 1.0 σ) is illustrated as mesh for both structures; $PHD2_{181-407}$.Mn(II).succinate (blue) and AsqJ-succinate (grey). Dashes (black) are representative of the highlighted polar interactions. Spheres are shown of metals (Mn-violet and Fe-orange) and waters (red). Abbreviations: Prolyl hydroxylase isoform 2 (PHD2), Succinate (SIN). PDB: 6KD9.

The apparent weak density for succinate methylenes was also manifested in the *Xtal-N* structure (discussed in section **2.4.1.1**) but was proposed to reflect acetate competition with succinate (*i.e.*, from the crystallisation condition). Further, acetate was not used in the purification of $PHD2_{181-407}$ and/or the crystallisation condition for the *Xtal-P* complex. However, 140 mM thiocyanate (SCN) was used in the crystallisation condition for the $PHD2_{181-407}$.Mn(II).succinate crystal (*Xtal-P*). SCN has been reported to form a Mn-SCN complex.[24] There is one reported structure of a quaternary ammonium Riseke monooxygenase (CntA) in complex with L-carnitine which contains a Fe-SCN complex (PDB: 6Y9D).[25] Therefore, it cannot be ruled out that SCN may be involved in the weak density of succinate in the *Xtal-P* structure as some portions of the crystal may contain the Mn-SCN complex.[24] Further spectroscopic studies, such as UV/vis, Raman, and X-ray absorption could provide evidence if the crystals contain the Mn-SCN complex.

Comparisons of $PHD2_{181-407}$.Mn(II).2OG (*Xtal-J*) and succinate bound structures (*Xtal-N* and *Xtal-P*) depicts the variation of binding positions for 2OG and succinate in the binding pocket (**Figure 3-11A**). The comparison reveals that the position of the C1 carboxylate of succinate in the $PHD2_{181-407}$.Mn(II).succinate complex can vary when compared with *Xtal-N* and *Xtal-P* structures (**Figure 3-11A**). The C1 carboxylate of succinate can interact with the phenolic sidechain of Tyr303 (which can adopt different conformations, **Figure 3-11A**). The shift of succinate may be involved in changes observed to active site residues Tyr303 and Tyr310, which will be discussed in more detail in section **3.4**.

The $PHD2_{181-407}$.Mn(II).succinate complex (*Xtal-P*) structure reveals the sidechain of Arg383 was shifted further (*i.e.*, away from the entrance of the active site) into the 2OG binding pocket relative to the *Xtal-J* and *Xtal-N* structures. The shift may relate to a previously uncharacterised active site water molecule (W1, **Figure 3-10A**).

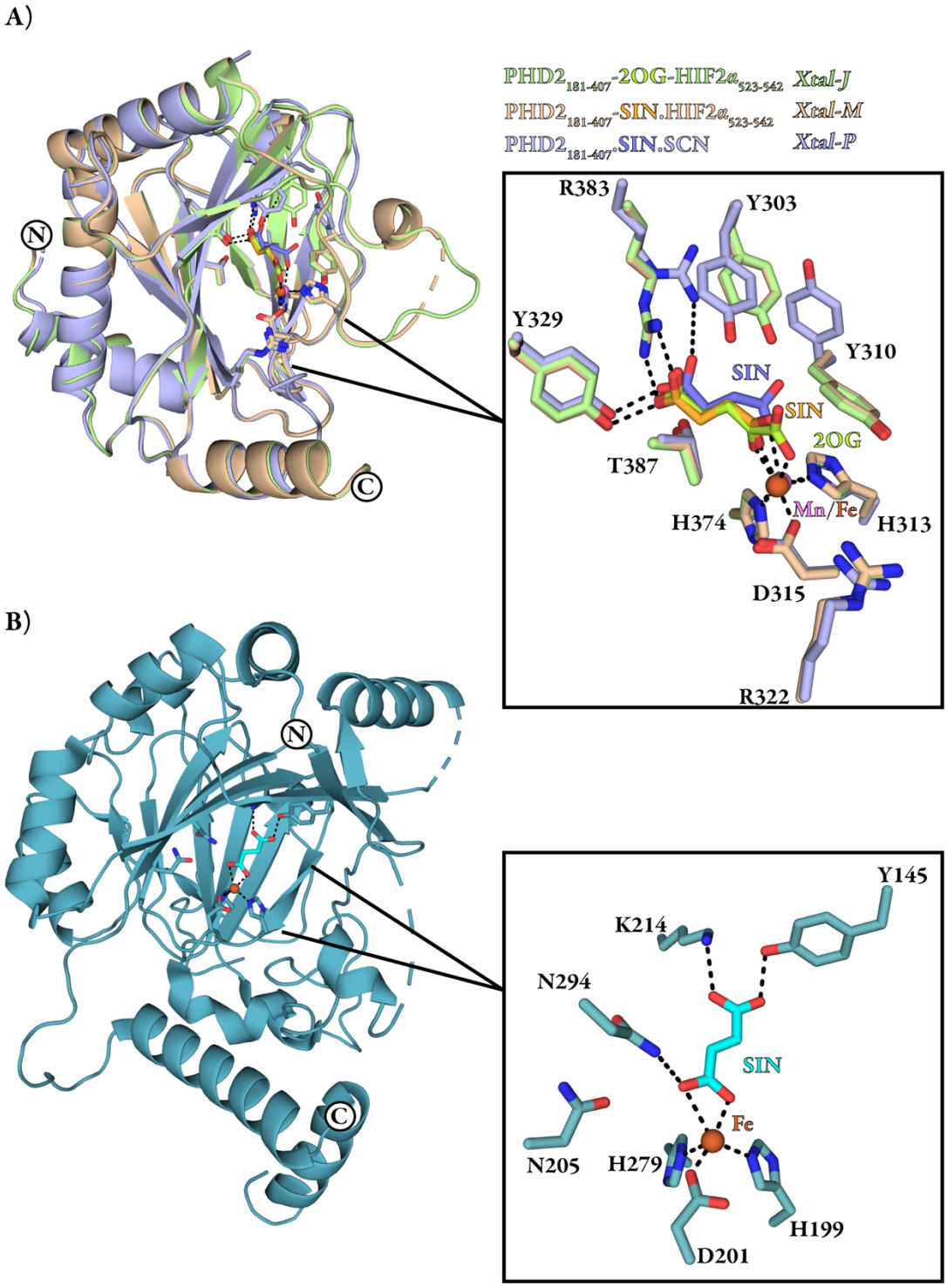


Figure 3-11| Views from the Active sites of PHD2$_{181-407}$.Mn(II).2OG, PHD2$_{181-407}$.Mn(II).Succinate, and FIH-1.Fe(II).Succinate Complexes. (A) Structural alignment of *Xtal-P* (light slate-slate), *Xtal-N* (orange-light orange), and *Xtal-J* (lemon-light lemon) structures. Active site residues and ligands are displayed as sticks. (B) Complex structure of FIH and succinate (cyan, PDB: 2CGN) is displayed as a cartoon (teal). Active site residues are shown as sticks (teal). (A-B) Spheres (Fe-orange and Mn-violet) depict metal ions and dashes (black) represent highlighted active site interactions. Abbreviations: Prolyl hydroxylase isoform 2 (PHD2), Factor-inhibiting hypoxia-inducible factor (FIH), 2-Oxoglutarate (2OG). PDB: 2CGN. *Xtal-IDs*: *J*, *N*, *P*.

An electrostatic interaction is observed between the 2OG C1 carboxylate and the guanidinium of β2-β3 loop residue Arg252 in the *Xtal-J* and *Xtal-N* structures; 3.95 Å and 4.92 Å, respectively. This electrostatic interaction with the guanidinium portion of Arg252 is not observed in the *Xtal-P* crystal form (*i.e.*, the β2-β3 loop is disordered). In the FIH-succinate complex, a bidentate coordination of the C1 carboxylate to metal was observed (**Figure 3-12B**).[18] However, in the *Xtal-P* structure, monodentate coordination is observed of the C1 carboxylate to the metal (seen also in PDB: 6KD9).[23]

Structural comparisons of $PHD2_{181-407}$.Mn(II).succinate complexes in different states and FIH-succinate complexes can potentially provide a better insight into the biophysical characteristics of the ligand induced-fit processes (as discussed further in section **3.4**). Following work on $PHD2_{181-407}$.Mn(II).succinate complex (*Xtal-P*, without substrate) structure, a further aim was to obtain a fumarate (FUM) complex with $PHD2_{181-407}$ to enable the comparison of the effects of a rigid alkene of FUM on binding compared to the more flexible succinate.

3.2.3 Structural analysis of $PHD2_{181-407}$ in Complex with Fumarate

Initially, co-crystallisation of $PHD2_{181-407}$ with fumaric acid (FUM) was investigated to have a representative comparison to the $PHD2_{181-407}$.Mn(II).succinate complex. It was envisaged that such investigations may provide further evidence of reported solution NMR data that showed a broader peak for the tPHD2.FUM compared to the sharper tPHD2-succinate complex peak, *i.e.*, the fumarate likely forms a tighter complex with tPHD2 than succinate, which may reflect in peak shapes. Another study has reported a tPHD2 K_D FUM of 200 ± 70 μM, an IC_{50} of 220 μM, and that FUM displaces 2OG (reported K_D for 2OG <1 μM and IC_{50} for succinate >10 mM).[17,26] The

same study showed that succinate inhibition of tPHD2 required a 40-molar excess ratio of succinate to tPHD2 and no 2OG displacement was observed.[17]

From a medicinal point-of-view, FUM and fumaric acid derivatives are of interest as 'natural' inhibitors of the PHDs (including when FUM is upregulated due to mutation of the gene for fumarate hydratase, as reportedly occurs in some cancer cells and may be a viable alternative to 2OG-mimicking derivatives.[27–29] Due to the structural similarities between fumaric acid and succinic acid, the $PH2_{181-407}$.fumarate mixture was prepared in a similar manner as $PHD2_{181-407}$.Mn(II).succinate. The batch of three-column purified $PHD2_{181-407}$ (1 mM, **3.2.2**, **Figure 3-6**)-fumaric acid (2.2 mM) was screened against conditions in the PEG/Ion Screen™ I/II (Hampton Research Corp., **6.8.3**). Crystal hits appeared in two conditions: 0.2 M sodium citrate and 20% (w/v) PEG 3350 and 0.2 M sodium iodide and 20% (w/v) PEG 3350. Due to concerns that citrate could compete with FUM, the sodium iodide condition was selected for optimisation. The crystallisation conditions were then optimised around 0.2 M sodium iodide pH 7 and 17-22.5% (w/v) PEG 3350 (**6.6.3** and **6.8.3**). After 3-days of equilibration, 150 μm x 100 μm x 40 μm rhombohedral crystal formed (**6.8.3**) and was harvested (**6.6.6.2**) for data collection (**6.6.7.2**, **Tables 3-3** and **3-8**). The $PHD2_{181-407}$.Mn(II).fumarate complex structure (*Xtal-Q*) diffracted to a resolution of 2.34 Å at a synchrotron source (**6.6.7.2**, **Table 3-4**). (*Thank you to Dr. Edward Lowe for collecting the $PHD2_{181-407}$.FUM crystal dataset.)*

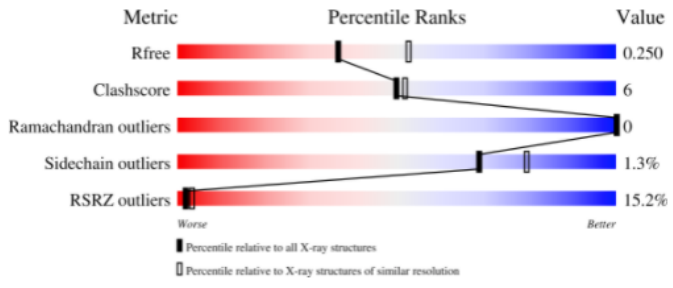
Table 3-4| Crystallographic Data Processing and Refinement Statistics (*Xtal-Q*).

	$PHD2_{181-407}$.FUM (*Xtal-Q*)
Beamline	SOLEIL-Proxima-1
Detector	Dectris Eiger-X 16M
Data Processing	XDS & AIMLESS
Wavelength (Å)	0.9786
Resolution range (Å)	19.73 - 2.34 (2.42 - 2.34)
Space group	$P\,1\,2_1\,1$
Unit cell (Å, °)	76.02 75.22 128.11, 93.22
Total reflections	119791 (12004)
Unique reflections	60984 (6084)
Multiplicity	2.0 (2.0)
Completeness (%)	99.65 (99.98)
Mean I/sigma(I)	7.47 (1.00)
Wilson B-factor (Å²)	55.85
R-merge†	0.05657 (0.6963)
R-meas	0.08 (0.9847)
R-pim	0.05657 (0.6963)
CC1/2	0.996 (0.478)
CC*	0.999 (0.804)
Reflections used in refinement	60984 (6084)
Reflections used for R-free	1864 (189)
R-work✧	0.2197 (0.3543)
R-free✧	0.2495 (0.3519)
CC(work)	0.949 (0.677)
CC(free)	0.949 (0.624)
Number of non-hydrogen atoms	9823
macromolecules	9455
ligands	249
solvent	171
Protein residues	1187
RMS(bonds, Å)	0.003
RMS(angles, °)	0.62
Ramachandran favored (%)	98.79
Ramachandran allowed (%)	1.21
Ramachandran outliers (%)	0.00
Rotamer outliers (%)	1.54
Clashscore	6.74
Average B-factor (Å²)	75.72
macromolecules	76.05
ligands	70.70
solvent	63.31
Number of TLS groups	35

Single crystal diffraction data was collected from samples held at 100 K with conventional, rotation-based methods. Ligands: Mn, FUM, Cl, I, and Na. Statistics for the highest-resolution shell are shown in parentheses.

† R-merge (or Rsym) is equal to $\sum|I-\langle I\rangle|/\sum I$. R-merge represents the data quality of merged reflection data. *I* is equal to the intensity of individual measurments and <I> is equal to the average of multiple measurements. ✧R_{free} is the R_{factor} for 5% of the reflections which are excluded during refinement.

R_{factor} is equal to $\sum_{hkl}||Fobs_{(hkl)}| - |Fcalc_{(hkl)}||/\sum_{hkl}|Fobs_{(hkl)}|$ and was calculated for the working set of reflections (R_{work}). **Appendix I** contains *Xtal-ID*s. Validation heat map generated by the PDB validation service.



The PHD2$_{181-407}$.Mn(II).FUM complex structure (*Xtal-Q*) crystallised in the same *P* 2_1 crystal form as the PHD2$_{181-407}$.Mn(II).succinate crystals (*Xtal-P*). The two-chain protomer model (*Xtal-P*) of the PHD2$_{181-407}$.Mn(II).succinate was used as a starting model for MR-phasing of the data (**6.6.9.2**). The structure was successfully solved, and six-chains were observed for the ASU of the *Xtal-Q* structure. Structural investigation of the active sites of each chain revealed binding of fumarate within the *Xtal-Q* complex (**Figure 3-12**). Notably, the observed complex of fumarate lacks the anticipated mode of direct coordination to the active site metal in all chains of the ASU (**Figure 3-12**). The primary hydrogen bond interactions of fumarate with PHD2$_{181-407}$ are between the C1 and C4 carboxylates with the sidechains of active site residues Thr387 and Tyr329, respectively (**Figure 3-12**). In chain B, however, the C1 carboxylate of fumarate interacts with the metal coordinated water (W1) at the 2OG C2 binding site (note the C1 refers to the carboxylate of FUM towards the metal, **Figure 3-12B**).

The C4 carboxylate of FUM forms a salt bridge interaction with the guanidinium moiety of Arg383 in chains E and F (2.3-2.8 Å), forms a hydrogen bond in chains A and D (3.0-3.1 Å), and electrostatic interactions in chains B-C (3.8-5.3 Å **Figure 3-12C** and **3-12F**). The guanidinium functionality of Arg383 is observed in different conformations throughout the ASU of PHD2$_{181-407}$.Mn(II).fumarate complex structure. The C1 carboxylate of FUM in chains A, C, D, E, and F interacts with the metal coordinated water that is proposed to be displaced upon O_2-binding (**Figure 3-12**).[14] FUM is also observed to be bound in other sites between chains A-C (**Figure 3-12A** and **3-12C)**. In chain A, the carboxylates of FUM2 interact with imidazole sidechain of His205 and the main chain carbonyl oxygen of Glu196 (both residues part of the α1 helix, **Figure 3-12A**).

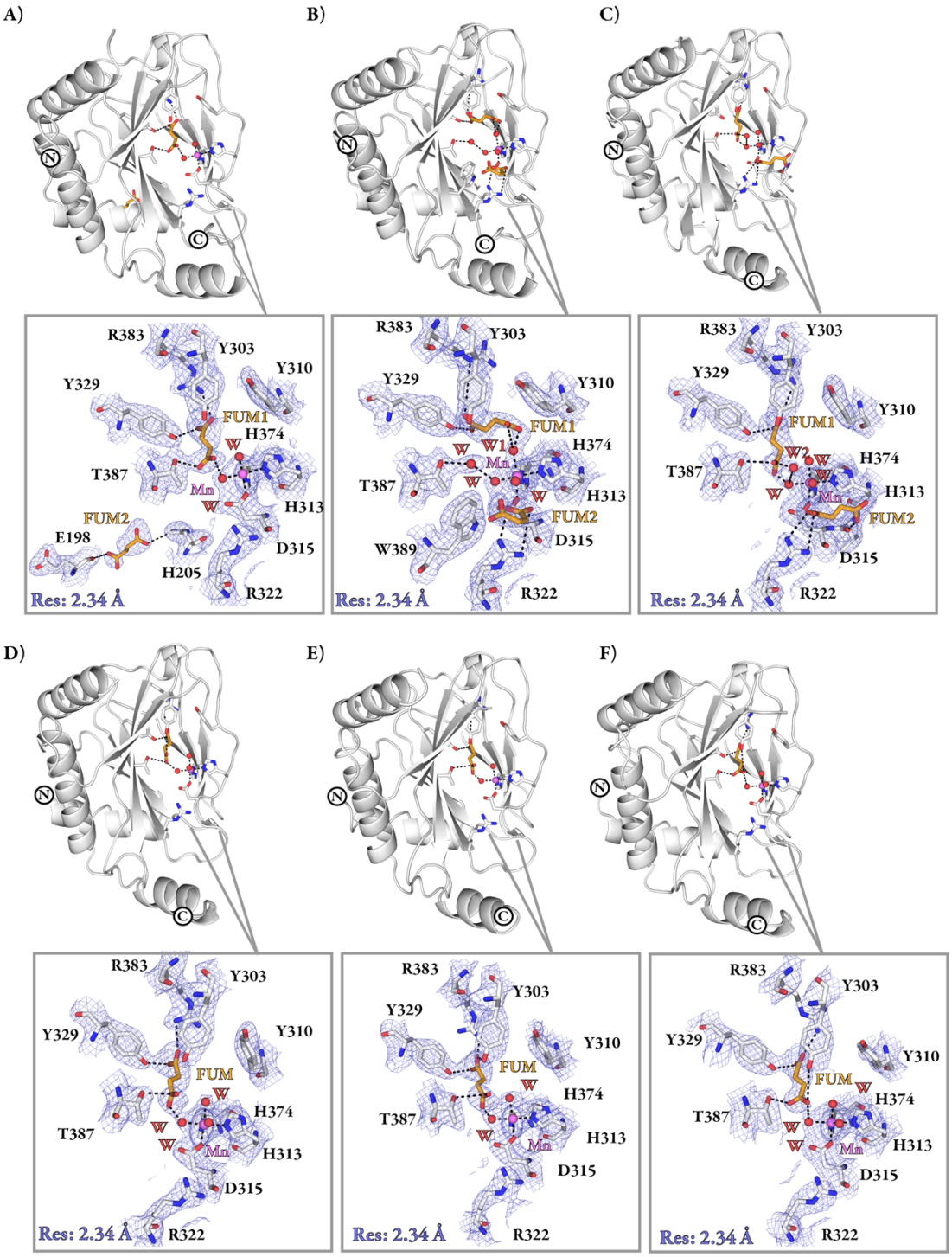


Figure 3-12| A View from the Active Sites of the Six-Chains of the PHD2$_{181-407}$ in complex with Fumarate. (A-F) Each chain (A, B, C, D, E, and F corresponding the labelled panel) is depicted as a cartoon (white). Active site residues (white) and fumarate (orange) ligand of each chain are displayed as sticks. Dashes (black) represent key active site interactions and spheres are shown of waters (red) and Mn ion (violet). 2mF$_o$-DF$_c$ density maps (contoured to 1.0 σ) are illustrated as mesh (blue). Abbreviations: Prolyl hydroxylase isoform 2 (PHD2). *Xtal-ID*: Q.

It is important to note that the binding mode of the active site complexed FUM is different to that of succinate in the *Xtal-Q* structure. The *E* (*trans*) geometry of FUM is

maintained as there is density for the two CH groups of FUM; thus, the solved FUM structure (*Xtal-Q*) supports the proposal that the density in the succinate derived structure (*Xtal-P*) is likely due to succinate binding itself. In chain B and C, the second binding event of FUM2 interacts with the active site guanidinium motif of Arg322 *via* a salt-bridge interaction (for chain B the geometry of FUM2 is in the *Z* (*cis*) conformation, **Figure 3-12B**-**C**). In chain C, another active site water molecule (W2) is observed to hydrogen bond with the C1 carboxylate of FUM (**Figure 3-12C**). Apart from the conformational changes of the guanidinium motif of Arg383 and FUM, active site residues and metals are in similar structural positions when compared between the chains of the *Xtal-Q* and *Xtal-P* complexes (**Figure 3-12**).

Furthermore, in the reported FIH.Fe(II).FUM structure (PDB: 2CGO), FUM is observed to bind in a similar position between FIH chains, in a manner similar to that observed for 2OG binding (PDB: 3D8C)[30], as well as to the succinate binding pocket in the FIH.Fe(II).succinate complex (**Figure 3-11B** and **3-13**; PDB: 2CGN).[18] Structural insights from the $PHD2_{181-407}$.Mn(II).fumarate complex have the potential to yield improved inhibitors based on structural analogues of this natural product.[27] The binding mode of FUM in $PHD2_{181-407}$ is distinct as it targets the alcohol sidechain of Thr387, which has been reported to be involved in the O_2-kinetics of PHD2.[31] While previous studies have shown inhibition of the PHDs with fumaric acid in the μM range, FIH was not inhibited by FUM.[17,18,28] New potential inhibitors utilising fumaric acid as a structural motif to construct novel selective-inhibitors of the PHDs, are therefore of interest.[17,18,28]

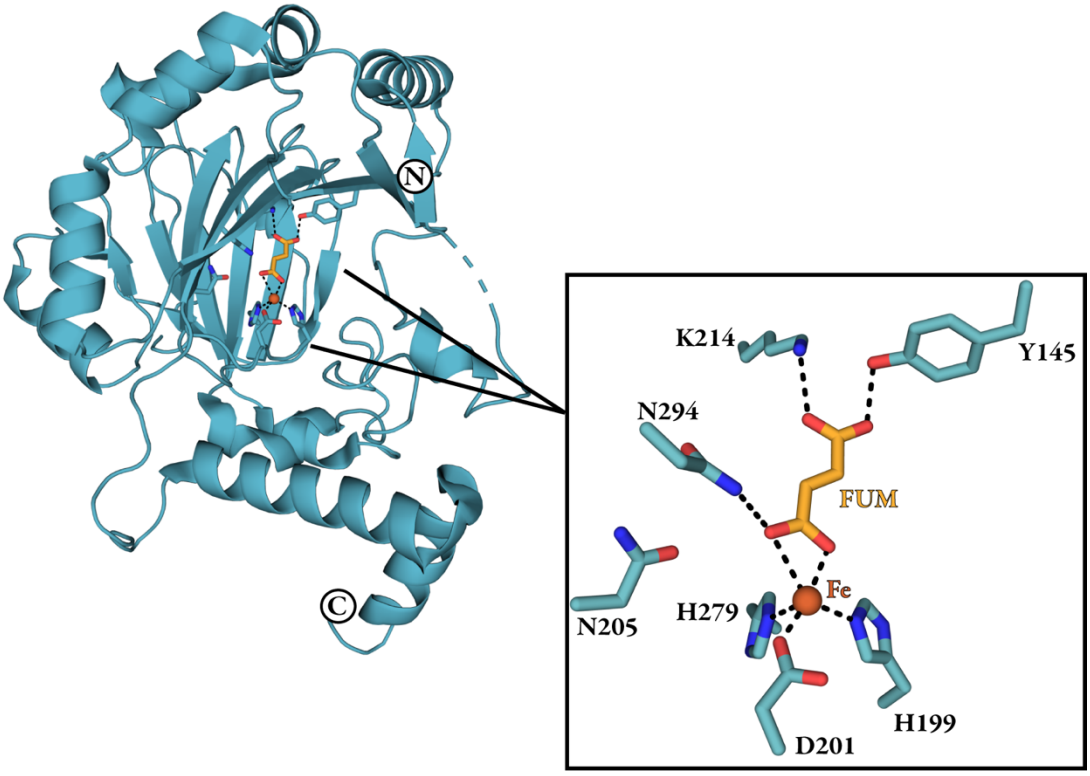


Figure 3-13| A View from the Active Sites FIH in complex with Fumarate. FIH is depicted as a cartoon (teal). Active site residues (teal) and fumarate (orange) ligand are displayed as sticks. Dashes (black) represent key active site interactions and spheres are shown of Fe ion (orange). Abbreviations: Factor inhibiting-hypoxia inducible factor (FIH).PDB: 2CGO.

3.2.4 Co-Crystallisation of PHD2$_{181-407}$ with Molidustat, IOX4, and Takeda-17 using the Succinate *P* 2$_1$ Crystal System

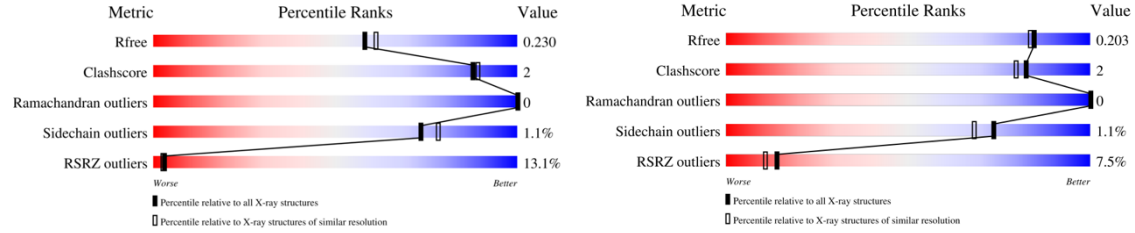
As previously mentioned (**3.2.2**), it was proposed that the PHD2$_{181-407}$.Mn(II).succinate crystal form (*Xtal-P*) could be used to potentially obtain co-crystallised inhibitor complexes with biophysically uncharacterised clinically applied inhibitors, *e.g.,* Molidustat (**20**), Roxadustat (**22**), Daprodustat (**24**), and Desidustat (**26**, **Figure 3-2**). Other inhibitors of the PHDs and 2OG oxygenase inhibitors, such IOX1 (**31**)[32], IOX4 (**28**)[33], Takeda-17 (**17**), MK-8617 (**32**)[34], and BNS (**34**)[17] were evaluated in co-crystallisation studies using the PHD2$_{181-407}$.Mn(II).succinate condition (**Figure 3-2**). The proposal was that the selected inhibitors may exchange with the succinate during a 0.5-1 hr incubation before preparing the crystallisation plates (**6.6.1** and **6.8.2**).

Table 3-5| Crystallographic Data Processing and Refinement Statistics (Xtal-R and Xtal-S).

	$PHD2_{181-407}$.IOX4 (PDB: 6ZBN or *Xtal-S*)	$PHD2_{181-407}$.Molidustat (PDB: 6ZBO or *Xtal-R*)
Beamline	Diamond Light Source-I04	Diamond Light Source-I04
Detector	Dectris Eiger2 XE 16M	Dectris Eiger2 XE 16M
Data Processing	Xia2 DIALS	Xia2 DIALS
Wavelength (Å)	0.9795	0.9795
Resolution range (Å)	19.97 - 2.01 (2.082 - 2.01)	53.71 - 1.79 (1.85 - 1.79)
Space group	$P\ 1\ 2_1\ 1$	$P\ 1\ 2_1\ 1$
Unit cell (Å, °)	77.06 75.47 127.56, 95.04	77.12 75.15 127.22, 95.31
Total reflections	194111 (19357)	268399 (26276)
Unique reflections	97123 (9699)	134369 (13146)
Multiplicity	2.0 (2.0)	2.0 (2.0)
Completeness (%)	99.64 (99.49)	98.25 (96.75)
Mean I/sigma(I)	13.41 (1.10)	15.12 (1.19)
Wilson B-factor (Å²)	46.55	36.96
R-merge†	0.02276 (0.6275)	0.02229 (0.5392)
R-meas	0.03219 (0.8874)	0.03152 (0.7625)
R-pim	0.02276 (0.6275)	0.02229 (0.5392)
CC1/2	1 (0.752)	0.999 (0.779)
CC*	1 (0.927)	1 (0.936)
Reflections used in refinement	96894 (9654)	133987 (13069)
Reflections used for R-free	4823 (494)	6820 (682)
R-work✧	0.2056 (0.3615)	0.1776 (0.3274)
R-free✧	0.2301 (0.3792)	0.2033 (0.3262)
CC(work)	0.963 (0.805)	0.963 (0.890)
CC(free)	0.956 (0.730)	0.951 (0.881)
Number of non-hydrogen atoms	9865	10381
macromolecules	9421	9599
ligands	156	157
solvent	288	625
Protein residues	1197	1218
RMS(bonds, Å)	0.002	0.006
RMS(angles,°)	0.47	0.75
Ramachandran favored (%)	96.93	97.80
Ramachandran allowed (%)	3.07	2.20
Ramachandran outliers (%)	0	0
Rotamer outliers (%)	1.45	1.61
Clashscore	2.36	2.78
Average B-factor (Å²)	67.10	52.56
macromolecules	67.66	52.94
ligands	51.68	42.77
solvent	57.11	49.24
Number of TLS groups	39	43

Single crystal diffraction data was collected from samples held at 100 K with conventional, rotation-based methods. Ligands: Mn, QEE, QEQ, and Cl. Statistics for the highest-resolution shell are shown in parentheses.

† R-merge (or Rsym) is equal to $\sum|I-\langle I\rangle|/\sum I$. R-merge represents the data quality of merged reflection data. *I* is equal to the intensity of individual measurments and <I> is equal to the average of multiple measurements. ✧R_{free} is the R_{factor} for 5% of the reflections which are excluded during refinement. R_{factor} is equal to $\sum_{hkl}||Fobs_{(hkl)}| - |Fcalc_{(hkl)}||/\sum_{hkl}|Fobs_{(hkl)}|$ and was calculated for the working set of reflections (R_{work}). *Xtal-IDs are listed in* ***Appendix I.*** Validation heat maps generated by the PDB validation service. *Table edited from Figg Jr, W.D. et al., ChemMedChem* ***2021****. Figg Jr., W. D.; McDonough, M. A.; Chowdhury, R.; Nakashima, Y.; Zhang, Z.; Holt-Martyn, J. P.; Krajnc, A.; Schofield, C. J. Structural Basis of Prolyl Hydroxylase Domain Inhibition by Molidustat. ChemMedChem* ***2021****, 16 (13), 2082–2088, Open Access, Wiley-VCH. https://doi.org/10.1002/cmdc.202100133. CC BY License 4.0.*



Rhombohedral crystals of similar morphologies to those of the $PHD2_{181-407}$.Mn(II).succinate (*Xtal-P*) formed after 3 days of equilibration in crystallisation conditions with Molidustat (**20**), Daprodustat (**24**), Desidustat (**26**), IOX1 (**31**), IOX4 (**28**), and Takeda-17 (**17**, **6.8.4**-**6.8.6**). Upon structural characterisation, evidence for binding with $PHD2_{181-407}$ was observed of only Molidustat (**20**, 180 μm x 60 μm x 40 μm, 1.79 Å), IOX4 (**28**, 100 μm x 100 μm x 15 μm, 2.01 Å), and Takeda-17 (**17**, 150 μm x 100 μm x 25 μm, 2.13 Å; **Tables 3-5**, **3-6**, and **3-8**).[3](*Thank you to Dr. Michael McDonough for fishing and collecting data on the crystals in **3.2.4.1**. Thank you to Dr. Yu Nakashima for his help in refinement of the dataset in **3.2.4.2**.*)

3.2.4.1 Biophysical Characterisation of $PHD2_{181-407}$ Complex Structures with Molidustat and IOX4†

As observed in other tPHD2 structures, Molidustat (**20**, PDB: 6ZBO or *Xtal-R*) and IOX4 (**28**, PDB: 6ZBN or *Xtal-S*), a brain-penetrating derivative of **20**, both complex the active site metal in a bidentate manner similar to 2OG *via* the chelation of their pyrimidine (2.15 Å)/pyridine (2.14 Å) N1 atom (*trans* to His374 ε-N2 atom, **Figure 3-14**).[3] The pyrazolone N1 nitrogen complexes *trans* to Asp315 Oδ1 atom, 2.27 Å and 2.24 Å, respectively (**Figure 3-14**).[3] The active site metal is coordinated by a conserved triad of residues; His313, Asp315, and His374 (**Figure 3-14**).[3]

Consistent with the reported carboxylate bioisosteric properties of the triazole sidechains, those of **20** and **28** bind in the predominantly hydrophobic 2OG binding pocket (except for Tyr329 and Arg383) in a manner similar to the C5 carboxylate as 2OG (**Figure 3-14**).[3,35] However, the binding mode of the triazole containing inhibitors differs

† Section **3.2.4.1** was paraphrased with permission from Figg Jr., W. D.; McDonough, M. A.; Chowdhury, R.; Nakashima, Y.; Zhang, Z.; Holt-Martyn, J. P.; Krajnc, A.; Schofield, C. J. Structural Basis of Prolyl Hydroxylase Domain Inhibition by Molidustat. ChemMedChem **2021**, 16 (13), 2082–2088, Open Access, Wiley-VCH. https://doi.org/10.1002/cmdc.202100133. CC BY 4.0 License.

from that of 2OG and close analogues such as the glycinamide containing inhibitors (*e.g.*, **21** and **23**; PDB: 4BQX and 5OX6, respectively).[2,3,7] By contrast, the triazole moieties of **20** and **28** bind *via* a direct electrostatic interaction with one terminal guanidino NH(2) group of Arg383, 3.27 Å and 3.25 Å, respectively (**Figure 3-14B** and **14D**).[3]

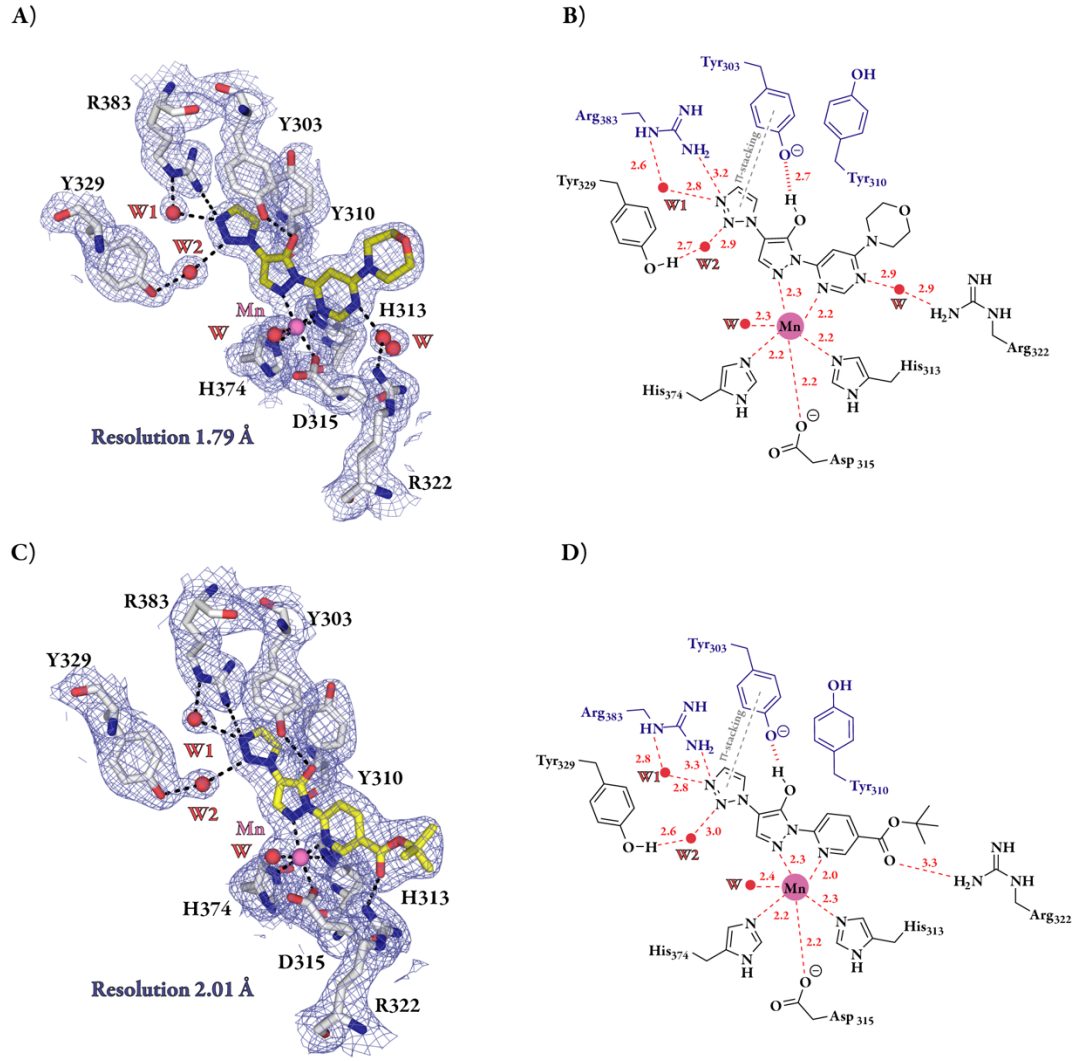


Figure 3-14| A View from 3D and 2D Active Site Representations of PHD2$_{181-407}$ in Complex with Molidustat (20) and IOX4 (28). (A) Structural determination of the active site of PHD2$_{181-407}$ in complex with **20**. (B) 2D illustration of PHD2$_{181-407}$ in complex with **20** (PDB: 6ZBO). (C) Structural determination of the active site of PHD2$_{181-407}$ in complex with **28**. (D) 2D illustration of PHD2$_{181-407}$ in complex with **28** (PDB: 6ZBN). (A-B) The 2mF_o-DF_c electron density maps (contoured to 1.0 σ) are displayed as mesh (blue). The ligands (black) and active site (black) and key active site (blue) residues are displayed as sticks. Active site waters (red) and metal (violet) is depicted as spheres. Key active site interactions are shown as dashes (black). Abbreviations: 3-Dimensional (3D), 2-Dimensional (2D), Prolyl hydroxylase isoform 2 (PHD2). PDB: 6ZBN (*Xtal-S*), 6ZBO (*Xtal-R*). *Figg Jr., W. D.; McDonough, M. A.; Chowdhury, R.; Nakashima, Y.; Zhang, Z.; Holt-Martyn, J. P.; Krajnc, A.; Schofield, C. J. Structural Basis of Prolyl Hydroxylase Domain Inhibition by Molidustat. ChemMedChem* ***2021****, 16 (13), 2082–2088, Open Access, Wiley-VCH. https://doi.org/10.1002/cmdc.202100133. CC BY 4.0 License.*

Two hydrogen bond interactions are observed between the triazole sidechain of both **20** and **28** with the active site waters (W1 and W2, *Xtal-R* and *Xtal-S*, **Figure 3-14**).[3] In both complex structures, W1 forms a hydrogen bond with the N1 of the triazoles and ε-NH of Arg383 (*Xtal-R* and *Xtal-S*, **Figure 3-14**).[3] The triazole N2 atom is positioned to make an interaction with the phenolic OH of Tyr329 *via* a hydrogen bond between W2 (*Xtal-R* and *Xtal-S*, **Figure 3-14**).[3] Finally, the triazole does not hydrogen bond with the phenolic sidechain of Tyr303, but is instead positioned to form a π-π stacking interaction with the aromatic ring (*Xtal-R* and *Xtal-S*, **Figure 3-14**).[3] Thus, it is likely that the pyrazolone rings of **20** and **28** are complexed in their enolic forms and interact with the Tyr303 phenolic OH sidechains *via* hydrogen bonds (*Xtal-R* and *Xtal-S*, **Figure 3-14**).[3,36] The biophysical characterisation of $PHD2_{181-407}$.**20** and **28** structures imply the pyrazolone based inhibitors complex, at least, predominantly in their enolic form (*Xtal-R* and *Xtal-S*, **Figure 3-14**).[3,36] Furthermore, supported by the apparent presence of a 'shared' hydrogen bond between the phenol of Tyr303 and the pyrazolone enol of **28**, *i.e.*, metal ligation is likely observed from the pyrazolone imine N2 atom (*Xtal-R* and *Xtal-S*, **Figure 3-14**).[3]

The morpholine and *tert*-butyl ester sidechains of **20** and **28**, respectively, extend out of the active site of $PHD2_{181-407}$ into the substrate binding groove (*Xtal-R* and *Xtal-S,* **Figure 3-14**).[3] Through NMR studies, both **20** and **28** have been observed to compete with 2OG binding, but both inhibitors incompletely displace HIFα-substrates.[3,5,7] When $PHD2_{181-407}$ is in complex with HIFα-substrates, the guanidino NH1 atom of Arg322 forms a hydrogen bond with the backbone carbonyl of $Pro564_{HIF1α-CODD}$, $Pro402_{HIF1α-NODD}$, and $Pro531_{HIF2α-CODD}$ (PDB: 3HQR, 5L9V, and *Xtal-A*, respectively), and likely makes an analogous interaction with structurally uncharacterised ODDs.[3,6,14] **28** forms an interactions between the *tert*-butyl ester carbonyl oxygen atom with the NH(2) sidechain of Arg322 (*Xtal-S*, **Figure 3-14C-D**).[3] This interaction may, in part, reflect the

observation that **28** more effectively displaces HIF1α$_{395-413}$-NODD than **20**.[3,5,7] Although, it is unclear how this occurs, it is thought that correlated motions may be involved in displacement of HIFα.[3]

In contrast to the PHD2$_{181-407}$.**20** complex structure, the triazole sidechain forms electrostatic and hydrogen bond interactions with ε-NH_2 of Lys214 and the phenolic OH of Tyr145 in the FIH.**20** complex, respectively (**Figure AIII-1**, PDB: 5OP8).[3,7] The triazole interactions are analogous to those observed in the FIH.2OG complex structure (PDB: 1MZF).[3,37] Thus, despite weaker inhibition of FIH with **20** and **28**, the interactions made by the triazole ring appear to more closely reflect those with the C5 carboxylate of 2OG in FIH (PDB: 3D8C) when compared to *Xtal-R* and *Xtal-S* (PHD2$_{181-407}$.**20** and **28**, respectively).[3,37] Furthermore, the interactions observed in the PHD2$_{181-407}$.**20** away from the 2OG binding pocket, *e.g.*, the π-π-stacking interaction between the triazole and Tyr303 aromatics rings, are seemingly important in the case of PHD inhibition.[3]

The results demonstrate that **20** and **28** inhibit PHD2, and by implication, other PHD paralogues, *via* complexation of the enol form of their pyrazolone ring in a manner that competes with 2OG for binding in the 2OG-pocket.[3,36] The triazole functionality is accommodated in the relatively similar position as the C5 carboxylate of 2OG.[3] However, structural analyses reveal that physio-chemical properties of the triazole (as a bioisostere of the carboxylic acid function) do not allow for a simple exchange with the 2OG carboxylate, as evidenced by the presence of the previously uncharacterised active site water molecules (W1-W2 in *Xtal-S* and *Xtal-R*).[3]

3.2.4.2 Complex Structure of PHD2$_{181-407}$ with Takeda-17

Structural characterisation of PHD2$_{181-407}$ in complex with Takeda-17 (**17**) was investigated to determine if **17** can complex in the PHD2$_{181-407}$.Mn(II).succinate crystals (*Xtal-P*, **Table 3-6**).

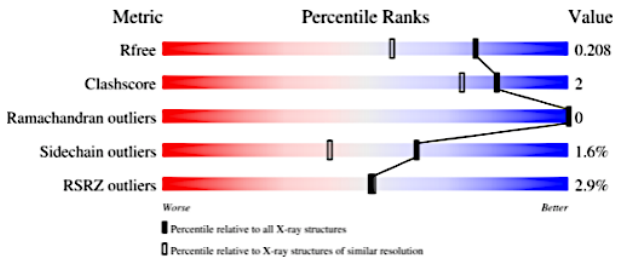
Table 3-6| Crystallographic Data Processing and Refinement Statistics (*Xtal-T*).

	$PHD2_{181-407}$.Takeda (*Xtal-T*)
Beamline	Diamond Light Source-I04
Detector	Dectris Eiger2 XE 16M
Data Processing	Xia2 DIALS
Wavelength (Å)	0.9795
Resolution range (Å)	19.85 - 2.13 (2.20 - 2.13)
Space group	P 1 21 1
Unit cell (Å, °)	75.79 75.21 126.21, 92.51
Total reflections	552426 (52021)
Unique reflections	79405 (7874)
Multiplicity	7.0 (6.6)
Completeness (%)	99.79 (99.96)
Mean I/sigma(I)	14.51 (1.34)
Wilson B-factor (Å²)	48.47
R-merge†	0.06361 (1.327)
R-meas	0.06885 (1.442)
R-pim	0.02611 (0.5579)
CC1/2	0.999 (0.636)
CC*	1 (0.882)
Reflections used in refinement	79369 (7872)
Reflections used for R-free	3905 (366)
R-work✧	0.1908 (0.3301)
R-free✧	0.2190 (0.3482)
CC(work)	0.959 (0.804)
CC(free)	0.950 (0.786)
Number of non-hydrogen atoms	9680
macromolecules	9347
ligands	178
solvent	211
Protein residues	1187
RMS(bonds, Å)	0.008
RMS(angles, °)	0.95
Ramachandran favored (%)	98.28
Ramachandran allowed (%)	1.63
Ramachandran outliers (%)	0.09
Rotamer outliers (%)	0.85
Clashscore	6.97
Average B-factor (Å²)	69.67
macromolecules	70.05
ligands	66.43
solvent	55.13
Number of TLS groups	45

Single crystal diffraction data was collected from samples held at 100 K with conventional, rotation-based methods. Ligands: Mn, 8UY, GOL, and Cl. Statistics for the highest-resolution shell are shown in parentheses.

† R-merge (or Rsym) is equal to $\sum|I-\langle I\rangle|/\sum I$. R-merge represents the data quality of merged reflection data. *I* is equal to the intensity of individual measurements and <I> is equal to the average of multiple measurements. ✧R_{free} is the R_{factor} for 5% of the reflections which are excluded during refinement.

R_{factor} is equal to $\sum_{hkl}||Fobs_{(hkl)}| - |Fcalc_{(hkl)}||/\sum_{hkl}|Fobs_{(hkl)}|$ and was calculated for the working set of reflections (R_{work}). **Appendix I** contains the *Xtal-ID*. The validation heat map was generated with PDB validation service.



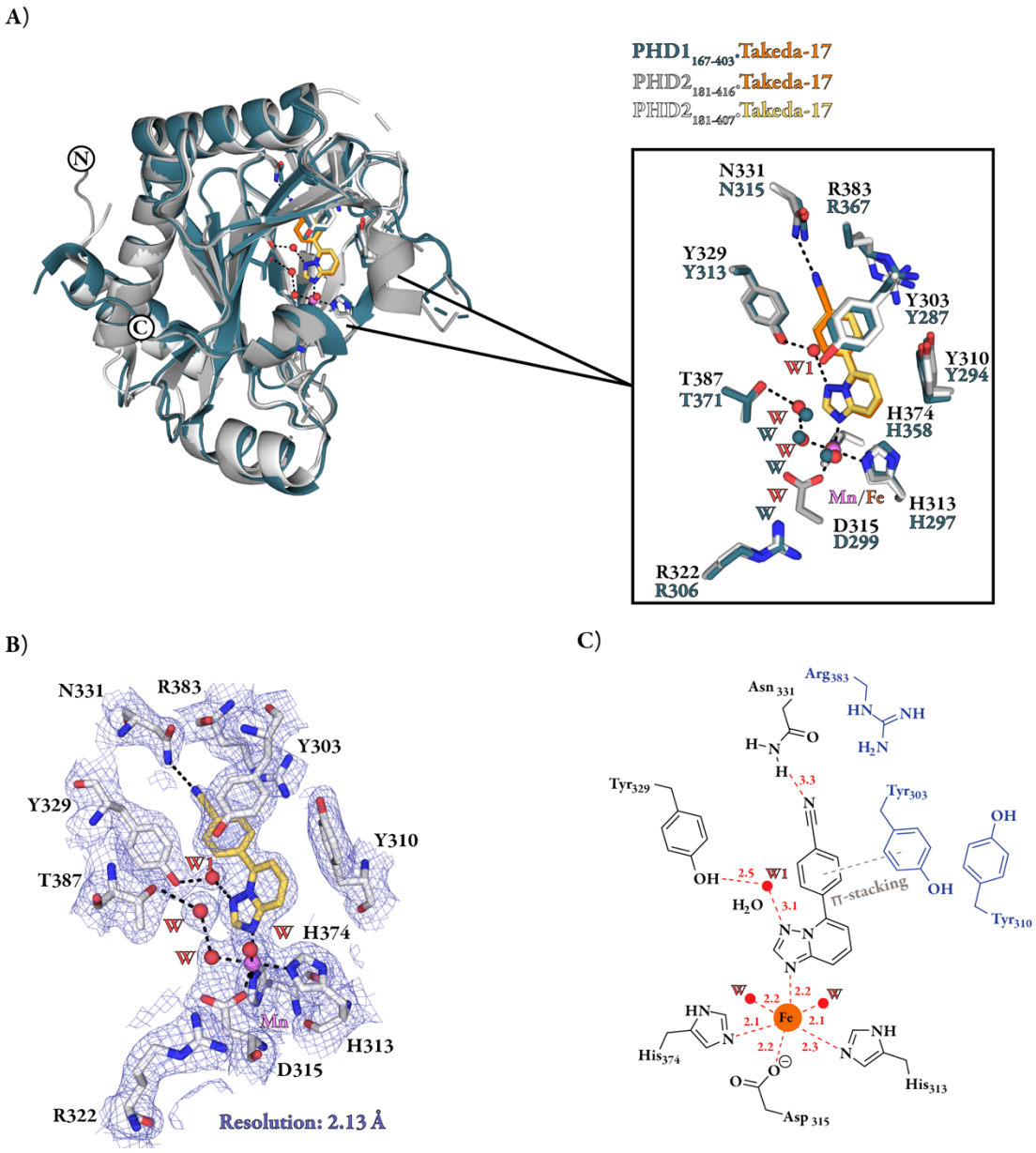


Figure 3-15 | A View from the Active Site of Aligned Complex Structures of PHD1, PHD2$_{181-416}$, and PHD2$_{181-407}$ Complexed with Takeda-17 (17). (A) PHD1, PHD2$_{181-416}$, and PHD2$_{181-407}$ are displayed as cartoons. (A-B) Active site residues (PHD1-teal, PHD2$_{181-416}$-grey, PHD2$_{181-407}$-white) and ligands (**17**-orange and *P* 2$_1$-**17**-light orange) are depicted as sticks. The key active site interactions are represented as dashes (black). (B) The 2mF$_o$-DF$_c$ electron density maps (contoured to 1.0 σ) are illustrated as mesh (blue). (C) A 2D representation of the active site of PHD2$_{181-407/416}$ in complex with **17**. (A-C) Spheres and circles represent water molecules and metal ions (Mn-violet and Fe-orange). Abbreviations: Prolyl hydroxylase isoform 1 and 2 (PHD1 and PHD2), 2-Dimensional (2D). PDB: 5V1B, 5V18, *Xtal-ID*: *T*.

A PHD2$_{181-407}$.**17** complex could be used to compare differences between the published structures of PHD1$_{167-403}$ (PDB: 5V1B) and PHD2$_{181-416}$ (PDB: 5V18, *P* 4$_1$ space group) in complex with **17**.[8] The previously discussed crystal (**3.2.4**) diffracted to a resolution of 2.13 Å (*Xtal-T*, **6.8.6**, **Tables 3-6** and **3-8**). The structural investigation reveals the

monodentate complexation of **17** to PHD2$_{181-407}$ *via* metal ligation of the triazolopyridine N1 atom (**Figure 3-15**).[8] *Xtal-T* complex structure was similar to reported complex structures with the **17** (PDB: 5V1B and 5V18).[8] The benzonitrile functionality was observed to interact *via* its Nδ2 atom with the aminoethanol moieties of Asn315$_{PHD1}$ and Asn331$_{PHD2}$ (**Figure 3-15**).[8] The benzonitrile of **17** also forms a π-π-stacking interaction with the phenol ring of Tyr303, in a manner similar to the triazole containing inhibitors discussed earlier (**3.2.4.1**, **Figure 3-15**).[8]

Overall, there are no significant conformational changes between the previously reported complex structures of PHD1$_{167-403}$, PHD2$_{181-416}$, and PHD2$_{181-407}$ with **17** (PDB: 5V1B, 5V18, and *Xtal-T*, **Figure 3-15**).[8] The RMSD (calculated in PyMOL™, **6.1**) for both tPHD2.**17** structures was 0.252, thus confirming the above observations. An active site water (W1) interacts *via* a hydrogen bond with the N2 of the triazole ring and the phenolic OH of Tyr329 (**Figure 3-15**).[8] The water molecule is observed in all three of the complex structures and may be useful for further investigations. This work additionally reveals that small-molecules, which bind in a monodentate fashion, can complex in the PHD2$_{181-407}$.Mn(II).succinate crystal form (*Xtal-P,* linked with section **4.3**).

3.3 A Novel PHD2$_{181-407}$ *P* 6$_1$ 2 2 Crystal Form in Complex with Pre-Clinical Candidate ZXJ-1

As the glycinamide containing inhibitors did not complex in the PHD2$_{181-407}$.Mn(II).succinate crystallisation condition (*Xtal-P*, **3.2.4**), a novel system was required to obtain further structural data on carboxylic acid-based PHD inhibitors. A biophysically uncharacterised pre-clinical candidate, ZXJ-1 (**33**), was chosen for a screen of conditions in the Crystal Screen™ I/II (Hampton Research, Corp.) at 1 mM PHD2$_{181-407}$ (two-column

purified batch of protein, **3.2.2**), 1.2 mM Mn(II)Cl_2, and 2.2 mM **33** concentrations (**6.8.7**).[38] Through reported docking and modelling studies of **33** in complex with tPHD2, the chlorobenzene sidechain of the ligand was proposed to target and form π-π-stacking interaction with the guanidinium of Arg322 and T-shaped interaction with the indole of Trp389.[38]

After 1-day of equilibration of the $PHD2_{181-407}$.**33**, a 20 μm x 20 μm x 5 μm crystal with the morphology of a tear drop formed in 0.1 M Tris-HCl pH 8.5 and 2 M ammonium sulfate (*Xtal-U*, **6.8.7**, **Figure 3-16A-B**). A 3.10 Å resolution dataset was collected and reported in a novel *P* 6_1 2 2 space group for $PHD2_{181-407}$ (**Tables 3-7** and **3-8**, **Figure 3-16C**). Unfortunately, the crystal form was not reproducible and 3.10 Å was the highest resolution obtained. The ASU was estimated to contain four-chains, and MR-phasing (**6.6.9.2**) was attempted with the two-chain model used for phasing of the $PHD2_{181-407}$.Mn(II).succinate crystal form (*Xtal-P*). However, the $PHD2_{181-407}$.**33**, *Xtal-U*) structure could not be solved with the previously used two-chain model (**3.2.2**). Again, a truncated model (PDB: 3HQR) was used to solve the structure of *Xtal-U*. A solution was obtained with a translation function Z (TFZ) score of 53.9 and log-likelihood gain (LLG) 4,362.05; a TFZ >8 indicates that the solution is most likely correct.[39] Two dimeric protomers formed *via* interactions between residues $Thr382_{Chain-A}$-$Gln220_{Chain-B}$-$Lys322_{Chain-B}$ and $Asp231_{Chain-A}$-$Thr382_{Chain-B}$ (**Figure 3-16D**). Although at 3.10 Å resolution, **33** was observed in complex with $PHD2_{181-407}$. A similar interaction forms between the second protomer of chains C and D (**Figure 3-16D**). (*Thank you to Prof. Xiaojin Zhang for providing the ZXJ-1 inhibitor for crystallisation with* $PHD2_{181-407}$.)

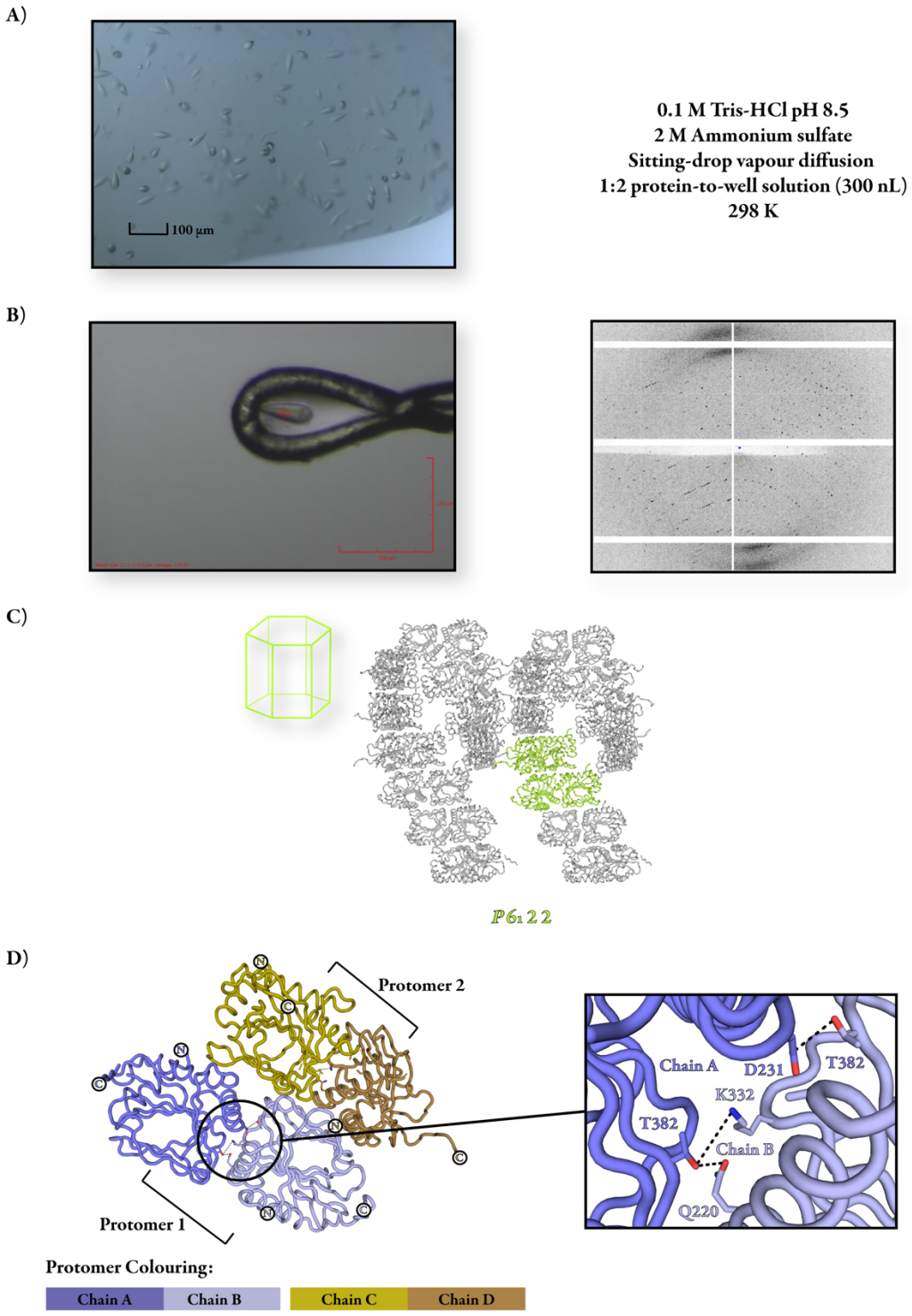


Figure 3-16| Overview of PHD2$_{181-407}$ *P* 6$_1$ 2 2 Crystal Form with the Pre-Clinical Candidate ZXJ-1 (33). (A) Crystallisation condition and tear drop morphology crystals of PHD2$_{181-407}$.Mn(II).**33**. (B) A mounted crystal of PHD2$_{181-407}$.Mn(II).**33** (*Xtal-U*) and detector image (Eiger2 XE 16M, I04 Beamline-Diamond Light Source Ltd.). (C) The crystal packing of PHD2$_{181-407}$ in *P* 6$_1$ 2 2 space group in the hexagonal system. The chains of the asymmetric unit (lemon) and symmetry-related chains (grey) are displayed as a cartoon. (D) Inter-chain interaction of the 2-chain protomers of the asymmetric unit are depicted as cartoons and colour based on pairs (chains A-B-blue and chains C-D-olive). A view from the protomer electrostatic interactions is illustrated with the residue sidechains shown as sticks (chain A-slate and chain-B-light blue) and key interactions displayed as dashes (black). Abbreviations: Prolyl hydroxylase isoform 2 (PHD2). *Xtal-ID*: *U*.

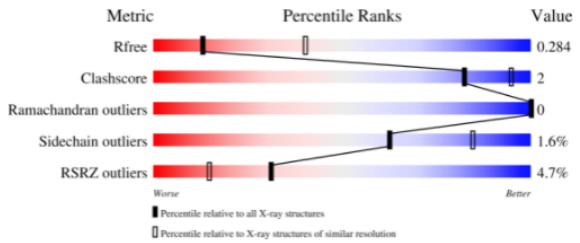
Table 3-7| Crystallographic Data Processing and Refinement Statistics (*Xtal-U*).

	$PHD2_{181-407}$.ZXJ-1 (*Xtal-U*)
Beamline	Diamond Light Source-I04
Detector	Dectris Eiger2 XE 16M
Data Processing	Xia2 DIALS
Wavelength (Å)	0.9795
Resolution range (Å)	19.99 - 3.10 (3.20 - 3.10)
Space group	*P* 6_1 2 2
Unit cell (Å, °)	117.79 117.79 384.17 90 90 120
Total reflections	1117615 (114115)
Unique reflections	29521 (2851)
Multiplicity	37.9 (40.0)
Completeness (%)	99.15 (98.88)
Mean I/sigma(I)	3.64 (0.44)
Wilson B-factor (Å²)	97.62
R-merge†	1.354 (20.44)
R-meas	1.372 (20.7)
R-pim	0.2214 (3.239)
CC1/2	0.994 (0.563)
CC*	0.999 (0.849)
Reflections used in refinement	29521 (2819)
Reflections used for R-free	1436 (148)
R-work✧	0.2551 (0.3922)
R-free✧	0.2851 (0.3719)
CC(work)	0.945 (0.641)
CC(free)	0.915 (0.469)
Number of non-hydrogen atoms	6130
macromolecules	6006
ligands	157
solvent	15
Protein residues	789
RMS(bonds, Å)	0.003
RMS(angles, °)	0.62
Ramachandran favored (%)	95.47
Ramachandran allowed (%)	4.53
Ramachandran outliers (%)	0.00
Rotamer outliers (%)	1.22
Clashscore	2.58
Average B-factor (Å²)	104.89
macromolecules	105.03
ligands	98.02
solvent	100.25
Number of TLS groups	13

Single crystal diffraction data was collected from samples held at 100 K with conventional, rotation-based methods. Ligands: Mn, ZXJ-1, and Cl. Statistics for the highest-resolution shell are shown in parentheses.

† R-merge (or Rsym) is equal to $\sum|I-\langle I\rangle|/\sum I$. R-merge represents the data quality of merged reflection data. *I* is equal to the intensity of individual measurements and <I> is equal to the average of multiple measurements. ✧R_{free} is the R_{factor} for 5% of the reflections which are excluded during refinement.

R_{factor} is equal to $\sum_{hkl}||Fobs(_{hkl})| - |Fcalc(_{hkl})||/\sum_{hkl}|Fobs(_{hkl})|$ and was calculated for the working set of reflections (R_{work}). **Appendix I** contains the *Xtal-ID*. The validation heat map was generated with PDB validation service.



The structural analysis reveals complexation of **33** with $PHD2_{181-407}$ active site metal *via* the N1 atom of the pyridine (*trans* to His374 ε-N2, *Xtal-U*, **Figure 3-17A-B**).[38] Similarly to the binding of Vadadustat (**23**), the **33** glycinamide carbonyl oxygen coordinates Mn (*trans* to Asp315 Oδ1, PDB: 5OX6, **Figure 3-17-C**).[7,38] The pyridine of **33** is observed to form a π-π-stacking interaction with the phenolic sidechain of Tyr310 (**Figure 3-17A-B**).[38] The carboxylate of **33** sidechain interacts with the guanidino group of Arg383 and the phenolic sidechain of Tyr329 (**Figure 3-17A-B**).[38]

However, there is a slight shift in the conformation of the glycinamide sidechain of **33** (*Xtal-U*) when aligned with the Vadadustat complex (PDB: 5OX6, **Figure 3-17**).[7] The bond distances between the **33** carboxylate and NH(2) atoms of Arg383 are 2.31 Å and 3.61 Å for chain C (*Xtal-U*, **Figure 3-17B**).[38] Whereas, in the $PHD2_{181-426}$.**23** complex, the observed distances are 2.70 Å and 2.90 Å to the NH(2) atoms of Arg383 (PDB: 5OX6, **Figure 3-17C**).[7] The observed variations in bond length may reflect the lower resolution of the *Xtal-U* structure, but could also be a consequence of different pHs used in both crystallisation conditions (pH 8.5-ZXJ-1 and pH 6.5-Vadadustat; PDB: 5OX6).[7,38] Overall, the results may reflect insights into the active site chemistry of tPHD2 at different pHs, but this work needs further validation through solution studies.

The pyridine core of **33** is positioned to form a hydrogen bond interaction with Tyr303 and forms a π-π-stacking interaction with the aromatic sidechain of Tyr310 similar to Vadadustat (*Xtal-U* and PDB: 5OX5, **Figure 3-16A**). The chlorobenzene moiety forms a π-π-stacking interaction with the guanidinium of Arg322 and indole of Trp389 (**Figure 3-17A-B**).[38]

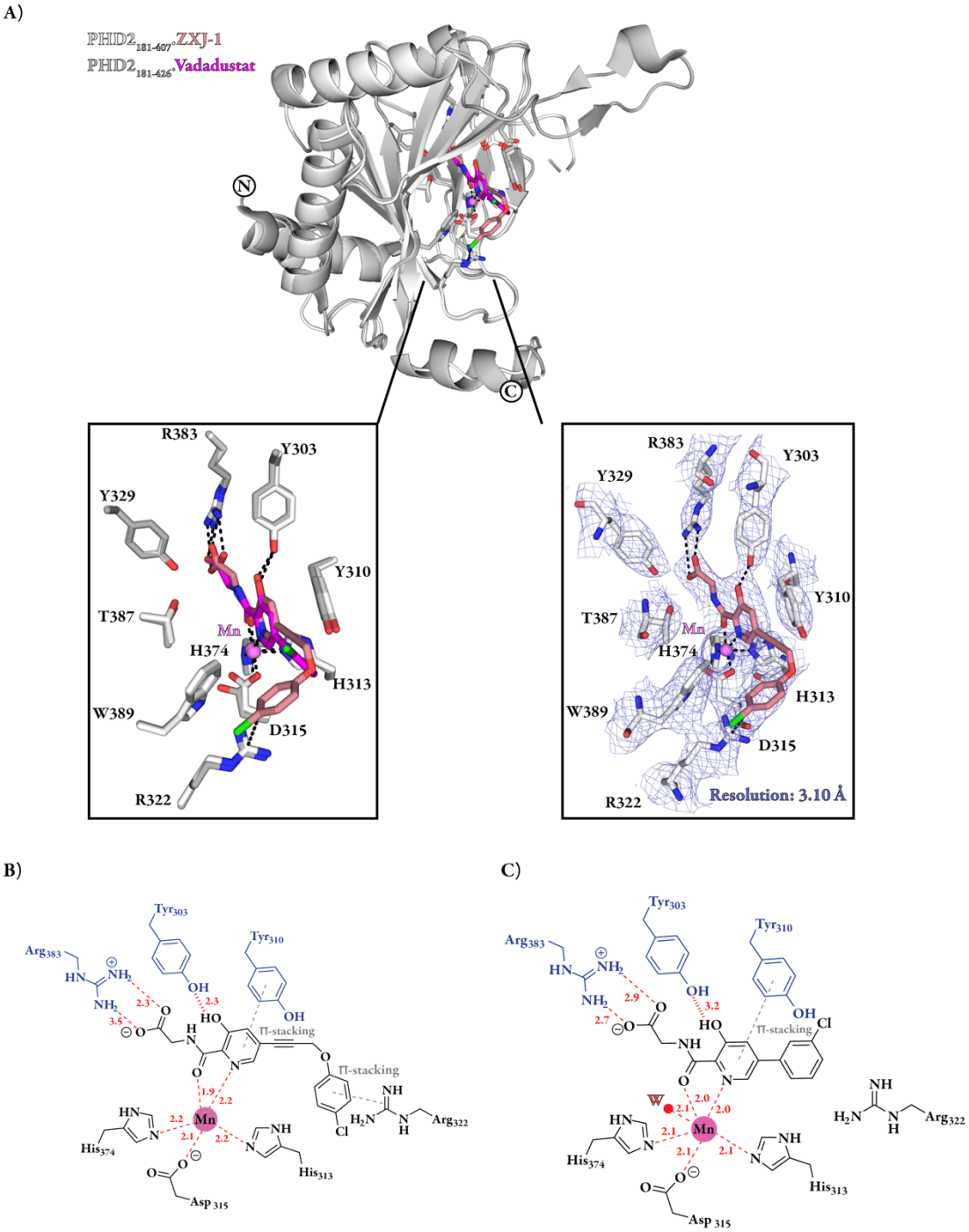


Figure 3-17| A View from Structure of PHD2$_{181-407/426}$ in Complex with ZXJ-1 (33) and Vadadustat (23). (A) Structural alignment of PHD2$_{181-407}$ and PHD2$_{181-426}$ in complex with **33** (*Xtal-U*) and **23** (PDB: 5OX6), respectively. Protein chains are displayed as cartoons (**33**-white and **23**-grey). A close-up view of the active sites depicts key residues as sticks (**33**-white and **23**-grey). Both inhibitors are shown as sticks (**33**-pink and **23**-magenta). Active site interactions are depicted as dashes (black) and spheres are of metal ions (Mn-violet). The 2mF$_o$-DF$_c$ electron density maps (contoured to 1.0 σ) are illustrated as mesh (blue). (B) 2D active site interactions of the PHD2$_{181-407}$ complex with **33** (*Xtal-U*). (C) 2D active site interactions of the PHD2$_{181-426}$ complex with **23** (PDB: 5OX6). Abbreviations: Prolyl hydroxylase isoform 2 (PHD2). PDB: 5OX6. *Xtal-ID*: *U*.

The interaction of **33** with the sidechains of Arg322 and Trp389 are similar to those observed in the complex structures of the 4-hydroxypyrimidines (*e.g.*, **30**) and spiro[4.5]decanones (*e.g.*, **31**) with $PHD2_{181-426}$ (*Xtal-U*, PDB: 4JZR, 6QGV, and 6ST3).[10,11,40]

Structural characterisation of the $PHD2_{181-407}$.Mn(II).ZXJ-1 complex (*Xtal-U*) provides insights into the mode of inhibition of this pre-clinical candidate.[38] Targeting the Arg322-Trp389 active site pocket of PHDs may be a useful tool for future inhibitor design and is likely a target for at least some of the clinically approved inhibitors, such as, Roxadustat (**22**) or Enarodustat (**25**), which both contain conformationally flexible aromatic sidechains.

3.4 The Substrate Binding Induced-Fit-Mechanism by tPHD2‡

Structural and biophysical investigations of the PHDs, including in relation to the mobile β2-β3 finger loop and active site residues Tyr303, Tyr310, and Arg383 have revealed conformational changes on substrate/ligand binding (**Figure 3-18** and **3-19**).[3] Further characterisation of the dynamic features of the PHDs may provide unique solutions for potent inhibition in the future. As the tPHDs sequences manifest the most variation in the β2-β3 finger loop region, development if small-molecule inhibitors targeting this loop may also inhibit other PHD paralogues in an isoform-selective manner (**Figure 3-18** and **3-19**).[3]

‡ Section **3.4** was paraphrased with permission from Figg Jr., W. D.; McDonough, M. A.; Chowdhury, R.; Nakashima, Y.; Zhang, Z.; Holt-Martyn, J. P.; Krajnc, A.; Schofield, C. J. Structural Basis of Prolyl Hydroxylase Domain Inhibition by Molidustat. *ChemMedChem* **2021**, 16 (13), 2082–2088, Open Access, Wiley-VCH. https://doi.org/10.1002/cmdc.202100133. CC BY 4.0 License.

During crystallisation the well conditions can either promote or hinder nucleation of specific protein conformations.[3] Thus, the precise nature of the structure obtained likely reflects the range of conditions used for crystallisation of tPHD2 structures in complex with weak binding ligands to potent inhibitors (**Figures 3-18** and **3-19**).[3]

In the $PHD2_{181-407}$.Mn(II).*P* 2_1-succinate crystal form, the β2-β2 loop (residues 231-253) is disordered between residues 234-253 (**Figure 3-18F**).[3] Partial disorder of the loop is observed in: (i) $PHD2_{181-416}$.2OG-*P* 4_1 (residues 244-249), (ii) $PHD2_{181-426}$.IOX4-A-*P* 3_2 1 2 (residues 232-252), (iii) $PHD2_{181-416}$.Takeda-17-*P* 4_1 (residues 244-254), (iv) $PHD2_{180-392}$.Carboxamide-*H* 3_2 (residues 236-254), (v) $PHD2_{181-392}$.benzimidazole-*P* 2_1 2_1 2_1 (residues 239-250), (vi) $PHD2_{181-407}$.Mn(II).4-hydroxypyrimidines-*P* 2_1 2 2_1 (residues 243-251), (vii) and $PHD2_{181-407}$.Mn(II).ZXJ-1-*P* 6_1 2 2 (residues 236-253, **3.3**) crystal forms (**Figures 3-18B**, **3-19D**, and **3-18E**; and **3-19A-D**, PDB/*Xtal-ID*: 3OUJ, 5A3U, 5V18, 6NMQ, 3OUI, 6ST3, and *U*, respectively).[3,4,8,9,11] In contrast, the $PHD2_{181-426}$.HIF1α-*P* 2_1 2_1 2_1/*P* 2_1 (PDB: 3HQR, 5L9V) and most of the $PHD2_{181-426}$-glycinamide-based inhibitors-*P* 6_3 crystal forms manifest electron density for the residues of the β2-β2 finger loop (**Figure 3-17**).[2,3,6,7,14] The conformation of active site residues Tyr303, Tyr310, Tyr329, and Arg383 were compared with $HIF1\alpha_{558-574}$-CODD substrate, various complexed ligands, and crystal forms (**Figures 3-18**, **3-19,** and **3-20**)[3].

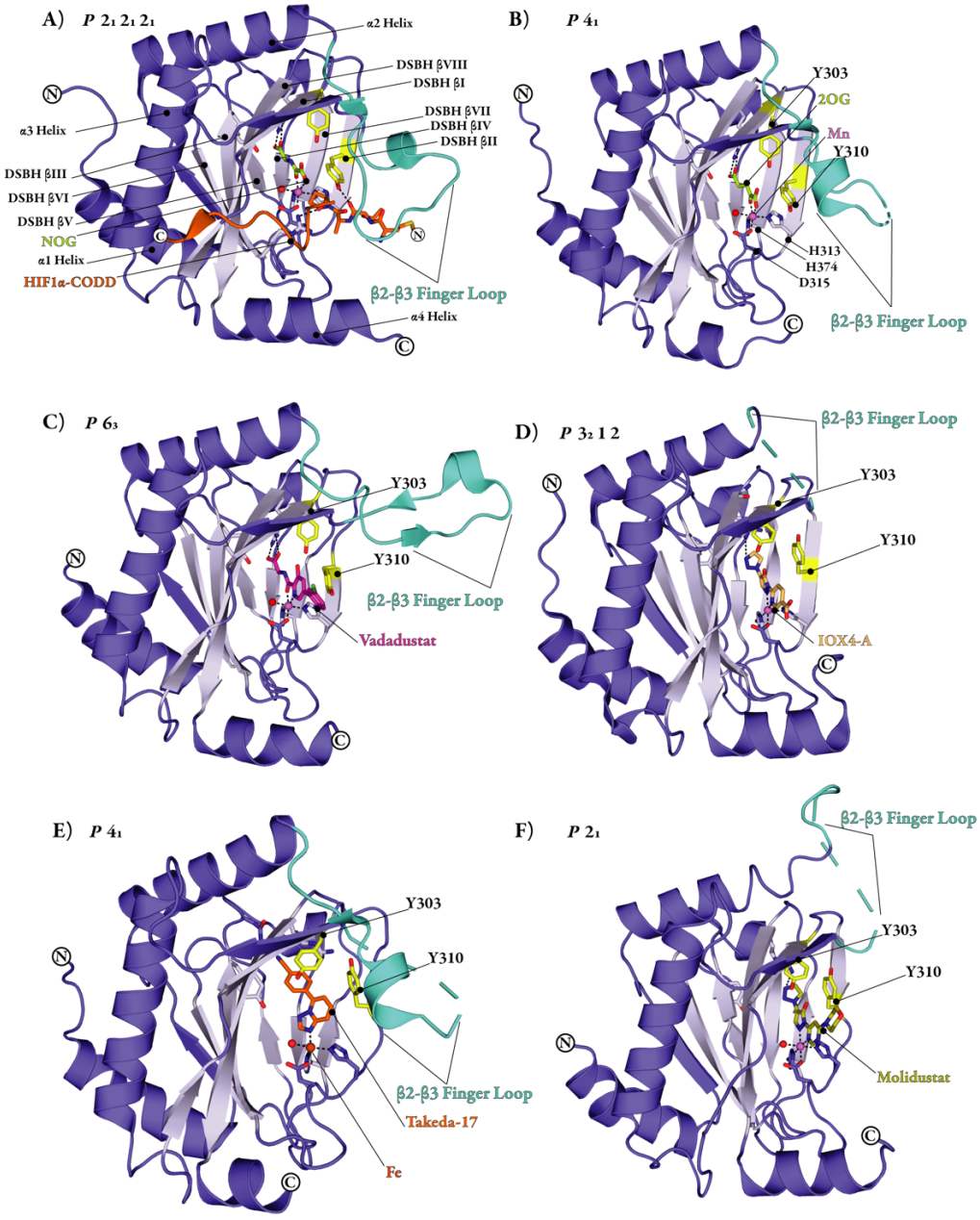


Figure 3-18| An Overview of Variation of the β2-β3 Finger Loop of tPHD2 Between Crystal Forms and Ligands Bound. (A) The *P* 2_1 2_1 2_1 crystal form of $PHD2_{181-426}$ in complex with HIF1α-substrate (cartoon-orange, PDB: 3HQR). (B) *P* 4_1 crystal form of $PHD2_{181-416}$ in complex with 2OG (lemon, PDB: 3OUJ). (C) *P* 6_3 crystal form of $PHD2_{181-426}$ in complex with Vadadustat (magenta, PDB: 5OX6). (D) *P* 3_2 1 2 crystal form in complex with IOX4-A (**34**, tan, acid derivative, PDB: 5A3U). (E) The *P* 41 crystal form of $PHD2_{181-417}$ in complex with Takeda-17 (orange, **17**, PDB: 5V18). (F) The *P* 2_1 crystal form of $PHD2_{181-407}$ in complex with Molidustat (**20**, olive, PDB: 6ZBO). (A-F) tPHD2 (purple) and the β2-β3 finger loop (cyan) are depicted as cartoons. The cartoon DSBH (light blue) is displayed as a cartoon. Active site residues are shown as sticks (purple, light blue, and yellow); yellow residues are Tyr303 and Tyr310 to highlight orientation between crystal forms. Spheres and dashes (black) represent active site waters (red)-metal ions (Mn-violet and Fe-orange) and key interactions, respectively. Broken cartoon dashes indicate the residues are disordered. Abbreviations: Prolyl hydroxylase isoform 2 (PHD2), Hypoxia inducible-factor isoform 1α (HIF1α), and Double-stranded beta-helix (DSBH). PDB: 3HQR, 3OUJ, 5OX6, 5A3U, 5V18, 6ZBO (*Xtal-R*). *Figure edited from Figg Jr., W. D.; McDonough, M. A.; Chowdhury, R.; Nakashima, Y.; Zhang, Z.; Holt-Martyn, J. P.; Krajnc, A.; Schofield, C. J. Structural Basis of Prolyl Hydroxylase Domain Inhibition by Molidustat. ChemMedChem* ***2021****, 16 (13), 2082–2088, Open Access, Wiley-VCH. https://doi.org/10.1002/cmdc.202100133. CC BY 4.0 License.*

Tyr303, Tyr310, and Arg383 are conserved throughout metazoan PHDs and in the bacterial orthologue PPHD.[3,41,42] Tyr303, Tyr310, and Tyr329 are conserved in the active site of CP4H as evidenced by the AlphaFold predicted structure (UniProt: P13674, DeepMind Technologies, Ltd.); the sidechain of Lys510 interacts with the C5 carboxylate of 2OG (discussed in section **3.5**).[43] The induced-fit-mechanism involving of these residues is likely important for catalysis and in the preparation of the PHDs for substrate and/or cosubstrate binding.[3]

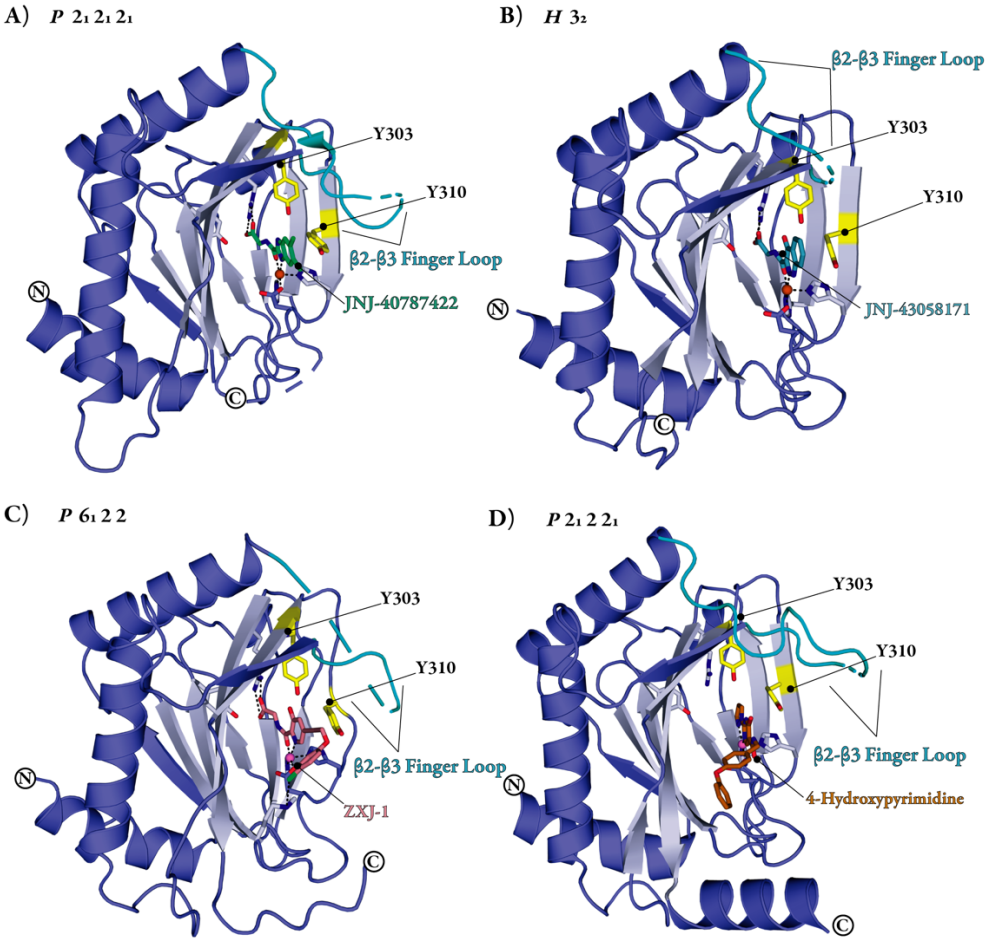


Figure 3-19| A Continued Overview of Variation of the β2-β3 Finger Loop of tPHD2 Between Crystal Forms and Ligands Bound. (A) The *P* 2_1 2_1 2_1 crystal form of $PHD2_{181-392}$ in complex with in complex (PDB: 3OUI). (B) *H* 3 2 crystal form of $PHD2_{180-392}$ in complex with JNJ-43058171 (teal, PDB: 6NMQ). (C) *P* 6_1 2 2 crystal form of $PHD2_{181-407}$ in complex with ZXJ-1(pink). (D) *P* 2_1 2 2_1 crystal form of $PHD2_{181-407}$ in complex with a 4-hydroxypyrimidine (rust, PDB: 6ST3). (A-D) tPHD2 (purple) and the β2-β3 finger loop (cyan) are depicted as cartoons. The cartoon DSBH (light blue) is displayed as a cartoon. Active site residues are shown as sticks (purple, light blue, and yellow); yellow residues are Tyr303 and Tyr310 to highlight orientation between crystal forms. Spheres and dashes (black) represent active site waters (red)-metal ions (Mn-violet and Fe-orange) and key interactions, respectively. Abbreviations: Truncated prolyl hydroxylase isoform 2 (tPHD2), Double-stranded beta-helix (DSBH). PDB: 3OUI, 6NMQ, 6ST3. *Xtal-ID*: *U. The figure was adapted from Figg Jr, W.D., et al., ChemMedChem* ***2021****.*

Together the Tyr303, Tyr310, and Arg383 active site and other residues (*e.g.*, *C*-terminal and β2-β3 finger loop residues) are involved in a dynamic induced-fit process during HIFα-substrate complexation to tPHD2; as evidenced by both crystallographic and NMR studies (**Figure 3-20**).[3,5–7,14,26] The conformational changes of active site residues imply a role for induced-fit motion upon 2OG and 2OG competing inhibitor binding to tPHD2 (**Figure 3-20**).[3] Recent investigation of Y303A, Y310F, and Y329F mutants revealed the importance of these residues for binding of a monocyclic Fe(II) inhibitor, with reduced binding observed in the Y303A and Y310F variants.[44]

Although the full details of the tPHDs dynamics remain to be solved, these conformational changes likely contribute to the ordered sequential mechanism of catalysis and pre-organisation of tPHD2's active site for HIFα-substrate complexation as prior 2OG binding promotes ODD binding (**Figure 3-20**).[3,6,14,26] It is notable that the extent of the β2-β3 finger loop disorder and conformation plays a key role in productive substrate binding with variation throughout the 2OG-competetive inhibitor complexes.[3] With growing structural data on tPHD2, it seems likely that the mobile nature of the β2-β3 finger loop (potentially other regions), are involved in the substrate binding induced-fit and are linked to changes in the 2OG pocket region *via* correlated motions. A better insight into dynamic motions may provide answers as to the extent of substrate displacement by Molidustat (**20**) and IOX4 (**28**) as evidenced by NMR studies (**Figure 3-20**).[3,5,7]

Further biophysical characterisation of tPHD2, coupled with more detailed in-depth characterisation of PHD1 and PHD3, may potentially aid an improved inhibitor design in the future with scope for exploiting the ability of Tyr303, Tyr310, and Arg383 to adopt different conformations; indeed at least one inhibitor has been shown to specifically target the conformation of Tyr310, *i.e.*, JPHM-2-167 (**30**, PDB: 6QGV,

Figure 3-20D).[3,10] It is possible that the potential differences in the substrate interacting loop and active site dynamics vary between the PHDs and CP4H enzymes could provide a target for isoform-selective and specific inhibitors.[3]

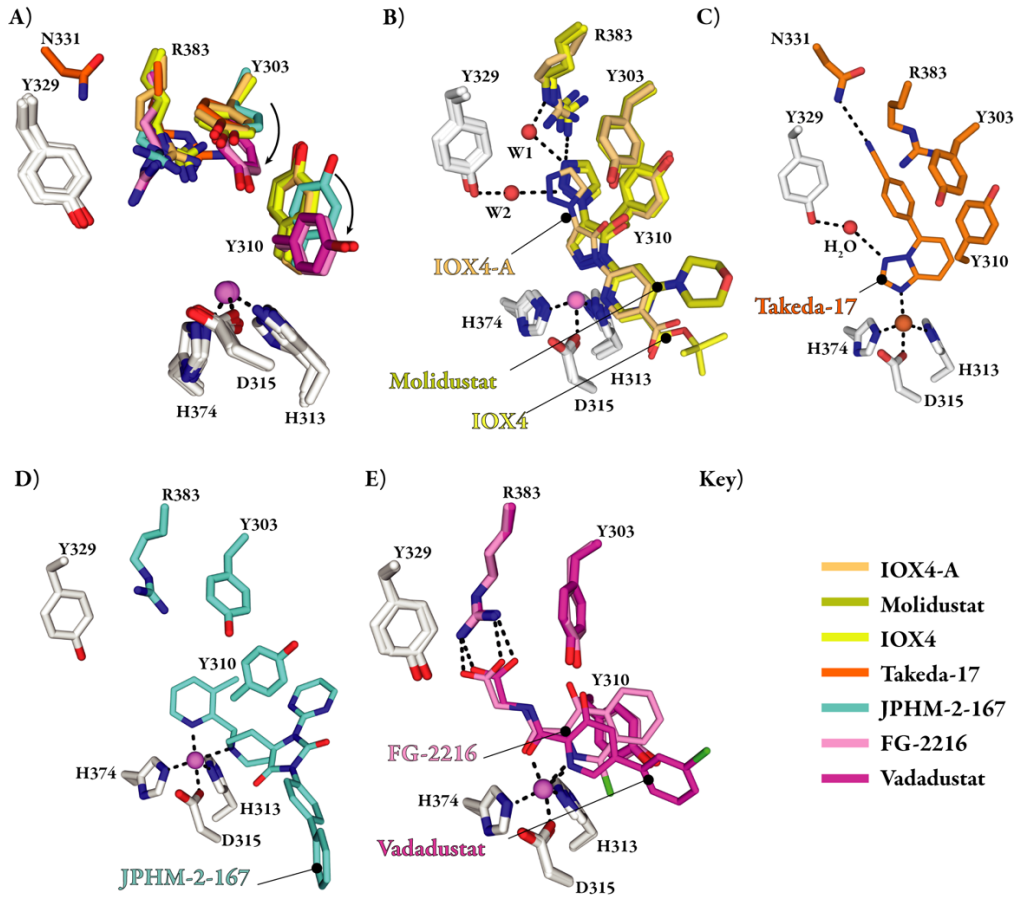


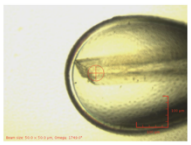
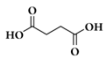
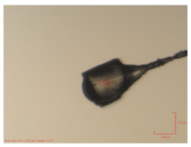
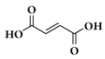
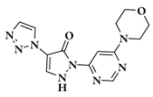
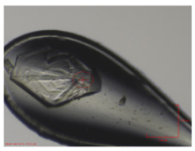
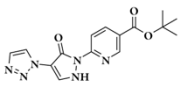
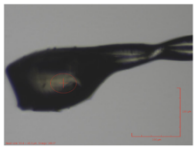
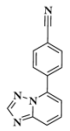
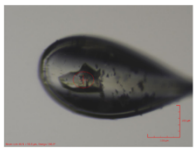
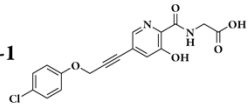
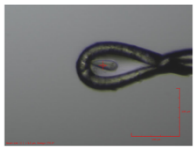
Figure 3-20| A View of tPHD2's Active Site Residues Induced-Fit Mechanism Between Various Complex Structures. (A) Alignment of complex structures of PHD2 and depiction of the sidechains of active site residues Tyr303, Tyr310, and Arg383 (coloured based on the ligand in complex, Key). (B) $PHD2_{181-407/426}$ in complex with inhibitors with a triazole sidechain (Molidustat (**20**)-olive, IOX4 (**28**)-yellow, and IOX4-A (**34**)-light orange; PDB: 6ZBO, 6ZBN, and 5A3U, respectively). (C) Structure of $PHD2_{181-416}$ in complex with Takeda-17 (PDB: 5V18). (D) The complex structure of $PHD2_{181-407}$ and spiro[4.5]decanone, JPHM-2-167 (PDB: 6QGV). (E) The complex structure of $PHD2_{181-426}$ with glycinamide-containing inhibitors (PDB: 5OX6-Vadadustat and PDB: 4BQX-FG-2216). (A-E) Static (white) and dynamic (coloured based on bound ligand, Key) active site residues are displayed as sticks. The inhibitors are depicted as sticks (coloured based on the Key in coordination with dynamic residues). Abbreviations: Prolyl hydroxylase isoform 2 (PHD2). PDB: 4BQX, 5A3U, 5OX6, 5V18, 6QGV, 6ZBN (or *Xtal-S*), 6ZBO (or *Xtal-R*). *The figure was edited from Figg Jr., W. D.; McDonough, M. A.; Chowdhury, R.; Nakashima, Y.; Zhang, Z.; Holt-Martyn, J. P.; Krajnc, A.; Schofield, C. J. Structural Basis of Prolyl Hydroxylase Domain Inhibition by Molidustat. ChemMedChem* ***2021****, 16 (13), 2082–2088, Open Access, Wiley-VCH. https://doi.org/10.1002/cmdc.202100133. CC BY 4.0 License.*

3.5 Summary and Future Directions

Using three novel crystallisation systems in two different space groups (*P* 2_1 and *P* 6_1 2 2), seven new $PHD2_{181-407/426}$ complex structures were obtained (**Table 3-8**) and solved. The structures provide a better insight into the observed dynamics of the β2-β3 finger loop; from binding into the neighbouring chain active site *via* Asp250 in the $PHD2_{181-426}$.Mn complex (*Xtal-O*) to complete disordering in the *P* 2_1-succinate crystal form (*Xtal-P*). Both $PHD2_{181-407}$ succinate (*Xtal-P*) and FUM (*Xtal-Q*) complexes provide insight into the binding modes of these tricarboxylic acid (TCA)-cycle intermediates (**Figure 3-21**).

Both succinate and fumarate ligands in the *Xtal-P* and *Xtal-Q* complexes, respectively, exhibit an apparently closer interaction with the Tyr329 phenolic sidechain than the guanidinium of Arg383, as evidenced by comparisons with *Xtal-M* (Product 1) and *Xtal-N* (Product 2) structures, respectively, **Figure 3-21**). The electrostatic binding of both succinate and fumarate C4 carboxylate and the NH(2) atom of Arg383 may be involved in the order sequential mechanism of tPHD2 upon 2OG binding. The interaction could potentially be a release/ejection mechanism of succinate and hydroxylated HIFα-product and is likely coupled to the induced-fit mechanism of Tyr303-Tyr310-Arg383-β2/β3 loop dynamics (as discussed in section **3.4**).[3] In comparison to succinate, FUM interacts with the alcohol sidechain of Thr387. FUM is observed to disrupt the hydrogen bond network of waters in the active site from Thr387 to the metal bound water that is typically observed in tPHD2 complex structures (**Figure 3-21**, discussed in section **2.1**).

Table 3-8| Harvested Crystals from Co-Crystallised Complex Structures of $PHD2_{181-407}$.

Crystal ID	Structure	Mount	Beamline	Res (Å)	Incub. (Min)	Cryo-protectant
$PHD2_{181-426}$-Mn *Xtal-O*			I04-1	2.97	10	Glycerol
$PHD2_{181-407}$-SIN *Xtal-P*			I03	1.90	5	DMSO
$PHD2_{181-407}$-FUM *Xtal-Q*			Proxima-1	2.34	5	Glycerol
$PHD2_{181-407}$-Molidustat *Xtal-R*			I04	1.79	30	Glycerol
$PHD2_{181-407}$-IOX4 *Xtal-S*			I04	2.01	30	Glycerol
$PHD2_{181-407}$-Takeda-17 *Xtal-T*			I04	2.13	30	Glycerol
$PHD2_{181-407}$-ZXJ-1 *Xtal-U*			I04	3.10	15	Glycerol

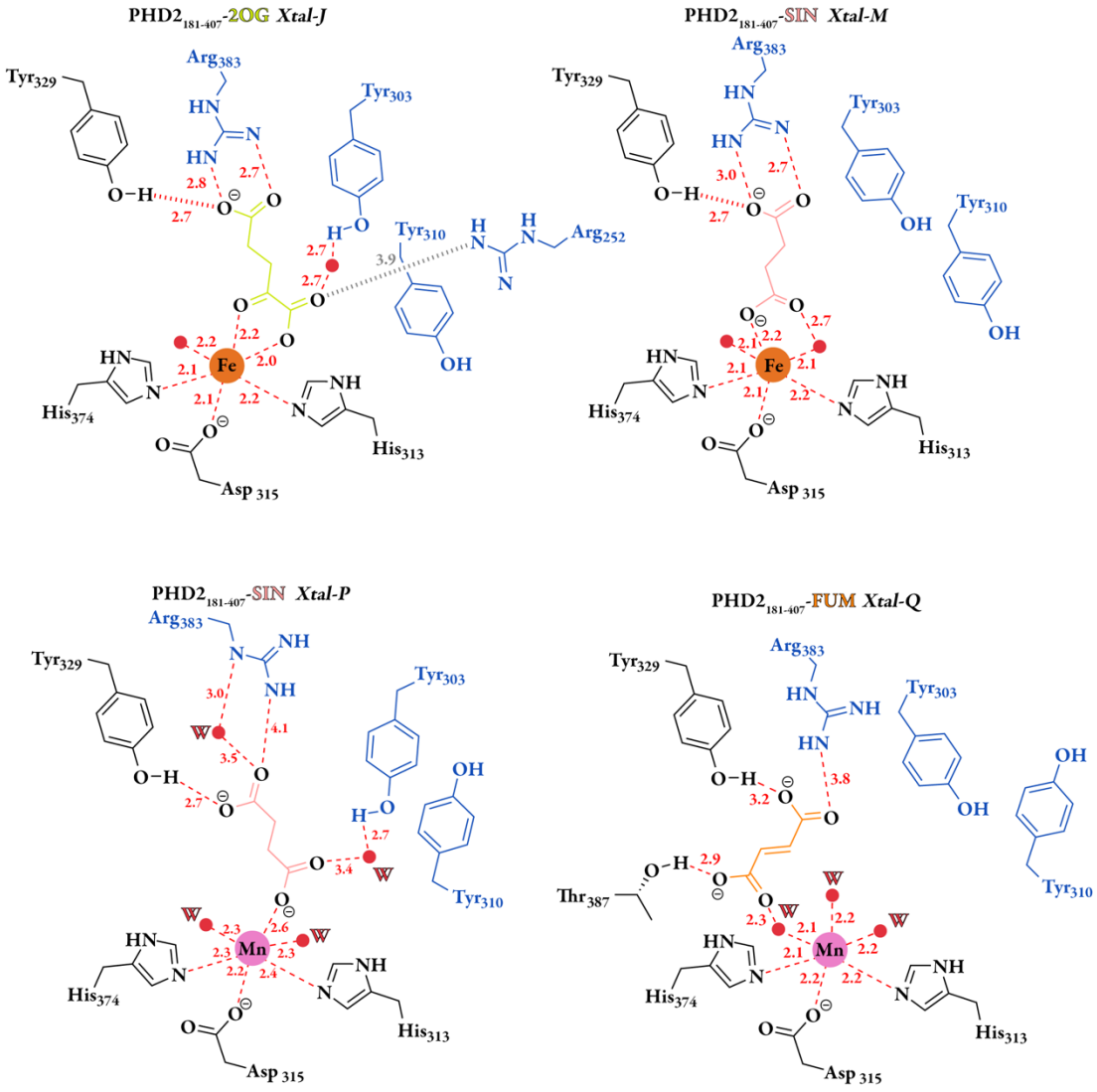


Figure 3-21| 2D Depiction of the PHD2$_{181-407}$ Active site in Complex with 2OG (Anaerobic), SIN (O_2-Exposed), SIN (Condition), and FUM (Condition). The ligands (2OG-yellow, SIN-salmon, SCN-lime, and FUM-orange) and key dynamic active site residues (blue) are coloured. Metal ions (Fe-orange and Mn-violet) and water molecules (red) are displayed as spheres. Important interactions are represented by dashes (red or grey). Abbreviations: Prolyl hydroxylase isoform 2 (PHD2), 2-Oxoglutarate (2OG), Succinate (SIN), Fumarate (FUM). *Xtal-IDs*: *J*, *M*, *P*, *Q*.

Structures of PHD2$_{181-407}$ in complex with the clinically relevant inhibitor (Molidustat, **20**), a related brain-penetrating analogue (IOX4, **28**), a non-conventional monodentate inhibitor (**17**), and a pre-clinical candidate (ZXJ-1, **33**) were successfully determined (*Xtal-R-U*). The previously uncharacterised active site water interactions in the *Xtal-R* (**20**) and *Xtal-S* (**28**) structures apparently revealed the triazole functionality does not simply exchange for the carboxylic acid moiety of the isoquinoline inhibitors (*e.g.*, **21**) .[3,8,38] The morpholine group of Molidustat (**20**, through an indirect water molecule), the *tert*-butyl

ester group of IOX4 (**28**), and the chlorobenzene group of ZXJ-1 (**33**) interact with the guanidinium moiety of Arg322. The *Xtal-T* structure in complex with Takeda-17 (**17**) was observed to have an RMSD of 0.252 when compared with a reported structure of $PHD2_{181-417}$.**17** (*P* 4_1, PDB: 5V18), *i.e.*, indicating the structures are comparable with no significant conformational changes observed.[8]

The phenolic sidechains of Tyr303 and Tyr310 are in different conformations in the $PHD2_{181-407}$.Mn(II).succinate crystal form (*Xtal-P*) when compared to the tPHD2-glycinamide-containing complex structures (PDB: 2G1M and 5OX6). The *Xtal-P* crystal form apparently cannot accommodate the carboxylic acid-based inhibitors. Thus, new conditions are being explored to obtain complex structures of $PHD2_{181-407}$ with Roxadustat (**22**) and Daprodustat (**24**). Currently, there are hit conditions with 1 mM $PHD2_{181-407}$, 2.4 mM Zn(II)Cl_2, 2.2 mM inhibitor, and 6 mM deoxycholic acid detergent that have produced rod morphology crystals of a *C* 2 space group (a=269.21 Å, b=97.67 Å, c=186.61 Å, β=129.34°) and an estimated 17-chain ASU. The crystals unfortunately diffracted to a resolution of 3.5 Å (in most cases 5-6 Å resolutions). Optimisation of the crystal form is required; either through (i) changing the cryo-protectant (attempted 20% (v/v) glycerol, 35% (v/v) ethylene glycol, and (20% (v/v) PEG 400), (ii) potentially crystal humidity control to reduce the size of the ASU, (iii) or room-temperature/*in situ* diffraction.[45]

As previously mentioned (section **3.4**), knowledge of how ligands bind may help understand modulation of dynamic active site features and can potentially provide ideas for the design of more potent PHD inhibitors.[10] The recent creation of AlphaFold Protein Structure Database (DeepMind Technologies, Ltd. and European Molecular Biology Laboratory-European Bioinformatics Institute, EMBL-EBI) has allowed researchers another tool to investigate the structures of previously uncharacterised proteins through

modelling of experimental data.[43] Comparison of the AlphaFold predicted model of CP4H suggests high structural conservation of the active site residues when superimposed with $PHD2_{181-426}$ (PDB: 5OX6, **Figure 3-22**).[43] The variation of residues observed between the aligned model of CP4H and $PHD2_{181-426}$ included (i) $Arg383_{PHD2}$-$Lys510_{CP4H}$, (ii) $Thr387_{PHD2}$-$Asn514_{CP4H}$, (iii) $Asn311_{PHD2}$-$Ser458_{CP4H}$, and (iv) $Asp254_{PHD2}$-$Ser381_{CP4H}$ (**Figure 3-22**, PDB: 5OX6).[7,43]

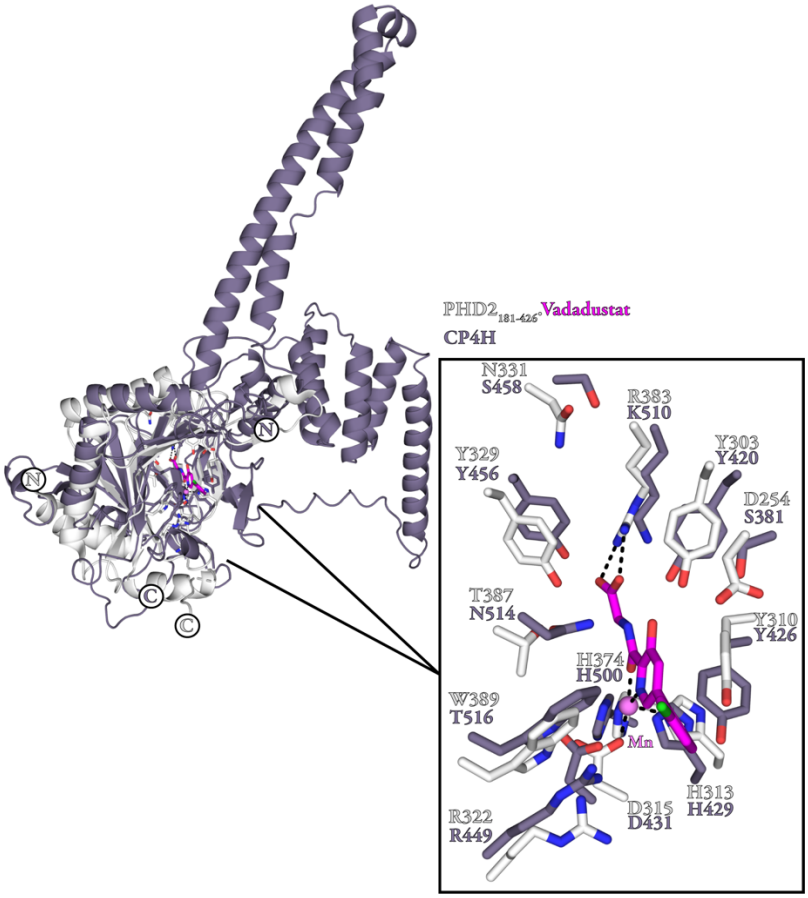


Figure 3-22| Structural Alignment of AlphaFold Predicted Collagen P4H and $PHD2_{181-426}$ with a View of the Active Site Residues. Both CP4H and $PHD2_{181-426}$ are depicted as cartoons. The active site residues (PHD2-white and CP4H-purple) and ligands are displayed as sticks (magenta). The metal ion of PHD2 is shown as a sphere (Mn-violet). Key active site interactions are represented as dashes (black). Abbreviations: Collagen prolyl-4-hydroxylase (CP4H), Prolyl hydroxylase isoform 2 (PHD2). PDB: 5OX6. AlphaFold Uniprot: P13674.

High levels of structural conservation indicates that some of the PHD inhibitors are likely not specific and could potentially inhibit CP4H (**Figure 3-22**, PDB: 5OX6).[7,43] Future work should therefore focus on the design of novel inhibitors that target regions other

than the 2OG binding pocket and exploit various distinct features of the PHDs in order to facilitate a more potent and selective inhibition. Thus, an XChem fragment-based and soaking-based screens of small-molecule fragments and derivatives of Takeda-17 (**17**), respectively, were conducted. Structure-guided drug discovery approach was utilised as a means to explore novel scaffolds that target the active site, discover potential allosteric binding pockets (as seen in reported complex structures PDB: 2Y34 and 3OUI), and investigate orthosteric pockets with derivatives of Takeda-17 (**17**, discussed in Chapter **4**).[4,8,46]

3.6 References

(1) McDonough, M. A.; Li, V.; Flashman, E.; Chowdhury, R.; Mohr, C.; Liénard, B. M. R.; Zondlo, J.; Oldham, N. J.; Clifton, I. J.; Lewis, J.; McNeill, L. A.; Kurzeja, R. J. M.; Hewitson, K. S.; Yang, E.; Jordan, S.; Syed, R. S.; Schofield, C. J. Cellular Oxygen Sensing: Crystal Structure of Hypoxia-Inducible Factor Prolyl Hydroxylase (PHD2). *Proceedings of the National Academy of Sciences of the United States of America* **2006**, *103* (26), 9814–9819. https://doi.org/10.1073/pnas.0601283103.

(2) Chowdhury, R.; Candela-Lena, J. I.; Chan, M. C.; Greenald, D. J.; Yeoh, K. K.; Tian, Y. M.; McDonough, M. A.; Tumber, A.; Rose, N. R.; Conejo-Garcia, A.; Demetriades, M.; Mathavan, S.; Kawamura, A.; Lee, M. K.; van Eeden, F.; Pugh, C. W.; Ratcliffe, P. J.; Schofield, C. J. Selective Small Molecule Probes for the Hypoxia Inducible Factor (HIF) Prolyl Hydroxylases. *ACS Chemical Biology* **2013**, *8* (7), 1488–1496. https://doi.org/10.1021/cb400088q.

(3) Figg Jr., W. D.; McDonough, M. A.; Chowdhury, R.; Nakashima, Y.; Zhang, Z.; Holt-Martyn, J. P.; Krajnc, A.; Schofield, C. J. Structural Basis of Prolyl Hydroxylase Domain Inhibition by Molidustat. *ChemMedChem* **2021**, *16* (13), 2082–2088. https://doi.org/10.1002/cmdc.202100133.

(4) Rosen, M. D.; Venkatesan, H.; Peltier, H. M.; Bembenek, S. D.; Kanelakis, K. C.; Zhao, L. X.; Leonard, B. E.; Hocutt, F. M.; Wu, X.; Palomino, H. L.; Brondstetter, T. I.; Haugh, P. v.; Cagnon, L.; Yan, W.; Liotta, L. A.; Young, A.; Mirzadegan, T.; Shankley, N. P.; Barrett, T. D.; Rabinowitz, M. H. Benzimidazole-2-Pyrazole HIF Prolyl 4-Hydroxylase Inhibitors as Oral Erythropoietin Secretagogues. *ACS Medicinal Chemistry Letters* **2010**, *1* (9), 526–529. https://doi.org/10.1021/ml100198y.

(5) Chan, M. C.; Atasoylu, O.; Hodson, E.; Tumber, A.; Leung, I. K. H.; Chowdhury, R.; Gómez-Pérez, V.; Demetriades, M.; Rydzik, A. M.; Holt-Martyn, J.; Tian, Y. M.; Bishop, T.; Claridge, T. D. W.; Kawamura, A.; Pugh, C. W.; Ratcliffe, P. J.; Schofield, C. J. Potent and Selective Triazole-Based Inhibitors of the Hypoxia-Inducible Factor Prolyl-Hydroxylases with Activity in the Murine Brain. *PLoS ONE* **2015**, *10* (7), e0132004. https://doi.org/10.1371/journal.pone.0132004.

(6) Chowdhury, R.; Leung, I. K. H.; Tian, Y. M.; Abboud, M. I.; Ge, W.; Domene, C.; Cantrelle, F. X.; Landrieu, I.; Hardy, A. P.; Pugh, C. W.; Ratcliffe, P. J.; Claridge, T. D. W.; Schofield, C. J. Structural Basis for Oxygen Degradation Domain Selectivity of the HIF Prolyl Hydroxylases. *Nature Communications* **2016**, *7* (1), 12673. https://doi.org/10.1038/ncomms12673.

(7) Yeh, T.-L.; Leissing, T. M.; Abboud, M. I.; Thinnes, C. C.; Atasoylu, O.; Holt-Martyn, J. P.; Zhang, D.; Tumber, A.; Lippl, K.; Lohans, C. T.; Leung, I. K. H.; Morcrette, H.; Clifton, I. J.; Claridge, T. D. W.; Kawamura, A.; Flashman, E.; Lu, X.; Ratcliffe, P. J.; Chowdhury, R.; Pugh, C. W.; Schofield, C. J. Molecular and Cellular Mechanisms of HIF Prolyl Hydroxylase Inhibitors in Clinical Trials. *Chemical Science* **2017**, *8* (11), 7651–7668. https://doi.org/10.1039/C7SC02103H.

(8) Ahmed, S.; Ayscough, A.; Barker, G. R.; Canning, H. E.; Davenport, R.; Downham, R.; Harrison, D.; Jenkins, K.; Kinsella, N.; Livermore, D. G.; Wright, S.; Ivetac, A. D.; Skene, R.; Wilkens, S. J.; Webster, N. A.; Hendrick, A. G. 1,2,4-Triazolo-[1,5-a]Pyridine HIF Prolylhydroxylase Domain-1 (PHD-1) Inhibitors with a Novel Monodentate Binding Interaction. *Journal of Medicinal Chemistry* **2017**, *60* (13), 5663–5672. https://doi.org/10.1021/acs.jmedchem.7b00352.

(9) Bembenek, S. D.; Venkatesan, H.; Peltier, H. M.; Rosen, M. D.; Barrett, T. D.; Kanelakis, K. C.; Palomino, H. L.; Brondstetter, T. I.; Mirzadegan, T.; Rabinowitz, M. H. Beyond Traditional Structure-Based Drug Design: The Role of Iron Complexation, Strain, and Water in the Binding of Inhibitors for Hypoxia-Inducible Factor Prolyl Hydroxylase 2. *ACS Omega* **2019**, *4* (4), 6703–6708. https://doi.org/10.1021/acsomega.9b00199.

(10) Holt-Martyn, J. P.; Tumber, A.; Rahman, M. Z.; Lippl, K.; Figg, W.; McDonough, M. A.; Chowdhury, R.; Schofield, C. J. Studies on Spiro[4.5]Decanone Prolyl Hydroxylase Domain Inhibitors. *MedChemComm* **2019**, *10* (4), 500–504. https://doi.org/10.1039/c8md00548f.

(11) Holt-Martyn, J. P.; Chowdhury, R.; Tumber, A.; Yeh, T. L.; Abboud, M. I.; Lippl, K.; Lohans, C. T.; Langley, G. W.; Figg, W.; McDonough, M. A.; Pugh, C. W.; Ratcliffe, P. J.; Schofield, C. J. Structure-Activity Relationship and Crystallographic Studies on 4-Hydroxypyrimidine HIF Prolyl Hydroxylase Domain Inhibitors. *ChemMedChem* **2020**, *15* (3), 270–273. https://doi.org/10.1002/cmdc.201900557.

(12) Chowdhury, R.; Abboud, M. I.; McAllister, T. E.; Banerji, B.; Bhushan, B.; Sorensen, J. L.; Kawamura, A.; Schofield, C. J. Use of Cyclic Peptides to Induce Crystallization: Case Study with Prolyl Hydroxylase Domain 2. *Scientific Reports* **2020**, *10* (1). https://doi.org/10.1038/s41598-020-76307-8.

(13) McAllister, T. E.; Yeh, T. L.; Abboud, M. I.; Leung, I. K. H.; Hookway, E. S.; King, O. N. F.; Bhushan, B.; Williams, S. T.; Hopkinson, R. J.; Münzel, M.; Loik, N. D.; Chowdhury, R.; Oppermann, U.; Claridge, T. D. W.; Goto, Y.; Suga, H.; Schofield, C. J.; Kawamura, A. Non-Competitive Cyclic Peptides for Targeting Enzyme-Substrate Complexes. *Chemical Science* **2018**, *9* (20), 4569–4578. https://doi.org/10.1039/c8sc00286j.

(14) Chowdhury, R.; McDonough, M. A.; Mecinović, J.; Loenarz, C.; Flashman, E.; Hewitson, K. S.; Domene, C.; Schofield, C. J. Structural Basis for Binding of Hypoxia-Inducible Factor to the Oxygen-Sensing Prolyl Hydroxylases. *Structure* **2009**, *17* (7), 981–989. https://doi.org/10.1016/j.str.2009.06.002.

(15) Matthews, B. W. Solvent Content of Protein Crystals. *Journal of Molecular Biology* **1968**, *33* (2), 491–497. https://doi.org/10.1016/0022-2836(68)90205-2.

(16) Demetriades, M.; Leung, I. K. H.; Chowdhury, R.; Chan, M. C.; McDonough, M. A.; Yeoh, K. K.; Tian, Y.-M.; Claridge, T. D. W.; Ratcliffe, P. J.; Woon, E. C. Y.; Schofield, C. J. Dynamic Combinatorial Chemistry Employing Boronic Acids/Boronate Esters Leads to Potent Oxygenase Inhibitors. *Angewandte Chemie International Edition* **2012**, *51* (27), 6672–6675. https://doi.org/https://doi.org/10.1002/anie.201202000.

(17) Leung, I. K. H.; Demetriades, M.; Hardy, A. P.; Lejeune, C.; Smart, T. J.; Szöllössi, A.; Kawamura, A.; Schofield, C. J.; Claridge, T. D. W. Reporter Ligand NMR Screening Method for 2-Oxoglutarate Oxygenase Inhibitors. *Journal of Medicinal Chemistry* **2013**, *56* (2), 547–555. https://doi.org/10.1021/jm301583m.

(18) Hewitson, K. S.; Liénard, B. M. R.; McDonough, M. A.; Clifton, I. J.; Butler, D.; Soares, A. S.; Oldham, N. J.; McNeill, L. A.; Schofield, C. J. Structural and Mechanistic Studies on the Inhibition of the Hypoxia-Inducible Transcription Factor Hydroxylases by Tricarboxylic Acid Cycle Intermediates. *Journal of Biological Chemistry* **2007**, *282* (5), 3293–3301. https://doi.org/10.1074/jbc.M608337200.

(19) Liu, H. F.; Ma, J.; Winter, C.; Bayer, R. Recovery and Purification Process Development for Monoclonal Antibody Production. *mAbs* **2010**, *2* (5), 480–499. https://doi.org/10.4161/mabs.2.5.12645.
(20) Chowdhury, R. Structural and Mechanistic Studies on Prolyl Hydroxylases, Oxford University, UK, 2008.
(21) Sheriff, S.; Hendrickson, W. A. Description of Overall Anisotropy in Diffraction from Macromolecular Crystals. *Acta Crystallographica Section A* **1987**, *43* (1), 118–121. https://doi.org/10.1107/S010876738709977X.
(22) Jittam, P.; Ruenwongsa, P.; Panijpan, B. Applying Symmetries of Common Objects to Help Students Understand Stereoselectivity for Apparently Symmetric Substrates. *Bioscience Education* **2008**, *12* (1), 1–8. https://doi.org/10.3108/beej.12.6.
(23) Li, J.; Liao, H. J.; Tang, Y.; Huang, J. L.; Cha, L.; Lin, T. S.; Lee, J. L.; Kurnikov, I. v.; Kurnikova, M. G.; Chang, W. C.; Chan, N. L.; Guo, Y. Epoxidation Catalyzed by the Nonheme Iron(II)- A Nd 2-Oxoglutarate-Dependent Oxygenase, AsqJ: Mechanistic Elucidation of Oxygen Atom Transfer by a Ferryl Intermediate. *Journal of the American Chemical Society* **2020**, *142* (13), 6268–6284. https://doi.org/10.1021/jacs.0c00484.
(24) Davydova, M. P.; Bauer, I. A.; Brel, V. K.; Rakhmanova, M. I.; Bagryanskaya, I. Y.; Artem'ev, A. v. Manganese(II) Thiocyanate Complexes with Bis(Phosphine Oxide) Ligands: Synthesis and Excitation Wavelength-Dependent Multicolor Luminescence. *European Journal of Inorganic Chemistry* **2020**, *2020* (8), 695–703. https://doi.org/10.1002/ejic.201901213.
(25) Quareshy, M.; Shanmugam, M.; Townsend, E.; Jameson, E.; Bugg, T. D. H.; Cameron, A. D.; Chen, Y. Structural Basis of Carnitine Monooxygenase CntA Substrate Specificity, Inhibition, and Intersubunit Electron Transfer. *Journal of Biological Chemistry* **2021**, *296*, 100038. https://doi.org/https://doi.org/10.1074/jbc.RA120.016019.
(26) Abboud, M. I.; Chowdhury, R.; Leung, I. K. H.; Lippl, K.; Loenarz, C.; Claridge, T. D. W.; Schofield, C. J. Studies on the Substrate Selectivity of the Hypoxia-Inducible Factor Prolyl Hydroxylase 2 Catalytic Domain. *ChemBioChem* **2018**, *19* (21), 2262–2267. https://doi.org/10.1002/cbic.201800246.
(27) Arbiser, J. L. Fumarate Esters as Angiogenesis Inhibitors: Key to Action in Psoriasis. *Journal of Investigative Dermatology* **2011**, *131* (6), 1189–1191. https://doi.org/10.1038/jid.2011.45.
(28) Koivunen, P.; Hirsilä, M.; Remes, A. M.; Hassinen, I. E.; Kivirikko, K. I.; Myllyharju, J. Inhibition of Hypoxia-Inducible Factor (HIF) Hydroxylases by Citric Acid Cycle Intermediates: Possible Links between Cell Metabolism and Stabilization of HIF. *Journal of Biological Chemistry* **2007**, *282* (7), 4524–4532. https://doi.org/10.1074/jbc.M610415200.
(29) Isaacs, J. S.; Yun, J. J.; Mole, D. R.; Lee, S.; Torres-Cabala, C.; Chung, Y. L.; Merino, M.; Trepel, J.; Zbar, B.; Toro, J.; Ratcliffe, P. J.; Linehan, W. M.; Neckers, L. HIF Overexpression Correlates with Biallelic Loss of Fumarate Hydratase in Renal Cancer: Novel Role of Fumarate in Regulation of HIF Stability. *Cancer Cell* **2005**, *8* (2), 143–153. https://doi.org/10.1016/j.ccr.2005.06.017.
(30) Hewitson, K. S.; Holmes, S. L.; Ehrismann, D.; Hardy, A. P.; Chowdhury, R.; Schofield, C. J.; McDonough, M. A. Evidence That Two Enzyme-Derived Histidine Ligands Are Sufficient for Iron Binding and Catalysis by Factor

Inhibiting HIF (FIH). *Journal of Biological Chemistry* **2008**, *283* (38), 25971–25978. https://doi.org/10.1074/jbc.M804999200.

(31) Pektas, S.; Taabazuing, C. Y.; Knapp, M. J. Increased Turnover at Limiting O2 Concentrations by the Thr387 → Ala Variant of HIF-Prolyl Hydroxylase PHD2. *Biochemistry* **2015**, *54* (18), 2851–2857. https://doi.org/10.1021/bi501540c.

(32) Hopkinson, R. J.; Tumber, A.; Yapp, C.; Chowdhury, R.; Aik, W.; Che, K. H.; Li, X. S.; Kristensen, J. B. L.; King, O. N. F.; Chan, M. C.; Yeoh, K. K.; Choi, H.; Walport, L. J.; Thinnes, C. C.; Bush, J. T.; Lejeune, C.; Rydzik, A. M.; Rose, N. R.; Bagg, E. A.; McDonough, M. A.; Krojer, T. J.; Yue, W. W.; Ng, S. S.; Olsen, L.; Brennan, P. E.; Oppermann, U.; Müller, S.; Klose, R. J.; Ratcliffe, P. J.; Schofield, C. J.; Kawamura, A. 5-Carboxy-8-Hydroxyquinoline Is a Broad Spectrum 2-Oxoglutarate Oxygenase Inhibitor Which Causes Iron Translocation. *Chem. Sci.* **2013**, *4* (8), 3110–3117. https://doi.org/10.1039/C3SC51122G.

(33) Yeh, T. L.; Leissing, T. M.; Abboud, M. I.; Thinnes, C. C.; Atasoylu, O.; Holt-Martyn, J. P.; Zhang, D.; Tumber, A.; Lippl, K.; Lohans, C. T.; Leung, I. K. H.; Morcrette, H.; Clifton, I. J.; Claridge, T. D. W.; Kawamura, A.; Flashman, E.; Lu, X.; Ratcliffe, P. J.; Chowdhury, R.; Pugh, C. W.; Schofield, C. J. Molecular and Cellular Mechanisms of HIF Prolyl Hydroxylase Inhibitors in Clinical Trials. *Chemical Science* **2017**, *8* (11), 7651–7668. https://doi.org/10.1039/c7sc02103h.

(34) Debenham, J. S.; Madsen-Duggan, C.; Clements, M. J.; Walsh, T. F.; Kuethe, J. T.; Reibarkh, M.; Salowe, S. P.; Sonatore, L. M.; Hajdu, R.; Milligan, J. A.; Visco, D. M.; Zhou, D.; Lingham, R. B.; Stickens, D.; Demartino, J. A.; Tong, X.; Wolff, M.; Pang, J.; Miller, R. R.; Sherer, E. C.; Hale, J. J. Discovery of N-[Bis(4-Methoxyphenyl)Methyl]-4-Hydroxy-2-(Pyridazin-3-Yl)Pyrimidine-5-Carboxamide (MK-8617), an Orally Active Pan-Inhibitor of Hypoxia-Inducible Factor Prolyl Hydroxylase 1-3 (HIF PHD1-3) for the Treatment of Anemia. *Journal of Medicinal Chemistry* **2016**, *59* (24), 11039–11049. https://doi.org/10.1021/acs.jmedchem.6b01242.

(35) Bonandi, E.; Christodoulou, M. S.; Fumagalli, G.; Perdicchia, D.; Rastelli, G.; Passarella, D. The 1,2,3-Triazole Ring as a Bioisostere in Medicinal Chemistry. *Drug Discovery Today*. Elsevier Ltd October 1, 2017, pp 1572–1581. https://doi.org/10.1016/j.drudis.2017.05.014.

(36) Elguero, J.; Martíanez, A.; Singh, S. P.; Grover, M.; Tarar, L. S. A 1H and 13c Nmr Study of the Structure and Tautomerism of 4-pyrazolylpyrazolinones. *Journal of Heterocyclic Chemistry* **1990**, *27* (4), 865–870. https://doi.org/10.1002/jhet.5570270409.

(37) Dann, C. E.; Bruick, R. K.; Deisenhofer, J. Structure of Factor-Inhibiting Hypoxia-Inducible Factor 1: An Asparaginyl Hydroxylase Involved in the Hypoxic Response Pathway. *Proceedings of the National Academy of Sciences of the United States of America* **2002**, *99* (24), 15351–15356. https://doi.org/10.1073/pnas.202614999.

(38) Zhang, X.; Lei, Y.; Hu, T.; Wu, Y.; Li, Z.; Jiang, Z.; Yang, C.; Zhang, L.; You, Q. Discovery of Clinical Candidate (5-(3-(4-Chlorophenoxy)Prop-1-Yn-1-Yl)-3-Hydroxypicolinoyl)Glycine, an Orally Bioavailable Prolyl Hydroxylase Inhibitor for the Treatment of Anemia. *Journal of Medicinal Chemistry* **2020**, *63* (17), 10045–10060. https://doi.org/10.1021/acs.jmedchem.0c01161.

(39) McCoy, A. J.; Grosse-Kunstleve, R. W.; Adams, P. D.; Winn, M. D.; Storoni, L. C.; Read, R. J. Phaser Crystallographic Software. *Journal of Applied Crystallography* **2007**, *40* (4), 658–674. https://doi.org/10.1107/S0021889807021206.

(40) Deng, G.; Zhao, B.; Ma, Y.; Xu, Q.; Wang, H.; Yang, L.; Zhang, Q.; Guo, T. B.; Zhang, W.; Jiao, Y.; Cai, X.; Zhang, J.; Liu, H.; Guan, X.; Lu, H.; Xiang, J.; Elliott, J. D.; Lin, X.; Ren, F. Novel Complex Crystal Structure of Prolyl Hydroxylase Domain-Containing Protein 2 (PHD2): 2,8-Diazaspiro[4.5]Decan-1-Ones as Potent, Orally Bioavailable PHD2 Inhibitors. *Bioorganic and Medicinal Chemistry* **2013**, *21* (21), 6349–6358. https://doi.org/10.1016/j.bmc.2013.08.046.

(41) Scotti, J. S.; Leung, I. K. H.; Ge, W.; Bentley, M. A.; Paps, J.; Kramer, H. B.; Lee, J.; Aik, W.; Choi, H.; Paulsen, S. M.; Bowman, L. A. H.; Loik, N. D.; Horita, S.; Ho, C. H.; Kershaw, N. J.; Tang, C. M.; Claridge, T. D. W.; Preston, G. M.; McDonough, M. A.; Schofield, C. J. Human Oxygen Sensing May Have Origins in Prokaryotic Elongation Factor Tu Prolyl-Hydroxylation. *Proceedings of the National Academy of Sciences of the United States of America* **2014**, *111* (37), 13331–13336. https://doi.org/10.1073/pnas.1409916111.

(42) Lippl, K.; Boleininger, A.; McDonough, M.; Abboud, M. I.; Tarhonskaya, H.; Chowdhury, R.; Loenarz, C.; Schofield, C. J. Born to Sense: Biophysical Analyses of the Oxygen Sensing Prolyl Hydroxylase from the Simplest Animal Trichoplax Adhaerens. *Hypoxia* **2018**, *6*, 57–71. https://doi.org/10.2147/hp.s174655.

(43) Jumper, J.; Evans, R.; Pritzel, A.; Green, T.; Figurnov, M.; Ronneberger, O.; Tunyasuvunakool, K.; Bates, R.; Žídek, A.; Potapenko, A.; Bridgland, A.; Meyer, C.; Kohl, S. A. A.; Ballard, A. J.; Cowie, A.; Romera-Paredes, B.; Nikolov, S.; Jain, R.; Adler, J.; Back, T.; Petersen, S.; Reiman, D.; Clancy, E.; Zielinski, M.; Steinegger, M.; Pacholska, M.; Berghammer, T.; Bodenstein, S.; Silver, D.; Vinyals, O.; Senior, A. W.; Kavukcuoglu, K.; Kohli, P.; Hassabis, D. Highly Accurate Protein Structure Prediction with AlphaFold. *Nature* **2021**, *596* (7873), 583–589. https://doi.org/10.1038/s41586-021-03819-2.

(44) Yeoh, K. K.; Chan, M. C.; Thalhammer, A.; Demetriades, M.; Chowdhury, R.; Tian, Y. M.; Stolze, I.; McNeill, L. A.; Lee, M. K.; Woon, E. C. Y.; MacKeen, M. M.; Kawamura, A.; Ratcliffe, P. J.; Mecinović, J.; Schofield, C. J. Dual-Action Inhibitors of HIF Prolyl Hydroxylases That Induce Binding of a Second Iron Ion. *Organic and Biomolecular Chemistry* **2013**, *11* (5), 732–745. https://doi.org/10.1039/c2ob26648b.

(45) Lechtenberg, B. C.; Rajput, A.; Sanishvili, R.; Dobaczewska, M. K.; Ware, C. F.; Mace, P. D.; Riedl, S. J. Structure of a HOIP/E2~ubiquitin Complex Reveals RBR E3 Ligase Mechanism and Regulation. *Nature* **2016**, *529* (7587), 546–550. https://doi.org/10.1038/nature16511.

(46) Chowdhury, R.; Flashman, E.; Mecinović, J.; Kramer, H. B.; Kessler, B. M.; Frapart, Y. M.; Boucher, J. L.; Clifton, I. J.; McDonough, M. A.; Schofield, C. J. Studies on the Reaction of Nitric Oxide with the Hypoxia-Inducible Factor Prolyl Hydroxylase Domain 2 (EGLN1). *Journal of Molecular Biology* **2011**, *410* (2), 268–279. https://doi.org/10.1016/j.jmb.2011.04.075.

Chapter 4

Structural Analyses on PHD2 Inhibition *via* Soaking-Based Studies

Chapter 4

4.1 Background

4.1.1 Technical Overview of XChem Fragment-Based Screening

The technique of fragment-based screening in drug discovery has evolved significantly in recent years.[1] The development of synchrotron beamlines to accommodate >15-20 data collections per hour has allowed for robust fragment screening of crystallographic targets with small-molecule libraries.[2] The developments include the use of Diamond BART robotic sample changers (Diamond Light Source Ltd.), faster pixel-array detectors (Pilatus or Eiger2 series, Dectris AG), improved data processing pipelines (Xia2 and autoPROC), X-ray centring-unattended data collection (UDC), and even automated crystal harvesting with CrystalDirect® (ESRF).[2–12] The beamline upgrades have been coupled with improved wet laboratory facilities to streamline the number of crystals that can be soaked and harvested.[13–16] The ability to screen >1,000 small-molecule fragments in crystals provides an alternative approach to drug discovery than the commonly used HTS by the pharmaceutical industry.[1,13] Efforts would then focus on the structural determination of the lead candidates. Furthermore, an inverse in the process allows for structural characterisation of small-molecule fragment binding events that begin to reveal insights into allosteric sites. The fragments also provide scaffold for further functionalisation through linking of fragment moieties that

bind in the same position or at neighbouring sites. The developments may allow for a structure-guided approach to drug discovery.[1,17]

The pipeline of the XChem fragment-based screen (I04-1 beamline, Lab34, Diamond Light Source Ltd.) includes crystal preparation, wet, and dry laboratory components for the HTS (**Figure 4-1**). [13–16,18–21]

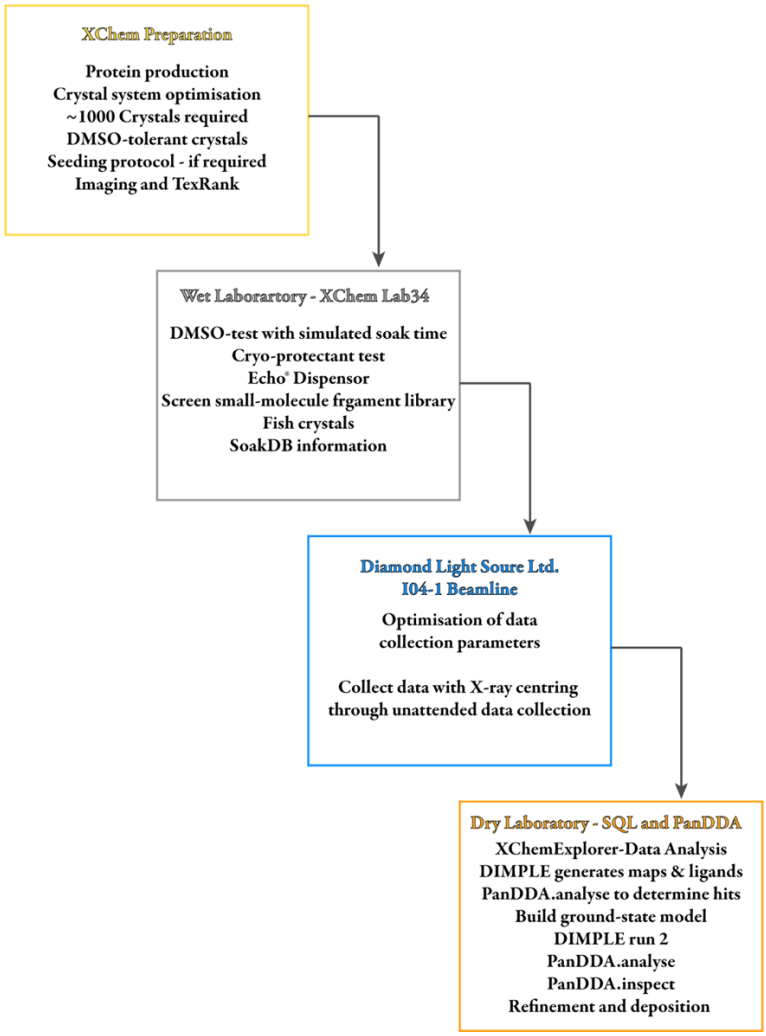


Figure 4-1| Introduction and Overview of the XChem Fragment Screen Pipeline at Diamond. Prior to use of XChem, preparation of the crystals for large-scale production of high-resolution diffracting crystals is conducted and crystals are tested for DMSO-tolerance (yellow). Crystal plates are imaged, and drops are targeted for dispensation of the small-molecule fragments (yellow). During a training week, the crystals undergo a simulated soak with DMSO that has been dispensed by an acoustic Echo® dispenser (grey). Small-molecule fragments are dispensed in the same way and screen multiple libraries of compounds, *e.g.,* DSI-poised and Fraglites libraries (grey). Soaked crystals are harvested using a robotic plate shifter (OLT) and soak information is stored in SoakDB (grey). Data collection parameters are optimised during the training week to obtain the best quality datasets during the unattended data collection *via* X-ray centring (blue). The dry laboratory uses XChemExplorer for analysis of datasets, Dimple to generate maps/ligand CIF files, and PanDDA to aid in structural determination of hits and build a ground-state model. Abbreviations: Diamond Light Source Ltd. (Diamond), Dimethyl sulfoxide (DMSO), Oxford Lab Technologies Ltd. (OLT), Soak Database (SoakDB), Pan-Dataset Density Analysis (PanDDA).

Prior to laboratory access and beamtime, the crystallisation of the target must be optimised. The optimisation includes the size of the crystals, morphology, and/or X-ray diffraction resolution under rotation-based cryogenic data collection at Diamond Light Source Ltd. (including the amount of DMSO dispensed from the fragment library). Once crystals are prepared, crystals are imaged using a Rock Imager® 1000 (Formulatrix, Inc., Research Complex at Harwell, Diamond Light Source Ltd.) and crystal drops are ranked based on the optical quality of crystal and the level of precipitation within the crystallisation drop using an automated software, TexRank (**Figures 4-1** and **4-2**, Diamond Light Source Ltd.).[16] TexRank allows the user to manually select a target within the crystal drop where the fragment should be dispensed (*i.e.*, to prevent damage to the crystal during fragment injection, **Figures 4-1** and **4-2**).[16] The plate coordinates are generated from the user defined target and are uploaded into an Echo® liquid handler (**6.9.3**, Labcytes Inc.) that acoustically dispenses the fragments (30 nL) from a DMSO-solubilised library of fragment compounds into 300 nL drops (**6.9.3**, **Figures 4-1** and **4-2**, DSI-poised and FragLites libraries).[15,18,22] Soaked crystals (typically 1-3 hr soaks) are then harvested into MicroLoops LD™ loops (MiTeGen, LLC, **6.9.3**) using a robotic crystal plate shifter (Oxford Lab Technologies Ltd.) that moves to a specified well containing a soaked crystal. After the soaked crystal is manually looped, it is plunged into liquid-N_2 for cryo-cooling (**6.9.3**, **Figures 4-1** and **4-2**); soak information is uploaded into SoakDB that is linked with a SQLite database (**6.9.4**-**6.9.5**).[14] Cryogenically stored crystals in universal pucks (uni-pucks) are loaded into a storage Dewar vessel (stores ~600 crystals) within the beamline experimental hutch (**6.9.5**).[2,5,7] The robotic sample changer (Mitsubishi Electric Corp.) loads the crystal pins (MiTeGen, LLC) onto the goniometer and crystals are centred using fully automatic X-ray centring (**Figures 4-1** and **4-2**, I04-1 beamline, **6.9.6**).[5,7] The datasets are automatically processed *via* Xia2 (3dii or DIALS) or

autoPROC pipelines (**6.6.8.2**-**6.6.8.3**). The auto-processing results can be extracted with XChemExplorer (XCE) software (**Figure 4-1**).[8,11,19,23,24]

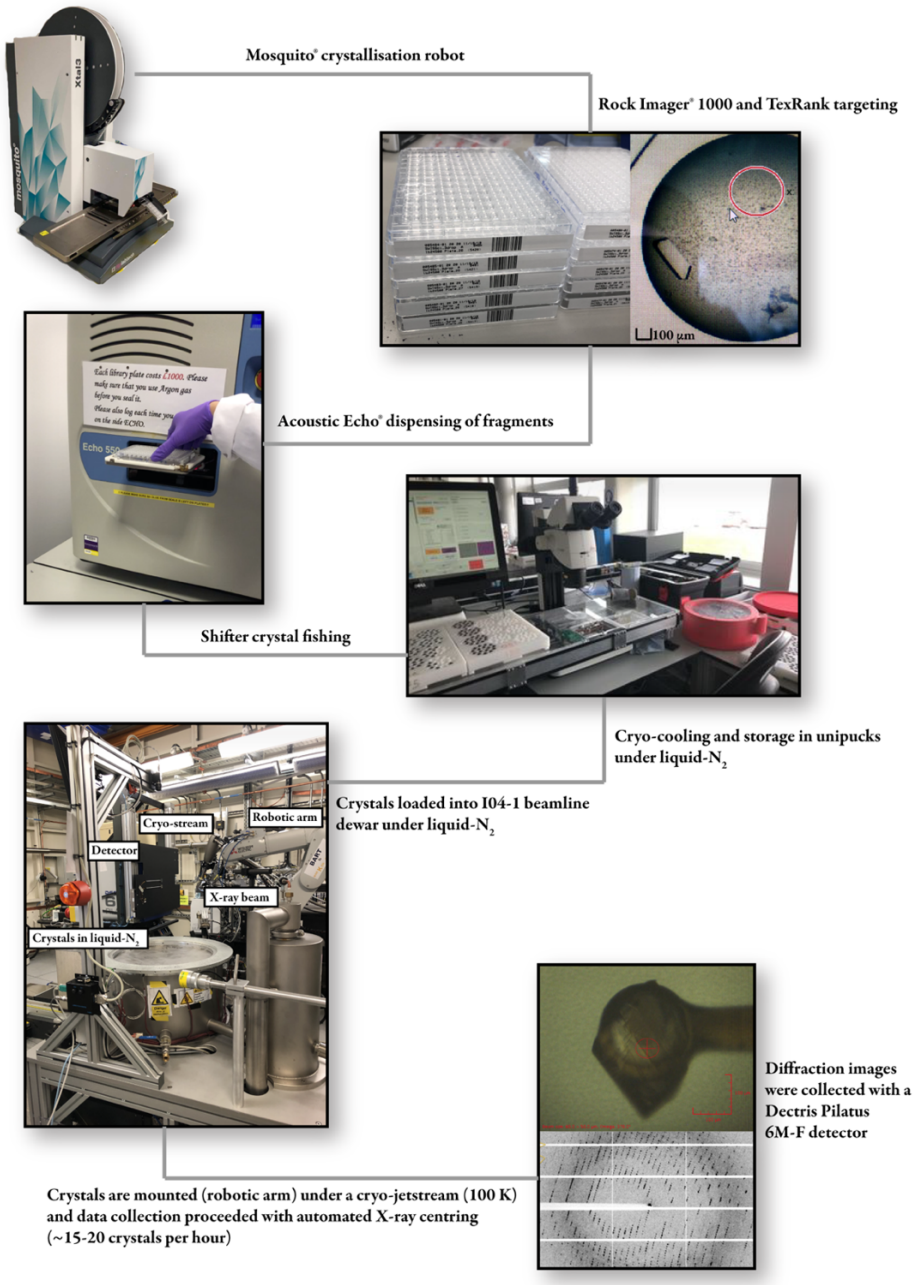


Figure 4-2| Overview of the Wet Laboratory XChem Pipeline. Crystal plates are set-up using a Mosquito® robot (SPT Labtech Ltd.) into 3 Lens crystallisation plates (SWISSCI AG). Crystal drops are imaged using a Rock Maker® 1000 (Formulatrix, Inc.) and targeted (red circle where the SM fragment will be dispensed) using TexRank software. SM fragments are dispensed using an acoustic Echo® dispenser. Soaked crystals were harvested using the crystal shifter (OLT) and stored in uni-pucks under liquid-N_2. Uni-pucks were loaded into the I04-1 beamline Dewar vessel (Diamond Light Source Ltd.) and a six-axis robotic arm (Mitsubishi Electric Corp.) mounted the crystal pins onto the multi-axis goniometer under a cryo-jetstream at 100 K. Unattended data collection proceeded with X-ray centring and diffraction images were collected with a Pilatus 6M-F detector (Dectris AG). Abbreviations: Small-molecule (SM), Oxford Lab Technology (OLT). *The photo of the Mosquito® robot was taken by Mr. Freddie Foster.*

Datasets less than 2.80 Å and complete in all resolution bins (>95%) were selected and phased with a prior MR-model with DIMPLE to generate fragment ligands crystallographic information files (CIF) and electron density maps for the datasets (**Figure 4-1**).[19,25,26] DIMPLE maps and ligand CIF files are analysed using PanDDA software to identify fragment hits by averaging all input datasets to account for any smearing of electron density caused by weak binding fragments (**Figure 4-1**).[20,21,25] Simultaneously with PanDDA.analyse, PanDDA builds a ground-state model from a good quality and representative dataset that does not contain a bound fragment (**Figure 4-1**).[20,21] The built ground-state model can be refined further and used for downstream PanDDA.analyse runs (**Figure 4-1**,).[20,21] It is typically expected that multiple DIMPLE-PanDDA.analyse runs are required to achieve the best quality PanDDA multiple dataset (**Figure 4-1**).[20,21,25] Fragment hits can be inspected through PanDDA inspect and tagged for further refinement (**Figure 4-1**).[20,21] Once the structures with fragments are refined, they can then be deposited into the PDB as a group deposition and be further analysed using Fragalysis webtool (**Figure 4-1**).[19,27]

4.1.2 Biological Background

The development of isoform-selective inhibitors has been an objective in the medicinal chemistry of PHD inhibition.[28] As the PHD isoforms contain a high sequence conservation of their active sites (**3.5**; **Figure 3-20**), targeting allosteric or orthosteric pockets may modulate the PHDs activity in tissue-specific manner. PHD-isoform inhibition may potentially regulate alternative cellular processes within different tissues.[29] The selectivity and safety of current clinically applied inhibitors, possibly apart from Molidustat (**20**), may relate to their likely direction to the liver due to the polarity of

glycinamide sidechains (e.g., **22** and **23,** discussed in section **1.4**) and targeted for metabolism.[30]

A recent example of isoform-selectivity was reported for human phosphodiesterase 5A1 (PDE5) with Avanafil, a highly selective and potent PDE5 inhibitor that mimics cyclic guanosine monophosphate (cGMP, **Figure 4-3**).[28]

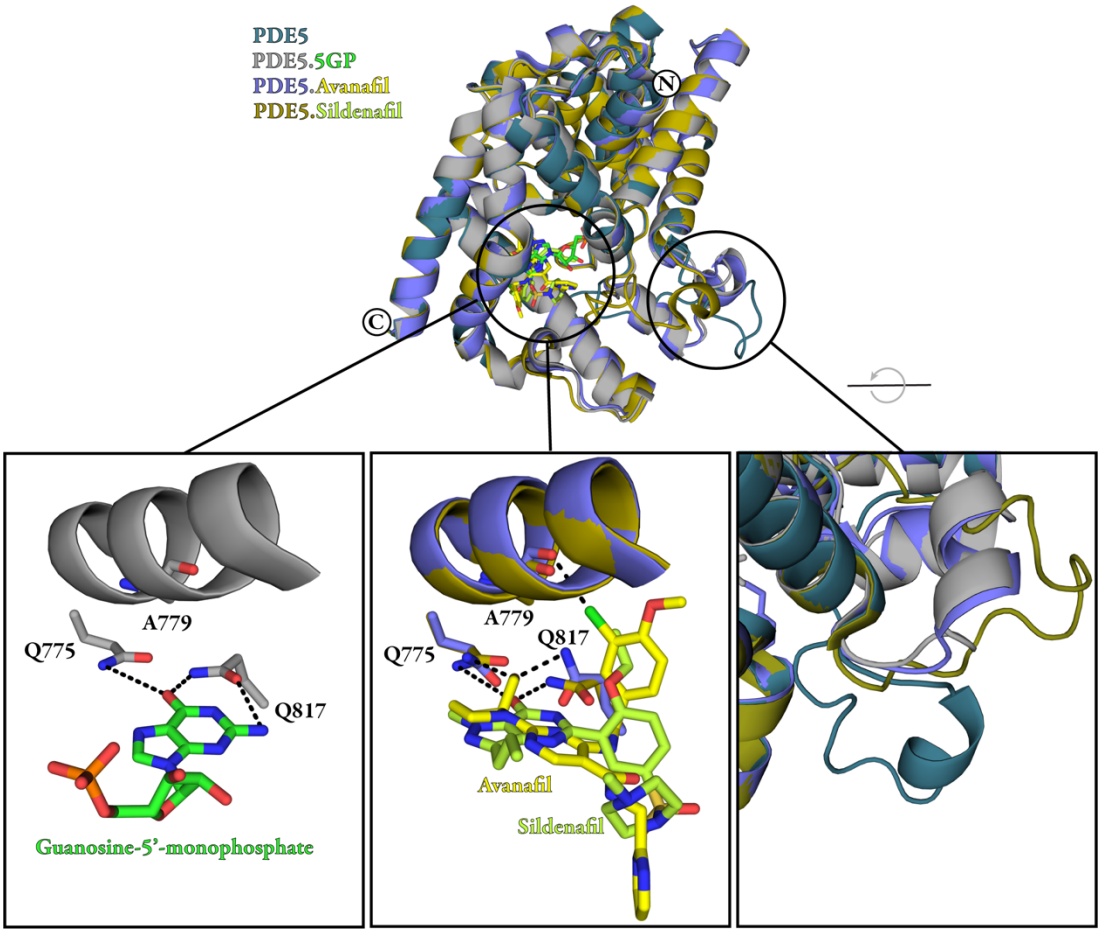


Figure 4-3| Alignment of Complex Structures of PDE5 and View of the Active Site and Dynamic Loop Regions. Complex structures of PDE5 (dark teal, PDB: 2H40), PDE5-GMP (grey, PDB: 1T9S), PDE5-Avanafil (slate, PDB: 6L6E), and PDE5-Sildenafil (olive, PDB: 2H42) are displayed as cartoons. The ligands (GMP-green, Avanafil-yellow, Sildenafil-lemon) and active site residues are depicted as sticks. Key active site interactions are represented by dashes (black). Abbreviations: Phosphodiesterase type 5 (PDE5), Guanosine-5'-monophosphate (5GP). PDB: 2H40, 1T9S, 6L6E, 2H42.

The small-molecule inhibitor Avanafil is proposed to display selectivity for isoform PDE5 due to a backbone-ligand interaction between the chloro-methoxybenzene sidechain and residue Ala779 (**Figure 4-3**).[28] Conformational changes are observed between un-

complexed PDE5, PDE5.cGMP, and PDE5.Sildenafil complexes, in particular as observed in an allosteric loop region (**Figure 4-3,** PDB: 2H40, 1T9S, 6L6E, 2H42). Binding in a 'halogen bonding hole' (residues Ala779, Val782, and Ala783) in PDE5 isoform is proposed to increase the potency and selectivity of Avanafil for PDE5; the other PDE isoforms do not contain the 'halogen bonding hole', as evidenced by computational modelling (**Figure 4-3**).[28]

The recently discovered triazolopyridine based PHD inhibitors (Takeda-17, **17**), provide a non-conventional mode of inhibition as they contain only one metal ligation atom of the triazole-core ring. The monodentate binding inhibitors could potentially be expanded through structure-guided drug design following their structural characterisation *via* soaking-based studies with the $PHD2_{181-407}$ *P* 2_1 crystal form (*Xtal-P*).[17,31]

With a combination of fragment-based screening and soaking-based studies, biophysical features, such as allosteric and orthosteric pockets, of the PHDs could potentially be revealed. Structural characterisation of bound fragments and monodentate binding derivatives may aid the future development of specific, isoform-selective, and/or allosteric PHD inhibitors. Evidence for potentially allosteric pockets have been provided by the complex structures of (i) $PHD2_{181-426}$.FG2216 (**21**), (ii) $PHD2_{181-392}$.JNJ-40787422, and (iii) $PHD2_{181-426}$-3C cyclic peptide (PDB: 2Y34, 3OUI, and 6YW3).[32–34] It was envisaged that the binding pockets of **21**, JNJ-40787422, and 3C may be explored further with the results from a XChem fragment-based screen.

4.2 XChem Fragment-Based Screen of PHD2

The $PHD2_{181-407}$.formate (*Xtal-A*) and succinate (*Xtal-P*) crystal forms (discussed earlier in Chapter **3**) were considered as candidates for the XChem screen.[13] The 1.17 Å resolution formate-derived crystals were initially preferred (discussed in section **2.2**), but to date it has not been feasible to generate ~1000 crystals of suitable size for analysis that are required for a full XChem screen with the *Xtal-A* crystal form. A second option was to use $PHD2_{181-407}$.Mn(II).succinate crystal form (*Xtal-P*) which could produce consistent crystals for screening. The potential benefit of the *Xtal-P* form was that it was envisaged fragments could potentially exchange with succinate due to the weak binding nature of co-product (see section **3.2.2**). However, the resolution for the *Xtal-P* crystal form (1.90 Å) diffracted to a lower resolution than the formate-derived crystals. The resolution of the *Xtal-P* form also varied across different crystals, being 1.79-3.00 Å or lower. The range of the resolution obtained for the datasets may complicate downstream analysis of the fragment hits as the best results from a full XChem analysis came from a crystal system with a resolution of 1.50 Å or better.[27] As the *Xtal-P* crystal form was the more reliable system to carry forward as laboratory access and beamtime approached, all efforts were focused on maximising the results obtained from the fragment-based screen of $PHD2_{181-407}$.Mn(II).succinate crystals. (*Thank you to Dr. Michael McDonough for organising the laboratory access and beamtime for the PHD2 XChem fragment screen. Also, thank you for his help in the fishing of the crystals and analysis of the data for the first 100 datasets during the training week.*)

100 crystals from the $PHD2_{181-407}$.Mn(II).succinate crystal form (*Xtal-P*) were taken to Lab34 (XChem Diamond Light Source Ltd.) and were prepared for solvent and cryo-protectant optimisation of *Xtal-P* system for the fragment screen (**Figure 4-4**, **6.9.2**).[13] The optimal conditions, after a solvent characterisation (**6.9.2**), were determined to be 1 hr soaks of fragments with 10% (v/v) DMSO in the crystallisation drop (*i.e.*, a final of

50.6 mM for each fragment, **Figure 4-4**, **6.9.2**). The DSI-poised and FragLite libraries were prepared with 500 mM concentrated DMSO-solubilised fragments (**6.9.3**).[18,22] A small screen of ~70 crystals was conducted, and data collection parameters were optimised for unattended data collection; λ=0.9119 Å, Flux=3.50e+11, Beamsize=60x50 μm, 1500 images, 0.16° oscillation, 2.00 Å detector distance, 0.060 second exposure, and 100% transmission (**Figure 4-4**, I04-1 beamline, **6.9.6**).[13] (*Thank you to beamline staff Dr. Alice Douangamath and Dr. Romain Talon for their significant support and help in optimising the* $PHD_{181\text{-}407}$ *crystallisation system for fragment-based screening.*)

Preparation of the large-batch of $PHD2_{181\text{-}407}$.Mn(II).succinate (*Xtal-P*) crystals began with a goal of >1000 crystals for the fragment screen (**Figure 4-4**, **6.8.2**). 35 plates were prepared, using 60 mg of $PHD2_{181\text{-}407}$, with four different optimisation blocks of the potassium thiocyanate condition (**Figure 4-4**, **6.6.3**). Due to robot inaccuracies (Crystal Phoenix, Art Robbins Instruments, LLC.) and a requirement to transition from INTELLI-PLATES® 3-drop vapour diffusion plates (Art Robbins Instruments, LLC.) to the XChem compatible 3 lens crystallisation plates (SWISSCI AG); most crystals were of 20 μm x 20 μm x 5 μm dimensions and each drop contained ~20 crystals (**Figure 4-4**, **6.9.1**). With so many crystals in the drop, the harvesting of crystals was very difficult (especially the 200 nL drops due to evaporation). All 35 plates with $PHD2_{181\text{-}407}$.Mn(II).succinate crystals were brought to Lab34 and ~400 crystals were harvested (Diamond Light Source Ltd., **6.9.5**). Unfortunately, data collection was halted due to weak diffraction of the crystals (**Figure 4-4**, **6.9.6**). Both the size and quality of the crystals were required to achieve <2.00 Å resolution. (*Thank you to Dr. Yu Nakashima for his help in setting-up some of the crystal plates and fishing crystals on the second visit to Lab34.*)

Further optimisation of the crystal form was required to obtain numerous ~200 μm x 100 μm x 50 μm crystals. The *Xtal-P* system was optimised with a seeding

protocol using a Mosquito® crystallisation robot (**Figure 4-2**, SPT Labtech Ltd.) to produce a plate full of optimal crystals for the fragment screen (**Figure 4-4**, **6.9.1**). Seed stocks were prepared from crystals in 5-6 different crystallisation drops using 100 µL of the well solution that contained the highest PEG 3350 concentration (**Figure 4-4**, **6.9.1**). An optimised screen was prepared of 0.140 M potassium thiocyanate and 18-21.5% (w/v) PEG 3350, crystal plates were prepared with 200 nL of $PHD2_{181-407}$.Mn(II).succinate protein mixture, 30 nL of concentrated seed stock, and 70 nL of the reservoir solution (**6.9.1**). Approximately 50 single crystals would appear per plate after one week of equilibration (**Figure 4-4**). (*Thank you to Dr. Therese Bergfors for providing a seeding protocol to optimise the crystallisation condition. Thank you to Dr. Alice Douangamath and Dr. Edward Lowe for their help with optimising the seeding protocol on the Mosquito®(SPT Labtech Ltd.))*

In total, 825 and 41 crystals were screened with the DSI-Poised and FragLite fragments, respectively. Approximately 390 datasets diffracted and were processed (**6.6.8.2**-**6.6.8.3**). All the datasets that were lower than 2.80 Å resolution were filtered out for further characterisation in XCE (**6.9.7**).[19] As the resolution and unit cell dimensions of the *Xtal-P* crystal form varied (>3.0% variance in most cases), the dry lab component of the project proved to be challenging (**Figure 4-5**, **6.9.7**). An accurate starting model was required for generation of DIMPLE phased maps for input into PanDDA (**Figure 4-5**, **6.9.7**).[20,21,25] Initially, DIMPLE was run with a six-chain model of $PHD2_{181-407}$ in complex with Molidustat (PDB: 6ZBO or *Xtal-R*). Approximately 220 datasets that (i) processed, (ii) complete in all resolution bins, and (iii) passed the resolution cut-off were phased in DIMPLE (**Figure 4-5**, **6.9.7** and **6.6.9.1**).[25] The DIMPLE generated maps and ligands were analysed with PanDDA.analyse (**Figure 4-5**, **6.9.7**).[19] The averaged maps in PanDDA.inspect were of very poor quality and contained many gaps the electron density (**Figure 4-5**).[20,21]

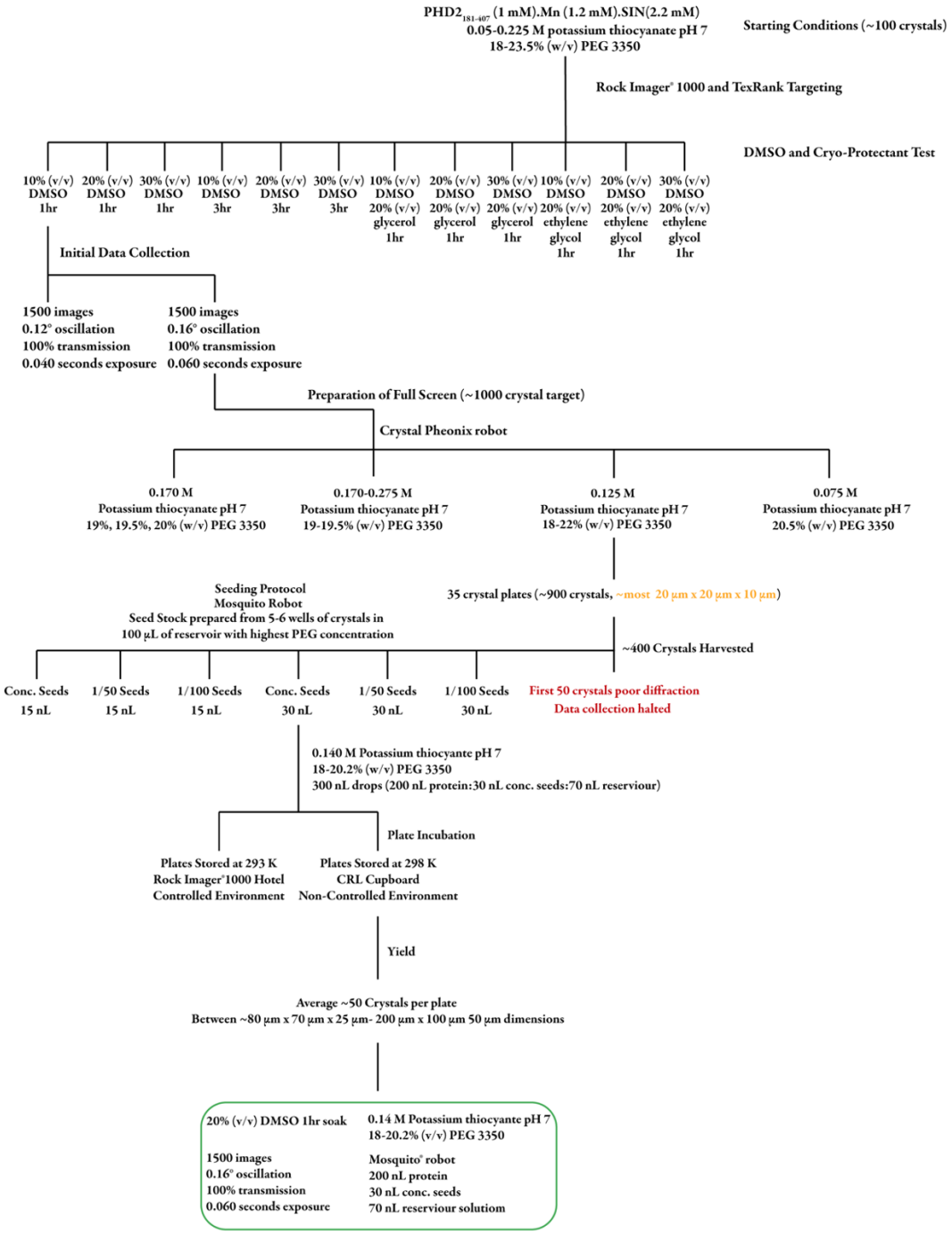


Figure 4-4| Optimisation Flowchart of the PHD2$_{181-407}$.Mn(II).Succinate-*P* 2$_1$ Crystal form for Use in the XChem Fragment Screen at Diamond. Abbreviations: Prolyl hydroxylase isoform 2 (PHD2), Diamond Light Source Ltd. (Diamond).

The chains in the ASU were not correctly phased in most cases. PanDDA built a ground-state model in parallel to PanDDA.analyse (**Figure 4-5**).[20,21] The PHD2$_{181-407}$.x0525 (1.95 Å resolution) dataset was selected to build the ground-state model. PHD2$_{181-407}$.x0525 was refined *via* PHENIX.refine (**6.6.9.4**) to obtain a correct model (*i.e.*,

including refinement of solvent and succinate, a=75.46 Å, b=74.37 Å, c=127.32 Å, β=94.84°, **Figure 4-5**, **6.9.7**).[35,36]

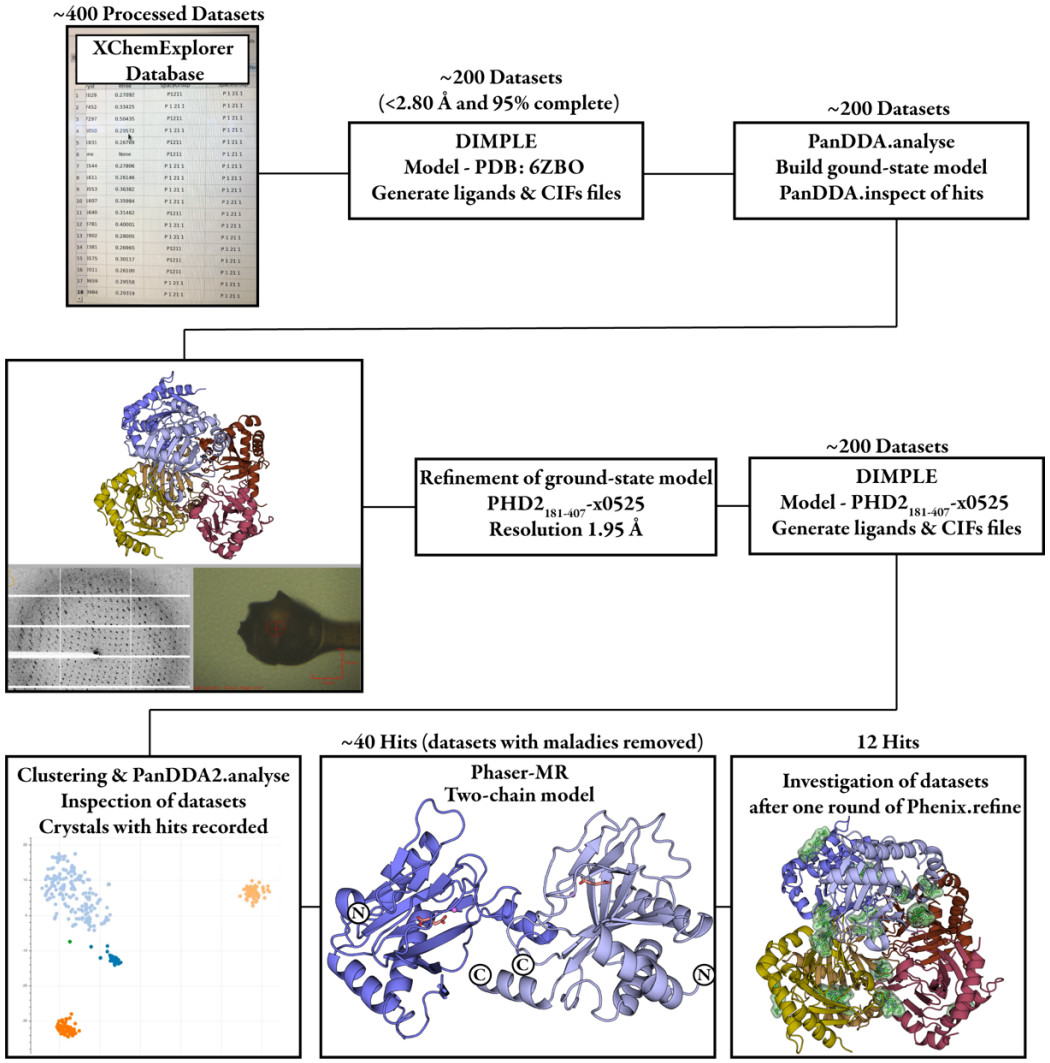
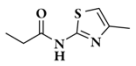
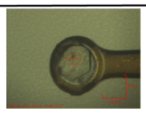
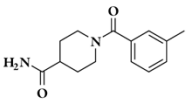
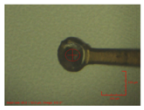
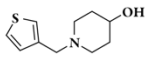
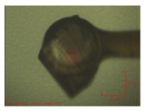
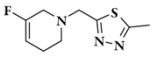
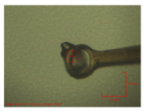
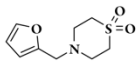
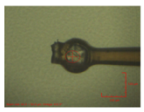
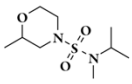
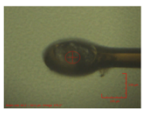
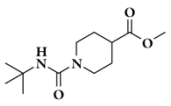
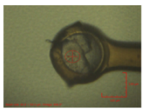
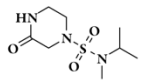
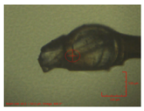
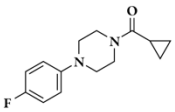
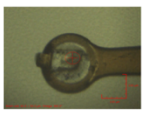
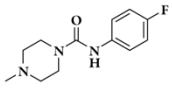
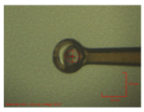
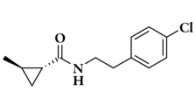
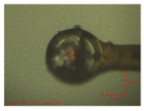
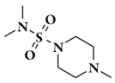
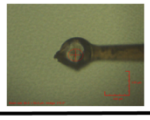


Figure 4-5 | An Overview Flowchart of the Dry Laboratory Component and Data Processing Steps of the XChem Pipeline. Crystal soak information in SoakDB and datasets in ISPyB are linked through an SQLite database. XCE can extract the information from the SQLite server and downstream data analysis can be completed. DIMPLE, using PDB: 6ZBO as an input model, generates maps, ligand coordinates, and CIF files for further hit investigation. PanDDA.analyse identifies bound fragment hits and builds a ground-state model for further analysis. $PHD2_{181-407}$.x0525 was selected as the ground-state model and was refined for a second DIMPLE run. Datasets were clustered based on resolution and unit cell dimensions into four clusters. PanDDA2.analyse was run on each individual cluster of datasets. Identified fragment hits were analysed in PanDDA.inspect and recorded. Datasets were phased with Phaser-MR with a refined two-chain model of $PHD2_{181-407}$.x0525. One round of Phenix.refine was carried out on all phased datasets and investigated if any fragments were bound. Abbreviations: Soak database (SoakDB), Information system for protein crystallography beamlines (ISPyB), XChemExplorer (XCE), Crystallographic information file (CIF), Pan-Dataset Density Analysis (PanDDA), Prolyl hydroxylase isoform 2 (PHD2), and Molecular replacement (MR).

Due to large variations in resolution and unit cell dimensions, the datasets were clustered based on the crystallographic and diffraction features of the crystals into four

clusters (**6.9.7**). PanDDA2 was run on each cluster using the DIMPLE maps generated with the refined ground-state model (**Figure 4-5**, **6.9.7**).[20,21,25] Fragment hits were inspected with PanDDA.inspect on the various clusters and any large positive PanDDA maps were recorded (**Figure 4-5**).[20,21] With the ground-state model and data clustering, the DIMPLE maps were only slightly improved in comparison with the previous PanDDA.analyse output (**Figure 4-5**).[20,21,25] As there was a consistent problem with the PanDDA maps caused by the nonisomorphism of the crystal form, a full MR-phasing (**6.6.9.2**) was required using a two-chain model ($PHD2_{181-407}$.x0525) with Phaser (**Figure 4-5**, **6.6.9.2**).[37] The 34 identified datasets were analysed with PHENIX.Xtriage (**6.6.9.1**) and crystals with pathologies (*e.g.*, twinning or negative Wilson B-factors) were removed from further analysis.[35,38] 24 datasets were further refined with one round of refinement completed with PHENIX.refine (**6.6.9.4**).[35,36] As the fragments can be weak binders, one round of refinement may help reduce the noise or smearing of density observed of fragments in the electron density maps generated through Phaser (*i.e*, they are not pan-averaged like the PanDDA maps).[20,21,37] Post refinement, the mF_o-DF_c difference maps of the refined datasets were inspected in COOT (**6.6.9.3**) for unexplained positive density.[39] 12 ordered fragment hits were identified from the DSI-poised library in five different binding sites of $PHD2_{181-407}$ (**Table 4-1** and **Figures 4-6** and **4-7**; Validation and Crystallographic Data Processing and Refinement Statistic tables are given in **Appendix I** & **II**).[18] In a recently reported fragment-based XChem study, the hit rate was ~4.5%. In this study, the hit rate was ~1.5%.[27] Of note, none of the XChem ligands displaced succinate from the active site of $PHD2_{181-407}$. Some fragments are observed to bind in some of the chains of the ASU; likely due to the nature of the solvent channels in the $PHD2_{181-407}$.Mn(II).succinate (*Xtal-P*) crystal form (**Figure 4-6**). Furthermore, some fragments are observed in different binding sites within the crystal structure.

Table 4-1 | Overview of Soak Conditions from SoakDB and Datasets Collected During the $PHD2_{181-407}$ XChem Fragment Screen.

Crystal ID	Fragment ID	Structure	Mount	Res (Å)	Soak (min)	Drop Cond.	Crystal Cond.
$PHD2_{181-407}$-x0033 *Xtal-V*	Z30820160			2.13	39	Clear	Normal
$PHD2_{181-407}$-x0042 *Xtal-W*	Z32400357			2.31	53	Clear	Normal
$PHD2_{181-407}$-x0524 *Xtal-X*	Z2856434899			2.13	92	Clear	Normal
$PHD2_{181-407}$-x0534 *Xtal-Y*	Z1619978933			2.07	102	Clear	Cracked
$PHD2_{181-407}$-x0555 *Xtal-Z*	Z2856434926			2.53	122	Clear	Normal
$PHD2_{181-407}$-x0582 *Xtal-AA*	Z416341642			2.78	172	Clear	Cracked
$PHD2_{181-407}$-x0594 *Xtal-BB*	Z44567722			2.20	35	Clear	Normal
$PHD2_{181-407}$-x0613 *Xtal-CC*	Z431807512			2.07	65	Clear	Normal
$PHD2_{181-407}$-x0630 *Xtal-DD*	Z30620520			2.20	83	Precipitated	Cracked
$PHD2_{181-407}$-x0723 *Xtal-EE*	Z2856434944			2.15	58	Clear	Normal
$PHD2_{181-407}$-x0747 *Xtal-FF*	Z1802166390			2.05	78	Clear	Cracked
$PHD2_{181-407}$-x0807 *Xtal-GG*	Z2735592898			2.50	72	Clear	Cracked

***N.B.* All complex structures soaked with XChem fragments still contain succinate in the active site.**

(*Thank you to Dr. Alexandre Dias for his help in clustering the datasets and running PanDDA2 on each individual cluster.*)

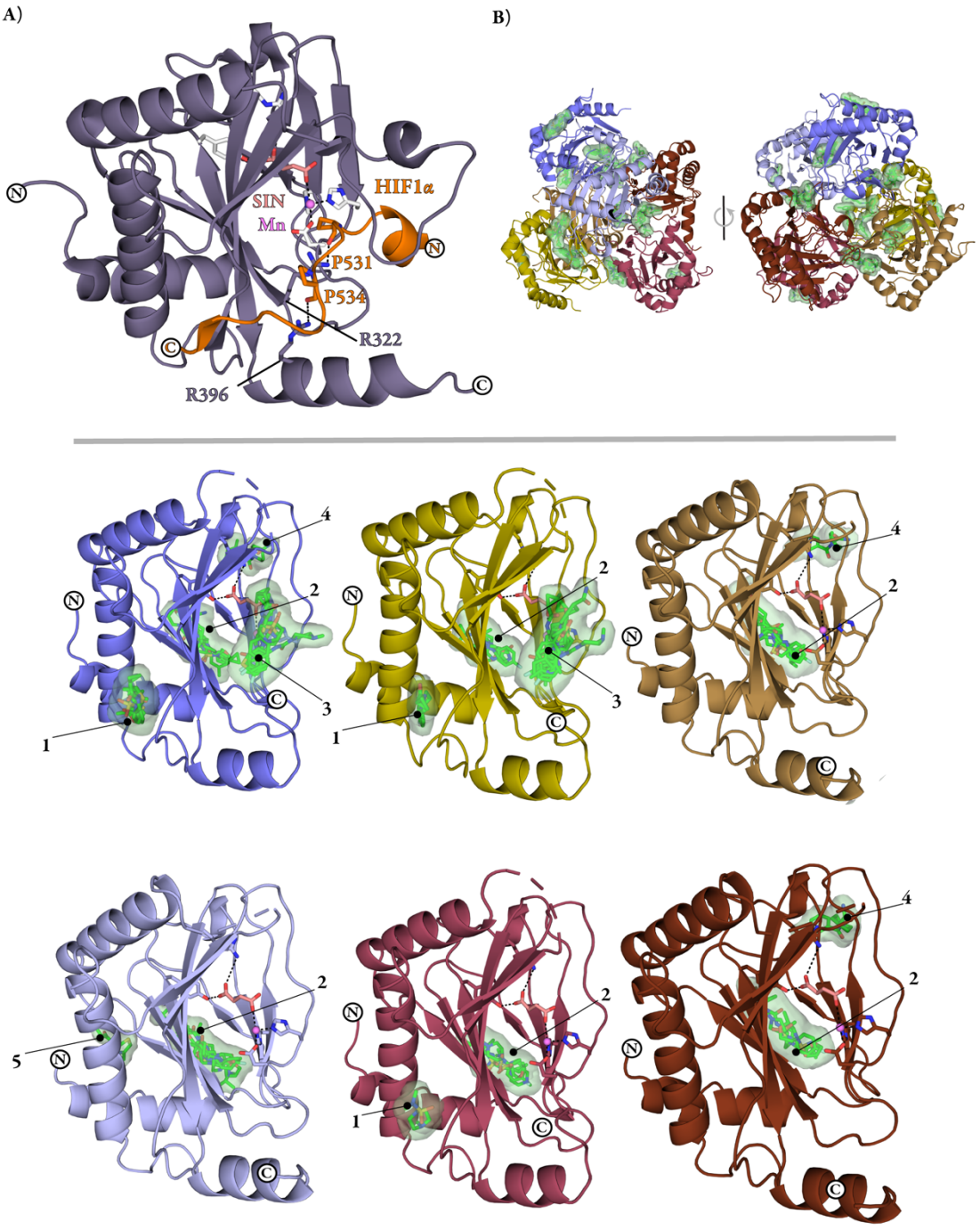


Figure 4-6| An Overview of the Five Binding Sites of PHD2$_{181-407}$.Mn(II).Succinate Identified for the Soaked XChem Fragments. Alignment of the 6-chains ASUs of the 12 datasets with a fragment/s bound are displayed as cartoons (chain A-slate, chain B-olive, chain c-sand, chain D-light blue, chain E-raspberry, and chain F-chocolate) and sticks (green), respectively. Individual chains and fragments are depicted below in cartoons and sticks, respectively. The surface representation (green) is illustrated for all ligand binding sites. PHD2$_{181-426}$.Mn(II).NOG.HIF1α complex (purple-grey), displayed as a cartoon, is provided for a visual reference of HIFα (orange) binding. Mn(II) ion (violet) is displayed as a sphere and succinate as sticks (salmon). Abbreviations: Prolyl hydroxylase isoform 2 (PHD2). *Xtal-IDs*: *V*, *W*, *X*, *Y*, *Z*, *AA*, *BB*, *CC*, *DD*, *EE*, *FF*, *GG*. PDB: 3HQR.

Of the identified binding modes, two were previously uncharacterised and potentially allosteric sites (**Figures 4-7A** and **4-7C-E**). However, it is important to note sites 1, 2, 4, and 5 are exposed to bulk solvent (**Figures 4-6** and **4-7**). Binding site 3 is buried within PHD2$_{181-407}$. Two of the binding interactions, site 3 and site 4, are in surface pockets that provide a suitable cavity for the fragments to bind (**Figures 4-7A** and **4-7E**).

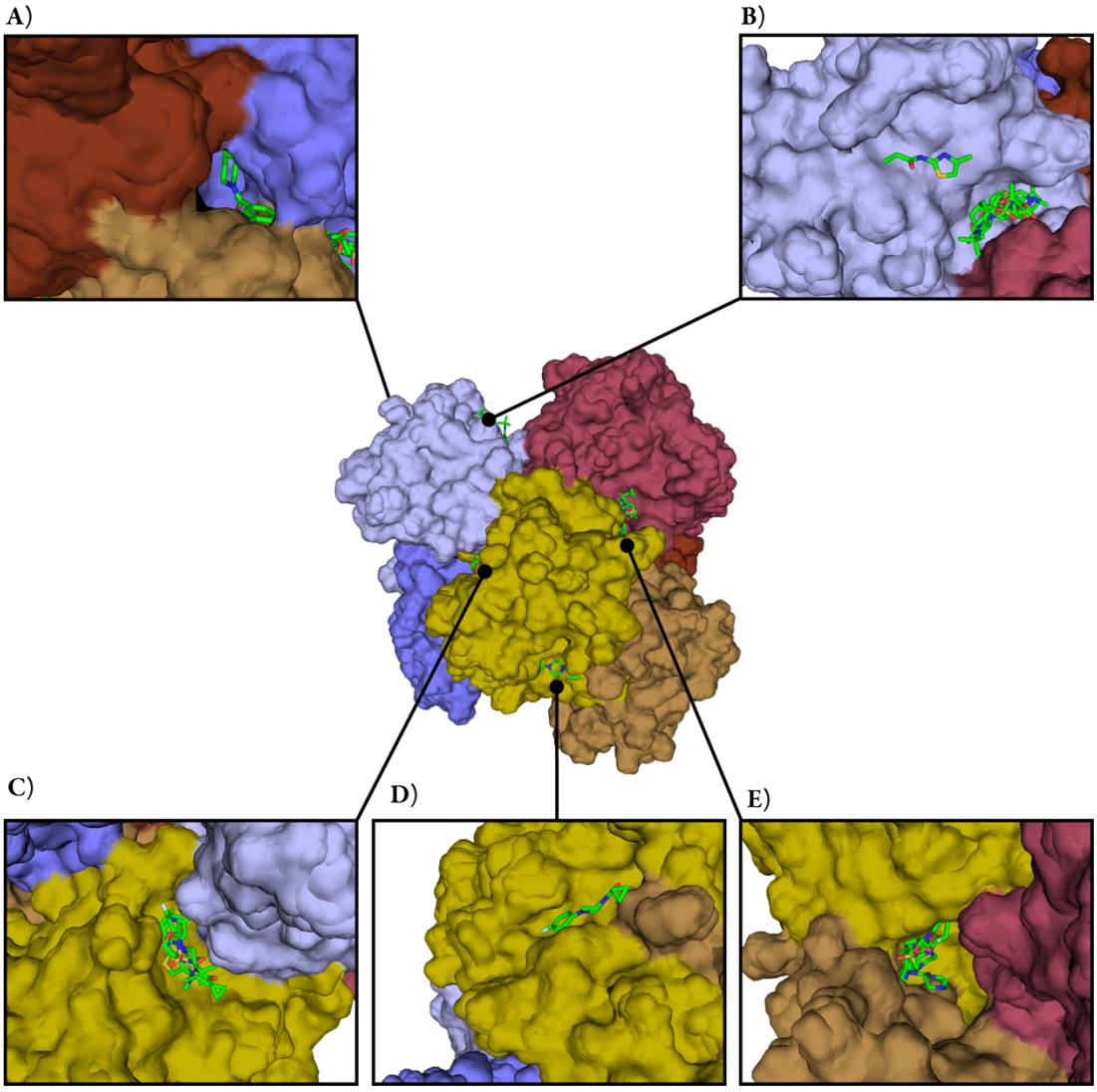


Figure 4-7| Surface Representation View of the Five Binding Sites of Soaked XChem Fragments and PHD2$_{181-407}$. (A) Surface depiction of binding site 4. (B) Surface depiction of binding site 5. (C) Surface depiction of binding site 2. (D) Surface depiction of binding site 1. (E) Surface hole of binding site 3 in the active site. (A-E) Surface representation is displayed for each chain (chain A-slate, chain B-olive, chain C-sand, chain D-light blue, chain E-raspberry, and chain F-chocolate). Abbreviations: Prolyl hydroxylase isoform 2 (PHD2). *Xtal-IDs*: *V*, *W*, *X*, *Y*, *Z*, *AA*, *BB*, *CC*, *DD*, *EE*, *FF*, *GG*.

4.2.1 XChem Binding Site 1

The first solvent exposed binding site (1) is a shallow pocket located between the *N*-terminal α3 and *C*-terminal α4 helices that interacts with the *C*-terminal residues of the HIFα-peptides. The pocket contains two positively charged Arg281 and Arg295 residues and one aromatic sidechain from Tyr390 (**Figure 4-8**). Evidence for four sulfur containing (*e.g.*, thiopene and sulfanediol) and one electronegative (fluorobenzene) fragments were observed to be bound at the site (**Figure 4-8**).

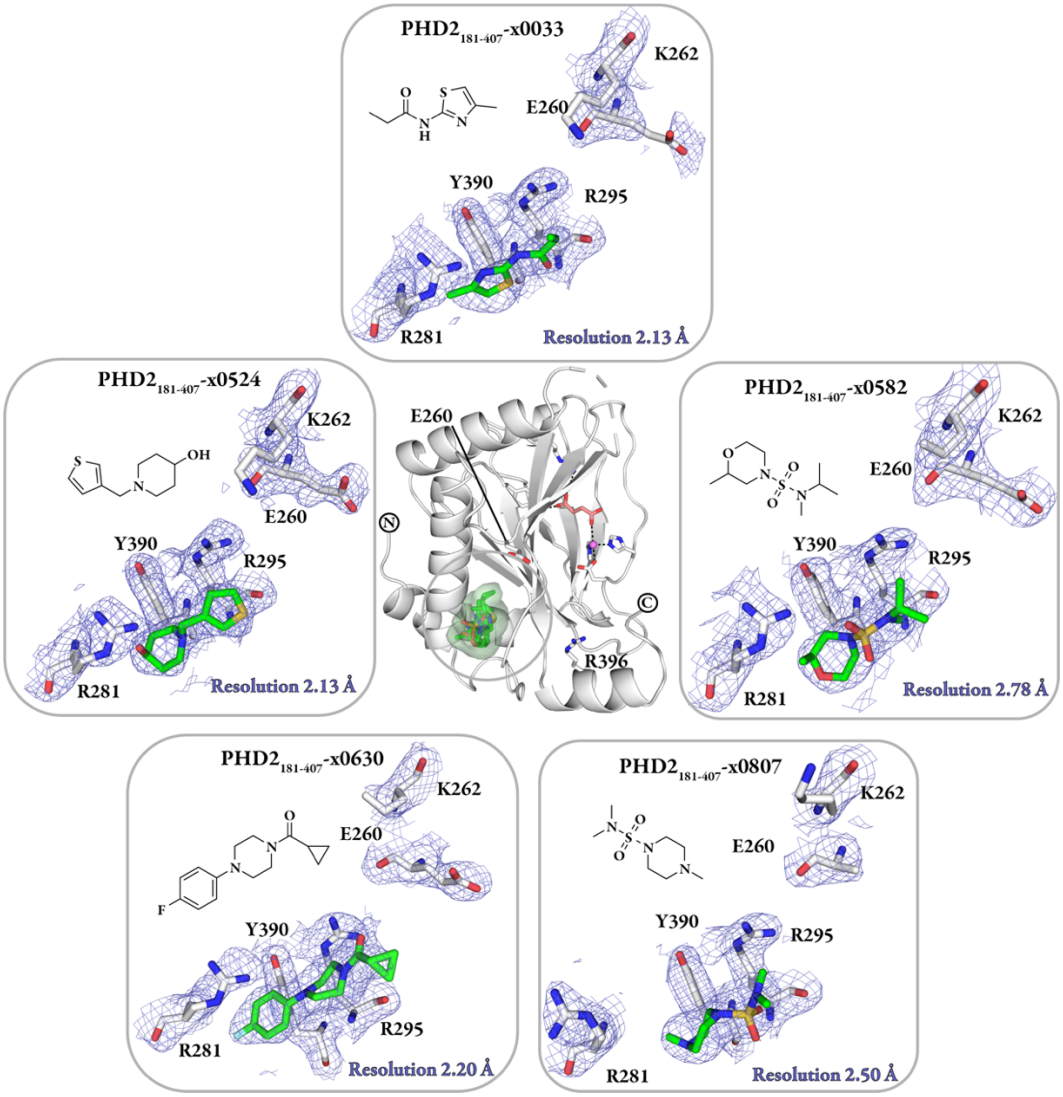


Figure 4-8| View of Binding Site 1 of PHD2$_{181-407}$ with Soaked XChem Fragments. The binding modes of the XChem fragments in binding site 1 are displayed as sticks (green). Key residues of the pocket are depicted as sticks (white). The 2mF_o-DF_c electron density maps (contoured to 1.0 σ) are illustrated as mesh (blue). In the centre, a cartoon representation of PHD2$_{181-407}$ (white) shown with the surface representation (green) of the aligned fragments. Abbreviations: Prolyl hydroxylase isoform 2 (PHD2). *Xtal-IDs: V, X, AA, DD, GG.*

Binding site 1 was observed only in chains A, B, and E of the crystal form (**Figure 4-6**). The carboxylate sidechain of Glu260 near the is positioned ~8-9 Å (measured using COOT, **6.6.9.3**) from the binding site 1 and may provide a target for further fragment modification (**Figure 4-8**). Fragment x0033 (*Xtal-V*) is one of the smallest fragments observed to bind to complex site 1; the carbonyl of x0033 is positioned 9-10 Å away from *C*-terminal residues, specifically, the guanidinium moiety of Arg396 (measured using COOT, **6.6.9.3**, **Figure 4-8**). A linker from the fragments that targets the residues of the *C*-terminal α4 helix could potentially affect HIFα-substrate binding. It should be noted that the Arg396 sidechain is observed in two different conformations in the complex structures of $PHD2_{181-426}$ with both $HIF1\alpha_{395-413}$-NODD and $HIF1\alpha_{556-575}$-CODD, indicating its flexibility (PDB: 5L9V and 5L9B, discussed in section **2.1**, **Figure 2-2**).[40]

Binding site 1 provides a previously uncharacterised pocket for inhibition or activation of PHD2 (**Figure 4-8**). Further work will be required to better understand the nature of targeting a small-molecule to site 1 of PHD2.

4.2.2 XChem Binding Site 2

The second solvent exposed identified binding site (2) of the $PHD2_{181-407}$ is located between the α1 helix, the β1 *N*-terminal extension strand, and the βV DSBH strand (**Figure 4-9**). Binding site 2 is formed from: (i) His205, (ii) Ile207, (iii) Lys350, (iv) Gln352, (v) Asp355, and (vi) Arg362 (**Figure 4-9**). Site 2 is of interest as the 3C cyclic peptide bind in the position (PDB: 6YW3).[34] Eight fragments were observed in the site, five of them contain sulfur based functional groups (thiopene and sulfanediols, **Figure 4-9**). The three other bound fragments contain flexible morpholine/cyclic ring systems that apparently enable them to mould into binding site 2 (**Figure 4-9**). Partially charged atoms (S1-thiopene, O1-aminoethanol, O1-furan, O01-sulfanediol, carbonyl O1-*tert*-

butyl, and F1-fluorobenzene) of the fragments interact with the polar sidechains of the site 2 residues (imidazole of His205, aminoethanol of Asn352, and guanidinium of Arg362, **Figure 4-9**). As the fragments exhibit variation in their binding position in the pocket, potential linking of fragments may be a viable option for future inhibitor/or enhancer design (**Figure 4-9**). Thus, the furan sidechain of x0555 (*Xtal-Z*) could be linked with the aminoethanol sidechain of x0042 (*Xtal-W*) fragment to form an interaction spanning the length of the pocket of site 2 (**Figure 4-9**).

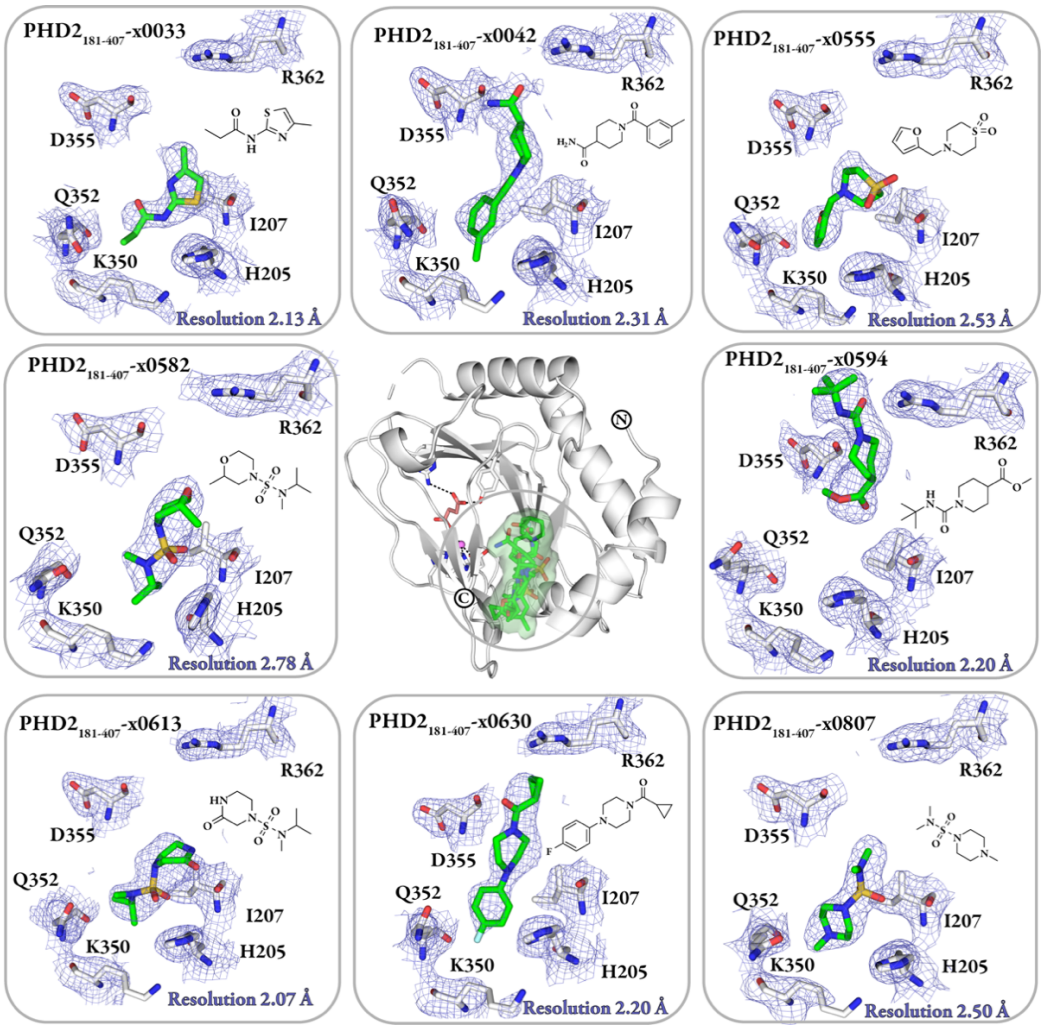


Figure 4-9| Views from Binding Site 2 of PHD2$_{181-407}$ with Soaked XChem Fragments. The binding events of the XChem fragments in binding site 2 are displayed as sticks (green). Key residues of the pocket are depicted as sticks (white). The 2mF_o-DF_c maps (contoured to 1.0 σ) are illustrated as mesh (blue). The centre is a cartoon representation of PHD2$_{181-407}$ (white) shown with the surface representation (green) of the aligned fragments. Abbreviations: Prolyl hydroxylase isoform 2 (PHD2). *Xtal-IDs*: *V*, *W*, *Z*, *AA*, *BB*, *CC*, *DD*, *GG*.

As a large portion of the fragments bind to site 2, as well as the 3C cyclic peptide, it is of interest to characterise the biological relevance of the pocket in the PHDs. Future work will be conducted to determine the biophysics of targeting small-molecules at site 2.[41] The observed structural data of complexed ligands at binding site 2 may provide an alternative route to PHD inhibition or enhancement of the PHDs activity (*i.e.*, the 3C binding site was reported to not be specific for one PHD isoform).[42]

4.2.3 XChem Binding Site 3

Binding site 3, buried within the active site, is formed from the substrate interacting guanidinium functionality of Arg322 and the indole sidechain of Trp389 (**Figure 4-10**).[43–45] Seven fragments were observed to bind in Site 3. Five of the fragments contain six-membered aromatic rings (fluorobenzene, chlorobenzene, and toluene) and two of the fragments contain five-membered aromatic rings (furan and thiolene sidechains, **Figure 4-10**).

The fragments bind with a double π-π-stacking interaction with the guanidinium side of Arg322 and *via* a T-shaped π-interaction with the indole sidechain of Trp389 (**Figure 4-10**).[45] A similar interaction is observed between the bi-phenyl (**28** and **29**) and chlorophenoxy (**32**) sidechains of the 4-hydroxypyrimidines (JPHM-8, **28**), spiro[4.5]decanones (JPHM-2-167, **29**), and monopyridine (ZXJ-1, **32**, *Xtal-U*).[43–45] The fragmentd x0534 (*Xtal-Y*) and x0555 (*Xtal-Z*) contain sulfur-based functional groups (thiadiazole and sulfanediol, respectively) which interact with the sulfur atom in the sidechain of active site residue Met299 (**Figure 4-10**).

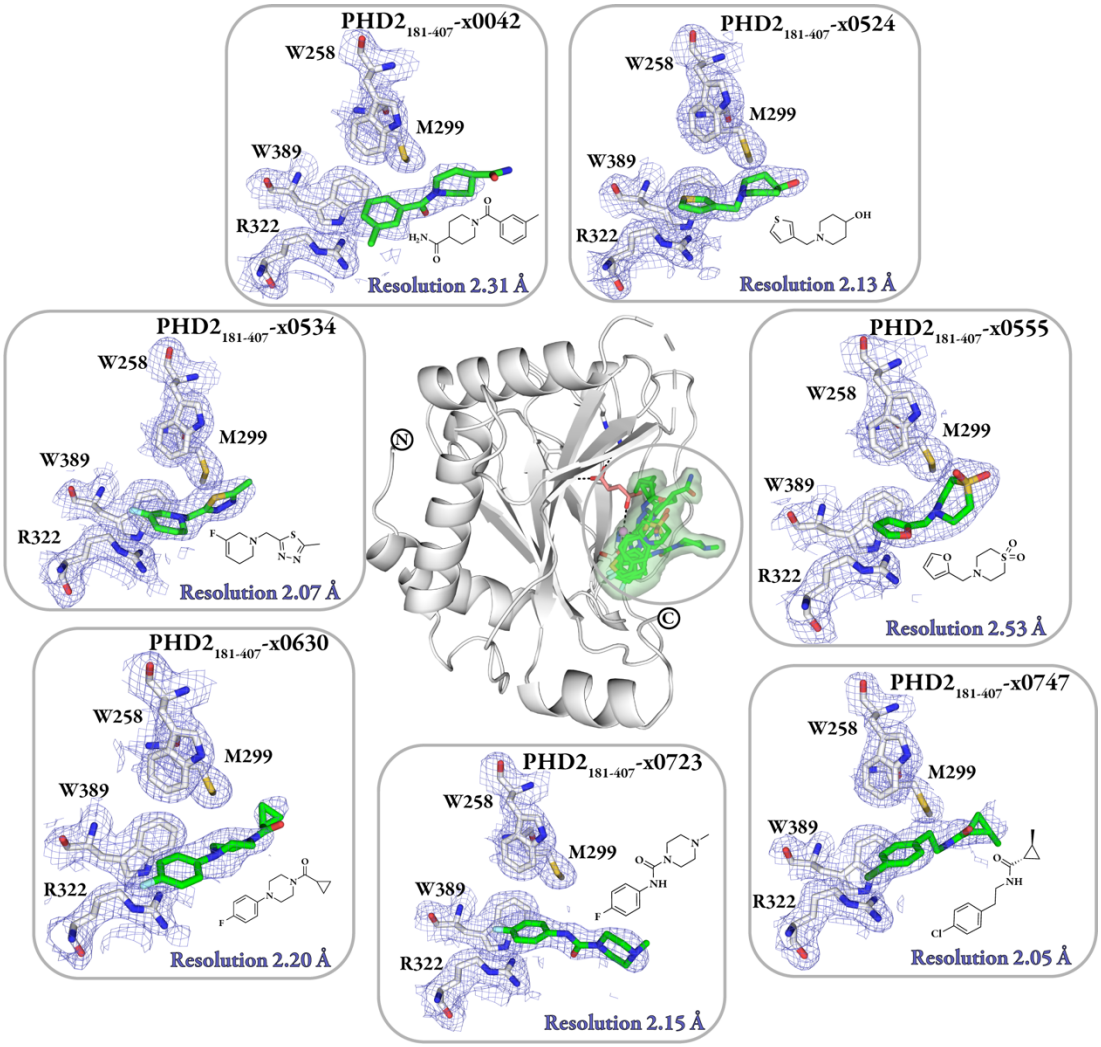


Figure 4-10| Views from Binding Site 3 of PHD2$_{181-407}$ with Soaked XChem Fragments. The binding events of the XChem fragments in binding site 3 are displayed as sticks (green). Key residues of the pocket are depicted as sticks (white). The 2mF$_o$-DF$_c$ electron density maps (contoured to 1.0 σ) are illustrated as mesh (blue). In the middle is a cartoon representation of PHD2$_{181-407}$ (white) shown with the surface representation (green) of the aligned fragments. Abbreviations: Prolyl hydroxylase isoform 2 (PHD2). *Xtal-IDs*: *W*, *X*, *Y*, *Z*, *DD*, *EE*, *FF*.

The structure of fragments occupying binding site 3, although not novel, illustrate the importance of the binding site for substrate/ligand interactions. Further medicinal chemistry could exploit Site 3 and link it with other features in the active site, such as metal coordination. Solution NMR studies should be conducted to observe whether ligands targeting binding site 3 have implications for substrate competition or displacement.[40,46–48]

4.2.4 XChem Binding Site 4

The solvent exposed binding site 4 is a 'tight'-pocket between the βIII and βIV strands of the DSBH fold (**Figure 4-11**). Furthermore, the binding site is formed from chains A, C, and F, and is not observed in chains B, D, and E (**Figure 4-11**). Three molecules of fragment x0042 (*Xtal-W*) are complexed at site 4, *i.e.*, one x0042 fragment per chain **(Figure 4-11**). The aminoethanol sidechain of x0042 interacts with the aminoethanol side of Asn377 (**Figure 4-11**). The toluene sidechain of x0042 (*Xtal-W*) forms a π-π-stacking interaction with the phenolic sidechain of Tyr380 from the neighbouring chain (ligand A-chain C, ligand C-chain F, and ligand F-chain A; **Figure 4-11**).

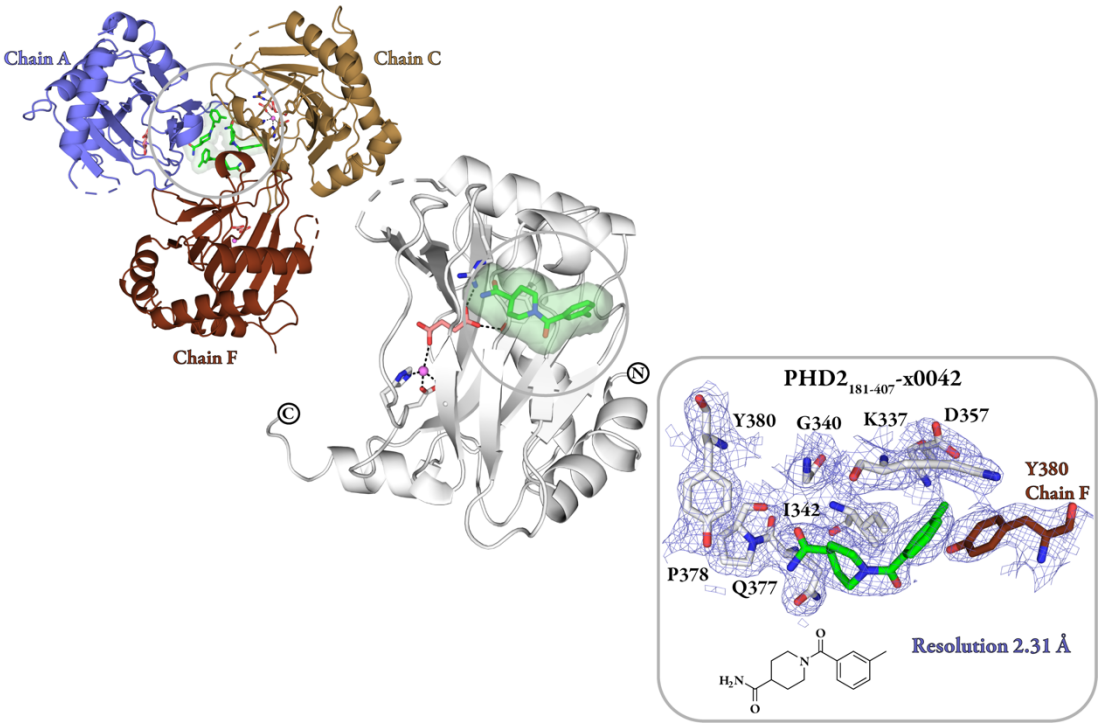


Figure 4-11| A View from Binding Site 4 of PHD2$_{181-407}$ in Complex with Fragment-x0042. The binding event of fragment-x0042 (chain C) at binding site 4 is displayed as sticks (green). Key residues of the pocket and of chain F residue Tyr380 (raspberry) are depicted as sticks. The 2mF$_o$-DF$_c$ electron density maps (contoured to 1.0 σ) are illustrated as mesh (blue). On the left and middle are a cartoon representation of PHD2$_{181-407}$ (chain A-slate, chain-C-sand/white, and chain-F-chocolate) shown with the surface representation (green) of fragment-x0042. Abbreviations: Prolyl hydroxylase isoform 2 (PHD2). *Xtal-ID*: *W*.

The fragment interaction at Site 4 is most likely due to the crystal packing of the PHD2$_{181-407}$.Mn(II).succinate crystal form (*Xtal-P*). However, Site 4 might have a biological role in complexation of another unknown protein and further studies could be conducted to investigate the significance of the region in the positive or negative modulation of PHD activity.[41]

4.2.5 XChem Binding Site 5

Solvent exposed binding site 5 was observed at the *N*-terminal α1 helix of PHD2$_{181-407}$ in complex with x0033 (*Xtal-V*, **Figure 4-12**). The thiazole ring of x0033 is positioned to bind *via* π-π-stacking interactions to the phenolic sidechain of Tyr197 (**Figure 4-12**).

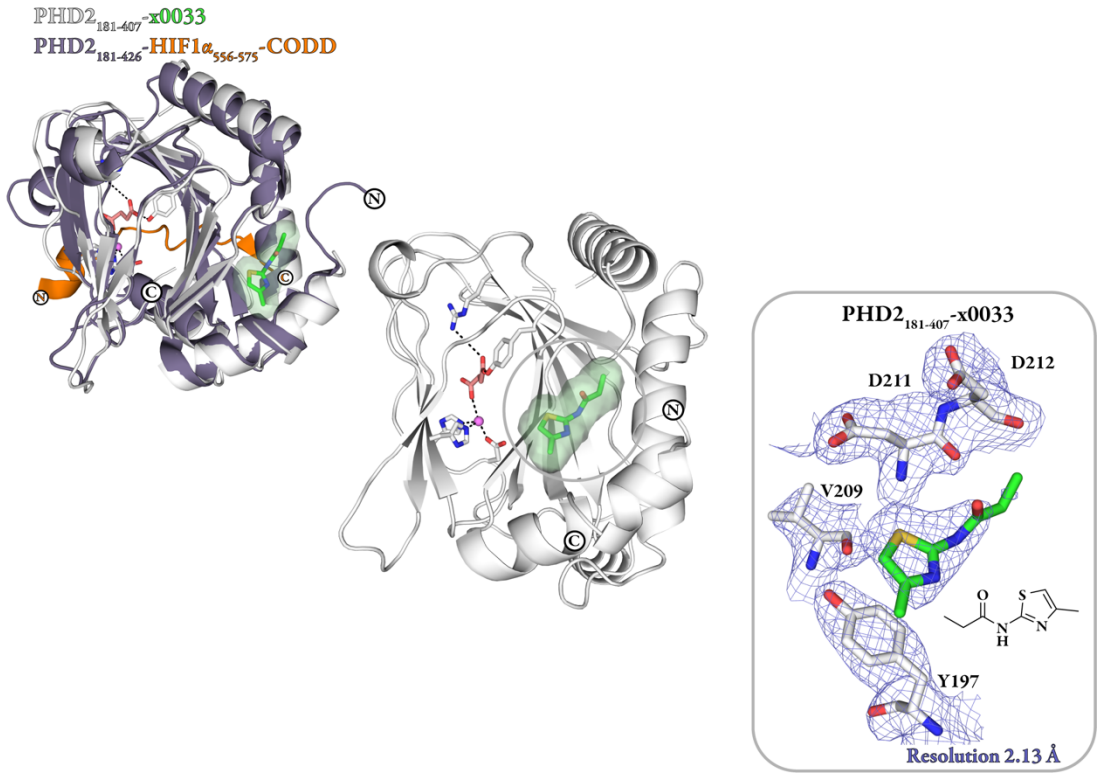


Figure 4-12| A View from Binding Site 5 of PHD2$_{181-407}$ in Complex with Fragment-x0033 and Superimposed with the PHD2$_{181-426}$.HIF1α$_{556-574}$-Substrate Structure. The binding event of fragment-x0033 at binding site 5 is displayed as sticks (green). Key residues of the pocket are depicted as sticks (white). The 2mF$_o$-DF$_c$ maps (contoured to 1.0 σ) are illustrated as mesh (blue). On the left is the aligned structure of PHD2$_{181-407}$ (white)-x0033 fragment (green) and PHD2$_{181-426}$ (purple)-HIF1α$_{556-575}$-CODD peptide (orange). On the middle is a cartoon representation of PHD2$_{181-407}$ (white) is shown with the surface representation (green) of fragment-x0033. Abbreviations: Prolyl hydroxylase isoform 2 (PHD2), Hypoxia-inducible-factor isoform 1α (HIF1α). *Xtal-IDs*: *V*.

The observed $2mF_o$-DF_c electron density map displays some smearing which may reflect the apparently weak binding nature of fragment x0033 (*Xtal-V*, **Figure 4-12**). The ethyl sidechain of the fragment could be modified for a charged group, *i.e.*, such as an aminoethanol group, that may interact with the carboxylate of Asp212. Modifications of x0033 (*Xtal-V*) could improve the binding strength of small-molecule at site 5 (**Figure 4-12**). Targeting the *N*-terminus has previously shown that a non-competitive cyclic peptide can bind to tPHD2, including the site 5 pocket, and positively influence the activity of the enzyme (PDB: 6YW3).[34,42]

Further medicinal and biophysical characterisation will be required to better understand the nature of site 5 and to improve its targeting with small-molecules. Since the pocket is near the *N*-terminus, small-molecule binding at site 5 might affect interactions with the *N*-terminal residues in the full-length PHD2 as seen with the 3C cyclic peptide.[42] (*Thank you to Diamond Light Source Ltd. for access to the XChem fragment screening facility and DSI-Poised and FragLite libraries. Also, thank you to the beamline staff and for the allocated beamtime on beamline I04-1.)*

4.2.6 XChem Summary

The XChem-PHD2 project was the first attempt at a fragment-based-drug discovery approach to inhibitor design of the PHDs. The identified hits and crystallisation conditions are a starting point for future studies, either by screening more XChem fragments or by developing/or linking the fragments with other reported PHD inhibitors.

Fragment Binding Site Rank

1) Site 3
2) Site 1
3) Site 2
4) Site 4
5) Site 5

Four out of the five sites identified are bulk solvent exposed. The only site buried within $PHD2_{181-407}$ is site 3 that has been previously reported as the 'aromatic' pocket and targeted by both the 4-hydroxypyrimidine (**29**), spiroindolone (**30**), and ZXJ-1 (**33**) series of compounds.[43-45] Site 1 is of interest as the *C*-terminus of the HIFα-peptides interacts in this pocket and a potent inhibitor may prevent HIFα-substrate binding. In combination with a PHD inhibitor that coordinates the active site metal might produce a synergistic effect. Site 2 is the binding site of the non-competitive 3C cyclic peptide.[34] As the 3C peptide does not inhibit the PHDs, the site is likely not a good of a target for PHD inhibitor design. Sites 4 and Sites 5 are likely induced by the crystal lattice packing.

The identified fragments will be evaluated in solution-based studies to determine the IC_{50} values for each compound. The structural data will be aligned with other reported PHD2.inhibitor complexes to assess whether linking of fragments could be an option for further design.

4.3 $PHD2_{181-407}$ in Complex with Derivatives of Takeda-17

In parallel with the XChem fragment screen, a soaking-based study was conducted to investigate the $PHD2_{181-407}$ complex structures with derivatives of non-conventional, monodentate binding PHD inhibitors.[31] It was thought that the small-molecule inhibitors could be soaked into $PHD2_{181-407}$.Mn(II).succinate crystals (*Xtal-P*) in a similar fashion as the XChem fragments (**4.2**). The objective of the work described here was to explore the active site 'back'-pocket (*i.e.*, residues Lys332-Gly400) where Takeda-17 (**17**) interacts (Asn331) and to potentially design isoform-selective inhibitors (**Figure 4-13**).[31] **17** is reported to preferentially inhibit isoform $PHD1_{167-403}$ over $PHD2_{181-416}$.[31] Additional objectives were to make sequential substitutions or modifications to the monodentate

binding inhibitors using a structure-guided approach to inhibitor design.[17] As derivatives of **17** could be soaked into the PHD2$_{181-407}$ crystal form and replace succinate, eight complex structures with various derivatives were obtained. (*Thank you to Ms. Caitlin Gold and Mr. Marcin Bielinski for their efforts in the synthesis of the Takeda-17 derivatives used for the soaking-based studies.*)

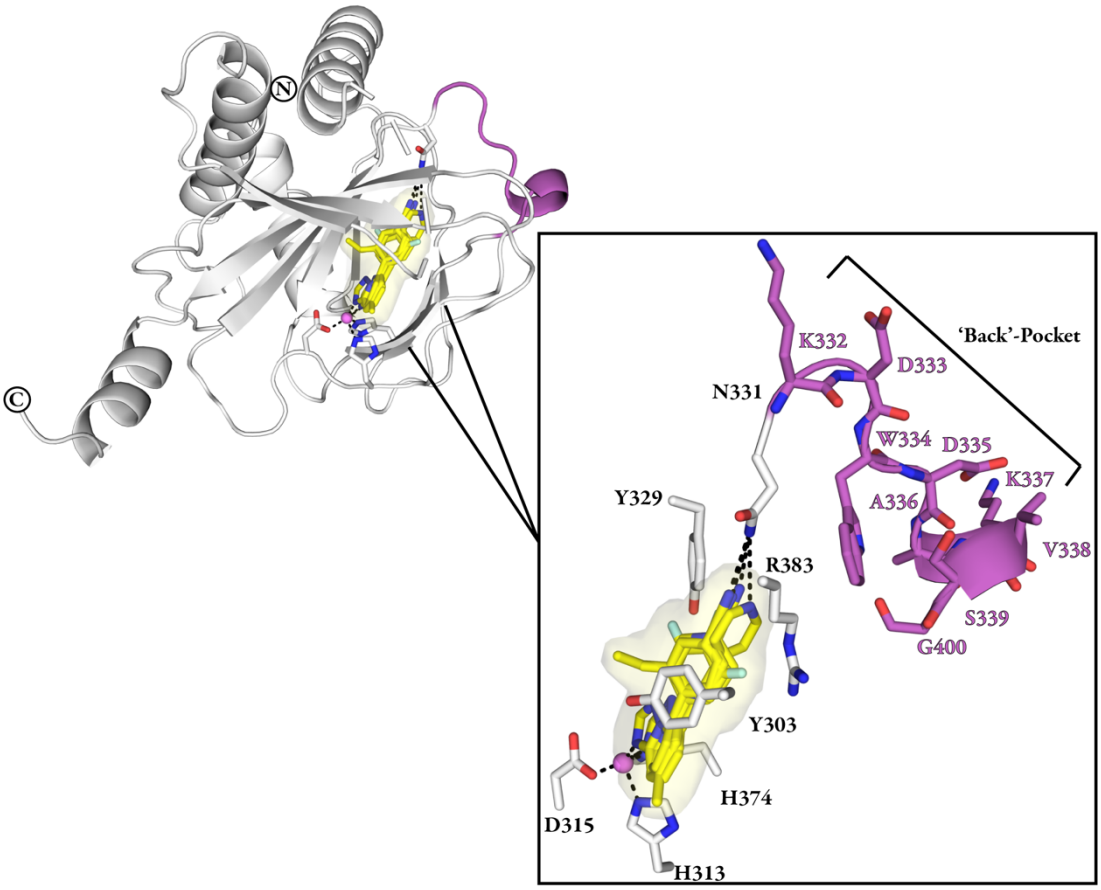
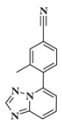
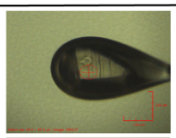
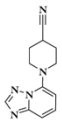
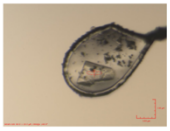
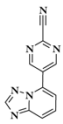
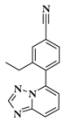
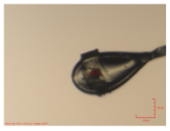
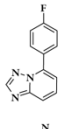
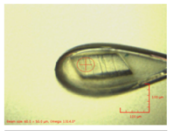
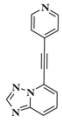
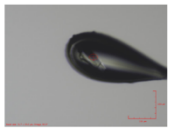
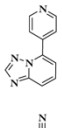
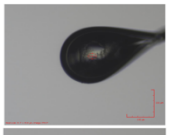
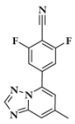
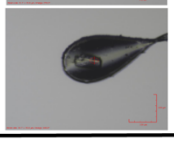


Figure 4-13| A View from Superimposed Monodentate Binding Derivatives in Complex with PHD2$_{181-407}$ and the Interaction with the Active Site 'Back'-Pocket. PHD2$_{181-407}$ is displayed as a cartoon (white). The key active site residues (white) and ligands (yellow, surface representation is illustrated) are depicted as sticks. The 'back'-pocket of residues Lys332-Gly400 is shown as a cartoon and sticks (purple). Active site interactions are represented by dashes (black). Mn ion is displayed as a sphere (violet). Abbreviations: Prolyl hydroxylase isoform 2 (PHD2). *Xtal-IDs*: *HH*, *II*, *JJ*, *KK*, *LL*, *MM*, *NN*, *OO*.

The inhibitors were soaked using various concentrations, times, and cryo-protectants as the methods of soaking evolved over the course of the project (**Table 4-2**). After the XChem fragment screen, 10% (v/v) DMSO was determined to be a suitable cryo-protectant for the *Xtal-P* crystal form (**Table 4-2**), whereas use of glycerol,

as a cryo-protectant, was observed to reduce the resolution of the datasets. 11 crystals with Takeda-**17** derived compounds were soaked (**6.9.8**) and cryo-cooled for data collection at a synchrotron source (**6.6.7.2**). However, only eight of the structures had derivatives of **17** complexed into the active site; (i) CG3, (ii) CG4, (iii) CG10, (iv) CG16, (v) CG17, (vi) CG22, (vii) CG28, and (viii) CG37 (**Table 4-2** and **Figure 4-14**; Validation and Crystallographic Data Processing and Refinement Statistic tables are given in **Appendix I** & **II**). During the soaking of inhibitors, the resolution was often affected due to cracks introduced in the crystals during the experiment. (*Thank you to Dr. Yu Nakashima for his help and assistance on the soaks, crystal harvesting, and refinement of some of the crystals and datasets.*)

Table 4-2| Overview of Soaked Based Studies of $PHD2_{181-407}$ in Complex with the Takeda-17 Derivatives.

Crystal ID	Structure	Mount	PHD2 IC_{50} (μM)	Res (Å)	Soak (min)	Concenstration	Cryo-protectant
$PHD2_{181-407}$-CG3 *Xtal-HH*			44.5	2.26	15	10 mM	DMSO,Glycerol
$PHD2_{181-407}$-CG4 *Xtal-II*			>100	2.40	20	6 mM	DMSO
$PHD2_{181-407}$-CG10 *Xtal-JJ*				2.68	20	6 mM	DMSO
$PHD2_{181-407}$-CG16 *Xtal-KK*			>100	2.70	20	6 mM	DMSO
$PHD2_{181-407}$-CG17 *Xtal-LL*			69.8	2.28	15	10 mM	DMSO,Glycerol
$PHD2_{181-407}$-CG22 *Xtal-MM*			5.98	2.38	20	5 mM	DMSO,Glycerol
$PHD2_{181-407}$-CG28 *Xtal-NN*			>100	2.26	20	5 mM	DMSO,Glycerol
$PHD2_{181-407}$-CG37 *Xtal-OO*			7.08	2.53	20	5 mM	DMSO,Glycerol

***NB: IC_{50} values are from unreported data with conditions: 0.15 μM $PHD2_{181-426}$, 10 μm $(NH_4)Fe(II)(SO_4)$, 100 μm sodium-L-ascorbate, 5.0 μm HIF1α-CODD peptide, and 10 μm 2OG (6.5.2.2).**

(Work conducted by Dr. Anthony Tumber and Ms. Caitlin Gold.)

The collected datasets were phased with MR using the two-chain model (*Xtal-P*, **3.2** and **4.2**). Biophysical and structural characterisations were carried out to investigate the monodentate binding derivatives in complex with $PHD2_{181-407}$ to investigate if certain modifications of the small-molecule inhibitors influenced the active site chemistry and/or the induced-fit mechanism (discussed in section **3.4**).

4.3.1 Active Site Chemistry with Monodentate Derivatives

The 'back'-pocket of the active site (which binds the C5 carboxylate of 2OG) can accommodate a range of functional groups from electronegative groups to small heterocyclic rings (note distances from the N1/F1 of the ligand sidechain to the Nδ2 atom of Asn331 are observed between 3.30-5.90 Å, **Figures 4-13**, **4-14**, and **4-15**). All the derivatives of **17** interact *via* the CN, N1, or F1 atoms with the Nδ2 atom of the sidechain of $Asn331_{PHD2}$.[31] As previously observed, the derivatives coordinate to the active site metal *via* the N1 atom of the triazolopyridine ring, in a similar manner (PDB: 5V18 and *Xtal-T*).[31] Each of the derivatives of **17** exhibit a π-π-stacking interaction with the phenol sidechain of Tyr303 (**Figure 4-14** and **4-15**).[31] In the case of CG37, methyl addition to the core pyridine extends towards the substrate binding groove and could potentially disrupt substrate complexation (*Xtal-OO*, **Figure 4-14H** and **4-15**).[40,49] Overall, the active site residues occupy similar positions in all the complex structures of the monodentate binding derivatives (**Figure 4-15**). CG22 and CG37 both influence the guanidinium sidechain of Arg383 relative to the other monodentate binding derivative complexes (*Xtal-MM* and *Xtal-OO*, respectively, **Figure 4-15**). The difluorobenzene of CG37 interacts with the phenolic sidechain of Tyr329 and apparently disorders the sidechain of Arg383; weak density is observed for the guanidino group (*Xtal-OO*, **Figure 4-15**).

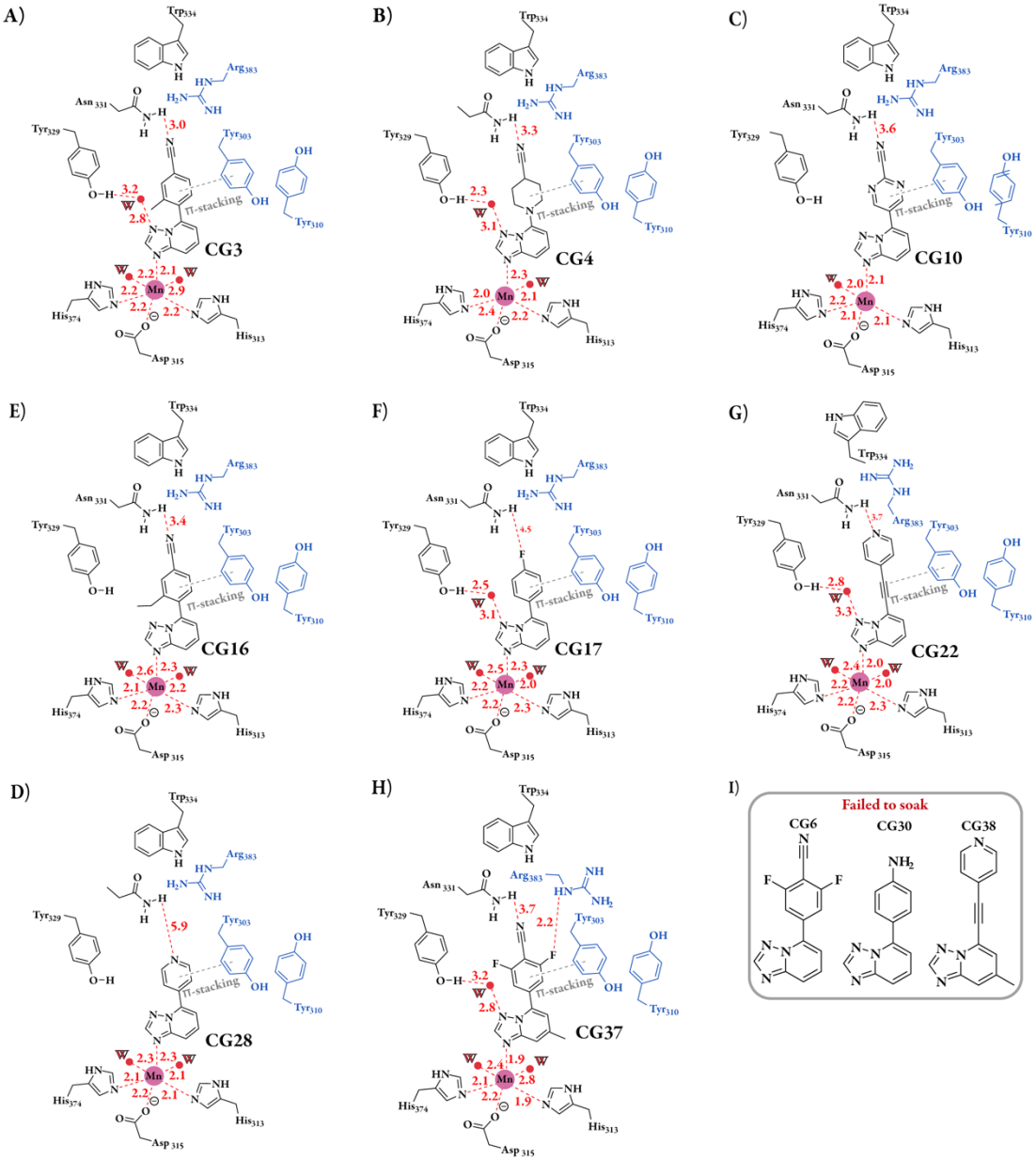


Figure 4-14| 2D Overview of the PHD2$_{181-407}$ Active Site in Complex with Takeda-17 Derivatives. (A-H) The chemical sidechains of the active site residues of PHD2$_{181-407}$ are displayed. Key active site residues are shown (blue). Metal ions and water molecules are depicted as circles. Chemical interactions are represented as dashes (red) with bond lengths (Å). (I) Takeda-17 (**17**) derivatives that failed to soak into the PHD2$_{181-407}$.Mn(II).succinate crystal form. Abbreviations: Prolyl hydroxylase isoform 2 (PHD2). *Xtal-IDs*: *HH*, *II*, *JJ*, *KK*, *LL*, *MM*, *NN*, *OO*.

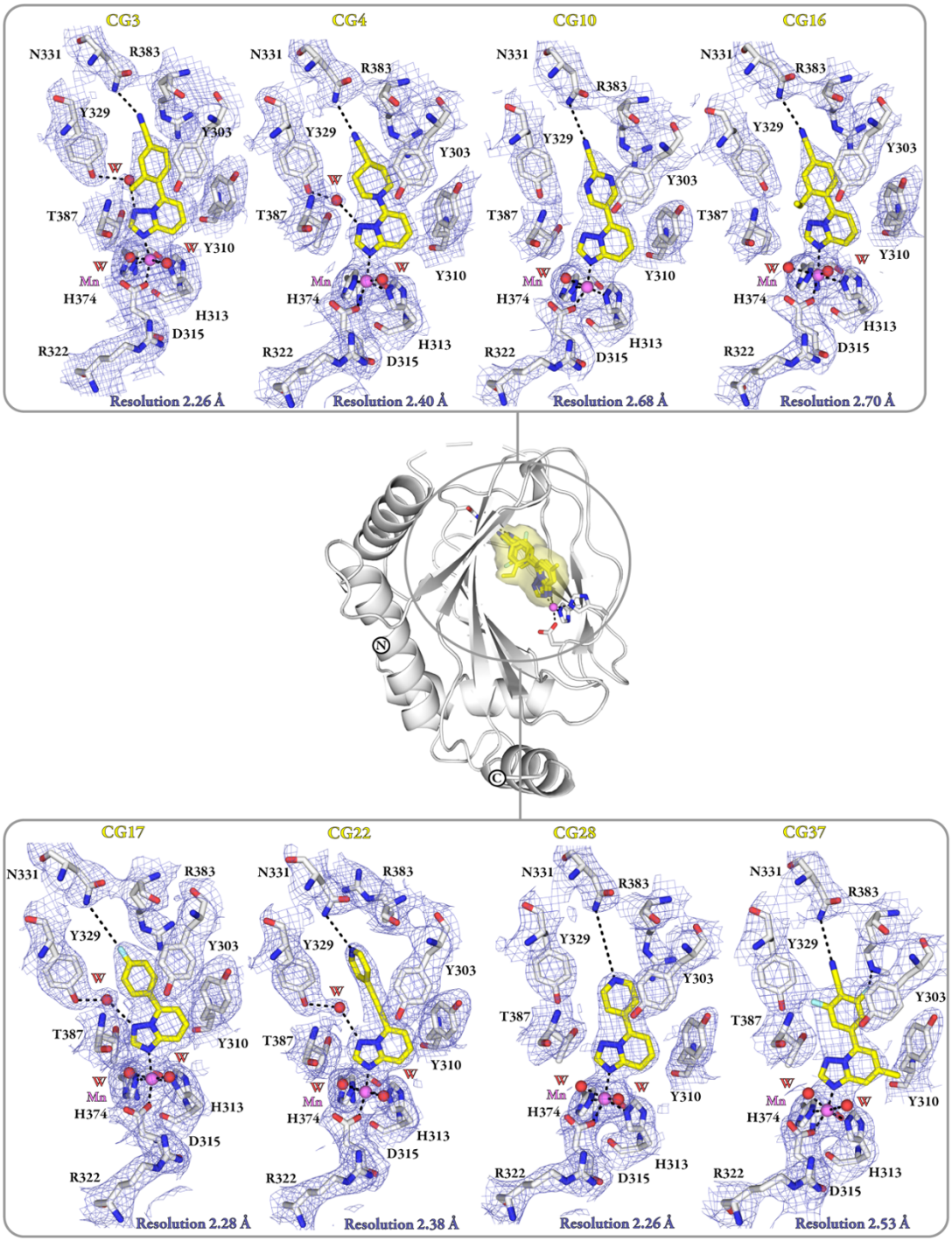


Figure 4-15 | Structures of PHD2$_{181-407}$ in Complex with Derivatives of Takeda-17 (17) and Views of the Active Site Interactions. PHD2$_{181-407}$ is depicted as a cartoon (white) and the surface representation of the aligned ligands is shown (yellow). Active site residues (white) and Takeda-17 (**17**) derivatives (yellow) are displayed as sticks. The $2mF_o$-DF_c electron density maps (contoured to 1.0 σ) are illustrated as mesh (blue). Key interactions are represented as dash (black). The metal ions (Mn-violet) and water molecules (red) are shown as spheres. Abbreviations: Prolyl hydroxylase isoform 2 (PHD2). *Xtal-IDs*: *HH*, *II*, *JJ*, *KK*, *LL*, *MM*, *NN*, *OO*.

The acetylene of CG22 creates a significant conformational change *via* an interaction with the guanidinium moiety of Arg383, which is observed to be shifted further into the 'back'-pocket of the active site (*Xtal-MM,* **Figures 4-13** and **4-16**). Comparisons with a reported structure of PHD1 in complex with **17** (PDB: 5V1B) and with the AlphaFold predicted model of PHD3, reveals $PHD2_{181-407}$ has more sequence variation of the 'back'-pocket when compared to $PHD1_{167-403}$ and PHD3 (**Figure 4-16**).[50] Significant work has been attempted to find a suitable crystallisation condition for PHD3 and truncated mutant of PHD3 (*work conducted by Dr. Rasheduzzaman Chowdhury*).[51] Furthermore, crystallisation of both PHD1 and PHD3 isoforms would provide the ability to biophysically characterise the potential isoform-selectivity induced by the conformational change (**Figure 4-16**). [28] If the 'back'-pocket interaction only occurs in the PHD2 isoform, then it may be a feature to exploit in the design of isoform-selective PHD inhibitors.[28] Solution studies are required to further characterise whether the conformational change has any effect on the inhibition or positive modulation of PHD2. Also, it cannot be ruled out that the Trp334 indole 'flip-out' could be a crystallographic artefact. However, visualisation of the effects introduced by the acetylene of CG22 in the 'back'-pocket of $PHD2_{181-407}$ provides a new target for structure-guided drug discovery that differs from the clinically applied 2OG-mimetics in use today (discussed in section **1.5**).[17]

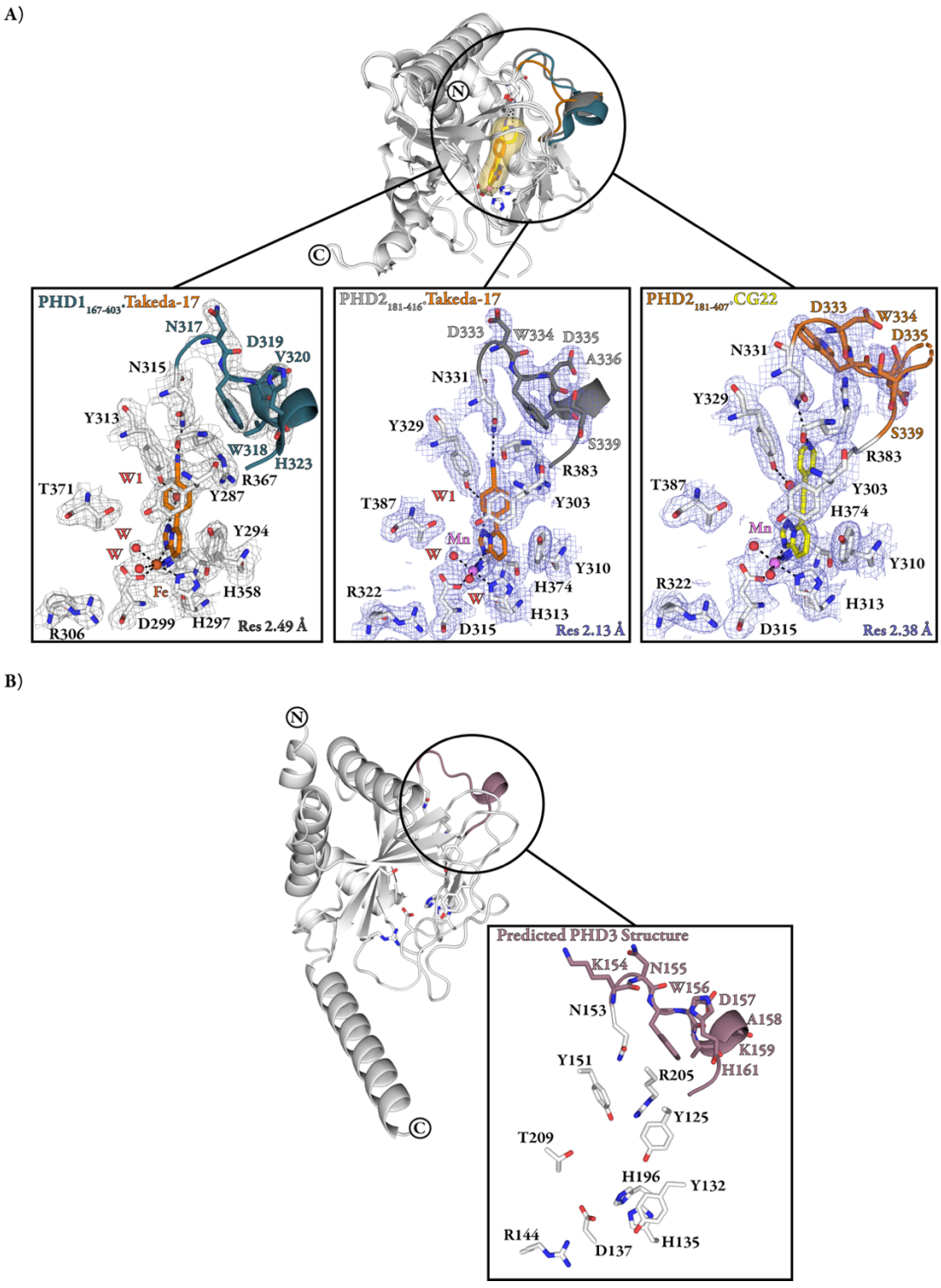


Figure 4-16| Comparison of the Back Pocket Loop between PHD1-3 Isoforms and View from the Active Site. (A) Alignment, surface representation (orange-yellow), and active site comparison of PHD1 (PDB: 5V1B) and PHD2$_{181-407}$ Complex structures with Takeda-17 (orange) and CG22 (yellow) monodentate ligands. The 2mF_o-DF_c electron density map (contoured at 1.0 σ) is illustrated as mesh (PHD1-dark grey and PHD2$_{181-407}$-blue). Metal ions and water molecules are depicted as spheres. Key active site interactions are represented by dashes (black). (B) AlphaFold predicted structure of PHD3. (A-B) PHD1-3 chains are shown as cartoons (white) and active site residues are represented as sticks. The back pocket loop conformation is highlighted for each isoform of the PHDs (PHD1-**17**-dark teal, PHD2$_{181-407}$.**17**-grey, PHD2$_{181-407}$.CG22-orange, and PHD3-red). Abbreviations: Prolyl hydroxylase isoforms 1-3 (PHD1-3). PDB: 5V1B. *Xtal-IDs*: *T*, *MM*.

4.4 Summary and Future Directions

The 20 previously unreported structures of $PHD2_{181-407}$ in complex with various small-molecule fragments and monodentate binding derivatives, provides a new platform for the design of novel selective PHD inhibitors. With a better insight into the subtle biophysical features of ligand binding to the PHDs, the regions may be targeted to maximise potency and selectivity. Potential isoform-selective PHD inhibition could regulate HIFα stabilisation in a tissue-specific manner.[29] The AlphaFold method to predict the structures of CP4H and PHD3, both challenging targets for crystallisation, has allowed comparisons of their models with structures of PHD1-2.[50] To achieve potent and selective inhibition of the PHDs, the distinct characteristics should be exploited to prevent potential off-target effects through inhibition of other 2OG oxygenases. Potentially, some of binding sites identified from the XChem screen may prove to be allosteric regulators of PHD inhibition and/or enhancement (discussed in section **4.2**).[41] Future studies will further characterise the binding sites identified from the fragment screen and may reveal the biological relevance of these regions in the PHDs.[41]

Future inhibitor design for the PHDs could exploit the observed interactions with the sidechains of residues: (i) Arg322, (ii) Trp389, (iii) Thr387, (iv) Arg383, (v) Tyr303, and (vi) Tyr310 (**Figure 4-17**). In particular, to design inhibitors that bind away from the 2OG binding pocket is of interest (**Figure 4-17**). Away from the 2OG pocket is a conserved Thr, present in PHD1-3 and *Ta*PHD.[52] Thr387 is likely an extremely important residue for catalysis and has been shown to alter the O_2-kinetics of tPHD2.[53] Fumaric acid, considered to be a natural inhibitor of the PHDs, is one of the few ligands to target and interact with the alcohol sidechain of Thr387 (*Xtal-Q*; **Figures 3-2** and **3-11**, respectively).[54] Fumaric acid derivatives, or small-molecules with similar properties as the

alkene of fumarate, in combination with a halogenated aromatic and acetylene moieties could potentially produce a potent and selective inhibitor of the PHDs (**Figure 4-16**).

Future work, both through crystallographic and solution studies, will be employed with the use of the acquired structural data to better characterise the biophysics of PHD inhibition or activation small-molecules ligand binding at the identified binding pockets, including potentially a further XChem screen using the reproducible acetate-derived PHD2$_{181-407}$.HIF2α$_{523-542}$-CODD crystallisation system (discussed earlier in **2.4**).

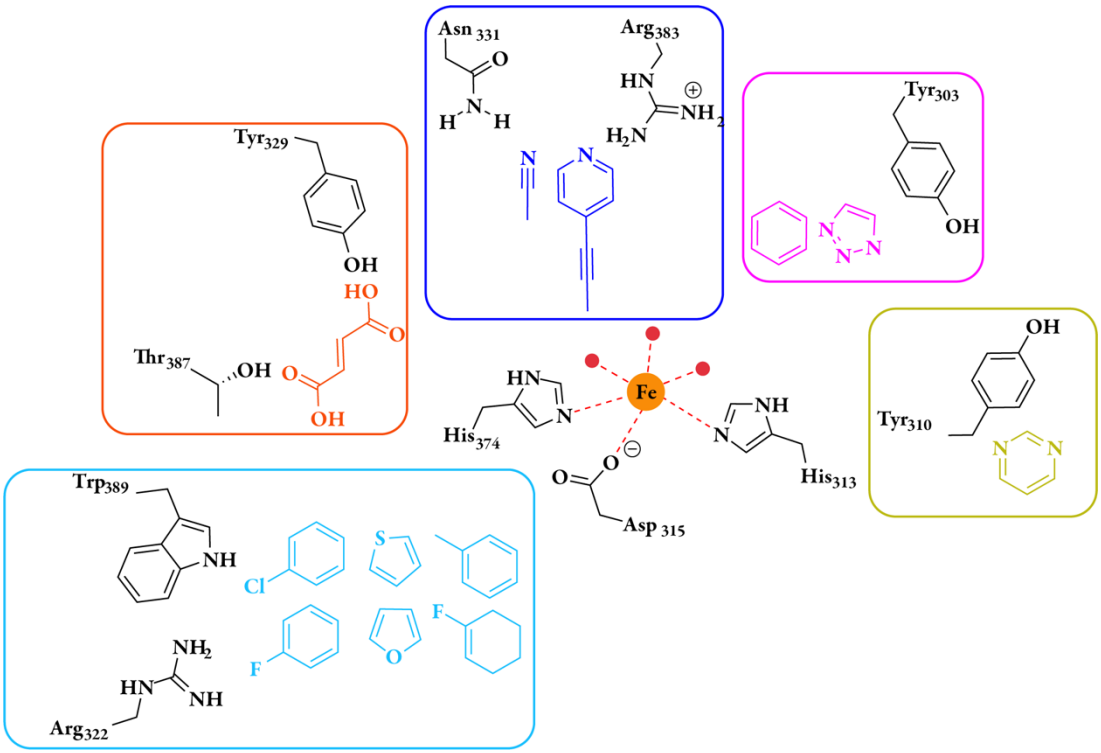


Figure 4-17| Chemical Moieties that can Modulate the Biophysics of the Paired PHD2$_{181-407}$ Active Site Sidechains. The guanidinium and indole sidechains of Arg322 and Trp389, respectively, have been observed to interact with aromatic motifs (cyan) through π-π-stacking interactions. The ethanoic and phenolic sidechains of Thr387 and Tyr329, respectively, have been observed to interact with the carboxylates of fumarate (orange, **3.2.3**). The acetamide and guanidinium of Asn331 and Arg383, respectively, have been observed to interact with the nitrile and acetylene of the Takeda-17 derivatives. The phenol ring of Tyr303 has been observed to interact form a π-π-stacking interaction with the triazole-containing inhibitors, i.e., Takeda-17 (**17**) and Molidustat (**20**). The conformation of the phenol ring of Tyr310 can be modulated *via* π-π-stacking interaction the aromatic sidechains of other inhibitors, *e.g.*, JPHM-2-167 (**30**, **3.4**). Abbreviations: Prolyl hydroxylase isoform 2 (PHD2). PDB: 5V18, and 6QGV. *Xtal-IDs*: *Q*, *R*, *S*, *T*, *W*, *X*, *Y*, *Z*, *EE*, *FF*, *MM*.

4.5 References

(1) Kirsch, P.; Hartman, A. M.; Hirsch, A. K. H.; Empting, M. Concepts and Core Principles of Fragment-Based Drug Design. *Molecules* **2019**, *24* (23). https://doi.org/10.3390/molecules24234309.

(2) Grimes, J. M.; Hall, D. R.; Ashton, A. W.; Evans, G.; Owen, R. L.; Wagner, A.; McAuley, K. E.; von Delft, F.; Orville, A. M.; Sorensen, T.; Walsh, M. A.; Ginn, H. M.; Stuart, D. I. Where Is Crystallography Going? *Acta Crystallographica Section D: Structural Biology* **2018**, *74* (2), 152–166. https://doi.org/10.1107/S2059798317016709.

(3) O'Hea, J. D.; Burt, M. H.; Fisher, S.; Jones, K. M. J.; McAuley, K. E.; Preece, G.; Williams, M. A. BART: Development of a Sample Exchange System for MX Beamlines. In *International Conference on Accelerator and Large Experimental Control Systems*; 2018; pp 1919–1922. https://doi.org/10.18429/JACoW-ICALEPCS2017-THPHA200.

(4) Förster, A.; Brandstetter, S.; Schulze-Briese, C. Transforming X-Ray Detection with Hybrid Photon Counting Detectors. *Philosophical Transactions of the Royal Society A: Mathematical, Physical and Engineering Sciences* **2019**, *377* (2147), 20180241. https://doi.org/10.1098/rsta.2018.0241.

(5) Svensson, O.; Malbet-Monaco, S.; Popov, A.; Nurizzo, D.; Bowler, M. W. Fully Automatic Characterization and Data Collection from Crystals of Biological Macromolecules. *Acta Crystallographica Section D: Biological Crystallography* **2015**, *71* (8), 1757–1767. https://doi.org/10.1107/S1399004715011918.

(6) Broennimann, C.; Eikenberry, E. F.; Henrich, B.; Horisberger, R.; Huelsen, G.; Pohl, E.; Schmitt, B.; Schulze-Briese, C.; Suzuki, M.; Tomizaki, T.; Toyokawa, H.; Wagner, A. The PILATUS 1M Detector. *Journal of Synchrotron Radiation* **2006**, *13* (2), 120–130. https://doi.org/10.1107/S0909049505038665.

(7) Bowler, M. W.; Nurizzo, D.; Barrett, R.; Beteva, A.; Bodin, M.; Caserotto, H.; Delagenière, S.; Dobias, F.; Flot, D.; Giraud, T.; Guichard, N.; Guijarro, M.; Lentini, M.; Leonard, G. A.; McSweeney, S.; Oskarsson, M.; Schmidt, W.; Snigirev, A.; von Stetten, D.; Surr, J.; Svensson, O.; Theveneau, P.; Mueller-Dieckmann, C. MASSIF-1: A Beamline Dedicated to the Fully Automatic Characterization and Data Collection from Crystals of Biological Macromolecules. *Journal of Synchrotron Radiation* **2015**, *22* (6), 1540–1547. https://doi.org/10.1107/S1600577515016604.

(8) Winter, G.; Waterman, D. G.; Parkhurst, J. M.; Brewster, A. S.; Gildea, R. J.; Gerstel, M.; Fuentes-Montero, L.; Vollmar, M.; Michels-Clark, T.; Young, I. D.; Sauter, N. K.; Evans, G. DIALS: Implementation and Evaluation of a New Integration Package. *Acta Crystallographica Section D: Structural Biology* **2018**, *74* (2), 85–97. https://doi.org/10.1107/S2059798317017235.

(9) Felisaz, F.; Sinoir, J.; Papp, G.; Pica, A.; Bowler, M. W.; Murphy, P.; Hoffmann, G.; Zander, U.; Lopez-Marrero, M.; Janocha, R.; Giraud, T.; Svensson, O.; Popov, S.; Leonard, G.; Mueller-Dieckmann, C.; Márquez, J. A.; McCarthy, A. A.; Cipriani, F. CrystalDirect-To-Beam: Opening the Shortest Path from Crystal to Data. *AIP Conference Proceedings* **2019**, *2054* (1), 50009. https://doi.org/10.1063/1.5084627.

(10) Mueller, M.; Wang, M.; Schulze-Briese, C. Optimal Fine φ-Slicing for Single-Photon-Counting Pixel Detectors. *Acta Crystallographica Section D: Biological Crystallography* **2012**, *68* (1), 42–56. https://doi.org/10.1107/S0907444911049833.

(11) Waterman, D. G.; Winter, G.; Gildea, R. J.; Parkhurst, J. M.; Brewster, A. S.; Sauter, N. K.; Evans, G. Diffraction-Geometry Refinement in the DIALS Framework. *Acta Crystallographica Section D: Structural Biology* **2016**, *72* (4), 558–575. https://doi.org/10.1107/S2059798316002187.
(12) Winter, G.; McAuley, K. E. Automated Data Collection for Macromolecular Crystallography. *Methods* **2011**, *55* (1), 81–93. https://doi.org/10.1016/j.ymeth.2011.06.010.
(13) Douangamath, A.; Powell, A.; Fearon, D.; Collins, P. M.; Talon, R.; Krojer, T.; Skyner, R.; Brandao-Neto, J.; Dunnett, L.; Dias, A.; Aimon, A.; Pearce, N. M.; Wild, C.; Gorrie-Stone, T.; von Delft, F. Achieving Efficient Fragment Screening at XChem Facility at Diamond Light Source. *Journal of visualized experiments : JoVE* **2021**, No. 171, e62414. https://doi.org/10.3791/62414.
(14) Wright, N. D.; Collins, P.; Koekemoer, L.; Krojer, T.; Talon, R.; Nelson, E.; Ye, M.; Nowak, R.; Newman, J.; Ng, J. T.; Mitrovich, N.; Wiggers, H.; von Delft, F. The Low-Cost Shifter Microscope Stage Transforms the Speed and Robustness of Protein Crystal Harvesting. *Acta Crystallographica Section D: Structural Biology* **2021**, *77* (1), 62–74. https://doi.org/10.1107/S2059798320014114.
(15) Collins, P. M.; Ng, J. T.; Talon, R.; Nekrosiute, K.; Krojer, T.; Douangamath, A.; Brandao-Neto, J.; Wright, N.; Pearce, N. M.; von Delft, F. Gentle, Fast and Effective Crystal Soaking by Acoustic Dispensing. *Acta Crystallographica Section D: Structural Biology* **2017**, *73* (3), 246–255. https://doi.org/10.1107/S205979831700331X.
(16) Ng, J. T.; Dekker, C.; Kroemer, M.; Osborne, M.; von Delft, F. Using Textons to Rank Crystallization Droplets by the Likely Presence of Crystals. *Acta Crystallographica Section D: Biological Crystallography* **2014**, *70* (10), 2702–2718. https://doi.org/10.1107/S1399004714017581.
(17) Williams, S. P.; Kuyper, L. F.; Pearce, K. H. Recent Applications of Protein Crystallography and Structure-Guided Drug Design. *Current Opinion in Chemical Biology* **2005**, *9* (4), 371–380. https://doi.org/10.1016/j.cbpa.2005.06.007.
(18) Cox, O. B.; Krojer, T.; Collins, P.; Monteiro, O.; Talon, R.; Bradley, A.; Fedorov, O.; Amin, J.; Marsden, B. D.; Spencer, J.; von Delft, F.; Brennan, P. E. A Poised Fragment Library Enables Rapid Synthetic Expansion Yielding the First Reported Inhibitors of PHIP(2), an Atypical Bromodomain. *Chemical Science* **2016**, *7* (3), 2322–2330. https://doi.org/10.1039/c5sc03115j.
(19) Krojer, T.; Talon, R.; Pearce, N.; Collins, P.; Douangamath, A.; Brandao-Neto, J.; Dias, A.; Marsden, B.; von Delft, F. The XChemExplorer Graphical Workflow Tool for Routine or Large-Scale Protein-Ligand Structure Determination. *Acta Crystallographica Section D: Structural Biology* **2017**, *73* (3), 267–278. https://doi.org/10.1107/S2059798316020234.
(20) Pearce, N. M.; Bradley, A. R.; Krojer, T.; Marsden, B. D.; Deane, C. M.; Delft, F. von. Partial-Occupancy Binders Identified by the Pan-Dataset Density Analysis Method Offer New Chemical Opportunities and Reveal Cryptic Binding Sites. *Structural Dynamics* **2017**, *4* (3), 32104. https://doi.org/10.1063/1.4974176.
(21) Pearce, N. M.; Krojer, T.; Bradley, A. R.; Collins, P.; Nowak, R. P.; Talon, R.; Marsden, B. D.; Kelm, S.; Shi, J.; Deane, C. M.; von Delft, F. A Multi-Crystal Method for Extracting Obscured Crystallographic States from Conventionally Uninterpretable Electron Density. *Nature Communications* **2017**, *8* (1), 15123. https://doi.org/10.1038/ncomms15123.
(22) Wood, D. J.; Lopez-Fernandez, J. D.; Knight, L. E.; Al-Khawaldeh, I.; Gai, C.; Lin, S.; Martin, M. P.; Miller, D. C.; Cano, C.; Endicott, J. A.; Hardcastle, I. R.;

Noble, M. E. M.; Waring, M. J. FragLites - Minimal, Halogenated Fragments Displaying Pharmacophore Doublets. An Efficient Approach to Druggability Assessment and Hit Generation. *Journal of Medicinal Chemistry* **2019**, *62* (7), 3741–3752. https://doi.org/10.1021/acs.jmedchem.9b00304.

(23) Winter, G.; Lobley, C. M. C.; Prince, S. M. Decision Making in Xia2. *Acta Crystallographica Section D: Biological Crystallography* **2013**, *69* (7), 1260–1273. https://doi.org/10.1107/S0907444913015308.

(24) Vonrhein, C.; Flensburg, C.; Keller, P.; Sharff, A.; Smart, O.; Paciorek, W.; Womack, T.; Bricogne, G. Data Processing and Analysis with the AutoPROC Toolbox. *Acta Crystallographica Section D: Biological Crystallography* **2011**, *67* (4), 293–302. https://doi.org/10.1107/S0907444911007773.

(25) Wojdyr, M.; Keegan, R.; Winter, G.; Ashton, A. DIMPLE - a Pipeline for the Rapid Generation of Difference Maps from Protein Crystals with Putatively Bound Ligands . *Acta Crystallographica Section A Foundations of Crystallography* **2013**, *69* (a1), s299–s299. https://doi.org/10.1107/s0108767313097419.

(26) Hall, S. R.; Allen, F. H.; Brown, I. D. The Crystallographic Information File (CIF): A New Standard Archive File for Crystallography. *Acta Crystallographica Section A* **1991**, *47* (6), 655–685. https://doi.org/10.1107/S010876739101067X.

(27) Douangamath, A.; Fearon, D.; Gehrtz, P.; Krojer, T.; Lukacik, P.; Owen, C. D.; Resnick, E.; Strain-Damerell, C.; Aimon, A.; Ábrányi-Balogh, P.; Brandão-Neto, J.; Carbery, A.; Davison, G.; Dias, A.; Downes, T. D.; Dunnett, L.; Fairhead, M.; Firth, J. D.; Jones, S. P.; Keeley, A.; Keserü, G. M.; Klein, H. F.; Martin, M. P.; Noble, M. E. M.; O'Brien, P.; Powell, A.; Reddi, R. N.; Skyner, R.; Snee, M.; Waring, M. J.; Wild, C.; London, N.; von Delft, F.; Walsh, M. A. Crystallographic and Electrophilic Fragment Screening of the SARS-CoV-2 Main Protease. *Nature Communications* **2020**, *11* (1), 5047. https://doi.org/10.1038/s41467-020-18709-w.

(28) Hsieh, C. M.; Chen, C. Y.; Chern, J. W.; Chan, N. L. Structure of Human Phosphodiesterase 5A1 Complexed with Avanafil Reveals Molecular Basis of Isoform Selectivity and Guidelines for Targeting α-Helix Backbone Oxygen by Halogen Bonding. *Journal of Medicinal Chemistry* **2020**, *63* (15), 8485–8494. https://doi.org/10.1021/acs.jmedchem.0c00853.

(29) Appelhoffl, R. J.; Tian, Y. M.; Raval, R. R.; Turley, H.; Harris, A. L.; Pugh, C. W.; Ratcliffe, P. J.; Gleadle, J. M. Differential Function of the Prolyl Hydroxylases PHD1, PHD2, and PHD3 in the Regulation of Hypoxia-Inducible Factor. *Journal of Biological Chemistry* **2004**, *279* (37), 38458–38465. https://doi.org/10.1074/jbc.M406026200.

(30) Casey Laizure, S.; Herring, V.; Hu, Z.; Witbrodt, K.; Parker, R. B. The Role of Human Carboxylesterases in Drug Metabolism: Have We Overlooked Their Importance? *Pharmacotherapy* **2013**, *33* (2), 210–222. https://doi.org/10.1002/phar.1194.

(31) Ahmed, S.; Ayscough, A.; Barker, G. R.; Canning, H. E.; Davenport, R.; Downham, R.; Harrison, D.; Jenkins, K.; Kinsella, N.; Livermore, D. G.; Wright, S.; Ivetac, A. D.; Skene, R.; Wilkens, S. J.; Webster, N. A.; Hendrick, A. G. 1,2,4-Triazolo-[1,5-a]Pyridine HIF Prolylhydroxylase Domain-1 (PHD-1) Inhibitors with a Novel Monodentate Binding Interaction. *Journal of Medicinal Chemistry* **2017**, *60* (13), 5663–5672. https://doi.org/10.1021/acs.jmedchem.7b00352.

(32) Chowdhury, R.; Flashman, E.; Mecinović, J.; Kramer, H. B.; Kessler, B. M.; Frapart, Y. M.; Boucher, J. L.; Clifton, I. J.; McDonough, M. A.; Schofield, C. J. Studies on the Reaction of Nitric Oxide with the Hypoxia-Inducible Factor

Prolyl Hydroxylase Domain 2 (EGLN1). *Journal of Molecular Biology* **2011**, *410* (2), 268–279. https://doi.org/10.1016/j.jmb.2011.04.075.

(33) Rosen, M. D.; Venkatesan, H.; Peltier, H. M.; Bembenek, S. D.; Kanelakis, K. C.; Zhao, L. X.; Leonard, B. E.; Hocutt, F. M.; Wu, X.; Palomino, H. L.; Brondstetter, T. I.; Haugh, P. v.; Cagnon, L.; Yan, W.; Liotta, L. A.; Young, A.; Mirzadegan, T.; Shankley, N. P.; Barrett, T. D.; Rabinowitz, M. H. Benzimidazole-2-Pyrazole HIF Prolyl 4-Hydroxylase Inhibitors as Oral Erythropoietin Secretagogues. *ACS Medicinal Chemistry Letters* **2010**, *1* (9), 526–529. https://doi.org/10.1021/ml100198y.

(34) Chowdhury, R.; Abboud, M. I.; McAllister, T. E.; Banerji, B.; Bhushan, B.; Sorensen, J. L.; Kawamura, A.; Schofield, C. J. Use of Cyclic Peptides to Induce Crystallization: Case Study with Prolyl Hydroxylase Domain 2. *Scientific Reports* **2020**, *10* (1). https://doi.org/10.1038/s41598-020-76307-8.

(35) Adams, P. D.; Afonine, P. v.; Bunkóczi, G.; Chen, V. B.; Davis, I. W.; Echols, N.; Headd, J. J.; Hung, L. W.; Kapral, G. J.; Grosse-Kunstleve, R. W.; McCoy, A. J.; Moriarty, N. W.; Oeffner, R.; Read, R. J.; Richardson, D. C.; Richardson, J. S.; Terwilliger, T. C.; Zwart, P. H. PHENIX: A Comprehensive Python-Based System for Macromolecular Structure Solution. *Acta Crystallographica Section D: Biological Crystallography* **2010**, *66* (2), 213–221. https://doi.org/10.1107/S0907444909052925.

(36) Afonine, P. v.; Grosse-Kunstleve, R. W.; Echols, N.; Headd, J. J.; Moriarty, N. W.; Mustyakimov, M.; Terwilliger, T. C.; Urzhumtsev, A.; Zwart, P. H.; Adams, P. D. Towards Automated Crystallographic Structure Refinement with Phenix.Refine. *Acta Crystallographica Section D: Biological Crystallography* **2012**, *68* (4), 352–367. https://doi.org/10.1107/S0907444912001308.

(37) McCoy, A. J.; Grosse-Kunstleve, R. W.; Adams, P. D.; Winn, M. D.; Storoni, L. C.; Read, R. J. Phaser Crystallographic Software. *Journal of Applied Crystallography* **2007**, *40* (4), 658–674. https://doi.org/10.1107/S0021889807021206.

(38) Afonine, P. v.; Grosse-Kunstleve, R. W.; Chen, V. B.; Headd, J. J.; Moriarty, N. W.; Richardson, J. S.; Richardson, D. C.; Urzhumtsev, A.; Zwart, P. H.; Adams, P. D. Phenix.Model-vs-Data: A High-Level Tool for the Calculation of Crystallographic Model and Data Statistics. *Journal of Applied Crystallography* **2010**, *43* (4), 669–676. https://doi.org/10.1107/S0021889810015608.

(39) Emsley, P.; Cowtan, K. Coot: Model-Building Tools for Molecular Graphics. *Acta Crystallographica Section D: Biological Crystallography* **2004**, *60* (12 I), 2126–2132. https://doi.org/10.1107/S0907444904019158.

(40) Chowdhury, R.; Leung, I. K. H.; Tian, Y. M.; Abboud, M. I.; Ge, W.; Domene, C.; Cantrelle, F. X.; Landrieu, I.; Hardy, A. P.; Pugh, C. W.; Ratcliffe, P. J.; Claridge, T. D. W.; Schofield, C. J. Structural Basis for Oxygen Degradation Domain Selectivity of the HIF Prolyl Hydroxylases. *Nature Communications* **2016**, *7* (1), 12673. https://doi.org/10.1038/ncomms12673.

(41) Lu, S.; Shen, Q.; Zhang, J. Allosteric Methods and Their Applications: Facilitating the Discovery of Allosteric Drugs and the Investigation of Allosteric Mechanisms. *Accounts of Chemical Research* **2019**, *52* (2), 492–500. https://doi.org/10.1021/acs.accounts.8b00570.

(42) McAllister, T. E.; Yeh, T. L.; Abboud, M. I.; Leung, I. K. H.; Hookway, E. S.; King, O. N. F.; Bhushan, B.; Williams, S. T.; Hopkinson, R. J.; Münzel, M.; Loik, N. D.; Chowdhury, R.; Oppermann, U.; Claridge, T. D. W.; Goto, Y.; Suga, H.; Schofield, C. J.; Kawamura, A. Non-Competitive Cyclic Peptides for Targeting

Enzyme-Substrate Complexes. *Chemical Science* **2018**, *9* (20), 4569–4578. https://doi.org/10.1039/c8sc00286j.
(43) Holt-Martyn, J. P.; Tumber, A.; Rahman, M. Z.; Lippl, K.; Figg, W.; McDonough, M. A.; Chowdhury, R.; Schofield, C. J. Studies on Spiro[4.5]Decanone Prolyl Hydroxylase Domain Inhibitors. *MedChemComm* **2019**, *10* (4), 500–504. https://doi.org/10.1039/c8md00548f.
(44) Holt-Martyn, J. P.; Chowdhury, R.; Tumber, A.; Yeh, T. L.; Abboud, M. I.; Lippl, K.; Lohans, C. T.; Langley, G. W.; Figg, W.; McDonough, M. A.; Pugh, C. W.; Ratcliffe, P. J.; Schofield, C. J. Structure-Activity Relationship and Crystallographic Studies on 4-Hydroxypyrimidine HIF Prolyl Hydroxylase Domain Inhibitors. *ChemMedChem* **2020**, *15* (3), 270–273. https://doi.org/10.1002/cmdc.201900557.
(45) Zhang, X.; Lei, Y.; Hu, T.; Wu, Y.; Li, Z.; Jiang, Z.; Yang, C.; Zhang, L.; You, Q. Discovery of Clinical Candidate (5-(3-(4-Chlorophenoxy)Prop-1-Yn-1-Yl)-3-Hydroxypicolinoyl)Glycine, an Orally Bioavailable Prolyl Hydroxylase Inhibitor for the Treatment of Anemia. *Journal of Medicinal Chemistry* **2020**, *63* (17), 10045–10060. https://doi.org/10.1021/acs.jmedchem.0c01161.
(46) Abboud, M. I.; Chowdhury, R.; Leung, I. K. H.; Lippl, K.; Loenarz, C.; Claridge, T. D. W.; Schofield, C. J. Studies on the Substrate Selectivity of the Hypoxia-Inducible Factor Prolyl Hydroxylase 2 Catalytic Domain. *ChemBioChem* **2018**, *19* (21), 2262–2267. https://doi.org/10.1002/cbic.201800246.
(47) Yeh, T.-L.; Leissing, T. M.; Abboud, M. I.; Thinnes, C. C.; Atasoylu, O.; Holt-Martyn, J. P.; Zhang, D.; Tumber, A.; Lippl, K.; Lohans, C. T.; Leung, I. K. H.; Morcrette, H.; Clifton, I. J.; Claridge, T. D. W.; Kawamura, A.; Flashman, E.; Lu, X.; Ratcliffe, P. J.; Chowdhury, R.; Pugh, C. W.; Schofield, C. J. Molecular and Cellular Mechanisms of HIF Prolyl Hydroxylase Inhibitors in Clinical Trials. *Chemical Science* **2017**, *8* (11), 7651–7668. https://doi.org/10.1039/C7SC02103H.
(48) Chan, M. C.; Atasoylu, O.; Hodson, E.; Tumber, A.; Leung, I. K. H.; Chowdhury, R.; Gómez-Pérez, V.; Demetriades, M.; Rydzik, A. M.; Holt-Martyn, J.; Tian, Y. M.; Bishop, T.; Claridge, T. D. W.; Kawamura, A.; Pugh, C. W.; Ratcliffe, P. J.; Schofield, C. J. Potent and Selective Triazole-Based Inhibitors of the Hypoxia-Inducible Factor Prolyl-Hydroxylases with Activity in the Murine Brain. *PLoS ONE* **2015**, *10* (7), e0132004. https://doi.org/10.1371/journal.pone.0132004.
(49) Chowdhury, R.; McDonough, M. A.; Mecinović, J.; Loenarz, C.; Flashman, E.; Hewitson, K. S.; Domene, C.; Schofield, C. J. Structural Basis for Binding of Hypoxia-Inducible Factor to the Oxygen-Sensing Prolyl Hydroxylases. *Structure* **2009**, *17* (7), 981–989. https://doi.org/10.1016/j.str.2009.06.002.
(50) Jumper, J.; Evans, R.; Pritzel, A.; Green, T.; Figurnov, M.; Ronneberger, O.; Tunyasuvunakool, K.; Bates, R.; Žídek, A.; Potapenko, A.; Bridgland, A.; Meyer, C.; Kohl, S. A. A.; Ballard, A. J.; Cowie, A.; Romera-Paredes, B.; Nikolov, S.; Jain, R.; Adler, J.; Back, T.; Petersen, S.; Reiman, D.; Clancy, E.; Zielinski, M.; Steinegger, M.; Pacholska, M.; Berghammer, T.; Bodenstein, S.; Silver, D.; Vinyals, O.; Senior, A. W.; Kavukcuoglu, K.; Kohli, P.; Hassabis, D. Highly Accurate Protein Structure Prediction with AlphaFold. *Nature* **2021**, *596* (7873), 583–589. https://doi.org/10.1038/s41586-021-03819-2.
(51) Chowdhury, R. Structural and Mechanistic Studies on Prolyl Hydroxylases, Oxford University, UK, 2008.
(52) Loenarz, C.; Coleman, M. L.; Boleininger, A.; Schierwater, B.; Holland, P. W. H.; Ratcliffe, P. J.; Schofield, C. J. The Hypoxia-Inducible Transcription Factor

Pathway Regulates Oxygen Sensing in the Simplest Animal, Trichoplax Adhaerens. *EMBO Reports* **2011**, *12* (1), 63–70. https://doi.org/10.1038/embor.2010.170.
(53) Pektas, S.; Taabazuing, C. Y.; Knapp, M. J. Increased Turnover at Limiting O2 Concentrations by the Thr387 → Ala Variant of HIF-Prolyl Hydroxylase PHD2. *Biochemistry* **2015**, *54* (18), 2851–2857. https://doi.org/10.1021/bi501540c.
(54) Arbiser, J. L. Fumarate Esters as Angiogenesis Inhibitors: Key to Action in Psoriasis. *Journal of Investigative Dermatology* **2011**, *131* (6), 1189–1191. https://doi.org/10.1038/jid.2011.45.

Chapter 5

Summary and Future Directions

Chapter 5

5.1 Chapter 2 – Mechanistic Studies of PHD2

The work discussed in Chapter **2** concentrated on laying the ground work for the time-resolved studies that provide snap-shots pictures of the catalysis of the PHDs and thus insights into the 'O_2-sensing' ability of the PHD family of enzymes compared to CP4H and other 2OG oxygenases.[1–5] Such knowledge may also enable the identification of PHD inhibitors with improved properties (*e.g.*, with respect to selectivity) and the development of compounds that enhance PHD activity (discussed in section **4.4**). The results may also inform on how O_2 diffuses through the channels within the PHDs and their hypoxia sensing properties.[6] One of the challenges to mechanistic based studies of tPHD2 has been the bottleneck of crystallisation of enzyme-substrate complexes that are catalytically competent.[7] The initial $PHD2_{181-426}$.Mn(II).NOG.$HIF1\alpha_{556-575}$-CODD complex crystals took approximately six months to crystallise.[2] Previous work has established the use of a non-competitively binding cyclic peptide (3C) to help promote nucleation of this crystal form.[8,9] However, this formate based crystallisation system did not yield crystals that were stable after O_2-exposure (*Xtal-A-F, Xtal-ID* listed in **Appendix I**; discussed in section **2.2**).

The work described in this thesis focused on finding a $PHD2_{181-407}$.HIFα crystallisation condition that could be grown anaerobically and was robust in nature (discussed in section **2.4.1**). The crystal form should be able to achieve high-resolution, be stable after O_2-exposure, and be reproducible in a relatively short timeframe. For

detailed mechanistic work to be carried out, multiple forms of experiments would be required to validate the crystallographic observations, requiring a consistent purification protocol to purify large batches of enzyme (10s of mg per batch). The crystallisation system should enable the generation of an abundance of crystals for the different experiments, *e.g.*, to crystallise different mutants, multiple inhibitors, and/or with modified substrates. The HIF2α-acetate condition (described in **2.4.1**) has proven to be such a crystallisation system. Under these conditions, it appears the HIF2$\alpha_{523\text{-}542}$-CODD peptide helps promote crystallisation due to the flexibility of Gly537$_{HIF2\alpha}$-Glu538$_{HIF2\alpha}$ insert that interacts with the symmetry-related chain (**Figure 2-8**, **2.2.1**). The *P* 2_1 2_1 2 crystal form (1.24-1.41 Å resolution) undergoes a point group change to *P* 2_1 (1.31-2.03 Å resolution) when exposed to O_2. Furthermore, O_2 induces a change in the crystal form where the symmetry-related chain prevents the release of hydroxylated product (**2.4**).

Initial O_2-exposure of the PHD2$_{181\text{-}407}$.Fe(II).2OG.HIF2$\alpha_{523\text{-}542}$-CODD crystals revealed the *in crystallo* turnover capabilities of this crystallisation system. Electron density consistent with the formation of *trans*-4-prolyl hydroxylation of Pro531 was observed along with the conversion of the cosubstrate 2OG to the coproduct succinate. Notably, there was no evidence for electron density corresponding to CO_2 in O_2-exposed complex structures (**Figure 5-1**). The first (i) PHD2$_{181\text{-}407}$.ACT.HIF2$\alpha_{523\text{-}542}$-CODD (*Xtal-I*), (ii) anaerobic-PHD2$_{181\text{-}407}$.Fe(II).2OG.HIF2$\alpha_{523\text{-}542}$-CODD.-O_2 (*Xtal-J*), (iii) two PHD2$_{181\text{-}407}$.Fe(II).2OG.HIF2$\alpha_{523\text{-}542}$-CODD.Rest-O_2-75-min and (iv) multiple PHD2$_{181\text{-}407}$.Fe(II).2OG.HIF2$\alpha_{523\text{-}542}$-CODD.Rest-O_2-1-min.+O_2.60/7,200-min complex structures were obtained with the HIF2α-acetate-derived crystallisation condition (*Xtal-K-N*, **Figure 5-1**). During the O_2-exposure studies, structures were obtained that likely correspond to both intermediate (*Xtal-K* and *Xtal-L*) and product complexes (*Xtal-M* and

Xtal-N, **2.4.1.1**). Structural analyses of the different timepoints revealed the likely formation of a peroxide-proline intermediate that formed from the C4 atom of the pyrrolidine ring of Pro531 (discussed in **2.4.1.1**, **Figure 5-1**). After 5-days O_2-exposure, the *Xtal-N* structure revealed apparently complete *trans*-4-hydroxylaiton of HIF2α$_{523-542}$-CODD peptide (**Figure 5-1**).

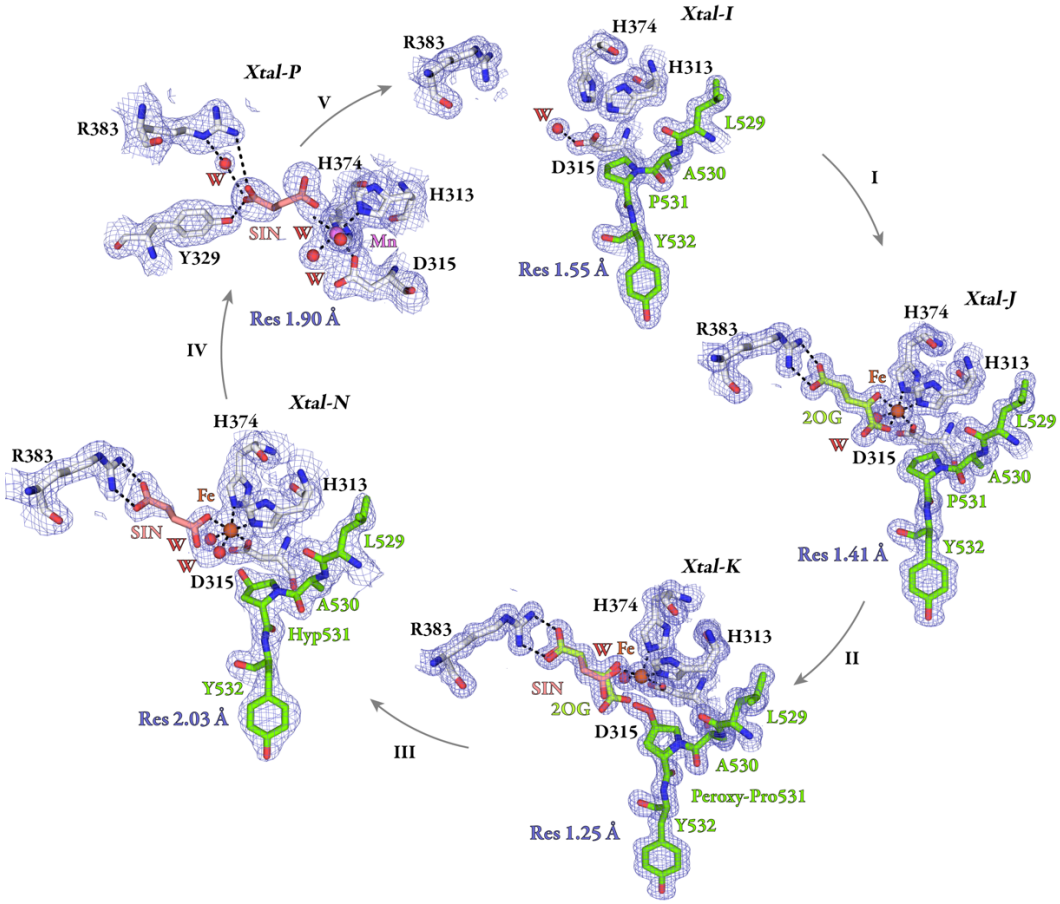


Figure 5-1| View from the Active Sites of PHD2$_{181-407}$ Crystals in Different States; Anaerobic, O_2-Exposed, and Aerobic Conditions (with or without Ligands). (I-V) The crystallographic snapshots allow for visualisation of different mechanistic stages of PHD2$_{181-407}$. (I) The complex structures represent the transition of PHD2$_{181-407}$ from a metal free state to a Fe and 2OG bound state. (II) 1hr O_2-exposed crystal where 2OG is decarboxylated and succinate is formed. The Pro531$_{HIF2α}$ has been hydroxylated, and the potential formation of a peroxyproline is observed on the C4 of the pyrrolidine ring. (III) After 5-days O_2-exposure, the peroxyproline is no longer observed. Hydroxylated-Pro531, a water molecule, and disordering of the methylene of succinate are observed. (IV) Succinate likely is involved in a shift of coordination from bi-coordination to mono-coordination in concert with the dynamics of the induced-fit mechanism of PHD2$_{181-407}$; potentially due to the disordering of the methylene and introduction of indirect contact between a water molecule and the C4 carboxylate of succinate. (V) The active site resets for catalysis. (I-V) Active site (white), ligands (2OG-yellow and succinate-salmon), and HIF2α$_{523-542}$-CODD (green) residues are depicted as sticks. Key interactions are represented by dashes (black). The 2mF_o-DF_c electron density maps (contoured at 1.0 σ) are displayed as mesh (blue). Metal ions (Fe-orange and Mn-violet) and water molecules (red) are displayed as spheres. Abbreviations: Prolyl hydroxylase isoform 2 (PHD2), 2-oxoglutarate (2OG), Succinate (SIN), Hour (hr), Hypoxia-inducible factor isoform 2α (HIF2α), *C*-terminal oxygen-degradation domain (CODD). *Xtal-IDs: I, J, K, N, P.*

The acquired structural data on PHD2$_{181-407}$.HIF2α$_{523-542}$-CODD complex has revealed previously uncharacterised features of the protein-substrate complex: (i) including a Gly537$_{HIF2α}$-Glu538$_{HIF2α}$ insert 'flip-out' (**Figure 2-8**, **2.2.1**) when compared with HIF1α$_{556-575}$-peptide (PDB: 3HQR) and (ii) Zn ions that interact with thiol sidechains of residues Cys201 and Cys208 that can form a disulfide bond (*Xtal-G*, **2.3**). Other interesting features include an ordered active site water molecule that interacts with the Oδ1 atom of Asp315 in the PHD2$_{181-407}$.ACT.HIF2α$_{523-542}$-CODD structure (*Xtal-I*) and the observed *in crystallo* turnover in the PHD2$_{181-407}$.Fe(II).2OG.HIF2α$_{523-542}$-CODD crystals (*Xtal-K-N*).

The results should be regarded as a starting point for detailed mechanistic-based crystallographic studies, such as synchrotron based VMXi serial MX ± X-ray emission spectroscopy, to fully understand the nature of the observed (**Figure 5-2**, **2.4.1.1**).[10]

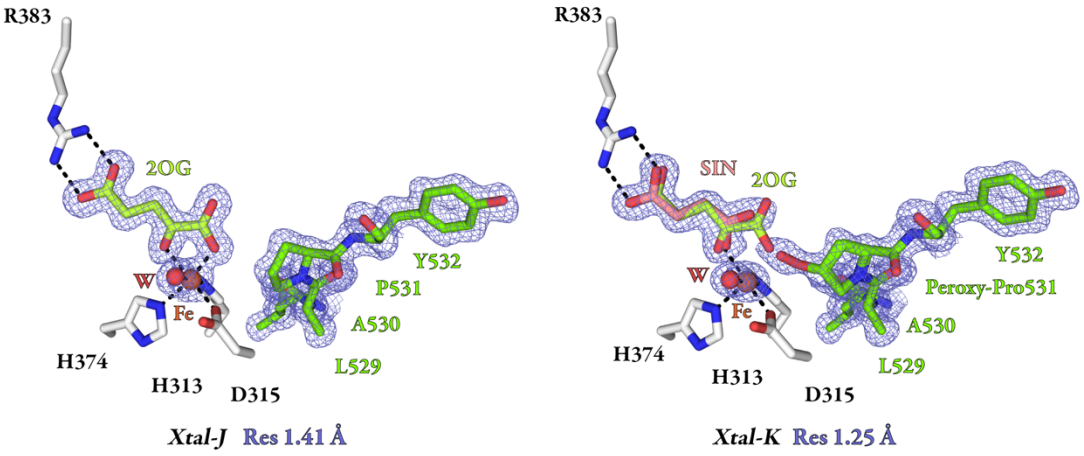


Figure 5-2| A Close-up View of Anaerobic and Intermediate PHD2$_{181-407}$.HIF2α$_{523-542}$-CODD Complex Structures. *Xtal-J* represents the anaerobic complex structure of PHD2$_{181-407}$ with Fe, 2OG, and HIF2α$_{523-542}$-CODD bound. *Xtal-K* represents O_2-exposed intermediate structure obtained with SIN and hydroxylated HIF2α$_{523-542}$-CODD. Active site (white) and HIF2α$_{523-542}$-CODD (green) residues are displayed as sticks. The interactions are represented by dashes (black). Fe ions (orange) and water molecules (red) are depicted as spheres. The $2mF_o$-DF_c electron density map (contoured at 1.0 σ) is illustrated as mesh (blue). The potential peroxide-proline intermediate is modelled at 60% occupancy and product at 40% occupancy. Abbreviations: Prolyl hydroxylase isoform 2 (PHD2), 2-Oxoglutarate (2OG), Succinate (SIN), Hypoxia-inducible factor isoform 2α (HIF2α), C-terminal oxygen-degradation domain (CODD). *Xtal-IDs*: *J, K.*

Furthermore, recent studies have a taken place at the High-Pressure-Macromolecular Crystallography (HPMX) laboratory, involving exposure of anaerobically grown crystals

to 55 Bar of O_2 (The European Synchrotron Research Facility, ESRF).[11] A 1.55 Å resolution PHD2$_{181-407}$.Fe(II).2OG.HIF2$\alpha_{523-542}$-CODD.~Rest-15-min-+O_2 structure was obtained and revealed the apparent binding of O_2 to the Fe-centre and displacement of the metal bound water (*work completed in collaboration with Dr. Michael McDonough, Dr. Philippe Carpentier, and Ms. Giorgia Fiorini*). Future plans are to further characterise the initial O_2-PHD2$_{181-407}$ structure with high-pressure experiments using noble gases for derivatisation, *i.e.*, Kr and Xe gases, to investigate how gases diffuse through PHD2$_{181-407}$.[11–13] Experiments are also planned to use *in crystallo* UV/Vis and Raman spectroscopy capabilities at the ESRF in order to characterise intermediates in catalysis.[14] Simultaneous efforts have been undertaken to prepare the PHD2$_{181-407}$.HIF2$\alpha_{523-542}$-CODD-acetate-derived crystallisation condition for future serial-MX with microcrystal slurries for fixed-target experiments (non-conventional serial data collection at room-temperature, I24 beamline, Diamond Light Source Ltd.). The aim is to obtain room-temperature and NO structures to compare with current cryogenic and O_2-exposed complexes (*Xtal-I-M*).[15] Future work may incorporate XFEL studies aimed to obtain and validate the observed intermediate complex (*Xtal-K-L*). Optimisation of microcrystal batch methods has already begun to be used for these experiments (*on-going work by Ms. Giorgia Fiorini*).[15,16] (*Thank you to Dr. Philippe Carpentier for conducting the HPMX experiment at ESRF. Thank you to ESRF and beamline staff for allocated lab access, beamtime, and assistance during the experiment.*)

5.2 Chapter 3 – Structural Analysis of PHD2 Inhibition *via* Co-Crystallisation

Additional structural data may aid the ongoing design of PHD inhibitors (**Table 3-1**, **3.1**).[17,18] Due to the bottleneck of obtaining useful crystals,[7] a novel crystal

form that permits robust crystallisation of $PHD2_{181-407/426}$ with small-molecule inhibitors was the aim of the work described in Chapter **3**.

The work presented highlights the use of three different crystal forms to obtain seven new complex structures with $PHD2_{181-407/426}$ (**Figure 5-2**).

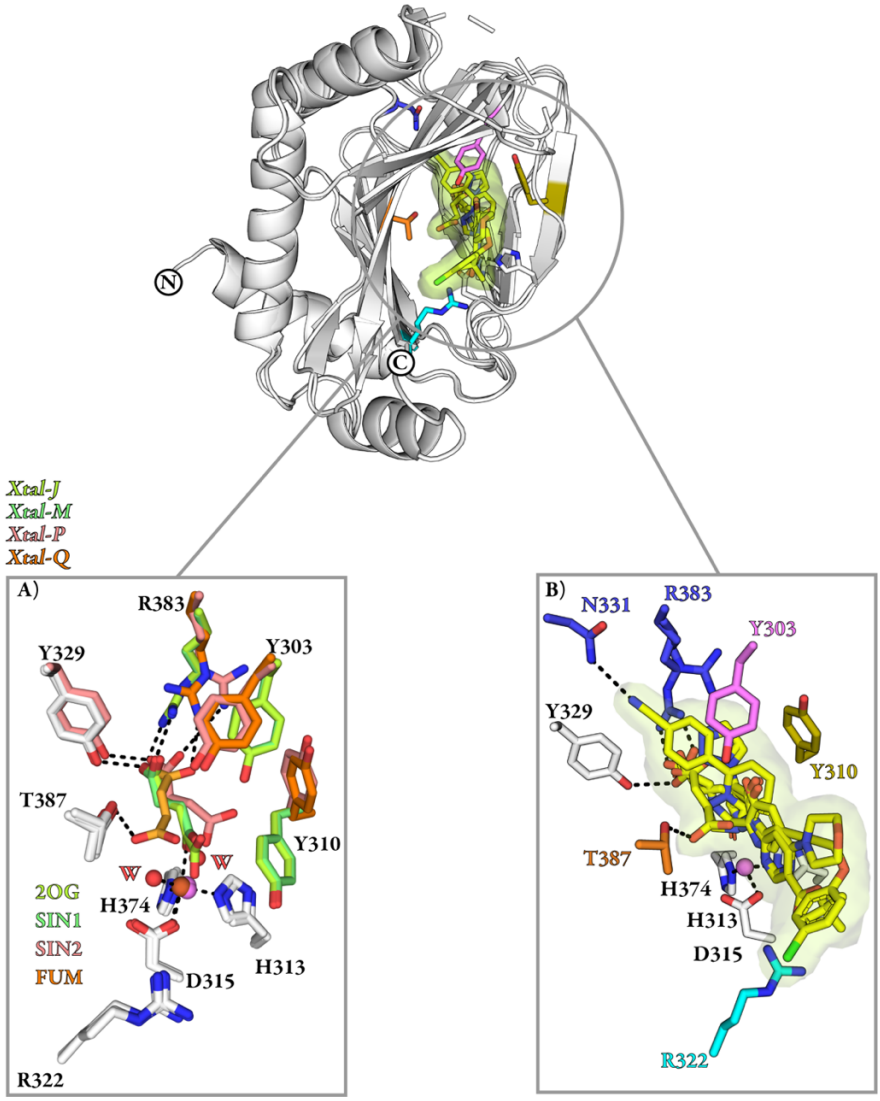


Figure 5-3| An Alignment and View from $PHD2_{181-407}$ Complex Structures with Co-Substrates, Co-Products, and Inhibitors. (A) Superimposition of $PHD2_{181-407}$ in complex with 2OG (lemon), SIN1 (lime, succinate from turnover), SIN2 (pink, succinate from the crystallisation condition), and FUM (orange). The mobile active site residues are coloured based on bound cofactor/cosubstrates/or coproduct. (B) Superimposition of $PHD2_{181-407}$ complexes obtained through co-crystallisation. The guanidinium of Arg322 (cyan) forms a π-π-stacking interaction with the aromatic sidechain with certain inhibitors, *e.g.*, ZXJ-1 (**32**). The alcohol sidechain of Thr387 (orange) interacts with the C1 carboxylate of fumarate. The acetamide of Asn331 (blue) interacts with the nitrile sidechain of Takeda-17 (**17**). The phenolic sidechains of Tyr303 (violet) and Tyr310 (olive) form π-π-stacking interactions with triazole-containing inhibitors. (A-B) $PHD2_{181-407}$ is depicted as a cartoon. The complexed ligands are shown as sticks. The active site residues are displayed as sticks (metal chelating residues-white and key residues-coloured). Key interactions are represented by dashes (black). Mn ion is displayed as a sphere (violet). Abbreviations: Prolyl hydroxylase isoform 2 (PHD2). PDB: 6ZBN, 6ZBO. *Xtal-IDs: J, M, P, Q, R, S, T, U.*

The first structure was of $PHD2_{181-426}$ in complex with Mn without any complexed ligands (*Xtal-O*). The β2-β3 finger loop is observed to coordinate the active site metal *via* the carboxylate of Asp250 in the *Xtal-O* structure (**3.2.1**). The efforts to crystallise the *Xtal-O* complex led to the use of succinate to mimic the interaction between the β2-β3 finger loop in the $PHD2_{181-426}$.Mn complex (*i.e.*, to add stability for crystallisation). Two complex structures of $PHD2_{181-407}$ with succinate and fumarate were obtained along with four further structures with small-molecule inhibitors: Molidustat (**20**), IOX4 (**28**), Takeda-17 (**17**), and ZXJ-1(**33**, **Figure 5-2**).[18–21] Comparison of structural data for the different PHD complexes reveal new insights into the interactions of the ligands with active site water molecules and the dynamic substrate/cosubstrate induced-fit processes of the PHDs (**3.4**).[18]

The $PHD2_{181-407}$.Mn(II).succinate and fumarate (along with those with 2OG) complex structures reveal variations in the binding of these TCA cycle intermediates in the active site of $PHD2_{181-407}$ (**Figure 5-2**).[22] A shift of the succinate C1 carboxylate position is observed relative to that of 2OG, which apparently is coupled with the movement of the phenolic sidechain of Tyr303. The C4 carboxylate of succinate likely forms a weaker interaction with the guanidino moiety of Arg383 when compared to 2OG, which may reflect, in part, the shorter length and lack of bidentate chelation of succinate (**Figure 5-1**, discussed in **3.2.2**). The weak electron density observed for succinate, potentially reflects the release of the co-product during the, ordered sequential mechanism of 2OG and HIFα-substrate oxidation.[18,23,24] If succinate remained in the 2OG binding pocket, this would most likely inhibit the enzyme. It has been reported that inhibition of the PHDs by succinic acid, due to mutations in succinate dehydrogenase (SDH), is associated with some cancer types.[22] This 'oncogenic' signal is proposed to be due to succinate inhibition of the PHDs which results in HIF stabilisation.[22,23,25] However,

it must be noticed that succinate is a poor PHD inhibitor and it may be that the reported HIFα stabilisation is not due to direct succinate inhibition of the PHDs. It cannot be ruled out that succinate inhibition of the PHDs is linked with the experimental conditions used for the *in vitro* cellular work and/or a route to modulation of catalytic activity upon dysregulation of the TCA cycle leads to an induced 'pseudo'-hypoxic state.[22,23,26,27] From a 'sensing' and evolutionary perspective, tight binding of succinate co-product to the metazoan's main 'O_2-sensor' would not seem to be advantageous.[1] This feature is likely reflected in the weak binding observed in the complex structure of succinate to $PHD2_{181-407}$.[24,28]

But in contrast with the typical binding mode for succinic acid, with fumaric acid, which is a more potent PHD inhibitor,[28] the complex structure with $PHD2_{181-407}$ unexpectedly illustrates the multiple binding conformations that fumarate can adopt in the active site. Fumarate is also observed to bind in some potentially allosteric sites. The $PHD2_{181-407}$.Mn(II).fumarate complex structure exhibits a previously uncharacterised interaction between the alcohol sidechain of Thr387 and the C1 carboxylate of fumaric acid (**Figure 5-2**). Thr387 is important for PHD2 catalysis and exploitation of this interaction could lead to a potent and selective inhibitor; an Asn514 replaces the Thr387 residue in the active site of CP4H (**Figures 5-2**; **3.5**).[29,30] The results correlate with previous studies reporting inhibition of the PHDs by fumaric acid.[23,28,31] Although further work is required to connect the *in vitro* and *in vivo* observations, the results represented here are consistent with PHD inhibition in cancers manifesting upregulated fumaric acid, but raise further questions as to the relevance of direct PHD inhibition from upregulated succinic acid in cancer cells.[22,32]

The structures of $PHD2_{181-407}$ and triazole-containing inhibitor complexes were obtained through co-crystallisation using the poorly binding succinic acid to stabilise the

active site for addition of DMSO-solubilised inhibitors (*Xtal-R* and *Xtal-S* or PDB: 6ZBO or 6ZBN). The solubilised inhibitors were added to the $PHD2_{181-407}$ protein mixture after the addition of succinate (**3.2.4**). The structures revealed a π-π-stacking interaction between the triazole moiety of the ligands and the phenolic sidechains of Tyr303 in the $PHD2_{181-407}$ *P* 2_1 crystal form (**Figure 5-2**).[18] In the Molidustat (**20**) and related analogue IOX4 (**28**) complex structures with $PHD2_{181-407}$, two previously uncharacterised active site waters are observed to interact indirectly with the triazole sidechain of these small-molecule inhibitors (**Figure 3-13**, PDB: 6ZBO and 6ZBN, respectively).[18,20] The presences of these water molecules could have implications for the potency these inhibitors.[18] Further, interactions between the guanidinium functionality of Arg322 and the sidechains of **20** and **28** illustrate how these interaction can disrupt and displace HIFα-substrates, with **28** exhibiting more efficient substrate displacement in NMR solution studies compared to **20**.[20,33] The interaction with the guanidinium sidechain of Arg322 is also observed in the $PHD2_{181-407}$ structure in complex with the pre-clinical candidate ZXJ-1 (**33**) that formed in a novel *P* 6_1 2 2 crystal form (*Xtal-U*, **Figure 5-2**).[21] The interaction between the chlorobenzene functionality and the guanidinium motif of Arg322 may, in part, have implications on substrate displacement in a manner similar to the *tert*-butyl sidechain of **28**.[20]

One current aim is to acquire additional tPHD2 structural data with other clinically-relevant inhibitors that are late-stage/approved, *e.g.*, Roxadustat (**22**), Daprodustat (**24**), Enarodustat (**25**), and Desidustat (**26**, **Figure 1-19**, **1.4.4**). Structural determination of these small-molecules, and other ligands, may reveal better insights into the biophysics of potent inhibition of the PHDs. These efforts, coupled with a structure guided approach to drug discovery, could yield new therapeutics that target the PHDs.[17]

5.3 Chapter 3 – Structural Analysis of PHD2 Inhibition *via* Soaking-based Studies

The current field of drug discovery, with recent advances in fragment-based HTS capabilities, has made fragment a high interest area (**4.1**). In parallel with the work to obtain more $PHD2_{181-407}$ complex structures with various ligands through co-crystallisation methods, simultaneous efforts were made to develop a condition for HT soaking-based studies of $PHD2_{181-407}$. Fragment screening and soaking-based crystallisation methods can provide vast amounts of structural data at immense speeds.[34–36]

5.3.1 Soaked-Based Studies with XChem Fragment Screening

The *P* 2_1 crystal system was optimised for the XChem fragment screening, because large amounts of $PHD2_{181-407}$.Mn(II).succinate crystals that could be generated (**3.2.2,** Diamond Light Source Ltd.).[37] In this crystal form (*Xtal-P*), fragments could potentially displace succinate and coordinate to the active site metal. Approximately 390 crystals diffracted and were processed (**4.2**). Of the ~390 XChem datasets, 12 datasets revealed fragment hits (**Figure 5-3**).[37]

The screen revealed five binding sites in $PHD2_{181-407}$; one orthosteric pocket (*i.e.*, active site) and four potentially allosteric binding sites (*i.e.*, not directly overlapping with cosubstrate/substrate binding sites, **Figure 5-3**; **4.2**). Of the apparent binding sites, fragments bound to *N*-terminal, DSBH, and *C*-terminal formed pockets. The *N*-terminal pockets are at between the α3-α4 helices (Site 1), β1-βV strands (Site 2), and α1-helix (Site 5, **Figure 5-3**; **4.2**). The DSBH pocket is formed between the βIII-βIV strands (Site 4).

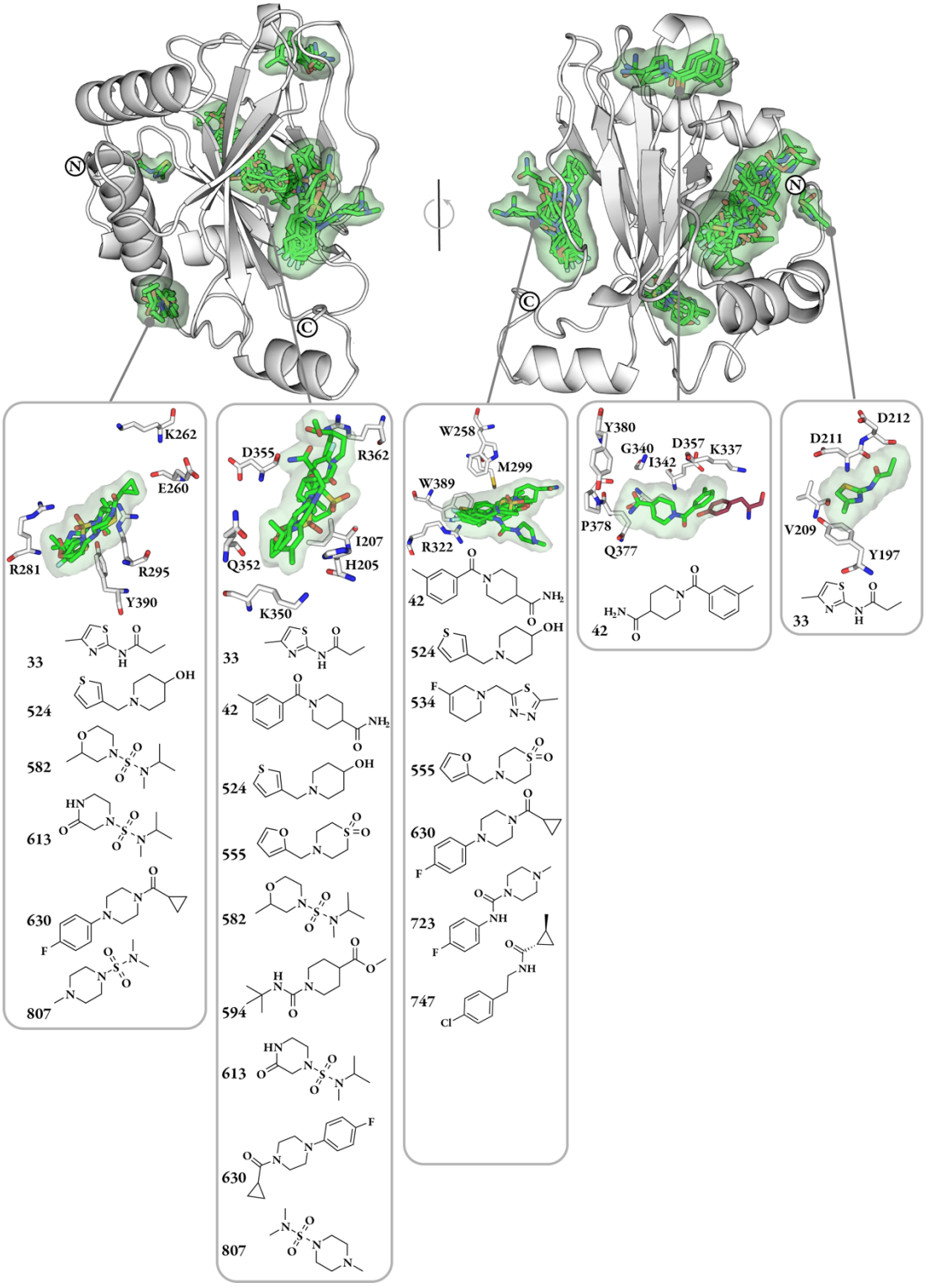


Figure 5-4| Structural Alignment of Complex Structures and Asymmetric Unit Chains of the 12 XChem Fragment Hits and Depiction of the Five Binding Sites. $PHD2_{181-407}$ is displayed as a cartoon. Pocket residues and ligands are depicted as sticks. The surface representation (green) is illustrated for the bound fragments. The chemical structures are shown of the fragment hits at each binding site. Abbreviations: Prolyl hydroxylase isoform 2 (PHD2). *Xtal-IDs: V, W, X, Y, Z, AA, BB, CC, DD, EE, FF, GG.*

Further validation will be required to determine if the binding pockets with complexed XChem fragments can be exploited for future inhibitor design. The bindings events illustrate the usefulness of crystallographic fragment screening as a powerful tool in drug discovery.[17,34,38]

Future work will be to carry out solution studies of these fragments, computational efforts (such as Fragalysis)[37], and potentially conduct further fragment-based screening with other small-molecule libraries, *e.g.*, covalent library.[37]

5.3.2 Soaking-Based Studies with Monodentate Binding Derivatives

The soaking-based studies with the $PHD2_{181-407}$.Mn(II).succinate crystal form (*Xtal-P*) were also utilised in the structural characterisation of several monodentate binding derivatives of Takeda-17 (**17**).[19] Eight complex structures were obtained and revealed a conserved metal coordination site and 'back'-pocket (*i.e.*, Asn331-Ser339) interaction with $Asn331_{PHD2}$ (**Figure 5-4**, **4.3**). The monodentate binding derivative structures display the area in the 'back'-pocket *via* modification of the benzonitrile sidechains of **17** (**4.3**). Furthermore, upon complexation of CG22 to $PHD2_{181-407}$, the acetylene group of CG22 appeared to cause a significant conformational change within the active site (**Figure 5-4**). The increase in electron density caused the guanidinium moiety of Arg383 to push further into the pocket which induces a 'flip-out' of the indole side chain of Trp334 (**Figure 5-4**). The conformational change can potentially be exploited as both PHD1 and PHD3 contain the residue His323 and His161, respectively. At the analogous position, PHD2 contains residue Ser339. Ser339, in comparison to $His323_{PHD1}$/$His161_{PHD3}$, likely accommodates the guanidinium functionality of Arg383 into the 'back'-pocket. However, the like-charge of the imidazole side chain of $His323_{PHD1}$/$His161_{PHD3}$ and the guanidinium motif of $Arg367_{PHD1}$/$Arg205_{PHD3}$ might, to

some extent, restrict the Trp334 'flip-out' that is seen in PHD2, *i.e.*, due to the repulsion of the 'like-like' sidechains.[39] Further solution studies will be required to fully understand the impact of this conformational change on catalysis. (**Figure 5-4**).[40]

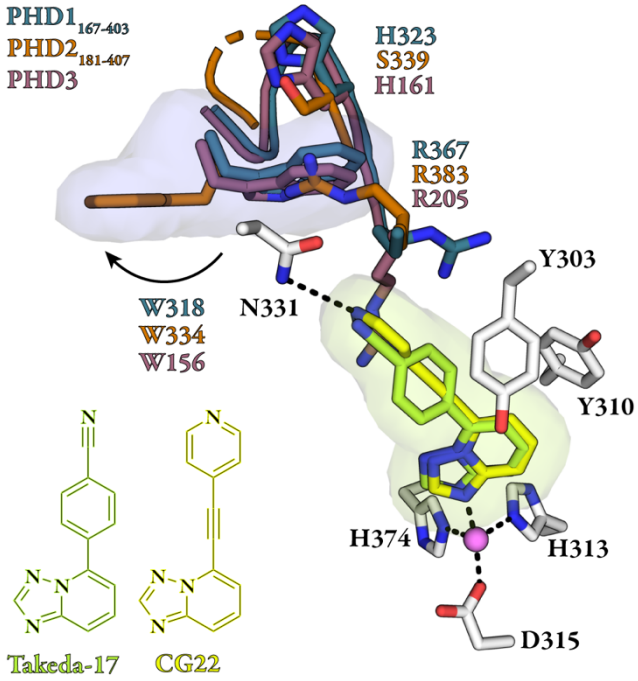


Figure 5-5| An Alignment of PHD1-3 Active Sites with the Acrive Site Conformational Change Induced by the Monodentate Binding Derivative, CG22. The active site residues (white) and inhibitors (Takeda-17 (17)-lemon and CG22-yellow) are displayed as sticks. Key interactions are represented by dashes (black). The Mn ion is depicted as a sphere. The 'back'-pocket loops of the PHD isoforms are displayed as cartoons (PHD1$_{167-403}$-teal, PHD2$_{181-407}$-orange, and predicted structure of PHD3-dark purple). Key sidechains of loop residues are shown as sticks. Surface representation is shown for the ligands and mobile Trp residue. Abbreviations: Prolyl hydroxylase isoform 1-3 (PHD1-3). PDB: 5V1B. Appendix I *Xtal-MM. AlphaFold predicted structure of PHD3*.[30]

5.4 Summary and Future Outlook

Further structural studies on the PHDs that is coupled with other experimental and computational techniques has the potential to reveal valuable insights into the precise nature of the catalysis of the PHDs and provide a better understanding of dynamic elements induced through substrate/ligand binding.[18]

The ongoing work within the group aims to characterise the unknown species observed in the mechanistic studies (discussed in Chapter **2**) of $PHD2_{181-407}$ through crystallographic approaches, *in crystallo* spectroscopy, and solution studies. Significant efforts are aimed at obtaining additional complex structures of the PHDs with clinically applied inhibitors (discussed in Chapter **3**); as there are several lead conditions that may be optimised. The soaking-based studies require validation *via* solution studies and further medicinal chemistry to determine if novel inhibitors can be designed from the fragment hits obtained (discussed in Chapter **4**). Also, future fragment screening to identify potential allosteric modulators could be carried out using the $PHD2_{181-407}$.$HIF2\alpha_{523-542}$-CODD acetate-derived crystal form instead of the $PHD2_{181-407}$.Mn(II).succinate crystals (*Xtal-P*, described in **3.2.2**), as the acetate-derived condition is more reproducible, robust, and the crystals diffract to a higher resolution. Additional studies should also consider obtaining room temperature $PHD2_{181-407}$.ligand complexes in parallel to assess if the cryogenic structures are temperature biased in one structural conformation.[41]

With the ever increasing amount of data that is obtained, a symbiosis of both experimental and computational techniques will likely be required.[35,42] Artificial intelligence (AI) employing computers may provide a better insight into the medicinal chemistry of target proteins.[30,35,42] On-going initiatives, such as Accelerating Therapeutics Opportunity in Medicine (ATOM) Modelling PipeLine (AMPL), are using AI-machine learning to understand why some clinically applied therapies are successful and why others fail, *i.e.*, due to toxicities or poor pharmacokinetic (PK) profiles.[42] AI-driven computational efforts may one day be expanded to include the machine learning of the available PHD structural data and aid the development of potent, selective inhibitors/or activators that have a high chance of success in the clinic.[42]

5.5 References

(1) Schofield, C. J.; Ratcliffe, P. J. Oxygen Sensing by HIF Hydroxylases. *Nat. Rev. Mol. Cell Biol.* **2004**, *5* (5), 343–354. https://doi.org/10.1038/nrm1366.

(2) Chowdhury, R.; McDonough, M. A.; Mecinović, J.; Loenarz, C.; Flashman, E.; Hewitson, K. S.; Domene, C.; Schofield, C. J. Structural Basis for Binding of Hypoxia-Inducible Factor to the Oxygen-Sensing Prolyl Hydroxylases. *Structure* **2009**, *17* (7), 981–989. https://doi.org/10.1016/j.str.2009.06.002.

(3) Chowdhury, R.; Leung, I. K. H.; Tian, Y. M.; Abboud, M. I.; Ge, W.; Domene, C.; Cantrelle, F. X.; Landrieu, I.; Hardy, A. P.; Pugh, C. W.; Ratcliffe, P. J.; Claridge, T. D. W.; Schofield, C. J. Structural Basis for Oxygen Degradation Domain Selectivity of the HIF Prolyl Hydroxylases. *Nature Communications* **2016**, *7* (1), 12673. https://doi.org/10.1038/ncomms12673.

(4) Flashman, E.; Hoffart, L. M.; Hamed, R. B.; Bollinger, J. M.; Krebs, C.; Schofield, C. J. Evidence for the Slow Reaction of Hypoxia-Inducible Factor Prolyl Hydroxylase 2 with Oxygen. *FEBS Journal* **2010**, *277* (19), 4089–4099. https://doi.org/10.1111/j.1742-4658.2010.07804.x.

(5) Rabe, P.; Kamps, J. J. A. G.; Sutherlin, K. D.; Linyard, J. D. S.; Aller, P.; Pham, C. C.; Makita, H.; Clifton, I.; McDonough, M. A.; Leissing, T. M.; Shutin, D.; Lang, P. A.; Butryn, A.; Brem, J.; Gul, S.; Fuller, F. D.; Kim, I.-S.; Cheah, M. H.; Fransson, T.; Bhowmick, A.; Young, I. D.; O'Riordan, L.; Brewster, A. S.; Pettinati, I.; Doyle, M.; Joti, Y.; Owada, S.; Tono, K.; Batyuk, A.; Hunter, M. S.; Alonso-Mori, R.; Bergmann, U.; Owen, R. L.; Sauter, N. K.; Claridge, T. D. W.; Robinson, C. v.; Yachandra, V. K.; Yano, J.; Kern, J. F.; Orville, A. M.; Schofield, C. J. X-Ray Free-Electron Laser Studies Reveal Correlated Motion during Isopenicillin N Synthase Catalysis . *Science Advances* **2021**, *7* (34), eabh0250. https://doi.org/10.1126/sciadv.abh0250.

(6) Domene, C.; Jorgensen, C.; Schofield, C. J. Mechanism of Molecular Oxygen Diffusion in a Hypoxia-Sensing Prolyl Hydroxylase Using Multiscale Simulation. *Journal of the American Chemical Society* **2020**, *142* (5), 2253–2263. https://doi.org/10.1021/jacs.9b09236.

(7) Doerr, A. Widening the Protein Crystallization Bottleneck. *Nature Methods* **2006**, *3* (12), 961. https://doi.org/10.1038/nmeth1206-961.

(8) Chowdhury, R.; Abboud, M. I.; McAllister, T. E.; Banerji, B.; Bhushan, B.; Sorensen, J. L.; Kawamura, A.; Schofield, C. J. Use of Cyclic Peptides to Induce Crystallization: Case Study with Prolyl Hydroxylase Domain 2. *Scientific Reports* **2020**, *10* (1). https://doi.org/10.1038/s41598-020-76307-8.

(9) McAllister, T. E.; Yeh, T. L.; Abboud, M. I.; Leung, I. K. H.; Hookway, E. S.; King, O. N. F.; Bhushan, B.; Williams, S. T.; Hopkinson, R. J.; Münzel, M.; Loik, N. D.; Chowdhury, R.; Oppermann, U.; Claridge, T. D. W.; Goto, Y.; Suga, H.; Schofield, C. J.; Kawamura, A. Non-Competitive Cyclic Peptides for Targeting Enzyme-Substrate Complexes. *Chemical Science* **2018**, *9* (20), 4569–4578. https://doi.org/10.1039/c8sc00286j.

(10) Sanchez-Weatherby, J.; Sandy, J.; Mikolajek, H.; Lobley, C. M. C.; Mazzorana, M.; Kelly, J.; Preece, G.; Littlewood, R.; Sørensen, T. L.-M. VMXi: A Fully Automated, Fully Remote, High-Flux *In situ* Macromolecular Crystallography Beamline. *Journal of Synchrotron Radiation* **2019**, *26* (1), 291–301. https://doi.org/10.1107/S1600577518015114.

(11) Kalms, J.; Schmidt, A.; Frielingsdorf, S.; Utesch, T.; Gotthard, G.; von Stetten, D.; van der Linden, P.; Royant, A.; Mroginski, M. A.; Carpentier, P.; Lenz, O.;

Scheerer, P. Tracking the Route of Molecular Oxygen in O2-Tolerant Membrane-Bound [NiFe] Hydrogenase. *Proceedings of the National Academy of Sciences of the United States of America* **2018**, *115* (10), E2229–E2237. https://doi.org/10.1073/pnas.1712267115.

(12) Carpentier, P.; Leprêtre, C.; Basset, C.; Douki, T.; Torelli, S.; Duarte, V.; Hamdane, D.; Fontecave, M.; Atta, M. Structural, Biochemical and Functional Analyses of TRNA-Monooxygenase Enzyme MiaE from Pseudomonas Putida Provide Insights into TRNA/MiaE Interaction. *Nucleic Acids Research* **2020**, *48* (17), 9918–9930. https://doi.org/10.1093/nar/gkaa667.

(13) Kalms, J.; Schmidt, A.; Frielingsdorf, S.; van der Linden, P.; von Stetten, D.; Lenz, O.; Carpentier, P.; Scheerer, P. Krypton Derivatization of an O2-Tolerant Membrane-Bound [NiFe] Hydrogenase Reveals a Hydrophobic Tunnel Network for Gas Transport. *Angewandte Chemie - International Edition* **2016**, *55* (18), 5586–5590. https://doi.org/10.1002/anie.201508976.

(14) von Stetten, D.; Giraud, T.; Carpentier, P.; Sever, F.; Terrien, M.; Dobias, F.; Juers, D. H.; Flot, D.; Mueller-Dieckmann, C.; Leonard, G. A.; de Sanctis, D.; Royant, A. In Crystallo Optical Spectroscopy (IcOS) as a Complementary Tool on the Macromolecular Crystallography Beamlines of the ESRF. *Acta Crystallographica Section D: Biological Crystallography* **2015**, *71* (1), 15–26. https://doi.org/10.1107/S139900471401517X.

(15) Rabe, P.; Beale, J. H.; Butryn, A.; Aller, P.; Dirr, A.; Lang, P. A.; Axford, D. N.; Carr, S. B.; Leissing, T. M.; McDonough, M. A.; Davy, B.; Ebrahim, A.; Orlans, J.; Storm, S. L. S.; Orville, A. M.; Schofielda, C. J.; Owen, R. L. Anaerobic Fixed-Target Serial Crystallography. *IUCrJ* **2020**, *7* (5), 901–912. https://doi.org/10.1107/S2052252520010374.

(16) Orville, A. M. Recent Results in Time Resolved Serial Femtosecond Crystallography at XFELs. *Current Opinion in Structural Biology* **2020**, *65*, 193–208. https://doi.org/10.1016/j.sbi.2020.08.011.

(17) Williams, S. P.; Kuyper, L. F.; Pearce, K. H. Recent Applications of Protein Crystallography and Structure-Guided Drug Design. *Current Opinion in Chemical Biology* **2005**, *9* (4), 371–380. https://doi.org/10.1016/j.cbpa.2005.06.007.

(18) Figg Jr., W. D.; McDonough, M. A.; Chowdhury, R.; Nakashima, Y.; Zhang, Z.; Holt-Martyn, J. P.; Krajnc, A.; Schofield, C. J. Structural Basis of Prolyl Hydroxylase Domain Inhibition by Molidustat. *ChemMedChem* **2021**, *16* (13), 2082–2088. https://doi.org/10.1002/cmdc.202100133.

(19) Ahmed, S.; Ayscough, A.; Barker, G. R.; Canning, H. E.; Davenport, R.; Downham, R.; Harrison, D.; Jenkins, K.; Kinsella, N.; Livermore, D. G.; Wright, S.; Ivetac, A. D.; Skene, R.; Wilkens, S. J.; Webster, N. A.; Hendrick, A. G. 1,2,4-Triazolo-[1,5-a]Pyridine HIF Prolylhydroxylase Domain-1 (PHD-1) Inhibitors with a Novel Monodentate Binding Interaction. *Journal of Medicinal Chemistry* **2017**, *60* (13), 5663–5672. https://doi.org/10.1021/acs.jmedchem.7b00352.

(20) Chan, M. C.; Atasoylu, O.; Hodson, E.; Tumber, A.; Leung, I. K. H.; Chowdhury, R.; Gómez-Pérez, V.; Demetriades, M.; Rydzik, A. M.; Holt-Martyn, J.; Tian, Y. M.; Bishop, T.; Claridge, T. D. W.; Kawamura, A.; Pugh, C. W.; Ratcliffe, P. J.; Schofield, C. J. Potent and Selective Triazole-Based Inhibitors of the Hypoxia-Inducible Factor Prolyl-Hydroxylases with Activity in the Murine Brain. *PLoS ONE* **2015**, *10* (7), e0132004. https://doi.org/10.1371/journal.pone.0132004.

(21) Zhang, X.; Lei, Y.; Hu, T.; Wu, Y.; Li, Z.; Jiang, Z.; Yang, C.; Zhang, L.; You, Q. Discovery of Clinical Candidate (5-(3-(4-Chlorophenoxy)Prop-1-Yn-1-Yl)-3-

Hydroxypicolinoyl)Glycine, an Orally Bioavailable Prolyl Hydroxylase Inhibitor for the Treatment of Anemia. *Journal of Medicinal Chemistry* **2020**, *63* (17), 10045–10060. https://doi.org/10.1021/acs.jmedchem.0c01161.

(22) Selak, M. A.; Armour, S. M.; MacKenzie, E. D.; Boulahbel, H.; Watson, D. G.; Mansfield, K. D.; Pan, Y.; Simon, M. C.; Thompson, C. B.; Gottlieb, E. Succinate Links TCA Cycle Dysfunction to Oncogenesis by Inhibiting HIF-α Prolyl Hydroxylase. *Cancer Cell* **2005**, *7* (1), 77–85. https://doi.org/10.1016/j.ccr.2004.11.022.

(23) Hewitson, K. S.; Liénard, B. M. R.; McDonough, M. A.; Clifton, I. J.; Butler, D.; Soares, A. S.; Oldham, N. J.; McNeill, L. A.; Schofield, C. J. Structural and Mechanistic Studies on the Inhibition of the Hypoxia-Inducible Transcription Factor Hydroxylases by Tricarboxylic Acid Cycle Intermediates. *Journal of Biological Chemistry* **2007**, *282* (5), 3293–3301. https://doi.org/10.1074/jbc.M608337200.

(24) Abboud, M. I.; McAllister, T. E.; Leung, I. K. H.; Chowdhury, R.; Jorgensen, C.; Domene, C.; Mecinović, J.; Lippl, K.; Hancock, R. L.; Hopkinson, R. J.; Kawamura, A.; Claridge, T. D. W.; Schofield, C. J. 2-Oxoglutarate Regulates Binding of Hydroxylated Hypoxia-Inducible Factor to Prolyl Hydroxylase Domain 2. *Chemical Communications* **2018**, *54* (25), 3130–3133. https://doi.org/10.1039/c8cc00387d.

(25) Li, Z.; Zhen, S.; Su, K.; Tumber, A.; Yu, Q.; Dong, Y.; McDonough, M.; Schofield, C. J.; Zhang, X. A Small-Molecule Probe for Monitoring Binding to Prolyl Hydroxylase Domain 2 by Fluorescence Polarisation. *Chemical Communications* **2020**, *56* (91), 14199–14202. https://doi.org/10.1039/d0cc06353c.

(26) Martínez-Reyes, I.; Chandel, N. S. Mitochondrial TCA Cycle Metabolites Control Physiology and Disease. *Nature Communications* **2020**, *11* (1), 102. https://doi.org/10.1038/s41467-019-13668-3.

(27) Tennant, D. A.; Frezza, C.; MacKenzie, E. D.; Nguyen, Q. D.; Zheng, L.; Selak, M. A.; Roberts, D. L.; Dive, C.; Watson, D. G.; Aboagye, E. O.; Gottlieb, E. Reactivating HIF Prolyl Hydroxylases under Hypoxia Results in Metabolic Catastrophe and Cell Death. *Oncogene* **2009**, *28* (45), 4009–4021. https://doi.org/10.1038/onc.2009.250.

(28) Leung, I. K. H.; Demetriades, M.; Hardy, A. P.; Lejeune, C.; Smart, T. J.; Szöllössi, A.; Kawamura, A.; Schofield, C. J.; Claridge, T. D. W. Reporter Ligand NMR Screening Method for 2-Oxoglutarate Oxygenase Inhibitors. *Journal of Medicinal Chemistry* **2013**, *56* (2), 547–555. https://doi.org/10.1021/jm301583m.

(29) Pektas, S.; Taabazuing, C. Y.; Knapp, M. J. Increased Turnover at Limiting O2 Concentrations by the Thr387 → Ala Variant of HIF-Prolyl Hydroxylase PHD2. *Biochemistry* **2015**, *54* (18), 2851–2857. https://doi.org/10.1021/bi501540c.

(30) Jumper, J.; Evans, R.; Pritzel, A.; Green, T.; Figurnov, M.; Ronneberger, O.; Tunyasuvunakool, K.; Bates, R.; Žídek, A.; Potapenko, A.; Bridgland, A.; Meyer, C.; Kohl, S. A. A.; Ballard, A. J.; Cowie, A.; Romera-Paredes, B.; Nikolov, S.; Jain, R.; Adler, J.; Back, T.; Petersen, S.; Reiman, D.; Clancy, E.; Zielinski, M.; Steinegger, M.; Pacholska, M.; Berghammer, T.; Bodenstein, S.; Silver, D.; Vinyals, O.; Senior, A. W.; Kavukcuoglu, K.; Kohli, P.; Hassabis, D. Highly Accurate Protein Structure Prediction with AlphaFold. *Nature* **2021**, *596* (7873), 583–589. https://doi.org/10.1038/s41586-021-03819-2.

(31) Abboud, M. I.; McAllister, T. E.; Leung, I. K. H.; Chowdhury, R.; Jorgensen, C.; Domene, C.; Mecinović, J.; Lippl, K.; Hancock, R. L.; Hopkinson, R. J.;

Kawamura, A.; Claridge, T. D. W.; Schofield, C. J. 2-Oxoglutarate Regulates Binding of Hydroxylated Hypoxia-Inducible Factor to Prolyl Hydroxylase Domain 2. *Chemical Communications* **2018**, *54* (25), 3130–3133. https://doi.org/10.1039/c8cc00387d.

(32) Isaacs, J. S.; Yun, J. J.; Mole, D. R.; Lee, S.; Torres-Cabala, C.; Chung, Y. L.; Merino, M.; Trepel, J.; Zbar, B.; Toro, J.; Ratcliffe, P. J.; Linehan, W. M.; Neckers, L. HIF Overexpression Correlates with Biallelic Loss of Fumarate Hydratase in Renal Cancer: Novel Role of Fumarate in Regulation of HIF Stability. *Cancer Cell* **2005**, *8* (2), 143–153. https://doi.org/10.1016/j.ccr.2005.06.017.

(33) Yeh, T.-L.; Leissing, T. M.; Abboud, M. I.; Thinnes, C. C.; Atasoylu, O.; Holt-Martyn, J. P.; Zhang, D.; Tumber, A.; Lippl, K.; Lohans, C. T.; Leung, I. K. H.; Morcrette, H.; Clifton, I. J.; Claridge, T. D. W.; Kawamura, A.; Flashman, E.; Lu, X.; Ratcliffe, P. J.; Chowdhury, R.; Pugh, C. W.; Schofield, C. J. Molecular and Cellular Mechanisms of HIF Prolyl Hydroxylase Inhibitors in Clinical Trials. *Chemical Science* **2017**, *8* (11), 7651–7668. https://doi.org/10.1039/C7SC02103H.

(34) Kirsch, P.; Hartman, A. M.; Hirsch, A. K. H.; Empting, M. Concepts and Core Principles of Fragment-Based Drug Design. *Molecules* **2019**, *24* (23). https://doi.org/10.3390/molecules24234309.

(35) Grimes, J. M.; Hall, D. R.; Ashton, A. W.; Evans, G.; Owen, R. L.; Wagner, A.; McAuley, K. E.; von Delft, F.; Orville, A. M.; Sorensen, T.; Walsh, M. A.; Ginn, H. M.; Stuart, D. I. Where Is Crystallography Going? *Acta Crystallographica Section D: Structural Biology* **2018**, *74* (2), 152–166. https://doi.org/10.1107/S2059798317016709.

(36) Douangamath, A.; Powell, A.; Fearon, D.; Collins, P. M.; Talon, R.; Krojer, T.; Skyner, R.; Brandao-Neto, J.; Dunnett, L.; Dias, A.; Aimon, A.; Pearce, N. M.; Wild, C.; Gorrie-Stone, T.; von Delft, F. Achieving Efficient Fragment Screening at XChem Facility at Diamond Light Source. *Journal of visualized experiments : JoVE* **2021**, No. 171, e62414. https://doi.org/10.3791/62414.

(37) Douangamath, A.; Fearon, D.; Gehrtz, P.; Krojer, T.; Lukacik, P.; Owen, C. D.; Resnick, E.; Strain-Damerell, C.; Aimon, A.; Ábrányi-Balogh, P.; Brandão-Neto, J.; Carbery, A.; Davison, G.; Dias, A.; Downes, T. D.; Dunnett, L.; Fairhead, M.; Firth, J. D.; Jones, S. P.; Keeley, A.; Keserü, G. M.; Klein, H. F.; Martin, M. P.; Noble, M. E. M.; O'Brien, P.; Powell, A.; Reddi, R. N.; Skyner, R.; Snee, M.; Waring, M. J.; Wild, C.; London, N.; von Delft, F.; Walsh, M. A. Crystallographic and Electrophilic Fragment Screening of the SARS-CoV-2 Main Protease. *Nature Communications* **2020**, *11* (1), 5047. https://doi.org/10.1038/s41467-020-18709-w.

(38) Lu, S.; Shen, Q.; Zhang, J. Allosteric Methods and Their Applications: Facilitating the Discovery of Allosteric Drugs and the Investigation of Allosteric Mechanisms. *Accounts of Chemical Research* **2019**, *52* (2), 492–500. https://doi.org/10.1021/acs.accounts.8b00570.

(39) Gitlin, I.; Carbeck, J. D.; Whitesides, G. M. Why Are Proteins Charged? Networks of Charge–Charge Interactions in Proteins Measured by Charge Ladders and Capillary Electrophoresis. *Angewandte Chemie International Edition* **2006**, *45* (19), 3022–3060. https://doi.org/https://doi.org/10.1002/anie.200502530.

(40) Hsieh, C. M.; Chen, C. Y.; Chern, J. W.; Chan, N. L. Structure of Human Phosphodiesterase 5A1 Complexed with Avanafil Reveals Molecular Basis of Isoform Selectivity and Guidelines for Targeting α-Helix Backbone Oxygen by

Halogen Bonding. *Journal of Medicinal Chemistry* **2020**, *63* (15), 8485–8494. https://doi.org/10.1021/acs.jmedchem.0c00853.
(41) Bradford, S. Y. C.; el Khoury, L.; Ge, Y.; Osato, M.; Mobley, D. L.; Fischer, M. Temperature Artifacts in Protein Structures Bias Ligand-Binding Predictions. *Chemical Science* **2021**, *12* (34), 11275–11293. https://doi.org/10.1039/d1sc02751d.
(42) Minnich, A. J.; Mcloughlin, K.; Tse, M.; Deng, J.; Weber, A.; Murad, N.; Madej, B. D.; Ramsundar, B.; Rush, T.; Calad-Thomson, S.; Brase, J.; Allen, J. E. AMPL: A Data-Driven Modeling Pipeline for Drug Discovery. *Journal of Chemical Information and Modeling* **2020**, *60* (4), 1955–1968. https://doi.org/10.1021/acs.jcim.9b01053.

Chapter 6

Material and Methods

Chapter 6

6.1 General Methods and Reagents

Reagents, chemicals, and solvents were purchased from Sigma-Aldrich-Merck Millipore Company Ltd., unless otherwise stated. All yeast, tryptone, agar, and NaCl reagents were either from Thermo Fisher Scientific Inc., Oxoid Ltd. or Melford Laboratories Ltd. All single-use tubes of 0.5-2 mL volumes were from Eppendorf Ltd. 6-50 mL tubes used were from Sarstedt, AG & Co. KG. Isopropyl-β-D-1-thiogalactoyranoside (IPTG) was from Apollo Scientific Ltd. SDS-PAGE gel staining solutions (Expedeon Instant Blue™) were from Abcam, Plc. All biologicals, unless otherwise stated, were from New England Biolabs Ltd. Custom peptides were ordered from GL Biochem Ltd., all with a *C*-terminal amide.

All water used was purified using a Millipore Elix® 10 system (Merck Life Sciences KGaA). 'Milli-Q' purification refers to water purified by filtration (0.22 μm nylon filter, Merck Life Sciences KGaA) after distillation. Water, media, and equipment were further sterilised with an LTE TouchClave® II bench top autoclave (LTE Scientific Ltd.), Crystal 300-RP25 controlled autoclave (300 L capacity, Rodwell Engineering Group Ltd.), or a LTE Falcon benchtop autoclave (LTE Scientific Ltd.) at 121°C at 1 Bar for 15 minutes for use in cell-culture and molecular biology protocols (**6.2** and **6.3**). All other solutions and buffers were purified using Millipore 0.22 μm porous nylon filters (Merck Life Sciences KGaA), unless otherwise stated, either using a vacuum suction (CVC2

controller, Vacuubrand GmbH & Co. KG) or by syringe filtration (Injekt® Luer Solo, B. Braun Medical Ltd.). Aqueous solutions were measured using PIPETMAN® pipettes (Gilson Scientific Ltd.) for volumes of 0.25 µL-5 mL using PIPETMAN® Diamond® tips (Gilson Scientific Ltd.). For volumes from 5 mL-25 mL, a pipette gun (PIPETBOY 2, Integra Biosciences™ Ltd.) and serological pipettes (Sarstedt, AG & Co. KG) were used. For volumes of greater than 25 mL, measuring cylinders, indicated bottle volumes, and 100-5000 mL Pyrex® borosilicate glass and Corning® plastic beakers (Corning Inc.) and were used for measurement. Balances that were used were: Electronic Balance FA-2000 (A&D Instruments Ltd., Pioneer™ (Ohaus, GmbH), and Explorer™ (Ohaus, GmbH) scales. Some solutions were degassed under vacuum (CVC2 controller, Vacuubrand, GMBH & CO KG) with a magnetic stirrer bar rotating at 300 rpm on a magnetic stirrer (FB15045, Thermo Fisher Scientific Inc.). The pH values of buffers and solutions were adjusted using an Oakton® PH 550 benchtop pH meter kit using 12 M hydrochloric (HCl) acid and 5 M NaOH base (Oakton Instruments).

ChemDraw® (version 18.1, Perkin Elmer, Inc.) was used to draw chemical structures and create 2D active site interactions figures. PyMOL™ molecular graphics system, (version 2.1-14.7.8, Schrödinger, Inc.) was used to create crystallography derived figures and to measure RMSD values between complex structures. Adobe® Illustrator 2021 (version 25.4.1, Adobe Inc.) was used to format, edit, and export high resolution figures. Jalview (version 2.10.5, University of Oxford, EMBL, and University of Dundee) was also used to create sequence alignment figures.[1] ImageLab™ software (version 6.0.1, Bio-Rad Laboratories, Inc.) was used to edit SDS-PAGE gel images. Prism 9 (GraphPad Software Inc.) was used to create graphical figures presented.

$PHD_{181-407}$-pET-28a(+) and $PHD_{181-426}$-pET-28a(+) ($PHD2_{181-426}$) constructs were used throughout this work.[2] (*Thank you to Dr. Kirsty Hewitson and Dr. Emily Flashman for their design of the $tPHD2_{181-426}$ construct and to Dr. Rasheduzzaman Chowdhury for his design of the $tPHD2_{181-407}$ and the cloning of the $PHD2_{181-426}$ constructs into an N-terminal His_6-tagged vector. (**Appendix Table AIII-1**).*)

6.2 Molecular Biology

6.2.1 SDS-PAGE

The SDS-PAGE gels were made following the protocols defined in **Table 6-1,** using 0.5 M tris(hydroxymethyl)aminomethane (Tris)-HCl pH 7.5/6.8, Milli-Q, 30% (w/v) acrylamide/1.03% (w/v) bis-acrylamide, 10% (w/v) ammonium persulfate (APS), *N,N,N′,N′*-tetramethylethylenediamine (TEMED). The resolving gel polymerises in ~10 minutes and the stacking gel polymerises in ~30 minutes. Bio-Rad casts, cast stands, and 17-well combs were used to make the gels (Bio-Rad Laboratories, Inc.). Once polymerised, the gels were transferred to a Bio-Rad gel electrophoresis tank (Bio-Rad Laboratories, Inc.). 1X gel running buffer diluted from a 10X stock buffer (tris-hydrochloric acid (HCl) 30 g, glycine 144 g, SDS 10 g and Milli-Q topped up to 1 L) was used during electrophoresis. 10-15 µl of protein solutions were taken from fractions and mixed with 2X loading buffer (200 mM *β*-mercaptoethanol, 4% (w/v) SDS, 100 mM Tris-HCl pH 6.8, 0.2% (w/v) bromophenol blue, and 20% (v/v) glycerol). Protein samples were then boiled for 3 minutes at 95 °C to heat denature the protein. PageRuler™ Plus prestained protein 10-250 kDa ladder (6 µL, Thermo Fisher Scientific, Inc) was used as a reference to estimate the molecular weight (MW) of the loaded protein. SDS-PAGE gels were run at 180 V for 55 minutes. The gels were removed from the casts and left for 10-

15 minutes in Expedeon InstantBlue™. Once bands were visible, gels were imaged on a Bio-Rad Universal Hood III (Bio-Rad Laboratories, Inc.).

Invitrogen Bis-Tris 7-11% 17-well precast gels (Thermo Fisher Scientific Inc.) were used for protein characterisation. Gel electrophoresis analyses with precast gels were run in 1X Invitrogen 3-morpholinopropane-1-sulfonic acid (MOPS) running buffer (Thermo Fisher Scientific Inc.).

Table 6-1| Reagents and Buffers Used to Prepare a 12.5% SDS-PAGE Gel.

Reagents	Resolving Gel (µL)	Stacking Gel (µL)
0.5 M Tris-HCl	2,500 (pH 7.5)	1,260 (pH 6.8)
Milli-Q	2,300	3,140
Acrylamide	5,000	500
SDS	100	50
APS	100	50
TEMED	8	4

6.2.2 Plasmid Deoxyribonucleic Acid (DNA) Mini-Prep

Cultures were grown at 37 °C overnight; 5 mL of cell culture was centrifuged at 6,800 rpm (3,500 × *g*) for 2 minutes (Sigma 1-14 Microfuge, Sigma Laborzentrifugen, GmbH). Plasmid DNA from cells was isolated with a GeneJET Plasmid Miniprep kit (Thermo Fisher Scientific Inc.). Plasmids were eluted from spin-columns with 20-40 µL of sterile water. Concentrations were determined following a standard protocol (**6.2.4**).

6.2.3 Sequencing

Plasmid DNA samples were sent to Eurofins Genomics Ltd. for sequencing using the T7 forward and T7 reverse sequences as primers. The plasmid DNA concentration for submission was 50-100 ng/µL and a final volume of 15 µL. DNA sequences were converted to protein sequences in SnapGene® viewer (version 5.1.5, GSL Biotech LLC.)

on the correct open-reading frame and then aligned to the reported UniProt protein sequence using Clustal Omega alignment tool (version 1.2.4, EMBL-EBI).

6.2.4 DNA Concentration – NanoDrop™

DNA concentration was determined using a Nanodrop™ One spectrophotometer (Thermo Fisher Scientific Inc.). 1.5 μL of sample was spotted onto the spectrophotometer. The DNA concentration was determined measuring the absorbance at 260_{nm}.

6.3 Microbiology Techniques

6.3.1 Luria-Bertani (LB) and 2xYeast and Tryptone (2YT) Media

LB media were made using the reagents in **Table 6-2** and 31 g/L of 2YT mixture, respectively**.** All media was autoclaved before use.

Table 6-2| Reagents used to Prepare LB Broth Media.

Reagents	LB (g/L)	2YT (g/L)
Tryptone	10	16
Yeast extract	5	10
Sodium chloride	10	5

6.3.2 LB Agar Media

LB agar plates were made following reagent list in **Table 6-3**.

Table 6-3| Reagents used to Prepare LB Agar media.

Reagents	Amount (g/600 mL)
Tryptone	6
Yeast extract	3
Sodium chloride	5
Agar	9

LB agar was autoclaved and cooled to approximately 45-50 °C, and subsequently, 50 mL of media was measured into a 50 mL falcon tube. A 50 μL (1/1000 dilution) of antibiotic was added to the LB agar media and gently mixed before plating onto a petri-dish (Sarstedt, AG & Co. KG). LB agar plates were left to dry in a laminar flow microbiological safety cabinet (SAFE 2020, Thermo Fisher Scientific Inc.).

6.3.3 Antibiotic Preparation

Kanamycin was used for antibiotic selection. 30 mg of kanamycin was weighed and dissolved into 10 mL of autoclaved Milli-Q and syringe filtered (0.22 μm) for a final concentration of 30 mg/mL (62 mM). Sterile work was conducted in a laminar flow hood (SAFE 2020, Thermo Fisher Scientific Inc.).

6.3.4 Transformations

The heat-shock method of transformation was used to insert plasmids into *Escherichia coli* cells.[3] 10-50 μL of BL21(DE3) cells (New England Biolab, Inc.) were incubated with 0.5-1 μL plasmid DNA. The cells were then incubated on ice for 5 minutes. Once cells had been equilibrated with the plasmid DNA, the cells were heat-shocked in a 42 °C water bath (FB60301, Thermo Fisher Scientific Inc.) for 20-42 seconds. Immediately after heat shock, the cells were cooled on ice for at least 5 minutes. To allow for recovery, 230 μL of super optimal broth media (SOC, New England Biolab, Inc.) was added to the cells and then samples were transferred to a 37 °C shaking incubator (ThermoMixer F1.5, Eppendorf Ltd.). Cells were plated on pre-warmed (37 °C) petri-dishes (Sarstedt, AG & Co KG) with antibiotic selective agar media using a spreader (L Shaped Spreader, Microspec Ltd.) and left overnight at 37 °C (Heraeus B6030 plate incubator, Heraeus Holding GmbH)

6.3.5 Small-Scale Bacterial Culture

Starter cultures of BL21(DE3) cells (New England Biolabs, Inc.) were grown overnight at 30 °C in an orbital shaker (New Brunswick™ , Eppendorf Ltd.) at 300 rpm. 100 µL (1/1000 dilution) of antibiotic was added to 100 mL of 2YT (**6.3.1**) starter culture in 200 mL Erlenmeyer flasks. The culture was initiated through subsequent looping of a freshly transformed colony or a glycerol stock (**6.3.9**). Foil was left over the flask stopper to prevent contamination. (*Thank you to Mr. Herminio Manso Jubier for preparing the starter culture flasks.*)

6.3.6 Optical Density (OD) Calculation-UV/Vis Spectrophotometry

2 mL of water was pipetted into a standard cuvette (FB55147, Thermo Fisher Scientific Inc.) and used as a reference sample (WPA CO8000, Biochrom Ltd.) at wavelength 600 nm. 2 mL of the cell culture was pipetted using a standard or serological pipette into a cuvette while in the laminar flow cupboard (SAFE 2020, Thermo Fisher Scientific Inc.). The cuvette with cell culture was inserted into the referenced spectrophotometer and the $OD_{600\ nm}$ was measured for the culture.

6.3.7 Large-Scale Bacterial Culture and Induction

10 mL of starter culture ($OD_{600\ nm}$ 0.6-1.2) was added to 1 L of pre-prepared autoclaved 2YT (**6.3.1**) media in 2 L glass Erlenmeyer flasks. 990 µL of antibiotic was added to culture flasks. Cultures were grown at 37 °C in orbital shakers (New Brunswick™ Innova® or Excella® E25, Eppendorf Ltd.) at 180-200 rpm for 3-4 hours. Once cells reached an $OD_{600\ nm}$ of 0.6-0.8, the shaker temperature was reduced to 18 or 30 °C. 1 mL of 0.5 M IPTG was added to flasks in a 1/1000 dilution for a final concentration of 0.5 mM to induce gene expression overnight or for 4-6 hours, respectively. Foil was left over

the stopper of the flasks to prevent any contamination. (*Thank you to Mr. Herminio Manso Jubier who helped autoclave and clean flasks used for large-scale bacterial cultures.)*

6.3.8 Cell Harvesting and Storage

Cells were harvested using a 6 L-JLA-8.1000 rotor at (5,000 × *g*) and 4 °C for 10 minutes (Avanti®-JHC centrifuge, Beckman Coulter Ltd.). Cell pellets were transferred and stored at -80 °C. (*Thank you to Prof. Carol Robinson's group for access to their 6 L rotor.*)

6.3.9 Glycerol Stocks

15% (v/v) glycerol stocks were used to store cells from cultures for long-term storage in the -80 °C freezer. An aqueous solution of 30% (v/v) of glycerol and LB broth was autoclaved. 500 μL of cells were mixed with 500 μL of 30% (v/v) glycerol-LB stock in a cryo-tube (Sarstedt AG & Co KG), and cell suspension was vortexed (Vortex-Genie 2, Scientific Industries, Inc.) before storage at -80 °C.

6.4 Protein Purification

6.4.1 Pre-Purification Cell Treatment

Cell pellets (~50-200g) were thawed in an appropriate amount of Ni(II)-affinity lysis buffer (**6.4.7**, 4X the mass of the cell pellet) in a 250 mL glass beaker/s. EDTA-free protease inhibitor tablet/s (Roche Holding, AG) and DNaseI (~1 mg, Roche Holding, AG) were added to the cell slurry.[4] Cells were left to thaw for ~30 minutes to 1 hour at 4 °C. Cells were sonicated using Cole-Parmer®-500-Watt ultrasonic homogenizer (Cole-Parmer Instruments Company Ltd.) for 3 seconds (on/off pulses) for a total elapsed time of 10 minutes.[4] After sonication, cell suspensions were placed in mass balanced 30 mL

polyethylene centrifuge tubes (Beckman Coulter Ltd.) and centrifuged in a Beckmans Coulter-JA-25.50 rotor at 20,000 rpm (or 48,384 × *g*) and 4 °C for 30 minutes (Avanti®-JHC Centrifuge, Beckmans Coulter Ltd.).[4] The supernatant lysate was then filtered (0.45 μm filter) into a measuring cylinder for direct injection on an ÄKTA™ Pure fast-protein liquid chromatography (FPLC) apparatus (Cytiva Ltd., formerly GE Healthcare Ltd.) at 4 °C.[4]

6.4.2 Ni(II)-Affinity Chromatography

A 5 mL HisTrap™ High Performance (HP, Cytiva Ltd.) column was used for the initial step of protein purification at a flow rate of 2 mL per minute at 4 °C.[4] The 5 mL HisTrap HP is charged with 5 column volumes (CV) of Ni(II) sulfate buffer (**6.4.7**), followed by addition of 5 CV of lysis buffer (**6.4.7**), 5 CV of elution buffer, and 5 CV of lysis buffer to equilibrate the column.[4] The ~150 mL of filtered lysate is loaded directly onto the column with a flow rate of 2 mL per minute.[4] After loading, the column was washed with 3 CV of lysis buffer (**6.4.7**) to clear the system of residual lysate.[4] The column was washed with 30 CV of wash buffer (**6.4.7**).[4] The target protein was eluted with a step gradient of increasing elution buffer (16% (v/v), 34% (v/v), and 100% (v/v). 5 CV was used for successive steps of the elution gradient. 3-4 mL fractions were collected, and purity was analysed by SDS-PAGE gel electrophoresis (>75% estimated purity).[4] The column was then washed with an EDTA buffer, 50 mM Tris-HCl pH 7.5, 500 mM NaCl, and 100 mM EDTA.[4] The column was stored at 4 °C.

6.4.3 Gel-Filtration (Size-Exclusion Chromatography)

300 mL Superdex®-75 resin columns (Cytiva Ltd.) was used to further purify protein after Ni(II)-affinity chromatography at a flow rate of 1 mL per minute at 4 °C.[4] Gel-filtration columns were equilibrated overnight with 1 CV of degassed Milli-Q water and 1.5 CV of degassed gel filtration buffer (**6.4.7**).[4] The protein sample (5 mL) was loaded onto the column using a 10 mL Superloop™ (Cytiva Ltd.) that had been pre-washed with 2 CV of degassed Milli-Q and equilibrated with 2 CV of degassed gel-filtration buffer (**6.4.7**).[4] 4 mL fractions were collected and the purity was analysed by SDS-PAGE gel electrophoresis (>90 estimated purity, **6.4.7**).[4] The column was washed with 1 CV of degassed Milli-Q and stored at 4 °C.[4]

6.4.4 Ion-Exchange (IX) Chromatography

1 mL Mono S™ cation exchange (Cytiva Ltd.) was used to further purify the three-column purified batch of protein at a flow rate of 1 mL per minute at 4 °C (**3.2.2**).[4] The Mono S™ column was pre-equilibrated with 5 CV of loading buffer, 50 mM MES pH 5.8 (**6.4.7**).[4,5] The protein (5 mL or ~200 mg) was buffer exchanged into 50 mM MES pH 5.8 prior to IX.[4] Buffer exchanged protein (2.5 mL) was loaded onto the Mono S™ column using a 10 mL Superloop™ (Cytiva Ltd.).[4] The volume of protein injected was based on the binding capacity of the 1 mL Mono S™column (50 mg per 1 mL of resin, based on manufacturer's protocol). Protein was eluted with a linear gradient to 100% (v/v) elution buffer (50 mM MES pH 5.8 1 M NaCl, **6.4.7**) over 5 CV. The IX column was washed with 5 CV of elution buffer. 1 mL fractions were collected and characterised for purity by SDS-PAGE gel electrophoresis (>95% estimated purity).[4] The Mono S™ column was

thoroughly cleaned following the manufacturer's protocol and stored in 20% (v/v) ethanol and stored at 4 ºC.

6.4.5 Protein Concentration

Purified protein was concentrated in chilled Amicon® 15 mL nitrocellulose membrane centrifuge tubes (Merck Life Sciences KGaA).[4] The concentrator tubes had a MW cut-off of 10 kDa. The concentrator tubes that contained the target protein were centrifuged in a bench-top Allegra® X-22 centrifuge (Beckman Coulter Ltd.) at 4,000 rpm (3,500 × *g*) in a SX4250 rotor at 4 °C for 5 minutes.[4] Subsequently, samples were mixed to prevent aggregation of protein in between the 5-minute centrifuge spins. The protein was concentrated to between 25-26 mg/mL (1 mM) and aliquoted into 0.5 mL tubes at a final volume of 65 µL.[4]

6.4.6 Buffer Exchange

PD-10 desalting columns (Cytiva Ltd.) were pre-equilibrated with 25 mL of desired buffer using a 25 mL reservoir through gravity flow at 4 °C. Once equilibrated, 2.5 mL of tPHD2 (approximately 50 mg/mL) was buffer exchanged into either 50 mM MES pH 5.8 or the crystallisation buffer at 4 °C (**Table 6-4**). 3.5 mL of buffer was used to elute protein from the PD-10 column. Elution was collected in a 6 mL tube or Amicon® 4 mL nitrocellulose membrane centrifuge tubes (Merck Life Sciences KGaA).

6.4.7 Protein Purification Buffers

All purification buffers are listed in **Table 6-4**.[4–7] (*Thank you to Dr. Rasheduzzaman Chowdhury for his optimisation of the buffers used to purify tPHD2.*)

Table 6-4| List of tPHD2 Protein Purification Buffers.

Chromatography Method	Buffer	Reagents
Ni(II)-affinity	Charge	100 mM $Ni(II)SO_4$
	Lysis (Binding)	20 mM Tris-HCl pH 7.5 500 mM NaCl 5 mM imidazole 5% (v/v) glycerol
	Wash	20 mM Tris-HCl pH 7.5 500 mM NaCl 30 mM imidazole 5% (v/v) glycerol
	Elution	20 mM Tris-HCl pH 7.5 500 mM NaCl 500 mM imidazole 5% (v/v) glycerol
Gel-filtration	SEC	50 mM Tris-HCl pH 7.5 100 mM NaCl 1% (v/v) glycerol
Ion-exchange	Loading	50 mM MES pH 5.8
	Elution	50 mM MES pH 5.8 1 M NaCl
Crystallisation buffer (Final)	Storage/Crystallisation	50 mM Tris-HCl pH 7.5 1% (v/v) glycerol

6.4.8 NanoDrop™ Protein Concentration Analysis

Protein concentrations were determined with a NanoDrop™ One UV/Vis spectrophotometer (Thermo Fisher Scientific Inc). NanoDrop™ concentrations were obtained using absorbance at 280 nm. The construct MW and extinction coefficient (assuming reduced cysteines) were used to calculate an estimated protein concentration (**Appendix III**, **Figures AIII-2-5**). 1.5 μL of buffer is used as a blank for the

NanoDrop™. 1.5 μL of sample was spotted on the spectrophotometer and the estimated sample concentration was reported.

6.4.9 His_6-Tag Cleavage

The His_6-tag were removed with thrombin protease-restriction grade (Merck Life Sciences KGaA) overnight at 4 °C on a fixed speed roller mixer (SRT9, Stuart®, Cole-Parmer Instruments Company Ltd.).[4] Thrombin cleavage was optimised to 1 unit of thrombin per 4 mg of protein purified after Ni(II)-affinity chromatography.[4] As per the manufacturer's protocol, a 10X solution of 200 mM Tris-HCl pH 8.4, 1.5 M NaCl and 25 mM $CaCl_2$ was diluted to a final of 1X concentration.

6.4.10 EDTA-Treatment for Apo-Enzyme

100 mg of tPHD2 was washed overnight on a roller mixer at 4 °C (SRT9, Stuart®, Cole-Parmer Instruments Company Ltd.) with 50 mM Tris-HCl pH 7.5, 0.5 M NaCl, 250 mM EDTA, and 5% (v/v) glycerol. Precipitated protein (~20%) was filtered (0.22 μm) and sample was prepared for buffer exchange (**6.4.6**) to remove EDTA.

6.5 tPHD2 Turnover Assays

6.5.1 Cofactor Preparation

Solutions of 250 mM $(NH_4)_2Fe(II)(SO_4)$, 100 mM sodium-L-ascorbate, and 100 mM 2OG disodium salt were prepared.[8] Sodium-L-ascorbate and 2OG stocks were made up in 50 mM Tris-HCl pH 7.5.[8] $(NH_4)_2Fe(II)(SO_4)$ stock was made in 20 mM HCl. $(NH_4)_2Fe(II)(SO_4)$ was further diluted to 500 μM in Milli-Q water.[9]

6.5.2 Hydroxylation Reaction

6.5.2.1 Analysis by Liquid Chromatography (LC)-Mass Spectrometry

The final concentrations of $(NH_4)_2Fe(II)(SO_4)$, sodium-L-ascorbate, and 2OG in the hydroxylation assay of HIFα-peptides were: 50 μM $(NH_4)_2Fe(II)(SO_4)$, 300 μM sodium-L-ascorbate, and 300 μM 2OG.[8] 1 μM $PHD2_{181-407}$ and 100 μM HIFα-peptides concentrations were used for the assay. Reaction was initiated upon addition of protein to the cofactors-substrate mixture.[8] Samples were left at 37 °C for 30 minutes or room temperature for 1 hour. Reactions were quenched with 0.1% (v/v) formic acid and HIFα peptide substrate/products analysed by mass spectrometry (MS, **6.5.3**).[8] A +16 mass-to-charge ratio (*m*/z) shift compared to the no-enzyme control HIFα peptide mass indicated hydroxylation of the peptide and activity of the enzyme.[8]

6.5.2.2 Analysis by Solid Phase Extraction (SPE) Coupled Mass Spectrometry

The final concentrations of $(NH_4)_2Fe(II)(SO_4)$, sodium-L-ascorbate, and 2OG in the hydroxylation assay of $HIF1\alpha_{556-575}$-CODD were 10 μM $(NH_4)_2Fe(II)(SO_4)$, 100 μM sodium-L-ascorbate, and 10 μM 2OG. $tPHD2_{181-407}$ and $HIF1\alpha_{556-575}$-CODD peptide were diluted to a final concentrations of 150 nM and 5 μM, respectively, in a 96-well polypropylene plate (Labcyte, Inc.).[9] Cosubstrates/FAS and protein were incubated for 15 minutes and the reaction was initiated upon addition of substrate.[9] Reactions were quenched with 10% (v/v) formic acid.[9] The assay plates were transferred to a RapidFire® RF365 sampling robot (Agilent Technologies, Inc.).[9] (*Thank you to Dr. Anthony Tumber for his work on the tPHD2 RapidFire® Assays.*)

6.5.3 Mass Spectrometry (MS)

6.5.3.1 Protein LC-MS

Protein samples were prepared in Thermo 300 µL Chromacol MS vials (Thermo Fisher Scientific Inc.) with split bonded septa screw caps (Agilent Technologies, Inc.) at concentrations between 1-2 µM; samples were injected into the machines and purified using a reverse-phase monolith 4.6 mm x 50 mm polystyrene-divinylbenzene (PSDVB) ProSwift™ RP-1S phenyl LC column (ThermoFisher Scientific Inc.) at a flow rate of 0.3 mL/minute. The LC-MS column attached to a Waters® instruments tandem ACQUITY ultra-performance-LC (UPLC)™-Xevo G2/G2-XS-quadrople-time-of-flight (QTOF)-MS (Micromass Ltd.). A 10-minute separation protocol of solution A (0.1% (v/v) formic acid and Milli-Q) and solution B (0.1% (v/v) formic acid and acetonitrile) was run on a gradient of 5% (v/v) A (1 minute) to 95% (v/v) B (6 minutes), 95% (v/v) B (1 minute) 5% (v/v) B (0.1 minute) 5% (v/v) B (1.9 minutes). Following separation, protein samples were injected directly into an electrospray ion source. The data generated were analysed using MassLynx™ version 4.1 (Micromass Ltd.). Deconvolution was set to a range of 10,000-50,000 Da +/- of the MW of the protein and a resolution of 1 Da using the MaxEnt1 function.

6.5.4 RapidFire® - Solid Phase Extraction (SPE)-Coupled MS

The RapidFire® RF365 sampling robot (Agilent Technologies, Inc.) was linked with a Agilent 6550 QTOF-MS (Agilent Technologies, Inc.).[9] A C4 SPE cartridge was loaded and cleaned with both aqueous A (water with 0.1% (v/v) formic acid and solvent B (acetonitrile) washes to remove contaminants.[9] Reaction mixtures were aspirated under vacuum and washed with the aqueous solution.[9] Peptides were extracted with the SPE

cartridge and eluted with 85% (v/v) solvent B and 15% aqueous A.[9] Peptide charge states were recorded by MassHunter (Agilent Technologies, Inc.) in the positive ion mode.[9] RapidFire Integrator software (Agilent Technologies, Inc.) was used to integrate the peak area data and calculate the % conversion of HIF1$\alpha_{556\text{-}575}$-CODD to +16 hydroxylated product.[9]

6.6 X-ray Crystallography

6.6.1 Protein Sample and Reagents Preparation

65 µL aliquots of tPHD2 were thawed on ice. $(NH_4)_2Fe(II)(SO_4)$, $Mn(II)Cl_2$, 2OG (disodium salt or diacid states), and succinic acid were dissolved in water to make stocks of 100 mM concentrations.[4] Fumaric acid and PHD inhibitors were dissolved into DMSO stocks of 100 mM concentration (if inhibitors were insoluble they were diluted to 50 mM stock concentration). HIFα-peptides (19-mer) were weighed out for a final concentration of 2-4 mM.[2] The 3C cyclic peptide was also weighed out for a final concentration of 2 mM and protein was added directly to the peptide to solubilise.[2] Samples were centrifuged using a Fresco™ 21 Microfuge (Thermo Fisher Scientific Inc.) at 14,000 rpm (18,800 × *g*) at 4 ºC for 10 minutes. The samples were stored on ice after centrifugation until the set-up of the crystallisation trays.

6.6.2 Broad Screen

Broad screens were performed with the aim of identifying different crystallisation conditions. The screens used were Pact premier™, JCSG-plus™, PEG/Ion™, PEGrX™, SaltRX™, Wizard™, Morpheus®, Crystal™, Classics Lite suite™, Anion suite™, Cation

suite™, Natrix™, ProPlex™, and Index, (Hampton Research Corp.; Molecular Dimensions Ltd.; and Qiagen N.V.). Screens were set up on 96-well sitting-drop vapour-diffusion plates using a Phoenix robot (Art Robbins Instruments, LLC.). Plates were stored both at 277 K and 298 K. Plates were checked every other day during the first week and then once a week over the equilibration period. (*Please note in some cases a 'focused'-screen was conducted with only one or two of the aforementioned crystallisation screens to reduce amount of protein sample required.*)

6.6.3 Optimisation Blocks

Optimisation blocks were designed with the Make Tray tool (Hampton Research, Corp.) to generate the block map. Stock solutions of salts and precipitants were dissolved in Milli-Q and filter (0.22 μm) sterilised. The pH of the potassium thiocyanate, sodium iodide, and ammonium/sodium acetate solutions were adjusted to pH 7 with 12 M HCl acid. PEG precipitants were warmed in a 42 °C water bath to dissolve them. An automated 1 mL serological pipette (Eppendorf Ltd.) was used to pipette solutions into the optimisation block. Once completed, blocks were sealed with adhesive aluminium StarSeals (StarLabs Ltd.), centrifuged in an Allegra X-12R centrifuge using SX4750 plate carriers (Beckman Coulter Ltd.) for a 10 second pulse spin and stored at 4 °C.

6.6.4 Crystallisation Robot

96-well-3-sitting drop vapour-diffusion plates (INTELLI-PLATES, Art Robbins Instruments, LLC.; 3 Lens Crystallisation Plate, SWISSCI Ltd.) were used with the Crystal Phoenix liquid dispenser (Art Robbins Instruments, LLC.). A total of 55 μL of the prepared protein at 4 ºC was required to plate out drops in ratios 2:1 (300 nL), 1:1 (200 nL), and 1:2 (300 nL) protein-to-well solution (final volume). Plates were removed from

the PhoenixRE and carefully sealed with ClearVue™ sealing sheets (Molecular Dimension Ltd.) and stored in a cupboard at predominantly 298 K (room temperature).

6.6.5 Additive and Detergent Screens

The Silver Bullets™, GrasX™, and Detergent Screen™ (Hampton Research Corp.) reagents were utilised to promote the crystallisation of challenging protein-ligand complexes. Screens were conducted following the manufacturers protocol on the crystallisation robot (**6.6.4**). Deoxycholic acid was identified as a detergent to aid in crystallisation of $PHD2_{181-407}$. A 60 mM solution of deoxycholic acid was prepared and added to the $PHD2_{181-407}$ mixture to a final of 6 mM concentration (note this detergent was used only to in the attempts to obtain complexes of $PHD2_{181-407}$ with Roxadustat (**22**) and Daprodustat (**24**).

6.6.6 Crystal Manipulation

6.6.6.1 Cryo-protectant

A 20-25% (v/v) glycerol solution was prepared by diluting the crystallisation reservoir solution with glycerol to be used as cryo-protectant. Other cryo-protectants used were prepared in the same manner; 10-20% (v/v) DMSO, 25% (v/v) ethylene glycol, and 30% (v/v) PEG 400. The orthorhombic $PHD2_{181-407}$ crystals reached equilibration and were stable in the cryo-protectant. The monoclinic tPHD2 crystals cracked and displayed weaker diffraction with longer exposures to cryo-protectant (>30 min 20% (v/v) glycerol and > 1 hr 10% (v/v) DMSO).

6.6.6.2 Crystal Harvesting

For wells containing crystal crystals, plate seals were cut with a dissecting knife (Swann Morton Ltd.) and ~1-2 μL of cryo-protectant was added to the crystallisation drop. Any protein skin formed on the surface of the drop was carefully removed with a D100 acupuncture needle (Dongbang AcuPrime Ltd.). Crystals were viewed under a Leica M205-C encoded stereozoom microscope (Leica Microsystems, GmbH), attached to a Motic® MLC-150C light source (MoticEurope, S.L.U.), single crystals were manually harvested using with 0.05-0.5 μm nylon CryoLoops™ (Hampton Research Corp.) mounted on CrystalCap™ SPINE HT bases (Hampton Research Corp.) and temporaily attached to a magnetic CrystalWand™ (Hampton Research Corp.).

6.6.6.3 Cryo-Cooling

Once installed in the loops, crystals were immediately cryo-cooled by plunging into liquid-N_2 contained in a Spearlab cryogenic foam Dewar vessel (Hampton Research Corp.) and covered until use. Liquid-N_2 was carefully monitored for ice build-up over time and refreshed as needed. The crystal pins were quickly transferred to cryo-cooled magnetic CryoVials (MiTeGen, LLC) using a curved Vial Clamp™ (Hampton Research Corp.).

6.6.6.4 Crystal Storage

Mounted crystals in CryoVials were either transferred to CryoCanes or uni-pucks and stored under liquid-until data collection. CryoCanes were stored in a 34XT Jencons Dewar vessel (Taylor-Wharton, Labmode Ltd.). The uni-pucks were transferred with a

bent cryo-tong (MiTegen, LLC.) and stored in Shelved Puck Shipping Canes (MiTegen, LLC.) in pre-cryo-cooled CX100 Cryo Express Dry Shippers (MiTegen, LLC.).

6.6.7 Data Collection

6.6.7.1 CuK$_\alpha$ Radiation Diffraction Analyses

Crystals were often screened using a FR-E+ SuperBright rotating anode generator in-house source (Rigaku Corp.) for diffraction quality, unit cell dimensions, and space group characterisation. Mounted crystals in cryo-vials were removed from storage canes and placed on an AFC11 partial χ four-axis goniometer (Rigaku Corp.) under a 100 K cryo-jet-stream (700 series cryostream cooler, Oxford Cryosystems Ltd.) attached to a 25 L Jencons liquid-N_2 Dewar vessel (Taylor-Wharton, Labmode Ltd.). Mounted crystals were aligned to the beam collimator using an optical analyser (Hitachi High-Tech Corp.) attached to a thin-film-transistor (TFT) liquid crystal display (LCD) colour monitor; centring was performed by rotating the crystal 90º on each axis while adjusting position of the crystal respective to the beam centre. A lead beam-stop was put in place and an initial screen of two images was carried out at 20-30 seconds of exposure with 45º of rotation around the Ω-axis. Diffraction images were collected on a Saturn 944+ charge coupled device detector (CCD, Rigaku Corp.). For a full dataset, 180 images with a 1º oscillation were collected for a total of 180º rotation around the Ω-axis with 30 seconds exposure per image (a max radiation dose of ~1.75 MGy, whereas for the synchrotron source (Diamond-I04) max dose was ~18.56 MGy calculated by RADDOSE-3D with PDB: 6ZBO (*Xtal-R*); **Figures AIII-6-7**).[10,11] CrystalClear™ software was used for data collection (Rigaku Corp.). Based on the resolution, crystals were either placed back into storage for collection at a synchrotron radiation source (**6.6.7.2**) or thawed. (*Thank you to*

Prof. Elspeth Garman and Dr. Shu En Lee calculated the FHWM beamsize and flux of the rotating anode diffractometer.)

6.6.7.2 Synchrotron Radiation Diffraction Analyses

Crystals were shipped to Diamond Light Source Ltd. and the SOLEIL synchrotrons in cryo-cooled C100X Dry Ship Dewar vessels (MiTeGen, LLC.) that contains loop-mounted crystals in uni-pucks. The uni-pucks were loaded into the liquid-N_2 storage Dewar vessels within the beamline experimental hutch of the macromolecular crystallography (MX) beamlines. MX beamlines where crystals were shipped: (i) Diamond (Didcot, UK) beamlines I03, I04, I04-1, I24, and (ii) SOLEIL (Paris, FR) beamline Proxima-1. At Diamond beamlines, automated loading of crystal pins onto the six-axis goniometer of the MX beamlines was carried out by using BART robotic sample changers (Diamond Light Source Ltd. and Mitsubishi Electric Corp.). Data collection was conducted *via* remote access of the Generic Data Acquisition (GDA) software graphical user interface (GUI, Diamond Light Source Ltd.) using NoMachine Enterprise Client (version 7.6.2, NoMachine S.à.r.l.) or by unattended data collection utilizing automated X-ray centring of crystals. Diffraction data collection parameters are listed in **Table-AI-2**. Diffraction data were collected using pixel-array detectors (Pilatus and Eiger series, Dectris AG; depending on the specific beamline).[12,13]

6.6.8 Data Processing

6.6.8.1 HKL-2000®

Crystal datasets collected on the in-house source (**6.6.7.1**) were uploaded into HKL-2000®.[14] The peak search function was initiated to find diffracted reflections. The reflections are then indexed, and the predicted crystal system and unit cell dimensions are

output (the user can also mask the beamstop and define the beam centre).[14] After the user defines the Bravais lattice, the unit cell dimensions are refined. The reflection images are then integrated in the chosen space group.[14] All unique reflections, *i.e.*, accounting for symmetry-related reflections, from the individual frames were merged into one file.[14] Output reflection files were generated and exported to PHENIX (**6.6.9**) in scalepack (SCA) file format.[14]

6.6.8.2 Xia2

Xia2 (DIALS or 3dii, Diamond Light Source Ltd.) automated data processing was initiated post-data collection and results were accessible online through information system for protein crystallography (ISPyB).[15–18] The Xia2 DIALS strategy uses Collaborative Computational Project Number 4 (CCP4), Xia2, DIALS.scale, and DIALS programs.[15–17,19] The Xia2 3dii strategy uses CCP4, DIALS, POINTLESS, XDS, and Xia2.[15–17,19–21] The automatic default free Mclaughlin, Terry, and Zelinka file (MTZ), unmerged MTZ, and LOG files (from default processing parameters) were exported from ISPyB to local PCs for further data analysis, structure solution, and refinement.[18]

6.6.8.3 autoPROC

autoPROC (Diamond Light Source Ltd.), another automated data processing pipeline, was successfully carried out on some of the datasets.[22] The processing results were accessible through ISPyB.[18] The autoPROC data processing strategy uses CCP4, XDS, POINTLESS, AIMLESS, STARANISO, and autoPROC programs to process and scale unmerged datasets.[19–24] Truncate-unique/staraniso-alldata-unique MTZ and LOG files were exported from ISPyB to local PCs for further data analysis, structure solution, and refinement.[18]

6.6.9 PHENIX Software Suite (version 1.19.1)

6.6.9.1 Xtriage

The PHENIX.Xtriage tool was used to analyse the quality of the processed crystal reflection files and determine if there are any abnormalities or pathologies with the dataset.[25–27] The Matthews coefficient and solvent content were estimated based on the unit cell dimensions and number of residues in the crystallised construct. Data completeness was displayed by resolution bin and average Wilson B-factors were assessed. Potential for twinning, ice rings, anisotropy, and pseudotranslational symmetry were all analysed in the datasets.[25–28]

6.6.9.2 PHENIX-Phaser-Molecular Replacement (MR)

Phaser-Molecular replacement (PHASER-MR) was used to phase the processed diffraction data for each structure.[29] A previously determined model of tPHD2 (PDB: 3HQR) used as a search model, the protein construct sequence in a fast-all sequence (FASTA) file format, the MW (either 26 kDa ($PHD2_{181-407}$) or 28 kDa ($PHD2_{181-426}$)), and the percent of sequence identity (100%) were all input into the GUI for MR-phasing.[29] PHASER-MR outputs the structure solution with the rotation and translation applied to the protein coordinates as PDB format files and structure factors with map coefficients in MTZ file format for visualisation and fitting in COOT.[27,29] The quality of output solutions were assessed by the TFZ scores and LLGs.

6.6.9.3 COOT

COOT (version 0.9.5, CCP4) was used to visualise the phased models with overlaid $2mF_o$-DF_c and mF_o-DF_c difference electron density maps to aid semi-manual model building based on the observed density.[19,30] The geometry of the model was

adjusted and improved in COOT based in calculated electron density maps prior to subsequent refinement cycles using PHENIX.Refine (**6.6.9.4**).17,25,28,29

6.6.9.4 PHENIX-Refine

PHENIX-Refine was used to modify and improve the model in iterative cycles.[27,31] Model improvement was assessed by the decreasing and converging of R_{work}/R_{Free} values between cycles of refinement.[27,31] MolProbility, a validation tool within PHENIX-refine, was used to assess the geometric quality, Ramachandran restraints, rotamers outliers, and clash score of the refined model and guide re-building in COOT.[32] Crystal resolution was defined depending on the completeness of the resolution bin (>95% in all resolution bins). PHENIX.Readyset was used to incorporate pre-generated CIFs (GRADE, Global Phasing Ltd. or PHENIX Elbow) for ligands and non-standard amino acids.[27,31] The general refinement strategy was to use Torsion-Liberation-Screw (TLS) refinement, individual B-factors, and reciprocal space refinement.[27,31] The TLS groups were modified and automatically determined through PHENIX.refine.[27,31,33,34] Optimisation of both X-ray/stereochemistry and X-ray/atomic displacement parameters (ADP) weight was automatically configured and depended on data resolution.[27,31] In the model interpretation, after the first refinement, Ramachandran restraints were used for all residues in structures for which reoccurring Ramachandran outliers were a problem.[27,31] Addition of hydrogen atoms (only for bumping restraints) and correction of N/Q/H errors were also configured.[27,31]Three cycles were typically run for each refinement round before manual fitting.[27,31]

6.6.9.5 Structure Comparison Tool

The Structure Comparison Tool in PHENIX was used to compare different models and chains within the ASU for differences in refined B-factors (**2.2.3.1** and **2.4.1.1**).[27,35]

6.6.9.6 Table Generation Tool

Crystallographic data tables were generated post the final refinements using the 'Generate Table 1 for Journal' tool in PHENIX.[25,27] The coordinates (PDB), structure factors, and unmerged reflections (MTZ) were uploaded into PHENIX to generate the tables.[25,27]

6.6.10 Protein Data Bank (PDB) Extract Tool

The online 'PDB extract' tool (version 3.24, Research Collaboratory for Structural Bioinformatics PDB) was used to prepare coordinate and structure factors files in macromolecular CIF (mmCIF) format to be uploaded to the PDB Validation or Onedep servers.[36–39] The log files of the Xia2 autoprocessing and Phaser were also uploaded for data statistics extraction.[15,29] The FASTA sequence of the protein construct was included.

6.6.11 PDB Validation Service

The coordinate and structure factor CIF files were uploaded to the PDB validation service as a final check of the overall quality of diffraction data and model prior to deposition into the PDB.[36,39] The validation service was also used to validate each of the complex structures and generate the heat-map validation.[36] Often the server detected errors such as too close contacts, distance solvent molecules, and incorrect occupancies which had to be corrected and resubmitted to obtain a final model for deposition.[36]

6.6.12 PDB Onedep Server

Coordinates and structure factors were uploaded into the Onedep server as mmCIF files.[37–39] Information about the experiment, ligand/s, protein, data collection, data processing, data refinement, authors, and funding bodies were input with the deposition.[38,39] The structures were deposited and validated by the RCSB PDB curators.[37–39] A unique PDB code and PDB ligand code was generated for each deposit. Deposits were generally held until release of publication.[38,39] (*Note the only deposited structures were PDB: 6ZBN (Xtal-S) and 6ZBO (Xtal-R). As the other structures are not deposited, the models of the structures may be further refined to correct any validation issues before publishing into the PDB.*)

6.7 Chapter 2 Methods

6.7.1 Formate Condition Protein-Substrate Preparation

$PHD2_{181-407}$ was purified through *via* the two-column purification strategy (affinity and SEC chromatography) was used to obtain the $PHD2_{181-407}$.$HIF2\alpha_{523-542}$-CODD complex structures (**2.2**).[2,7] Protein solutions were prepared following standard protein preparation procedures (**6.4**). An 80 mM stock of NOG pH 7-8 or 100 mM 2OG disodium salt was diluted to a final concentration of 2 mM in the protein sample. The protein/ligand mixture was pipetted into lyophilised 3C cyclic peptide (**2.1.2** and **6.6.1**) and left to equilibrate on a Cole-Parmer® tube rotator (Cole-Parmer Instrument Company Ltd.) at 4 ºC for 2.5 hours.[2,40] $PHD2_{181-407}$ was centrifuged at 12,000 rpm (9,600 × *g*) for 10 minutes at 4 ºC. The protein, cofactors, and cyclic peptide mixture were added to lyophilised $HIF2\alpha_{523-542}$-CODD peptide (**6.6.1**).[2,40] The protein-substrate mixture was left overnight to equilibrate on the tube rotator at 4 ºC. The next day the incubated sample was centrifuged at 14,000 rpm (18,800 × *g*) and the supernatant harvested for

crystallisation. The protein-substrate sample volume was adjusted to a final volume of 70 μL before preparation of the crystallisation plates. (*Initial optimisation was conducted by Dr. Rasheduzzaman Chowdhury.*)

6.7.2 $PHD2_{181-407}$.HIF2α-CODD Complex Structure

The $PHD2_{181-407}$.Mn(II).NOG/or 2OG.$HIF2\alpha_{523-542}$-CODD.3C (*Xtal-A* and *Xtal-B*) mixture was screened against 0.25-0.39 M magnesium formate disodium salt and 18-22% (w/v) PEG 3350.[2] The protein-substrate mixture was prepared with 1 mM $PHD2_{181-407}$, 1 mM Mn(II)Cl2, 2 mM NOG/or 2OG, 2 mM $HIF2\alpha_{523-542}$-CODD peptide, and 2 mM 3C peptide dispensed into crystallisation plates following the standard protocol (**6.6.4**) and stored at 298 K. A 1 mm x 100 μm x 80 μm (*Xtal-A*) and a 240 μm x 50 μm x 30 μm (*Xtal-B*) plate-like crystals appeared after 1-week of equilibration in 0.31 M magnesium formate and 16.6% (w/v) PEG 3350 (200 nL, 1:1 protein-to-well ratio, 298 K). Crystals were cryo-cooled (**6.6.6.3**) and stored (**6.6.6.4**) until data collection at a synchrotron source (**6.6.7.2**).

6.7.3 Anaerobic Formate-Derived Crystal

Anaerobic $PHD2_{181-407}$.Fe(II).2OG.$HIF2\alpha_{523-542}$-CODD.3C (*Xtal-C*) complex crystals were produced with 1 mM $PHD2_{181-407}$, 1 mM Mn(II)Cl2, 2 mM 2OG, 2 mM $HIF2\alpha_{523-542}$-CODD peptide, and 2 mM 3C peptide. $HIF2\alpha_{523-542}$-peptides (**Figure 1-7**, **1.3.1**) were not added to the protein sample until all solution were equilibrated in a modular anaerobic glovebox (O_2-levels maintained at 2 parts per million or less, Belle Technologies Ltd.) to prevent substrate turnover. 24-well vapour-diffusion hanging drop VDX plates with sealant (Hampton Research Corp.) and N_2-sparged precipitant solutions were ported into the anaerobic glovebox through the main port using a 2X 15-minute N_2-

valve purge protocol. The protein-cofactor mixture equilibrated overnight on a tube rotator at 4 ºC and subsequently ported into the glovebox *via* the smaller rapid port (a 5-minute N_2-purge was completed to prepare the rapid port). The protein mixture was kept cold on a chilled sample block (IsoFreeze®, Scientific Specialties, Inc.). $(NH_4)_2Fe(II)(SO_4)$ was added to protein mixture and incubated for 5 minutes. The sample was added to lyophilised HIF2$\alpha_{523\text{-}542}$-CODD peptide (**6.6.1**). Crystallisation drops (2 µL) were prepared at a 1:1 protein-to-precipitant ratio. An optimised screen of 0.33-0.39 M magnesium formate and 17-20.81% (w/v) PEG 3350 conditions was prepared with 500 µL of reservoir solution in each well in a 24-well VDX hanging-drop plates. A 500 µm x 250 µm fan cluster of rod morphology crystals appeared after 1-2 weeks 0.39 M magnesium formate and 19.15% (w/v) PEG 3350 (2 µL drop, 1:1 protein-to-well ratio, 298 K). A Dewar vessel, filled with liquid-N_2, was connected to the glovebox for cryo-cooling samples under anaerobic conditions. The anaerobic crystal (*Xtal-C*) was separated into single crystal fragments, and 20% (v/v) glycerol-precipitant was used as a cryo-protectant (**6.6.6.1**). A single crystal was cryo-cooled (**6.6.6.3**) in a Dewar vessel containing liquid-N_2. The Dewar vessel port was sealed, and the crystal pins were transferred and stored (**6.6.6.4**) under liquid-N_2 in canes or uni-pucks until data collection at a synchrotron source (**6.6.7.2**).

6.7.4 O_2-Exposure Formate condition Crystals

A highly purified O_2 gas source was bubbled (~1.22 mM of O_2)[41] into 1 mL of 0.39 M magnesium formate and 19.15% (w/v) PEG 3350 precipitant solution from the crystal well condition. The crystal plate that contained the anaerobic PHD2$_{181\text{-}407}$.Fe(II).2OG.HIF2$\alpha_{523\text{-}542}$-CODD.3C clustered crystal was ported out of the glovebox and the O_2-saturated precipitant solution was mixed with 20% (v/v) glycerol-precipitant

cryo-protectant (~976 μM dissolved O_2, **6.6.6.1**). Crystals of ~90 μm x 25 μm x 10 μm - ~120 μm x 60 μm x 20 μm were soaked with 1 μL of the cryo-O_2 solution (2 μL drops; ~374 μM) from 5-25 minutes (T5-T25). A total of eight O_2-exposed crystals (*Xtal-D-F*) were cryo-cooled (**6.6.6.3**) and stored (**6.6.6.4**) under liquid-N_2 until data collection at a synchrotron source (**6.6.7.2**). Only T17, T19, and T25 timepoints diffracted and did not contain abnormalities in the datasets.

6.7.5 Zn Condition Crystals

The PHD2$_{181-407}$.Mn(II).2OG.HIF2α$_{523-542}$-CODD.3C mixture was prepared with 1.2-1.5 mM Mn(II)Cl_2, and 2 mM HIF2α$_{523-542}$-CODD peptide (**6.6.1** and **6.6.4**).The 2OG-disodium salt was replaced the 2OG-diacid (5 mM) and 3C peptide was added at a final concentration of ~600-700 μM (**6.6.1**). A screen of the Classic Lite Suite™, Anion Suite™, and Cation Suite™ (Qiagen N.V.) was conducted in an attempt to find a PEG free crystallisation condition. After 1 day of equilibration, a 20 μm x 10 μm x 5 μm rhombohedral crystal (*Xtal-G*) appeared in 0.01 M Zn(II)SO_4, 11% (w/v) PEG MME, and 26 mM MES pH 6.5 (200 nL drop, 1:1 protein-to-well ratio, 298 K). The crystal was cryo-protected (20% (v/v) glycerol-precipitant, **6.6.6.1**), cryo-cooled under liquid-N_2 (**6.6.6.3**), stored (**6.6.6.4**), and sent for data collection at a synchrotron source (**6.6.7.2**).

6.7.6 Acetate Condition Anaerobic Crystals

The PHD2$_{181-407}$.HIFα substrate mixture was optimised to produce reliable crystals of PHD2$_{181-407}$.Fe(II)/Mn(II).2OG.HIF2α$_{523-542}$-CODD complex. HIF2α$_{523-542}$-CODD peptide was prepared at a 100 mM stock concentration in DMSO. 1 mM apo-PHD2$_{181-407}$ (EDTA-treated) was used for the anaerobic studies. Protein-substrate mixture contained final concentrations of 1.2-1.5 mM $(NH_4)_2$Fe(II)(SO_4), 5-7 mM 2OG, 1.5 mM

HIF2$\alpha_{523-542}$-CODD peptide. All reagents were prepared in the glovebox, except for the protein and substrate stock solutions. The protein solution was ported into the anaerobic glovebox following the standard protocol (**6.7.3**) and carefully pipetted up and down to purge the solution of O_2. The protein sample was stored in a mini-fridge at 6-8 ºC during incubation with the HIFα-substrate (Great Gadgets Ltd.). Reagents were added in successive order (metal, cosubstrate, and substrate) with 5-minute incubations. Subsequently, after addition of the substrate, the sample was stored in a mini-fridge for 1 hour until plate set-up in a 24-well Cryschem sitting-drop plates (Hampton Research Corp.) with 500 µL of precipitant-reservoir solution. The plate was sealed with (Xtra-Clear Advanced Polyolefin StarSeal Film, StarLabs Ltd.) and the largest crystal obtained was 600 µm x 200 µm x 75 µm rod crystal (*Xtal-J*) appeared after 3 days equilibration in 0.2 M ammonium acetate 0.3 M sodium acetate trihydrate pH 5.6, and 25% (w/v) PEG4000 (1.5 µL drops, 1:1 protein-to-well ratio, 298 K). Crystals were cryo-protected (20% (v/v) glycerol-precipitant, **6.6.6.1**), cryo-cooled under liquid-N_2 (**6.6.6.3**) and stored (**6.6.6.4**) under liquid-N_2 until data collection at a synchrotron source (**6.6.7.2**). (*Crystals plates were prepared by Ms. Giorgia Fiorini.*)

6.7.7 O_2-Exposure Acetate condition Crystals

The previous protocol for O_2-exposure of anaerobic PHD2$_{181-407}$.Fe(II)/Mn(II).2OG.HIF2$\alpha_{523-542}$-CODD crystals was used (**6.7.4**). Crystal were prepared with 1 mM apo-PHD2$_{181-407}$, 1.2-1.5 mM $(NH_4)_2Fe(II)(SO_4)$, 5-7 mM 2OG, 1.5 mM HIF2$\alpha_{523-542}$-CODD peptide. An O_2-sparged (~1.22 mM dissolved O_2)[41] solution of 0.2 M ammonium acetate, 0.3 M sodium acetate trihydrate, 25% (v/v) PEG 4000 pH 5.6 was used. Cryo-protectant was prepared with (10-20% (v/v) DMSO-precipitant, ~976 µM dissolved O_2). Crystals of ~100 µm x 30 µm x 10 µm-280 µm x 75 µm x 20 µm

dimensions were ported out of the anaerobic glovebox and had a 1-min or 75-min rest in atmospheric O_2. *Xtal-M* (60-min incubation with supplemental O_2) and *Xtal-N* (~7,200-min with supplemental O_2) were exposed to the O_2-cryoprotectant solution (1 µL into 1.5 µL drops; ~645 µM dissolved O_2). The crystals were exposed for 45 minutes to 5 days, and 14 crystals were cryo-cooled under liquid-N_2 (*Xtal-K-N*, **6.6.6.2**). Only four datasets without abnormalities are shown in this study. Two crystals (*Xtal-K* and *Xtal-L*) were exposed to atmospheric levels of O_2 for a rest of 75-min. *Xtal-K* and *Xtal-L* were soaked with 5 mM DMSO-solubilised Roxadustat (**22,** 10-minute soak) at 75 minutes O_2-exposure prior to cryo-cooling.

6.8 Chapter 3 Methods

6.8.1 $PHD2_{181-426}$.Mn(II) Complex Structure

A broad screen (**6.6.2**) of conditions was conducted to find crystallisation conditions for a $PHD2_{181-426}$ (0.8 mM) in complex with Mn (2.2 mM). Crystal hits were observed after 1 week of equilibration in condition 0.02 M sodium/potassium phosphate and 20% (v/v) PEG 3350 of the Pact premier™ screen at 298 K. An optimized screen (**6.6.3**) was prepared around the initial hit; 0.05-0.035 M sodium/potassium phosphate and 15-26% (w/v) PEG 3350. The optimisation produced relatively large (400 µm x 90 µm x 15 µm) rod crystals and 30 x 10 x 5 µm plate crystals were observed after 3-5 days in 5 mM sodium/potassium phosphate and 15% (w/v) PEG 3350 (300 nL drop, 1:2 protein-to-well ratio, 298 K). The crystal was cryo-protected with (20% (v/v) glycerol-precipitant), harvested (**6.6.6.2**), and screened on the in-house source (**6.6.7.1**). Data collection was carried out *via* synchrotron radiation (**6.6.7.2**) due to weak diffraction of the crystals on the in-house source (**6.6.7.1**).

6.8.2 $PHD2_{181-407}$.Mn(II).Succinate Complex Structure

The $PHD2_{181-407}$.Mn(II).succinate complex solution with 1 mM $PHD2_{181-407}$, 1.2 mM Mn(II)Cl_2, and 2.2 mM succinate. Crystallisation conditions were screened with the PEG/Ion screen™ I/II. The largest 90 μm x 80 μm x 10 μm rhombohedral crystal formed after 3-days in well condition B2 (0.2 M potassium thiocyanate pH 7 and 20% (w/v) PEG 3350, 200 nL drop, protein-to-well ratio 1:1, 298 K). The largest 200 μm x 120 μm x 35 μm rhombohedral crystal formed in 0.140 M potassium thiocyanate pH 7 17% (w/v) PEG 3350. Crystals were cryo-protected (10% (v/v) DMSO-precipitant, **6.6.6.1**) and cryo-cooled under liquid-N_2 (**6.6.6.3**). Data was collected *via* synchrotron radiation (**6.6.7.2**).

6.8.3 $PHD2_{181-407}$.Mn(II).Fumarate Complex Structure

The $PHD2_{181-407}$.Mn(II).fumarate complex structure with 1 mM $PHD2_{181-407}$, 1.2 mM Mn(II)Cl_2, and 2.2 mM fumarate. Crystallisation conditions were screened against the PEG/Ion Screen™ I/II and plated (**6.6.4**) and stored at 298 K. Clustered crystal hits formed in well precipitant condition 0.2 M sodium iodide pH 7 and 20% (w/v) PEG 3350. An optimisation block was used to improve crystal quality and screened 0.2 M sodium iodide pH 7 and 17-22.5% (w/v) PEG 3350. 150 μm x 100 μm x 40 μm rod crystals formed after 3-days in well condition 0.2 M sodium iodide pH 7 and 18% (v/v) PEG 3350 (300 nL volume drops, protein-to-precipitant solution ratio 2:1, 298 K) and were cryo-protected (20% (v/v) glycerol-precipitant, **6.6.6.1**), cryo-cooled (**6.6.6.3**), and stored under liquid-N_2 (**6.6.6.3**) until data collection at a synchrotron source (**6.6.7.2**).

6.8.4 $PHD2_{181-407}$.Mn(II).Molidustat Complex Structure

The $PHD2_{181-407}$.Mn(II).Molidustat (**20**) complex was prepared with 1 mM $PHD2_{181-407}$, 1.2 mM $Mn(II)Cl_2$, and 2.2 mM succinate.[4] $PHD2_{181-407}$ was incubated for 30-60 minutes with 2.2 mM of **20**.[4] The sample was plated following a standard protocol (**6.6.4**) using an optimised screen (**6.6.3**) of 0.050-0.225 M potassium thiocyanate pH 7 and 18-23.5% (w/v) PEG 3350 and stored at 298 K.[4] A 180 μm x 60 μm x 40 μm rhombohedral crystal formed in well condition 0.2 M potassium thiocyanate pH 7 and 21% (w/v) PEG 3350 (300 nL drops, 2:1 protein-to-well ratio, 298 K) after 3-5 days.[4] The crystal was cryo-protected (20% (v/v) glycerol-precipitant, **6.6.6.1**), cryo-cooled (**6.6.6.3**), and stored under liquid-N_2 (**6.6.6.3**). Data were collected on both the in-house (**6.6.7.1**) and synchrotron radiation (**6.6.7.2**) sources.

6.8.5 $PHD2_{181-407}$.Mn(II).IOX4 Complex Structure

The $PHD2_{181-407}$.Mn(II).IOX4 (**28**) complex was prepared with 1 mM $PHD2_{181-407}$, 1.2 mM $Mn(II)Cl_2$, and 2.2 mM succinate.[4] **28** was incubated with $PHD2_{181-407}$ for 30-60 minutes at a final concentration of 2.2 mM. The sample was plated following a standard protocol (**6.6.4**) using an optimised screen of 0.050-0.225 M potassium thiocyanate pH 7 and 18-23.5% (w/v) PEG 3350 conditions and stored at 298 K.[4] A 100 μm x 100 μm x 15 μm rhombohedral crystal formed in condition 0.15 M potassium thiocyanate pH 7 and 21% (w/v) PEG 3350 (300 nL, 2:1 protein-to-well ratio, 298 K) after 3-5 days.[4] The crystal were cryo-protected (20% (v/v) glycerol-precipitant, **6.6.6.1**) and cryo-cooled (**6.6.6.3**) and data was collected *via* synchrotron radiation (**6.6.7.2**).

6.8.6 $PHD2_{181-407}$.Mn(II).Takeda-17 Complex in the *P* 2_1 Crystal Form

The $PHD2_{181-407}$.Mn(II).Takeda-17 (**17**) complex was prepared with 1 mM $PHD2_{181-407}$, 1.2 mM Mn(II)Cl_2, and 2.2 mM succinate.[42] **17** was incubated with $PHD2_{181-407}$ for 30-60 minutes at a final concentration of 2.2 mM.[42] The sample was plated following a standard protocol (**6.6.4**) using an optimised screen of 0.050-0.225 M potassium thiocyanate pH 7 and 18-23.5% (w/v) PEG 3350 and stored at 298 K. A 150 μm x 100 μm x 25 μm rhombohedral crystal formed in well condition 0.3 M potassium thiocyanate pH 7 and 22% (w/v) PEG 3350 after 3-5 days (300 nL, 1:2 protein-to-well ratio, 298 K). The crystal was cryo-protected (20% (v/v) glycerol-precipitant, **6.6.6.1**) and cryo-cooled (**6.6.6.3**) and data was collected *via* synchrotron radiation (**6.6.7.2**).

6.8.7 $PHD2_{181-407}$.Mn(II).ZXJ1 Complex Structure Ammonium Sulfate Condition

The Crystal Screen™ I/II was set-up following the standard protein preparation and conditions in (**6.6.1**). ZXJ-1 (**33**) was incubated with 1 mM $PHD2_{181-407}$ and 1.2 mM Mn(II)Cl_2 for 30 minutes at a final concentration of 2.2 mM.[43] $PHD2_{181-407}$.Mn(II).**33** complex was plated following a standard protocol (**6.6.1**) at 298 K.[43] A 10 μm x 2 μm tear drop hit crystal formed in 3-5-days in 0.1 M Tris-HCl pH 8.5 and 2 M $(NH_4)_2SO_4$ (300 nL, 1:2 protein-to-well ratio, 298 K). The crystals were not reproducible and could not be optimised for higher resolution. The hit crystal was cryo-protected (20% (v/v) glycerol-precipitant, **6.6.6.1**) and cryo-cooled (**6.6.6.3**) and sent for data collection *via* synchrotron radiation (**6.6.7.2**).

6.9 Chapter 4 Methods

6.9.1 Seeding Protocol

A seeding protocol was optimised to increase the number of 80 μm x 70 μm x 25 μm-200 μm x 100 μm x 50 μm rhombohedral $PHD2_{181-407}$.Mn(II).succinate crystals (1 mM $PHD2_{181-407}$, 1.2 mM Mn(II)Cl_2, and 2.2 mM succinate) to give ~50 crystals per 3 Lens Crystallisation Plate (SWISSCI Ltd.). A Mosquito® robot (STP Labtech Ltd.) was used for seeding. $PHD2_{181-407}$.Mn(II).succinate seeds were prepared with a SeedBead™ kit from (Hampton Research Corp.) with $PHD2_{181-407}$.Mn(II).succinate crystals from 5-6 drops. 100 μL of precipitant from the well condition of the highest PEG concentration was added to the crystals. 300 nL drops contained 200 nL of $PHD2_{181-407}$, 30 nL of seeds, and 70 nL of precipitant. The plate condition contained 140 mM potassium thiocyanate pH 7 and 18-20.2% (w/v) PEG 3350. Protein was prepared following a standard protocol (**6.6.1**) and seeds were stored on ice. Seeds were vortexed (Vortex-Genie 2, Scientific Industries, Inc.) prior to use and stored at -20 ºC for 1-2 freeze-thaw cycles. Seeded crystal plates were stored at 298 K. Crystals appeared after 1 week of equilibration.

6.9.2 Solvent Characterisation

Crystals were characterised with varying concentrations of 10-40% (v/v) DMSO and with glycerol to determine a soaking condition for the fragment screen and concentrations of fragments to dispense.[44] 10-30% (v/v) DMSO with either 20% (v/v) glycerol or 20% (v/v) ethylene glycol were tested on the $PHD2_{181-407}$.Mn(II).succinate crystals.[44] One hour soaks with 10% (v/v) DMSO was selected as the optimal condition for fragment screening as use as a cryo-protectant (**6.6.6.1**).

6.9.3 TexRank and Echo® Dispensing

Crystal plates were imaged with a Rock Imager® 1000 (Formulatrix, Inc.) plate imager. Crystal drop images were uploaded into TexRank (Diamond Light Source Ltd.).[45] TexRank allowed for efficient selection of useable crystals for the screen and generated coordinates for Echo® dispensing of the fragments into the crystal drops (30 nL into 300 nL drops).[45,46] The fragment dispense target was used to prevent damage to the crystals upon dispensing of the fragments.[46] Comma-separated values (CSV) file with the crystal plate coordinates was input into the Echo® 550 acoustic liquid handler (Labcyte Inc.) dispenser and the DSI-poised or FragLite fragment libraries (Diamond Light Source, Ltd and University of Newcastle, respectively) were dispensed into the crystal plates.[46–48] After the run, crystal plates were sealed with QuickSeal PCR™ self-adhesive film (IST Scientific. LLP.) and stored for 15-30 minutes in an incubator at 293 K. The fragment libraries were stored under Ar and sealed with adhesive aluminium StarSeals (StarLabs Ltd.).

6.9.4 SoakDB

The SoakDB spreadsheet was used to record all the information about the crystals selected from TexRank, small-molecule fragment Simplified Molecular Input Line Entry System (SMILES) code, plates coordinates, soak times, crystal/drop conditions, puck position, pin codes, and ISPyB data identification/identifier (IDs). The input data and recorded information was stored from SoakDB into an SQLite (version 3.34.0) database and could be accessed for downstream data processing in XCE (version 1.7.16, Diamond Light Source Ltd.).[44,49]

6.9.5 Crystal Shifter

CSV files with soaked crystal plate coordinates were uploaded into the crystal shifter (Oxford Lab Technologies Ltd.).[50] Uni-pucks were scanned, and positions were recorded automatically to linked uni-puck IDs. 4-5 uni-pucks were cryo-cooled and stored under liquid-N_2. The skin that formed on the surface of the crystallisation drop was removed carefully using an acupuncture needle. Crystals were harvested with 33 μm, 75 μm, and 150 μm MicroSD™ loops (MiTeGen, LLC., **6.6.6.3**). Crystal harvesting began after 15-30 minutes of soaking with the small-molecule fragments and crystals were cryo-cooled. The drop condition *(e.g.*, precipitated, clear, or crystalline state of the fragment), the crystal condition (*e.g.*, cracked, jelly, normal, and melted states), and total soak times were recorded using the shifter and information uploaded into SoakDB.[44,50] To fish ~100 crystals required ~2-3 hours, including the soak time. Uni-pucks were stored in a shelved uni-puck cane in storage Dewar vessel until data collection. Scanned uni-puck and crystal pin information was uploaded into ISPyB *via* SoakDB.[18] Harvested crystals were numbered and required information was generated for data collection. Beamline staff loaded the uni-pucks into the Dewar vessel within the experimental hutch (**6.6.7.2**).

6.9.6 Data Collection and Parameters

The data collection proceeded *via* unattended data collection with X-ray centring (**6.6.7.2**). Data collection was conducted at beam energies (λ) of either 0.9159 Å or 0.9119 Å, 60 μm x 50 μm beam size, 1500 images, 0.040 or 0.060 seconds exposure, 100% transmission, 0.16º oscillation, and 2.00 Å detector distance (Pilatus 6M-F, Dectris AG, Diamond Light Source-I04-1; **Table AI-2**).

6.9.7 XCE and Downstream Processing (DIMPLE and PanDDA)

Crystal information in SoakDB was linked to an SQLite database. Crystal datasets in ISPyB were imported into XCE GUI from SQLite database and could be selected for further analysis.[49] Correct space group and resolution cut-offs (>2.80 Å) were used to select the best datasets for downstream processing. Once datasets had been compiled, DIMPLE was used to phase datasets with a previously refined model (PDB: 6ZBO) and generated electron density maps.[4,51] The fragment's ligand restraints were generated using the corresponding SMILES code. Electron density maps and ligand restraints were analysed with PanDDA.analyse with simultaneous building of the ground-state model (Diamond Light Source Ltd.).[52,53] Results were viewed with PanDDA.inspect.[52,53] The ground-state model was refined following a standard protocol (**6.6.9.3** and **6.6.9.4**).[52,53] The built ground-state model, with correctly placed solvent and ligands, was run as the starting model for DIMPLE. Datasets were clustered into four groups based on unit cell dimensions and resolution. Each individual cluster was analysed with PanDDA2.analyse.[52,53] PanDDA fragment hits were visualised through PanDDA.inspect.[52,53] Medium-to-high confidence hits were recorded and merged reflection MTZ files were downloaded from ISPyB.[18] The reflection MTZ files were checked with Xtriage for abnormalities or pathologies (**6.6.9.1**).[26] Good quality datasets were phased with Phaser-MR (**6.6.9.2**).[27,29] One round of PHENIX.refine was conducted on the datasets post Phaser-MR.[27,29,31] Subsequently, fragments ligand coordinates were placed into structures through successive rounds of refinement (PHENIX-Refine).[27,31] Structures with low quality ligand maps were rejected. (*Clustering and PanDDA2 was work conducted by Dr. Alexandre Dias.*)

6.9.8 Crystal Soaking with Monodentate Binding Derivatives

The crystal soaking protocol was based on the soaking method used in the XChem fragment screen (**4.2**).[54] Crystals were prepared with 1 mM $PHD2_{181-407}$, 1.2 mM $Mn(II)Cl_2$, and 2.2 mM succinate. 20% (v/v) glycerol was initially used as a cryo-protectant, and subsequently DMSO was used (**6.6.6.1**). Takeda-17 (**17**) derivatives at 50 mM DMSO stock concentration were diluted to final concentration between 2-10 mM in either 15-20% (v/v) glycerol-precipitant solution or 10% (v/v) DMSO-precipitant solution.[42] As the inhibitors were diluted in the cryo-protectant (**6.6.6.1**), 1-2 μL was added to the crystal drops (either 200 or 300 nL) and sealed with Sellotape® (Henkel AG & Co KGaA). Crystals were soaked for 15-20 minutes and monitored for degradation. Once crystals started to dissolve or crack, crystal were cryo-cooled under liquid-N_2. Harvested crystals (**6.6.6.2**) were stored cryogenically until data collection (**6.6.7.2**).

6.10 References

(1) Waterhouse, A. M.; Procter, J. B.; Martin, D. M. A.; Clamp, M.; Barton, G. J. Jalview Version 2-A Multiple Sequence Alignment Editor and Analysis Workbench. *Bioinformatics* **2009**, *25* (9), 1189–1191. https://doi.org/10.1093/bioinformatics/btp033.

(2) Chowdhury, R.; Abboud, M. I.; McAllister, T. E.; Banerji, B.; Bhushan, B.; Sorensen, J. L.; Kawamura, A.; Schofield, C. J. Use of Cyclic Peptides to Induce Crystallization: Case Study with Prolyl Hydroxylase Domain 2. *Scientific Reports* **2020**, *10* (1). https://doi.org/10.1038/s41598-020-76307-8.

(3) van Die, I. M.; Bergmans, H. E. N.; Hoekstra, W. P. M. Transformation in Escherichia Coli: Studies on the Role of the Heat Shock in Induction of Competence. *Journal of General Microbiology* **1983**, *129* (3), 663–670. https://doi.org/10.1099/00221287-129-3-663.

(4) Figg Jr., W. D.; McDonough, M. A.; Chowdhury, R.; Nakashima, Y.; Zhang, Z.; Holt-Martyn, J. P.; Krajnc, A.; Schofield, C. J. Structural Basis of Prolyl Hydroxylase Domain Inhibition by Molidustat. *ChemMedChem* **2021**, *16* (13), 2082–2088. https://doi.org/10.1002/cmdc.202100133.

(5) Chowdhury, R. Structural and Mechanistic Studies on Prolyl Hydroxylases, Oxford University, UK, 2008.

(6) Chowdhury, R.; McDonough, M. A.; Mecinović, J.; Loenarz, C.; Flashman, E.; Hewitson, K. S.; Domene, C.; Schofield, C. J. Structural Basis for Binding of Hypoxia-Inducible Factor to the Oxygen-Sensing Prolyl Hydroxylases. *Structure* **2009**, *17* (7), 981–989. https://doi.org/10.1016/j.str.2009.06.002.

(7) Chowdhury, R.; Leung, I. K. H.; Tian, Y. M.; Abboud, M. I.; Ge, W.; Domene, C.; Cantrelle, F. X.; Landrieu, I.; Hardy, A. P.; Pugh, C. W.; Ratcliffe, P. J.; Claridge, T. D. W.; Schofield, C. J. Structural Basis for Oxygen Degradation Domain Selectivity of the HIF Prolyl Hydroxylases. *Nature Communications* **2016**, *7* (1), 12673. https://doi.org/10.1038/ncomms12673.

(8) Cockman, M. E.; Lippl, K.; Tian, Y. M.; Pegg, H. B.; Figg, W. D.; Abboud, M. I.; Heilig, R.; Fischer, R.; Myllyharju, J.; Schofield, C. J.; Ratcliffe, P. J. Lack of Activity of Recombinant HIF Prolyl Hydroxylases (PHDs) on Reported Non-HIF Substrates. *eLife* **2019**, *8*, e46490. https://doi.org/10.7554/eLife.46490.

(9) Richardson, N. L.; O'Malley, L. J.; Weissberger, D.; Tumber, A.; Schofield, C. J.; Griffith, R.; Jones, N. M.; Hunter, L. Discovery of Neuroprotective Agents That Inhibit Human Prolyl Hydroxylase PHD2. *Bioorganic and Medicinal Chemistry* **2021**, *38*, 116115. https://doi.org/10.1016/j.bmc.2021.116115.

(10) Zeldin, O. B.; Gerstel, M.; Garman, E. F. RADDOSE-3D: Time- and Space-Resolved Modelling of Dose in Macromolecular Crystallography. *Journal of Applied Crystallography* **2013**, *46* (4), 1225–1230. https://doi.org/10.1107/S0021889813011461.

(11) Bury, C. S.; Brooks-Bartlett, J. C.; Walsh, S. P.; Garman, E. F. Estimate Your Dose: RADDOSE-3D. *Protein Science* **2018**, *27* (1), 217–228. https://doi.org/https://doi.org/10.1002/pro.3302.

(12) Mueller, M.; Wang, M.; Schulze-Briese, C. Optimal Fine φ-Slicing for Single-Photon-Counting Pixel Detectors. *Acta Crystallographica Section D: Biological Crystallography* **2012**, *68* (1), 42–56. https://doi.org/10.1107/S0907444911049833.

(13) Broennimann, C.; Eikenberry, E. F.; Henrich, B.; Horisberger, R.; Huelsen, G.; Pohl, E.; Schmitt, B.; Schulze-Briese, C.; Suzuki, M.; Tomizaki, T.; Toyokawa, H.;

Wagner, A. The PILATUS 1M Detector. *Journal of Synchrotron Radiation* **2006**, *13* (2), 120–130. https://doi.org/10.1107/S0909049505038665.

(14) Otwinowski, Z.; Minor, W. Processing of X-Ray Diffraction Data Collected in Oscillation Mode. In *Methods in Enzymology*; Methods in Enzymology; Academic Press, 1997; Vol. 276, pp 307–326. https://doi.org/10.1016/S0076-6879(97)76066-X.

(15) Winter, G.; Lobley, C. M. C.; Prince, S. M. Decision Making in Xia2. *Acta Crystallographica Section D: Biological Crystallography* **2013**, *69* (7), 1260–1273. https://doi.org/10.1107/S0907444913015308.

(16) Waterman, D. G.; Winter, G.; Gildea, R. J.; Parkhurst, J. M.; Brewster, A. S.; Sauter, N. K.; Evans, G. Diffraction-Geometry Refinement in the DIALS Framework. *Acta Crystallographica Section D: Structural Biology* **2016**, *72* (4), 558–575. https://doi.org/10.1107/S2059798316002187.

(17) Winter, G.; Waterman, D. G.; Parkhurst, J. M.; Brewster, A. S.; Gildea, R. J.; Gerstel, M.; Fuentes-Montero, L.; Vollmar, M.; Michels-Clark, T.; Young, I. D.; Sauter, N. K.; Evans, G. DIALS: Implementation and Evaluation of a New Integration Package. *Acta Crystallographica Section D: Structural Biology* **2018**, *74* (2), 85–97. https://doi.org/10.1107/S2059798317017235.

(18) Delagenière, S.; Brenchereau, P.; Launer, L.; Ashton, A. W.; Leal, R.; Veyrier, S.; Gabadinho, J.; Gordon, E. J.; Jones, S. D.; Levik, K. E.; Mcsweeney, S. M.; Monaco, S.; Nanao, M.; Spruce, D.; Svensson, O.; Walsh, M. A.; Leonard, G. A. ISPyB: An Information Management System for Synchrotron Macromolecular Crystallography. *Bioinformatics* **2011**, *27* (22), 3186–3192. https://doi.org/10.1093/bioinformatics/btr535.

(19) Winn, M. D.; Ballard, C. C.; Cowtan, K. D.; Dodson, E. J.; Emsley, P.; Evans, P. R.; Keegan, R. M.; Krissinel, E. B.; Leslie, A. G. W.; McCoy, A.; McNicholas, S. J.; Murshudov, G. N.; Pannu, N. S.; Potterton, E. A.; Powell, H. R.; Read, R. J.; Vagin, A.; Wilson, K. S. Overview of the CCP4 Suite and Current Developments. *Acta Crystallographica Section D: Biological Crystallography* **2011**, *67* (4), 235–242. https://doi.org/10.1107/S0907444910045749.

(20) Kabsch, W. XDS. *Acta Crystallographica Section D* **2010**, *66* (2), 125–132. https://doi.org/10.1107/S0907444909047337.

(21) Evans, P. R. An Introduction to Data Reduction: Space-Group Determination, Scaling and Intensity Statistics. *Acta Crystallographica Section D: Biological Crystallography* **2011**, *67* (4), 282–292. https://doi.org/10.1107/S090744491003982X.

(22) Vonrhein, C.; Flensburg, C.; Keller, P.; Sharff, A.; Smart, O.; Paciorek, W.; Womack, T.; Bricogne, G. Data Processing and Analysis with the AutoPROC Toolbox. *Acta Crystallographica Section D: Biological Crystallography* **2011**, *67* (4), 293–302. https://doi.org/10.1107/S0907444911007773.

(23) Vonrhein, C.; Tickle, I. J.; Flensburg, C.; Keller, P.; Paciorek, W.; Sharff, A.; Bricogne, G. Advances in Automated Data Analysis and Processing within AutoPROC , Combined with Improved Characterisation, Mitigation and Visualisation of the Anisotropy of Diffraction Limits Using STARANISO . *Acta Crystallographica Section A Foundations and Advances* **2018**, *74* (a1), a360–a360. https://doi.org/10.1107/s010876731809640x.

(24) Evans, P. R.; Murshudov, G. N. How Good Are My Data and What Is the Resolution? *Acta Crystallographica Section D: Biological Crystallography* **2013**, *69* (7), 1204–1214. https://doi.org/10.1107/S0907444913000061.

(25) Liebschner, D.; Afonine, P. v.; Baker, M. L.; Bunkoczi, G.; Chen, V. B.; Croll, T. I.; Hintze, B.; Hung, L. W.; Jain, S.; McCoy, A. J.; Moriarty, N. W.; Oeffner, R. D.; Poon, B. K.; Prisant, M. G.; Read, R. J.; Richardson, J. S.; Richardson, D. C.; Sammito, M. D.; Sobolev, O. v.; Stockwell, D. H.; Terwilliger, T. C.; Urzhumtsev, A. G.; Videau, L. L.; Williams, C. J.; Adams, P. D. Macromolecular Structure Determination Using X-Rays, Neutrons and Electrons: Recent Developments in Phenix. *Acta Crystallographica Section D: Structural Biology* **2019**, *75* (10), 861–877. https://doi.org/10.1107/S2059798319011471.

(26) Afonine, P. v.; Grosse-Kunstleve, R. W.; Chen, V. B.; Headd, J. J.; Moriarty, N. W.; Richardson, J. S.; Richardson, D. C.; Urzhumtsev, A.; Zwart, P. H.; Adams, P. D. Phenix.Model-vs-Data: A High-Level Tool for the Calculation of Crystallographic Model and Data Statistics. *Journal of Applied Crystallography* **2010**, *43* (4), 669–676. https://doi.org/10.1107/S0021889810015608.

(27) Adams, P. D.; Afonine, P. v.; Bunkóczi, G.; Chen, V. B.; Davis, I. W.; Echols, N.; Headd, J. J.; Hung, L. W.; Kapral, G. J.; Grosse-Kunstleve, R. W.; McCoy, A. J.; Moriarty, N. W.; Oeffner, R.; Read, R. J.; Richardson, D. C.; Richardson, J. S.; Terwilliger, T. C.; Zwart, P. H. PHENIX: A Comprehensive Python-Based System for Macromolecular Structure Solution. *Acta Crystallographica Section D: Biological Crystallography* **2010**, *66* (2), 213–221. https://doi.org/10.1107/S0907444909052925.

(28) Matthews, B. W. Solvent Content of Protein Crystals. *Journal of Molecular Biology* **1968**, *33* (2), 491–497. https://doi.org/10.1016/0022-2836(68)90205-2.

(29) McCoy, A. J.; Grosse-Kunstleve, R. W.; Adams, P. D.; Winn, M. D.; Storoni, L. C.; Read, R. J. Phaser Crystallographic Software. *Journal of Applied Crystallography* **2007**, *40* (4), 658–674. https://doi.org/10.1107/S0021889807021206.

(30) Emsley, P.; Cowtan, K. Coot: Model-Building Tools for Molecular Graphics. *Acta Crystallographica Section D: Biological Crystallography* **2004**, *60* (12 I), 2126–2132. https://doi.org/10.1107/S0907444904019158.

(31) Afonine, P. v.; Grosse-Kunstleve, R. W.; Echols, N.; Headd, J. J.; Moriarty, N. W.; Mustyakimov, M.; Terwilliger, T. C.; Urzhumtsev, A.; Zwart, P. H.; Adams, P. D. Towards Automated Crystallographic Structure Refinement with Phenix.Refine. *Acta Crystallographica Section D: Biological Crystallography* **2012**, *68* (4), 352–367. https://doi.org/10.1107/S0907444912001308.

(32) Chen, V. B.; Arendall, W. B.; Headd, J. J.; Keedy, D. A.; Immormino, R. M.; Kapral, G. J.; Murray, L. W.; Richardson, J. S.; Richardson, D. C. MolProbity: All-Atom Structure Validation for Macromolecular Crystallography. *Acta Crystallographica Section D: Biological Crystallography* **2010**, *66* (1), 12–21. https://doi.org/10.1107/S0907444909042073.

(33) Schomaker, V.; Trueblood, K. N. On the Rigid-Body Motion of Molecules in Crystals. *Acta Crystallographica Section B Structural Crystallography and Crystal Chemistry* **1968**, *24* (1), 63–76. https://doi.org/10.1107/s0567740868001718.

(34) Winn, M. D.; Isupov, M. N.; Murshudov, G. N. Use of TLS Parameters to Model Anisotropic Displacements in Macromolecular Refinement. *Acta Crystallographica Section D: Biological Crystallography* **2001**, *57* (1), 122–133. https://doi.org/10.1107/S0907444900014736.

(35) Moriarty, N. W.; Liebschner, D.; Klei, H. E.; Echols, N.; Afonine, P. v.; Headd, J. J.; Poon, B. K.; Adams, P. D. Interactive Comparison and Remediation of Collections of Macromolecular Structures. *Protein Science* **2018**, *27* (1), 182–194. https://doi.org/10.1002/pro.3296.

(36) Gore, S.; Sanz García, E.; Hendrickx, P. M. S.; Gutmanas, A.; Westbrook, J. D.; Yang, H.; Feng, Z.; Baskaran, K.; Berrisford, J. M.; Hudson, B. P.; Ikegawa, Y.; Kobayashi, N.; Lawson, C. L.; Mading, S.; Mak, L.; Mukhopadhyay, A.; Oldfield, T. J.; Patwardhan, A.; Peisach, E.; Sahni, G.; Sekharan, M. R.; Sen, S.; Shao, C.; Smart, O. S.; Ulrich, E. L.; Yamashita, R.; Quesada, M.; Young, J. Y.; Nakamura, H.; Markley, J. L.; Berman, H. M.; Burley, S. K.; Velankar, S.; Kleywegt, G. J. Validation of Structures in the Protein Data Bank. *Structure* **2017**, *25* (12), 1916–1927. https://doi.org/10.1016/j.str.2017.10.009.

(37) Hall, S. R.; Allen, F. H.; Brown, I. D. The Crystallographic Information File (CIF): A New Standard Archive File for Crystallography. *Acta Crystallographica Section A* **1991**, *47* (6), 655–685. https://doi.org/10.1107/S010876739101067X.

(38) Young, J. Y.; Westbrook, J. D.; Feng, Z.; Sala, R.; Peisach, E.; Oldfield, T. J.; Sen, S.; Gutmanas, A.; Armstrong, D. R.; Berrisford, J. M.; Chen, L.; Chen, M.; di Costanzo, L.; Dimitropoulos, D.; Gao, G.; Ghosh, S.; Gore, S.; Guranovic, V.; Hendrickx, P. M. S.; Hudson, B. P.; Igarashi, R.; Ikegawa, Y.; Kobayashi, N.; Lawson, C. L.; Liang, Y.; Mading, S.; Mak, L.; Mir, M. S.; Mukhopadhyay, A.; Patwardhan, A.; Persikova, I.; Rinaldi, L.; Sanz-Garcia, E.; Sekharan, M. R.; Shao, C.; Swaminathan, G. J.; Tan, L.; Ulrich, E. L.; van Ginkel, G.; Yamashita, R.; Yang, H.; Zhuravleva, M. A.; Quesada, M.; Kleywegt, G. J.; Berman, H. M.; Markley, J. L.; Nakamura, H.; Velankar, S.; Burley, S. K. OneDep: Unified WwPDB System for Deposition, Biocuration, and Validation of Macromolecular Structures in the PDB Archive. *Structure* **2017**, *25* (3), 536–545. https://doi.org/10.1016/j.str.2017.01.004.

(39) Berman, H. M.; Battistuz, T.; Bhat, T. N.; Bluhm, W. F.; Bourne, P. E.; Burkhardt, K.; Feng, Z.; Gilliland, G. L.; Iype, L.; Jain, S.; Fagan, P.; Marvin, J.; Padilla, D.; Ravichandran, V.; Schneider, B.; Thanki, N.; Weissig, H.; Westbrook, J. D.; Zardecki, C. The Protein Data Bank. *Acta Crystallographica Section D: Biological Crystallography* **2002**, *58* (6 I), 899–907. https://doi.org/10.1107/S0907444902003451.

(40) McAllister, T. E.; Yeh, T. L.; Abboud, M. I.; Leung, I. K. H.; Hookway, E. S.; King, O. N. F.; Bhushan, B.; Williams, S. T.; Hopkinson, R. J.; Münzel, M.; Loik, N. D.; Chowdhury, R.; Oppermann, U.; Claridge, T. D. W.; Goto, Y.; Suga, H.; Schofield, C. J.; Kawamura, A. Non-Competitive Cyclic Peptides for Targeting Enzyme-Substrate Complexes. *Chemical Science* **2018**, *9* (20), 4569–4578. https://doi.org/10.1039/c8sc00286j.

(41) Xing, W.; Yin, M.; Lv, Q.; Hu, Y.; Liu, C.; Zhang, J. 1 - Oxygen Solubility, Diffusion Coefficient, and Solution Viscosity. In *Rotating Electrode Methods and Oxygen Reduction Electrocatalysts*; Xing, W., Yin, G., Zhang, J., Eds.; Elsevier: Amsterdam, 2014; pp 1–31. https://doi.org/https://doi.org/10.1016/B978-0-444-63278-4.00001-X.

(42) Ahmed, S.; Ayscough, A.; Barker, G. R.; Canning, H. E.; Davenport, R.; Downham, R.; Harrison, D.; Jenkins, K.; Kinsella, N.; Livermore, D. G.; Wright, S.; Ivetac, A. D.; Skene, R.; Wilkens, S. J.; Webster, N. A.; Hendrick, A. G. 1,2,4-Triazolo-[1,5-a]Pyridine HIF Prolylhydroxylase Domain-1 (PHD-1) Inhibitors with a Novel Monodentate Binding Interaction. *Journal of Medicinal Chemistry* **2017**, *60* (13), 5663–5672. https://doi.org/10.1021/acs.jmedchem.7b00352.

(43) Zhang, X.; Lei, Y.; Hu, T.; Wu, Y.; Li, Z.; Jiang, Z.; Yang, C.; Zhang, L.; You, Q. Discovery of Clinical Candidate (5-(3-(4-Chlorophenoxy)Prop-1-Yn-1-Yl)-3-Hydroxypicolinoyl)Glycine, an Orally Bioavailable Prolyl Hydroxylase Inhibitor

for the Treatment of Anemia. *Journal of Medicinal Chemistry* **2020**, *63* (17), 10045–10060. https://doi.org/10.1021/acs.jmedchem.0c01161.

(44) Douangamath, A.; Powell, A.; Fearon, D.; Collins, P. M.; Talon, R.; Krojer, T.; Skyner, R.; Brandao-Neto, J.; Dunnett, L.; Dias, A.; Aimon, A.; Pearce, N. M.; Wild, C.; Gorrie-Stone, T.; von Delft, F. Achieving Efficient Fragment Screening at XChem Facility at Diamond Light Source. *Journal of visualized experiments : JoVE* **2021**, No. 171, e62414. https://doi.org/10.3791/62414.

(45) Ng, J. T.; Dekker, C.; Kroemer, M.; Osborne, M.; von Delft, F. Using Textons to Rank Crystallization Droplets by the Likely Presence of Crystals. *Acta Crystallographica Section D: Biological Crystallography* **2014**, *70* (10), 2702–2718. https://doi.org/10.1107/S1399004714017581.

(46) Collins, P. M.; Ng, J. T.; Talon, R.; Nekrosiute, K.; Krojer, T.; Douangamath, A.; Brandao-Neto, J.; Wright, N.; Pearce, N. M.; von Delft, F. Gentle, Fast and Effective Crystal Soaking by Acoustic Dispensing. *Acta Crystallographica Section D: Structural Biology* **2017**, *73* (3), 246–255. https://doi.org/10.1107/S205979831700331X.

(47) Cox, O. B.; Krojer, T.; Collins, P.; Monteiro, O.; Talon, R.; Bradley, A.; Fedorov, O.; Amin, J.; Marsden, B. D.; Spencer, J.; von Delft, F.; Brennan, P. E. A Poised Fragment Library Enables Rapid Synthetic Expansion Yielding the First Reported Inhibitors of PHIP(2), an Atypical Bromodomain. *Chemical Science* **2016**, *7* (3), 2322–2330. https://doi.org/10.1039/c5sc03115j.

(48) Wood, D. J.; Lopez-Fernandez, J. D.; Knight, L. E.; Al-Khawaldeh, I.; Gai, C.; Lin, S.; Martin, M. P.; Miller, D. C.; Cano, C.; Endicott, J. A.; Hardcastle, I. R.; Noble, M. E. M.; Waring, M. J. FragLites - Minimal, Halogenated Fragments Displaying Pharmacophore Doublets. An Efficient Approach to Druggability Assessment and Hit Generation. *Journal of Medicinal Chemistry* **2019**, *62* (7), 3741–3752. https://doi.org/10.1021/acs.jmedchem.9b00304.

(49) Krojer, T.; Talon, R.; Pearce, N.; Collins, P.; Douangamath, A.; Brandao-Neto, J.; Dias, A.; Marsden, B.; von Delft, F. The XChemExplorer Graphical Workflow Tool for Routine or Large-Scale Protein-Ligand Structure Determination. *Acta Crystallographica Section D: Structural Biology* **2017**, *73* (3), 267–278. https://doi.org/10.1107/S2059798316020234.

(50) Wright, N. D.; Collins, P.; Koekemoer, L.; Krojer, T.; Talon, R.; Nelson, E.; Ye, M.; Nowak, R.; Newman, J.; Ng, J. T.; Mitrovich, N.; Wiggers, H.; von Delft, F. The Low-Cost Shifter Microscope Stage Transforms the Speed and Robustness of Protein Crystal Harvesting. *Acta Crystallographica Section D: Structural Biology* **2021**, *77* (1), 62–74. https://doi.org/10.1107/S2059798320014114.

(51) Wojdyr, M.; Keegan, R.; Winter, G.; Ashton, A. DIMPLE - a Pipeline for the Rapid Generation of Difference Maps from Protein Crystals with Putatively Bound Ligands . *Acta Crystallographica Section A Foundations of Crystallography* **2013**, *69* (a1), s299–s299. https://doi.org/10.1107/s0108767313097419.

(52) Pearce, N. M.; Bradley, A. R.; Krojer, T.; Marsden, B. D.; Deane, C. M.; Delft, F. von. Partial-Occupancy Binders Identified by the Pan-Dataset Density Analysis Method Offer New Chemical Opportunities and Reveal Cryptic Binding Sites. *Structural Dynamics* **2017**, *4* (3), 32104. https://doi.org/10.1063/1.4974176.

(53) Pearce, N. M.; Krojer, T.; Bradley, A. R.; Collins, P.; Nowak, R. P.; Talon, R.; Marsden, B. D.; Kelm, S.; Shi, J.; Deane, C. M.; von Delft, F. A Multi-Crystal Method for Extracting Obscured Crystallographic States from Conventionally Uninterpretable Electron Density. *Nature Communications* **2017**, *8* (1), 15123. https://doi.org/10.1038/ncomms15123.

(54) Douangamath, A.; Fearon, D.; Gehrtz, P.; Krojer, T.; Lukacik, P.; Owen, C. D.; Resnick, E.; Strain-Damerell, C.; Aimon, A.; Ábrányi-Balogh, P.; Brandão-Neto, J.; Carbery, A.; Davison, G.; Dias, A.; Downes, T. D.; Dunnett, L.; Fairhead, M.; Firth, J. D.; Jones, S. P.; Keeley, A.; Keserü, G. M.; Klein, H. F.; Martin, M. P.; Noble, M. E. M.; O'Brien, P.; Powell, A.; Reddi, R. N.; Skyner, R.; Snee, M.; Waring, M. J.; Wild, C.; London, N.; von Delft, F.; Walsh, M. A. Crystallographic and Electrophilic Fragment Screening of the SARS-CoV-2 Main Protease. *Nature Communications* **2020**, *11* (1), 5047. https://doi.org/10.1038/s41467-020-18709-w.

Appendix I

Table AI-1| The *Xtal-ID* Information Reported in this Thesis and Coupled with the Data Quality and Refinement Statistics.

Crystal ID	Protein Mixture	Crystal Information	Space Group	Resolution (Å)	R_{Work}	R_{Free}	ΔR: R_{Free}-R_{work} (%)	Rama Outliers (%)	Rotamers (%)	Bonds (Å)	Angles (°)	Clashscore	Average B-factor (Å^2)	TLS Groups
Xtal-A	Mn.NOG.HIF2α.3C	Formate, NOG	$P\ 2_1\ 2_1\ 2$	1.17	0.1613	0.1852	2.39	0	1.37	0.008	1.02	5.94	20.46	9
Xtal-B	Mn.2OG.HIF2α.3C	Formate, 2OG	$P\ 2_1\ 2_1\ 2$	1.21	0.1598	0.1792	1.94	0	1.43	0.011	1.22	4.63	22.72	10
Xtal-C	Fe.2OG.HIF2α.3C.-O_2	Formate, Anaerobic	$P\ 2_1\ 2_1\ 2$	1.48	0.2494	0.2774	2.80	0	0.99	0.013	1.08	3.34	31.81	6
Xtal-D	Fe.2OG.HIF2α.3C.T17.+O_2	Formate, O_2 T17	$P\ 2_1\ 2_1\ 2$	1.65	0.1816	0.2013	1.97	0	1.9	0.004	0.78	3.26	23.31	9
Xtal-E	Fe.2OG.HIF2α.3C.T19.+O_2	Formate, O_2 T19	$P\ 2_1\ 2_1\ 2$	1.65	0.1808	0.2113	3.05	0	1.42	0.007	0.99	2.48	20.66	9
Xtal-F	Fe.2OG.HIF2α.3C.T25.+O_2	Formate, O_2 T25	$P\ 2_1\ 2_1\ 2$	1.48	0.1748	0.2061	3.13	0	1.39	0.010	0.96	1.39	25.76	9
Xtal-G	Mn.2OG.HIF2α.3C	Zn condition	$P\ 2_1\ 2_1\ 2$	2.07	0.2041	0.2243	2.02	0	1.93	0.004	0.65	3.18	52.36	15
Xtal-H	Mn.2OG.HIF2α	Acetate screen	$P\ 2_1\ 2_1\ 2$	1.70	0.1687	0.1976	2.89	0	2.16	0.004	0.84	3.31	21.71	9
Xtal-I	Fe.2OG.ACT.HIF2α	Acetate, No Metal	$P\ 2_1\ 2_1\ 2$	1.55	0.1859	0.2173	3.14	0	1.48	0.005	0.81	3.79	28.77	9
Xtal-J	Fe.2OG.HIF2α.-O_2	Acetate, Anaerobic	$P\ 2_1\ 2_1\ 2$	1.41	0.1596	0.1819	2.23	0	1.48	0.008	1.02	2.30	18.95	10
Xtal-K	Fe.2OG.HIF2α.Rest-O_2-75-min	Acetate, O_2 Intermediate 1	$P\ 2_1\ 2_1\ 2$	1.25	0.1579	0.1735	1.56	0	1.46	0.010	1.20	2.49	16.97	10
Xtal-L	Fe.2OG.HIF2α.Rest-O_2-75-min	Acetate, O_2 Intermediate 2	$P\ 2_1\ 2_1\ 2$	1.24	0.1593	0.1784	1.91	0	2.82	0.001	1.46	3.95	19.28	8
Xtal-M	Fe.2OG.HIF2α.+O_2.60-min	Acetate, O_2 Product 1	$P\ 2_1$	1.31	0.1884	0.2114	2.30	0	1.51	0.009	1.03	2.07	22.93	17
Xtal-N	Fe.2OG.HIF2α.+O_2.7,200-min	Acetate, O_2 Product 2	$P\ 2_1$	2.03	0.1949	0.2252	3.03	0	2.3	0.003	0.61	1.71	38.92	14
Xtal-O	Mn	Mn, 181-426 construct	$P\ 2_1$	2.97	0.2451	0.2672	2.21	0	1.46	0.005	0.77	6.69	105.29	26
Xtal-P	Mn.SIN	SIN	$P\ 2_1$	1.90	0.2071	0.2264	1.93	0	2.82	0.006	0.90	4.78	53.05	35
Xtal-Q	Mn.FUM	FUM	$P\ 2_1$	2.34	0.2197	0.2495	2.98	0	1.54	0.003	0.62	6.74	75.72	35
Xtal-R	Mn.SIN.Molidustat	Molidustat (**20**)	$P\ 2_1$	1.79	0.1776	0.2033	2.57	0	1.61	0.006	0.75	2.78	52.94	43
Xtal-S	Mn.SIN.IOX4	IOX4 (**28**)	$P\ 2_1$	2.01	0.2056	0.2301	2.45	0	1.45	0.002	0.47	2.36	67.10	39
Xtal-T	Mn.SIN.Takeda	Takeda-17 (**17**)	$P\ 2_1$	2.13	0.1908	0.2190	2.82	0	0.85	0.008	0.95	6.97	69.67	45
Xtal-U	Mn.ZXJ-1	ZXJ-1 (**33**)	$P\ 6_1\ 2\ 2$	3.10	0.2551	0.2851	3.00	0	1.22	0.003	0.62	2.58	104.89	13
Xtal-V	Mn.SIN.33	$PHD2_{181-407}$-x0033	$P\ 2_1$	2.13	0.2539	0.2734	1.95	0	4.46	0.004	0.73	3.40	70.70	26
Xtal-W	Mn.SIN.42	$PHD2_{181-407}$-x0042	$P\ 2_1$	2.31	0.2546	0.2758	2.12	0	2.32	0.008	0.80	4.25	60.44	28
Xtal-X	Mn.SIN.524	$PHD2_{181-407}$-x0524	$P\ 2_1$	2.13	0.2520	0.2671	1.51	0	1.69	0.007	0.83	7.49	61.45	26
Xtal-Y	Mn.SIN.534	$PHD2_{181-407}$-x0534	$P\ 2_1$	2.07	0.2456	0.2685	2.29	0	2.12	0.006	0.94	11.72	64.14	33
Xtal-Z	Mn.SIN.555	$PHD2_{181-407}$-x0555	$P\ 2_1$	2.53	0.2620	0.2785	1.65	0	2.05	0.003	0.64	5.82	89.59	31
Xtal-AA	Mn.SIN.582	$PHD2_{181-407}$-x0582	$P\ 2_1$	2.78	0.2832	0.2949	1.17	0	2.25	0.008	0.97	4.81	68.17	50
Xtal-BB	Mn.SIN.594	$PHD2_{181-407}$-x0594	$P\ 2_1$	2.20	0.2378	0.2613	2.35	0	3.57	0.006	0.84	5.65	68.50	29
Xtal-CC	Mn.SIN.613	$PHD2_{181-407}$-x0613	$P\ 2_1$	2.07	0.2626	0.2759	1.33	0	4.38	0.007	0.89	6.25	71.76	26
Xtal-DD	Mn.SIN.630	$PHD2_{181-407}$-x0630	$P\ 2_1$	2.20	0.2482	0.2666	1.84	0	2.66	0.007	0.82	8.42	75.99	29
Xtal-EE	Mn.SIN.723	$PHD2_{181-407}$-x0723	$P\ 2_1$	2.15	0.2363	0.2623	2.60	0	2.99	0.003	0.73	5.48	63.27	31
Xtal-FF	Mn.SIN.747	$PHD2_{181-407}$-x0747	$P\ 2_1$	2.05	0.2596	0.2840	2.44	0	3.23	0.006	0.85	5.41	58.01	27
Xtal-GG	Mn.SIN.807	$PHD2_{181-407}$-x0807	$P\ 2_1$	2.50	0.2596	0.2826	2.30	0	1.91	0.004	0.66	5.63	77.96	27
Xtal-HH	Mn.SIN.CG3	CG3	$P\ 2_1$	2.26	0.2662	0.2853	1.91	0	1.76	0.004	0.70	8.33	87.13	35
Xtal-II	Mn.SIN.CG4	CG4	$P\ 2_1$	2.40	0.2544	0.2751	2.07	0	1.62	0.008	0.83	6.09	89.85	34
Xtal-JJ	Mn.SIN.CG10	CG10	$P\ 2_1$	2.68	0.2579	0.2759	1.80	0	0.8	0.004	0.70	6.48	106.38	31
Xtal-KK	Mn.SIN.CG16	CG16	$P\ 2_1$	2.70	0.2569	0.2855	2.86	0.09	1.13	0.004	0.73	8.96	99.75	38
Xtal-LL	Mn.SIN.CG17	CG17	$P\ 2_1$	2.28	0.2177	0.2457	2.80	0	1.16	0.010	0.92	6.34	88.50	38
Xtal-MM	Mn.SIN.CG22	CG22	$P\ 2_1$	2.38	0.2408	0.2582	1.74	0	1.97	0.007	0.85	10.46	84.69	38
Xtal-NN	Mn.SIN.CG28	CG28	$P\ 2_1$	2.26	0.2400	0.2684	2.84	0	1.78	0.011	0.87	4.23	87.89	35
Xtal-OO	Mn.SIN.CG37	CG37	$P\ 2_1$	2.53	0.2529	0.2689	1.60	0	1.53	0.007	0.76	8.17	94.38	30

* All data collected at 100 K and conventional rotation-based single crystal diffraction.

Table AI-2| Conventional Rotation-Based Macromolecular Crystallography Diffraction Parameters.

Crystal ID	Protein Mixture	Beamline	Wavelength (Å)	Distance (Å)	Transmission (%)	Exposure (s)	Beamsize (μm x μm)	Temperature (K)	Images	Ω Osc (°)	Flux (ph/s)	Phasing Type
Xtal-A	Mn.NOG.HIF2α.3C	I24	0.9686	1.22	10.09	0.010	7x7	100	3600	0.10	3.10E+12	SAD
Xtal-B	Mn.2OG.HIF2α.3C	I24	0.9796	1.23	19.26	0.020	30x30	100	3600	0.10	3.10E+12	SAD
Xtal-C	Fe.2OG.HIF2α.3C.-O_2	I24	0.9688	1.21	29.91	0.010	50x50	100	3600	0.10	3.10E+12	SAD
Xtal-D	Fe.2OG.HIF2α.3C.T17.+O_2	I24	0.9688	1.21	29.91	0.010	50x50	100	3600	0.10	3.10E+12	SAD
Xtal-E	Fe.2OG.HIF2α.3C.T19.+O_2	I24	0.9688	1.21	29.91	0.010	50x50	100	3600	0.10	3.10E+12	SAD
Xtal-F	Fe.2OG.HIF2α.3C.T25.+O_2	I24	0.9688	1.21	29.91	0.010	50x50	100	3600	0.10	3.10E+12	SAD
Xtal-G	Mn.2OG.HIF2α.3C	I24	0.9686	2.00	20.01	0.020	20x20	100	3600	0.10	3.10E+12	SAD
Xtal-H	Mn.2OG.HIF2α	I04	0.9795	1.40	100.00	0.020	32x20	100	3600	0.10	2.92E+11	SAD
Xtal-I	Fe.2OG.ACT.HIF2α	I03	0.9763	1.50	100.00	0.002	80x20	100	3600	0.10	3.81E+12	SAD
Xtal-J	Fe.2OG.HIF2α.-O_2	I03	0.9763	1.50	100.00	0.002	80x20	100	3600	0.10	3.92E+12	SAD
Xtal-K	Fe.2OG.HIF2α.Rest-O_2-75-min	I03	0.9763	1.30	87.89	0.002	80x20	100	3600	0.10	3.42E+12	SAD
Xtal-L	Fe.2OG.HIF2α.Rest-O_2-75-min	I03	0.9763	1.30	87.89	0.002	80x20	100	3600	0.10	3.46E+12	SAD
Xtal-M	Fe.2OG.HIF2α.+O_2.60-min	I03	0.9763	1.30	87.89	0.002	80x20	100	3600	0.10	3.44E+12	SAD
Xtal-N	Fe.2OG.HIF2α.+O_2.7,200-min	I03	0.9763	1.30	43.95	0.002	80x20	100	3600	0.10	1.72E+12	SAD
Xtal-O	Mn	I04-1	0.9159	1.50	100.00	0.400	50x50	100	900	0.20	3.50E+11	SAD
Xtal-P	Mn.SIN	I03	0.9763	1.50	100.00	0.002	80x20	100	3600	0.10	3.63E+12	SAD
Xtal-Q	Mn.FUM	PX-1	0.9786	2.00	100.00	0.020	40x20	100	3600	0.10	2.00E+12	SAD
Xtal-R	Mn.SIN.Molidustat	I04	0.9795	1.33	100.00	0.040	63x50	100	3600	0.10	3.65E+11	SAD
Xtal-S	Mn.SIN.IOX4	I04	0.9795	1.33	100.00	0.020	54x40	100	3600	0.10	2.94E+11	SAD
Xtal-T	Mn.SIN.Takeda	I04	0.9795	1.33	100.00	0.040	63x50	100	3600	0.10	3.66E+11	SAD
Xtal-U	Mn.ZXJ-1	I04	0.9795	1.40	100.00	0.040	11x5	100	3600	0.10	2.69E+11	SAD
Xtal-V	Mn.SIN.33	I04-1	0.9159	2.00	100.00	0.060	60x50	100	1500	0.16	3.50E+11	SAD
Xtal-W	Mn.SIN.42	I04-1	0.9159	2.00	100.00	0.060	60x50	100	1500	0.16	3.50E+11	SAD
Xtal-X	Mn.SIN.524	I04-1	0.9119	2.00	100.00	0.060	60x50	100	1500	0.16	3.50E+11	SAD
Xtal-Y	Mn.SIN.534	I04-1	0.9119	2.00	100.00	0.060	60x50	100	1500	0.16	3.50E+11	SAD
Xtal-Z	Mn.SIN.555	I04-1	0.9119	2.00	100.00	0.060	60x50	100	1500	0.16	3.50E+11	SAD
Xtal-AA	Mn.SIN.582	I04-1	0.9119	2.00	100.00	0.060	60x50	100	1500	0.16	3.50E+11	SAD
Xtal-BB	Mn.SIN.594	I04-1	0.9119	2.00	100.00	0.060	60x50	100	1500	0.16	3.50E+11	SAD
Xtal-CC	Mn.SIN.613	I04-1	0.9119	2.00	100.00	0.060	60x50	100	1500	0.16	3.50E+11	SAD
Xtal-DD	Mn.SIN.630	I04-1	0.9119	2.00	100.00	0.060	60x50	100	1500	0.16	3.50E+11	SAD
Xtal-EE	Mn.SIN.723	I04-1	0.9119	2.00	100.00	0.060	60x50	100	1500	0.16	3.50E+11	SAD
Xtal-FF	Mn.SIN.747	I04-1	0.9119	2.00	100.00	0.060	60x50	100	1500	0.16	3.50E+11	SAD
Xtal-GG	Mn.SIN.807	I04-1	0.9119	2.00	100.00	0.060	60x50	100	1500	0.16	3.50E+11	SAD
Xtal-HH	Mn.SIN.CG3	I04-1	0.9119	1.42	100.00	0.200	60x50	100	3600	0.10	3.50E+11	SAD
Xtal-II	Mn.SIN.CG4	I03	0.9763	1.50	100.00	0.002	80x20	100	1500	0.16	3.63E+12	SAD
Xtal-JJ	Mn.SIN.CG10	I03	0.9763	1.50	100.00	0.002	80x20	100	1500	0.16	3.61E+12	SAD
Xtal-KK	Mn.SIN.CG16	I03	0.9763	1.50	100.00	0.002	80x20	100	3600	0.10	3.59E+12	SAD
Xtal-LL	Mn.SIN.CG17	I04-1	0.9119	1.42	100.00	0.200	60x50	100	1500	0.10	3.50E+11	SAD
Xtal-MM	Mn.SIN.CG22	I04	0.9795	1.45	70.02	0.020	32x20	100	1500	0.16	2.10E+11	SAD
Xtal-NN	Mn.SIN.CG28	I04	0.9795	1.45	60.02	0.020	32x20	100	1500	0.16	1.72E+11	SAD
Xtal-OO	Mn.SIN.CG37	I05	0.9795	1.45	60.02	0.020	32x21	100	1500	0.16	1.72E+11	SAD

Appendix II

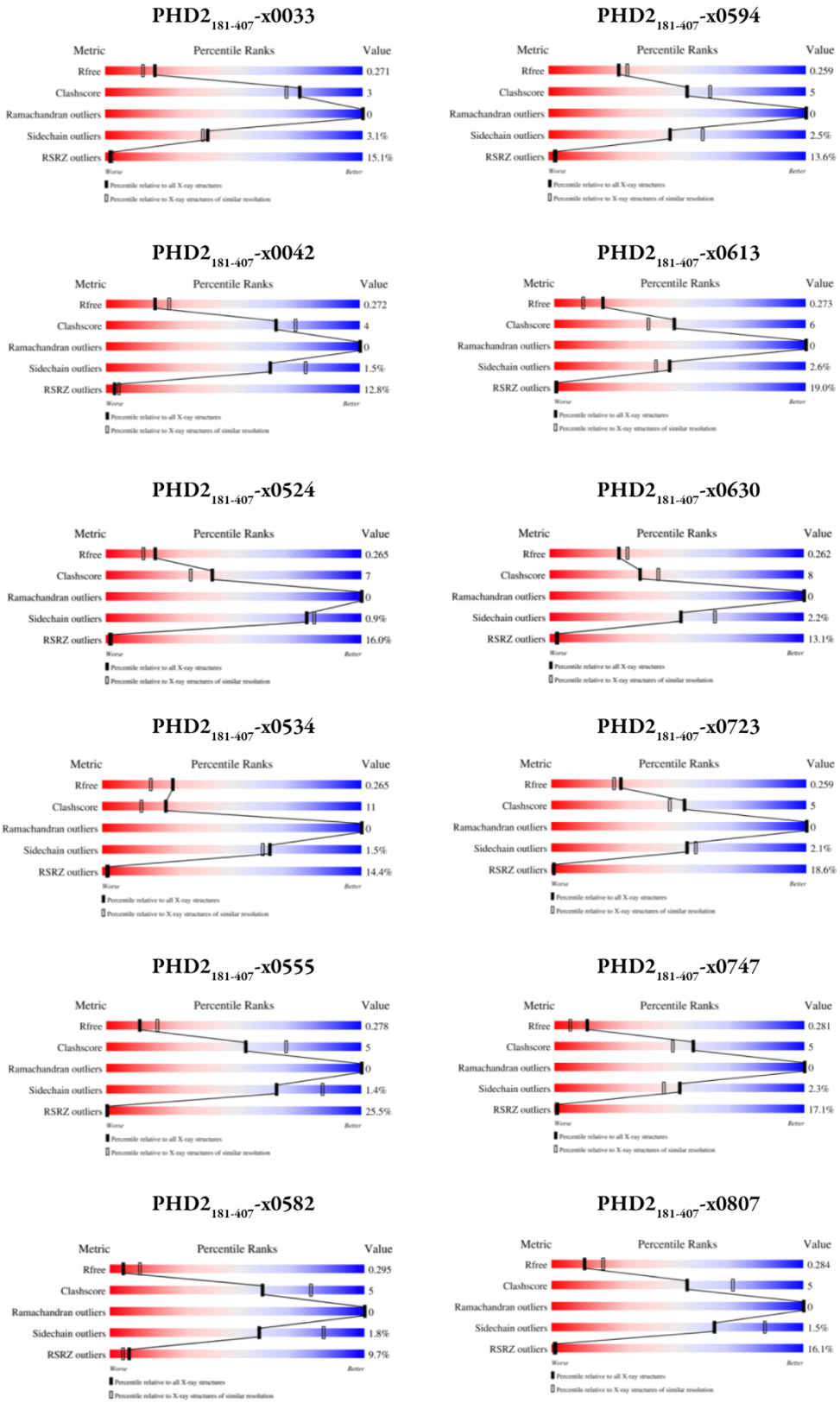


Figure AII-1| Validation Tables for the Crystallographic Data from the XChem Fragment Screen. Tables were generated using the PDB validation service. Abbreviations: Protein Data Bank (PDB).

Table AII-1| The XChem Fragment Screen Crystallographic Data and Refinement Statistics.

	PHD2$_{181-407}$-x0033 (*V*)	**PHD2$_{181-407}$-x0042 (*W*)**	**PHD2$_{181-407}$-x0524 (*X*)**	**PHD2$_{181-407}$-x0534 (*Y*)**	**PHD2$_{181-407}$-x0555 (*Z*)**	**PHD2$_{181-407}$-x0582 (*AA*)**
Beamline	DLS-I04-1	DLS-I04-1	DLS-I04-1	DLS-I04-1	DLS-I04-1	DLS-I04-1
Detector	Dectris Pilatus 6M-F	Dectris Pilatus 6M-F	Dectris Pilatus 6M-F	Dectris Pilatus 6M-F	Dectris Pilatus 6M-F	Dectris Pilatus 6M-F
Data Processing	Xia2 DIALS	Xia2 DIALS	Xia2 DIALS	Xia2 DIALS	Xia2 DIALS	Xia2 DIALS
Wavelength (Å)	0.9159	0.9159	0.9119	0.9119	0.9119	0.9119
Resolution range (Å)	67.10 - 2.13 (2.20 - 2.13)	66.80 - 2.31 (2.39 - 2.31)	128.20 - 2.13 (2.20 - 2.13)	75.16 - 2.07 (2.14 - 2.07)	74.43 - 2.53 (2.62- 2.53)	19.73 - 2.78 (2.87 - 2.78)
Space group	$P\ 1\ 2_1\ 1$	$P\ 1\ 2_1\ 1$	$P\ 1\ 2_1\ 1$	$P\ 1\ 2_1\ 1$	$P\ 1\ 2_1\ 1$	$P\ 1\ 2_1\ 1$
Unit cell (Å, °)	76.19 75.30 128.86, 93.18	75.77 75.11 128.10, 93.28	75.89 75.11 128.42, 93.27	75.25 74.56 124.73, 92.81	74.52 74.48 124.31, 92.88	76.15 74.80 128.49, 93.28
Total reflections	363197 (36991)	273789 (25528)	335482 (33774)	367039 (37824)	199009 (20435)	154485 (16018)
Unique reflections	81616 (8095)	63202 (6243)	80600 (7959)	84076 (8333)	45572 (4495)	36253 (3616)
Multiplicity	4.5 (4.6)	4.3 (4.1)	4.2 (4.2)	4.4 (4.5)	4.4 (4.5)	4.3 (4.4)
Completeness (%)	99.82 (99.64)	99.85 (99.66)	99.64 (99.30)	99.59 (98.08)	99.37 (96.63)	98.90 (99.42)
Mean I/sigma(I)	4.92 (1.11)	4.09 (1.09)	5.11 (0.77)	9.23 (0.50)	7.60 (0.39)	4.22 (1.55)
Wilson B-factor (Å^2)	44.49	37.37	38.28	43.33	62.81	47.16
R-merge†	0.1298 (1.126)	0.1698 (1.123)	0.1294 (0.5494)	0.0888 (1.395)	0.1157 (1.392)	0.2129 (0.532)
R-meas	0.1487 (1.275)	0.1955 (1.295)	0.1494 (0.6315)	0.1013 (1.577)	0.1324 (1.575)	0.246 (0.6097)
R-pim	0.07121 (0.5868)	0.09514 (0.6325)	0.07318 (0.3044)	0.04768 (0.7207)	0.06297 (0.725)	0.1213 (0.2945)
CC1/2	0.958 (0.67)	0.966 (0.544)	0.988 (0.824)	0.997 (0.575)	0.992 (0.583)	0.96 (0.853)
CC*	0.989 (0.896)	0.991 (0.839)	0.997 (0.951)	0.999 (0.855)	0.998 (0.858)	0.99 (0.959)
Reflections used in refinement	81616 (8075)	63174 (6235)	80600 (7952)	84077 (8179)	45573 (4385)	36253 (3611)
Reflections used for R-free	4170 (433)	3232 (298)	3964 (435)	4188 (443)	2369 (240)	1697 (162)
R-work✧	0.2539 (0.4058)	0.2546 (0.3497)	0.2520 (0.3709)	0.2456 (0.4002)	0.2620 (0.4235)	0.2832 (0.3432)
R-free✧	0.2734 (0.4551)	0.2758 (0.3780)	0.2671 (0.3900)	0.2685 (0.4077)	0.2785 (0.4345)	0.2949 (0.3671)
CC(work)	0.919 (0.765)	0.894 (0.746)	0.931 (0.756)	0.934 (0.684)	0.928 (0.635)	0.880 (0.768)
CC(free)	0.914 (0.667)	0.841 (0.646)	0.869 (0.772)	0.924 (0.600)	0.807 (0.556)	0.883 (0.593)
Number of non-hydrogen atoms	9682	9398	9691	9524	9507	9549
macromolecules	9562	9247	9534	9428	9319	9382
ligands	204	269	261	144	245	326
solvent	0	2	19	6	45	5
Protein residues	1201	1177	1197	1188	1170	1186
RMS(bonds, Å)	0.004	0.008	0.007	0.006	0.003	0.008
RMS(angles, °)	0.73	0.80	0.83	0.94	0.64	0.97
Ramachandran favored (%)	97.71	98.09	97.87	97.77	98.78	96.13
Ramachandran allowed (%)	2.29	1.91	2.13	2.23	1.22	3.87
Ramachandran outliers (%)	0.00	0.00	0.00	0.00	0.00	0.00
Rotamer outliers (%)	4.46	2.32	1.69	2.12	2.05	2.25
Clashscore	3.40	4.25	7.49	11.72	5.82	4.81
Average B-factor (Å^2)	70.70	60.44	61.45	64.14	89.59	68.17
Macromolecules	70.77	60.59	61.63	64.25	89.85	68.39
ligands	64.92	51.17	52.24	54.31	80.71	56.37
solvent	0.00	32.02	37.97	39.59	63.36	41.07
Number of TLS groups	26	28	26	33	31	50

Single crystal diffraction data was collected from samples held at 100 K with conventional, rotation-based methods. Ligands: Mn, SIN, DMS, and Cl. Statistics for the highest-resolution shell are shown in parentheses.

† R-merge (or R-sym) is equal to $\sum|I-\langle I\rangle|/\sum I$. R-merge represents the data quality of merged reflection data. *I* is equal to the intensity of individual measurements and <I> is equal to the average of multiple measurements. ✧R_{free} is the R_{factor} for 5% of the reflections which are excluded during refinement.

R_{factor} is equal to $\sum_{hkl}||Fobs_{(hkl)}| - |Fcalc_{(hkl)}||/\sum_{hkl}|Fobs_{(hkl)}|$ and was calculated for the working set of reflections (R_{work}). *Xtal-IDs* listed in **Appendix I.**

Table AII-2|The XChem Fragment Screen Crystallographic Data and Refinement Statistics.

	PHD2$_{181-407}$-x0594 (*BB*)	PHD2$_{181-407}$-x0613 (*CC*)	PHD2$_{181-407}$-x0630 (*DD*)	PHD2$_{181-407}$-x0723 (*EE*)	PHD2$_{181-407}$-x0747 (*FF*)	PHD2$_{181-407}$-x0807 (*GG*)
Beamline	DLS-I04-1	DLS-I04-1	DLS-I04-1	DLS-I04-1	DLS-I04-1	DLS-I04-1
Detector	Dectris Pilatus 6M-F	Dectris Pilatus 6M-F	Dectris Pilatus 6M-F	Dectris Pilatus 6M-F	Dectris Pilatus 6M-F	Dectris Pilatus 6M-F
Data Processing	Xia2 DIALS	Xia2 DIALS	Xia2 DIALS	Xia2 DIALS	Xia2 DIALS	Xia2 DIALS
Wavelength (Å)	0.9119	0.9119	0.9119	0.9126	0.9126	0.9126
Resolution range (Å)	127.30 - 2.20 (2.27 - 2.20)	64.16 - 2.07 (2.144- 2.07)	65.14 - 2.20 (2.28 - 2.20)	66.51 - 2.15 (2.22 - 2.15)	75.53 - 2.05 (2.12 - 2.05)	125.70- 2.50 (2.58- 2.50)
Space group	$P\ 1\ 2_1\ 1$	$P\ 1\ 2_1\ 1$	$P\ 1\ 2_1\ 1$	$P\ 1\ 2_1\ 1$	$P\ 1\ 2_1\ 1$	$P\ 1\ 2_1\ 1$
Unit cell (Å, °)	75.60 74.62 127.46, 93.04	75.67 74.58 125.99, 92.44	74.44 74.50 124.98, 92.47	75.73 74.55 126.54, 93.13	75.64 74.58 126.30, 93.05	73.58 73.46 126.12, 94.62
Total reflections	308660 (30898)	379560 (38949)	300967 (29800)	329630 (33779)	373049 (39083)	203082 (20971)
Unique reflections	72037 (7146)	85072 (8407)	68399 (6720)	76682 (7666)	87881 (8764)	46588 (4635)
Multiplicity	4.3 (4.3)	4.5 (4.6)	4.4 (4.4)	4.3 (4.4)	4.2 (4.5)	4.4 (4.5)
Completeness (%)	99.57 (97.85)	97.24 (98.55)	98.45 (97.37)	99.33 (96.42)	99.42 (98.67)	98.81 (93.05)
Mean I/sigma (I)	8.42 (0.60)	10.16 (0.50)	8.07 (0.81)	5.50 (0.47)	6.95 (0.57)	6.48 (0.45)
Wilson B-factor (Å^2)	46.49	44.51	51.50	39.15	35.54	56.75
R-merge†	0.09671 (0.6515)	0.07731 (0.9649)	0.09607 (1.942)	0.1478 (1.117)	0.1117 (0.8375)	0.1252 (0.9211)
R-meas	0.1112 (0.7461)	0.08744 (1.086)	0.109 (2.195)	0.169 (1.273)	0.1286 (0.9585)	0.1437 (1.047)
R-pim	0.05397 (0.357)	0.04011 (0.4904)	0.0506 (1.01)	0.08035 (0.5985)	0.06238 (0.4547)	0.06912 (0.4859)
CC1/2	0.992 (0.618)	0.997 (0.701)	0.993 (0.432)	0.991 (0.646)	0.994 (0.4)	0.99 (0.56)
CC*	0.998 (0.874)	0.999 (0.908)	0.998 (0.777)	0.998 (0.886)	0.998 (0.756)	0.998 (0.847)
Reflections used in refinement	72037 (6995)	85076 (8370)	68399 (6702)	76682 (7396)	87881 (8684)	46587 (4322)
Reflections used for R-free	3540 (298)	3975 (401)	3346 (330)	3856 (365)	4398 (493)	2193 (244)
R-work✧	0.2378 (0.3784)	0.2626 (0.4422)	0.2482 (0.3566)	0.2363 (0.3701)	0.2596 (0.3989)	0.2596 (0.3564)
R-free✧	0.2613 (0.3871)	0.2759 (0.4548)	0.2666 (0.3589)	0.2623 (0.3693)	0.2840 (0.4016)	0.2826 (0.3789)
CC(work)	0.933 (0.759)	0.932 (0.724)	0.945 (0.621)	0.933 (0.710)	0.915 (0.713)	0.918 (0.547)
CC(free)	0.888 (0.710)	0.953 (0.800)	0.879 (0.672)	0.908 (0.710)	0.887 (0.663)	0.903 (0.572)
Number of non-hydrogen atoms	9699	9656	9635	9892	9577	9531
macromolecules	9562	9532	9370	9524	9467	9451
ligands	243	210	438	154	171	138
solvent	6	6	21	276	7	0
Protein residues	1201	1198	1181	1196	1192	1188
RMS(bonds, Å)	0.006	0.007	0.007	0.003	0.006	0.004
RMS(angles, °)	0.84	0.89	0.82	0.73	0.85	0.66
Ramachandran favored (%)	97.37	97.87	98.44	97.87	97.86	98.37
Ramachandran allowed (%)	2.63	2.13	1.56	2.13	2.14	1.63
Ramachandran outliers (%)	0.00	0.00	0.00	0.00	0.00	0.00
Rotamer outliers (%)	3.57	4.38	2.66	2.99	3.23	1.91
Clashscore	5.65	6.25	8.42	5.48	5.41	5.63
Average B-factor (Å^2)	68.50	71.76	75.99	63.27	58.01	77.96
macromolecules	68.59	71.96	76.20	63.87	58.15	78.14
ligands	63.31	57.62	70.22	49.65	47.11	57.64
solvent	34.82	32.79	50.72	46.99	30.13	0.00
Number of TLS groups	29	26	29	31	27	27

Single crystal diffraction data was collected from samples held at 100 K with conventional, rotation-based methods. Ligands: Mn, SIN, DMS, and Cl. Statistics for the highest-resolution shell are shown in parentheses.

† R-merge (or R-sym) is equal to $\sum|I-\langle I\rangle|/\sum I$. R-merge represents the data quality of merged reflection data. *I* is equal to the intensity of individual measurements and <I> is equal to the average of multiple measurements. ✧R_{free} is the R_{factor} for 5% of the reflections which are excluded during refinement.

R_{factor} is equal to $\sum_{hkl}||Fobs_{(hkl)}| - |Fcalc_{(hkl)}||/\sum_{hkl}|Fobs_{(hkl)}|$ and was calculated for the working set of reflections (R_{work}). *Xtal-IDs* listed in **Appendix I.**

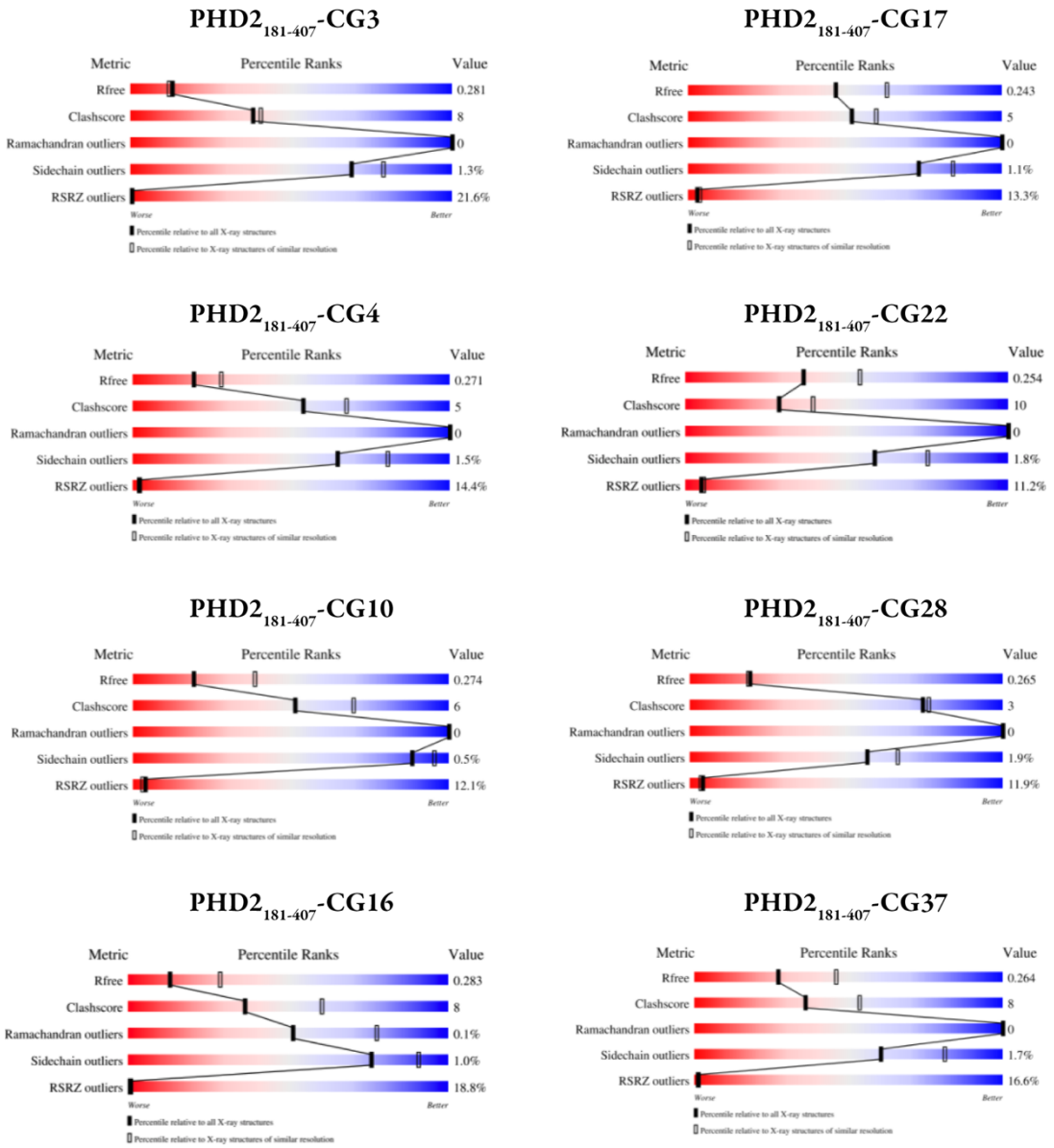


Figure AII-2| Validation Tables for the Crystallographic Data from the Soaking-Based Studies with Monodentate Binding Derivatives. Tables were generated using the PDB validation service. Abbreviations: Protein Data Bank (PDB)

Table AII-3| The Crystallographic Data and Refinement Statistics for $PHD2_{181-407}$ in Complex with Takeda-17 (17) Derivatives.

	$PHD2_{181-407}$.CG3 (*Xtal-HH*)	$PHD2_{181-407}$.CG4 (*Xtal-II*)	$PHD2_{181-407}$.CG10 (*Xtal-JJ*)	$PHD2_{181-407}$.CG16 (*Xtal-KK*)
Beamline	Diamond Light Source-I04-1	Diamond Light Source-I03	Diamond Light Source-I03	Diamond Light Source-I03
Detector	Dectris Pilatus3 6M	Dectris Eiger2 XE 16M	Dectris Eiger2 XE 16M	Dectris Eiger2 XE 16M
Data Processing	autoPROC	Xia2 DIALS	Xia2 DIALS	Xia2 3dii
Wavelength (Å)	0.9119	0.9762	0.9762	0.9762
Resolution range (Å)	65.33 - 2.26 (2.34 - 2.26)	48.94 - 2.40 (2.48 - 2.40)	49.13 - 2.68 (2.77 - 2.68)	49.24 - 2.70 (2.79 - 2.70)
Space group	$P\,1\,2_1\,1$	$P\,1\,2_1\,1$	$P\,1\,2_1\,1$	$P\,1\,2_1\,1$
Unit cell (Å, °)	74.54 74.39 125.88, 92.48	73.43 74.98 125.43, 92.59	74.54 74.90 125.66, 92.03	74.47 74.77 126.79, 92.56
Total reflections	127277 (12529)	366649 (34532)	270695 (28017)	266997 (27535)
Unique reflections	63794 (6271)	53506 (5311)	39148 (3909)	38517 (3796)
Multiplicity	2.0 (2.0)	6.9 (6.5)	6.9 (7.2)	6.9 (7.3)
Completeness (%)	98.55 (97.33)	99.50 (97.03)	99.30 (95.19)	99.82 (99.68)
Mean I/sigma(I)	8.03 (1.37)	11.91 (0.47)	7.38 (0.37)	9.96 (0.55)
Wilson B-factor (Å²)	54.29	63.55	72.31	73.98
R-merge†	0.0346 (0.5525)	0.1105 (2.449)	0.1456 (1.677)	0.1033 (1.167)
R-meas	0.04893 (0.7813)	0.1197 (2.661)	0.1576 (1.808)	0.1119 (1.258)
R-pim	0.0346 (0.5525)	0.04542 (1.031)	0.05968 (0.6715)	0.04246 (0.4654)
CC1/2	0.999 (0.752)	0.998 (0.435)	0.997 (0.729)	0.998 (0.755)
CC*	1 (0.926)	1 (0.779)	0.999 (0.918)	1 (0.928)
Reflections used in refinement	63794 (6263)	53506 (5153)	39148 (3721)	38517 (3784)
Reflections used for R-free	3194 (301)	2630 (264)	1850 (162)	1881 (154)
R-work✧	0.2662 (0.3870)	0.2544 (0.4365)	0.2579 (0.4787)	0.2569 (0.4344)
R-free✧	0.2853 (0.3931)	0.2751 (0.4210)	0.2759 (0.4539)	0.2855 (0.4493)
CC(work)	0.918 (0.763)	0.942 (0.584)	0.944 (0.654)	0.940 (0.691)
CC(free)	0.905 (0.720)	0.928 (0.659)	0.932 (0.701)	0.909 (0.777)
Number of non-hydrogen atoms	9281	9068	9132	9539
macromolecules	9098	8872	8984	9367
ligands	208	242	192	238
solvent	49	58	16	26
Protein residues	1172	1163	1180	1188
RMS(bonds, Å)	0.004	0.008	0.004	0.004
RMS(angles, °)	0.70	0.83	0.70	0.73
Ramachandran favored (%)	97.74	97.98	96.54	97.51
Ramachandran allowed (%)	2.26	2.02	3.46	2.41
Ramachandran outliers (%)	0.00	0.00	0.00	0.09
Rotamer outliers (%)	1.76	1.62	0.80	1.13
Clashscore	8.33	6.09	6.48	8.96
Average B-factor (Å²)	87.13	89.85	106.38	99.75
macromolecules	87.50	90.31	106.72	100.22
ligands	72.25	72.85	87.68	75.15
solvent	60.40	59.31	71.92	66.02
Number of TLS groups	35	34	31	38

Single crystal diffraction data was collected from samples held at 100 K with conventional, rotation-based methods. Ligands: Mn, SIN, DMS, and Cl. Statistics for the highest-resolution shell are shown in parentheses.

† R-merge (or R-sym) is equal to $\sum|I-\langle I\rangle|/\sum I$. R-merge represents the data quality of merged reflection data. *I* is equal to the intensity of individual measurements and <I> is equal to the average of multiple measurements. ✧R_{free} is the R_{factor} for 5% of the reflections which are excluded during refinement.

R_{factor} is equal to $\sum_{hkl}||Fobs_{(hkl)}| - |Fcalc_{(hkl)}||/\sum_{hkl}|Fobs_{(hkl)}|$ and was calculated for the working set of reflections (R_{work}). *Xtal-IDs* listed in **Appendix I.**

Table AII-4| The Crystallographic Data and Refinement Statistics for $PHD2_{181-407}$ in Complex with Takeda-17 (17) Derivatives.

	$PHD2_{181-407}$.CG17 (*Xtal-LL*)	$PHD2_{181-407}$.CG22 (*Xtal-MM*)	$PHD2_{181-407}$.CG28 (*Xtal-NN*)	$PHD2_{181-407}$.CG37 (*Xtal-OO*)
Beamline	Diamond Light Source-I04-1	Diamond Light Source-I04	Diamond Light Source-I04	Diamond Light Source-I04
Detector	Dectris Pilatus 6M-F	Dectris Eiger2 XE 16M	Dectris Eiger2 XE 16M	Dectris Eiger2 XE 16M
Data Processing	Xia2 DIALS	Xia2 DIALS	autoPROC	Xia2 DIALS
Wavelength (Å)	0.9118	0.9795	0.9795	0.9795
Resolution range (Å)	63.88 - 2.28 (2.36 - 2.28)	63.35 - 2.38 (2.46 - 2.38)	65.69 - 2.26 (2.34 - 2.26)	64.19 - 2.53 (2.62 - 2.53)
Space group	$P\ 1\ 2_1\ 1$	$P\ 1\ 2_1\ 1$	$P\ 1\ 2_1\ 1$	$P\ 1\ 2_1\ 1$
Unit cell (Å,°)	75.04 74.72 127.93 92.88	75.15 75.05 128.44, 92.99	74.99 75.00 125.90, 92.60	74.90 74.78 125.30, 92.94
Total reflections	180725 (18338)	400812 (38044)	131056 (12923)	325157 (32016)
Unique reflections	64208 (6361)	57533 (5715)	65534 (6461)	46309 (4562)
Multiplicity	2.8 (2.9)	7.0 (6.7)	2.0 (2.0)	7.0 (7.0)
Completeness (%)	99.10 (98.72)	99.62 (98.43)	99.80 (99.22)	99.31 (98.59)
Mean I/sigma(I)	7.31 (0.83)	10.14 (0.47)	12.44 (1.05)	9.01 (0.39)
Wilson B-factor (Å²)	59.55	61.32	59.74	71.19
R-merge†	0.07795 (0.8462)	0.1014 (1.724)	0.02665 (0.7362)	0.119 (2.102)
R-meas	0.09667 (1.03)	0.1097 (1.872)	0.03769 (1.041)	0.1286 (2.268)
R-pim	0.05622 (0.5792)	0.04139 (0.7219)	0.02665 (0.7362)	0.04838 (0.8466)
CC1/2	0.992 (0.686)	0.999 (0.6)	1 (0.551)	0.998 (0.636)
CC*	0.998 (0.902)	1 (0.866)	1 (0.843)	1 (0.882)
Reflections used in refinement	64210 (6343)	57533 (5625)	65533 (6456)	46310 (4529)
Reflections used for R-free	3219 (314)	2816 (258)	3213 (278)	2257 (209)
R-work✧	0.2177 (0.3417)	0.2408 (0.4027)	0.2400 (0.3720)	0.2529 (0.4946)
R-free✧	0.2457 (0.3649)	0.2582 (0.4115)	0.2684 (0.3876)	0.2689 (0.4847)
CC(work)	0.950 (0.793)	0.937 (0.658)	0.943 (0.688)	0.945 (0.695)
CC(free)	0.929 (0.773)	0.920 (0.634)	0.853 (0.604)	0.916 (0.579)
Number of non-hydrogen atoms	9529	9405	9567	9308
macromolecules	9269	9070	9310	9125
ligands	289	240	265	214
solvent	91	183	106	35
Protein residues	1184	1174	1180	1178
RMS(bonds, Å)	0.010	0.007	0.011	0.007
RMS(angles, °)	0.92	0.85	0.87	0.76
Ramachandran favored (%)	98.19	97.55	98.53	97.91
Ramachandran allowed (%)	1.81	2.45	1.47	2.09
Ramachandran outliers (%)	0.00	0.00	0.00	0.00
Rotamer outliers (%)	1.16	1.97	1.78	1.53
Clashscore	6.34	10.46	4.23	8.17
Average B-factor (Å²)	88.50	84.19	87.89	94.38
macromolecules	88.96	84.69	88.26	94.74
ligands	76.16	74.47	78.63	77.96
solvent	64.10	67.24	68.73	69.95
Number of TLS groups	38	38	35	30

Single crystal diffraction data was collected from samples held at 100 K with conventional, rotation-based methods. Ligands: Mn, SIN, DMS, and Cl. Statistics for the highest-resolution shell are shown in parentheses.

† R-merge (or Rsym) is equal to $\sum|I-\langle I\rangle|/\sum I$. R-merge represents the data quality of merged reflection data. *I* is equal to the intensity of individual measurements and <I> is equal to the average of multiple measurements. ✧R_{free} is the R_{factor} for 5% of the reflections which are excluded during refinement.
R_{factor} is equal to $\sum_{hkl}||Fobs_{(hkl)}| - |Fcalc_{(hkl)}||/\sum_{hkl}|Fobs_{(hkl)}|$ and was calculated for the working set of reflections (R_{work}). *Xtal-IDs* listed in **Appendix I.**

Appendix III

Table AIII-1| tPHD2 Constructs Used in the Research Described this Thesis.

Construct	Length	Vector	Cloning Site	Tag	Source
$PHD2_{181-407}$	181-407	pET-28a(+)	NheI/BamHI	His_6	Chowdhury R.[1]
$PHD2_{181-426}$	181-426	pET-28a(+)	NheI/BamHI	His_6	Chowdhury R.[2]

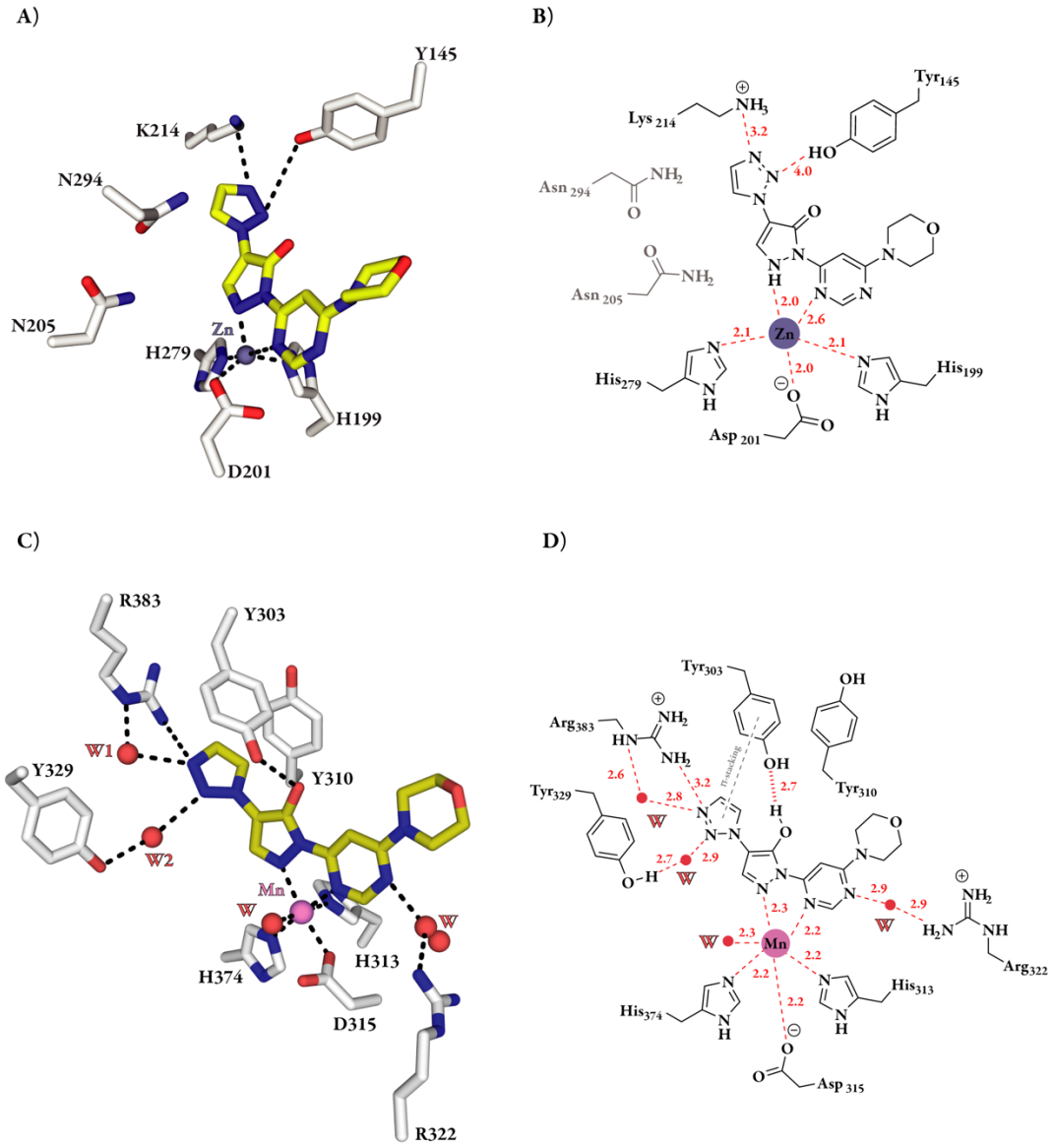
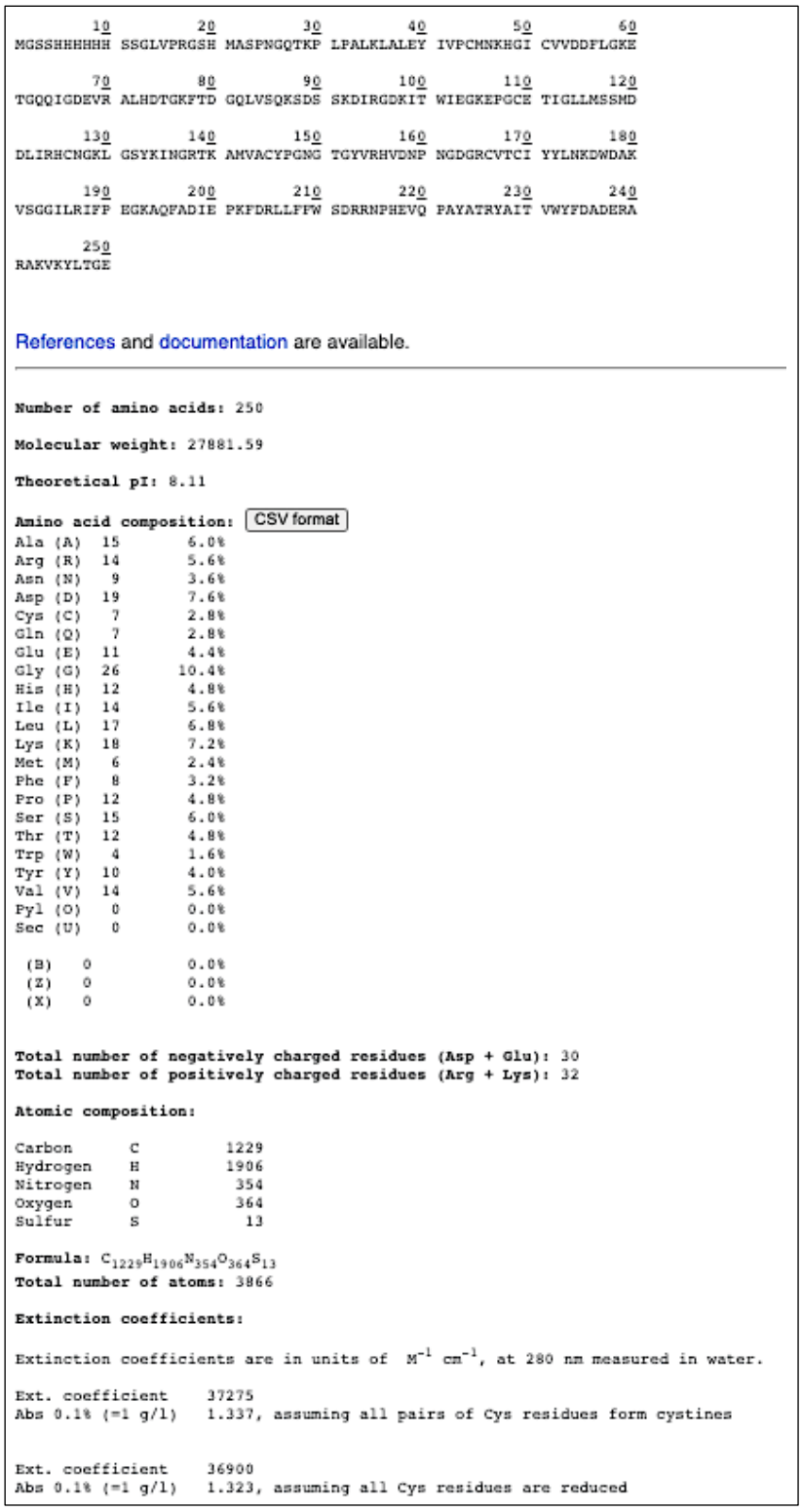


Figure AIII-1| 3D and 2D Active Site Comparisons of FIH and PHD2$_{181-407}$ Complex Structures with Molidustat (20). (A) A 3D view of the active site of the FIH.Molidustat complex structure (PDB: 5OP8). (B) A 2D representation of FIH's active site residues and Molidustat (PDB: 5OP8).[3] (A) A 3D view of the active site of the PHD2$_{181-407}$.Molidustat complex structure (PDB: 6ZBO or *Xtal-R*).[4] (B) A 2D representation of PHD2$_{181-407}$'s active site residues and Molidustat (PDB: 6ZBO or *Xtal-R*). (A-C) Active site residues (white) and Molidustat (A-yellow and C-olive) are displayed as sticks. (B-D) Active sites residues and Molidusta are shown as sticks (black) (A-D) Water molecules (red) and metal ions (Zn-blue and Mn-violet) are depicted as spheres. The key active site interactions are represented by dashes (A-C-black and B-D-red). Abbreviations: 3/2-Dimensional (3D/2D), Factor-inhibiting hypoxia-inducible factor (FIH), Prolyl hydroxylase isoform 2 (PHD2). PDB: 5OP8, 6ZBO. *Xtal-ID*: R. *Figure edited with permission from Figg Jr., W. D.; McDonough, M. A.; Chowdhury, R.; Nakashima, Y.; Zhang, Z.; Holt-Martyn, J. P.; Krajnc, A.; Schofield, C. J. Structural Basis of Prolyl Hydroxylase Domain Inhibition by Molidustat. ChemMedChem* ***2021****, 16 (13), 2082–2088, Open Access, Wiley-VCH. https://doi.org/10.1002/cmdc.202100133. CC BY 4.0 License.*



```
        10         20         30         40         50         60
MGSSHHHHHH SSGLVPRGSH MASPNGQTKP LPALKLALEY IVPCMNKHGI CVVDDFLGKE

        70         80         90        100        110        120
TGQQIGDEVR ALHDTGKFTD GQLVSQKSDS SKDIRGDKIT WIEGKEPGCE TIGLLMSSMD

       130        140        150        160        170        180
DLIRHCNGKL GSYKINGRTK AMVACYPGNG TGYVRHVDNP NGDGRCVTCI YYLNKDWDAK

       190        200        210        220        230        240
VSGGILRIFP EGKAQFADIE PKFDRLLFFW SDRRNPHEVQ PAYATRYAIT VWYFDADERA

       250
RAKVKYLTGE
```

References and documentation are available.

Number of amino acids: 250

Molecular weight: 27881.59

Theoretical pI: 8.11

Amino acid composition: CSV format

Ala (A)	15	6.0%
Arg (R)	14	5.6%
Asn (N)	9	3.6%
Asp (D)	19	7.6%
Cys (C)	7	2.8%
Gln (Q)	7	2.8%
Glu (E)	11	4.4%
Gly (G)	26	10.4%
His (H)	12	4.8%
Ile (I)	14	5.6%
Leu (L)	17	6.8%
Lys (K)	18	7.2%
Met (M)	6	2.4%
Phe (F)	8	3.2%
Pro (P)	12	4.8%
Ser (S)	15	6.0%
Thr (T)	12	4.8%
Trp (W)	4	1.6%
Tyr (Y)	10	4.0%
Val (V)	14	5.6%
Pyl (O)	0	0.0%
Sec (U)	0	0.0%
(B)	0	0.0%
(Z)	0	0.0%
(X)	0	0.0%

Total number of negatively charged residues (Asp + Glu): 30
Total number of positively charged residues (Arg + Lys): 32

Atomic composition:

Carbon	C	1229
Hydrogen	H	1906
Nitrogen	N	354
Oxygen	O	364
Sulfur	S	13

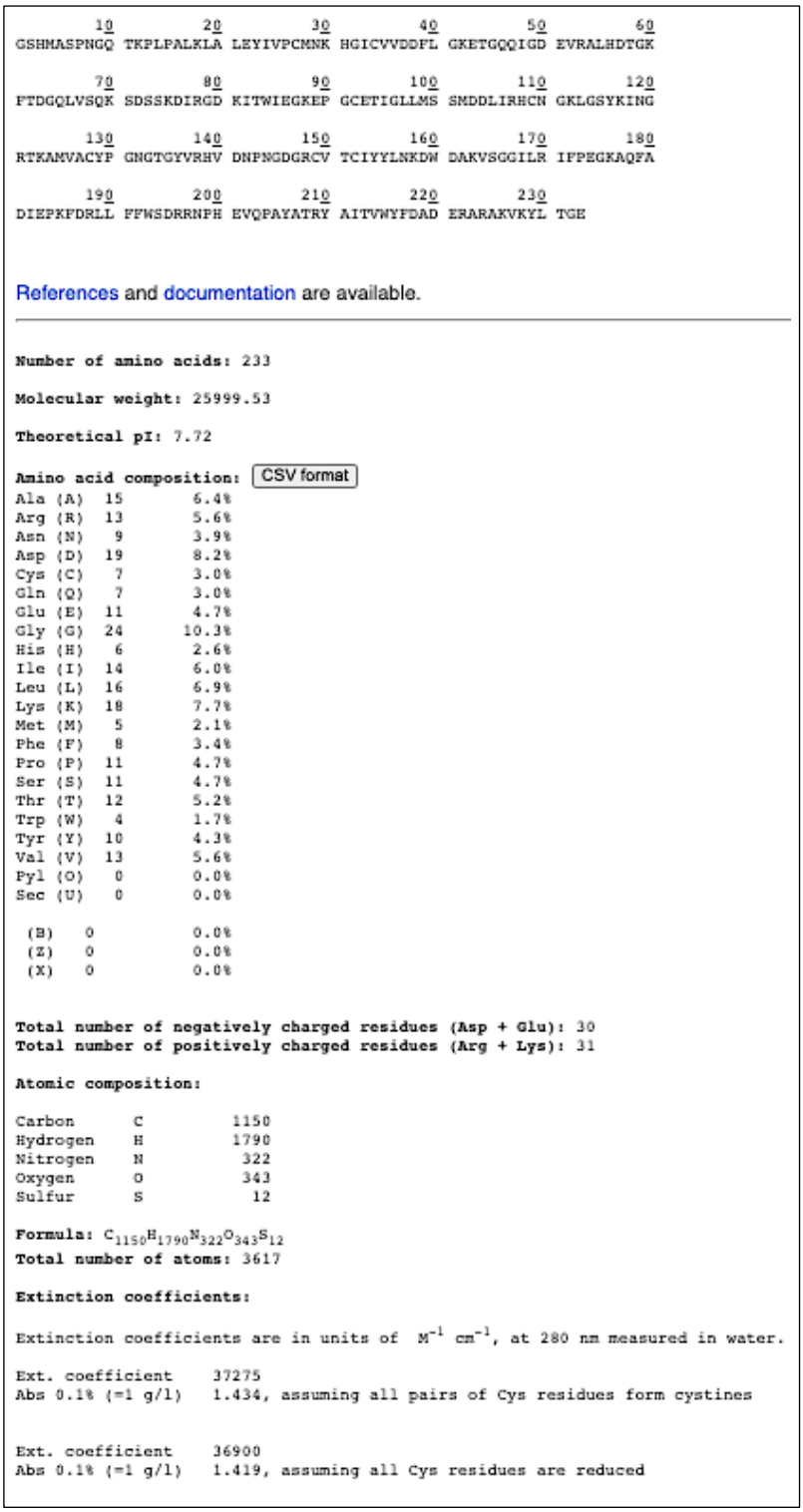
Formula: $C_{1229}H_{1906}N_{354}O_{364}S_{13}$
Total number of atoms: 3866

Extinction coefficients:

Extinction coefficients are in units of M^{-1} cm^{-1}, at 280 nm measured in water.

Ext. coefficient	37275
Abs 0.1% (=1 g/l)	1.337, assuming all pairs of Cys residues form cystines
Ext. coefficient	36900
Abs 0.1% (=1 g/l)	1.323, assuming all Cys residues are reduced

Figure AIII-2| Sequence and Amino Acid Composition of the PHD2$_{181-407}$ Construct with an *N*-Terminal His$_6$ Affinity-Tag. The data sheet was generated using the ProtParam tool (ExPASy, SIB). Abbreviations: Prolyl hydroxylase isoform 2 (PHD2), Hexa-histidine (His$_6$), Swiss Institute of Bioinformatics (SIB).



```
        10         20         30         40         50         60
GSHMASPNGQ TKPLPALKLA LEYIVPCMNK HGICVVDDFL GKETGQQIGD EVRALHDTGK

        70         80         90        100        110        120
FTDGQLVSQK SDSSKDIRGD KITWIEGKEP GCETIGLLMS SMDDLIRHCN GKLGSYKING

       130        140        150        160        170        180
RTKAMVACYP GNGTGYVRHV DNPNGDGRCV TCIYYLNKDW DAKVSGGILR IFPEGKAQFA

       190        200        210        220        230
DIEPKFDRLL FFWSDRRNPH EVQPAYATRY AITVWYFDAD ERARAKVKYL TGE
```

References and documentation are available.

Number of amino acids: 233

Molecular weight: 25999.53

Theoretical pI: 7.72

Amino acid composition: CSV format

Ala (A)	15	6.4%
Arg (R)	13	5.6%
Asn (N)	9	3.9%
Asp (D)	19	8.2%
Cys (C)	7	3.0%
Gln (Q)	7	3.0%
Glu (E)	11	4.7%
Gly (G)	24	10.3%
His (H)	6	2.6%
Ile (I)	14	6.0%
Leu (L)	16	6.9%
Lys (K)	18	7.7%
Met (M)	5	2.1%
Phe (F)	8	3.4%
Pro (P)	11	4.7%
Ser (S)	11	4.7%
Thr (T)	12	5.2%
Trp (W)	4	1.7%
Tyr (Y)	10	4.3%
Val (V)	13	5.6%
Pyl (O)	0	0.0%
Sec (U)	0	0.0%
(B)	0	0.0%
(Z)	0	0.0%
(X)	0	0.0%

Total number of negatively charged residues (Asp + Glu): 30
Total number of positively charged residues (Arg + Lys): 31

Atomic composition:

Carbon	C	1150
Hydrogen	H	1790
Nitrogen	N	322
Oxygen	O	343
Sulfur	S	12

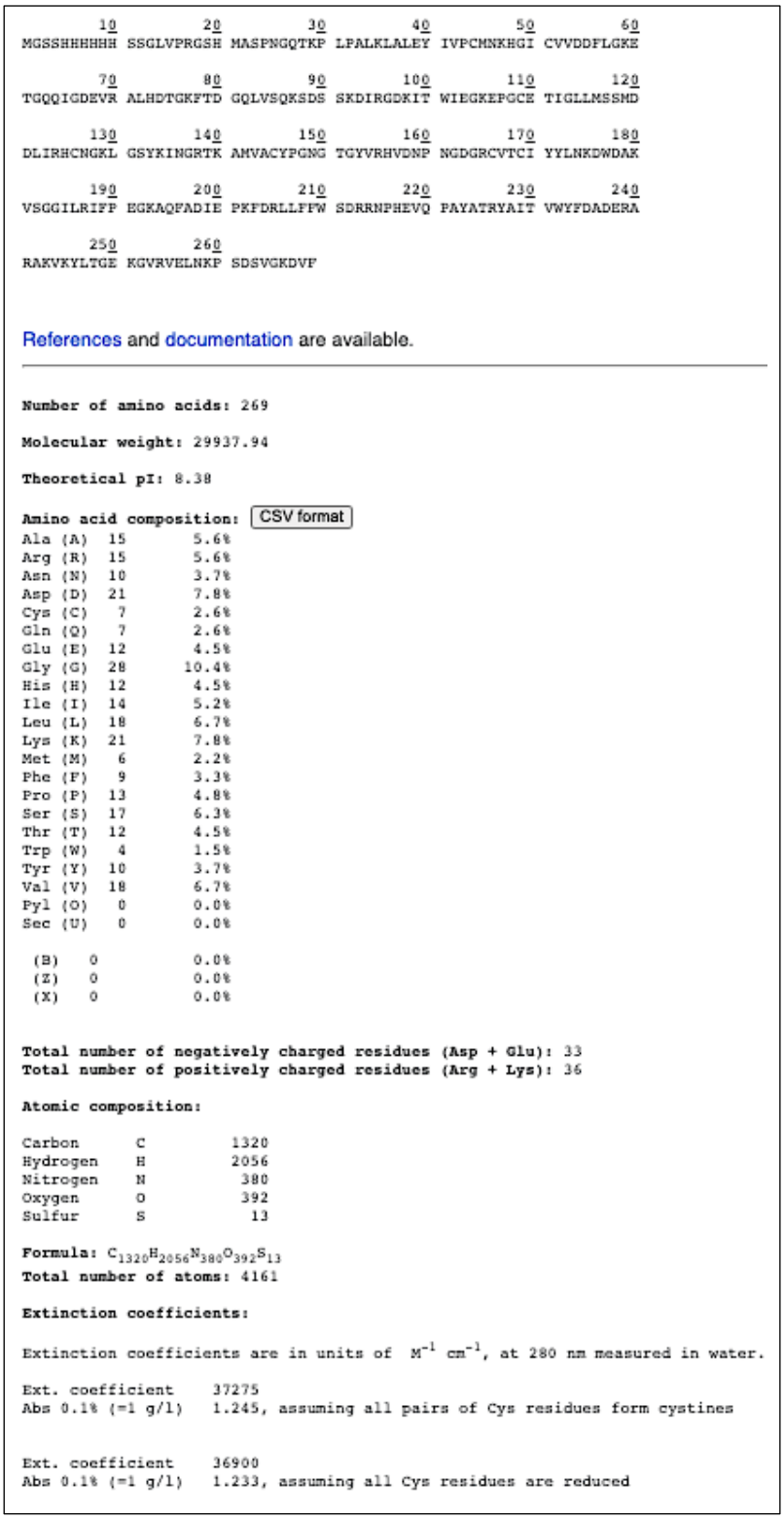
Formula: $C_{1150}H_{1790}N_{322}O_{343}S_{12}$
Total number of atoms: 3617

Extinction coefficients:

Extinction coefficients are in units of M^{-1} cm^{-1}, at 280 nm measured in water.

Ext. coefficient	37275	
Abs 0.1% (=1 g/l)	1.434,	assuming all pairs of Cys residues form cystines
Ext. coefficient	36900	
Abs 0.1% (=1 g/l)	1.419,	assuming all Cys residues are reduced

Figure AIII-3| Sequence and Amino Acid Composition of the PHD2$_{181-407}$ Construct Post Thrombin Cleavage of *N*-Terminal His$_6$-Tag. The data sheet was generated using the ProtParam tool (ExPASy, SIB). Abbreviations: Prolyl hydroxylase isoform 2 (PHD2), Hexa-histidine (His$_6$), Swiss Institute of Bioinformatics (SIB).



```
        10         20         30         40         50         60
MGSSHHHHHH SSGLVPRGSH MASPNGQTKP LPALKLALEY IVPCMNKHGI CVVDDFLGKE

        70         80         90        100        110        120
TGQQIGDEVR ALHDTGKFTD GQLVSQKSDS SKDIRGDKIT WIEGKEPGCE TIGLLMSSMD

       130        140        150        160        170        180
DLIRHCNGKL GSYKINGRTK AMVACYPGNG TGYVRHVDNP NGDGRCVTCI YYLNKDWDAK

       190        200        210        220        230        240
VSGGILRIFP EGKAQFADIE PKFDRLLFFW SDRRNPHEVQ PAYATRYAIT VWYFDADERA

       250        260
RAKVKYLTGE KGVRVELNKP SDSVGKDVF
```

References and documentation are available.

Number of amino acids: 269

Molecular weight: 29937.94

Theoretical pI: 8.38

Amino acid composition: CSV format

Ala (A)	15	5.6%
Arg (R)	15	5.6%
Asn (N)	10	3.7%
Asp (D)	21	7.8%
Cys (C)	7	2.6%
Gln (Q)	7	2.6%
Glu (E)	12	4.5%
Gly (G)	28	10.4%
His (H)	12	4.5%
Ile (I)	14	5.2%
Leu (L)	18	6.7%
Lys (K)	21	7.8%
Met (M)	6	2.2%
Phe (F)	9	3.3%
Pro (P)	13	4.8%
Ser (S)	17	6.3%
Thr (T)	12	4.5%
Trp (W)	4	1.5%
Tyr (Y)	10	3.7%
Val (V)	18	6.7%
Pyl (O)	0	0.0%
Sec (U)	0	0.0%
(B)	0	0.0%
(Z)	0	0.0%
(X)	0	0.0%

Total number of negatively charged residues (Asp + Glu): 33
Total number of positively charged residues (Arg + Lys): 36

Atomic composition:

Carbon	C	1320
Hydrogen	H	2056
Nitrogen	N	380
Oxygen	O	392
Sulfur	S	13

Formula: $C_{1320}H_{2056}N_{380}O_{392}S_{13}$
Total number of atoms: 4161

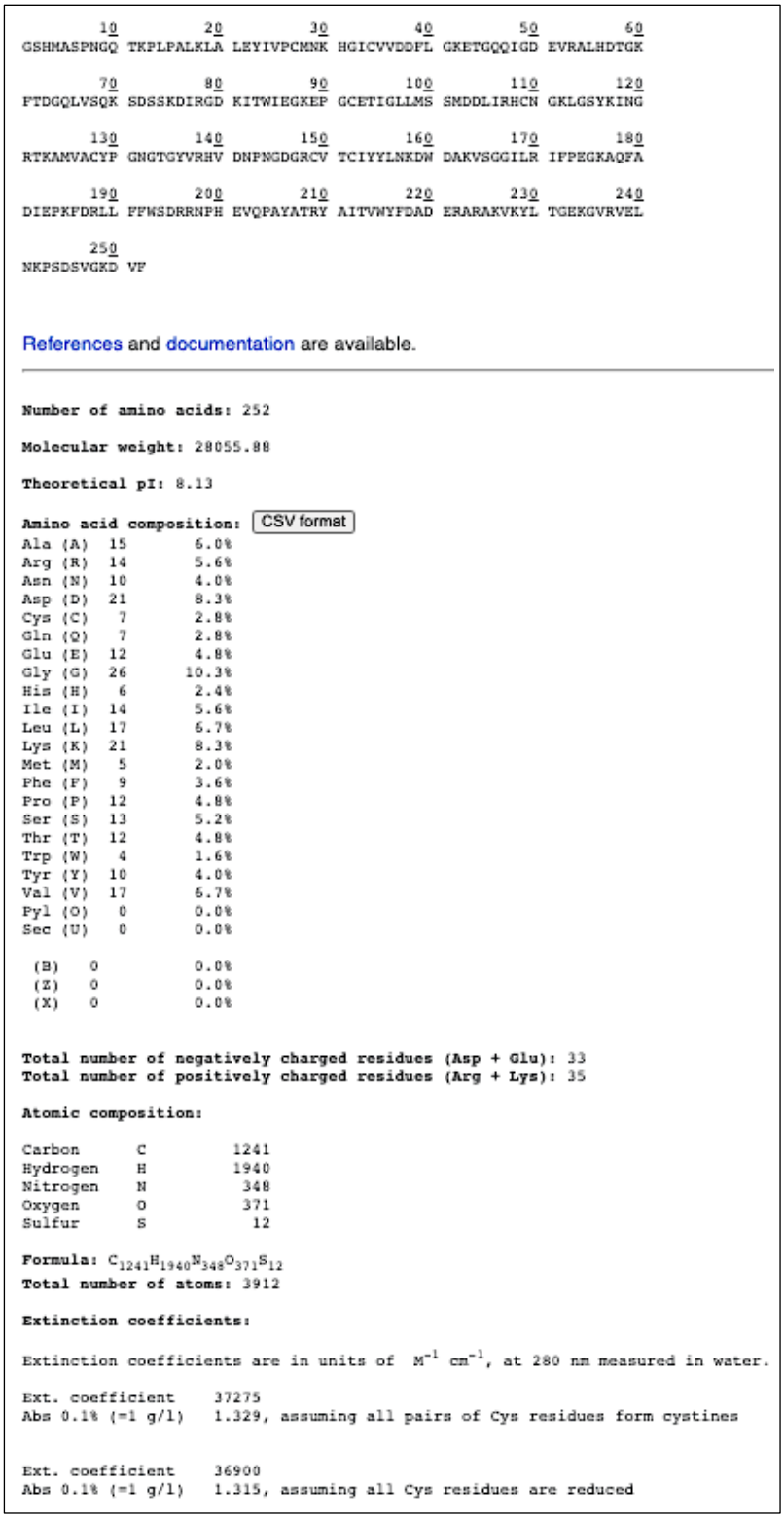
Extinction coefficients:

Extinction coefficients are in units of M^{-1} cm^{-1}, at 280 nm measured in water.

Ext. coefficient 37275
Abs 0.1% (=1 g/l) 1.245, assuming all pairs of Cys residues form cystines

Ext. coefficient 36900
Abs 0.1% (=1 g/l) 1.233, assuming all Cys residues are reduced

Figure AIII-4| Sequence and Amino Acid composition of the PHD2$_{181-426}$ Construct with an *N*-Terminal His$_6$ Affinity-Tag. The data sheet was generated using the ProtParam tool (ExPASy, SIB). Abbreviations: Prolyl hydroxylase isoform 2 (PHD2), Hexa-histidine (His$_6$), Swiss Institute of Bioinformatics (SIB).



```
        10         20         30         40         50         60
GSHMASPNGQ TKPLPALKLA LEYIVPCMNK HGICVVDDFL GKETGQQIGD EVRALHDTGK

        70         80         90        100        110        120
FTDGQLVSQK SDSSKDIRGD KITWIEGKEP GCETIGLLMS SMDDLIRHCN GKLGSYKING

       130        140        150        160        170        180
RTKAMVACYP GNGTGYVRHV DNPNGDGRCV TCIYYLNKDW DAKVSGGILR IFPEGKAQFA

       190        200        210        220        230        240
DIEPKFDRLL FFWSDRRNPH EVQPAYATRY AITVWYFDAD ERARAKVKYL TGEKGVRVEL

       250
NKPSDSVGKD VF
```

References and documentation are available.

Number of amino acids: 252

Molecular weight: 28055.88

Theoretical pI: 8.13

Amino acid composition: CSV format

Ala (A)	15	6.0%
Arg (R)	14	5.6%
Asn (N)	10	4.0%
Asp (D)	21	8.3%
Cys (C)	7	2.8%
Gln (Q)	7	2.8%
Glu (E)	12	4.8%
Gly (G)	26	10.3%
His (H)	6	2.4%
Ile (I)	14	5.6%
Leu (L)	17	6.7%
Lys (K)	21	8.3%
Met (M)	5	2.0%
Phe (F)	9	3.6%
Pro (P)	12	4.8%
Ser (S)	13	5.2%
Thr (T)	12	4.8%
Trp (W)	4	1.6%
Tyr (Y)	10	4.0%
Val (V)	17	6.7%
Pyl (O)	0	0.0%
Sec (U)	0	0.0%
(B)	0	0.0%
(Z)	0	0.0%
(X)	0	0.0%

Total number of negatively charged residues (Asp + Glu): 33
Total number of positively charged residues (Arg + Lys): 35

Atomic composition:

Carbon	C	1241
Hydrogen	H	1940
Nitrogen	N	348
Oxygen	O	371
Sulfur	S	12

Formula: $C_{1241}H_{1940}N_{348}O_{371}S_{12}$
Total number of atoms: 3912

Extinction coefficients:

Extinction coefficients are in units of M^{-1} cm^{-1}, at 280 nm measured in water.

Ext. coefficient	37275
Abs 0.1% (=1 g/l)	1.329, assuming all pairs of Cys residues form cystines
Ext. coefficient	36900
Abs 0.1% (=1 g/l)	1.315, assuming all Cys residues are reduced

Figure AIII-5| Sequence and Amino Acid Composition of the PHD2$_{181-426}$ Construct Post Thrombin Cleavage of *N*-Terminal His$_6$-Tag. The data sheet was generated using the ProtParam tool (ExPASy, SIB). Abbreviations: Prolyl hydroxylase isoform 2 (PHD2), Hexa-histidine (His$_6$), Swiss Institute of Bioinformatics (SIB).

```
Cuboid (Polyhedron) crystal of size [180, 60, 40] um [x, y, z] at a resolution of 2.00
microns per voxel edge.
Simple DDM.
Gaussian beam, 189.0x150.0 um with 63.00 by 50.00 FWHM (x by y) and 3.7e+11 photons
per second at 12.60 keV.
Wedge 1:
Collecting data for a total of 144.0s from phi = 0.0 to 360.0 deg.

Crystal coefficients calculated with RADDOSE-3D.
Photelectric Coefficient: 8.06e-04 /um.
Inelastic Coefficient: 2.02e-05 /um.
Elastic Coefficient: 2.55e-05 /um.
Attenuation Coefficient: 8.52e-04 /um.
Density: 1.25 g/ml.

Average Diffraction Weighted Dose         : 5.221407 MGy
Last Diffraction Weighted Dose            : 11.892850 MGy
Elastic Yield                             : 6.74e+10 photons
Diffraction Efficiency (Elastic Yield/DWD): 1.29e+10 photons/MGy
Average Dose (Whole Crystal)              : 7.968095 MGy
Average Dose (Exposed Region)             : 7.968095 MGy
Max Dose                                  : 18.556643 MGy
Average Dose (95.0 % of total absorbed energy threshold (3.74 MGy)): 8.765912 MGy
Dose Contrast (Max/Threshold Av.)         : 2.12
Used Volume                               : 100.0%
Absorbed Energy (this Wedge)              : 4.40e-03 J.
Dose Inefficiency (Max Dose/mJ Absorbed)  : 4.2 1/g
Dose Inefficiency PE (Max Dose/mJ Deposited): 4.3 1/g
Final Dose Histogram:
Bin  1,  0.0 to  0.1 MGy:  0.0 %
Bin  2,  0.1 to  3.4 MGy: 10.7 %
Bin  3,  3.4 to  6.7 MGy: 37.2 %
Bin  4,  6.7 to 10.1 MGy: 23.6 %
Bin  5, 10.1 to 13.4 MGy: 14.9 %
Bin  6, 13.4 to 16.7 MGy: 10.8 %
Bin  7, 16.7 to 20.0 MGy:  2.9 %
Bin  8, 20.0 to 23.4 MGy:  0.0 %
Bin  9, 23.4 to 26.7 MGy:  0.0 %
Bin 10, 26.7 to 30.0 MGy:  0.0 %
Bin 11, 30.0 MGy upwards:  0.0 %
```

Figure AIII-6|RADDOSE-3D[5,6] Calculation of the X-ray dosage of PHD2$_{181-407}$.Mn.Molidustat crystal (20, *Xtal-R*) Collected at the Diamond-I04 Beamline. The diffraction data collection parameters (144s total exposure, 0.9795 Å (λ), 3.65e+11 flux (ph/s), 12.6 keV, Gaussian beam with 63 μm x 50 μm size (FWHM), and 360 degrees 0.10° oscillation) were used to calculate the synchrotron light source X-ray radiation dose of the crystal with RADDOSE-3D online interface.

```
Cuboid (Polyhedron) crystal of size [180, 60, 40] um [x, y, z] at a resolution of
2.00 microns per voxel edge.
Simple DDM.
Gaussian beam, with 216.00 by 142.00 FWHM (x by y) and 4.0e+09 photons per second at
8.05 keV.
Wedge 1:
Collecting data for a total of 5400.0s from phi = 0.0 to 180.0 deg.

Crystal coefficients calculated with RADDOSE-3D.
Photelectric Coefficient: 2.93e-03 /um.
Inelastic Coefficient: 1.68e-05 /um.
Elastic Coefficient: 4.50e-05 /um.
Attenuation Coefficient: 3.00e-03 /um.
Density: 1.25 g/ml.

Average Diffraction Weighted Dose         : 0.754882 MGy
Last Diffraction Weighted Dose            : 1.509165 MGy
Elastic Yield                             : 9.66e+09 photons
Diffraction Efficiency (Elastic Yield/DWD): 1.28e+10 photons/MGy
Average Dose (Whole Crystal)              : 1.502874 MGy
Average Dose (Exposed Region)             : 1.502874 MGy
Max Dose                                  : 1.751784 MGy
Average Dose (95.0 % of total absorbed energy threshold (1.30 MGy)): 1.519041 MGy
Dose Contrast (Max/Threshold Av.)         : 1.15
Used Volume                               : 100.0%
Absorbed Energy (this Wedge)              : 8.23e-04 J.
Dose Inefficiency (Max Dose/mJ Absorbed)  : 2.1 1/g
Dose Inefficiency PE (Max Dose/mJ Deposited): 2.2 1/g
Final Dose Histogram:
Bin  1,  0.0 to  0.1 MGy:  0.0 %
Bin  2,  0.1 to  3.4 MGy: 100.0 %
Bin  3,  3.4 to  6.7 MGy:  0.0 %
Bin  4,  6.7 to 10.1 MGy:  0.0 %
Bin  5, 10.1 to 13.4 MGy:  0.0 %
Bin  6, 13.4 to 16.7 MGy:  0.0 %
Bin  7, 16.7 to 20.0 MGy:  0.0 %
Bin  8, 20.0 to 23.4 MGy:  0.0 %
Bin  9, 23.4 to 26.7 MGy:  0.0 %
Bin 10, 26.7 to 30.0 MGy:  0.0 %
Bin 11, 30.0 MGy upwards:  0.0 %
```

Figure AIII-7|RADDOSE-3D[5,6] Calculation of the X-ray dosage of PHD2$_{181-407}$.Mn.Molidustat crystal (20, *Xtal-R*) Collected on an In-House FR-E+ SuperBright Rotating Anode Source. The diffraction data collection parameters (5,400s total exposure, 1.54 Å (λ), 4.00e+9 flux (ph/s), 8.05 keV, Gaussian beam with 216 μm x 142 μm size (FWHM), and 180 degrees 1° oscillation) were used to calculate the in-house source X-ray radiation dose of the crystal with RADDOSE-3D online interface.

Appendices I-III References:

(1) Chowdhury, R.; Abboud, M. I.; Mcallister, T. E.; Banerji, B.; Bhushan, B.; Sorensen, J. L.; Kawamura, A.; Schofield, C. J. Use of Cyclic Peptides to Induce Crystallization: Case Study with Prolyl Hydroxylase Domain 2. *Scientific Reports* **2020**, *10* (21964). https://doi.org/10.1038/s41598-020-76307-8.

(2) Chowdhury, R.; Candela-Lena, J. I.; Chan, M. C.; Greenald, D. J.; Yeoh, K. K.; Tian, Y.-M.; McDonough, M. A.; Tumber, A.; Rose, N. R.; Conejo-Garcia, A.; Demetriades, M.; Mathavan, S.; Kawamura, A.; Lee, M. K.; van Eeden, F.; Pugh, C. W.; Ratcliffe, P. J.; Schofield, C. J. Selective Small Molecule Probes for the Hypoxia Inducible Factor (HIF) Prolyl Hydroxylases. *ACS Chemical Biology* **2013**, *8* (7), 1488–1496. https://doi.org/10.1021/cb400088q.

(3) Yeh, T.-L.; Leissing, T. M.; Abboud, M. I.; Thinnes, C. C.; Atasoylu, O.; Holt-Martyn, J. P.; Zhang, D.; Tumber, A.; Lippl, K.; Lohans, C. T.; Leung, I. K. H.; Morcrette, H.; Clifton, I. J.; Claridge, T. D. W.; Kawamura, A.; Flashman, E.; Lu, X.; Ratcliffe, P. J.; Chowdhury, R.; Pugh, C. W.; Schofield, C. J. Molecular and Cellular Mechanisms of HIF Prolyl Hydroxylase Inhibitors in Clinical Trials. *Chemical Science* **2017**, *8* (11), 7651–7668. https://doi.org/10.1039/C7SC02103H.

(4) Figg Jr, W. D.; McDonough, M. A.; Chowdhury, R.; Nakashima, Y.; Zhang, Z.; Holt-Martyn, J. P.; Krajnc, A.; Schofield, C. J. Structural Basis of Prolyl Hydroxylase Domain Inhibition by Molidustat. *ChemMedChem* **2021**, *16* (13), 2082–2088. https://doi.org/https://doi.org/10.1002/cmdc.202100133.

(5) Zeldin, O. B.; Gerstel, M.; Garman, E. F. RADDOSE-3D: Time- and Space-Resolved Modelling of Dose in Macromolecular Crystallography. *Journal of Applied Crystallography* **2013**, *46* (4), 1225–1230. https://doi.org/10.1107/S0021889813011461.

(6) Bury, C. S.; Brooks-Bartlett, J. C.; Walsh, S. P.; Garman, E. F. Estimate Your Dose: RADDOSE-3D. *Protein Science* **2018**, *27* (1), 217–228. https://doi.org/https://doi.org/10.1002/pro.3302.

Name: William Douglas Figg, Jr. **Candidate number: 1122055**
College: St. Hugh's College **Supervisor: Prof. Christopher J. Schofield**

Title of Thesis: Structural and Mechanistic Studies on PHD2 and the Discovery of Potential Inhibitors

Word count: 81,498

I have read and understood the University's disciplinary regulations concerning conduct in examinations and, in particular, the regulations on plagiarism (*The University Student Handbook* Section 8.7; available at https://www.ox.ac.uk/students/academic/student-handbook). ☑

I have read and understood the Education Committee's information and guidance on academic good practice and plagiarism at https://www.ox.ac.uk/students/academic/guidance/skills?wssl=1. ☑

The thesis I am submitting is entirely my own work except where otherwise indicated. ☑

It has not been submitted, either partially or in full, either for this Honour School or qualification or for another Honour School or qualification of this University (except where the Special Regulations for the subject permit this), or for a qualification at any other institution. ☑

I have clearly indicated the presence of all material I have quoted from other sources, including any diagrams, charts, tables or graphs. ☑

I have clearly indicated the presence of all paraphrased material with appropriate references. ☑

I have acknowledged appropriately any assistance I have received in addition to that provided by my [tutor/supervisor/adviser]. ☑

I have not copied from the work of any other candidate. ☑

I have not used the services of any agency providing specimen, model or ghost-written work in the preparation of this thesis. (See also section 2.4 of Statute XI on University Discipline under which members of the University are prohibited from providing material of this nature for candidates in examinations at this University or elsewhere: http://www.admin.ox.ac.uk/statutes/352-051a.shtml). ☑

I agree to retain an electronic copy of this work until the publication of my final examination result, except where submission in hand-written format is permitted. ☑

I agree to make any such electronic copy available to the examiners should it be necessary to confirm my word count or to check for plagiarism. ☑



Candidate's signature: …… Date: 12 October 2021 ……..